



**National Technical University of Athens**  
**School of Mechanical Engineering**  
**Department of Fluids**  
**Laboratory of Innovative Environmental Technologies**

**Development and optimization of a concentrating  
photovoltaic/thermal cogeneration system**

Doctoral Dissertation

IOANNIS K. KARATHANASSIS  
Mechanical Engineer, M.Sc.

**PhD Supervisors:**

G. Bergeles, NTUA Emeritus Professor  
E. Kakaras, NTUA Professor  
E. Papanicolaou, NCSR “Demokritos”  
Researcher A’

**Examination Committee:**

G. Bergeles, NTUA Emeritus Professor  
E. Kakaras, NTUA Professor  
D. Papantonis, NTUA Professor  
S. Tsangaris, NTUA Professor  
D. Bouris, NTUA Assistant Professor  
V. Belessiotis, NCSR “Demokritos”  
Researcher A’  
E. Papanicolaou, NCSR “Demokritos”  
Researcher A’

**Athens, April 2015**

Approval of the doctoral dissertation from the School of Mechanical Engineering of National Technical University of Athens (NTUA) does not imply acceptance of the opinions of the author (Law 5343/1932, Article 202).

The present work was financially supported by the Special Account for Scientific Research of the National Technical University of Athens.



The investigated CPVT system.

**“How often have I said to you that when you have eliminated the impossible, whatever remains, *however improbable*, must be the truth?”**

**- Sherlock Holmes**



# Summary

The term “photovoltaic/thermal cogeneration systems” refers to integrated configurations that can simultaneously produce electrical and thermal energy, using the solar irradiation. The scope of the present doctoral dissertation is the theoretical and experimental evaluation of a linear Concentrating Photovoltaic Thermal (CPVT) system. The system comprises three distinct constituents, namely the optical device to concentrate solar irradiation, the solar-cell module and the active cooling system. Concentrated solar irradiation is incident on the active surface of the solar-cell module at the backside of which, a suitable cooling device (heat sink) is thermally bonded to extract excess heat. The most significant parameters that affect the operation of a CPVT system are the intensity of the solar irradiation and the temperature of the solar cells. It is consequently of vital importance that an appropriate active cooling system be designed such as to allow the solar cells to operate under high irradiation intensity, but within a moderate temperature range.

Special attention was given to the selection and design of an appropriate cooling device. At a first stage, several heat-sink layouts were evaluated using three-dimensional, computational fluid dynamics and heat transfer models in terms of, among others, thermal resistance, temperature uniformity of the heated surface and cooling fluid pressure drop. The configurations taken into consideration can be divided into two general groups based on the cross-section of the ducts employed for the flow of the cooling fluid (water): configurations with orthogonal and circular ducts, respectively. The configurations with orthogonal ducts include heat sinks with channel width in the micro-(microchannels) and the mini-scale (minichannels), respectively. Besides, the evaluated configurations with circular ducts comprise tube-on-plate heat sinks with bent tubing in a serpentine layout embedded within a solid plate.

The most promising heat-sink designs were subsequently optimized using a novel, multi-objective optimization procedure which allows the determination of the optimal heat-sink geometrical parameters through the use of a genetic algorithm. In addition, a manifold system suitable for the distribution and collection of the working fluid from the cooling device was also designed and manufactured. The optimal devices were manufactured of aluminum bars and were experimentally evaluated. The performance evaluation of the manufactured heat sinks comprised the measurement of the induced fluid pressure drop (hydrodynamic performance) and the substrate temperature for constant heat-flux heating and negligible heat losses.

In reference to the development of the integrated CPVT system, the main focus initially was on the procurement of appropriate materials and the manufacturing of the custom-made components required for the development of the prototype system. More specifically, high-reflectivity anodized aluminum sheets and custom-made concentrating solar-cell modules were assembled. Special attention was given to the procurement and evaluation of a suitable thermally- conductive adhesive for bonding the heat sink onto the solar cells module, as a thermal bond of high quality has a beneficial impact on both the system performance and reliability. The manufacturing drawings for the concentrating system were created using a CAD software (Dassault Solidworks) and subsequently the metallic components comprising the system were manufactured. The optical quality of the parabolic trough was experimentally evaluated with the use of an appropriate measuring device that bears a grid of sensors (photodiodes), so that the irradiation distribution on the receiver surface and the achieved

concentration ratio can be determined. Besides, the main factors that have a significant effect on the trough optical quality were designated using a ray-tracing software (Lambda TracePro).

An experimental rig was developed for the evaluation of the integrated CPVT system. The rig comprises a closed hydraulic circuit, which is connected with the system under evaluation and allows the adjustment of the working fluid volumetric flow rate and inlet temperature. Besides, all the physical quantities necessary for the evaluation of the system performance (environmental conditions, fluid flow rate, temperatures, electricity voltage and current) are measured through instruments. The experimental evaluation led to the determination of the solar-cell modules voltage-current curves and temperature factor, as well as the electric and thermal efficiency of the system. In addition, the main thermal losses mechanisms were identified and the CPVT system thermal performance was compared to that of flat-plate thermal collectors, commercially available in the Greek market.

Finally, a computational code was developed in FORTRAN for the dynamic simulation of the CPVT system long-term performance. A dynamic theoretical model was formulated that allows the prediction of the system energetic and exergetic efficiency, as well as its output in a daily, monthly or annual basis. The CPVT system characteristics are taken into account by the model in a parametric manner, which makes possible the determination of the system optimal operating parameters. In addition, the constituents characteristics that have the most significant impact on the system exergetic performance are highlighted.

The complete design, manufacturing and evaluation procedure of the integrated CPVT system and the system sub-components clearly elucidated the advantages of concentrating photovoltaic/thermal applications. Furthermore, the know-how gained allows the identification and effective treatment of the technical aspects associated with such systems. Suggestions to further enhance the efficient operation of novel CPVT applications are given as recommendations for future research.

# Περίληψη

Με τον όρο “φωτοβολταϊκά/θερμικά συστήματα” αναφερόμαστε σε ολοκληρωμένες διατάξεις που έχουν τη δυνατότητα ταυτόχρονης παραγωγής ηλεκτρικής και θερμικής ενέργειας, χρησιμοποιώντας την ηλιακή ακτινοβολία. Στόχος της παρούσας διδακτορικής διατριβής είναι η θεωρητική και πειραματική διερεύνηση ενός πρωτότυπου συγκεντρωτικού φωτοβολταϊκού/θερμικού συστήματος γραμμικής εστίασης. Το σύστημα αποτελείται από τρεις διακριτές συνιστώσες: τη διάταξη συγκέντρωσης της ακτινοβολίας, τη συστοιχία ηλιακών κυψελών και το ενεργητικό σύστημα ψύξης (ψύκτρα). Η ηλιακή ακτινοβολία, με τη χρήση παραβολικού ανακλαστήρα, συγκεντρώνεται στην επιφάνεια της συστοιχίας κυψελών, στο πίσω μέρος της οποίας είναι προσκολλημένη κατάλληλη ψύκτρα (heat sink) η οποία απάγει την περίσσεια θερμικής ενέργειας. Οι κυριότερες παράμετροι που επηρεάζουν τη λειτουργία ενός συγκεντρωτικού φωτοβολταϊκού/θερμικού συστήματος είναι η ένταση της προσπίπτουσας ηλιακής ακτινοβολίας και η θερμοκρασία των ηλιακών κυψελών. Συνεπώς, κατά τη σχεδίαση ενός συστήματος θα πρέπει να ληφθεί μέριμνα για κατάλληλο σύστημα ψύξης, ώστε να είναι δυνατή η λειτουργία των κυψελών υπό υψηλή συγκέντρωση ακτινοβολίας, αλλά σε ελεγχόμενο θερμοκρασιακό εύρος.

Ιδιαίτερη έμφαση δόθηκε στην επιλογή και σχεδίαση της πλέον κατάλληλης διάταξης απαγωγής θερμότητας. Αρχικά, αξιολογήθηκαν, με χρήση μοντέλων υπολογιστικής ρευστοδυναμικής, διάφοροι τύποι διατάξεων, έχοντας ως κριτήρια, μεταξύ άλλων, τη θερμική αντίσταση που εμφανίζουν, τη θερμοκρασιακή ομοιομορφία στη θερμαινόμενη επιφάνεια και την πτώση πίεσης που προκαλούν στο εργαζόμενο μέσο. Οι διατάξεις που ελήφθησαν υπ’ όψιν μπορούν να χωριστούν σε δύο ευρύτερες κατηγορίες ανάλογα με τη διατομή των αγωγών που χρησιμοποιούνται για τη διέλευση του ψυκτικού μέσου (νερό): διατάξεις με αγωγούς ορθογωνικής και κυκλικής διατομής, αντίστοιχα. Στις διατάξεις ορθογωνικής διατομής που διερευνήθηκαν περιλαμβάνονται ψύκτρες που χρησιμοποιούν κανάλια με πλάτος στην περιοχή της μικρο-κλίμακας (microchannels) και της μίνι-κλίμακας (minichannels). Αντιστοίχως, οι διατάξεις κυκλικής διατομής που διερευνήθηκαν περιλαμβάνουν ψύκτρες τύπου «σωλήνα-σε-πλάκα» (tube-on-plate) με σωλήνωση σε μαιανδρική διαμόρφωση βυθισμένη εντός πλάκας με αυλακώσεις.

Ακολούθησε η διαδικασία βελτιστοποίησης των πιο αποδοτικών ψυκτικών διατάξεων, κατά την οποία αναπτύχθηκε ολοκληρωμένη μεθοδολογία πολύ-κριτηριακής (multi-objective) βελτιστοποίησης η οποία, με δεδομένη τη συνολική επιφάνεια των διατάξεων και μέσω της χρήσης γενετικού αλγορίθμου, οδήγησε στον προσδιορισμό των βέλτιστων γεωμετρικών παραμέτρων. Επιπροσθέτως, σχεδιάστηκε το σύστημα προσαγωγής-απαγωγής του ψυκτικού ρευστού. Οι βελτιστοποιημένες ψύκτρες κατασκευάστηκαν από τεμάχια αλουμινίου και αξιολογήθηκαν πειραματικά. Η αξιολόγηση περιλάμβανε τη μέτρηση της πτώσης πίεσης του ψυκτικού διαμέσου αυτών (υδροδυναμική απόδοση) και τη μέτρηση της θερμοκρασίας μετάλλου για θέρμανση μέσω σταθερής θερμοροής (θερμική απόδοση) σε συνθήκες αμελητέων θερμικών απωλειών.

Αναφορικά με την ανάπτυξη του ολοκληρωμένου συγκεντρωτικού φωτοβολταϊκού/θερμικού συστήματος πραγματικής κλίμακας, σε πρώτο στάδιο διενεργήθηκε εμπειρισματομένη έρευνα αγοράς ώστε να εξασφαλισθεί η προμήθεια των κατάλληλων υλικών και η δυνατότητα κατασκευής των μεταλλικών συνιστωσών που απαρτίζουν το συγκεντρωτικό σύστημα. Πιο συγκεκριμένα εξασφαλίστηκε η προμήθεια φύλλων ανοδιωμένου αλουμινίου υψηλής ανακλαστικότητας και συστοιχιών (panels) ηλιακών κυψελών ειδικής σχεδίασης. Ιδιαίτερη έμφαση δόθηκε στην προμήθεια

και αξιολόγηση του κατάλληλου υλικού για την προσκόλληση της ψύκτρας στη συστοιχία κυψελών, καθώς η επιτυχής θερμική σύζευξη έχει ευεργετική επίδραση στην απόδοση και την αξιοπιστία του συστήματος. Με τη χρήση λογισμικού τρισδιάστατης σχεδίασης (Dassault Solidworks) αναπτύχθηκαν τα μηχανολογικά σχέδια του συγκεντρωτικού συστήματος και στη συνέχεια κατασκευάστηκαν όλες οι μεταλλικές συνιστώσες που απαρτίζουν το σύστημα. Η οπτική ποιότητα του παραβολικού πλαισίου αξιολογήθηκε πειραματικά με χρήση κατάλληλης διάταξης, η οποία φέρει πλέγμα αισθητηρίων (φωτοδιόδων), ώστε να προσδιοριστεί η κατανομή της προσπίπτουσας ακτινοβολίας στην επιφάνεια του απορροφητή καθώς και ο επιτυγχανόμενος δείκτης συγκέντρωσης. Επιπλέον, με τη χρήση κατάλληλου λογισμικού «ιχνηλασίας ακτίνων» (Lambda TracePro), προσδιορίστηκαν οι βασικοί παράγοντες που επηρεάζουν την οπτική ποιότητα του παραβολικού πλαισίου.

Για την πειραματική αξιολόγηση του ολοκληρωμένου συστήματος αναπτύχθηκε κατάλληλη πειραματική διάταξη. Η διάταξη περιλαμβάνει κλειστό κύκλωμα νερού, το οποίο συνδέεται υδραυλικά με το υπό αξιολόγηση σύστημα και επιτρέπει την αξιολόγηση λειτουργίας του συστήματος για διάφορες τιμές της παροχής και της θερμοκρασίας εισόδου του ψυκτικού ρευστού. Επιπροσθέτως, όλα τα απαραίτητα για την αξιολόγηση του συστήματος φυσικά μεγέθη (περιβαλλοντικές συνθήκες, παροχή ρευστού, θερμοκρασίες, τάση και ένταση ρεύματος) μετρώνται μέσω διακριβωμένων μετρητικών οργάνων. Από την πειραματική αξιολόγηση προέκυψαν οι καμπύλες τάσης-έντασης και ο ρυθμός μείωσης της απόδοσης των συστοιχιών ηλιακών κυψελών ως συνάρτηση της θερμοκρασίας λειτουργίας, καθώς και ο ηλεκτρικός και θερμικός βαθμός απόδοσης του συστήματος για διαφορετικές παραμέτρους λειτουργίας. Επιπροσθέτως, προσδιορίστηκαν οι βασικοί μηχανισμοί θερμικών απωλειών από τον απορροφητή του συστήματος και η θερμική απόδοση του συστήματος συγκρίθηκε με επίπεδους ηλιακούς θερμικούς συλλέκτες που είναι εμπορικά διαθέσιμοι στην ελληνική αγορά.

Τέλος, για τη δυναμική προσομοίωση της λειτουργίας του ολοκληρωμένου φωτοβολταϊκού/θερμικού συστήματος αναπτύχθηκε υπολογιστικός κώδικας σε γλώσσα FORTRAN, ο οποίος έχει τη δυνατότητα πρόβλεψης της απόδοσης (ηλεκτρικής-θερμικής και εξεργειακής) του συστήματος. Το υπολογιστικό μοντέλο που αναπτύχθηκε είναι δυναμικό και επιτρέπει την πρόβλεψη της παραγόμενης από το σύστημα ισχύος σε ωριαία, μηνιαία και ετήσια βάση. Το μοντέλο λαμβάνει υπ' όψιν τα χαρακτηριστικά του συστήματος με παραμετρικό τρόπο, ώστε να είναι δυνατός ο καθορισμός των βέλτιστων παραμέτρων λειτουργίας και ο προσδιορισμός των συνιστωσών του συστήματος που έχουν τη σημαντικότερη επίδραση στη εξεργειακή απόδοση.

Η ολοκληρωμένη διαδικασία σχεδιασμού, κατασκευής και αξιολόγησης τόσο του ολοκληρωμένου συστήματος, όσο και των επί μέρους υπο-συστημάτων κατέδειξε με σαφήνεια τα πλεονεκτήματα της τεχνολογίας των συγκεντρωτικών φωτοβολταϊκών/θερμικών συστημάτων. Επιπλέον, η τεχνογνωσία που αποκτήθηκε επιτρέπει την αναγνώριση και αντιμετώπιση όλων των τεχνικών προκλήσεων που σχετίζονται με τέτοιου είδους συστήματα. Προτάσεις ώστε να ενισχυθεί περαιτέρω η αποδοτική λειτουργία πρωτότυπων φωτοβολταϊκών/θερμικών συστημάτων δίνονται ως θέματα για μελλοντική έρευνα.

# Acknowledgements

The present doctoral dissertation was assigned by the Department of Fluids of the National Technical University in collaboration with the Solar and other Energy Systems Laboratory of the National Center for Scientific Research “Demokritos”. First of all, I would like to thank Professor G. Bergeles, for the trust shown in me, his solid guidance through the whole work, as well as his commitment to the cause of this work. I would also like to thank Dr. E. Papanicolaou for his valuable assistance in various aspects I had to deal with in the course of the study and his kind spirit to discuss all the arising matters regarding the dissertation. Furthermore, a particular thank is addressed to Professor E. Kakaras for his willingness to participate in the committee of supervisors and his involvement during the execution of the thesis.

The experimental rigs required for the research activities of the dissertation were developed using the infrastructure of the Solar and other Energy Systems Laboratory. Cordial thanks are extended to the head of the laboratory Dr. V. Belessiotis for his useful advice throughout the preparation of the dissertation and, in addition, for providing the financial resources necessary for the experimental and other activities in the framework of the dissertation. Special thanks are addressed to Dr. M. Mathioulakis for his willingness to answer queries on instrumentation and experimental procedures. The simulations were performed using the NTUA Cloud Computing infrastructure. The staff of the computer center was eager to provide their technical support and is gratefully acknowledged for their smooth collaboration. Finally, I would like to thank my colleagues at the Solar and other Energy Systems Laboratory of NCSR “Demokritos” and especially G. Panaras, S. Kaloudis and K. Arvanitis for offering great work environment.

A lot of people were involved in the manufacturing of the CPVT system sub-components. In particular, the solar concentrator was manufactured by *MEVACO SA* and the heat sinks by *Petrekas Ltd*. I would like to thank Mr. E. Chaviaras and Mr. M. Toupalis of *MEVACO SA* and Mr. M. Petrekas of *Petrekas Ltd* for the excellent collaboration we had during the sub-component manufacturing.



## Nomenclature

a	fin thickness to channel width ratio
A	area, m <sup>2</sup>
Ar	Archimedes (or Richardson) number $Ar = \frac{Gr}{Re^2}$
Be	Bejan number $Be = \frac{\dot{S}'_{gen,\Delta T}}{\dot{S}'_{gen}}$
C <sub>p</sub>	pressure coefficient
C <sub>p</sub>	specific heat, J/kgK
CR	concentration ratio
De	Dean number $De = Re\sqrt{\delta}$
D	tube diameter, m
D <sub>h</sub>	channel hydraulic diameter $D_h = \frac{2W_{ch}H_{ch}}{(W_{ch} + H_{ch})}$ , m
$\dot{E}_x$	rate of exergy, W
F	focal length, m
f	friction factor $f = \Delta p D_i / (2\rho L \bar{w}^2)$
g	gravity acceleration, m/s <sup>2</sup>
G	solar radiation flux, W/m <sup>2</sup>
Gr	Graetz number $Gz = \frac{\pi Re Pr}{2\delta\phi}$
H	height, m
h	heat transfer coefficient $h = \frac{-k(\partial T / \partial n)_w}{(T_w - T_{f,m})}$
I	electric current, A
k	Boltzmann constant, J/K
k	thermal conductivity, W/mK
k	turbulent kinetic energy $k = \frac{1}{2}(\overline{(u')^2} + \overline{(v')^2} + \overline{(w')^2})$ , m <sup>2</sup> /s <sup>2</sup>
k*	non-dimensional turbulent kinetic energy $k^* = k/k_{FD}$
K	incidence angle modifier $K(\theta_{long}) = \frac{\eta_0 _{\theta_{long}=0}}{\eta_0 _{\theta_{long}}}$
L	length, m

M	mass, kg
M	Maranzana number $M = \frac{k_s t_s / L_{hs}}{\rho c_p H_{ch} \bar{w}}$
$N_s$	Entropy generation number $N_s = \frac{T_a \dot{S}_{gen}}{A_a G_b}$
m	fin parameter $m = \sqrt{\frac{2h}{k_s W_w}}$
$\dot{m}$	mass flow rate, kg/s
n	solar cell ideality factor
Nu	Nusselt number $Nu = \frac{h \cdot D}{k_f}$
p	pressure, Pa
PI	performance index $PI = \frac{\overline{Nu_{ove}}}{f}$
P	power, W
Pr	Prandtl number $Pr = \frac{\nu}{\alpha}$
P	perimeter, m
q	electron charge, C
q'	heat rate per unit length, W/m
q''	heat flux, W/m <sup>2</sup>
R	tube radius, m
Ra	Rayleigh number $Ra = GrPr$
$R_c$	tube radius of curvature, m
Re	Reynolds number for internal flow $Re = \frac{\bar{w}D}{\nu}$
$Re_L$	Reynolds number for external flow $Re = \frac{\bar{w}L}{\nu}$
R	electrical resistance, $\Omega$
$R_f$	fouling resistance, m <sup>2</sup> K/W
$R_{th}$	thermal resistance, K/W
s	unwound coordinate, m

$S^*$	non-dimensional unwound coordinate $S^* = \frac{s}{D_i}$
$\dot{S}_{gen}$	entropy generation rate, W/mK
St	Stanton number $St = \frac{Nu}{Re Pr}$
t	thickness, m
t	time
T	temperature, K
$T^*$	non-dimensional temperature $T^* = \frac{T - T_i}{q'' D / k_f}$
$t_s$	solid substrate thickness, m
U	value uncertainty
$U_0$	thermal losses coefficient
$\dot{V}$	volumetric flow rate, m <sup>3</sup> /s
V	electric voltage, V
W	width, m
u,v,w	velocity constituents, m/s
$w^*$	non-dimensional axial velocity $w^* = \frac{w}{\bar{w}}$
x,y,z	streamwise, vertical and spanwise coordinate respectively, m
$X^*$	non-dimensional span-wise coordinate
$Y^*$	non-dimensional height-wise coordinate
$Z^*$	non-dimensional streamwise coordinate

### Greek symbols

$\alpha$	absorptance
$\beta$	cell temperature coefficient
$\beta$	thermal expansion coefficient, K <sup>-1</sup>
$\gamma$	receiver intercept factor
$\delta$	radius ratio $\delta = \frac{R}{R_c}$
$\varepsilon$	emittance
$\eta_{el}$	electrical efficiency
$\eta_{fin}$	fin efficiency
$\eta_0$	optical efficiency
$\eta_{th}$	thermal efficiency
$\eta_{II}$	exergetic efficiency
$\mu$	dynamic viscosity, Pa·s
$\mu_t$	turbulent viscosity, Pa·s
$\nu$	kinematic viscosity, m <sup>2</sup> /s
$\rho$	density, kg/m <sup>3</sup>
$\rho$	reflectivity
$\sigma$	Stefan-Boltzmann constant, W/m <sup>2</sup> K <sup>4</sup>
$\tau$	transmittance
$\tau_w$	wall shear stress $\tau_w = \mu \left. \frac{\partial u_{\tan g}}{\partial y} \right _{y=0}$ , Pa
$\omega$	turbulent frequency

$\omega$	vorticity $\vec{\omega} = \vec{\nabla} \times \vec{U}$ , $s^{-1}$
$\omega^*$	non-dimensional vorticity $\omega^* = \omega D / \bar{w}$

### *Abbreviations*

a	aperture, ambient
adh	adhesive
al	aluminum
ave	average
b	beam
BR	blowing ratio
c	contraction, cold
cal	caloric
ch	channel
cond	conductive
conv	convective
cs	cross section
d	diffuse
d	developing
dest	destroyed
dt	time step
e	expansion
el	electric
eff	effective
ext	external
f	fluid
FC	forced convection
FD	fully developed
gen	generated
gl	glass
h	high fin density, hot
hs	heat sink
hy	hydrodynamic
HTR	heat transfer
gen	generation
i	number of section
i	inlet, inner
inc	incident
init	initial
ins	insulation
int	interface
l	low fin density
lam	laminar
max	maximum
MC	mixed convection
MPP	maximum power point
NC	natural convection
o	outlet, outer
OC	open circuit
opt	optical
ove	overall
pl	plate
proj	projection

PV	photovoltaic
rec	receiver
ref	reference
refl	reflector
res	residual
s	series, section
s	solid, substrate
SC	short circuit
scat	scattered
sh	shunt
tang	tangential
TC	thermocouple
th	thermal
turb	turbulent
tot	total
w	wall
$\mu$	microchannel



# Table of Contents

<b>1. Introduction .....</b>	<b>.....</b>
1.1 Energy today .....	1.1
1.2 Market penetration of solar technologies.....	1.2
1.3 Objectives of the thesis .....	1.5
1.4 Thesis structure .....	1.6
<b>2. The Basics on Photovoltaic Engineering .....</b>	<b>.....</b>
2.1 Solar cells-Current state of technology.....	2.1
2.2 Principle of operation of a silicon solar cell.....	2.3
2.3 Concentrating Photovoltaic (CPV) systems.....	2.6
2.4 Solar cell behavior under concentrated illumination .....	2.10
2.5 Cooling techniques .....	2.12
2.6 Concentrating Photovoltaic Thermal (CPVT) systems.....	2.13
2.7 Solar angles and tracking .....	2.16
2.8 Concluding remarks.....	2.18
<b>3. Investigation of Cooling Devices Appropriate for CPVT Systems .....</b>	<b>.....</b>
3.1 Cooling configurations .....	3.1
3.2 Formulation of the numerical models.....	3.4
3.2.1 Governing equations.....	3.4
3.2.2 Boundary conditions.....	3.5
3.2.3 Non-dimensional numbers .....	3.7
3.3 Selection of the main operating and geometrical parameters.....	3.9
3.4 Numerical investigation of the various configurations.....	3.11
3.4.1 Plate-fin heat sink with Fixed Width (FW) channels.....	3.11
3.4.1.1 Geometry and computational domain.....	3.16
3.4.1.2 Validation of the numerical model .....	3.16
3.4.1.3 Grid independence study.....	3.18
3.4.1.4 Flow and temperature fields.....	3.19
3.4.2 Tapered channels with gradually varying width (VW <sub>t</sub> ).....	3.22
3.4.2.1 Geometry and computational domain.....	3.23
3.4.2.2 Grid independence study.....	3.24
3.4.2.3 Flow and temperature fields.....	3.24
3.4.3 Plate-fin configuration with channels of stepwise varying width (VW).....	3.27
3.4.3.1 Literature survey-Extended surfaces and flow-area contraction phenomena.....	3.27

3.4.3.2	Geometry and computational domain .....	3.29
3.4.3.3	Validation of the numerical model. ....	3.31
3.4.3.4	Grid independence study-Forced convection conditions. ....	3.33
3.4.3.5	Grid independence-Mixed convection conditions .....	3.35
3.4.3.6	Flow field-Forced convection conditions.....	3.36
3.4.3.7	Effect of the Reynolds number-Parametric analysis.....	3.43
3.4.3.8	Temperature field and heat transfer-Forced convection conditions.....	3.45
3.4.3.9	Flow Field-Mixed convection conditions.....	3.49
3.4.3.10	Temperature field and heat transfer-Mixed convection conditions .....	3.53
3.4.4	Heat transfer enhancement: cold-fluid injection in the channels.....	3.58
3.4.4.1	Jets In Cross-Flow (JICF)-Literature survey .....	3.59
3.4.4.2	Geometry and computational domain.....	3.61
3.4.4.3	Grid independence study.....	3.63
3.4.4.4	Flow Field-JICF.....	3.64
3.4.4.5	Temperature field and heat transfer .....	3.71
3.5	Tube-on-plate configuration with serpentine tube.....	3.75
3.5.1	Geometry and computational domain .....	3.79
3.5.2	Validation of the numerical model .....	3.80
3.5.3	Grid independence study.....	3.81
3.5.4	Flow Field .....	3.82
3.5.5	Effect of the Reynolds number-Parametric analysis.....	3.89
3.5.6	Temperature field and heat transfer .....	3.92
3.6	Comparative evaluation of the various configurations .....	3.97
<b>4.</b>	<b>Heat Sink Design, Optimization and Evaluation .....</b>	
4.1	Introduction.....	4.1
4.2	Heat-sink theoretical model .....	4.2
4.3	Model validation.....	4.5
4.4	Optimization procedure .....	4.5
4.4.1	Determination of the objective functions and the design variables .....	4.5
4.4.2	Surrogate functions.....	4.6
4.4.3	Multi-objective optimization using the genetic algorithm .....	4.7
4.5	Optimal designs.....	4.9
4.6	Fabrication of the optimized heat sinks .....	4.14
4.7	Inlet-outlet manifold .....	4.15
4.7.1	Design concept .....	4.15
4.7.2	Fabrication of the inlet/outlet nozzles.....	4.17

4.7.3 Numerical investigation of the manifold system .....	4.18
4.7.4 Flow field in the manifold system .....	4.19
4.8 Evaluation of the implemented heat-sink designs .....	4.20
4.8.1 Experimental evaluation .....	4.20
4.8.1.1 Flow loop and test rigs .....	4.20
4.8.1.2 Uncertainty of the experimental data .....	4.23
4.8.2 Numerical analysis .....	4.24
4.8.2.1 Formulation of the numerical model.....	4.24
4.8.2.2 Grid independence .....	4.25
4.9 Results .....	4.26
4.9.1 Flow fields.....	4.27
4.9.2 Temperature fields and heat transfer .....	4.32
4.9.3 Comparative evaluation of the FW and VW designs.....	4.40
4.10 Effect of fouling on the heat-sink performance.....	4.42
<b>5. Design and Manufacturing of the CPVT System .....</b>	
5.1 Selection of the parabola.....	5.1
5.2 Position of the receiver .....	5.3
5.3 Supporting frame.....	5.4
5.4 Reflector sheet.....	5.7
5.5 Optical losses and slope error.....	5.8
5.6 Solar Tracking mechanism.....	5.9
5.6.1 Obtaining normal incidence .....	5.9
5.6.2 System orientation .....	5.10
5.7 System optical analysis.....	5.12
5.7.1 Ray-tracing.....	5.12
5.7.2 Measurement of the heat flux on the receiver .....	5.14
5.7.3 Irradiation flux distribution .....	5.16
5.8 Solar-cell module .....	5.22
5.9 Receiver .....	5.23
5.10 Thermally conductive adhesive materials.....	5.24
5.10.1 Thermal resistance of the adhesive materials.....	5.25
<b>6. Experimental evaluation of the CPVT system .....</b>	
6.1 Experimental rig and instrumentation.....	6.1
6.1.1 Direct beam radiation.....	6.1
6.1.2 Ambient temperature .....	6.2
6.1.3 Wind velocity .....	6.2

6.1.4 Volumetric flow rate.....	6.2
6.1.5 Fluid temperature.....	6.2
6.1.6 Solid temperature.....	6.2
6.1.7 Glass temperature .....	6.3
6.1.8 Photovoltaic module voltage and current.....	6.3
6.1.9 Data taking procedure.....	6.4
6.2 Experimental uncertainty analysis.....	6.4
6.3 CPVT system performance .....	6.5
6.3.1 System electrical performance .....	6.6
6.3.1.1 Efficiency of the PV modules.....	6.6
6.3.1.2 Effect of temperature on PV module performance .....	6.8
6.3.2 System overall performance.....	6.8
6.3.3 Incidence angle modifier (IAM).....	6.13
6.4 Temperature distribution on the glass cover .....	6.15
6.5 Thermal losses.....	6.18
6.6 Heat transfer at the thermal bond .....	6.23
6.7 Comparison to flat-plate solar thermal collector .....	6.25
<b>7. Simulation and optimization of the CPVT system .....</b>	
7.1 Introduction.....	7.1
7.2 Formulation of the dynamic model .....	7.3
7.3 Validation of the theoretical model .....	7.8
7.4 Prediction of the system long-term performance .....	7.11
7.5 System Optimization .....	7.18
7.5.1 Exergy analysis.....	7.19
7.5.2 Effect of the system parameters on overall performance.....	7.21
7.6 Concluding remarks.....	7.30
<b>8. Conclusions and recommendations for future work.....</b>	
8.1 Conclusions .....	8.1
8.2 Publications .....	8.5
8.3 Novelty of the work.....	8.6
8.4 Recommendations for future work .....	8.7
Appendix A1-Numerical schemes used by the ANSYS CFX package.....	A.1
Appendix A2-Catalogue of the CPVT system components and materials-Cost breakdown	A.3
Appendix A3-Dynamic simulation of the CPVT system-Algorithm description .....	A.5
Appendix A4-Dynamic simulation of the CPVT system-FORTRAN source code .....	A.8





### 1.1 Energy today

The intense human activities of the last half-century have a detrimental impact on the natural environment. Global warming has been identified as an ominous consequence of the twentieth century industrialization and constitutes one of the major concerns of the modern world, while also the “Living planet Index”, a metric of the planet’s biological diversity has declined by about 30% since 1970 [1.1]. The present total energy consumption (2012 values) exceeds 12000 Mtoes; approximately 47% of the total is intended for heating, 17% for electricity and 27% for transport. Residential and industrial sectors account for the 41% and 44% respectively of the total energy intended for heating [1.2]. Oil remains globally the leading fuel as it meets approximately 33% of the global energy needs (Fig. 1.1). The three fossil energy sources in aggregate meet 80% of the global demand [1.3]. Coal is the most abundant fossil fuel, in terms of reserves to production ration, while oil and natural gas reserves have also increased over time [1.1]. At least 70% of CO<sub>2</sub> emissions, which have a major contribution to global warming, are due to the combustion of fossil fuels [1.4]. In order to constrain climate change, a shift from carbon intensive energy production to clean energy is essential. Renewable forms of energy account today for 2.4% of the global energy consumption, but especially regarding power generation their contribution rises to 4.7%.

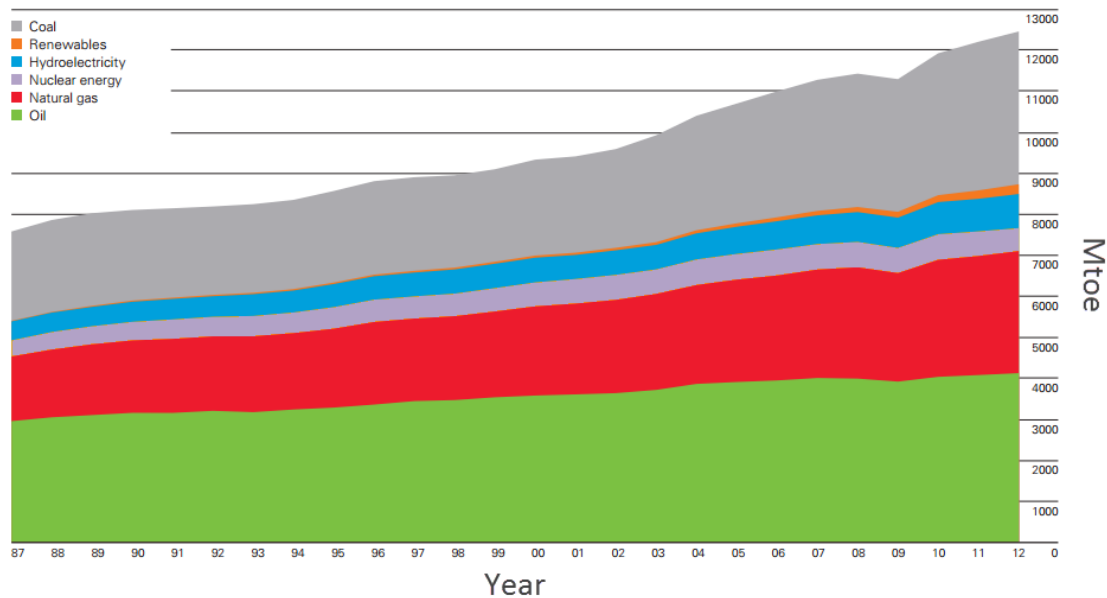


Fig. 1.1 Historical variation of the global energy consumption [1.3].

The United Nations framework convention on climate change through the Kyoto protocol [1.5] has set binding objectives for the time period 2008-2020, regarding the mitigation of greenhouse-gases emissions, on the industrialized nations that signed the treaty. With regard to the European Union in particular, the target is for the energy use to have been reduced by 20% by the year 2020, while a 20%

share of the total energy consumption must be met by renewable resources [1.1, 1.6]. In addition, renewables must account for 10% of the energy consumed in the transport sector [1.6]. Member states that will not meet these goals could face financial penalties from the EU.

Another important factor that makes the shift to non-fossil resources a necessity is energy-production security. As depicted in **Figure 1.2**, oil price has reached a historical peak in the last years despite the fact that the oil reserves worldwide have actually increased since 1992, as depicted in the inset of **Fig. 1.2**. The peak price of oil in recent years was up to two orders of magnitude higher than the cost of extraction, which implies that reasons not related to technical limitations determine modern oil prices. It can be therefore deduced that global energy market and thus the cost of energy production can be manipulated by corporate strategies and be prone to the localized nature of global reserves [1.7]. The most secure way to ensure the security of energy supply is through national energy independence.

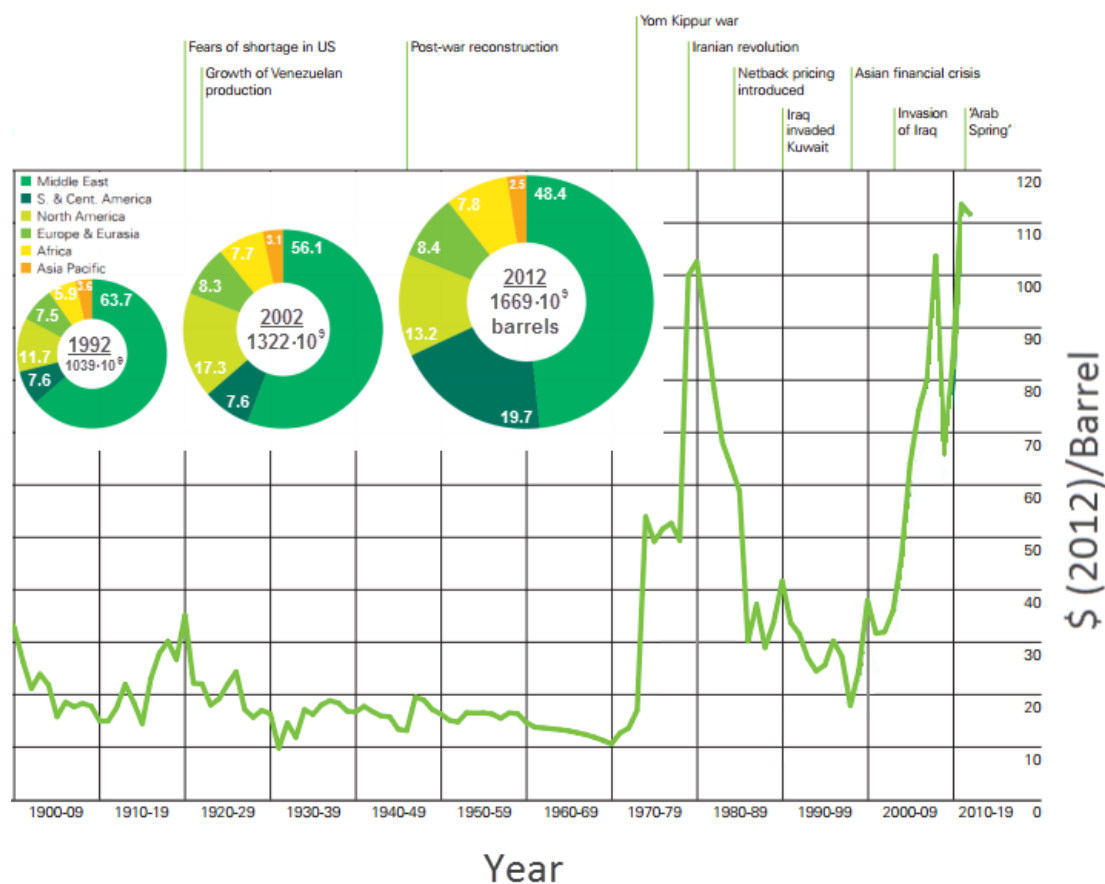


Figure 1.2 Historical variation of oil price [1.3].

## 1.2 Market penetration of solar technologies

In theory, the energy potential of solar irradiation, which is approximately equal to  $1.42 \cdot 10^9$  TWh per year, surpasses any other form of primary energy currently in use globally, as it exceeds the total primary energy consumption by approximately 7000 times. Solar thermal and photovoltaics are the two dominant categories of applications nowadays in order to exploit solar energy. Global venture capital and private equity investment in solar applications totaled \$2.3 billion in 2010 [1.8]. Despite

the rapid growth of the solar energy market in the last thirty years, its contribution to the total energy mix can be still considered negligible.

Approximately 40 GW of photovoltaics had been installed by the end of 2010 [1.8, 1.9], with Germany accounting for the 44% of the installed capacity. The most commonly used raw material is silicon with 80% of the cells being manufactured of silicon wafers, while the remaining 20% almost entirely accounts for thin film cells. Modern commercial “silicon” modules use cells of polycrystalline or monocrystalline silicon, thin films are made of amorphous silicon or CIGS or CdTe, while high efficiency multijunction cells are manufactured from elements in the groups III-V of the periodic table, which are exclusively intended for concentrating applications. Efficiencies of typical modules of each type are shown in **Table 1**.

**Table 1.1** Efficiency of average-production commercial solar-cell modules (2010 values) [1.8].

Technology	Commercial Module Efficiency
Monocrystalline silicon	14%
Multicrystalline silicon	14%
CdTe	11%
a-Si	6%
CIGS	11%
Low concentration CPV ( $\eta=20\%$ silicon cells)	15%
High concentration CPV ( $\eta=38\%$ MJ cells)	29%

China and Taiwan account for the 59% of total production of PV cells (2010 values). Europe is the second largest cell producer with 13% of global production. 17.4 GW of photovoltaics were shipped in 2010 [1.8], with 95% of the shipments being for silicon solar cells. The vast majority (80%) of these shipments was intended for Europe, in order to cover the increased demand arisen due to tax benefits. According to 2012 values, module price is estimated at  $\$0.85/W_p$  for Chinese multicrystalline silicon modules and  $\$1.01/W_p$  for non-Chinese monocrystalline silicon modules [1.10, 1.11]. Regarding Concentrating photovoltaics, the global installed capacity was 90MW (demonstration and commercial plants) at the end of 2012 accounting for the 0.1% of total PV deployment. The majority of the commercial plants, 75% of the total capacity, is located in Spain [1.12]. The cost of CPV technology is decreasing in the years after 2010 due to the growth of the production volume and at the end of 2012 it was estimated to be at  $3.0 \pm 0.7$   $\$/W$ . Based on current predictions this figure could be as low as 1.5  $\$/W$  by 2020 [1.13].

The globally installed solar thermal applications at the time being primarily comprise flat collectors for heat production and large-scale concentrated solar power (CSP) plants for electricity production. The total estimated capacity of flat-plate solar thermal collectors based on collector area amounted to 185-195  $GW_{th}$  [1.2, 1.9] in 2010, with approximately 80% of this installed in China. The prevailing technologies regarding solar thermal systems are the evacuated-tube and the glazed flat-plate collectors with 56% and 11% market share, respectively. The market growth of CSP experienced a significant idle time period in the last twenty years, as after the construction of plants with a total capacity of 350 MW in California in the late 1980s, new plants have only very recently been built, in the years 2007-2010. At the end of 2010, the global capacity of CSP was about 1300MW with 39% in the US and 57% in Spain. Parabolic trough technology accounts for approximately 96% of the total capacity [1.8, 1.14]. Globally, the regions that are suitable for installation of CSP applications lie in

latitudes within 35° about the equator, as the criterion of high direct insolation (at least 2200 kWh/m<sup>2</sup>/year) must be fulfilled. In addition, significant areas of flat and unoccupied lands are required for the installation of the solar fields. From an economic point of view, a major drawback regarding the deployment of CSP is the very high capital cost, which represents 80% percent of the total investment cost. Recent estimates place the capital cost for a CSP plant in the range \$3000-7500/kW where the upper limit refers to plants with thermal energy storage.

Different technologies can be compared in terms of levelized cost, a metric that takes into account the construction cost, as well as the annual operation, maintenance and fuel costs. As depicted in **Fig. 1.3**, the levelized cost for power generation using solar technologies is still high in comparison to fossil-fuel technologies, with the exception of single-cycle gas turbine. It is evident that lowering the high capital cost is a vital requirement for solar technologies. Wind and hydropower, among renewable-energy technologies, appear more competitive at the time being. However, it must be mentioned that there are additional cost factors associated with fossil-fuel technologies that are not taken into account by the levelized-cost metric. These cost factors refer to the negative environmental impact of applications that use conventional fuel at a local level through air pollution and at a global level through the emission of greenhouse gases. Referring to the power supply and industrial sectors, the cumulative amount of CO<sub>2</sub> emissions was equal to 22.2 Gt in 2004 [1.15] and is expected to be approximately equal to 24.3 Gt in 2030. Considering that cost of CO<sub>2</sub> in 2030 is forecasted as high as 58\$(2012)/t [1.16], it is made clear that the implementation of renewable-energy technologies offers a considerable cost reduction potential.

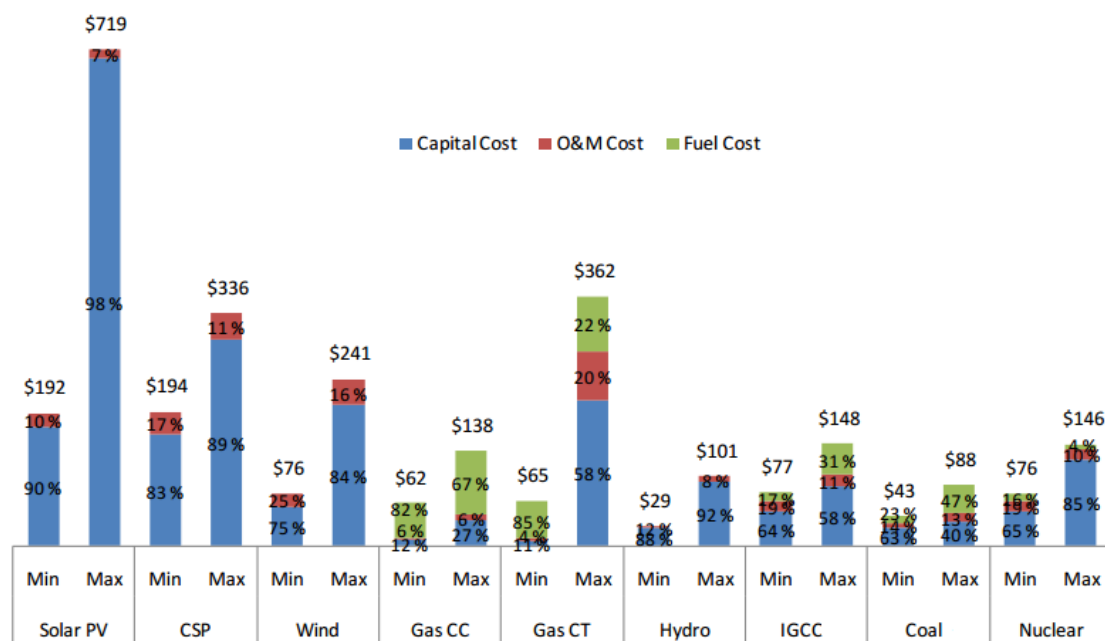


**Fig. 1.3** Levelized cost of various technologies (2008\$/MWh). The difference between minimum and maximum values is due to the large discrepancies in the construction cost (CC: combined cycle, IGCC: Integrated gasification combined cycle).

The “learning curve” analysis can be applied to assess an industry’s future potential for cost reductions. This method draws an empirical relationship between cost reduction and volume of manufacturing [1.13]. Regarding solar technologies, the learning curve has a rate of 21% for PV, 7%

for CSP, 20% for solar thermal applications and 20% for CPV [1.9, 1.13, 1.17]. For comparison, the curve for wind turbines is 8%. These figures indicate that there is a wide margin for cost reduction provided that the solar market expands accordingly. In addition, the cost for greenhouse gas emission mitigation associated with fossil-fuel technologies in conjunction with energy policy incentives that have been undertaken by many governments in favor of green energy deployment, enhance the viability of solar technologies from an economic point of view. For example the European Union has implemented a number of legislation measures in this direction, such as electricity feed-in laws, renewable energy certificates, subsidies, tax incentives, pollution tax exemptions grants and loans.

According to the predictions of the European Photovoltaic Industry Association, global PV capacity is expected to rise to 1000-1845GW by 2030 depending on the political commitment [1.18]. Total CSP installation capacity could reach 137 GW, while solar thermal technologies could account for as much as 60Mtoe of energy by 2030 [1.9]. Solar energy technologies in aggregate are projected to meet 11% of global energy consumption by 2040.

### **1.3 Objectives of the thesis**

In view of the above and as a contribution to the ongoing effort for promoting research in the area of solar energy utilization, an investigation that addresses all the main aspects related to design, optimization manufacturing and operation of a linear Concentrating Photovoltaic/Thermal (CPVT) system is conducted in the present thesis. The system under investigation simultaneously produces electricity and heat at temperatures suitable for domestic hot water and space heating. Heat is in fact a by-product of the limited efficiency of the direct solar energy conversion to electricity, which is being exploited through the use of a properly designed heat exchanging device. During the design procedure, various engineering challenges must be addressed regarding all the system sub-components and proper materials must be selected, in order to ensure an, as much as possible, robust and efficient operation of the prototype system. The three main components of the CPVT system are the reflectors along with supporting frame on which they are mounted, the solar cell module and the cooling device (heat sink). Especially regarding the solar-cell cooling device, for which the research undergone worldwide until now is relatively limited, a thorough investigation of various designs must be conducted. Based on these key technical parameters, the main objectives of this work are the following:

- Understanding of the physics associated with all the components of the CPVT system, such as concentrator optics, solar cell performance characteristics, e.g. effect of operating temperature and irradiation intensity on the produced power, and heat transfer in the cooling system.
- Development of experimental rigs and modification of already existing ones so that various systems sub-components can be experimentally evaluated.
- Sizing of the system and selection of appropriate materials for its sub-components, e.g. determination of the system aperture area and geometrical configuration, the receiver overall dimensions, selection of the reflector material, the PV module components and the thermally conductive adhesive resin.

- Comparative evaluation of different cooling devices using computational fluid dynamics. Proposal of novel heat-sink designs suitable for linear CPVT systems. In addition, design of an appropriate manifold system for an efficient supply and return of the cooling fluid (water).
- Optimization of the geometry of the most attractive heat sink designs using multi-objective algorithms. Fabrication of the optimal heat sink configurations and evaluation of their hydrodynamic and thermal performance.
- Characterization of the concentrator optical efficiency through concentration-ratio measurements and ray tracing simulation.
- Manufacturing of a fully integrated CPVT system and evaluation of its thermal and electrical performance. Characterization of the main energy loss mechanisms.
- Development of a transient model for the estimation of the system long term performance. Exergetic optimization of the integrated system.

As will be thoroughly discussed in the following chapters, the engineering issues raised above are properly addressed in the framework of the present thesis. The research activities conducted and the respective findings refer to two main axes, namely the investigation, development and experimental evaluation of novel cooling devices and the implementation and evaluation of all the aspects of performance of a prototype parabolic trough CPVT system.

#### **1.4 Thesis structure**

The content of the present thesis has been divided into eight chapters. Following this introductory chapter, background information regarding the basic principles of operation of solar cells is provided in **Chapter 2**. The effects of concentrated irradiation and elevated operation temperature on the cell efficiency are clarified. Besides, the advantages of irradiation concentration are reported and a survey on the recent research on CPV and CPVT systems is presented. Finally, the angles that characterize the position of a specified point on earth in relevance to the sun beams of incident irradiation are identified and correlations necessary for sun tracking and inevitable optical losses are given.

Different active cooling configurations suitable for extracting the excess heat from a CPVT system are evaluated in **Chapter 3**. A number of different plate-fin and tube-on-plate heat-sink designs are investigated using three dimensional numerical models. Special focus is given to designs that tend to enhance heat transfer by inducing beneficial secondary flow patterns. The distinctive flow and temperature fields that arise within each configuration are thoroughly illustrated and the heat transfer rates achieved are quantified. The various designs are comparatively evaluated using a number of well established criteria, such as the thermal resistance, the induced pressure drop and the entropy generation rate. Finally, the effect on the heat-sink performance of a potential heat transfer enhancement technique, namely the use of jet streams in cross flow, is examined.

The optimization procedure, construction and evaluation of the heat-sink designs, most favorable in terms of induced pressure drop and thermal resistance, are presented in **Chapter 4**. The heat-sink geometrical parameters are optimized using a stochastic multi-objective technique. Optimal (non-

dominated) solutions produced by the optimization procedure are further evaluated in order to reach a single optimum for each geometry. The design and fabrication of a manifold system that induces low pressure drop and ensures uniform distribution of the cooling fluid is also discussed. Experimental results regarding the induced pressure drop and the solid wall temperature distribution are presented in a comparative fashion, in order to point out the strengths and drawbacks of the two manufactured cooling devices. The distinct flow and temperature fields that emerge within the devices are illustrated with the use of three-dimensional models.

**Chapter 5** provides a comprehensive illustration of the design procedure for the CPVT system. Special attention is given to the design and manufacturing of the system supporting frame and an experimental and numerical (ray-tracing) evaluation is conducted in order to estimate the system optical efficiency. In addition, the critical properties and performance characteristics of all the system sub-components are discussed in detail and all the materials used throughout the system manufacturing are reported.

The experimental performance evaluation of the integrated CPVT system is discussed in **Chapter 6**. The developed experimental rig and instrumentation used are thoroughly described. Different receiver configurations are tested employing the two novel cooling devices and solar cells of different dimensions. Regarding the system electrical performance, the characteristic IV curves are obtained and the effect of temperature on the cell performance is quantified. The system electrical and thermal efficiencies are measured, under steady state conditions, for variable operating parameters and the thermal losses through the glass cover and the insulation are determined. The transient thermal behavior is characterized through the measurement of the system response time, while the incidence angle modifier is measured in order to account for the effect of non-perpendicular incident irradiation on the system performance.

A theoretical model suitable for the prediction of the CPVT system long-term performance is described in **Chapter 7**. The formulation of the mathematical model and the considered geometrical and operational parameters of the system are given in detail. The effect of heat capacity is taken into consideration in the thermal balances and thus the model is able to capture the transient behavior of the system. Besides, the model is validated using available experimental data. The annual yield of system variations with different receiver designs is obtained and the respective annual efficiency is calculated. In addition, a parametric analysis is conducted in order to point out the sensitivity of the system efficiency on the main sub-component characteristics and to determine the flow rate and aperture area that maximize the system exergetic efficiency.

The main findings and conclusions drawn in the present study are summarized in **Chapter 8**. Based on the experience gained, recommendations are made for future research on aspects that present great interest from an engineering point of view and could contribute to the improvement of the overall CPVT system performance.

**Chapter references**

- [1.1] N. Lior. Sustainable energy development: The present (2009) situation and possible paths to the future, *Energy* 35 (2010) 3976-3994.
- [1.2] M.P. del Pablo-Romero, A. Sánchez-Braza, E. Lerma, Solar Thermal Energy Use in EU-27 Countries: Evolution and Promotion, in G. Ferreira (Ed.): *Alternative Energies* Springer Verlag, Heidelberg 2013.
- [1.3] BP Statistical Review of World Energy, June 2013, available at [www.bp.com/statisticalreview](http://www.bp.com/statisticalreview).
- [1.4] V. Sardeshpande, I.R. Pillai, Effect of micro-level and macro-level factors on adoption potential of solar concentrators for medium temperature thermal applications, *Energy Sust. Dev.* 16 (2012) 216–223.
- [1.5] United Nations Framework Convention on Climate Change, Kyoto protocol, December 1997, available at [https://unfccc.int/kyoto\\_protocol/items/2830.php](https://unfccc.int/kyoto_protocol/items/2830.php)
- [1.6] A.N. Menegaki, Growth and renewable energy in Europe: A random effect model with evidence for neutrality hypothesis, *Energy Econ.* 33 (2011) 257–263.
- [1.7] J. D. Mondol, N. Koumpetsos, Overview of challenges, prospects, environmental impacts and policies for renewable energy and sustainable development in Greece, *Ren. Sust. Energy Rev.* 23 (2013) 431–442.
- [1.8] U.S. department of Energy, 2010 Solar Technologies Market Report, November 2011, available at <http://www.nrel.gov/docs/fy12osti/51847.pdf>.
- [1.9] G.R. Timilsina, L. Kurdgelashvili, P. a. Narbel, Solar energy: Markets, economics and policies, *Renew. Sustain. Energy Rev.* 16 (2012) 449–465.
- [1.10] V. Devabhaktuni, M. Alam, S.S.S.R. Depuru, R.C. Green II, D. Nims, C. Near, Solar energy: Trends and enabling technologies. *Ren. Sust. Energy Rev.* 19 (2013) 555–564.
- [1.11] M. Bazilian, I. Onyeji, M. Liebreich, I. MacGil, J. Chase, J. Shah, D. Gielen, D. Arent, D. Landfear, S. Zhengrong, Re-considering the economics of photovoltaic power, *Ren. Energy* 53 (2013) 329-338.
- [1.12] F. J. Gómez-Gila, X. Wang, A. Barnett, Energy production of photovoltaic systems: Fixed, tracking, and concentrating, *Ren. Sust. Energy Rev.* 16 (2012) 306– 313.
- [1.13] J.E. Haysom, O. Jafarieh, H. Anis, K. Hinzer, Concentrated photovoltaics system costs and learning curve analysis, *AIP Conf. Proc.* 239 (2013) 1556.
- [1.14] U.S. Department of Energy, Sunshot Vision Study, February 2012, available at <http://energy.gov/eere/sunshot/sunshot-vision-study>.
- [1.15] Intergovernmental Panel on Climate Change, Climate Change 2007-Mitigation of Climate Change, Chapter 11, 2007, available at <http://www.ipcc-wg3.de/assessment-reports/fourth-assessment-report>.
- [1.16] Synapse Energy Economics Inc., 2013 Carbon Dioxide Price Forecast, Cambridge, MA, 2013.
- [1.17] E. Taibi, D. Gielen, M. Bazilian, The potential for renewable energy in industrial applications, *Ren. Sust. Energy Rev.* 16 (2012) 735–744.
- [1.18] European Photovoltaic Industry Association, Solar Generation VI-2011, February 2011, available at <http://www.epia.org/news/publications/>.

## 2.1 Solar cells – Current state of technology

As it was stated in **Chapter 1**, the cell type (**Fig. 2.1**) that at the moment dominates the photovoltaics market is the silicon cell. Silicon is in abundance on earth, however not in a pure form, but as silicon dioxide in the form of quartz or sand. In order to separate the oxygen, silicon dioxide is heated together with carbon powder, coke and charcoal to a temperature of 1800-1900°C. This procedure produces carbon monoxide and 98% pure silicon. The raw silicon (polysilicon) is further purified in chemical processes. Different procedures must be consequently followed for the production of either mono- or polycrystalline silicon wafers, as illustrated in **Fig. 2.2**. In order to produce mono-crystalline silicon, the polysilicon is melted in a quartz crucible at around 1420°C. A seed crystal with a defined orientation is dipped into the silicon melt and slowly drawn upwards out of the melt. As drawn upwards, the crystal grows into a cylindrical mono-crystal, which is subsequently cut to form semi-round or square bars. The bars are divided to thin wafers using wire saws [2.1]. Poly-crystalline silicon is produced by the controlled solidification of the polysilicon melt see (**Fig. 2.2**). The melt is cast into a cuboid block, which cools evenly in one direction. During the solidification process homogeneous silicon crystals are formed, with grain sizes from a few millimeters to several centimeters. The grain boundaries constitute crystal defects and consequently the efficiency of polycrystalline solar cells is somewhat lower than that of mono-crystalline cells. The silicon blocks are subsequently sawn into bars, and then cut into wafers [2.1].

Once the silicon wafers are created, their upper surface is negatively doped (refer to **paragraph 2.2**) using phosphorous diffusion. After the application of an additional anti-reflective coating, metallic contacts are printed to both sides of the silicon wafer to enable the electrical current flow. A fine metal grid is used on the side facing the sun, so as not to limit the semiconductor area. The lines (contact fingers) have a typical width of about 0.1-0.2mm in this process. Two collector contact lines (busbars) run across the thin contact fingers.

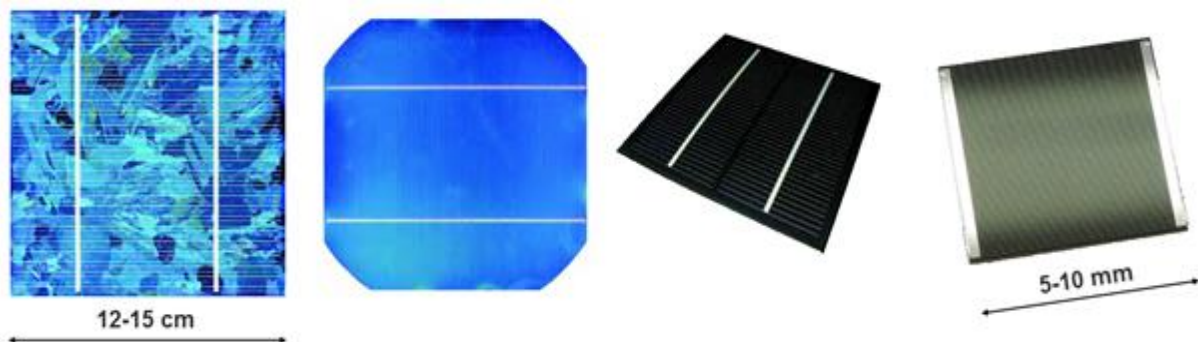


**Fig 2.1** Types of commercial solar cells: poly- and monocrystalline silicon, thin film, III-V multi-junction.

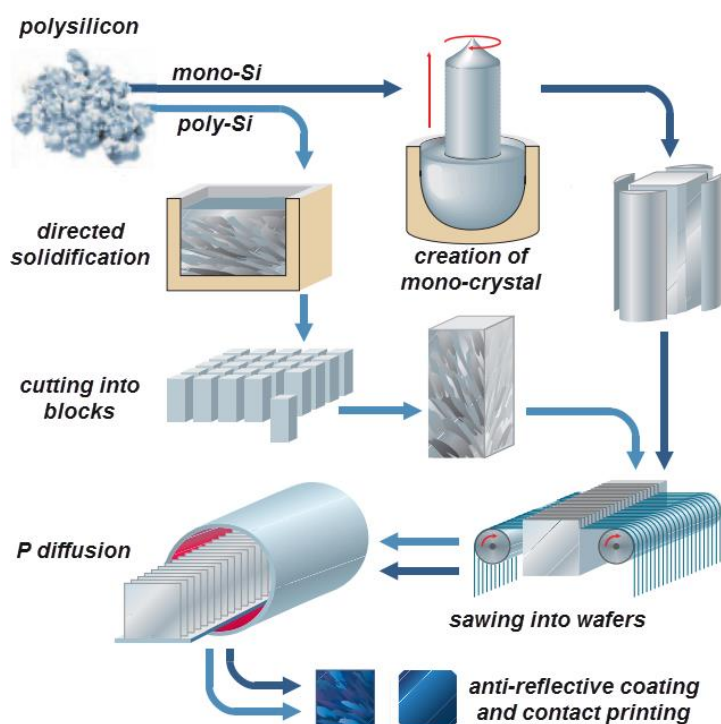


**Fig. 2.2** Silicon solar cells manufacturing procedure [2.1].

Thin film cells represent a small yet non-negligible part of the Photovoltaic (PV) market. Their manufacturing procedure is quite different in comparison to silicon cells, as photoactive semiconductors are applied as thin layers to a glass substrate. Amorphous silicon, copper indium diselenide (CIS) and cadmium telluride (CdTe) are the most commonly used semiconductor materials, while the methods used include vapor deposition, sputter processes and electrolytic baths. Besides, while crystalline solar cells are interconnected externally to a module, thin-film cells are interconnected during the coating and layering process. The electrical contact is created on the back with an opaque metal coating, while a highly transparent and conductive metal oxide layer serves as a front contact [2.1].

None of the aforementioned two cell types can withstand operation under high concentrated illumination ( $>100x$ , i.e. 100suns). On the other hand, the III-V cells are specifically designed in a tandem structure (multi-junction cells), as depicted in **Fig. 2.3**, in order to obtain very high efficiency under high sunlight concentration (400x). Cells of this type are manufactured from materials of the third and fifth element group of the periodic table such as indium gallium arsenide (InGaAs), indium gallium phosphide (InGaPh) or germanium. These semiconductors have band gaps that cover a large part of the solar spectrum [2.2]. A multi-junction cell usually comprises two to five layers with different band gaps that convert different parts of the solar spectrum to electricity. These sub-cell layers are connected in series and thus they must generate equal amounts of current, in order to achieve the maximum cell efficiency. This characteristic cell architecture poses a critical issue in the manufacturing precision required, as the subcell-layers lattices must be matched and this increases the cell cost.

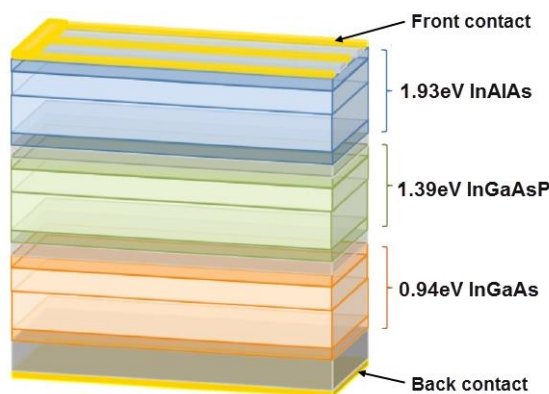


**Fig. 2.3** Typical structure of a triple-junction solar cell [2.2]. The energy values on the figure correspond to the bandgap of each layer.

As depicted in **Fig. 2.4** [2.3], the efficiency of III-V cells (purple line) is higher in comparison to monocrystalline silicon cells (blue line), with a top efficiency of 44.4% for triple junction cells. It is interesting to notice that single junction GaAs cells have achieved an efficiency of 29.1%. The reliability and performance degradation of non-silicon concentrator cells is a major concern, as they must prove reliable for a period of 25-30 years in order to be competitive with silicon cells. Indoor tests performed by Agora [2.4] on GaAs cells showed a possibility of 65% for a reliability time span of 25 years. However, a prototype module tested outdoors proved reliable for only 7080 hours.

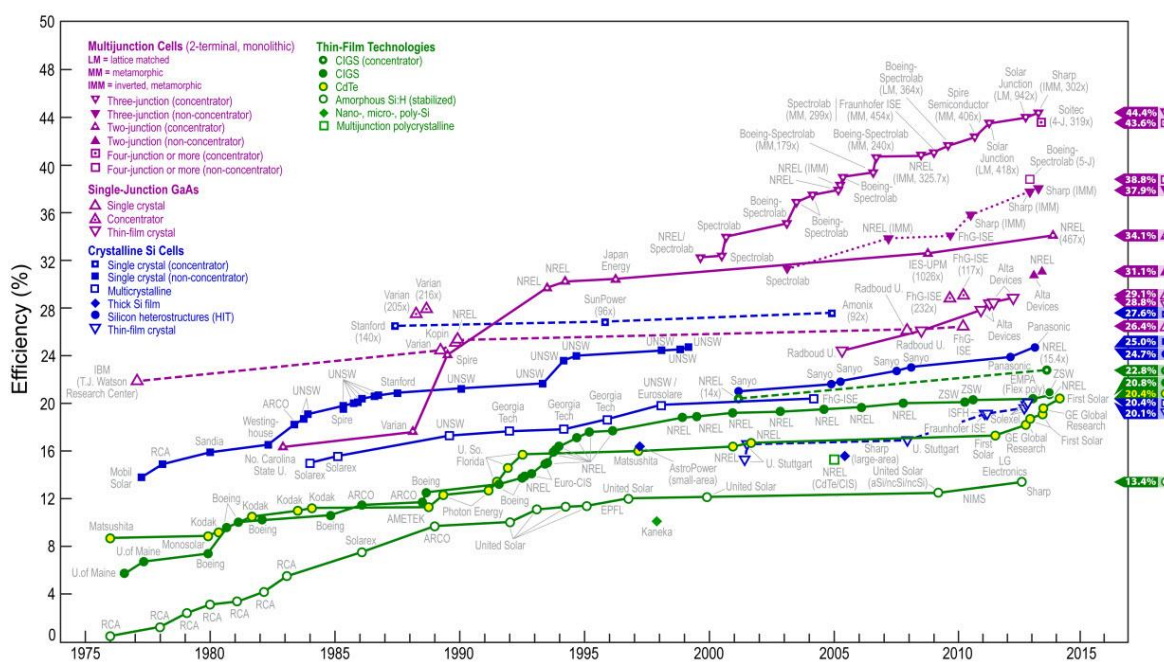


**Fig. 2.4** Histogram of research-cell efficiencies [2.3].

## 2.2 Principle of operation of a silicon solar cell.

A solar cell is in fact a diode comprising two differently doped semiconductor layers. The layer directly exposed to sunlight is negatively doped (n-type), meaning that there is a surplus of electrons

in the specific layer, while the layer below is positively doped (p-type) having a surplus of *electron holes*. A junction is formed at the interface of the p-type and n-type layers, called a p-n junction, **Fig. 2.5**. Electrons and holes have the tendency to diffuse across the p-n junction and consequently an electric field builds up at the unction to prevent this movement [2.5]. If an external voltage is applied to the p-n junction, a current is produced known as diode or dark current  $I_D$ :

$$I_D = I_0 \left[ \exp\left(\frac{qV}{nkT}\right) - 1 \right] \quad (2.1)$$

where  $I_0$  is the diode saturation current,  $V$  is the applied voltage,  $k$  is the Boltzmann constant,  $q$  is the electron charge and  $n$  is the ideality factor, a number between 1 and 2 that typically increases as the current decreases [2.6].

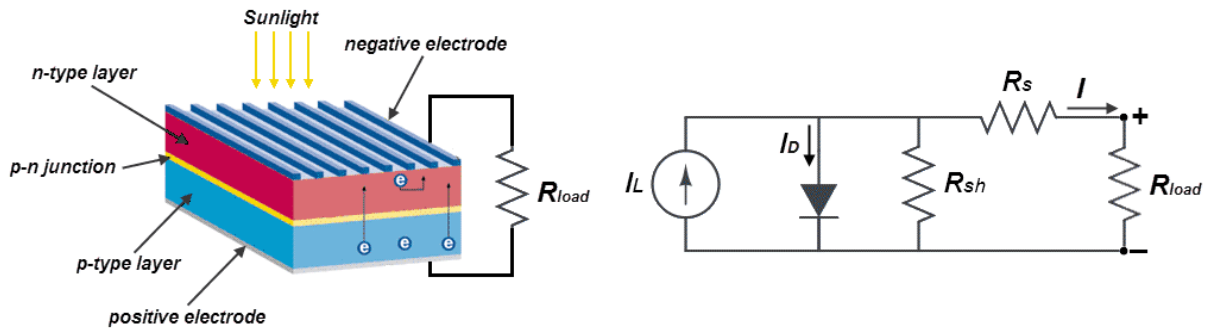


**Fig. 2.5** Schematic and equivalent circuit of a solar cell.

Under illumination, the incoming photons brake electron bonds and create electron-hole pairs. The released electrons are pulled by the electric field toward the n-type layer, while the holes migrate toward the p-type layer. If the two layers are connected through a load, current flows from the n-doped layer towards the p-doped layer and power can be extracted from the cell. A solar cell can be modeled using an equivalent circuit comprising a constant current source, a diode and two resistances corresponding to the series  $R_s$  and shunt  $R_{sh}$  internal resistances. The current  $I$  produced by the cell under illumination is the difference of the photocurrent and the dark current [2.7].

$$I = I_L - I_D - \frac{I(R_{load} + R_s)}{R_{sh}} \quad (2.2)$$

where  $I_L$  is the light generated current, which is equal to the short circuit current for an ideal solar cell. The open circuit voltage of the cell is given by the following relation [2.8]:

$$V_{oc} = \frac{kT}{q} \ln\left(\frac{I_L}{I_0} + 1\right) \quad (2.3)$$

The series resistance of the cell is primarily determined by the bulk resistance of the semiconductor material and the metallic electrodes and by the contact resistance between the front and back metallic

contacts and the semiconductor [2.6]. The shunt resistance is owed to the material impurities in the vicinity of the p-n junction that cause partial shorting. Proper design of solar cells dictates that the shunt resistance must be much larger and, respectively, the series resistance must be much smaller than the external load resistance, so that only a small amount of power is dissipated within the cell. A comprehensive review of the common methodologies used for the determination of the series and shunt resistances from the characteristic Current-Voltage (I-V) curves of the silicon solar cells can be found in [2.9].

The behavior of a solar cell is characterized through I-V curves, such as the one depicted in Fig. 2.6. There is a characteristic point at the curve of Fig. 2.6 where the product of the current and voltage becomes maximum; this point is referred to as the maximum power point. Furthermore, the potential building up at the terminals of an un-connected cell is known as open circuit voltage  $V_{OC}$ , while the current produced by the cell operating at an infinitesimally small load, is known as short circuit current  $I_{SC}$ , respectively. The efficiency of a solar cell is determined as the electric power produced by the cell under operation at the maximum power point to the incoming solar radiation. An additional factor indicative of the cell quality is the fill factor  $FF$  defined as the power produced at the maximum power point to the maximum power that could be ideally produced by the solar cell. Fill factors values above 80% indicate high cell efficiency. In conclusion, the cell efficiency obtains the following equivalent forms:

$$\eta_{cell} = \frac{V_{MPP} I_{MPP}}{A_{cell} G} = \frac{FF \cdot V_{OC} I_{SC}}{A_{cell} G} \quad (2.4)$$

where  $V_{MPP}$ ,  $I_{MPP}$  are the voltage and current produced by the cell at the maximum power point, while  $G$  is the irradiation intensity and  $A_{cell}$  the cell area.

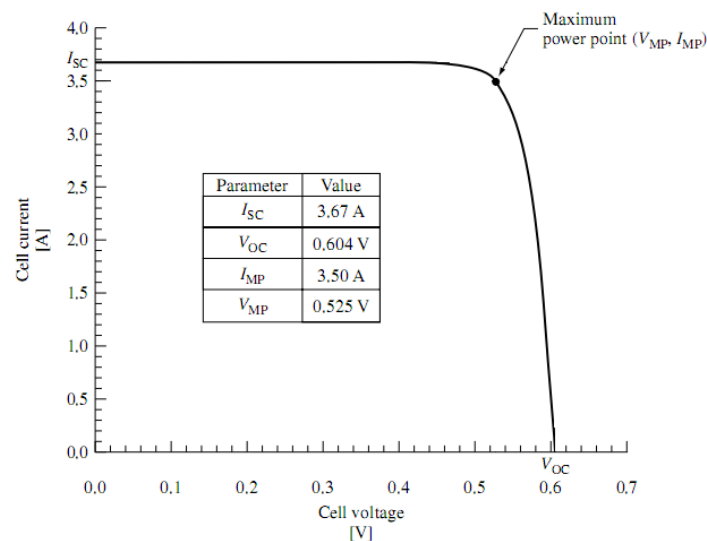


Fig. 2.6 I-V curve of a typical silicon solar cell.

It must be noted that if the cells are connected in series in a module, as it is common in linear Concentrating Photovoltaic (CPV) systems, the module current and thus efficiency are determined by the worst performing cell in the module (affected e.g. by local overheating or partial shading). The

most important effects of partial shading on series-connected silicon solar cells, such as multiple maximum power points and current mismatch losses, are discussed by Maki et al. [2.10]. The placement of bypass diodes between the solar cells, in order to isolate the ones with poor performance, has a beneficial effect on the module efficiency. In an array of solar cells, a bypass diode can be connected in parallel with each cell, as depicted in Fig. 2.7. Under normal operation, the diodes act as open circuits and thus the equal current produced by each cell flows through all the cells of the array. In the case of a current mismatch, e.g. due to a cell of the array being shaded, the diode provides a current path around the poorly performing cell and consequently the current produced by the module is not significantly affected.

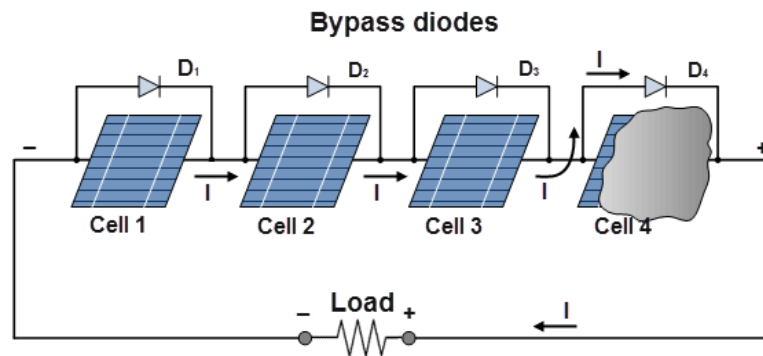
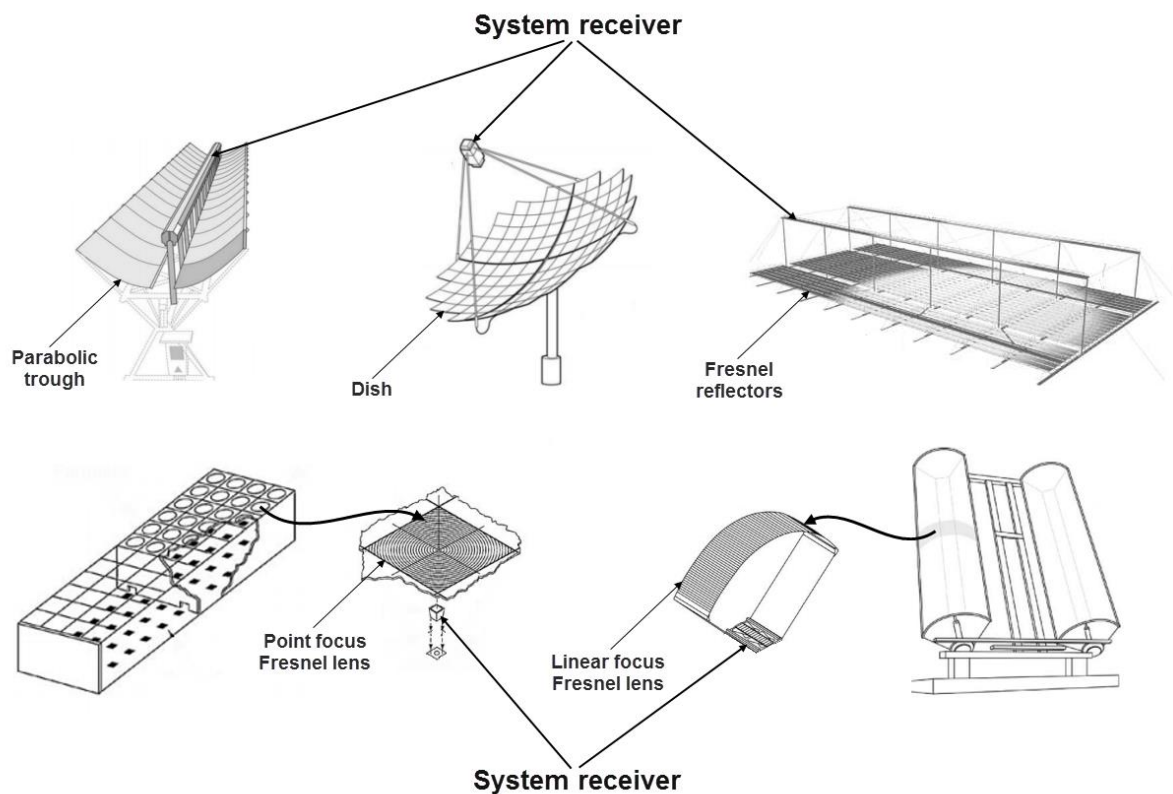


Fig. 2.7 Electrical connection of bypass diodes in an array of silicon cells.

### 2.3 Concentrating Photovoltaic (CPV) systems

The concept of concentrating photovoltaics is to use an optical device in order to focus sunlight onto a cell (or cell module) of small overall dimensions, serving as the receiver of the system. Thus, the cell area and consequently the required raw material are reduced by a factor equal to the concentration ratio  $CR$  [2.11, 2.12]. A major advantage of the substitution of semiconductor material by inexpensive reflective material (e.g. anodized aluminum) is the significant reduction of the overall system cost. With regard to the optical devices utilized, CPV systems can be grouped into two categories, namely point-focus and line-focus systems. Point-focus systems employ paraboloid dishes, Fresnel lenses or heliostats to focus sunlight, while parabolic mirrors and linear Fresnel lenses or mirrors are used by linear focus systems [2.11]. Schematics of the most typical concentrator configurations, which are also adopted by exclusively solar thermal systems [2.13], are depicted in Fig. 2.8 [2.14]. A wide variety of optical devices and variations of the main concentrator designs shown in Fig. 2.8 that have been proposed for the implementation of novel CPV systems can be found in the review article by Chong et al. [2.15].



**Fig. 2.8** Typical optical devices used in concentrated solar power applications [2.14].

There were less than thirty companies worldwide that manufactured CPV systems in 2012 [2.16, 2.17]. The vast majority of them had developed point focus systems that employed Fresnel lenses as primary concentrators and, usually multi-junction, III-V solar cells at the receiver, as depicted in **Table 2.1** [2.16, 2.18]. The systems efficiency lay in the range of 17-30%, while the cell efficiency in the range 27-39%, respectively. The lower efficiency of the integrated system is obviously due to the losses arising from the cell interconnection into a cell module and the quality of the optical device. Another common issue that leads to performance deterioration is cell overheating. The small overall dimensions of CPV cells facilitate the mounting of finned heat sinks in order to dissipate surplus heat to the environment. It must be noted that most of system efficiencies shown in **Table 2.1** are reported by the manufactures and are not necessarily field proven.

Extensive field measurements have been published by (Soitec) Concentrix [2.19, 2.20] for a 100KW power plant in Spain that verify annual system efficiency approximately equal to 23% (**Fig. 2.9a**). In addition, the monthly plant efficiency in months of high insolation was measured up to 26% and showed no deterioration through the years 2009-2011 [2.20]. Besides, a 30 kW CPV system manufactured by Daido Steel and located in Japan was reported to achieve a peak efficiency of 24% [2.21].

**Table 2.1** Commercial high concentration CPV systems characteristics and efficiencies ( $\eta_m$ : module efficiency,  $\eta_s$ : system efficiency [2.16, 2.18]. The cell efficiencies are 39% for Emcore, 38.5% for Spectrolab and 35% for Azur [2.22].

Company	Concentrator	Cell supplier	CR	$\eta_m$ [%]	$\eta_s$ [%]
Arima Eco Energy	Fresnel lens	Spectrolab	476	22-25	-
Concentrix Solar	Fresnel lens	Azur	385	27	23.5
Daido Steel	Fresnel lens	Azur	550	23	21
Delta Electronics	Fresnel lens	Spectrolab	470	26	23
Emcore	Fresnel lens	Emcore	500	-	27
Energy Innovations	Fresnel lens	Emcore	1440	28.8	23-25
Enfocus Engineering	Fresnel lens	-	300	20	-
Green and Gold	Fresnel lens	Emcore	1370	34	28
INER	Fresnel lens	Spectrolab	476	23	20
Opel International	Fresnel lens	Spectrolab	500	26-28	-
Pyron Solar	Fresnel lens	Spectrolab	500	22	21
Sharp	Fresnel lens	Sharp	700	-	-
SolarTec	Fresnel lens	ENE	600	20	17
Sol3G	Fresnel lens	Azur	476	24	22.7
Abengoa	Fresnel lens	Spectrolab	2000	-	-
Isofoton	Total Int. Refl. lens	-	1000	25	23
GreenVolts	Micro-dish	Spectrolab	625	28.5	-
Solfocus	Micro-dish	Spectrolab	500	25	23
Solar Systems	Dish (dense array rec.)	Spectrolab	500	35	30
Cool Earth Solar	Dish (dense array rec.)	-	400	30	-
Menova Energy	Fresnel reflector	Emcore	1450	26.4	23.2

Gómez-Gil et al. [2.23] conducted a comparative evaluation between three nearby located photovoltaics power plants comprising of fixed and tracking conventional (flat) and concentrating photovoltaic systems, respectively. The power plants were compared in terms of energy production (in kWh per  $W_p$  of installed power) by also applying a correction for the irradiation level, in order to allow a straightforward comparison. It must be noted that the concentrating system uses 500x Fresnel lenses and it is the second largest installation in the world with an overall capacity of 1.5 MW. The yield of single and dual-axis tracking CPV systems were higher by 22.3% and 25.2%, respectively, in comparison to the reference fixed PV system. On the other hand, the yield of the CPV system exceeded that of the reference system by only 0.6% indicating that there is a considerable margin for improvement regarding CPV technology. Saito et al. [2.24] compared a Fresnel lens CPV system developed by Sumitomo Electric Industries to a polycrystalline conventional PV module. The two modules were mounted on the same tracking mechanism and the daily yield of both was recorded. It was established that the CPV module had a twofold yield (in Wh per  $m^2$  of the system aperture area) in comparison to the flat module, with conversion efficiency approximately equal to 30%. Siaw et al. [2.25] optimized the electrical interconnection between the cells in a dense array receiver of a point-focus system. The optimization criterion was to minimize cell current mismatch due to the non-uniform irradiation on the receiver. A prototype system that was manufactured and employed planar reflectors and Emcore triple junction cells achieved very high instantaneous efficiency equal to 34%. High efficiency multi-junction cells are designed to exploit the typical solar light spectrum. Thus, the optical devices of high concentration point-focus systems, apart from being geometrically precise, must also not alter the irradiation spectrum at reflection. Consequently, the concentrator manufacturing materials must be of high quality and therefore the cost of the optical device increases.

For this reason, sun spectral splitting devices have been proposed to be used in conjunction to concentrators for CPV systems employing single junction cells, in order to reduce overall cost [2.26]. These devices act as selective absorbers that allow only the part of the solar spectrum that matches the cell bandgap to pass. Thus, the conversion efficiency is increased and furthermore the cell operating temperature is reduced, as the solar irradiation that cannot be converted to electricity is reflected by the splitting device.

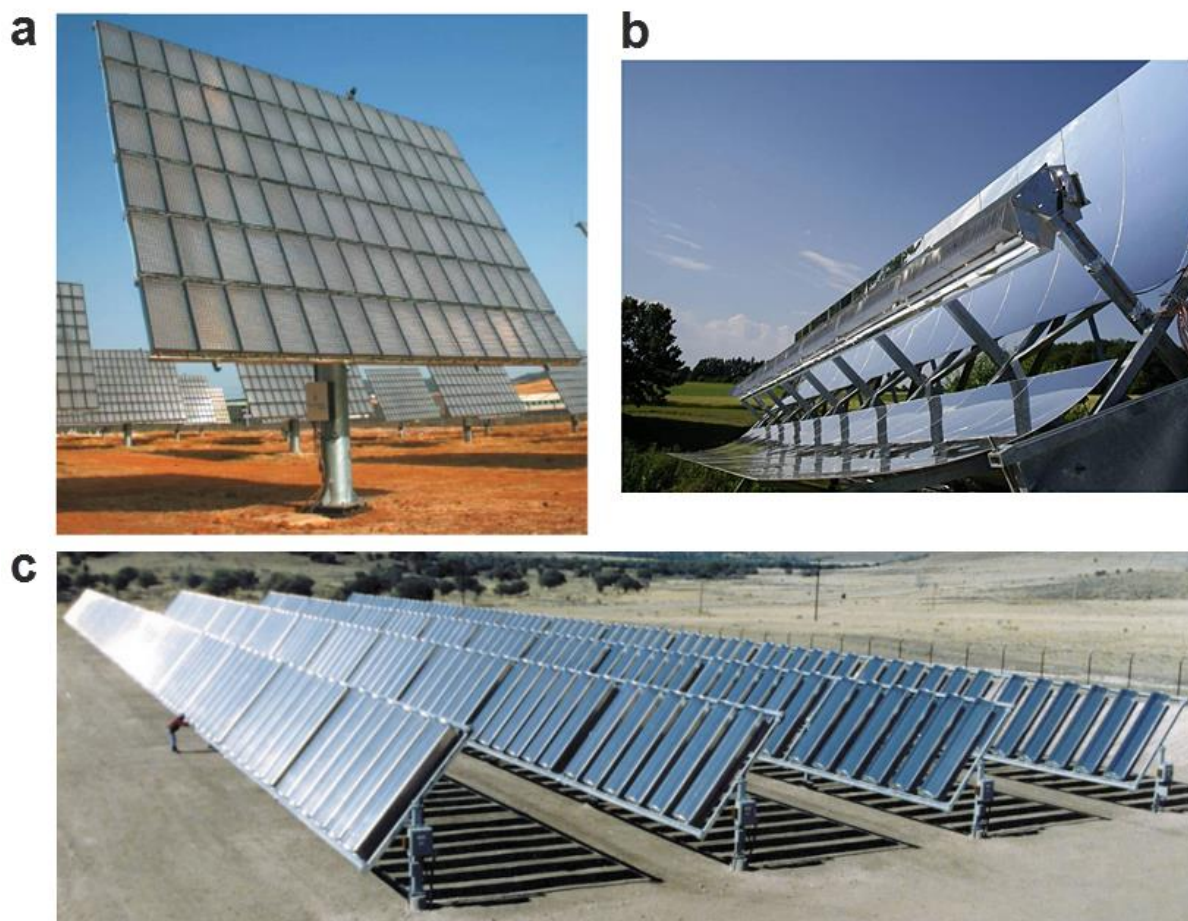


**Fig. 2.9** CPV systems that employ different optical devices: (a) Point-focus Concentrix system using Fresnel lenses, (b) linear parabolic trough Euclides prototype, (c) linear Entech system using Fresnel reflectors.

Few installations and demonstration prototypes that achieve low to medium concentration ( $CR < 100$ ) have been developed worldwide. The only parabolic trough linear CPV system for which there are available technical specifications and performance data in the open literature is the EUCLIDES system (**Fig. 2.9b**) that has been developed by the Polytechnic University of Madrid [2.27, 2.28]. The prototype system had a total aperture area of  $42 \text{ m}^2$  and a geometrical concentration ratio of  $32\times$ . Commercially available concentrator silicon solar-cell modules were mounted on the receiver, which also incorporated a plate fin heat dissipator. The single module efficiency was measured equal to 14%, while the efficiency of the interconnected modules in the 24m long receiver was approximately equal to 10.6%. As reported recently by Vivar et al. [2.28], the first two generations of EUCLIDES system proved inadequate to operate reliably under real outdoor conditions due to problems associated both with the concentrator and the solar-cell modules. In addition, the authors of [2.28] illustrate all the critical issues and challenges posed during the construction of a CPV

system both, in terms of appropriate materials and manufacturing processes. A third generation EUCLIDES system has been manufactured with two receivers operating at 12x and 24x concentration and nominal output of 2 kW. The improved solar cell modules achieved efficiencies of 17.4% (24x) and 16.6 (12x) as interconnected receiver modules under uniform illumination, nevertheless the system efficiency, as measured in two test sites, was approximately equal to 11%. A linear Fresnel lens CPV module (**Fig. 2.9c**) has been commercialized in 2012 by Entech [2.29]. The module, with overall dimensions 100 x 165 x 15 cm, comprises six linear acrylic lenses that focus irradiation at 20x on respective arrays of silicon cells with specially designed front contact. Due to the heavy metallization of the cell front contact, a refractive prismatic optical device has been incorporated into the module that increases the cell efficiency to 18-20%.

Low concentration static CPV systems have been manufactured by few research groups in order to demonstrate the feasibility of the manufacturing at a very low cost. Baig et al. [2.30] report the design and manufacturing process of a small prototype CPV with a concentration ratio of 3, suitable for building integration. The system employs an asymmetrical compound parabolic reflector and monocrystalline silicon solar cells. Hatwaambo et al. evaluated a 3.6x [2.31] compound parabolic concentrator system, while Sangani et al [2.32] investigated a 2x V-trough system. Grasso et al. [2.33] proposed a methodology, based on the levelized cost of energy, to determine the maximum cost of the concentrator with a specified optical efficiency, in order for low concentrating CPV systems to be financially competitive with standard PV modules. The authors manufactured a scaled CPV system with a concentration ratio of 5 using a static modified prism compound parabolic concentrator and commercial silicon cells. The system optical performance was evaluated and the cost for the concentrator was determined.

Lack of proper standardization is a vital issue that hinders the development of commercial CPV systems, as at the present there are no universally accepted test methods to certify the electrical efficiency of a CPV system under standard conditions [2.34]. It is consequently difficult for a product to achieve high market penetration without guarantee of its performance and reliability.

## 2.4 Solar cell behavior under concentrated illumination

Operation of solar cells under concentrated illumination offers an additional advantage in terms of efficiency. As it has been theoretically and experimentally established [2.11, 2.35], the short circuit current and the open circuit voltage increase in a linear and a logarithmic manner, respectively, in proportion to the irradiation intensity:

$$I_{SC,conc} = CR \cdot I_{SC,1-sun} \quad (2.5)$$

$$V_{OC,conc} = V_{OC,1-sun} + \frac{kT}{q} \ln CR \quad (2.6)$$

where CR is the concentration ratio and  $I_{SC,conc}$ ,  $V_{OC,conc}$  are the short circuit current and open circuit voltage, respectively, for operation under concentrated irradiation. The effect of illumination increase on the cell characteristic I-V curve is shown in **Fig. 2.10a**. The logarithmic increase of the open circuit voltage is expected considering **Eq. (2.3)**, as  $V_{OC}$  has a logarithmic dependence on the photocurrent  $I_L$

[2.12]. By taking into consideration Eqs. (2.5) and (2.6), Eq. 2.4 describing the cell efficiency becomes:

$$\eta_{conc} = \frac{FF_{conc} \cdot CR \cdot I_{SC,1-sun} \cdot \left( V_{OC,1-sun} + \frac{kT}{q} \ln CR \right)}{CR \cdot G \cdot A_{cell}} \quad (2.7)$$

Finally, the ratio of the cell efficiency under concentration to that at typical irradiation is:

$$\frac{\eta_{conc}}{\eta_{1-sun}} = \left( \frac{FF_{conc}}{FF_{1-sun}} \right) \left( 1 + \frac{\frac{kT}{q} \ln CR}{V_{OC,1-sun}} \right) \quad (2.8)$$

The cell fill factor increases as a function of the concentration ratio [2.36] and thus both factors at the right hand side of Eq. (2.8) are larger than unity proving the beneficial impact of elevated illumination. It must also be noted that the illumination distribution profile also has an effect on cell efficiency. Franklin and Coventry [2.37] tested a concentrator silicon cell under uniform illumination of 30 suns along the entire cell width and under partial illumination of 90 suns in the central third of the cell. The cell open-circuit voltage and efficiency decreased by 4.5% in the latter case.

However, Eq. (2.8) is valid only in the ideal case where the cell operating temperature is maintained constant for different levels of irradiation. In reality, high irradiation concentration induces elevated operating temperature. The cell temperature affects the p-n junction “built-in” potential, which is formed due to the existence of the electric field in that region [2.7]. Increase of the cell temperature leads to decrease of the built-in potential, a trend also followed by the open-circuit voltage, which in fact decreases in a linear manner. On the contrary, increase of the cell temperature leads to the reduction of the semiconductor band gap energy, which allows a greater part of the incident energy to interact with the semiconductor material and produce electron-hole pairs [2.7]. Thus, the generated photocurrent and short-circuit current increase with temperature [2.8]. Nevertheless, this effect is negligible in comparison to the decrease of the cell open circuit voltage, as depicted in Fig. 2.10b. In a real operating solar cell, the series resistance also increases with temperature, due to the different thermal expansion coefficient of the electric contact and the bulk cell material, and in fact in a linear manner [2.38]. Besides, it has been experimentally confirmed that the cell fill factor decreases with temperature [2.11] due to the effect of the series resistance [2.12]. The net effect of temperature increase is a linear decrease of the cell efficiency:

$$\eta_{cell} = \eta_{cell,ref} \left[ 1 - \beta_{ref} (T_{cell} - T_{ref}) \right] \quad (2.9)$$

where the temperature coefficient  $\beta_{ref}$  can be experimentally determined and it primarily depends on the cell material [2.39]. Typical values of  $\beta_{ref}$  for silicon solar cells range between 0.003 and 0.005 [2.8].

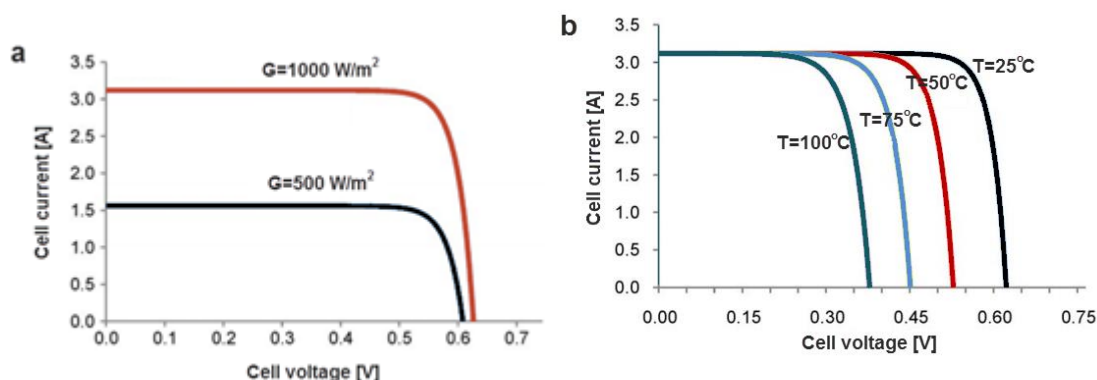


**Fig. 2.10** Effect of (a) irradiation intensity and (b) temperature on a silicon cell current-voltage (I-V) curve [2.8].

Braun et al. [2.40] theoretically investigated the combined effect of concentrated illumination and elevated temperature on the solar cell efficiency. It was concluded that the efficiency penalty decreases logarithmically with irradiance concentration. Materials with high band gap energy, such as III-V semiconductors, under extreme concentration ( $>1000x$ ) could have a minor efficiency decrease. Vossier et al. [2.41] experimentally investigated the possibility of operating III-V cells rated for concentration of a few hundred suns under extreme concentration up to  $3000x$ . The cell efficiency degradation at  $3000x$  ranged between 25%-50% of the peak efficiency at  $400-500x$ . In addition, it is reported in [2.42] that the temperature distribution, apart from its absolute value, has a non-negligible effect on the cell performance. The authors of [2.42] tested three cells with equal average temperature, yet with uniform, Gaussian and anti-Gaussian temperature profiles. It was established that the Gaussian distribution enhances the cell efficiency by 1.52%, whereas the anti-Gaussian distribution decreases the cell efficiency by 3.31%, in comparison to the uniform one. The authors attributed this effect to the local temperature at the cell busbar region, which is vital to the cell efficiency.

Apart from the efficiency deterioration, the mechanical impact of temperature on a solar-cell module can be significant, as the module consists of materials in contact (glass, semiconductor, electrodes etc.) that have considerably different thermal expansion coefficients. Thus, the materials when heated undergo dimensional changes of different magnitude and consequently mechanical stresses build up that can lead to cracking of the cells or the glass cover, as well as detachment of the metallic contacts. Even though overheating might not lead to immediate destruction of the module it will certainly reduce its life expectancy due to mechanical fatigue.

## 2.5 Cooling techniques

Cooling is a major concern regarding the design of concentrating photovoltaics, as the integration of a heat dissipating configuration can have a beneficial impact on the system electrical efficiency. A wide variety of cooling configurations that could potentially be suited for the cooling of solar cells are presented in the review articles by Du et al. [2.43] and Royne et al. [2.44]. Besides, Micheli et al. [2.45] focused on the cooling options for concentrating photovoltaics that are made available through micro and nano-technology, such as micro-fins (or micro-channels) configurations, micro heat pipes and the use of carbon nanotube suspension as cooling fluid. Royne and Dey [2.46] proposed an active cooling system for densely packed cells comprising a grid of impinging jets. An optimization

methodology, based on analytical models, was formulated in order to determine the layout and geometrical parameters of the cooling nozzles that maximize the cell electrical output. Barrau et al [2.47] proposed a hybrid device that combines the techniques of impingement jets and microchannel flow for cooling a dense array of solar cells under high concentration. A parametric study was conducted in order to determine the optimal flow rate for which the net electrical output, by also taking into account the required pumping power, was maximized. The hybrid scheme was proven to produce a more uniform temperature distribution at the cooled surface in comparison to straight rectangular microchannels. Rahimi et al. [2.48] experimentally evaluated the performance of a water-cooled silicon cell module. Microchannels of hydraulic diameter 0.667mm were machined onto a Plexiglas plate, which was subsequently bonded to a module with overall area 13x26 cm<sup>2</sup>. Indoor testing using a solar simulator of 1000 W/m<sup>2</sup> showed that the cell power output increased by 30% for a volumetric flow rate of the coolant equal to 198 mL/min. Although, single-phase flow is considered in the vast majority of studies, two-phase cooling has also been proposed as an effective technique that allows the irradiation concentration to be much higher, exceeding even 1000x, depending on the cooling fluid and the flow rate [2.49, 2.50].

The alternative technique of directly immersing a properly insulated PV module into the cooling fluid has also been examined. Han et al [2.51] conducted a comparative study in terms of optical transmittance and cooling capacity, in order to evaluate the applicability of different fluids for immersion cooling. Zhu et al. [2.52, 2.53] experimentally investigated the cooling effectiveness of direct immersion of a solar cell module under concentrated sunlight (CR=160-200) into a liquid. Initial indoor tests [2.52] using dimethyl silicon oil as a coolant showed promising results as the convective heat transfer coefficients achieved were higher than 3000 W/m<sup>2</sup>K. Zhu et al. [2.53] subsequently conducted an outdoor evaluation of an integrated system using a dish reflector capable of 250x concentration and a glass tube receiver, where a silicon cell module was immersed into deionized water. It was established that the cell temperature was kept under 50°C for a cooling flow rate and inlet temperature equal to 2.23m<sup>3</sup>/h and 30°C, respectively, while the overall convective heat transfer coefficient was equal to 6000 W/m<sup>2</sup>K. However, the efficiency of the module was significantly decreased after two days of operation due to the chemical effects of the immersion fluid on solar cells. A further experimental evaluation of the fluid immersion technique was conducted by the same research group on a linear Fresnel reflector CPV system with low concentration (10x) [2.54].

## **2.6 Concentrating Photovoltaic Thermal (CPVT) systems**

The integration of an active cooling system into the receiver of a CPV system, apart from increasing the system electrical efficiency, makes the surplus heat available for utilization in other applications, where heat at temperatures in the range 60-80°C can be exploited, such as water and space heating, (adsorption or desiccant) cooling [2.55, 2.56] or even desalination through membrane distillation [2.57, 2.58]. The reduced receiver dimensions, in comparison to a flat-plate solar thermal collector, render concentrating systems ideal for high-temperature operation as heat losses are limited, a beneficial feature in terms of system overall efficiency. However, the concept of simultaneous production of heat and electricity has been applied to flat-plate collectors as well. Various flat PVT designs are reviewed in [2.59-2.62].

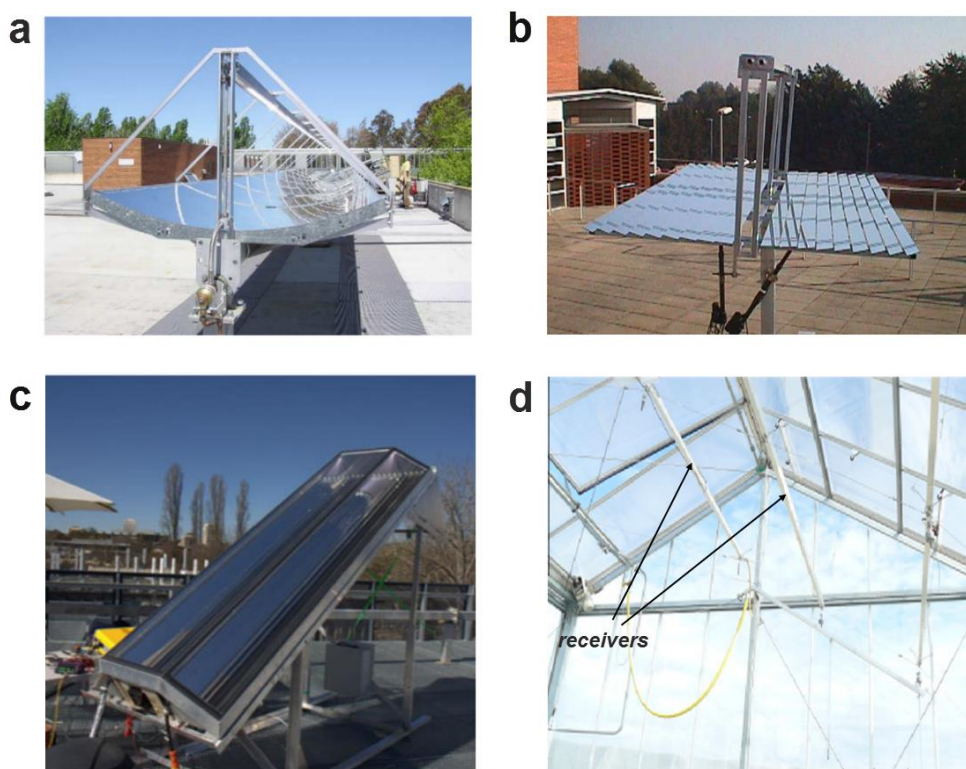


**Fig 2.11** Prototype CPVT systems: (a) Parabolic trough [2.65], (b) Fresnel reflector [2.68], (c) sealed separate arrays of Fresnel reflectors with two receivers [2.69], (d) building integrated Fresnel lens [2.71].

Few examples of integrated CPVT systems can be found in the open literature. Early studies by Chenlo and Cid [2.63] and Gibart [2.64] outlined the manufacturing procedure for prototype linear CPVT systems based on the Fresnel lens and the parabolic reflector technologies, respectively. Rectangular ducts were used to extract surplus heat in both studies. Coventry [2.65] designed and manufactured a parabolic trough linear CPVT system with a geometrical concentration ratio equal to 37 (**Fig. 2.11a**). The receiver comprised an array of custom designed mono-crystalline silicon cells cooled by water flowing inside an aluminium tube. The tube had internal fins in order to enhance heat transfer and a specially manufactured outer cross section with a flat lower surface so that the cell array can be adhered. The system achieved thermal and electrical performance equal to 58% and 11%, respectively, for mass flow rates in the range 37.5-42.5 mL/s. Li et al. [2.66] evaluated the overall performance of a 2m<sup>2</sup> prototype linear CPVT system manufactured at Yunnan university (Kunming) and which used a parabolic reflector to concentrate solar radiation up to 31 suns. Three different types of cells (monocrystalline silicon, “super cells” and GaAs) were tested. The heat sink used for the cooling of the cell array was similar to that reported in [2.65]. The system employing the GaAs cell array obtained a maximum overall efficiency of 50.6%, with 41.7% and 8.9% attributed to the thermal and electrical efficiency, respectively.

Yongfeng et al. [2.67] performed a separate experimental evaluation for a variation of the system investigated in [2.66], that achieves a concentration of 10x. The measured efficiency of the GaAs cells was 9.5% and the thermal efficiency of the system was 34%. Rossel et al. [2.68] manufactured a two-axis tracking 11x CPVT system, as depicted in **Fig. 2.11b**. The system has an overall aperture area of 3.6 m<sup>2</sup> and employs Fresnel reflectors to concentrate irradiation onto a silicon cell module thermally bonded to a water cooled channel. The daily thermal efficiency of the system, without electricity

production, was measured higher than 60%. Vivar et al. [2.69] report the performance evaluation of a Fresnel reflector linear system with concentration ratio 20x. A module of the system resembles a fully sealed case, which encloses two arrays of Fresnel reflectors that concentrate irradiation on two “micro-receivers” consisting of an array of silicon solar cells bonded to cylindrical tubes (Fig. 2.11c). Daily measurements established an average overall efficiency of 58% (50% thermal-8% electrical).

Chemisana et al. [2.70] proposed a design for a CPVT system that utilizes a linear Fresnel lens and a CPC (compound parabolic concentrator) as primary and secondary concentrators respectively. The system achieves a maximum concentration of 10x. A typical rectangular channel served as the cooling device with water flow inside it under laminar flow conditions. The electrical performance of the PV array and the thermal performance of the cooling system were experimentally evaluated and the data were compared against theoretical and numerical models. A 25x Fresnel lens linear CPVT system was integrated into a greenhouse in the University of Wageningen, as reported by Sonneveld et al. [2.71]. Fresnel lenses were mounted onto the top glazing of the green house and concentrated the solar irradiation on tracking hollow beams, which were supported by the steel frame of the green house (Fig. 2.11d). Silicon solar cells were thermally bonded on the beams and water was circulated through them. Daily performance measurements showed an overall efficiency of 67% (56% thermal and 11% electrical). Nevertheless, the system optical losses (equal to 30%) were excluded from the calculation of the efficiency.

Chaabane et al. [2.72] manufactured a linear CPVT system that comprises an asymmetric compound parabolic reflector and a mono-crystalline silicon solar cell module thermally bonded to a rectangular duct. The performance evaluation of the system showed that the maximum obtained thermal and electrical efficiencies were equal to 16% and 10%, respectively. Du et al. [2.73] evaluated the performance of an 8x linear Fresnel reflector system. At the system receiver, a silicon cell module was bonded to a tube-on-plate heat sink with a U-shaped tube. Hourly measurements illustrated that the system thermal and electrical efficiencies under steady state conditions were approximately equal to 39% and 8% for coolant flow rates larger than 0.035 kg/s. Kandilli [2.74] designed and evaluated a novel CPVT system based on the concept of irradiation spectral decomposition. The system comprises a paraboloidal dish reflector, a solar cell, which is laminated to a spectral splitting optical device and placed at the focal spot of the concentrator, and a vacuum tube serving as a secondary “thermal” receiver. The visible part of the irradiation is absorbed by the solar cell and converted to electricity, whereas the infrared and ultraviolet parts are reflected by the spectrum splitting device onto the vacuum tube to produce heat. The energetic and exergetic total efficiency of the system were measured equal to 7.3% and 1.16% respectively. Kribus et al. [2.75] proposed a miniature point-focus system with aperture area less than 1m<sup>2</sup> that uses a dish concentrator and high efficiency triple junction cells operating at concentration of 500x. Nevertheless, although the system was reported to be under construction, experimental data of the system actual performance have not been published yet.

The evaluation of low-concentration, static CPVT systems has also been reported by a number of researchers. Kong et al. [2.76] manufactured a low concentration static linear CPVT system that employs a Fresnel lens and flat reflectors, as primary and secondary concentrators respectively, with a geometrical concentration ration of 5.7. For a single daily measurement, the system was reported to achieve peak electrical and thermal efficiencies equal to 10% and 56% respectively for a flowrate equal to 72 Lt/h. Brogren et al. [2.77] discuss the optical properties of the main components (reflector, glazing cells) comprising a 4x compound parabolic concentrator photovoltaic thermal system. The

system optical efficiency was measured to be equal to 71%, while the system electrical and thermal output were measured equal to  $330\text{W/m}^2$  cell area and  $2300\text{W/m}^2$  cell area, respectively.

Nilsson et al. [2.78] focused on the annual performance of a static photovoltaic-thermal system employing asymmetrical parabolic concentrators, in order to be efficient regardless of the sun altitude. The annual electrical of the system was estimated at  $373\text{ kWh/m}^2$  cell area, while the thermal yield was  $145\text{ kWh/m}^2$  glazed area. It was mentioned by the authors that the thermal bond between the cooling tube and the receiver has a significant effect on the system performance. Bernardo et al. [2.79] experimentally evaluated the performance of a low-concentrating parabolic CPVT system ( $\text{CR}=7.8$ ) that has been designed and developed at the university of Lund. The receiver of the system is made of aluminium and has a V-shaped cross section, which allows two arrays of silicon solar cells to be adhered at the oblique surfaces. The cooling fluid (water) flows inside the receiver through a properly machined passage. From a thermal performance point of view, the optical efficiency and the heat loss coefficient of the system were measured equal to 45% and  $1.9\text{ W/}^\circ\text{C}\cdot\text{m}^2$ , respectively. The maximum electrical efficiency was 6.4%. Künnemeyer et al. [2.80] manufactured a static low-concentration V-trough CPVT module comprising four arrays of polycrystalline cells cooled by water flowing inside channels formed by the corrugated reflector frame. The overall efficiency of the system was in the order of 30%.

## 2.7 Solar angles and tracking

Since only the direct part of solar radiation can be reflected, it is necessary for concentrating solar systems with concentration ratios larger than 3 [2.81] to track the sun position during the daytime. The position of the sun in reference to a location with known spatial coordinates can be specified with the use of two angles referred to as the zenith  $\theta_z$  and the solar azimuth angle  $\gamma_s$ , respectively. As depicted in Fig. 2.12, the zenith angle is defined as the angle between the vertical and the line to the sun, whereas the solar azimuth angle is defined as the angular displacement from south of the projection of the sun's position on the horizontal plane. Analytical correlations for the determination of the solar angles at a specified location and time of the year can be found in various solar engineering handbooks [2.82, 2.83].

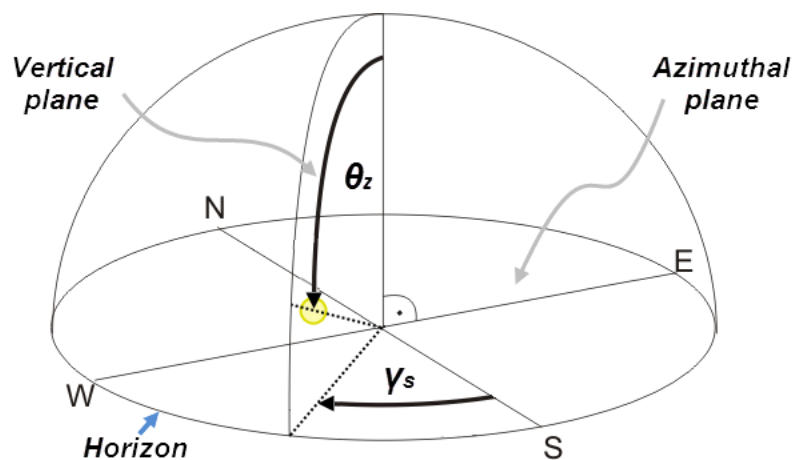
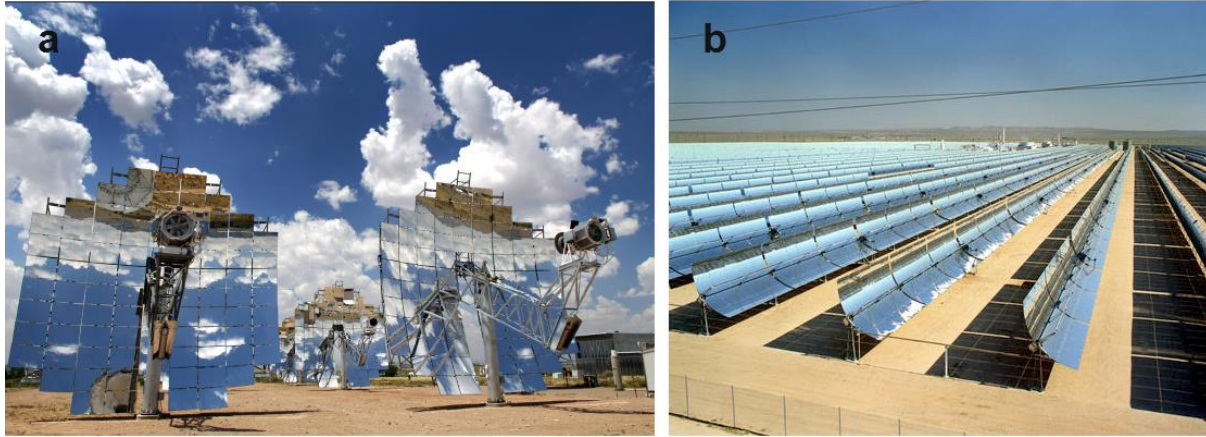


Fig. 2.12 Reference system for the position of the sun.

In order to maintain solar irradiation constantly perpendicular to the collector aperture, it is required that the solar position is followed along both the azimuthal and vertical planes (two-axes tracking). The incidence angle in the case of two-axes tracking is maintained equal to zero at all times and thus no optical losses associated with the collector orientation in relevance to the sun are introduced. Point-focus systems employ exclusively two-axes tracking systems, as the sunlight must be concentrated in a three-dimensional manner (**Fig. 2.13a**). On the other hand, linear-focus systems allow for single-axis tracking, along the vertical plane, which reduces the complexity of the utilized tracking system and thus the maintenance and operation cost (**Fig. 2.13b**).



**Fig. 2.13** Large-scale installations of (a) dual and (b) single-axis tracking concentrating solar power applications [2.84,2.85].

However single-axis tracking introduces optical losses, as the beam irradiation incidence angle  $\theta$  to the reflector aperture is generally not equal to zero. Two loss mechanisms are associated with single-axis tracking, known as cosine and end losses, respectively. Cosine losses arise, in the case of non-perpendicular incidence, as the irradiation flux intercepted by the reflector aperture is smaller in comparison to beam radiation, as depicted in **Fig. 2.10a**. The actual intercepted irradiation results as [2.86]:

$$G = G_b \cos \theta \quad (2.10)$$

where  $G_b$  is the direct beam radiation and  $\theta$  the incidence angle. In addition, as depicted in **Fig. 2.10b**, a part of the non-perpendicular irradiation is reflected beyond the edge of the receiver and consequently its initial part remains un-illuminated. The un-illuminated length  $l_e$  of the receiver can be calculated using the relation [2.86]:

$$l_e = f \tan \theta \quad (2.11)$$

where  $f$  is the focal length of the linear reflector. The contribution of end effects on the deterioration of the collector performance can be easily quantified through a correction factor:

$$\Gamma(\theta) = \frac{A_{rec,eff}}{A_{rec}} \quad (2.12)$$

where  $A_{rec,eff} = W_{rec}(l-l_e)$  is the receiver illuminated area. In general, the overall influence of non-perpendicular sunlight incidence on the efficiency of a concentrating system can be evaluated using the Incident Angle Modifier (IAM), as will be discussed in more detail in paragraph 6.3.2.3. The incidence angle that is required for the determination of the optical losses can be derived from the following simple analytical correlation for a linear, single-axis tracking, concentrating system at a specified time of the year and location. The system is also assumed to be horizontal, which is true in the vast majority of cases):

$$\cos \theta = \sin \delta \sin \phi + \cos \delta \cos \phi \cos \omega \quad (2.13)$$

where  $\delta$  is the sun declination,  $\phi$  is the location latitude and  $\omega$  is the hour angle. At a specified hour and day,  $\omega$  and  $\delta$  are known [2.84].

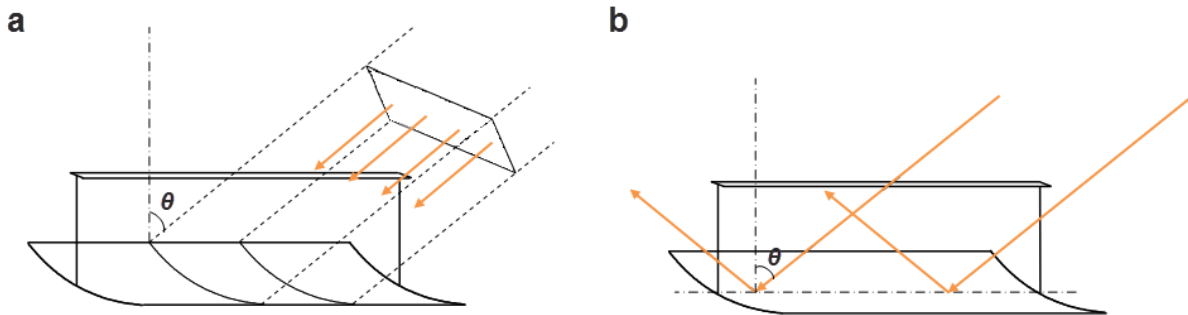


**Fig 2.10** Optical losses associated with single-axis tracking in a linear-focus system: (a) cosine losses, (b) end losses.

## 2.8 Concluding remarks

The discussion provided in this chapter leads to the deduction that although concentrating photovoltaics have reached the stage of commercial production, there are only few demonstration prototypes in regard to concentrating photovoltaic/thermal systems and the specific technology has not achieved a level of notable level of maturity until now. The main implementation issues that have been identified are the effect of the concentrated illumination distribution on the efficiency of the solar cells, the high temperature gradients that tend to develop within the receiver materials and the lack of innovative designs in respect to the cooling system.

The focus of the present work is to give further insight and to narrow the technological gap in respect to the implementation of CPVT systems. The main goal of the thesis is the successful development of a novel prototype CPVT system. The parabolic shape has been chosen for the concentrator, as it offers ease of manufacturing compared to paraboloid surfaces considering that it is actually a two dimensional shape extruded along the third dimension. Besides, it was considered that a parabolic trough with custom-made geometrical characteristics would be simpler to manufacture compared to a Fresnel lens, as it only requires machining of metallic items. In addition, parabolic concentrators usually achieve medium sunlight concentration ( $CR \approx 10-50$ ), which is preferable in the case of demonstration CPVT systems, as the receiver materials are not being subject to extreme

thermal loading that could compromise the reliable operation of the prototype system. Special effort has been made for the designation of the desired characteristics of the cooling system, as will be discussed in detail in the following chapter, so that the manufacturing of novel cooling devices of high thermal and hydrodynamic performance can be made feasible.

### Chapter references

[2.1] The German energy society, Planning and Installing Photovoltaic Systems: A Guide for Installers, Architects and Engineers, Earthscan, London, 2008, pp.23-52.

[2.2] M.S. Leite, Towards an optimized all lattice-matched InAlAs/InGaAsP/InGaAs multi-junction solar cell with efficiency > 50%, Appl. Phys. Letters 102, (2013) 033901.

[2.3] NREL, Research Cell Efficiency Records, March 2014, available at <http://www.nrel.gov/ncpv/>.

[2.4] C. Algora, Reliability of III–V concentrator solar cells, Microelectron. Reliab. 50 (2010) 1193–1198.

[2.5] S.A. Kalogirou, Solar Energy Engineering: Processes and Systems, first ed., Academic Press, San Diego, 2009, pp. 469-482.

[2.6] S.R. Wenham, M.A. Green, M.E. Watt, R. Corkish, Applied photovoltaics, second ed., Earthscan, London, 2007, pp. 31-54.

[2.7] M.E. Meral, F. Diner, A review of the factors affecting operation and efficiency of photovoltaic based electricity generation systems, Renew. Sustain. Energy Rev. 15 (2011) 2176–2184.

[2.8] A. Zahedi, Review of modelling details in relation to low-concentration solar concentrating photovoltaic, Renew. Sustain. Energy Rev. 15 (2011) 1609–1614.

[2.9] D.T. Cofas, P. a. Cofas, S. Kaplanis, Methods to determine the dc parameters of solar cells: A critical review, Renew. Sustain. Energy Rev. 28 (2013) 588–596.

[2.10] A. Mäki, S. Valkealahti, J. Leppäaho, Operation of series-connected silicon-based photovoltaic modules under partial shading conditions, Prog. Photovolt: Res. Appl. 20 (2012) 298-309.

[2.11] A. Blakers, Silicon concentrator solar cells and G. Martinelli, M. Stefancich, Solar cell cooling, in: A. Luque, V. Andreev (Eds.), Concentrator Photovoltaics, Springer Verlag, Heidelberg, 2007 pp. 51-66 and 133-149.

- [2.12] H. Cotal, C. Fetzer, J. Boisvert, G. Kinsey, R. King, P. Hebert, et al., III–V multijunction solar cells for concentrating photovoltaics, *Energy Environ. Sci.* 2 (2009) 174.
- [2.13] D. Barlev, R. Vidu, P. Stroeve, Innovation in concentrated solar power, *Sol. Energy Mater. Sol. Cells.* 95 (2011) 2703–2725.
- [2.14] IEC 62108:2007. Concentrator photovoltaic (CPV) modules and assemblies-design qualification and type approval. 1.0 ed., 2007.
- [2.15] K.K. Chong, S.L. Lau, T.K. Yew, P.C.L. Tan, Design and development in optics of concentrator photovoltaic system, *Renew. Sustain. Energy Rev.* 19 (2013) 598–612.
- [2.16] G. Zubi, J.L. Bernal-Agustín, G.V. Fracastoro, High concentration photovoltaic systems applying III-V cells, *Renew. Sustain. Energy Rev.* 13 (2009) 2645–2652.
- [2.17] D. Chemisana, Building integrated concentrating photovoltaics: A review, *Renew. Sustain. Energy Rev.* 15 (2011) 603–611.
- [2.18] A. Pereira, L. Dargent, G. Lorin, W. Schwartz, T. Baffie, C. Mangeant, et al., Electro-optical study of a  $\times 1024$  concentrator photovoltaic system, *Prog. Photovolt: Res. Appl.* 22 (2014) 383–393.
- [2.19] A. Gombert, I. Heile, J. Wüllner, T. Gerstmaier, A. Hakenjos, S. Van Riesen, M. Klein, M. Röttger, V. Bellini, Concentrator photovoltaic systems with AC system efficiencies > 23 % field proven, available at <http://www.cpvconsortium.org/cpvtechnology/resourcelibrary.aspx>.
- [2.20] A. Gombert, S.S. Gmbh, B. Str, Low Cost Reliable Highly Concentrating Photovoltaics – a Reality, *Photovolt. Spec. Conf. (PVSC)*, 2012 38th IEEE. (2011) 1651–1656.
- [2.21] K. Araki, T. Yano, Y. Kuroda, 30 kW concentrator photovoltaic system using dome-shaped Fresnel lenses., *Opt. Express.* 18 (2010) A53–A63.
- [2.22] P. Pérez-Higueras, E. Muñoz, G. Almonacid, P.G. Vidal, High Concentrator PhotoVoltaics efficiencies: Present status and forecast, *Renew. Sustain. Energy Rev.* 15 (2011) 1810–1815.
- [2.23] F.J. Gómez-Gil, X. Wang, A. Barnett, Energy production of photovoltaic systems: Fixed, tracking, and concentrating, *Renew. Sustain. Energy Rev.* 16 (2012) 306–313.
- [2.24] K. Saito, Y. Abiko, K. Toya, K. Mori, Y. Kogetsu, Development of Concentrator Photovoltaic System, *SEI Tech. Rev.* 76 (2013) 23–26.
- [2.25] F.L. Siaw, K.K. Chong, C.W. Wong, A comprehensive study of dense-array concentrator photovoltaic system using non-imaging planar concentrator, *Renew. Energy.* 62 (2014) 542–555.

- [2.26] A. Mojiri, R. Taylor, E. Thomsen, G. Rosengarten, Spectral beam splitting for efficient conversion of solar energy - A review, *Renew. Sustain. Energy Rev.* 28 (2013) 654–663.
- [2.27] A. Luque, G. Sala, J.C. Arboiro, T. Bruton, D. Cunningham, N. Mason, Some results of the EUCLIDES photovoltaic concentrator prototype, *Prog. Photovoltaics Res. Appl.* 5 (1997) 195–212.
- [2.28] M. Vivar, I. Antón, D. Pachón, G. Sala, Third-generation EUCLIDES concentrator results, *Prog. Photovolt: Res. Appl.* 20 (2012) 356-371.
- [2.29] M. O’Neill, J. McDanal, D. Spears, C. Stevenson, D. Gelbaum, Low-Cost 20X Silicon-Cell-Based Linear Fresnel Lens Concentrator Panel., *AIP Conf. Proc.* 1407 (2011) 120–124.
- [2.30] H. Baig, N. Sarmah, K.C. Heasman, T.K. Mallick, Numerical modelling and experimental validation of a low concentrating photovoltaic system, *Sol. Energy Mater. Sol. Cells.* 113 (2013) 201–219.
- [2.31] S. Hatwaambo, H. Hakansson, J. Nilsson, B. Karlsson, Angular characterization of low concentrating PV-CPC using low-cost reflectors, *Sol. Energy Mater. Sol. Cells.* 92 (2008) 1347–1351.
- [2.32] C.S. Sangani, C.S. Solanki, Experimental evaluation of V-trough (2 suns) PV concentrator system using commercial PV modules, *Sol. Energy Mater. Sol. Cells.* 91 (2007) 453–459.
- [2.33] G. Grasso, A. Righetti, M.C. Ubaldi, F. Morichetti, S.M. Pietralunga, Competitiveness of stationary planar low concentration photovoltaic modules using silicon cells: A focus on concentrating optics, *Sol. Energy.* 86 (2012) 1725–1732.
- [2.34] E. Muñoz, P.G. Vidal, G. Nofuentes, L. Hontoria, P. Pérez-Higueras, J. Terrados, et al., CPV standardization: An overview, *Renew. Sustain. Energy Rev.* 14 (2010) 518–523.
- [2.35] E. Cuce, P.M. Cuce, T. Bali, An experimental analysis of illumination intensity and temperature dependency of photovoltaic cell parameters, *Appl. Energy.* 111 (2013) 374–382.
- [2.36] J.L. Gray, The physics of the solar cell, in: A. Luque, S. Hegedus (Eds.), *Handbook of Photovoltaic Science and Engineering*, Wiley, Chichester, 2011, pp. 106-107.
- [2.37] E.T. Franklin, J.S. Coventry, Effects of highly non-uniform illumination distribution on electrical performance of solar cells, *Sol. Energy.* (2002) 2005–2008.
- [2.38] W.X.W. Xiao, W.G. Dunford, A. Capel, A novel modeling method for photovoltaic cells, 2004 IEEE 35th Annu. Power Electron. Spec. Conf. (IEEE Cat. No.04CH37551). 3 (2004) 1950–1956.
- [2.39] E. Skoplaki, J.A. Palyvos, On the temperature dependence of photovoltaic module electrical performance: A review of efficiency/power correlations, *Sol. Energy.* 83 (2009) 614–624.

- [2.40] A. Braun, E.A. Katz, J.M. Gordon, Basic aspects of the temperature coefficients of concentrator solar cell performance parameters, *Prog. Photovolt: Res. Appl.* 21 (2013) 1087-1094.
- [2.41] A. Vossier, D. Chemisana, G. Flamant, A. Dollet, Very high fluxes for concentrating photovoltaics: Considerations from simple experiments and modeling, *Renew. Energy.* 38 (2012) 31–39.
- [2.42] D. Chemisana, J.I. Rosell, Electrical performance increase of concentrator solar cells under Gaussian temperature profiles, *Prog. Photovolt: Res. Appl.* 21 (2013) 444-455.
- [2.43] D. Du, J. Darkwa, G. Kokogiannakis, Thermal management systems for Photovoltaics (PV) installations: A critical review, *Sol. Energy.* 97 (2013) 238–254.
- [2.44] A. Royne, C.J. Dey, D.R. Mills, Cooling of photovoltaic cells under concentrated illumination: A critical review, *Sol. Energy Mater. Sol. Cells.* 86 (2005) 451–483.
- [2.45] L. Micheli, N. Sarmah, X. Luo, K.S. Reddy, T.K. Mallick, Opportunities and challenges in micro- and nano-technologies for concentrating photovoltaic cooling: A review, *Renew. Sustain. Energy Rev.* 20 (2013) 595–610.
- [2.46] A. Royne, C.J. Dey, Design of a jet impingement cooling device for densely packed PV cells under high concentration, *Sol. Energy.* 81 (2007) 1014–1024.
- [2.47] J. Barrau, J. Rosell, D. Chemisana, L. Tadriss, M. Ibañez, Effect of a hybrid jet impingement/micro-channel cooling device on the performance of densely packed PV cells under high concentration, *Sol. Energy.* 85 (2011) 2655–2665.
- [2.48] M. Rahimi, E. Karimi, M. Asadi, P. Valeh-e-Sheyda, Heat transfer augmentation in a hybrid microchannel solar cell, *Int. Commun. Heat Mass Transf.* 43 (2013) 131–137.
- [2.49] T. Ho, S.S. Mao, R. Greif, The impact of cooling on cell temperature and the practical solar concentration limits for photovoltaics, *Int. J. Energy Res.* 35 (2011) 1250–1257.
- [2.50] P. Valeh-E-Sheyda, M. Rahimi, E. Karimi, M. Asadi, Application of two-phase flow for cooling of hybrid microchannel PV cells: A comparative study, *Energy Convers. Manag.* 69 (2013) 122–130.
- [2.51] X. Han, Y. Wang, L. Zhu, The performance and long-term stability of silicon concentrator solar cells immersed in dielectric liquids, *Energy Convers. Manag.* 66 (2013) 189–198.
- [2.52] L. Zhu, Y. Wang, Z. Fang, Y. Sun, Q. Huang, An effective heat dissipation method for densely packed solar cells under high concentrations, *Sol. Energy Mater. Sol. Cells.* 94 (2010) 133–140.
- [2.53] L. Zhu, R.F. Boehm, Y. Wang, C. Halford, Y. Sun, Water immersion cooling of PV cells in a high concentration system, *Sol. Energy Mater. Sol. Cells.* 95 (2011) 538–545.

- [2.54] Y. Sun, Y. Wang, L. Zhu, B. Yin, H. Xiang, Q. Huang, Direct liquid-immersion cooling of concentrator silicon solar cells in a linear concentrating photovoltaic receiver, *Energy*. 65 (2014) 264–271.
- [2.55] H.M. Henning, Solar assisted air conditioning of buildings - an overview, *Appl. Therm. Eng.* 27 (2007) 1734–1749.
- [2.56] G. Mittelman, A. Kribus, A. Dayan, Solar cooling with concentrating photovoltaic/thermal (CPVT) systems, *Energy Convers. Manag.* 48 (2007) 2481–2490.
- [2.57] J. Koschikowski, M. Wieghaus, M. Rommel, V.S. Ortin, B.P. Suarez, J.R. Betancort Rodríguez, Experimental investigations on solar driven stand-alone membrane distillation systems for remote areas, *Desalination*. 248 (2009) 125–131.
- [2.58] H. Chang, G.B. Wang, Y.H. Chen, C.C. Li, C.L. Chang, Modeling and optimization of a solar driven membrane distillation desalination system, *Renew. Energy*. 35 (2010) 2714–2722.
- [2.59] M.A. Hasan, K. Sumathy, Photovoltaic thermal module concepts and their performance analysis: A review, *Renew. Sustain. Energy Rev.* 14 (2010) 1845–1859.
- [2.60] V.V. Tyagi, S.C. Kaushik, S.K. Tyagi, Advancement in solar photovoltaic/thermal (PV/T) hybrid collector technology, *Renew. Sustain. Energy Rev.* 16 (2012) 1383–1398.
- [2.61] X. Zhang, X. Zhao, S. Smith, J. Xu, X. Yu, Review of R&D progress and practical application of the solar photovoltaic/thermal (PV/T) technologies, *Renew. Sustain. Energy Rev.* 16 (2012) 599–617.
- [2.62] T.T. Chow, A review on photovoltaic/thermal hybrid solar technology, *Appl. Energy*. 87 (2010) 365–379.
- [2.63] F. Chenlo, M. Cid, A linear concentrator photovoltaic module: analysis of non-uniform illumination and temperature effects on efficiency, *Sol. Cells* 20 (1987) 27–39.
- [2.64] C. Gibart, S.E. De Propulsion, Study of and tests on a hybrid photovoltaic-thermal collector using concentrated sunlight, *Sol. Cells* 4 (1981) 71–89.
- [2.65] J.S. Coventry, Performance of a concentrating photovoltaic/thermal solar collector, *Sol. Energy*. 78 (2005) 211–222.
- [2.66] M. Li, G.L. Li, X. Ji, F. Yin, L. Xu, The performance analysis of the Trough Concentrating Solar Photovoltaic/Thermal system, *Energy Convers. Manag.* 52 (2011) 2378–2383.
- [2.67] X. Yongfeng, L. Ming, W. Liuling, L. Wenxian, X. Ming, Z. Xinghua, et al., Performance analysis of solar cell arrays in concentrating light intensity, *J. Semicond.* 30 (2009) 084011.

- [2.68] J.I. Rosell, X. Vallverdú, M. a. Lechón, M. Ibáñez, Design and simulation of a low concentrating photovoltaic/thermal system, *Energy Convers. Manag.* 46 (2005) 3034–3046.
- [2.69] M. Vivar, V. Everett, M. Fuentes, A. Blakers, A. Tanner, P. Le Lievre, M. Greaves, Initial field performance of a hybrid CPV-T microconcentrator system, *Prog. Photovolt: Res. Appl.* 21 (2013) 1659-1671.
- [2.70] D. Chemisana, M. Ibáñez, J.I. Rosell, Characterization of a photovoltaic-thermal module for Fresnel linear concentrator, *Energy Convers. Manag.* 52 (2011) 3234–3240.
- [2.71] P.J. Sonneveld, G.L. a M. Swinkels, B. a J. Van Tuijl, H.J.J. Janssen, J. Campen, G.P. a Bot, Performance of a concentrated photovoltaic energy system with static linear Fresnel lenses, *Sol. Energy.* 85 (2011) 432–442.
- [2.72] M. Chaabane, W. Charfi, H. Mhiri, P. Bournot, Performance evaluation of concentrating solar photovoltaic and photovoltaic/thermal systems, *Sol. Energy.* 98 (2013) 315–321.
- [2.73] B. Du, E. Hu, M. Kolhe, Performance analysis of water cooled concentrated photovoltaic (CPV) system, *Renew. Sustain. Energy Rev.* 16 (2012) 6732–6736.
- [2.74] C. Kandilli, Performance analysis of a novel concentrating photovoltaic combined system, *Energy Convers. Manag.* 67 (2013) 186–196.
- [2.75] A. Kribus, D. Kaftori, G. Mittelman, A. Hirshfeld, Y. Flitsanov, A. Dayan, A miniature concentrating photovoltaic and thermal system, *Energy Convers. Manag.* 47 (2006) 3582–3590.
- [2.76] C. Kong, Z. Xu, Q. Yao, Outdoor performance of a low-concentrated photovoltaic-thermal hybrid system with crystalline silicon solar cells, *Appl. Energy.* 112 (2013) 618–625.
- [2.77] M. Brogren, P. Nostell, B. Karlsson, Optical efficiency of a PV thermal hybrid CPC module for high latitudes, *Sol. Energy* 69 (2000) 173-185.
- [2.78] J. Nilsson, H. Håkansson, B. Karlsson, Electrical and thermal characterization of a PV-CPC hybrid, *Sol. Energy.* 81 (2007) 917–928.
- [2.79] L.R. Bernardo, B. Perers, H. Håkansson, B. Karlsson, Performance evaluation of low concentrating photovoltaic/thermal systems: A case study from Sweden, *Sol. Energy.* 85 (2011) 1499–1510.
- [2.80] R. Künnemeyer, T.N. Anderson, M. Duke, J.K. Carson, Performance of a V-trough photovoltaic/thermal concentrator, *Sol. Energy.* 101 (2014) 19–27.
- [2.81] R. Winston, Principles of solar concentrators of a novel design. *Sol. Energy* 16 (1974) 89–95.
- [2.82] J.A. Duffie, W.A. Beckman, *Solar Engineering of Thermal Processes*, second ed., Wiley, New York, 1991 pp.10-31.

[2.83] W.B. Stine, R.W. Harrigan, Solar Energy Systems Design, Wiley, New York, 1986, Chap. 3, available at <http://www.powerfromthesun.net/>.

[2.84] Sandia Laboratory, Stirling Energy Systems set new world record for solar-to-grid conversion efficiency, 2008, available at <https://share.sandia.gov/news/resources/releases/2008/solargrid.html>.

[2.85] National Renewable Energy Laboratory, Solar Electric Generating Station III, 2013, available at [http://www.nrel.gov/csp/solarpaces/project\\_detail.cfm/projectID=30](http://www.nrel.gov/csp/solarpaces/project_detail.cfm/projectID=30)

[2.86] A.S. Hegazy, M.M. El-Kassaby, M.A. Hassab, Effect of parabolic trough solar collector orientation on its collection efficiency, Int. J. Sust. Energy 16 (1995) 173-183.



---

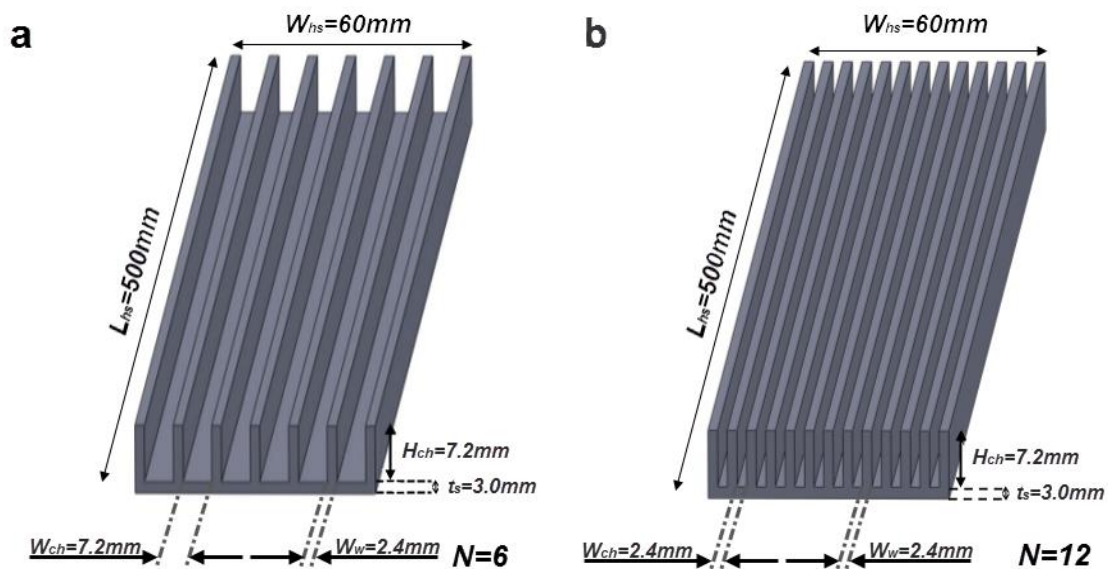
# Chapter 3 Investigation of cooling devices suitable for CPVT systems

---

## 3.1 Cooling configurations

The flow and heat transfer characteristics of heat-sink configurations suitable to serve as the active cooling system of a linear CPVT system will be numerically investigated in this chapter. The selection of the designs to be evaluated was primarily dictated by the structural constraints posed by the nature of the application, i.e. the cooling of a solar cell module, and the available manufacturing capabilities. From a manufacturing/structural point of view, the main criteria that were taken into consideration for the design of the cooling devices were the following:

- compact and lightweight layout
- reliable and leak-proof operation, viz. development of low internal pressure
- ease of fabrication using conventional machining and thus low cost
- convenient layout for thermal bonding to the solar cell module
- single inlet/single outlet arrangement for the cooling fluid so that the design of an elaborate manifold system is not required (in compliance to the criterion that the device must be compact)
- capability of the design to be scaled up, e.g. in order to be suitable for a linear CPVT system of larger overall length.



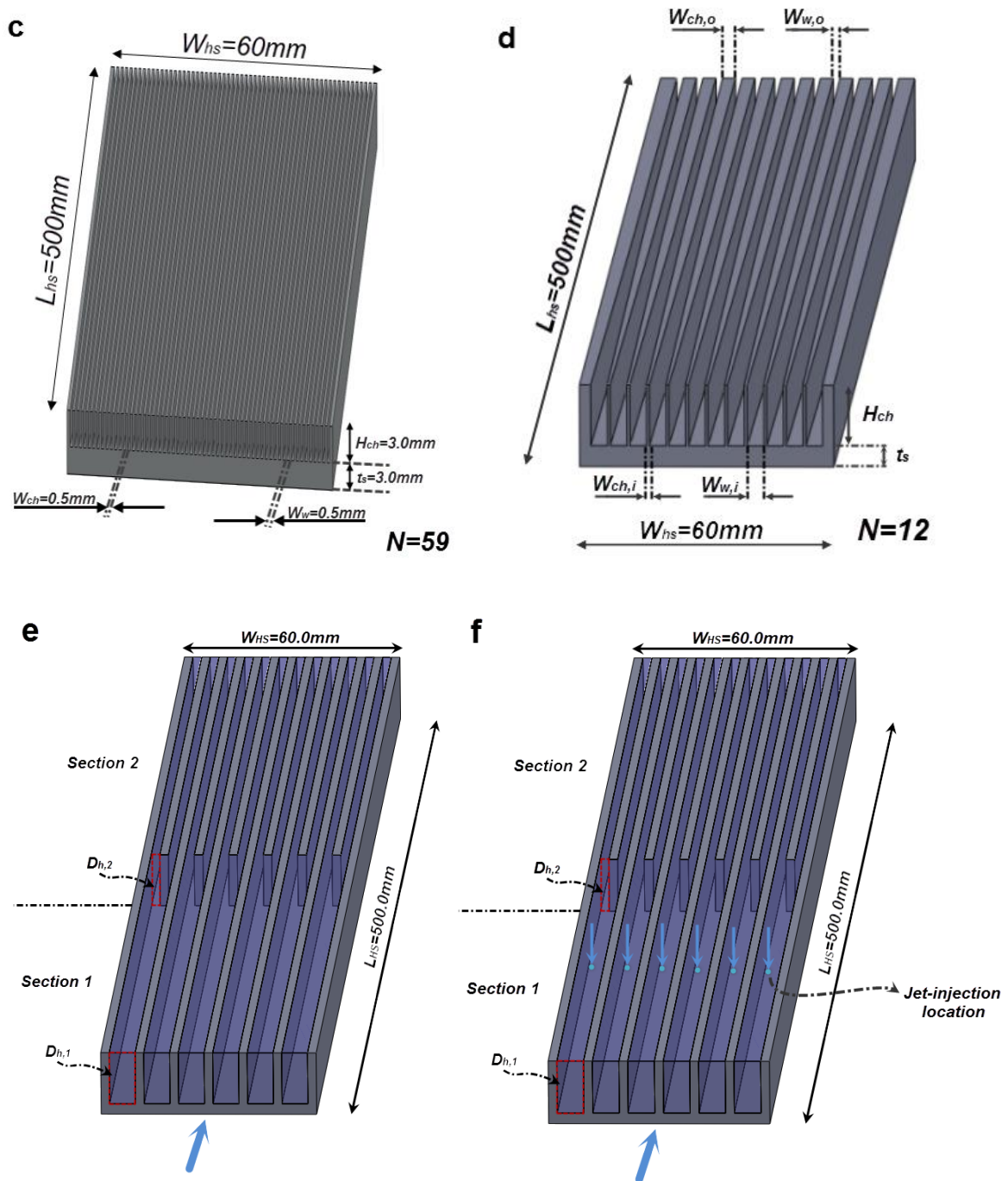


**Fig. 3.1** Geometric layout of the plate-fin heat sinks: (a)  $FW_l$  (low-fin density minichannels), (b)  $FW_h$  (high-fin density minichannels), (c)  $FW_\mu$  (microchannels), (d)  $VW_t$ , (e)  $VW$ , and (f)  $VW$ -JICF.

Apart from complying with the constraints posed above, the devices considered are evaluated in terms of thermal and hydrodynamic performance in order to designate the most efficient design. The following heat sink configurations have been evaluated in the course of the present thesis and relevant results will be presented in this chapter:

Plate-fin heat sinks (**Fig. 3.1**) employing:

- straight minichannels of rectangular cross-section ( $FW_l$ ,  $FW_h$ ) (**Figs. 3.1a-b**)
- straight microchannels of rectangular cross-section ( $FW_\mu$ ) (**Fig. 3.1c**)

- tapered minichannels of smoothly-varying channel width (VW<sub>t</sub>) (Fig. 3.1d)
- minichannels of stepwise-varying channel width (VW) (Fig. 3.1e)
- minichannels of stepwise-varying channel width and cold fluid injection (Jets In Cross-Flow or JICF) (Fig. 3.1f)

Tube-on-plate heat sinks (Fig. 3.2), employing serpentine tubing mounted on a rectangular plate with:

- a single U-bend or two-pass (2P) (Fig. 3.2a)
- consecutive U-bends or four-pass (4P) (Fig.3.2b)

and considering, in both cases, tubes partially or fully embedded within the plate.

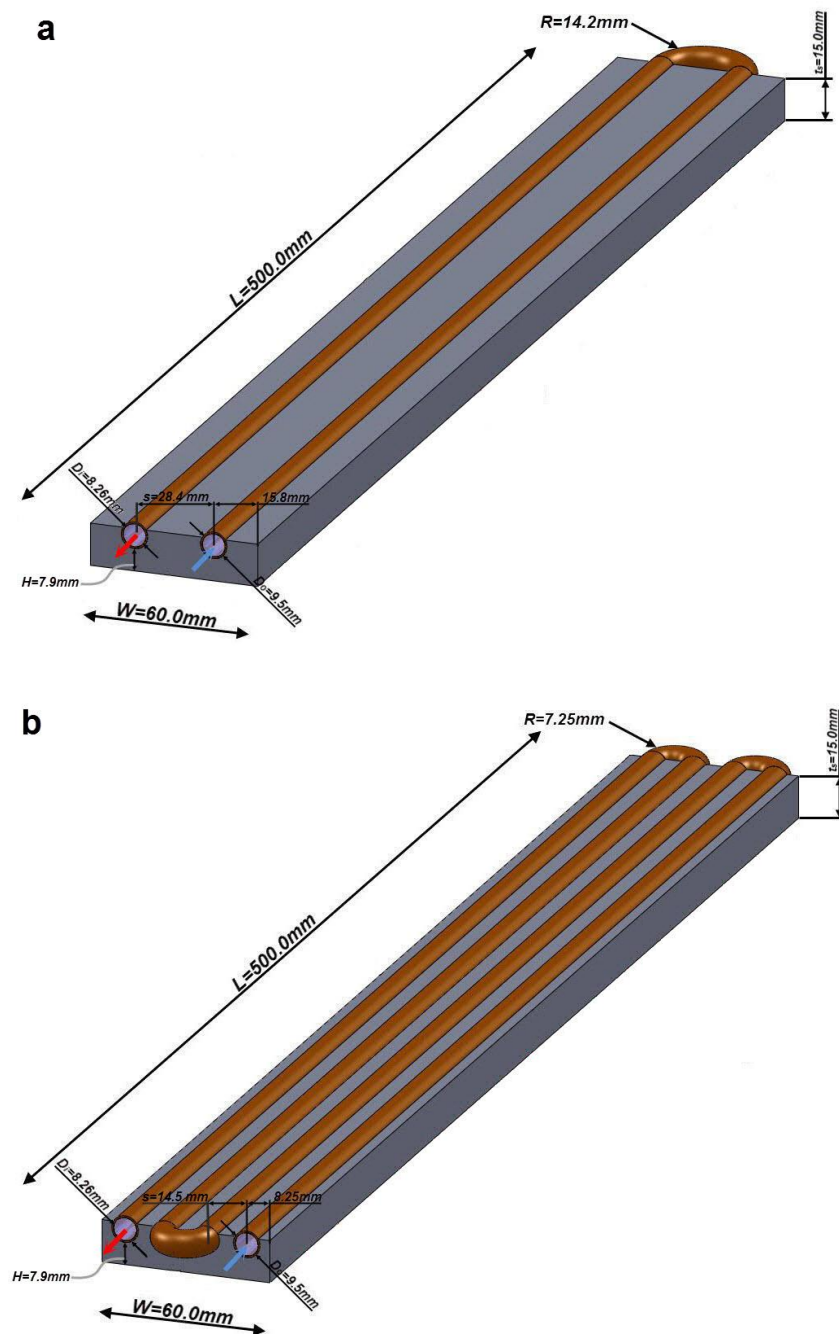


Fig. 3.2 Geometrical layout of the tube-on-plate configurations: (a) two-pass (2P), and (b) four-pass (4P).

### 3.2 Formulation of the numerical models

#### 3.2.1 Governing equations

The investigation in reference to the proposed cooling configurations is conducted in terms of three-dimensional numerical simulations. The typical governing equations associated with fluid flow and heat transfer that express the conservation of mass, momentum and energy are reduced to appropriate forms based on assumptions that have been established to be valid for heat-exchanging applications. Namely, the governing equations are simplified based on the following assumptions

- (1) steady fluid flow and heat transfer,
- (2) incompressible fluid,
- (3) negligible viscous dissipation and radiative heat transfer

As will be discussed in detail in the following paragraphs, the prevailing flow and heat transfer conditions differ in the examined cooling configurations. Based on the heat-sink layouts, laminar forced convection or laminar mixed convection is expected to occur in the plate-fin configurations, depending on the channel hydraulic diameter, while turbulent forced convection is expected in the tube-on-plate configurations, respectively. In the simplest case of laminar flow under forced convection conditions, the Navier-Stokes and energy equations obtain the following forms [3.1, 3.2]:

$$(continuity) \quad \frac{\partial \rho}{\partial t} + \nabla \cdot (\rho \vec{V}) = 0 \quad (3.1)$$

$$(momentum) \quad \frac{\partial}{\partial t} (\rho \vec{V}) + \vec{V} \cdot \nabla (\rho \vec{V}) = -\nabla p + \nabla (\mu \nabla \vec{V}) \quad (3.2)$$

$$(energy- fluid) \quad \frac{\partial}{\partial t} (\rho c_p T) + \vec{V} \cdot \nabla (\rho c_p T) = \nabla (k_f \nabla T) \quad (3.3)$$

$$(energy- solid) \quad \frac{\partial}{\partial t} (\rho_s C_s T_s) + \nabla (k_s \nabla T_s) = 0 \quad (3.4)$$

The effect of natural convection is not taken into account in the above formulated equations. However, in the case where buoyancy forces affect the flow field, the momentum equation must be modified accordingly:

$$(momentum) \quad \frac{\partial}{\partial t} (\rho \vec{V}) + \vec{V} \cdot \nabla (\rho \vec{V}) = -\nabla p + \nabla (\mu \nabla \vec{V}) + \Delta \rho \vec{g} \quad (3.5)$$

Where  $\Delta \rho = \rho - \rho_{ref}$  and  $\vec{g} = (0, -g, 0)$ . With reference to the fluid density, the Boussinesq approximation is applied [3.3]:

$$\rho - \rho_{ref} = -\rho_{ref} \beta (T - T_{ref}) \quad (3.7)$$

where  $\rho_{ref}$  is a reference density evaluated at a reference temperature  $T_{ref}$ .

With respect to turbulent flow under forced-convection heating conditions, case which refers to tube-on-plate configurations, the governing equations obtain the following forms [3.4]:

$$(continuity) \quad \frac{\partial \rho}{\partial t} + \frac{\partial}{\partial x_i} (\rho u_i) = 0 \quad (3.8)$$

$$(momentum) \quad \frac{\partial}{\partial t} (\rho \bar{u}_i) + \rho \frac{\partial}{\partial x_j} (\rho \bar{u}_i \bar{u}_j) = -\frac{\partial \bar{p}}{\partial x_i} + \frac{\partial}{\partial x_j} \left[ \mu \left( \frac{\partial \bar{u}_i}{\partial x_j} + \frac{\partial \bar{u}_j}{\partial x_i} \right) - \rho \overline{u'_i u'_j} \right] \quad (3.9)$$

$$(energy) \quad \frac{\partial}{\partial t} (\rho c_p \bar{T}) + \frac{\partial}{\partial x_i} (\rho c_p \bar{u}_i \bar{T}) = \frac{\partial}{\partial x_i} \left[ k \frac{\partial \bar{T}}{\partial x_i} - \rho c_p \overline{u'_i T'} \right] \quad (3.10)$$

The Reynolds Averaged Navier-Stokes (RANS) equations formulated above contain the Reynolds stresses terms  $-\rho \overline{u'_i u'_j}$  and the turbulent heat flux  $-\rho c_p \overline{u'_i T'}$ . The Shear Stress Transport (SST)  $k-\omega$  model introduced by Menter [3.5] is used for the calculation of these terms. The SST is a two-equation turbulence model based on the eddy-viscosity concept and thus the above mentioned terms are determined through the use of the turbulent viscosity  $\mu_t$ , which for the  $k-\omega$  model is defined as:

$$\mu_t = \rho \frac{k}{\omega} \quad (3.11)$$

where the turbulent kinetic energy  $k$  and the turbulent frequency  $\omega$  are determined by the additional transport equations introduced by the model. Furthermore, the SST model uses appropriate blending functions in order to switch between the  $k-\omega$  and the  $k-\varepsilon$  model formulations depending on the distance from the wall; therefore the  $k-\omega$  formulation is used in the near-wall region in order to avoid the use of any extra damping functions, while the  $k-\varepsilon$  formulation is used in the fluid-core region. The additional equations introduced for the turbulent kinetic energy  $k$  and the turbulent frequency  $\omega$ , as well as all the additional relations and coefficients used by the model are listed in [3.6, 3.7].

It must be noted that the transient term is included in the governing equations, **Eqs. (3.1)-(3.5) and (3.8)-(3.10)**, despite the fact that the flow and heat transfer are considered steady, as false transient time-stepping is used for the control of convergence, instead of explicit under-relaxation [3.7]. Thus, a proper physical time scale is selected in each case, equal to the 20% of the fluid residence time inside the heat sink in order to ensure convergence.

### 3.2.2 Boundary conditions

Appropriate hydrodynamic and thermal boundary conditions for the governing equations are imposed in accordance to the operating conditions of the heat sink. **Fig. 3.3** illustrates the computational domain for a simplified geometrical layout of the most common type of the heat sinks considered, along with the typical boundary conditions applied to the numerical models representing the considered cooling devices. It must be noted that the same types of boundary conditions apply to all the configurations, while the surfaces where they are imposed differ due to the layout of each heat sink and the possible existence of symmetry and will be specifically mentioned for each configuration

discussed in the following paragraphs. Besides, heat transfer was treated as conjugate in all cases with heat conduction and convection occurring in the solid and fluid domains, respectively.

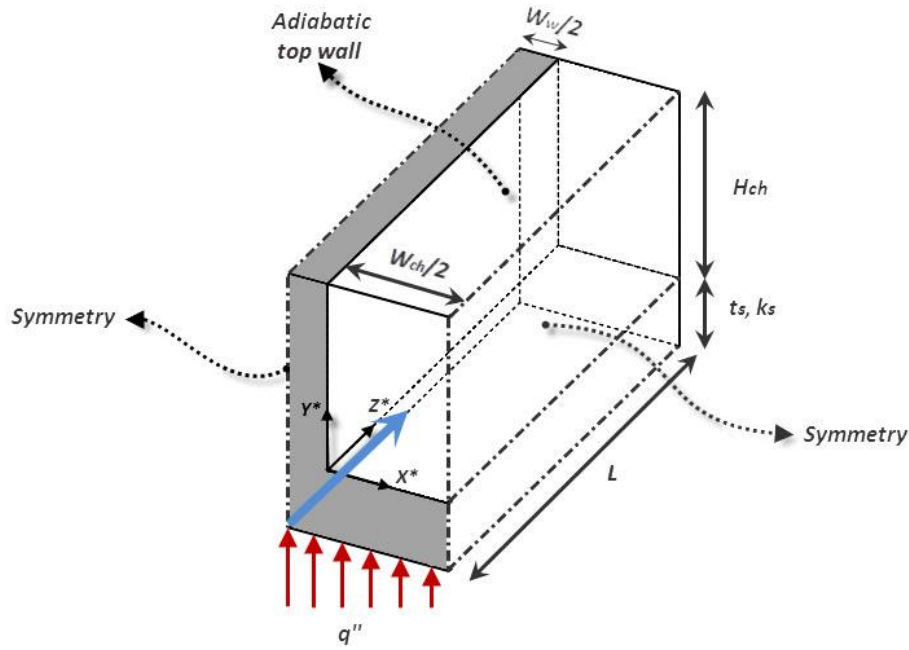


**Fig. 3.3** Computational domain for the simplified heat sink geometry.

The imposed boundary conditions as depicted in **Fig. 3.3** are the following:  
A uniform velocity profile is imposed at the prescribed inlet of the fluid domain:

$$z = 0, \quad w = w_i, \quad u = 0, \quad v = 0 \quad (3.12)$$

whereas the average static pressure is taken equal to zero at the domain outlet

$$z = L, \quad P_{ave} = 0 \quad (3.13)$$

A no-slip boundary condition is imposed on the fluid-wall interface:

$$u = v = w = 0 \quad (3.14)$$

A symmetry boundary condition (or adiabatic wall in the case of heat transfer) is applied on both the outer, parallel to the main flow, vertical planes of the domain. Furthermore, all the rest outer surfaces of the domain, apart from the bottom side, are also treated as adiabatic

$$\left. \begin{array}{l} x = -\frac{W_w}{2} \\ x = \frac{W_{ch}}{2} \\ z = 0 \\ z = L \\ y = H \end{array} \right\} -k_s \frac{\partial T}{\partial n} \Big|_w = 0 \quad (3.15)$$

At the bottom surface of the solid domain, a constant heat flux is applied:

$$y = -t_s, \quad -k_s \frac{\partial T}{\partial y} \Big|_w = q'' \quad (3.16)$$

The fluid temperature at the inlet is given, while at the outlet the temperature values are extrapolated using a constant gradient:

$$z = 0, \quad T_f = T_i \quad (3.17)$$

$$z = L, \quad \frac{\partial^2 T_f}{\partial z^2} = 0 \quad (3.18)$$

Finally, at the solid- fluid interface, continuity of both temperature and heat flux is imposed:

$$T_w \Big|_{int} = T_f \Big|_{int} \quad (3.19)$$

$$-k_s \frac{\partial T_w}{\partial n} \Big|_{int} = -k_f \frac{\partial T_f}{\partial n} \Big|_{int} \quad (3.20)$$

The set of governing equations along with the boundary conditions are fully coupled and solved simultaneously using the finite volume-based CFD package ANSYS CFX (v.13) [3.7].

### 3.2.3 Non-dimensional numbers

Three non-dimensional quantities are extensively used in **paragraph 3.4**, where the numerical results regarding the heat-sink configurations are presented, in order to demonstrate the prevailing flow and heat transfer conditions in each case. The quantities are namely the Reynolds, Archimedes and Nusselt numbers.

The Reynolds number used in this work is defined on the basis of the duct hydraulic diameter  $D_h$  as follows:

$$Re = \frac{\bar{w} D_h}{\nu} \quad (3.21)$$

where  $\bar{w}$  is the average flow velocity in the duct and  $\nu$  is the fluid dynamic viscosity. The hydraulic diameter is also used as the characteristic length scale in all the non-dimensional numbers reported. The tube internal diameter is used as length scale for circular cross sections, while the hydraulic diameter for rectangular cross-sections is defined as:

$$D_h = \frac{4A}{P} = \frac{2 \cdot w_{ch} \cdot H_{ch}}{(w_{ch} + H_{ch})} \quad (3.22)$$

where  $A$  and  $P$  are the duct cross-section and wetted perimeter, respectively. Especially regarding the configurations that do not maintain a constant cross-section, an averaged Reynolds number  $\overline{Re}$  is defined for the configurations of smoothly-varying tapered channels (**Fig. 3.1d**) based on the average channel hydraulic diameter, whereas, for the channels of stepwise-varying width (**Fig. 3.1e**), the different flow conditions in each heat-sink section  $i$  of constant hydraulic diameter are characterized by a different Reynolds number  $Re_i$ . The available theoretical correlations (e.g. in **[3.8]**) for the calculation of hydrodynamic and thermal quantities also make use of the duct hydraulic diameter as characteristic length and thus are used for comparison throughout the presented results.

The non-dimensional parameter that quantifies the relative strength of free and forced convection in mixed convection flows is the Archimedes number (also referred to as the Richardson number by other authors) defined as **[3.9]**:

$$Ar = \frac{Gr}{Re^2} \quad (3.23)$$

The Grashof number  $Gr$  is indicative of the magnitude of the buoyancy forces relative to that of the viscous forces **[3.9]**:

$$Gr = \frac{g\beta\bar{q}''D_h^4}{\nu^2 k_f} \quad (3.24)$$

where  $\bar{q}''$  is the average wall heat flux and  $\beta$  is the fluid volumetric thermal expansion coefficient.

The Nusselt number expresses the ratio of convective to conductive heat transfer normal to a specified boundary and constitutes an illustrative way to quantify the heat transfer rate inside the heat-sink configurations under different flow conditions. The distribution of the local Nusselt number values is utilized in the present analysis, in order to point out the effect of characteristic geometrical features of the configurations on the heat transfer rate. The local Nusselt number is defined as:

$$\overline{Nu}(Z^*) = \bar{h}(Z^*) \frac{D_h}{k_f} \quad (3.25)$$

The local convective heat transfer coefficient  $\bar{h}(Z^*)$  can be determined from the following relation:

$$\bar{h}(Z^*) = \frac{\bar{q}''(Z^*)}{\bar{T}_w(Z^*) - \bar{T}_f(Z^*)} \quad (3.26)$$

where  $\bar{q}''(Z^*)$  and  $\bar{T}_w(Z^*)$  are the circumferentially averaged wall heat flux and temperature values along the (non-dimensional) streamwise coordinate  $Z^*$ , which can be calculated, respectively, as follows:

$$\bar{q}''(Z^*) = \frac{1}{P} \int_P -k_s \left. \frac{\partial T}{\partial n} \right|_w dl \quad (3.27)$$

$$\bar{T}_w(Z^*) = \frac{1}{P} \int_P T_w dl \quad (3.28)$$

and  $P$  is the channel perimeter.  $\bar{T}_f(Z^*)$  is the local fluid bulk mean (mixing cup) temperature defined as:

$$\bar{T}_f(Z^*) = \frac{1}{\bar{w} A_{ch,cs}} \int_{A_{ch,cs}} w(x, y) T(x, y) dA_{ch,cs} \quad (3.29)$$

where  $\bar{w}$  is the mean, streamwise flow velocity inside the channel.

### 3.3 Selection of the main operating and geometrical parameters

The numerical investigation of the cooling devices has to be conducted in a uniform manner to allow for a straightforward comparison among them. Thus, all the heat-sink designs must be of the same overall dimensions and, in addition, they must operate under similar conditions. During the initial sizing of a CPVT system, the aperture area, which is a design variable, must be designated. As will be discussed in detail in **chapter 5**, the aperture area of the present CPVT system (module) was selected equal to 1.0m<sup>2</sup>. Considering that the typical “one-sun” normal incident solar irradiation on a sun-tracking plane for a clear day is equal to 1.0 kW/m<sup>2</sup> and postulating that the system optical losses are negligible ( $\eta_{opt}=1.0$ ), the irradiation on the system is 1.0 kW.

In a second stage, the overall dimensions of the heat sink had to be assigned, which would also determine the system geometrical concentration. The total active length of the heat sink was selected equal to 0.5 m, which is the maximum processing length that the milling machine used for the fabrication of the actual devices can handle in a single pass. The heat sink must have an adequate length, in order to allow for a measurable inlet-outlet temperature difference to be attained for a heat rate corresponding to the aperture area. The total width of the heat sink had to be maintained relatively small in order to avoid optical losses due to aperture shading by the receiver. In concentrating solar applications, the shading losses should not exceed 5% [3.10]. On the other hand, the heat sink cannot be made extremely slender for a number of practical reasons, such as:

- the need for device rigidity,
- the need for selection of an appropriate concentration ratio so that the solar cells can operate efficiently,

- prevention of possible solar radiation spillage if the solar band at the focal line is wider than the receiver,
- prevention of reduced thermal performance due to the decrease of the available heat transfer area.

Taking into account the technical aspects of suitable materials for the manufacturing of the solar-cell modules and the heat sink, the active width of the heat sink was selected equal to 0.06 m and consequently the system concentration ratio resulted equal to 33. The heat sink material selected for the present analysis is aluminum due to its high thermal conductivity ( $k_{al} = 237 \text{ W/mK}$ ), its corrosion resistance and its good machinability in conventional cutting processes. The excess heat to be extracted by the heat sink resulted equal to 850 W and the respective heat flux equal to  $28.33 \text{ kW/m}^2$  by considering the irradiation incident on the system aperture, whereas a rough estimate of the solar-cell modules efficiency was about 15%. Nevertheless, the absolute value of the imposed heat flux is not particularly important as the temperature values presented in the results are given in a non-dimensional form.

Water was selected as the cooling fluid with temperature at the heat sink inlet equal to the standard tap temperature ( $T_{f,in} = 298 \text{ K}$ ). The cooling fluid flow rate for the evaluation of the cooling devices was selected using a graphical optimization procedure proposed by Foli et al. [3.11] that results to minimal thermal resistance and pumping power for a specific cooling device. A one-dimensional model (discussed in detail in **paragraphs 3.6** and **4.2**) was developed, in order to calculate the device thermal resistance and required pumping power based on the heat sink geometrical and operating conditions. These two quantities ( $R_{th}$  and  $P_{pump}$ ) are indicative of the heat-sink thermal and hydrodynamic performance respectively, as will be discussed in **paragraph 3.6**. It must be noted that strictly heat sinks employing arrays of rectangular channels of equal channel width and fin thickness were considered for the optimization procedure. As depicted in **Fig. 3.4**, the quantities in question were plotted for a wide range of the cooling fluid flow rate and, as can be seen, they are of mutually opposing trends, both, nevertheless, tending to asymptotic values. According to the method, which is similar to the “intersection of asymptotes” method proposed by Bejan [3.12], the tangent lines must be drawn at the maximum (points A and B in **Fig. 3.4**) and minimum curvature points (points A' and B' in **Fig. 3.4**) of each curve and the intersection of the tangents corresponds to a specific value of the flow rate (points C and C' in **Fig. 3.4**). The optimal flow rate range lies between the two values produced by following this procedure for the thermal resistance and the pumping power curves.

In the present case, it was found that the minimum optimal flow rate is approximately equal to 30 mL/s ( $3 \cdot 10^{-5} \text{ m}^3/\text{s}$ ) for the three test cases considered, while the maximum flow rate lies in the range 58-65 mL/s. The minimum value of 30 mL/s was finally selected in order to produce a larger fluid temperature rise through the cooling device, as this would facilitate the subsequent experimental measurements. It was also taken into account that the volumetric flow rate that represents realistic operating conditions, as stated by the EN12975-2 [3.13] standard, for flat plate solar thermal collectors is equal to 20 mL/s. The thermophysical properties of water were regarded as constant in cases considered and were evaluated at the fluid overall mean temperature, which was estimated prior to the simulations through a global thermal balance.

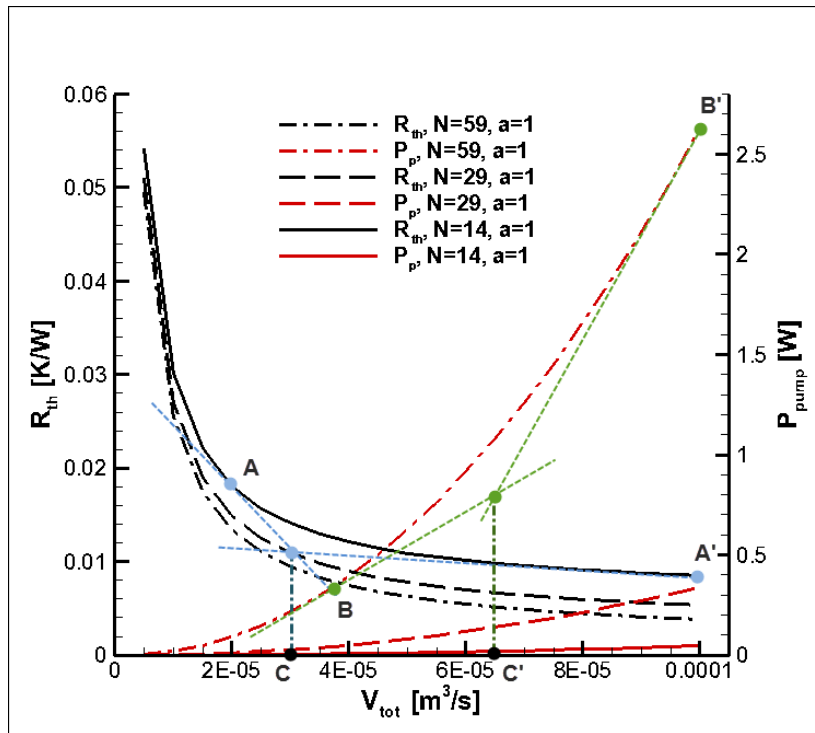


Fig. 3.4 Variation of the heat-sink thermal resistance and required pumping power with the cooling fluid volumetric flow rate.

### 3.4 Numerical investigation of the various configurations

The numerical results illustrating the flow and temperature fields that arise in the various cooling configurations considered are presented in this paragraph. In order to facilitate the interpretation of the results all the quantities of interest are presented in non-dimensional form and, furthermore, the coordinates are properly non-dimensionalized as  $X^*$  (horizontal direction),  $Y^*$  (vertical direction),  $Z^*$  (streamwise direction) using respective characteristic lengths for each configuration studied.

#### 3.4.1 Plate-fin heat sink with Fixed Width (FW) channels (Figs. 3.1a-c)

A practice commonly employed in various heat exchanging devices, in order to increase the overall heat transfer rate, is the use of extended surfaces, such as fins or pins, with a proper geometrical layout so that the ratio of the area available for heat transfer to the overall volume of the device is maximized. From a heat transfer point of view and for a constrained heat-sink width, it is beneficial to decrease the fin spacing, in order to employ as many additional heat-transfer surfaces as possible. The lower limit for the fin spacing is posed only by the manufacturing capabilities and it is feasible to construct plate-fin heat sinks employing channels with dimensions in the microscale ( $D_h \leq 1.0 \text{ mm}$ ). Although microchannel cooling is well-suited to the thermal management of electronics, its use can be extended to concentrating solar applications where there is also demand for high heat flux dissipation. Single phase liquid forced convection is the most commonly encountered flow condition in microchannel heat sinks [3.14]. However, two-phase or gas flow have also been considered as summarized in [3.15]. The preferred manufacturing materials for the devices are copper, aluminum and silicon.

Tuckerman and Pease [3.16] were the first to introduce the concept of liquid cooling by utilizing microchannels. They created three different heat sink configurations by chemically etching parallel channels onto silicon chips. Their experimental evaluation showed that the thermally superior configuration was able to dissipate a flux of  $790 \text{ W/cm}^2$ . Harms et al. [3.17] conducted an analytical and experimental evaluation of laminar flow and forced convection inside a heat sink of total dimensions  $2.5 \text{ cm} \times 2.5 \text{ cm}$  incorporating deep microchannels with an aspect ratio ( $H_{ch}/W_{ch}$ ) of 4.1. They pointed out that microchannels with a high aspect ratio exhibit enhanced thermal and hydrodynamic performance. Moreover, they demonstrated that the multiple-channel configuration exhibits superior thermal performance for a given pressure drop, in comparison to a single-channel heat sink designed for turbulent flow. The various methods available for the manufacturing of metallic microchannel heat sinks ranging from conventional machining to lithography were illustrated by Lu et al. [3.18]. The authors of [3.18] managed to manufacture copper microchannel heat sinks by compression molding with mold inserts. The experimental evaluation of the manufactured specimens showed that the experimental data for both the friction factor and overall Nusselt number were in agreement with conventional theory.

Park and Punch [3.19] experimentally evaluated the overall performance of microchannel heat sinks with hydraulic diameters in the range  $106\mu\text{m} < D_h < 307\mu\text{m}$  for Reynolds numbers up to 800. Regarding the induced pressure drop, their experimental results of the friction factor were in agreement with conventional theory. On the other hand, regarding heat transfer under constant heat flux conditions, the obtained average Nusselt number values deviated from the theoretical ones. The authors of [3.19] attributed these deviations to the effect of viscous dissipation. Wang and Feng [3.20] measured the overall Nusselt number for heat sink configurations with channel widths in the range 0.2-0.8mm for different heating conditions. Fully developed turbulent heat transfer was observed at a region of the Reynolds number in the range of 1000-1500. The transition was attributed to the effect of the fluid thermophysical properties on the local Reynolds number. Lee et al. [3.21] evaluated the thermal performance of microchannel heat sinks for a wide range of channel hydraulic diameters ( $D_h=318\mu\text{m}-903\mu\text{m}$ ) and Reynolds number ( $Re=300-3500$ ).

Experimental data and numerical predictions obtained using the continuum approach were found to be in close agreement. In a further study, Lee and Garimella [3.22] focused on the thermally developing flow in microchannels and derived correlations for predicting the local Nusselt number for a specified channel aspect ratio and dimensionless thermal entrance length. Peng and Peterson [3.23] presented experimental results for the friction factor and the average Nusselt number for microchannel single flow in both the laminar and turbulent flow regimes. The microchannels hydraulic diameters were in the range 0.133-0.367 mm and empirical correlations for the prediction of flow friction and heat transfer were proposed for the specified geometrical parameters. Jajja et al [3.24] evaluated the thermal performance of different heat sinks suitable for electronics' cooling with channel widths in the range 0.2-1.5mm. The heat sinks were made of copper and had the same fin thickness and channel height. The measurements showed that a very low thermal resistance of 0.033 K/W was achieved by the high channel density heat sink for a volumetric flow rate of 1 L/min.

Loh and Chu [3.25] compared experimental data for the pressure drop induced by minichannel heat sinks of different geometrical parameters against numerical predictions and commonly used theoretical correlations. It was concluded that both numerical results and Darcy correlations are valid for the prediction of the induced pressure drop. The thermal performance of a minichannel heat sink

has also been experimentally investigated in two-phase flow conditions by Wang et al. [3.26]. The experiments showed that the bubbles created due to fluid boiling were accumulated in the channel cross-section, reduced its wettability and thus the dissipated heat flux. Zhang et al. [3.27] manufactured three microchannel heat sink configurations of different geometrical layout using chemical etching and evaluated their transient thermal performance. The specimen employing U-shaped microchannels was proven to have the smallest response time for reaching steady state for a specified heat flux.

There is a large number of numerical studies in the available literature that discuss the thermohydraulic performance of microchannel heat sinks [3.28-3.41]. An early study by Fedorov and Viskanta [3.28] illustrated the temperature field and heat flux distribution inside a microchannel heat sink. Toh et al. [3.29] investigated the hydrodynamic and thermal performance of microchannel heat sinks with different hydraulic diameters under various flow and heating conditions. The thermophysical properties of the cooling fluid were considered as temperature dependent and the obtained numerical predictions compared well with experimental results. Chen et al. [3.30] and Zhuo et al. [3.31] evaluated the thermal performance of heat-sink configurations employing microchannels of triangular, rectangular and trapezoidal cross-sections. The trapezoidal microchannels were found to achieve superior thermal performance. A similar study was conducted by Gunnasegaran et al. [3.32], with the exception that a model of the entire heat sink was used, instead of a unit cell, in order to demonstrate that the temperature distribution along the heat sink width is uniform. Qu and Mudawar [3.33, 3.34] numerically investigated the three-dimensional laminar flow and heat transfer inside two heat sink configurations having channel widths of 57  $\mu\text{m}$  and 231  $\mu\text{m}$  with respective channel heights of 180  $\mu\text{m}$  and 713  $\mu\text{m}$ . Different heat sink materials were also selected for the two configurations, namely silicon and copper, respectively. The numerical analysis demonstrated that the average temperature rise along the flow direction, in both the fluid and solid part of the heat sink can be considered as linear. The numerical procedure was validated against the experimental evaluation that was also conducted for the second heat sink configuration, as close agreement was found between the predicted values and the experimental data for the heat sink temperature distribution and pressure drop.

The numerical results of Li et al. [3.35] regarding friction factor and Nusselt number values were in agreement with conventional theory. Numerical simulations were performed for both constant and variable fluid thermophysical temperatures and the predictions were validated using available experimental data. Choi et al. [3.36] conducted a comparative evaluation of microchannel heat sinks with channel walls of high aspect ratio ( $AR=8$ ) that have intermittent gaps. Two variations of the configurations were considered with one and two cooling fluid passages respectively. The numerical predictions, which were verified through experimental data for some of the configurations considered, showed that the introduction of gaps in the channel walls enhances heat transfer. The configurations with two passages and the higher gap density considered obtained a thermal resistance of 0.03 K/W for a mass flow rate of 2kg/min. Ryu et al. [3.37] formulated a three-dimensional numerical model and optimized the geometrical parameters of a microchannel heat sink in terms of thermal resistance for a constrained pumping power using a random search technique. It was found that the channel width had the most significant effect on thermal resistance.

Farnam et al. [3.38] examined the effect of the channel geometrical parameters on heat transfer under the constrain of constant pressure drop. A similar unconstrained investigation was performed by

Li and Peterson [3.39]. Kosar [3.40] focused on the effect of the substrate material on the heat sink thermal behavior. The Nusselt number distribution for low conductivity materials was found to deviate from the expected for constant heat flux heating due to the significant effect of axial heat transfer. Wei et al. [3.41] illustrated the effect of geometry deviation from a perfect rectangular cross section, which could result due to limitations of the manufacturing procedure, on pressure drop and heat transfer. It was shown that a 5° angle in the fin slope (fin with an angle larger than 90°) results to slightly (7%) lower pressure drop and up to 45% decreased thermal performance in comparison to rectangular channels.

Finally, two-layered, stacked microchannel heat sinks in cross-flow have also been evaluated, and it was established that the solid temperature increase along the heat-sink length is less steep in comparison to single-layer ones. Hence lower thermal resistance and increased performance can be achieved [3.42, 3.43].

A theoretical approach for the performance prediction of microchannel heat sinks was followed by a number of researchers [3.44-3.47]. Tsai and Chen [3.44] proposed a one-dimensional model in order to predict the thermal and hydrodynamic performance of a microchannel heat sink. The model was validated against experimental results. Fischer and Torrance [3.45] used a one-dimensional model to optimize the cross section curvature of non-rectangular channels in terms of thermal resistance. Zhao and Lu [3.46] used a fin approach, a porous medium approach and a two-dimensional numerical simulation to predict the temperature distribution and the overall Nusselt number achieved by a microchannel heat sink. Kim et al. [3.47] also used one and two-equation theoretical models for the prediction of heat transfer in microchannel heat sinks.

In general, the open literature is quite extensive on the subject of microchannel cooling and additional references concerning the flow and heat transfer inside microchannels can be found in review papers on high heat flux cooling technologies such as those by Agostini et al. [3.48], Ebadian and Lin [3.49] and Khandlikar and Bapat [3.48]. In the review article by Agostini et al. [3.48], it is concluded that the major drawback of microchannel cooling is the increased required pumping power. Ebadian and Lin [3.49] report that a heat flux removal up to 1430 W/cm<sup>2</sup> can be achieved by the use of microchannels, however the associated pressure drop penalty is also emphasized by the authors. Khandlikar and Bapat [3.50], after reviewing the open literature on jet impingement, microchannel and spray cooling, state that the use of microchannels is at the moment the most viable option for high-flux removal. A review of the most common configurations with different geometrical layouts of extended surfaces, such as annular, elliptical, longitudinal and pin fins, can be found in [3.49]. Experimental studies regarding single or two-phase flow and heat transfer in minichannels and microchannels of various cross sections were summarized by Mehendale et al. [3.52]. It is interesting to mention that most studies included in [3.52] report flow transition to the turbulent regime for a critical value of the Reynolds number approximately equal to  $Re_c=2300$ . In addition, the authors reported a number of methods suitable for manufacturing heat sinks in the microscale.

More recently, Dey et al. [3.53] reviewed a number of experimental studies conducted in reference to micro-flows. The authors distinguished the studies based on whether their findings were in agreement with classical macroscale theory regarding flow friction and heat transfer or not. It was reported that especially for smaller channel hydraulic diameter the effect of wall roughness on both pressure drop and heat transfer could be significant even in the laminar flow regime. The effect of surface roughness on microchannel flow and heat transfer is also discussed in [3.54-3.55]. Wagner and

Khandlikar [3.54] state that relative roughness  $\varepsilon/D_h$  is indicative of the effect of surface roughness on fluid flow. In addition, Shen et al. [3.55] measured lower values of the Nusselt number than the ones predicted by theory for a channel surface relative roughness equal to 4-6%. In the review article by Khan and Fartaj [3.56] it is stated that the classical correlations for liquid fluid friction are valid for a channel hydraulic diameter in the range  $0.25\text{mm} \leq D_h \leq 1.00\text{mm}$ , whereas the conventional correlations can predict heat transfer for a hydraulic diameter even as small as 0.001mm. The authors also inferred that a possible cause for the deviation between a number of experimental findings and theory is the effect of measurement uncertainty and especially to that associated with the actual dimensions of the microscale geometry.

Furthermore, the effect of axial conduction in the fluid region regarding flow in microchannels is non-negligible for low values of the Peclet number ( $Pe < 100$ ) and for configurations with thick walls and low channel length-to-height ratio [3.57]. Rosa et al. [3.58] thoroughly reviewed the possible causes for the discrepancies observed between experimental findings and theory. The authors reached the solid conclusion that flow in microchannels can be fully predicted by conventional theory provided that the effect of various parameters, such entry length, temperature dependent properties and surface roughness, which can be considerable when microscale geometries are in question are properly taken into consideration. In addition, the thermohydraulic performance of multiple-channel heat sinks is more probable to deviate from theory due to flow maldistribution and three-dimensional conjugate heat transfer arising from the manufacturing non-ideality of the actual configurations.

The effect of natural convection is negligible in microchannels due to the small length scale but can be considerable in channels with hydraulic diameter in the mini-scale. Heat transfer under mixed convection conditions in horizontal rectangular channels has been investigated by few researchers. Cheng et al. [3.59] theoretically investigated laminar mixed convection of a large Prandtl fluid in horizontal channels under constant heat flux. They demonstrated that the buoyancy effect enhances heat transfer and reduces the thermal entry length in comparison to pure forced convection. Furthermore, they concluded that the characteristic minimum that appears in the Nusselt number distribution at the thermally developing flow region is due to the combined entry- and secondary-flow effect. Nonino and Del Giudice [3.60] applied a finite-element procedure to predict laminar water flow and mixed convection in a duct of aspect ratio 0.5, under asymmetrical heating on different sides of the duct by means of a uniform heat flux. In the cases of two-surface heating they observed oscillations in the local Nusselt number, which they attributed to the instability of the temperature distribution on the heated walls. Chou [3.61] introduced a vorticity-velocity formulation of the Navier-Stokes equations to numerically examine the effect of the circumferential heat flux distribution on the laminar mixed convective air flow in a square duct. The greatest heat transfer enhancement was found to occur for a channel where the lower symmetrical half relative to the center-plane of the cross section had conductive walls, while the upper half was kept adiabatic. In a later study, Chou [3.62] focused on the heating of a rectangular channel under the thermal boundary condition of axial constant heat flux with circumferentially uniform wall temperature. The author considered thermal developing flow of air and water inside horizontal channels of various aspect ratios, ranging from 0.2 to 5, and it was demonstrated that, for high Rayleigh numbers, the Nusselt number distribution exhibits two local extrema and that the local maximum value occurs close to the location of the secondary flow maximum intensity. In general, it was concluded that the secondary flow induced by buoyancy significantly enhances heat transfer.

The results presented in this paragraph refer to plate-fin configurations comprising parallel channel arrays of different hydraulic diameters. The main objectives are to illustrate the emerging flow and temperature fields and to clarify the effect of the channel length scale on the basic flow and heat transfer characteristics.

### 3.4.1.1 Geometry and computational domain

The layout of the three FW configurations considered, along with their basic geometrical parameters are depicted in **Figs. 3.1a-c**. The heat sinks are denoted as  $FW_l$  (low-fin density),  $FW_h$  (high-fin density) and  $FW_\mu$  (microchannels) with corresponding hydraulic diameters of 9.60 mm, 4.11 mm and 0.86 mm, respectively. Mixed convection conditions are expected to occur in the  $FW_l$  configuration as the Archimedes number was calculated equal to 1.24 indicating that the inertial and buoyancy forces are nearly counterbalanced. On the other hand, the Archimedes number is negligibly small in the other two configurations and pure forced-convection conditions are expected to prevail.

The simulation of the entire configuration bears a great computational cost, especially in the case of the microchannel heat sink. By taking advantage of the existing symmetry instead, the computational domain is reduced to half of the microchannel width and half of the fin thickness [**3.22, 3.29, 3.35, 3.37, 3.43**], having the form depicted in **Fig. 3.3**, whereby the top lid thickness is not included in the domain. Considering the upper surfaces of the heat sink as adiabatic is actually an accurate representation of the real heating conditions. It is impossible to manufacture the heat sink as a one-piece component using conventional machining. Consequently, the heat sink is manufactured with its upper part open and the top lid is subsequently attached in place, usually by welding or mechanically clamping its edges to the two extreme fins of the heat sink body. The top lid is not in direct contact to the inner fins and thus there is no thermal bond between them which would have led to significant contact thermal resistance and significantly hindered heat transfer.

In order to further reduce the computational time, the domain for the microchannel configuration was truncated to a total length of  $L=0.1\text{m}$ , which exceeds the thermal entry length by more than five times. This simplification is valid since the pressure distribution and both the bulk fluid and bottom wall temperature distribution in the fully-developed region are linear along the flow direction [**3.8**]. The set of governing equations (**3.1**), (**3.3**)-(**3.5**) along with the boundary conditions, **Eqs. (3.12)-(3.20)** were solved on the computational domain, with a convergence criterion of  $10^{-6}$  set for the root mean square (RMS) mass, momentum and energy residuals.

### 3.4.1.2 Validation of the numerical model

Prior to the presentation of the numerical results, it is essential to confirm that the developed numerical model (as formulated in **paragraph 3.3**) can accurately predict the laminar flow and heat transfer in microchannels. For this reason, the experimental data presented by Qu and Mudawar [**3.34**] for the streamwise wall temperature distribution of a microchannel heat sink were compared against the predictions produced by the numerical model for a computational domain, depicted in Fig. 3.4a, that matched the dimensions of the actual test device. The authors did not construct a separate heat sink test device but instead machined twenty-one microchannels of hydraulic diameter equal to 353  $\mu\text{m}$  directly onto a copper block which also served as housing for the cartridge heaters that provided

the constant heat flux heating. As can be noticed in the computational domain, three rectangular slots were cut laterally from the actual copper block, in order to provide a more uniform heat flux distribution, as stated by the authors. Wall temperature was measured exactly at the same height as the top edge of the slots, as shown in **Fig. 3.5a**. The experimental evaluation covered a wide range of flow conditions within the laminar regime and furthermore two values (100 and 200 W/cm<sup>2</sup>) were considered for the imposed heat flux. **Figs 3.5b-c** present the axial wall distribution produced by the numerical model along with the experimental measurements in four streamwise locations. Good agreement is established and the predictions are expected to lie within the experimental uncertainty associated with the measured quantities and especially with the microchannel dimensions due to the manufacturing precision, which cannot be less than 20µm for conventional machining. Nevertheless, the experimental uncertainties were not reported by the authors of [3.34]. The local minima that can be discerned in the numerical results are due to the effect of the slots on the temperature field, as their axial locations coincide with the respective locations of the slots (see also **Fig. 3.5a**).

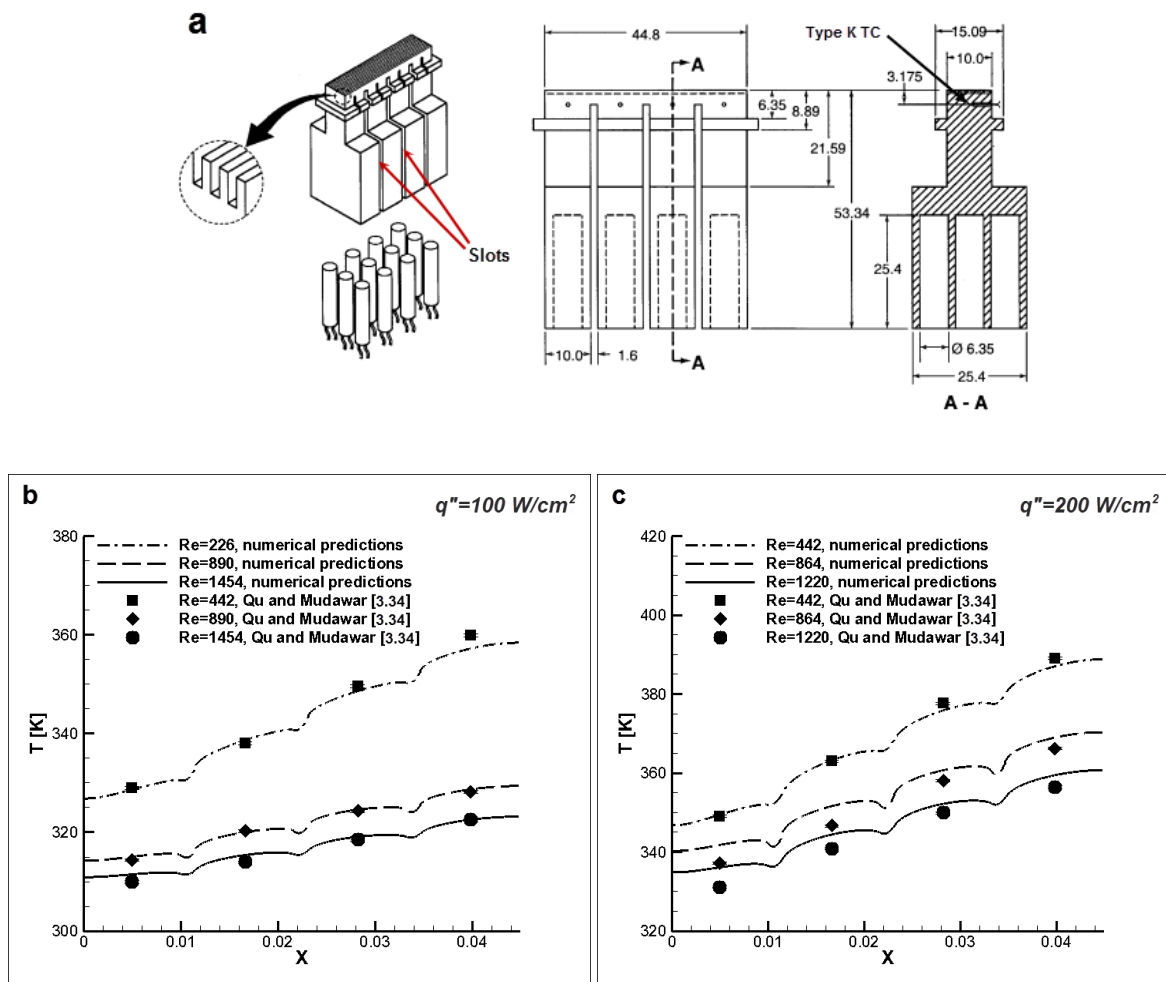


**Fig. 3.5** (a) Experimental setup of [3.34]. Comparison of the numerical predictions for a single microchannel against the experimental results of [3.34]. Longitudinal temperature distribution of the solid substrate: (b)  $q=100 \text{ W/cm}^2$ , (c)  $q=200 \text{ W/cm}^2$ .

3.4.1.3 Grid independence study

The computational domain was discretized using a structured hexahedral grid. The grid was locally refined toward the channel inlet, where the flow is hydrodynamically and thermally developing, as depicted in **Fig. 3.6a**. A non-uniform grid arrangement was employed across the domain cross-section as the grid was locally refined in the near-wall regions (**Fig. 3.6b**), in order to capture the steep velocity and temperature gradients. Numerical tests were conducted using grids of increased density in order to verify the grid independence of the results. The comparative results regarding the overall fluid pressure drop, the maximum bottom wall temperature and the overall value of the Nusselt number, respectively, for the three FW configurations are presented in **Table 3.1**. As can be seen, the intermediate grid used in each case is adequate for the production of accurate values of the quantities in question (maximum discrepancy of 1.6% with respect to the fine grid results for the case of the microchannels) and hence was used to produce the results presented below.

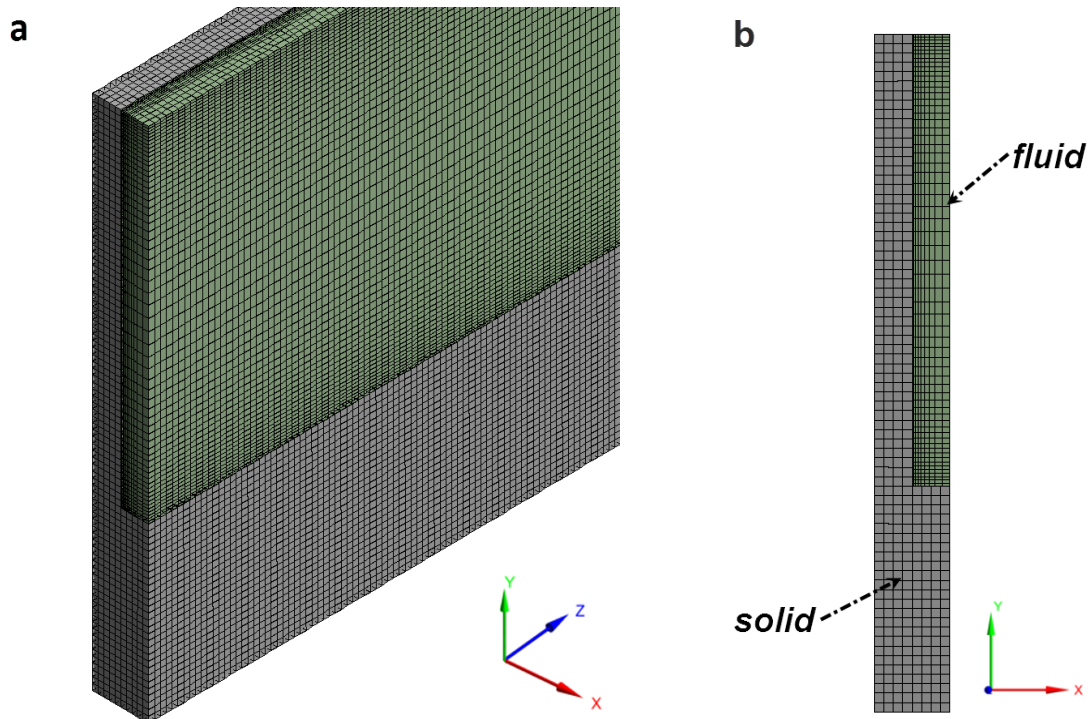


**Fig 3.6** Topology of the computational grid employed for the unit cell of the FW configurations: (a) detail view at the channel inlet and (b) cross-sectional view.

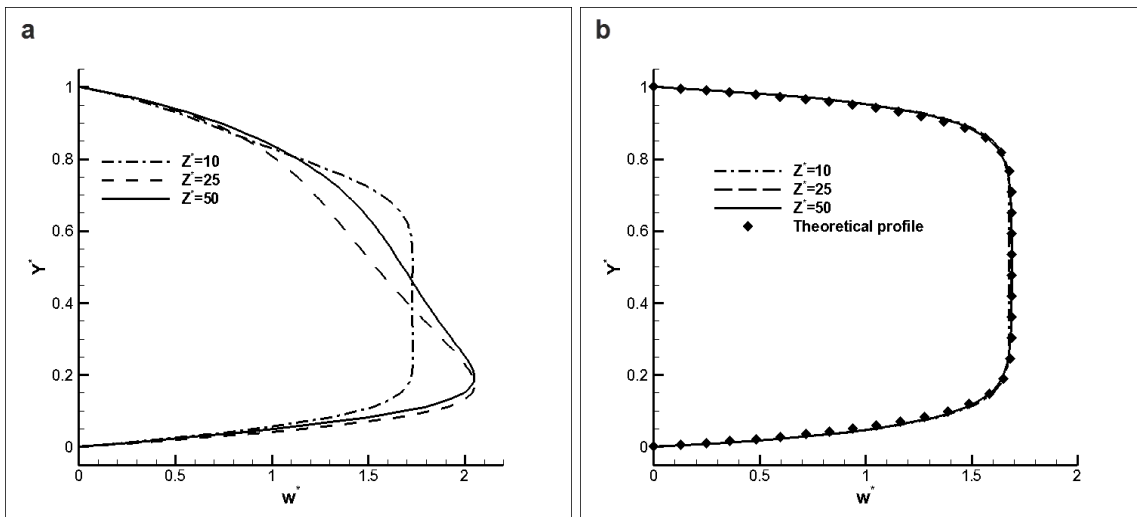
**Table 3.1** Grid independence study for the straight-channel configurations.

<b>FW<sub>h</sub></b>	<b>Coarse</b>	<b>Intermediate</b>	<b>Fine</b>
Elements	$1.00 \cdot 10^6$	$1.52 \cdot 10^6$	$2.37 \cdot 10^6$
Pressure drop [Pa]	74.0	74.3	74.8
T <sub>max</sub> [K]	310.0	310.1	310.0
Nu [-]	7.36	7.41	7.46
<b>FW<sub>l</sub></b>	<b>Coarse</b>	<b>Intermediate</b>	<b>Fine</b>
Elements	$0.9 \cdot 10^6$	$1.46 \cdot 10^6$	$2.08 \cdot 10^6$
Pressure drop [Pa]	10.3	10.6	10.8
T <sub>max</sub> [K]	315.5	315.6	315.8
Nu [-]	12.48	12.66	12.66

$FW_{\mu}$	Coarse	Intermediate	Fine
Elements	$1.00 \cdot 10^6$	$1.67 \cdot 10^6$	$2.34 \cdot 10^6$
Pressure drop [Pa]	7459.0	7668.5	7789.5
$T_{\max}$ [K]	306.3	306.3	306.3
Nu [-]	6.47	6.47	6.54

3.4.1.4 Flow and temperature fields

The results referring to the FW configurations are presented in a comparative manner. In order to have a clearer outlook on the effect of geometry on the flow development, the convention has been made to non-dimensionalize the streamwise coordinate using the hydraulic diameter of the  $FW_1$  configuration for all cases. The development of the vertical profile of the axial velocity in each configuration is presented in **Fig. 3.7**. In reference to the  $FW_1$  het sink (**Fig. 3.7a**), it is evident that the profiles are asymmetric with the maximum axial velocity obtained approximately at  $Y^*=0.2$ . The distorted profile shape is indicative of the effect of the buoyancy forces, which is manifested as a distinct secondary flow pattern (longitudinal rolls). The topology of the secondary flow is discussed in detail in **paragraph 3.4.3.9**. On the other hand, the profiles corresponding to the  $FW_h$  and  $FW_{\mu}$  configurations (**Figs. 3.7b-c**) exhibit a flat symmetrical form typical of rectangular channels with high aspect ratio. It is evident that the fully developed profiles are in perfect agreement with theoretical predictions **[3.8]**. Besides, the flow reaches hydrodynamic full development very rapidly, especially in the case of the microchannel heat sink, where a fully developed profile could be already detected 4.8cm ( $Z^*=5$ ) downstream of the inlet.



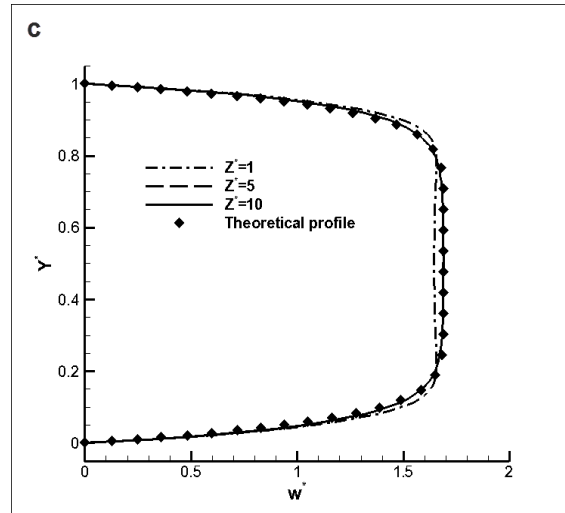


**Fig. 3.7** Vertical velocity profile development: (a)  $FW_1$ , (b)  $FW_h$ , (c)  $FW_\mu$ .

The temperature field that develops in the fluid and solid regions of the heat sinks is illustrated in **Fig. 3.8**. The cross-sectional temperature contours at the streamwise location  $Z^*=10$  (**Fig. 3.8a**) reveal that the temperature fields that arise within the  $FW_h$  and  $FW_\mu$  heat sinks are qualitatively similar, whereas the respective field arising within the  $FW_1$  configuration exhibits some distinct variations. As can be seen in the contour plot referring to the  $FW_1$  configuration, the fluid core maintains the inlet temperature, while a considerably thicker boundary layer in comparison to the  $FW_h$  and  $FW_\mu$  configurations develops at the near wall region, which is indicative of the inferior thermal performance of the  $FW_1$  heat sink. In addition, the effect of natural convection ( $Ar=1.24$ ) due to which water of higher temperature is pushed toward the upper part of the channel causes the upper thermal boundary layer to attain a larger thickness than the lower one. On the contrary, the fluid core is heated in the other two configurations and the minimum wall-fluid temperature difference occurs in the  $FW_\mu$  heat sink. In fact the flow has reached full thermal development in the case of the  $FW_\mu$  heat sink. As shown in **Fig. 3.8b**, the lateral temperature gradient at the channel bottom wall ( $Y^*=0$ ) is negligible in all configurations and therefore it can be deduced that the heat flow is exclusively in the upward direction, hence maintaining the solid substrate temperature uniform across its width.

In reference to the temperature gradient along the streamwise direction, the  $FW_1$  configuration exhibits a steep gradient in the developing flow region close to the channel inlet and subsequently the rate of temperature change decreases considerably. On the contrary, the temperature gradient remains relatively constant for the larger channel part in the  $FW_h$  and  $FW_\mu$  configurations. **Fig. 3.8c** depicts the streamwise distribution of the circumferentially averaged wall temperature. The steep increase of the wall temperature in the first part of the  $FW_1$  channel ( $Z^*<10$ ) is once again evident. Downstream of  $Z^*=10$  the temperature increase rate is much smaller due to the beneficial influence of the buoyancy-induced secondary flow on heat transfer. Regarding the  $FW_h$  configuration, two regions of non-linear and linear temperature increase can be discerned in the distribution marking the developing ( $Z^*<12$ ) and fully developed flow regions ( $Z^*>12$ ), respectively. Besides, the solid temperature increases in a linear manner throughout approximately the entire length of the  $FW_\mu$  configuration as the flow reaches full thermal development very rapidly. As expected the  $FW_\mu$  heat sink achieves the lowest wall maximum temperature, primarily due to the additional heat transfer surfaces and secondarily due to the accelerated flow in comparison to the two other configurations.

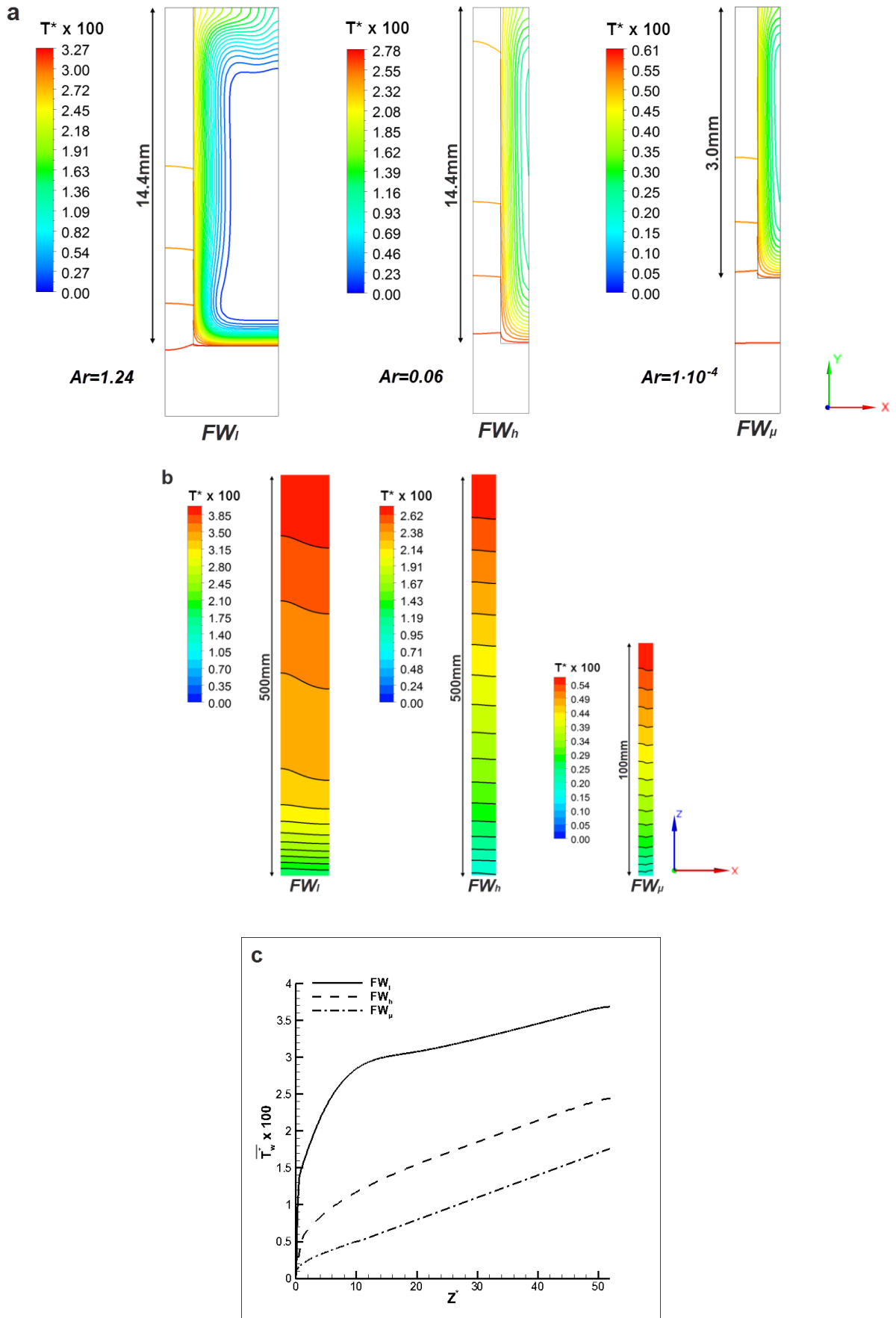


**Fig. 3.8** Temperature contour plots: (a) at the channel cross section ( $Z^* = 10$ ) and (b) at the channel bottom wall. (c) Streamwise distribution of the wall temperature.

**Fig. 3.9a** presents the circumferentially averaged Nusselt number distributions for the FW configurations considered. Regarding the  $FW_h$  and  $FW_\mu$  designs, the respective distributions indicate pure forced convection conditions and the fully developed values are in agreement with the theoretical prediction ( $Nu_{FD}=6.31$ ). Heat transfer appears more enhanced in the  $FW_l$  configuration due to the effect of buoyancy and the Nusselt number values after reaching a minimum point characteristic of mixed convection conditions [3.59], exhibit a slightly increasing trend. This behavior is indicative of the fact that the flow does not reach full thermal development until the outlet of the heat sink. However, the Nusselt number values can be misleading due to the use of a different hydraulic diameter in each case. The distribution of the heat transfer coefficient instead (**Fig. 3.9b**), which is independent of the geometrical parameters, reveals that heat transfer is significantly enhanced in the  $FW_\mu$  configuration due to the increased heat transfer area.

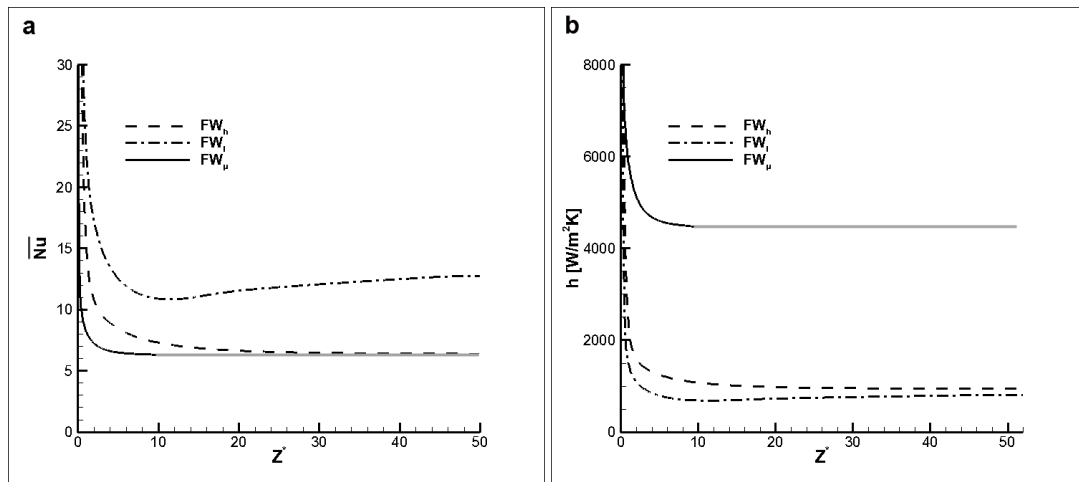


**Fig. 3.9** (a) Streamwise distribution of (a) the average Nusselt number and (b) the average heat transfer coefficient for the fixed-width configurations.

### 3.4.2 Tapered channels with smoothly varying width ( $VW_l$ )(Fig. 3.1d)

Morega and Bejan [3.63] illustrated that the maximum temperature at the base of a plate-fin heat sink can be decreased by gradually varying the cross-section of the fins in a wedge-like form. It was reported that a plate-fin heat sink with fins of non-uniform thickness, increasing in the streamwise direction, can have approximately 15% lower hotspot temperature in comparison to an identical one employing fins of fixed thickness under the same heating and flow conditions. In addition, the temperature distribution at the heat sink bottom surface was also found to be more uniform. The authors proposed an optimization procedure to determine the optimal plate sharpness parameter, which designates the fin thickness distribution, using a two-dimensional numerical model for the fin heat conduction, uncoupled from the heat convection to the cooling fluid. For constant heat-flux heating, the sharpness parameter was found to obtain an optimal value of 0.42, which was established to be insensitive to the fin height and the length. In addition, Hung and Yan [3.64] in their numerical investigation, illustrated that tapering the channel width along the flow direction improves the thermal performance of a microchannel heat sink in comparison to maintaining a constant channel width, for a constrained pumping power. In a later study [3.65], the same authors developed an optimization

procedure using the simplified conjugate gradient method in order to obtain the optimal value of the channel “tapering” ratio  $W_o/W_i$ , considering a linear decrease of the channel width.

In view of the above, a plate-fin heat sink employing tapered channels of smoothly Varying Width (VW<sub>t</sub>) is investigated in this paragraph, in order to point out the differences in the emerging flow and temperature fields in compared against the FW configurations presented in **paragraph 3.5.1**. The effect of the varying channel hydraulic diameter on heat transfer is discussed as well.

3.4.2.1 Geometry and computational domain

The heat sink layout is shown in **Fig. 3.1d**, where the wedge-like profile of the fins is clearly evident with the minimum and maximum thickness obtained at the heat-sink inlet and outlet, respectively. For a constrained overall volume of the fin (equal to  $t \times H \times L$ ) the fin thickness must vary according to the relation [3.63]:

$$\frac{t}{\bar{t}} = \left(1 + a\right) \left(\frac{z}{L}\right)^a \tag{3.30}$$

where the fin sharpness parameter  $a$  is equal to 0.42 and  $\bar{t}$  is the average fin thickness. The latter was chosen equal to 2.4mm so that the average channel width and fin thickness of the VW<sub>t</sub> configuration are equal to the respective dimensions of the FW<sub>n</sub> configuration and thus the effect of the fin tapering can be elucidated in a clear manner. In addition, the constraints posed by conventional machining processes would render the manufacturing of more slender VW<sub>t</sub> fins infeasible.

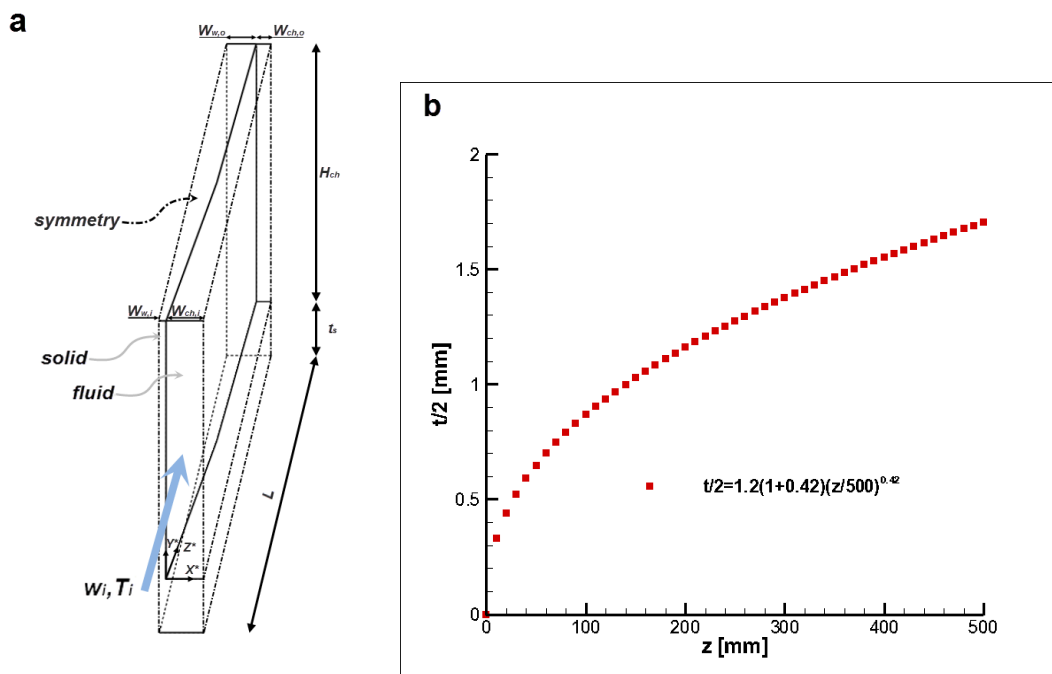


**Fig. 3.10** Heat-sink configuration with gradually developing channel width: (a) computational domain and (b) approximation of the fin profile.

In accordance to the FW configurations, the unit cell of the device comprising half the channel width along with half the fin thickness served as the computational domain for the simulations (**Fig. 3.10a**). The cross-sections of the fluid and solid domains were varying in a gradual manner as dictated by **Eq. (3.30)**, while the total width of the domain is maintained constant. The distribution of the half fin thickness along the streamwise coordinate is depicted in **Fig 3.10b**. The set of governing equations (3.10), (3.12)-(3.14) along with the boundary conditions (3.20)-(3.28) were solved on the computational domain, with a convergence criterion of  $10^{-6}$  set for the root mean square (RMS) mass, momentum and energy residuals.

### 3.4.2.2 Grid independence study

The computational domain was discretized using an unstructured hexahedral grid of increasing density towards the channel outlet, where the fluid domain obtains its minimum cross-section. The grid elements at the cross-stream direction were of varying width, so that the channel width and the fin thickness were discretized with the same number of elements throughout the domain length despite the variation in their hydraulic diameter. The grid independence of the results was verified by monitoring the discrepancy in characteristic quantities using grids of increasing density. By increasing the number of grid elements from  $0.79 \cdot 10^3$  to  $1.65 \cdot 10^3$  a discrepancy of 3.2% was detected in the values of the overall coolant pressure drop. The respective value for a grid of  $3.22 \cdot 10^3$  elements differed by 0.8%. Regarding heat transfer, the values of the overall averaged Nusselt number produced by the coarse and the intermediate mesh number exhibit a variation of 0.6%. The variation in the values produced by the intermediate and the fine grid was equal to 0.08% respectively.

### 3.4.2.3 Flow and temperature fields

The flow within the heat sink is expected to be constantly accelerating due to the decreasing hydraulic diameter and thus full hydrodynamic and thermal development cannot be reached. The velocity profiles at the channel horizontal mid-plane ( $Y^*=0.5$ ) at different streamwise locations are depicted in **Fig. 3.11a**. It must be noted that the  $X^*$  coordinate has been non-dimensionalized using the channel width at the inlet, so that the channel narrowing in the streamwise direction is pointed out ( $X^* < 1$ ). As can be seen, the channel width close to the outlet ( $Z^*=120$ ) is approximately 40% of the respective value at the inlet, while the maximum velocity is more than 38% higher than the fully developed value obtained by the  $FW_h$  configuration (compare **Figs. 3.7b** and **3.11a**). The horizontal profile retains a parabolic shape in all the streamwise locations considered.

Inevitably, the increased flow velocity is associated with increased pressure drop penalty and consequently the overall coolant pressure drop through the  $VW_t$  configuration is approximately 56% higher than in the case of the  $FW_h$  configuration (as will be shown in **paragraph 3.6**). As depicted in **Fig. 3.11b**, the rate of pressure loss, as illustrated though the pressure coefficient, is not linear as in the case of fixed rectangular channels but exhibits a gradually steeper gradient along the streamwise direction. The pressure loss rate obtains its maximum gradient, which also becomes linear, approximately after  $Z^*=95$ , as the fin thickness increases linearly downstream of this location as well (see **Fig. 3.10b**).

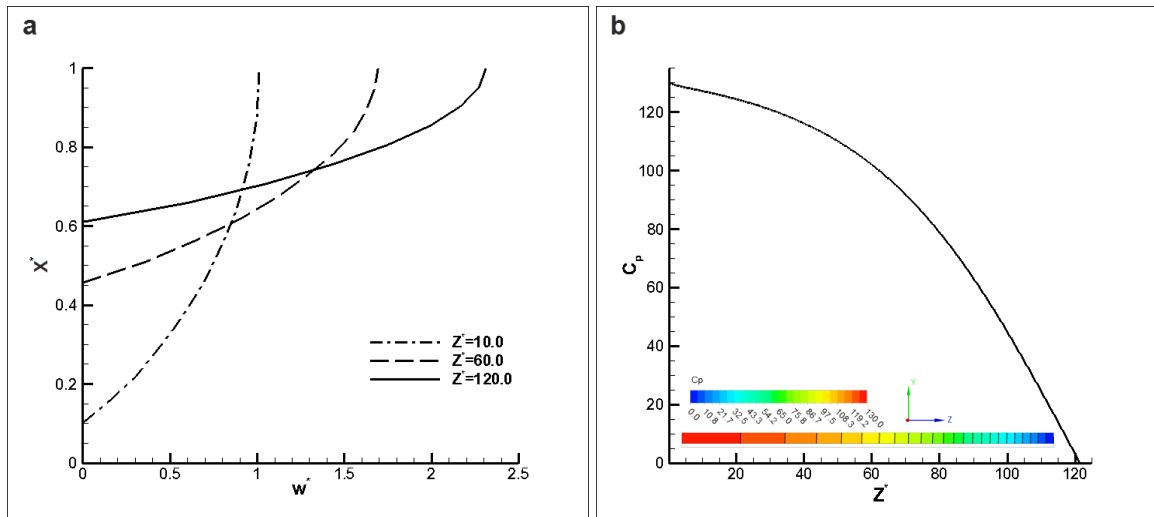


**Fig. 3.11** (a) Development of the horizontal velocity profile ( $Y^*=0.5$ ). (b) Streamwise distribution of the pressure coefficient.

**Fig. 3.12** depicts the development of the vertical temperature profiles along the streamwise direction at the channel symmetry plane ( $X^*=1$ ). The linear part of the profile for  $Y^*<0$  corresponds to the solid substrate, while the temperature profile in the fluid part clearly exhibits the thermal boundary layer growth near the bottom surface, where the heat transfer primarily takes place. The increase in the fluid temperature in the vicinity of the top wall is due to the lateral heat flux, combined with the reduced mass flux (reduced axial flow velocities) in the boundary layer of the upper wall of the channel. The constant decrease of the channel cross-sectional area affects the development of the thermal boundary layer and the temperature difference between the channel bottom wall ( $Y^*=0$ ) and the fluid core is constantly decreasing as the axial coordinate increases, indicating an increase in the heat transfer rate. The temperature field arising within the  $VW_t$  configuration is further elucidated through temperature contour plots on selected cross-flow planes (inset of **Fig. 3.12a**), which elucidate the redistribution of thermal energy as the fin thickness increases and the lateral thermal boundary layers approach each other. The wall temperature distribution depicted in **Fig. 3.12b** exhibits a non-linear behavior with varying gradient along the streamwise coordinate, whereas the average (bulk) fluid temperature increases in a linear manner after  $Z^*=30$ . However, the maximum wall temperature is reached at the heat sink outlet, as in the case of  $FW$  configurations. The relative wall temperature rise in reference to the fluid inlet temperature ( $T_{w,max}-T_{f,i}$ ) is decreased by 14% compared to the  $FW_h$  configuration and thus it is confirmed that the  $VW_t$  configuration achieves superior thermal performance.

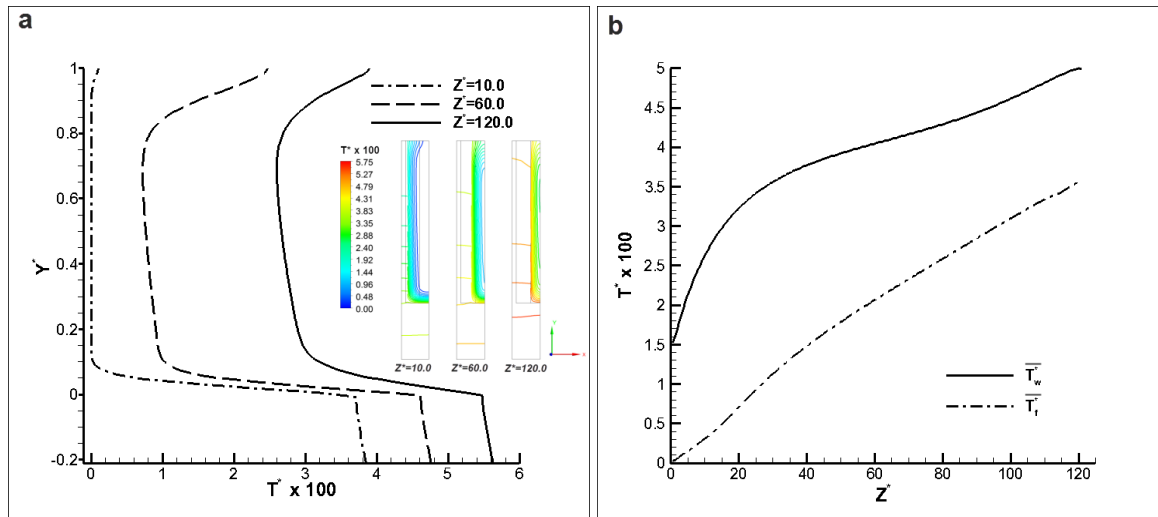


**Fig. 3.12** (a) Development of the vertical temperature profile ( $X^*=1$ ). (b) Distribution of the circumferentially averaged wall and fluid temperature.

**Fig. 3.13** depicts the circumferentially averaged heat transfer coefficient for the  $VW_t$  configuration, along with the derived Nusselt number (using the average channel hydraulic diameter as a length scale). As can be seen, the distributions exhibit a characteristic minimum point at  $Z^*=17.0$  due to the thermal entrance effect after which the beneficial influence of the channel increasing aspect ratio on heat transfer becomes evident [3.8]. More specifically, downstream of the minimum point, an increasing trend can be clearly discerned up to approximately  $Z^*=100.0$  and succeeded by a slightly decreasing trend due to the fact that the channel width remains relatively constant in that part of the channel. The overall heat transfer coefficient of the  $VW_t$  configuration is higher by 11% than that obtained by the  $FW_h$  configuration.

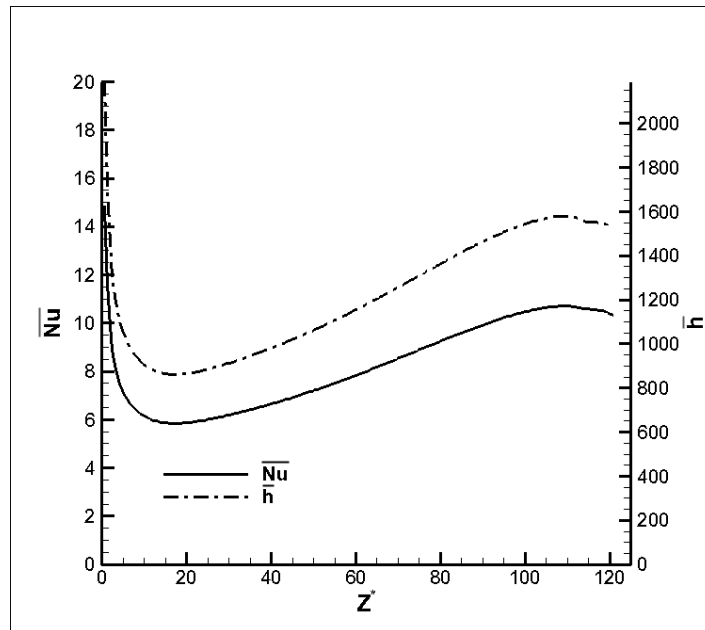


**Fig 3.13** Streamwise distribution of the circumferentially averaged heat transfer coefficient and Nusselt number.

### 3.4.3 Plate-fin configuration with channels of stepwise varying width (VW) (Fig. 3.1e)

#### 3.4.3.1 Literature survey – Extended surfaces and flow-area contraction phenomena

It is commonly employed practice in heat exchanging devices, and in an effort to increase the overall heat transfer rate, to disrupt the thermal boundary layer development along the heat transport surfaces and/or to provoke secondary-flow patterns [3.66]. These can arise, among others, due to the morphology of the device geometry, the effect of buoyancy forces or by some external excitation (e.g. surface vibration) [3.67, 3.68]. If the topology of these patterns is such as to allow free-stream fluid entrainment toward the heated surfaces, then the overall heat transfer rate is significantly enhanced due to the intense thermal mixing [3.67]. Research in the field of heat transfer enhancement is still ongoing especially regarding heat exchanging configurations employing extended surfaces, which are the most commonly encountered technique in industrial applications. Various fin designs have been proposed and investigated, e.g. wavy, louvered, corrugated or offset-strip fins and a comprehensive overview of the flow and heat transfer behavior of characteristic plate-fin configurations can be found in [3.69] and [3.70]. In addition, techniques used for heat transfer enhancement through control of the prevailing flow conditions are reported in the review articles by Jacobi and Shah [3.68] and Bergles [3.71].

A simple way to enhance the overall heat transfer rate in heat exchanging devices is the introduction of a flow-contracting geometry [3.72]. Two basic configurations of flow-contraction, typically encountered in heat dissipation applications, are the forward facing step and the flow entrance into an array of parallel fins, with the latter having been primarily investigated under forced convection conditions and using air as the cooling medium [3.73-3.75]. The two-dimensional flow over a forward-facing step exhibits three characteristic regions: a separation zone adjacent to the step salient corner, a recirculation zone at the step tip, and a re-attachment section downstream of the step. It is reported, [3.76, 3.77], that whereas the salient corner vortex is formed even for creeping flows, the tip vortex is detected only beyond a critical value of the Reynolds number. The formation of the separation bubble immediately downstream of the leading edge is a feature also encountered in the flow around blunt plates. The studies of Djilali [3.73] and Rahnema et al. [3.74] focused on the two-dimensional laminar steady flow around an array of plates and demonstrated two main findings: the linear increase of the separation bubble length with the Reynolds number (for a constant blockage ratio) and the significant heat transfer augmentation in the reattachment region. Marty et al. [3.78] expanded the two-dimensional steady-flow calculations to unsteady flow as well. They reported that the heat transfer for high Re numbers was enhanced by 50% in comparison to an infinite plate due to the unsteadiness of the recirculation bubble and they confirmed their numerical predictions by experimental measurements.

The three-dimensional nature of separated flows in the case of a geometrical confinement generates a complex velocity field manifested by the formation of distinct vortex structures [3.72, 3.79-3.81]. Stürer et al. [3.72] used the hydrogen bubble technique and particle tracking velocimetry to visualize the laminar three-dimensional flow ahead of a forward facing step. Their experiments were conducted in an open water channel, wide enough to exclude the side wall influence; it was concluded that the separation bubble at the step base corner is of the open type and that the entrained fluid, after undergoing a helical movement in the spanwise direction, is released over the step and transformed

into a longitudinal vortex in a quasi-periodic manner. A similar observation was made by Largeau and Moriniere [3.79] who experimentally examined turbulent air flow over a forward facing step in an open channel. They noticed a structure similar to a horseshoe vortex in front of the step and came to the conclusion that the flow passes the step over paths of approximately the same spanwise distance.

Wilhelm et al. [3.80] performed a computational analysis of the three-dimensional, laminar, incompressible flow of a Newtonian fluid over an infinite, in the spanwise direction, forward-facing step. The simulation was initialized with a two-dimensional solution and three-dimensional perturbations of different kind and intensity were superimposed. The formation of pairs of longitudinal counter-rotating vortices downstream of the step was established and it was observed that a characteristic sequence of streaks also appeared downstream of the step, marking the paths of fluid entrainment over the step. The topology of this streaky pattern was found to be closely related to the longitudinal vortices, as a periodic pair of counter rotating vortices was always located between two paths of fluid entrainment. Barbosa-Saldaña et al. [3.81] also investigated numerically the three-dimensional laminar forward-facing step flow using a finite volume method. They examined the effect of increased Reynolds number on the magnitude and location of the salient and tip vortices detected immediately upstream and at the edge of the step respectively, but they did not report the emergence of any periodic longitudinal vortices.

The *effect of flow confinement* on the local and overall heat transfer rate has been discussed by a number of researchers. Yaghoubi and Velayati [3.75] in their numerical investigation of the three-dimensional turbulent air flow and conjugate heat transfer around an array of rectangular parallel plates of finite thickness established that the flow was symmetric in that configuration. Consequently, they conducted their computations with respect to various plate geometrical parameters (aspect ratio, blockage ratio and spacing) on a reduced domain containing a half-section of the plate. The authors concluded their study by numerically deriving analytical correlations regarding the reattachment length and the overall Nusselt number. It was pointed out that the overall Nusselt number increases with the blockage ratio. Zhang et al. [3.82] conducted a numerical analysis in order to capture the topology of the unsteady three-dimensional flow around cascading blunt-plate arrays. The effect of the end walls was not taken into consideration as periodic conditions were imposed along all directions. The emergence of longitudinal vortices was established, which were furthermore found to interact and extract energy from the spanwise vortices that constitute a two-dimensional feature of the flow.

Yanaoka et al. [3.83] numerically investigated the three-dimensional laminar fluid flow and heat transfer around a blunt plate inside a square channel in order to point out the effects of the lateral walls. The blockage ratio defined as the ratio of the plate thickness to the channel width was equal to 10%. An interesting result of the study was the detection of a horseshoe vortex in the vicinity of the side wall downstream of the plate edge, resulting in a thinning of the thermal boundary layer in that region and significant enhancement of the local Nusselt number values. For  $Re=450$  (based on the plate thickness) the flow became unsteady and a single hairpin vortex with a spanwise scale of approximately twice the plate thickness was formed downstream of the plate leading edge. The horseshoe vortex is a pattern also encountered in flows around unconfined surface mounted obstacles. Nakamura et al. [3.84] visualized the turbulent air flow around a 30mm cube using an oil-film method. They noticed the formation of the horseshoe pattern on the floor adjacent to both the front and side regions of the cube. It was also stated that the heat transfer on the base wall was significantly enhanced because of the influence of the vortex. The formation of the horseshoe vortex at the leading

face of an obstacle was also observed by Meinders and Hanjalić [3.85] who visualized the air flow around a matrix of equidistant cubes.

Few studies are available in the open literature that discuss the *effect of buoyancy* on heat transfer in flow-contracting configurations. The published numerical and experimental results concerning laminar mixed convection over a forward-facing step are summarized in [3.86]. The effects of fin height and spacing on mixed-convection heat transfer around an array of longitudinal plates shrouded by a rectangular duct were investigated in depth in the experiments of Maughan and Incropera [3.87]. The bottom and upper duct walls were isothermally heated and cooled respectively. It was observed that for Reynolds numbers within the laminar regime and small fin height, the reduction of fin spacing reduced the overall heat transfer, despite the additional heat-transfer areas, due to the weakening of the buoyancy induced secondary vortices. However, the opposite trend was observed for fins of considerable height as the enhancement due to the extended surfaces had a decisive impact on the overall heat transfer rate.

Chong et al. [3.88] conducted an experimental investigation of the laminar mixed convection inside a horizontal rectangular duct having a vertical longitudinal plate at the middle of its cross-section. The imposed thermal boundary condition was that of axially uniform heat flux with circumferentially constant wall temperature. The authors concluded that heat transfer was enhanced with an increase in the Reynolds number, due to the increased impact of forced convection, while duct inclination was found to have either a beneficial or a hindering influence on heat transfer, depending on the orientation of the buoyancy force in comparison to the flow direction. More recently, Dogan and Sivrioglu [3.89] examined both numerically and experimentally the overall heat transfer from an array of longitudinal fins mounted inside a rectangular horizontal channel under mixed convection conditions. A constant heat flux was applied at the channel bottom wall, while the heat was dissipated through laminar air flow. The authors analyzed the effect of fin spacing and clearance gap between fin tips and the channel top surface on the average heat transfer coefficient inside the channel. They came to the conclusion that an optimal fin spacing exists that maximizes heat transfer, while a widening of the clearance gap had an adverse impact on heat transfer, a trend more pronounced for larger Reynolds numbers.

In view of the above, a heat sink where additional fins are added in the original configuration mid-length is investigated in this paragraph. The initial objective is to thoroughly investigate the effect of the flow-area contraction on the flow field by illustrating the topology of the emerging vortical structures and identifying the mechanisms that cause their onset. As mixed convection conditions are expected to occur in the first half of the heat sink, where channels are wider, for the operating conditions reported in **paragraph 3.3** the complex flow field, resulting from the combined effect of buoyancy and flow-contraction is also analyzed for increasing values of the Archimedes number. Subsequently, the influence of the developing secondary flow pattern on the temperature field and the overall heat transfer rate of the heat sink are investigated for both pure forced and mixed convection conditions.

#### 3.4.3.2 Geometry and computational domain

The relatively more complex heat-sink design to be addressed in this paragraph (**Fig. 3.1e**) comprises a series of rectangular channels with a stepwise width reduction occurring midway along

their length. Such a design was first implemented by Barrau et al. [3.90], albeit in a conceptually different configuration, namely in a jet impingement cooling device. Barrau et al. [3.90] manufactured a cooling device of overall area (2.5 x 6.0) cm<sup>2</sup> that employs a vertical rectangular slot at the heat-sink mid-length, serving as the cooling fluid inlet and two symmetrical arrays of stepwise-varying width microchannels on either side of the slot, where the flow branches into. Such a design offers additional heat-transfer surfaces and disrupts the development of the cooling-fluid thermal boundary layer, which would lead to steep temperature gradients. Both these effects are expected to have a positive impact on the heat sink thermal performance; however, the presence of additional channels in the heat sink second section leads to a higher pressure-drop penalty. This conceptual design can ideally be further developed into (*dendritic*) tree-like structures with enhanced thermal performance, by adding more sections with channel widths that extend down to the microscale. However, the increasing complexity of such a structure also leads to prohibitively high manufacturing costs, which is a hindering factor for the use of such heat sinks in practical applications. Therefore, this paragraph refers to the simplest, two-section configuration, which is adequate for the investigation of the three-dimensional flow features in the transition between two consecutive sections of the heat sink. The channel width ratio  $W_{ch,1}/W_{ch,2}$  is taken here equal to three, while the fin thickness  $W_w$ , which is maintained constant throughout the heat-sink length, is equal to the channel width of the second section. With respect to these geometrical constraints, the number of channels in each section can be explicitly determined through the relation:

$$N_i = \frac{W_{hs} - a_i W_{ch,i}}{(a_i + 1)W_{ch,i}} \quad (3.31)$$

where  $\alpha = W_w/W_{ch}$  and  $W_{hs}$  is the total heat-sink width. The total channel height  $H_{ch}$  is selected as the maximum structurally possible value for thermal performance purposes [3.8] and it is kept constant, resulting in channel aspect ratios equal to  $AR=2$  and  $AR=6$  for the upstream and downstream sections respectively. With the above choices, it turns out that the first and second sections consist of six and twelve channels, respectively, and are identical to the  $FW_1$  and  $FW_h$  configurations presented in **paragraph 3.4.1**.

It is computationally expensive to model the entire heat-sink and therefore the computational domain was truncated by taking advantage of the existing symmetries. This had to be done with caution since, as Chiang et al. [3.91] have demonstrated, in the case of sudden contraction flows in perfectly symmetrical domains, critical values of the aspect ratio  $AR$ , contraction ratio ( $W_{ch,1}/B_{ch,2}$ ) and Reynolds number exist, which lead to the onset of non-symmetrical flow features. The Reynolds number values arising from the flow conditions of the present study are sub-critical (as will be shown in **paragraph 3.4.3.7**) and thus symmetrical flow should be expected. Thus, a reduced, representative computational domain is defined as shown in **Fig.3.14**, consisting of a fluid and a solid sub-domain. Half the width of the first-section channel and the entire width of the second-section channel define the lateral extent of the fluid domain, while the solid domain is composed by the vertical fins (of half thickness) and the plate substrate. The set of governing equations (3.1)-(3.4) or (3.1) and (3.3)-(3.5) for the forced-convection and mixed convection cases, respectively, along with the boundary conditions (3.12)-(3.20) were solved on the computational domain, with a convergence criterion of  $10^{-6}$  set for the root mean square (RMS) mass, momentum and energy residuals.

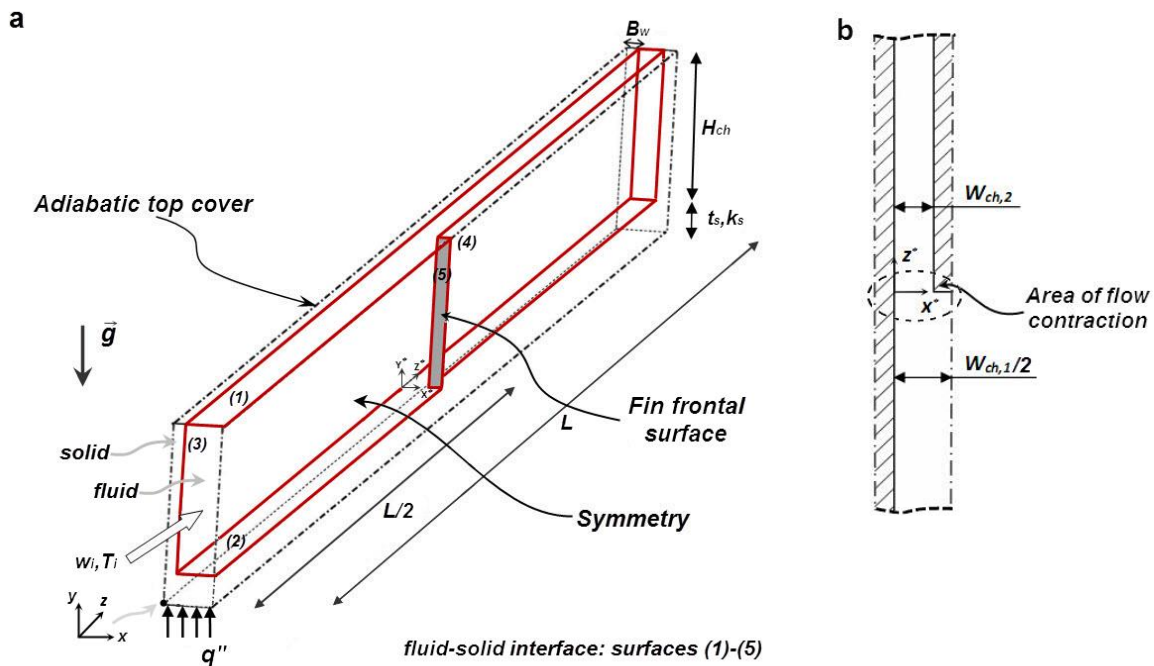


**Fig. 3.14** Computational domain for the variable-width configuration: (a) Perspective view, (b) top detailed view of the flow-contraction region.

### 3.4.3.3 Validation of the numerical model

It is essential to evaluate the reliability of the computational code in predicting the flow field emerging in confined, flow-contracting geometries, in order to confirm the accuracy of the results obtained. Experimental results in configurations that are closely related to the present one could not be found, therefore suitable numerical solutions were sought instead. Barbosa-Saldaña et al. [3.81] investigated the three-dimensional confined laminar flow over a forward-facing step, which is a configuration that exhibits the closest resemblance to the unit cell of the present work. Therefore, for validation purposes, the dimensions of the unit cell and the boundary conditions are adjusted, as a no-slip condition (wall) is placed at the base upstream of the step instead of a symmetry boundary, so as to match the corresponding configuration found in [3.81]. Fig. 3.15a indicates the flow configuration, along with the nomenclature as used in [3.81]. The step height  $s$  is taken equal to half the channel height  $H$  ( $H=2s$ ) and the step is placed at a distance  $l=20s$  downstream of the channel inlet, while the channel total length  $L$  and width  $W$  are  $L=60s$  and  $W=4s$ , respectively. The Reynolds number  $Re_{st}$  that characterizes the flow is equal to 800 based on the step height and the numerical grid consists of 320000 cells.

Axial velocity profiles are compared to published values at three representative positions, namely immediately upstream of the step ( $X/s=19.09$ ), downstream of the step tip ( $X/s=20.08$ ) and at the channel outlet ( $X/s=60$ ). The streamwise velocity profiles along the Y direction in the middle of the channel spanwise direction are in very good agreement with the respective values of [3.81], as shown in Fig. 3.15. A small recirculation region is detected slightly upstream of the step base, where the axial velocity obtains negative values (Fig. 3.15b), while an additional recirculation bubble of greater magnitude is evident downstream of the step leading edge, as depicted in Fig. 3.15c. Both regions of

flow separation, which are distinct features of the flow over a forward-facing step [3.76], are well captured qualitatively and quantitatively. Finally, the flow obtains a parabolic profile, Fig. 3.15d, which, however, has not yet reached full development at the channel outlet.

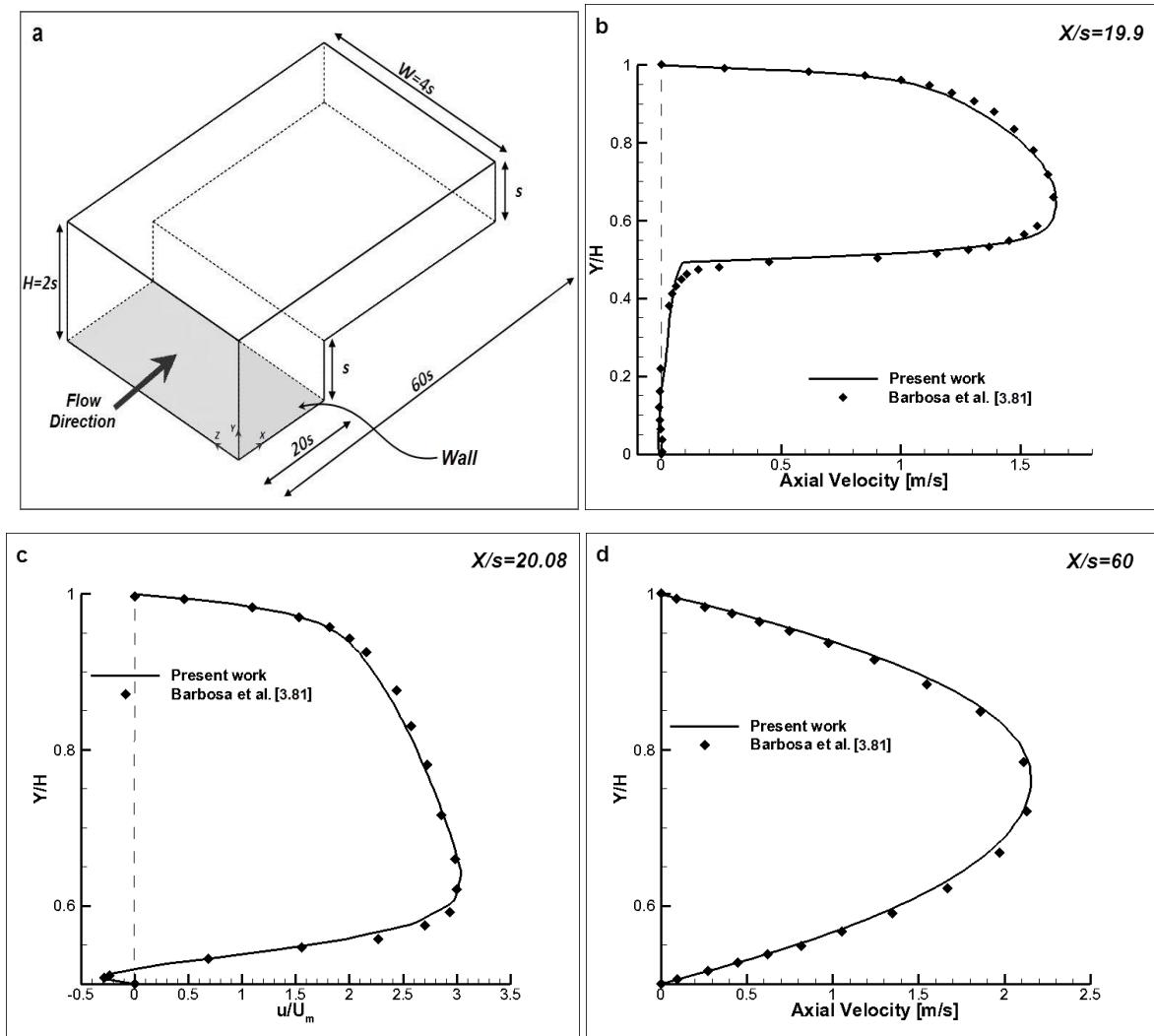


**Fig. 3.15** Code validation for the case of Barbosa-Saldaña et al. [3.81]. (a) Computational domain. Vertical velocity profiles on the domain symmetry plane ( $Z/W=0.5$ ) at  $Re_{st}=800$ : (b) immediately upstream of the vertical step wall, (c) downstream of the step edge ( $U_m=0.617$  m/s) and (d) at the channel outlet.

The case of laminar mixed convection around a shrouded array of parallel fins investigated by Maughan and Incropera [3.87] was used in order to verify the accuracy of the numerical scheme in cases where the effect of natural convection is considerable. The particular experimental study has been selected among others in the open literature as bearing the closest resemblance to the present investigation. It focuses on the effect of fin spacing and fin height on the overall heat transfer rate for increasing values of the Rayleigh number. The temperature of the bottom wall and the vertical fins is maintained constant at a prescribed value  $T_{bot}$  that also determines the value of the Rayleigh number, while the temperature of the top wall  $T_{top}$  is maintained constant in all cases and equal to the fluid inlet temperature ( $T_{top}=293K$ ). The overall Nusselt number is calculated by the expression:

$$Nu = \frac{Q}{A_{bot}(T_{bot} - T_{top})} \frac{H}{k_f} \quad (3.32)$$

where  $Q$  is the total heat transfer rate,  $A_{bot}$  is the unfinned area of the bottom wall and  $H$  is the distance between the bottom and the top wall.

The Nusselt number values obtained in the present numerical investigation were compared against the experimental ones for different values of the fin spacing  $s$  ( $0.5H$ ,  $1.0H$  and  $2.0H$ ) and for a fin height  $H_f=0.9H$ . The computational domain used for the validation study is limited to half the cross-section of adjacent fins for the two larger values of the fin spacing; however, the entire cross-section between fins is used for the closest fin spacing. The Reynolds number (based on the distance  $H$ ) that characterizes the flow is equal to 1000 and the Rayleigh number lies in the range  $3500 \leq Ra \leq 29700$ . The comparative results are presented in **Fig. 3.16** and, as can be seen, good agreement is established between the predicted and the experimental values. The maximum discrepancy detected between the comparative values is approximately equal to the minimum uncertainty of the experimental data (7%) stated by the authors, with the exception of the values regarding the highest Rayleigh number value for fin spacing, namely  $s=H$ . The discrepancy in the specific case is approximately equal to 10% but, as can be detected in **Fig. 3.16**, the experimental value does not follow the expected increasing trend of the Nusselt number upon increasing Rayleigh number, indicating possibly an underestimation of the specific value during the experimental evaluation.

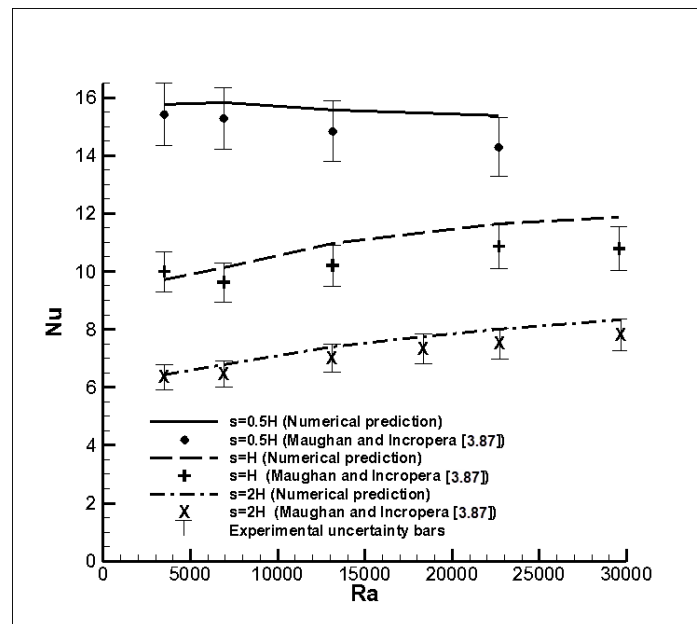


**Fig. 3.16** Validation of the numerical code with the experimental results of Ref. [3.87] for a shrouded array of parallel fins: Computed overall Nusselt number values for  $Re=1000$  and increasing Rayleigh number.

#### 3.4.3.4 Grid independence study-Forced convection conditions.

A structured hexahedral grid was used for the discretization of the computational domain, with a non-uniform arrangement along the flow direction (**Fig. 3.17**), as smaller control volumes were placed in the vicinity of the geometry constriction, in order to fully resolve the complex phenomena that

occur in that region (**Fig. 3.17a**). On the other hand, a uniform grid arrangement was employed across the domain cross-section (**Fig. 3.17b**).

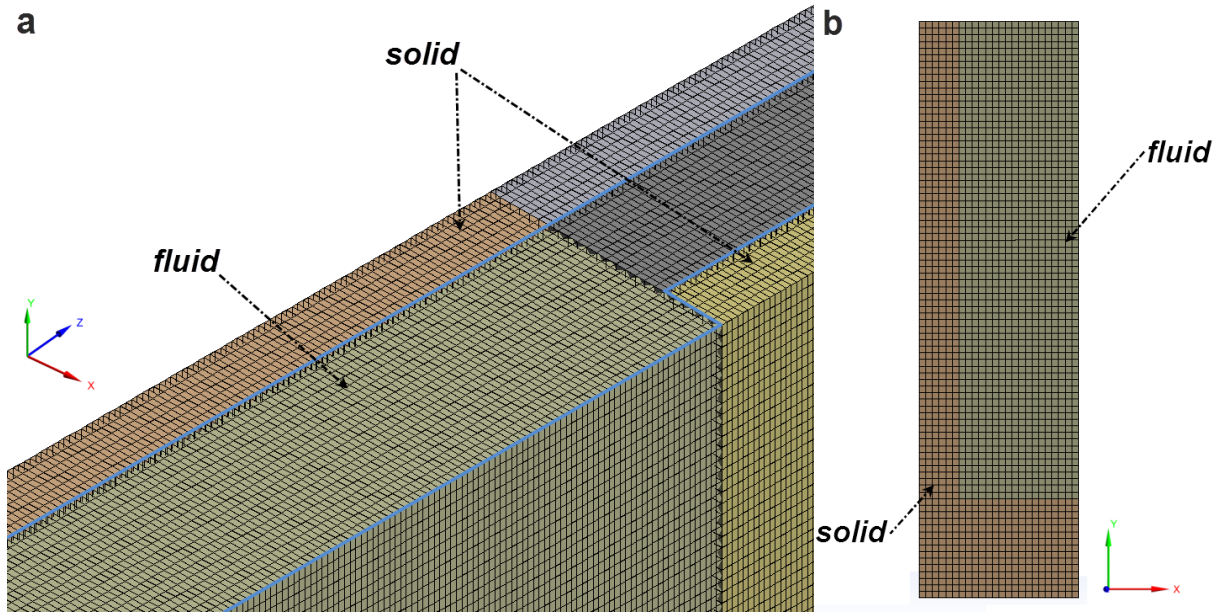


**Fig 3.17** Computational grid used for the simulations of the VW configuration: (a) detail view of the contraction area and (b) cross-sectional view.

A grid-independency analysis was conducted to verify that grid density had no effect on the derived solution for the three Reynolds numbers investigated ( $Re_1=519, 1038, 1557$ ). Regarding the fluid domain, grids of increasing density (coarse-intermediate-dense) were selected, with  $0.8, 2.1$  and  $2.5 \times 10^6$  cells, respectively. The horizontal axial velocity profiles at the channel mid-height at locations in the vicinity of the contraction were chosen as suitable measures to quantify the discrepancies between the different grids. As depicted in **Fig. 3.18**, the effect of the contraction on the streamwise velocity profile at an upstream to the step position is well captured by all three grids for all the Reynolds numbers considered. However, at downstream locations the velocity profile is not adequately captured by the coarse grid even for the lowest Reynolds number case (**Fig. 3.18a**). On the other hand, the intermediate grid can accurately represent the flow features for  $Re=519$  and  $Re=1038$ , as further grid refinement produces almost identical velocity profiles for both cases. For example, the discrepancy observed between the maximum velocity values produced by the intermediate and the dense grid for  $Re=1038$  is below 0.8%. For  $Re=1557$  (**Fig. 3.18c**), a slightly larger discrepancy of 1.5% is observed between the maximum velocity values, despite the fact that the profiles produced by the two grids are in qualitative agreement. Therefore the intermediate grid was selected for the production of results for  $Re=519$  and  $1038$ , while the dense grid was used for the case of  $Re=1557$ . A grid of  $1.5 \times 10^6$  cells was initially tested for the discretization of the solid domain at  $Re=1557$ . A grid refinement to  $2.3 \times 10^6$  cells produced an identical value of the bottom wall mean temperature, as the discrepancy between the values produced by the two grids was below 0.1%. Consequently, the initial grid was selected as adequate for the production of results in all cases.

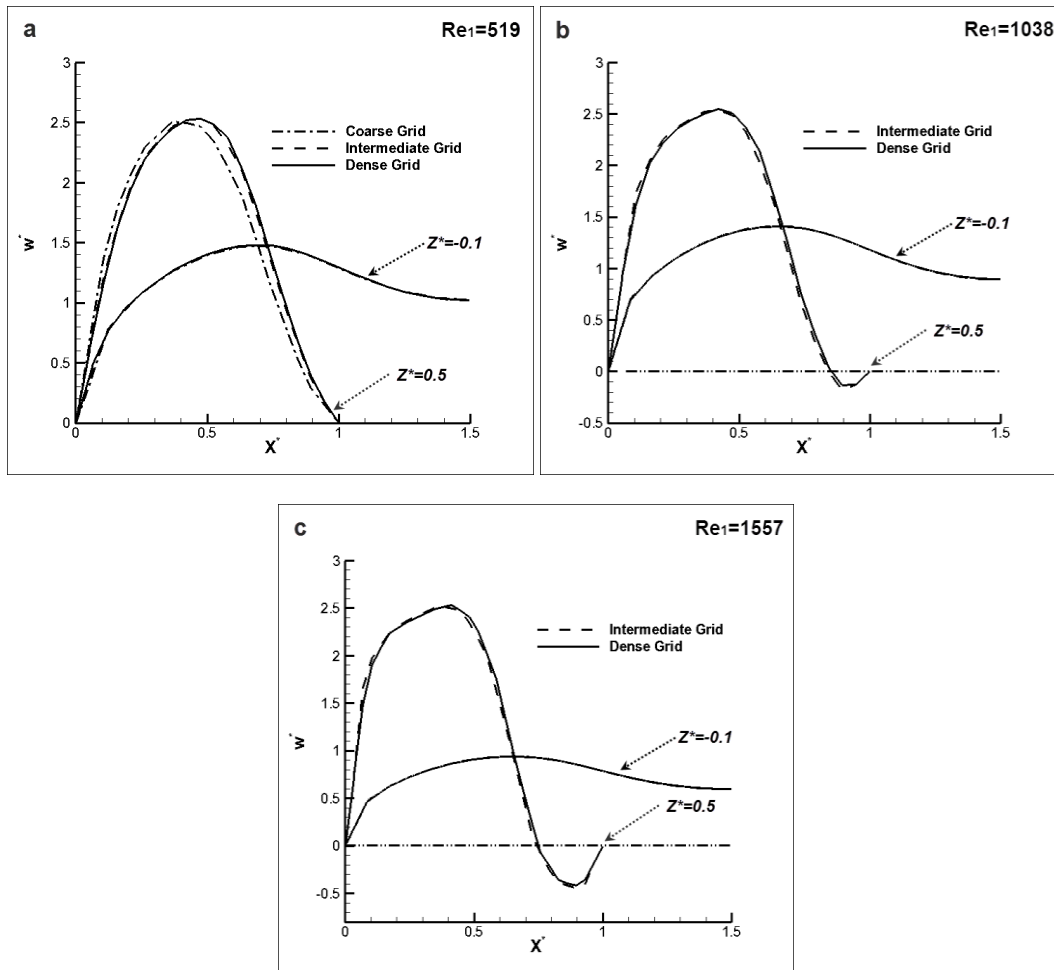


**Fig. 3.18** Effect of grid refinement. Axial velocity profiles at the channel mid-height ( $Y^*=0.5$ ): (a)  $Re_1=519$ , (b)  $Re_1=1038$  and (c)  $Re_1=1557$ .

### 3.4.3.5 Grid independence-Mixed convection conditions

The grid independence study was conducted for the case of the highest Archimedes number value ( $Ar_1=5.82$ ) considered and for  $Re_1=667$ . The computational domain was discretized using a non-uniform hexahedral grid, similar to that employed in the forced convection case. Uniform hexahedral elements were placed transversely to the flow direction, as uniform grid density is required in order to resolve buoyancy induced secondary-flow patterns [3.60, 3.92].

Three grids of increased density (coarse-intermediate-fine), consisting of  $2.5$ ,  $3.6$  and  $4.6 \times 10^6$  elements respectively, were tested in order to ensure grid independence of the solution. An increase of the grid density from  $2.5$  to  $3.6 \times 10^6$  elements produced a relative difference of 1.5% to the overall fluid pressure drop value. A further refinement caused a relative discrepancy of 0.6%; besides, the horizontal profiles of the axial velocity at  $Z=0.5^*$  were almost identical for all three grids considered (Fig. 3.19a). Regarding heat transfer, grid refinement from the coarse to the intermediate grid caused a variation of 2.7% to the value of the overall mean Nusselt number. A further refinement produced a variation of 1.3%. In addition, the bottom wall temperature distribution at  $X^*=0.5$  (Fig. 3.19b) was qualitatively captured by all three grids, with a maximum discrepancy between the values produced by the intermediate and the fine grid of 0.4%. Consequently, the intermediate grid, consisting of  $3.6 \times 10^6$  elements, was proven adequately accurate for the production of the results presented below.

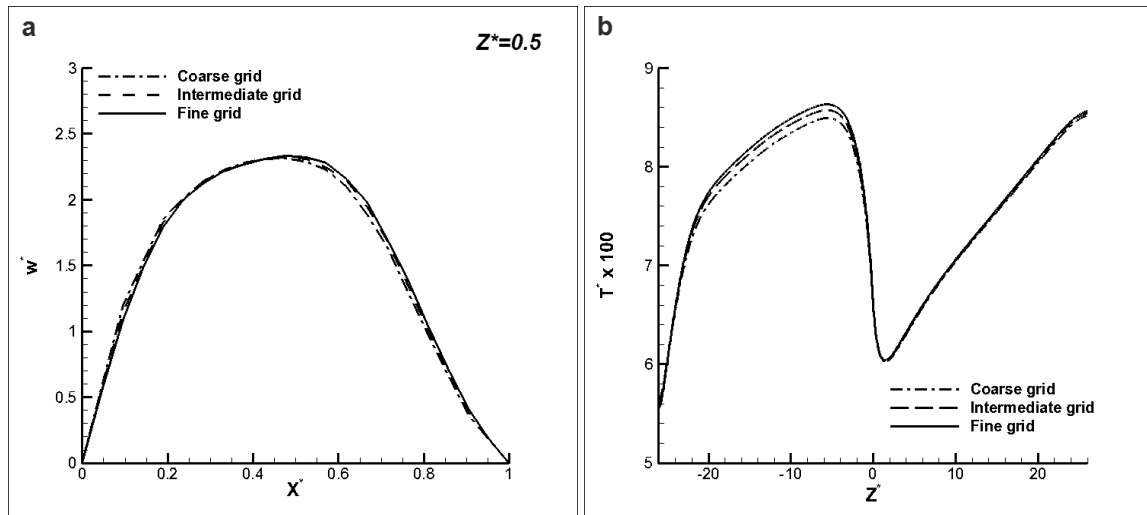


**Fig. 3.19** Grid independence study for  $Ar_1=5.82$  and  $Re_1=667$ : (a) Horizontal velocity profile ( $Y^*=0.5$ ) at  $Z^*=0.5$ , (b) bottom wall temperature distribution at  $X^*=0.5$  (centerline of the second section channel).

### 3.4.3.6 Flow field-Forced convection conditions

In order to facilitate the interpretation of the presented results, the coordinates have been properly non-dimensionalized so that the flow cross section is characterized by  $0 \leq X^* \leq 1$  (after contraction), while  $Z^* < 0$  denotes locations upstream and  $Z^* > 0$  downstream of the flow contraction respectively. The Reynolds number that characterizes the flow is defined using the hydraulic diameter in each section  $i$  ( $i=1,2$ ) and results equal to  $Re_1=519$  and  $Re_2=333$  respectively for a volumetric flow rate of 30 mL/s, with both values lying well within the laminar region. The streamwise velocity distributions in the upstream (larger  $D_h$ ) and the downstream (smaller  $D_h$ ) sections of the heat sink, on the vertical channel center planes ( $X^*=1.5$  and  $X^*=0.5$  respectively) are presented in **Fig. 3.20**. The flow velocity in the first section upstream of the contraction (channel aspect ratio of 2) develops from one of uniform distribution ( $Z^* \approx -26.042$ ) into a parabolic profile (**Fig. 3.20a**), which has not yet reached full development at the location of the contraction. The velocity profile at  $Z^* = -0.52$  appears similar to the one at  $Z^* = -5.21$ , due to the influence of the flow contraction which causes flow deceleration. On the other hand a fully developed velocity profile is formed at a distance of  $Z^* \approx 15.63$  downstream of the contraction (**Fig. 3.20b**). It is evident that the flow in the second section exhibits an almost flat fully developed velocity profile (on the Y-Z plane), due to the higher aspect ratio of the channel (channel aspect ratio of 6). The fully developed profile obtained in the second section was compared against the analytical prediction given in [3.8] for the same aspect ratio and excellent agreement is found. This agreement indicates that by that distance ( $Z^* > 15.63$ ), the three dimensional effects have become small and localized in the near wall regions.

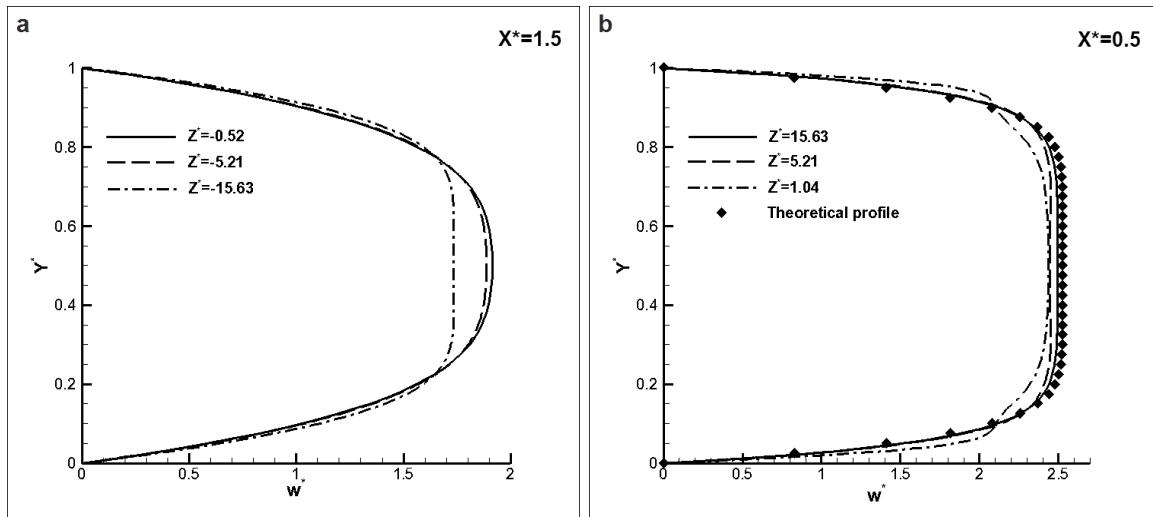


Fig. 3.20 Vertical profiles of w-velocity at the (a) first ( $Z^* < 0$ ) and (b) second section ( $Z^* > 0$ ) of the unit cell.

Vector plots on cross-flow and horizontal planes are created in the vicinity of the contraction, in order to point out the impact this has on the upstream velocity field (Fig. 3.21). As seen from Fig. 3.21, the flow approaching the contraction branches symmetrically into two directions along the Y axis and the oncoming fluid is pushed towards the endwalls and the opposite duct corners; furthermore, the flow distribution on the horizontal (XZ) plane near the bottom wall, Fig. 3.21, reveals the presence of flow reversal in the endwall regions, due to the upstream deflection of the downwards moving fluid after the impingement on the respective endwall.

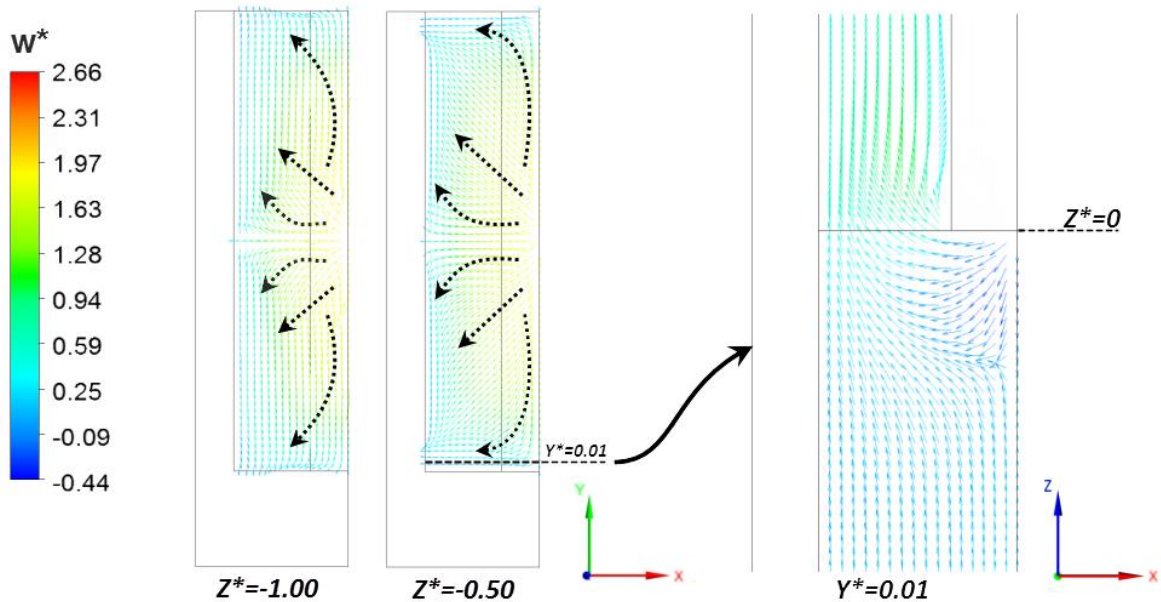
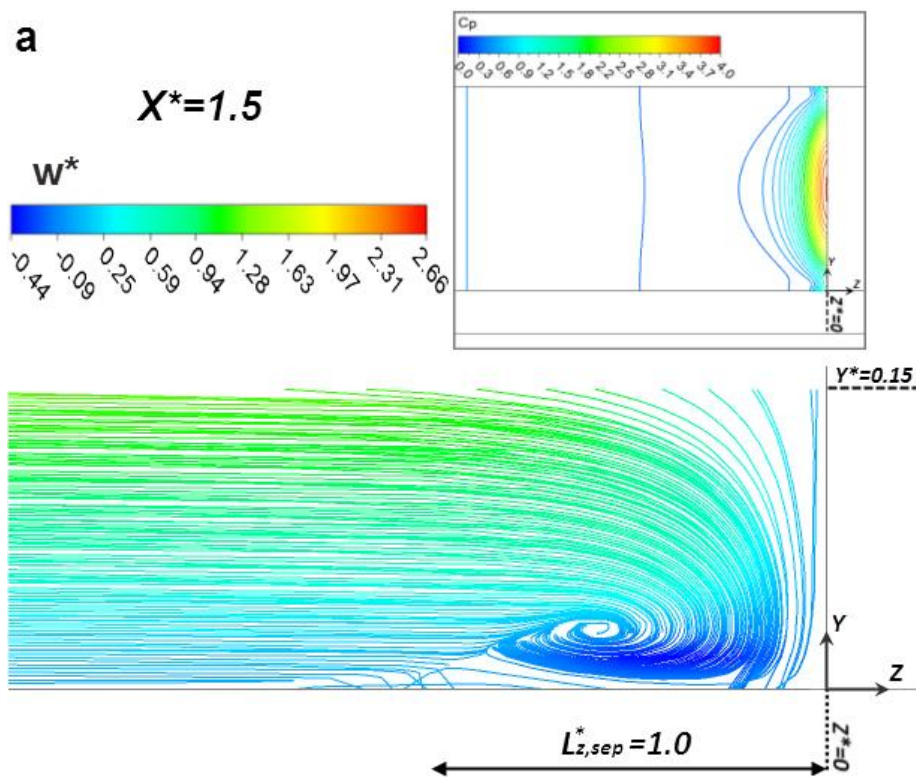
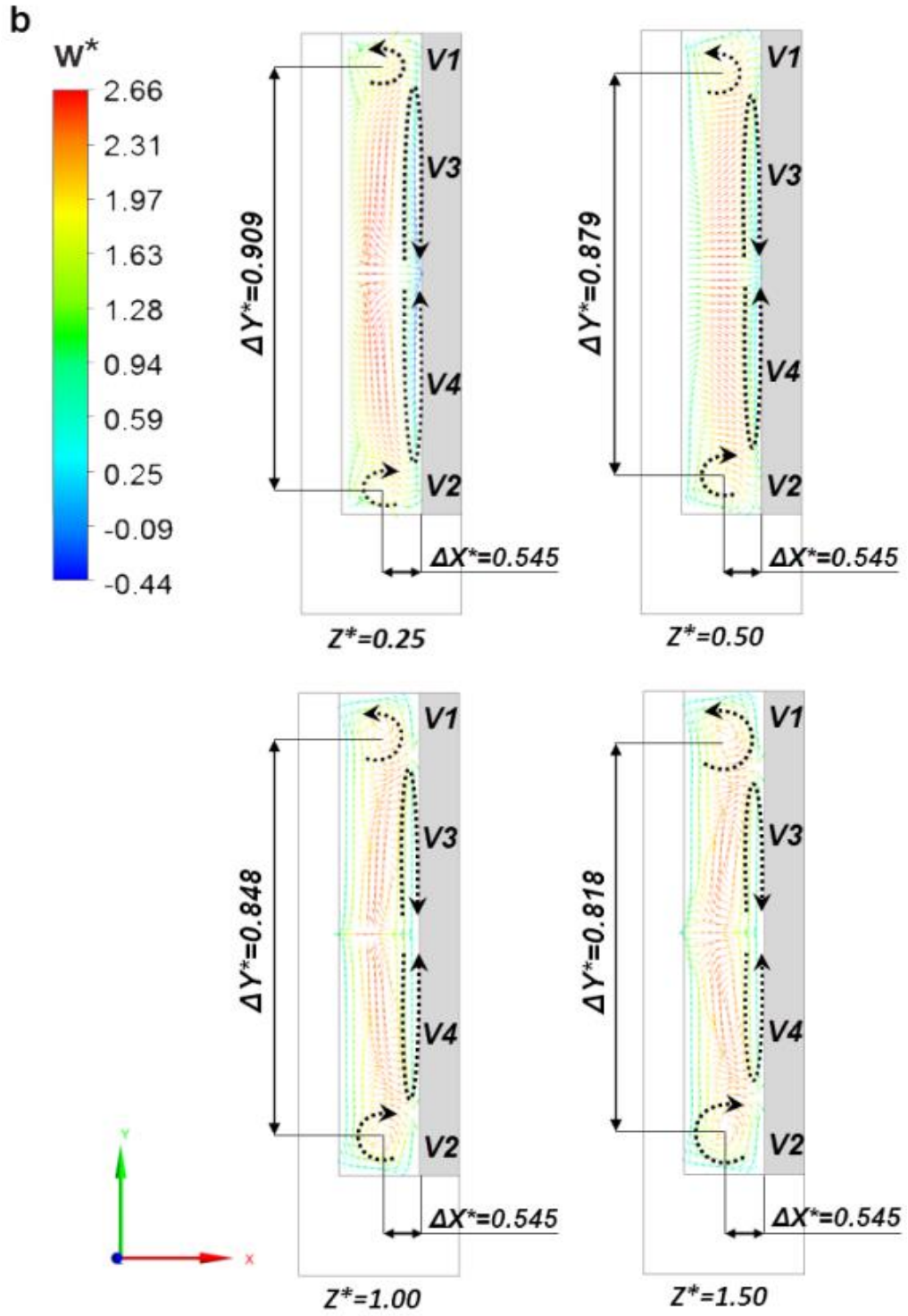


Fig. 3.21 Effect of the contraction on the upstream velocity field ( $Z^* < 0$ ) at  $Re_1 = 519$ .

The inset of Fig. 3.22a presents the distribution of the pressure coefficient  $C_p$  on the symmetry plane of the upstream channel ( $X^* = 1.5$ ). The streamwise positive pressure gradient causes a strong deceleration of the flow and leads to final separation upstream of the contraction, whilst the negative pressure gradient in the vertical direction pushes the flow towards the endwalls. The fluid whirling

motion, **Fig. 3.22a**, which is created at the end wall regions upstream of the flow contraction, develops into X-direction-oriented vortices towards the vertical channel sidewall ( $X^*=0$ ) and thus two counter-rotating vortices near the upper and lower walls of the channel are created. These are found to increase in strength, being continuously fed by the sideways deflected fluid. The vortices obtain maximum strength at the step location, where they are deflected into the longitudinal vortices V1-V2 (**Fig. 3.22b**) over the contraction (horseshoe type of vortices). Subsequently, downstream of the contraction the vortices decrease in strength and increase in size. The flow interaction with both the fin leading surface and the endwalls is an essential condition for the onset of the symmetrical horseshoe vortices flowing on both sides of the flow-contracting fin [3.93, 3.94]. The three-dimensional topology of the horseshoe vortex is shown in the detailed view of **Fig. 3.22c**, illustrating that the spiraling motion of the upstream boundary layer becomes more intense as the channel symmetry plane ( $X^*=1.5$ ) is approached.





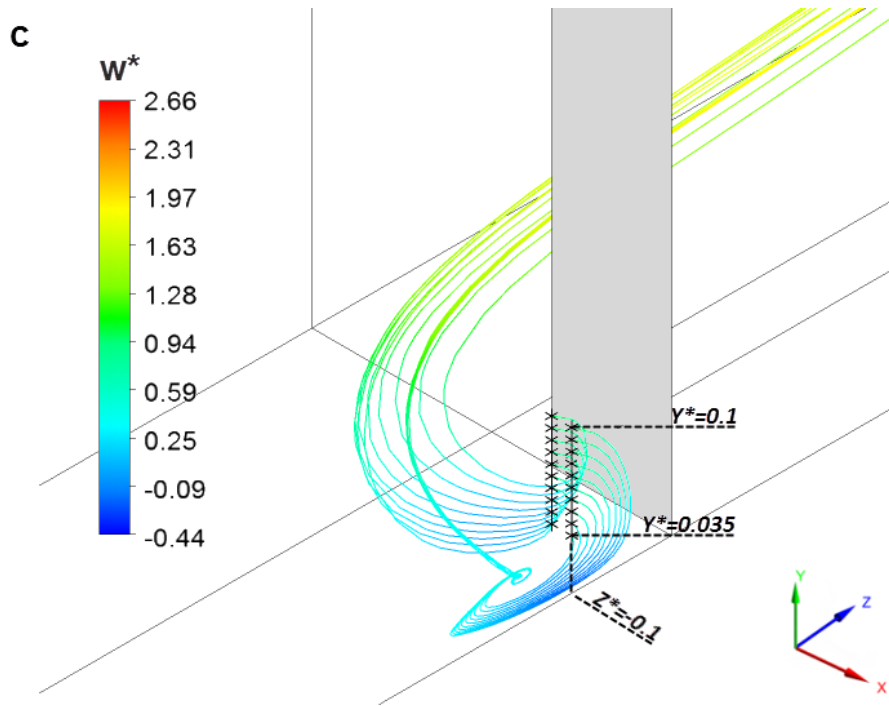


**Fig. 3.22** Reference case ( $Re_1=519$ ): (a) Rolling up of the bottom wall boundary layer. (b) Vector plots on cross-flow planes downstream of the contraction. (c) Three-dimensional streamlines originating from seed points at  $X^*=1.42$  and  $X^*=1.5$ , respectively.

The topology and magnitude of the secondary flow in the contraction region can be visualized even more clearly with the help of iso-surfaces of constant  $\omega_x$  and  $\omega_z$  vorticity, as presented in **Fig. 3.23**. As can be seen, the symmetric vortex structure onsets at the intersections of the fin leading surface and the endwalls, as illustrated by the regions of high  $\omega_x$  vorticity depicted in **Fig. 3.23a**. The structure is then transformed over the contraction to a pair of  $\omega_z$  vortices which persist for a significant distance downstream of the contraction before breaking down (**Fig. 3.23b**). The presence of another vortical structure of considerable magnitude close to the flow-contracting fin sidewall is detected in **Figs. 3.22b** and **3.23b**. However, these regions of high vorticity reduce in size further downstream due to the expansion of the horseshoe vortices. It must be pointed out that vortices of this kind have been observed by Yanaoka et al. [3.83] in their numerical investigation of confined flow around a blunt plate. This coherent pattern attached to the fin sidewall (V3-V4 in **Fig. 3.23b**) emerges due to the effect of the endwalls on the form of the downstream recirculation bubble, as illustrated by the iso-surface of the total vorticity depicted in **Fig. 3.23c**. The bubble appears distorted as the endwalls are approached and vortices V3-V4 are in fact the end branches of the same vortical structure. The source for the creation of this hairpin type of vortex is the parabolic flow reattachment on the fin sidewall [3.83].

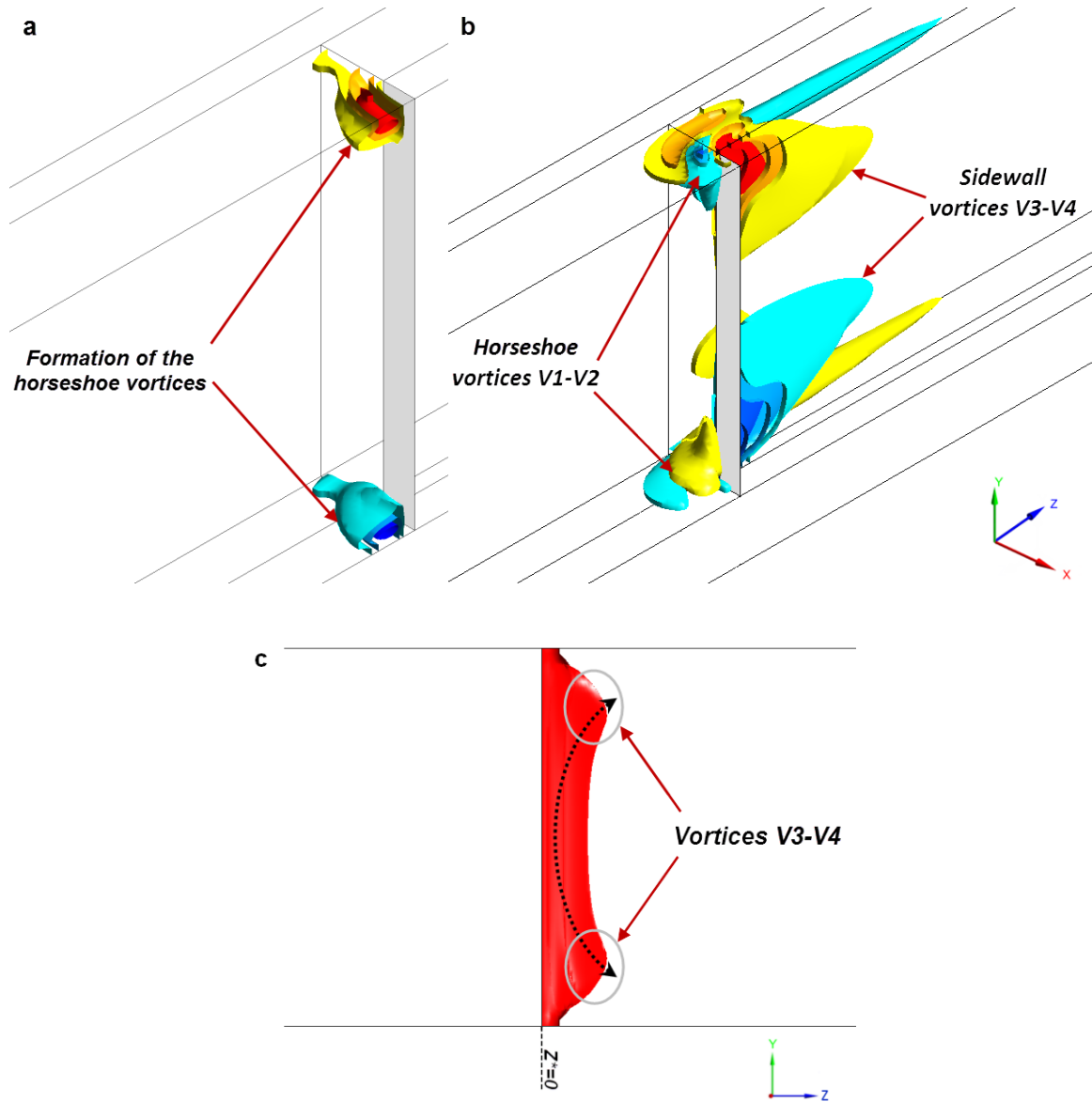


**Fig. 3.23** Iso-surfaces of (a) the  $\omega_x$  and (b) the  $\omega_z$  vorticity ( $Re_1=519$ ). Three pairs of surfaces of equal magnitude ( $\omega_x=100-75-50 \text{ s}^{-1}$ ,  $\omega_z=50 - 25 -12.5 \text{ s}^{-1}$ ) and opposite sign are presented (red-maximum vorticity, blue-minimum vorticity). (c) Iso-surface of the total vorticity  $|\omega|=200\text{s}^{-1}$ .

It is thus of interest to investigate the flow patterns that arise transversely to the channel side walls, where, even in the case of two-dimensional flow [3.73, 3.74], a characteristic recirculation region is clearly expected immediately downstream of the contraction. **Fig. 3.24a** presents streamwise velocity contours at different horizontal (XZ) planes in the vicinity of the geometry contraction, while **Fig. 3.24b** shows the velocity profiles along the spanwise direction ( $X^*$ ) at the channel mid-height ( $Y^*=0.5$ ) at three different streamwise positions: within the recirculation region ( $Z^*=0.10-0.25$ ) and after the flow reattachment ( $Z^*=0.50$ ) respectively. The three-dimensional nature of the flow is yet again evident as the separation bubble on each plane is of different size and it is also established that the recirculation bubble is symmetrical to the channel mid-height plane (not shown). Besides, the size of the recirculation is relatively small, as the non-dimensional reattachment length  $L_{Z,r}^*$  (defined as the streamwise distance from the contraction at which the wall shear stress  $\tau_w$  vanishes) at the channel mid-height is found equal to 1.14. The small value of the reattachment length is attributed primarily to

the low Reynolds number (based on the fin thickness  $W_w$  [3.83]) which is found equal to 130. The reattachment-length value obtained by the present numerical calculations is also smaller than the experimental and numerical values for flow around a blunt plate at the same Reynolds number published by Ota et al. [3.95] and Yanaoka et al. [3.83] respectively. This is justified due to the high blockage ratio of the present study ( $BR=0.33$ ) which tends to reduce the recirculation bubble size and has an overall stabilizing effect on the flow [3.75].

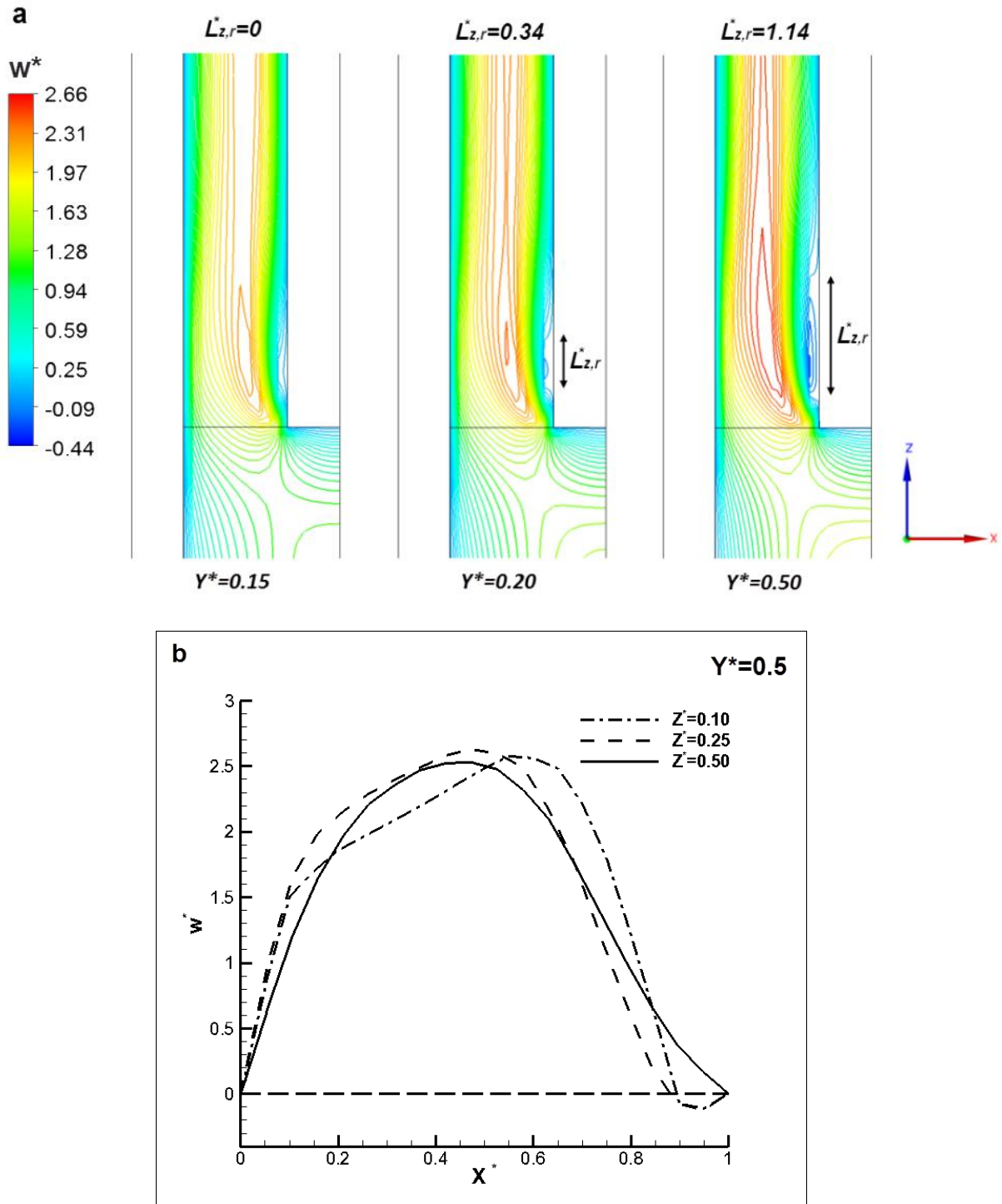


**Fig. 3.24** Reference case ( $Re_1=519$ ): (a)  $W$  – velocity contours at different horizontal planes and respective bubble lengths  $L_{z,r}^*$ , (b) Dimensionless axial velocity profiles along the spanwise direction.

The topology and magnitude of the entire secondary flow pattern has a crucial impact on the performance of the heat sink. It is therefore of use to further analyze the interaction between the longitudinal vortices and the recirculation bubble that forms downstream of the fin edge. It is shown in **Fig. 3.24a** that the bubble tends to reduce in streamwise length as the endwalls are approached. In fact, it disappears completely for  $Y^*$  values larger than 0.82 (and respectively lower than 0.18). **Fig. 3.25** elucidates the fact that the coherence of the bubble near the endwalls is destroyed due to the presence of the longitudinal vortices in that region. The action of these vortices is to bring high momentum fluid from the fluid-core region to the fin vertical wall, thus affecting the topology of the bubble. The longitudinal vortices are visualized using vorticity iso-surfaces, while streamlines are used in order to depict the downstream recirculation. As can be seen, the downstream recirculation bubble is present over most of the fin height, extending symmetrically from mid-height up to locations (along the Y axis) not influenced by the presence of the longitudinal vortices. Beyond these locations, the bubble breaks down as its energy is extracted from the vortices [3.82].

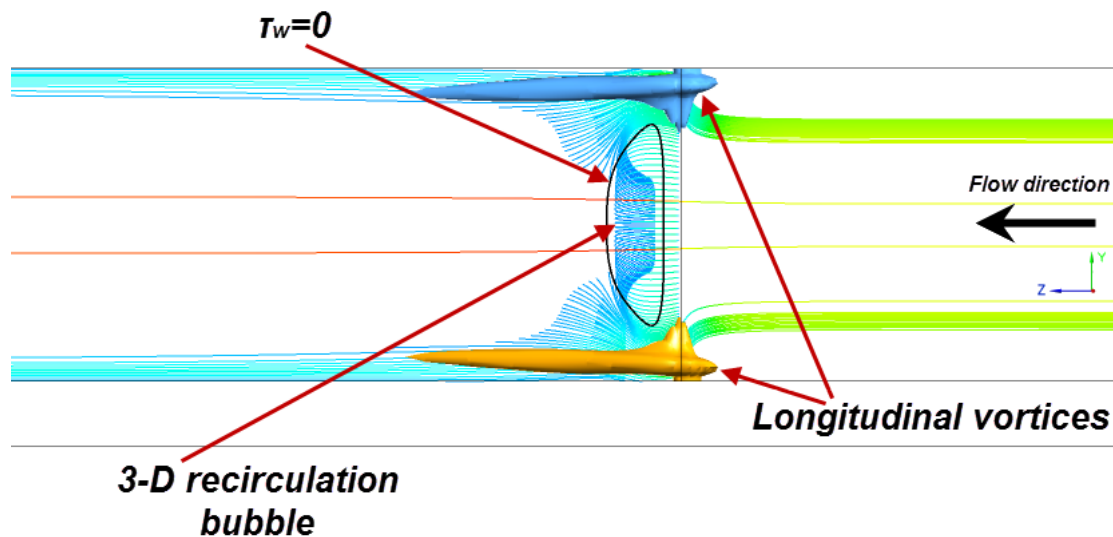


**Fig. 3.25** Interaction of the downstream vortical structures ( $Re_1=519$ ). The vortices are visualized using  $\omega_z$  iso-surfaces (of magnitude  $12.5 \text{ s}^{-1}$ ), while the bubble is illustrated through 3-D streamlines colored according to the axial velocity.

#### 3.4.3.7 Effect of the Reynolds number – Parametric analysis

The flow-topology examination has been further extended to larger values of the Reynolds number – $Re_1=1038$  and  $Re_1=1557$ – corresponding to twice and three times the flow rate of the base case, respectively. The corresponding Reynolds number in the latter case is 390 using the fin thickness as a characteristic length scale. The experimental investigation of Baker [3.93] revealed that no unsteady behavior of the horseshoe vortex did arise for Reynolds number values (based on the obstacle thickness) lower than 3000. Besides, numerical results for steady laminar confined flow around fins are available in the open literature for a value of the Reynolds number (based on the fin thickness) of 400 [3.73, 3.83], even for lower values of the blockage ratio. Thus, the assumption of steady and

laminar flow remains valid for the entire range of the examined Reynolds numbers. However, a steady-state solution could not be attained for higher values of the Reynolds number (e.g.  $1850 < Re < 2000$ ), as the steady-solver residuals exhibited a regular oscillatory pattern even for the dense grid considered, indicating non-convergence.

The objective of the present parametric investigation is to verify that the flow remains symmetric for the examined flow conditions. In order to examine the symmetric nature of the steady flow, a modified, extended computational domain was considered, comprising a full first-section channel divided into two by the additional fin inserted at its mid-length. It must be noted that the full domain comprised only fluid domains and was discretized using a grid consisting of twice number of elements of the fluid domains of the unit cell in each case.

**Fig. 3.26** depicts vorticity contours on two characteristic intersecting planes, which enable the characterization of the distinct flow features, for  $Re_1=1557$ . As can be seen in **Fig. 3.26a**, the flow remains perfectly symmetrical and the vortex structures that were apparent in the base case can once again be observed (vortices V1, V2, V3 and V4 of **Fig. 3.23b**); however, the vortices have an increased magnitude which is maintained for a substantial distance downstream of the contraction. Besides, the horseshoe vortices lay closer to the duct opposite wall in comparison to the base case ( $Re_1=519$ ), which indicates a more intense fluid deflection after the flow impingement on the fin frontal surface. **Fig. 3.26b** illustrates that, as the streamwise distance from the contraction increases, the downstream regions of high vorticity (vortices V3-V4) tend to completely detach from the fin sidewall and to move towards the channel center plane, whilst approaching each other. Likewise, the corner vortices (V1-V2) move towards the channel vertical center plane and tend to align with the vortices V3-V4, reducing at the same time the distance between them. The existence of symmetrical flow in the full domain validates the choice of truncating the computational domain to half the width for the investigation of the base case.

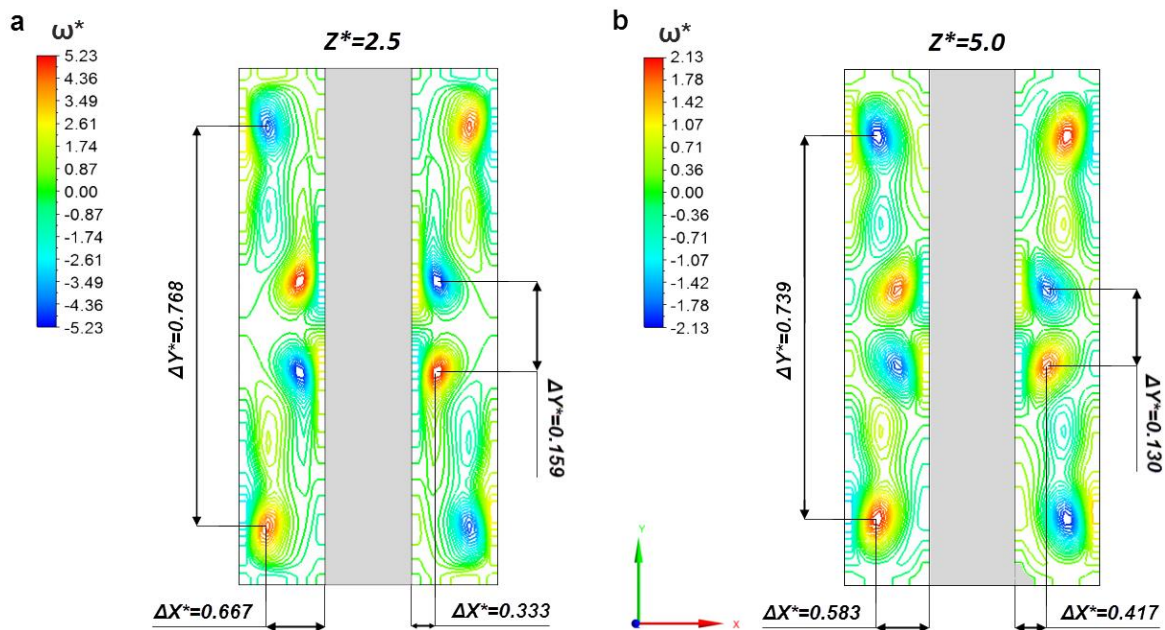


**Fig. 3.26** Symmetry verification on a laterally extended domain ( $Re_1=1557$ ): Contour plots of the  $\omega_z$  vorticity on cross-flow planes at (a)  $Z^*=2.5$  and (b)  $Z^*=5.0$ .

Fig. 3.27 presents the effect of the Reynolds number on the regions of the upstream and downstream recirculation bubbles. The minima of the pressure coefficient curves depicted in Fig. 3.27a correspond to the location of the upstream bubble locus [3.93] and indicate that the bubble moves upstream as the Reynolds number increases. Furthermore, only the two higher values of  $Re_1$  exhibit negative values of the  $C_p$  coefficient. This is due to the fact that the development of the recirculation leads to a local pressure drop to values lower than would have been attained without the presence of the fin, i.e. had the linear drop due to friction been extended to that location. Besides, an increase on the Reynolds number value causes an approximately linear expansion of the downstream recirculation to all three dimensions, a fact elucidated by the maximum bubble dimensions depicted in Fig. 3.27b for each Reynolds number value.

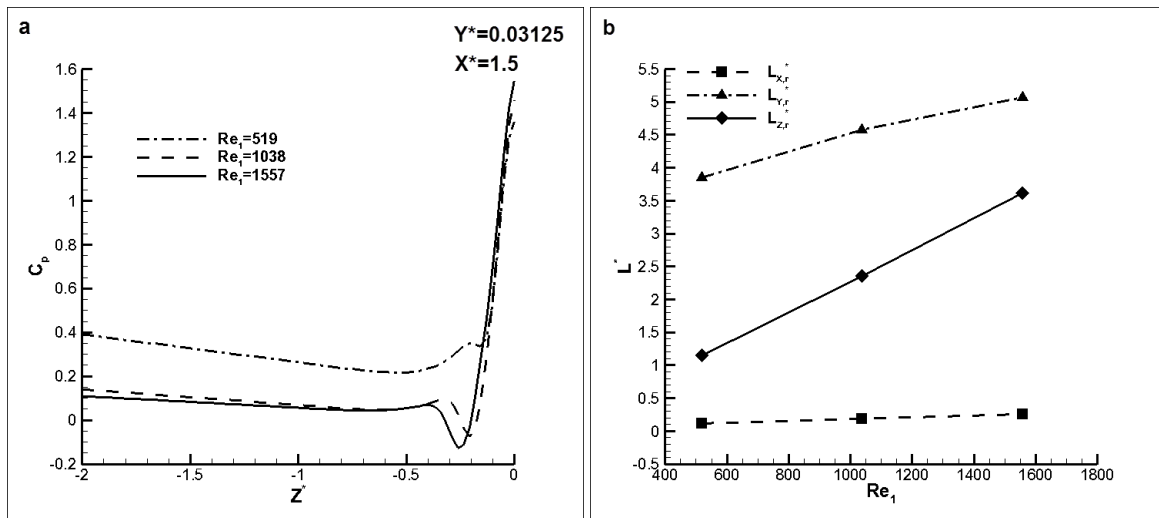


Fig. 3.27 (a) Upstream pressure variation in the vicinity of the lower endwall. (b) Maximum dimensions of the downstream separation bubble vs.  $Re_1$ .

### 3.4.3.8 Temperature field and heat transfer-Forced convection conditions

It is of importance from an engineering point of view to illustrate the impact of the contraction-induced recirculation pattern on the overall thermal performance of the heat-sink configuration. For this reason, forced convection conditions are considered in this section, in order to rule out the emergence of buoyancy-induced secondary flow that has a significant effect on the flow field, as will be illustrated in a following section. The imposed heat flux is properly selected, so that the Archimedes number has a value much smaller than unity. It is ensured thereby that buoyancy forces are orders of magnitude smaller than inertial forces.

It has been established that the flow remains symmetrical for the examined Reynolds number range and therefore the results concerning heat transfer are presented for the basic unit cell geometry (Fig. 3.14). Fig. 3.28 presents the temperature field in the flow contraction region on cross-flow, Fig. 3.28a, and streamwise planes Fig. 3.28b. Fig. 3.28a shows the development of the channel cross-section temperature distribution near the contraction, along the flow direction. The development of thermal boundary layers along the channel base and the side wall is clearly discernible for  $Z^* < 0$ . Downstream of the contraction ( $Z^* > 0$ ), the isotherms appear distorted at the locations of the longitudinal vortices, as warm fluid from the wall boundary layers is mixed with cold fluid from the

channel core. A high temperature area is evident at the “eye” of the lower vortex increasing in size downstream. This topology is not present at the symmetry position near the top wall as that endwall is adiabatic; clearly the temperature distribution on the cross stream planes is not symmetrical about the  $Y^*=0.5$  plane. A closer examination of **Fig. 3.28a** also reveals fluid cooling occurring at the bottom thermal boundary layer immediately upstream of the contraction (e.g., see plot at  $Z^*=-0.1$ ). This rather distinct temperature distribution can be explained by the presence of the reverse flow of cold fluid in the horseshoe-vortex region (**Fig. 3.22c**), which gives rise to axial heat transfer in the fluid thermal boundary layers and redistribution of thermal energy.

**Fig. 3.28b** exhibits a detailed view of the temperature distribution along the flow direction, particularly in the contraction region. A sequence of overlapping warm and cold water layers is evident close to the endwalls. The formation of characteristic streaks downstream of the contraction is accounted for, considering the entrainment back to the main flow of the elements of the fluid core that form the pair of horseshoe vortices which subsequently transform to longitudinal vortices downstream of the contraction. The fact that the distorted topology of the temperature contours, **Fig. 3.28a**, coincides with the streaks observed in **Fig. 3.28b**, also clarifies the effect of the vortices on the axial temperature distribution.

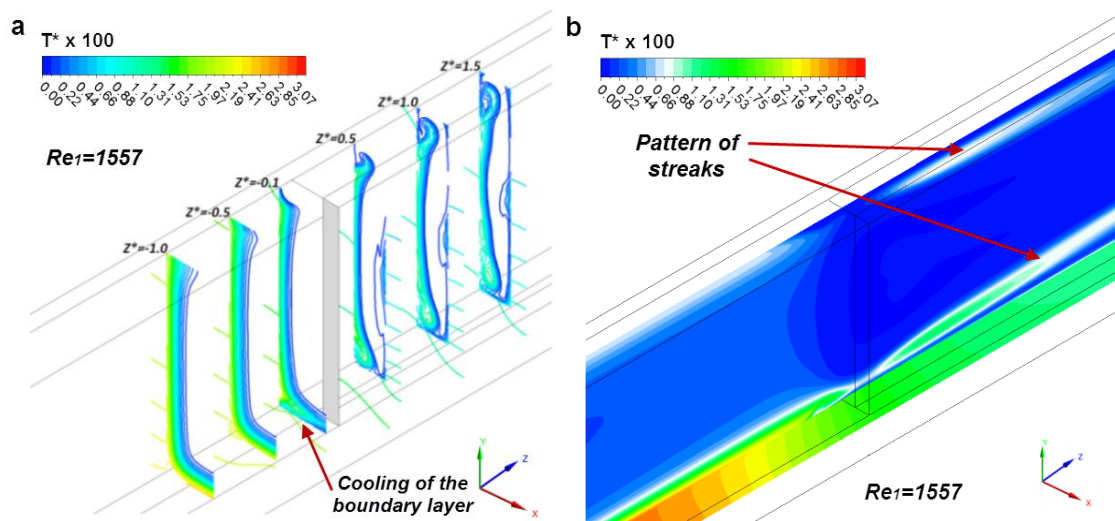


**Fig. 3.28** (a) Temperature contour plots on consecutive cross-flow planes in the vicinity of flow contraction and (b) on a longitudinal plane at  $X^*=0.5$ .

**Fig. 3.29** presents contours of the wall heat flux normalized by the mean overall heat flux  $\overline{q''}$  on the channel bottom wall (**Fig. 3.29a**) and on the fin sidewall (**Fig. 3.29b**), respectively. It is evident that the local wall heat flux at the bottom wall in the vicinity of the fin base obtains much larger values in comparison to the mean heat flux inside the heat sink (**Fig. 3.29a**), which is a clear evidence that heat transfer is significantly enhanced in the region under the influence of the lower horseshoe vortex. An interesting feature that may be observed is a region of local flux reversal (heat transfer from the fluid to the heat-sink base) which develops near the channel wall immediately upstream of the contraction. This is due to the cooling of the channel bottom wall under the action of the lower horseshoe vortex, while the fluid above and within the sidewall boundary layer maintains its elevated temperature. Although the occurrence of flux reversal is undesirable, the effect it has on heat transfer is localized and limited to a small area in the vicinity of the contraction. The effect of the horseshoe

vortex on heat transfer is also illustrated by the flux distribution at the fin sidewall, **Fig. 3.29b**, as the area influenced by the action of the lower vortex exhibits high local heat flux values. It is obvious, that the lower vortex predominantly contributes to the heat transfer enhancement due to the fact that this mainly takes place on the channel bottom wall, while the upper wall is adiabatic.

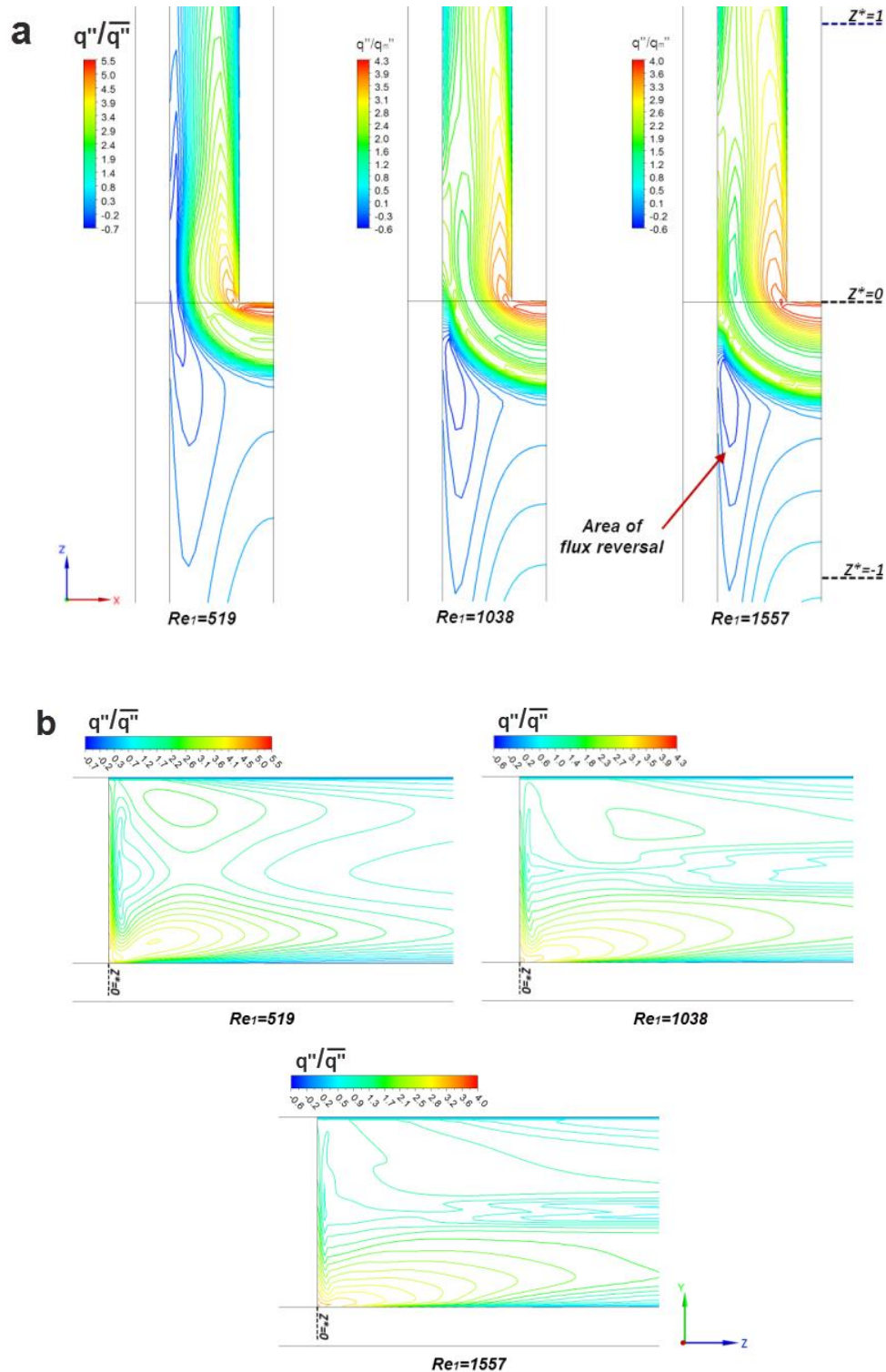
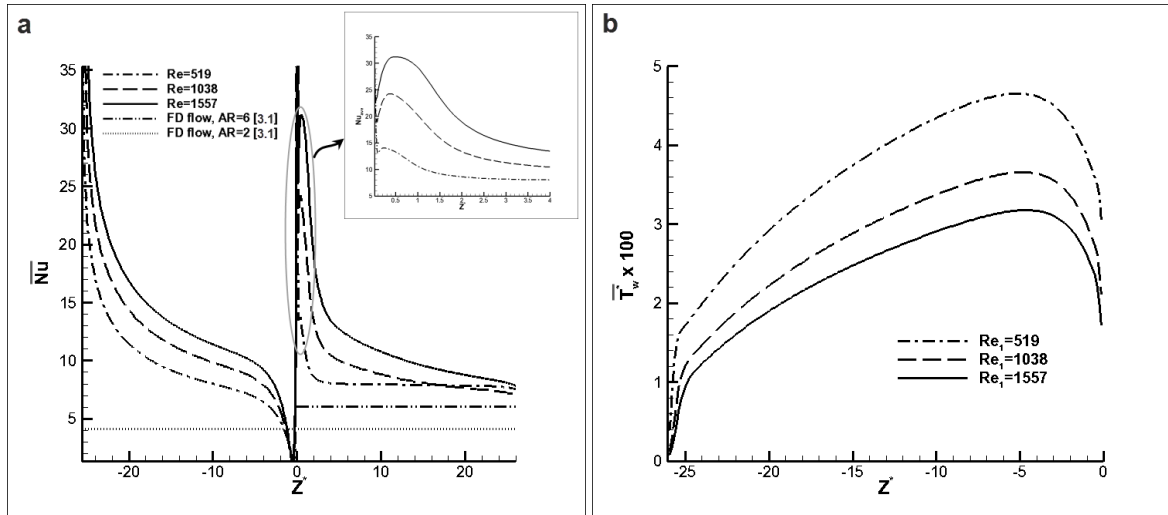


Fig. 3.29 Wall heat flux contours at the contraction region: (a) Channel bottom wall, (b) fin sidewall.

**Fig. 3.30a** shows the averaged local Nusselt number values along the flow direction for the three values of the Reynolds number considered. The theoretical values of the Nusselt number [3.8] for thermally fully developed parallel flow in channels having aspect ratios equal to the heat sink first (AR=2) and second section (AR=6), respectively, are also plotted in **Fig. 3.30a** for the sake of comparison. As can be seen, close to the channel inlet and away from the contraction influence the Nusselt number distribution behaves like a typical thermal entry flow. As the contraction is approached, the distribution shows a rapid decrease in the range of axial locations  $-4 < Z^* < 0$ . Nevertheless, this decrease of the heat transfer rate is not associated with a hot spot at the surface of the channel wall, as shown in **Fig. 3.30b**. The wall temperature in fact decreases prior to the contraction due to the influence of the second section and the action of the horseshoe vortices. On the other hand, fluid boundary layers of elevated temperature have developed adjacent to the walls. As a result, the temperature gradient  $dT/dy$  at the solid-fluid interface is considerably decreased in the specified region and consequently the heat flux ( $q'' = -kdT/dy$ ) and the Nusselt number values also decrease. The abrupt heat transfer augmentation in the contraction region is attributed to the flow impingement on the leading surface of the emerging fin. As can be seen from the inset of **Fig. 3.30a**, a second local Nusselt number maximum is observed due to the flow reattachment following the separation at the entrance to the second heat-sink section.

Downstream of the contraction, the Nusselt number maintains relatively constant values, which are higher than those expected for fully developed parallel flow in a channel of AR=6 [3.8]. This further heat transfer enhancement throughout the heat-sink second section is attributed to the presence of the two horseshoe vortices and especially of the one adjacent to the channel bottom wall. The vortex constantly feeds the heated bottom wall with cold fluid from the channel core causing disruption of the developing thermal boundary layer and thermal mixing. As a result, mixing zones consisting of cold and warm fluid layers emerge in the region of the boundary layer, which persist further downstream. If the channels of the first section were extended over the entire length of the heat sink and the flow remained parallel, the Nusselt number values would have gradually approached the fully developed value of 4.1. With the stepwise reduction of the channel hydraulic diameter however heat transfer is enhanced, as the aforementioned value is significantly exceeded.

A closer look at **Fig. 3.30a** reveals that the obtained Nusselt number values for  $Re_1=519$  are higher than the respective for  $Re_1=1038$  at axial locations of  $Z^* > 18$ . This slightly decreased heat transfer rate (by approximately 4%) for  $Re_1=1038$  is attributed to the three-dimensional effects and more specifically the effect of the sidewall vortex V4 on heat transfer, whereby fluid of elevated temperature is drawn from the thermal boundary layer near the bottom wall toward the channel mid-height (see **Fig. 3.22b**). Thus, the thermal boundary layer of the fin sidewall in the vicinity of the channel mid-height thickens locally and heat transfer is reduced. The effect appears to be significant for the two higher values of the Reynolds number as the Nusselt number values exhibit the same trend, while, on the contrary, the values for  $Re_1=519$  remain approximately constant. The influence of the sidewall vortex becomes more evident as thermal full development is approached and the Nusselt number tends to an asymptotic value.



**Fig. 3.30** (a) Circumferentially averaged local Nusselt number distribution against the fully-developed, parallel-flow result, (b) Wall average temperature at heat-sink first section ( $Z^* < 0$ ).

### 3.4.3.9 Flow Field-Mixed convection conditions

For a volumetric flow rate equal to 30 mL/s, in accordance to the reference case for forced convection conditions, the imposed heat flux is gradually increased, so as to cover the entire range of achievable concentration ratios for parabolic trough CPVT systems that can obtain values up to 100x [3.96]. The flow conditions in each of the two sections  $i$  ( $i=1$  or  $2$ ) of the VW configuration are characterized by the non-dimensional numbers summarized in **Table 3.2**. It should be taken in mind that the mean Archimedes number  $Ar_i$  and the corresponding Grashof number  $Gr_i$  are based on the circumferentially averaged heat flux, while the Reynolds number in each section  $Re_i$  varies between the different cases, despite the fact that the flow rate is maintained constant. This is due to the variation of the fluid kinematic viscosity  $\nu$ , which is evaluated at the fluid mean temperature in each case. Nevertheless, the Reynolds number for all three cases lies well within the laminar region. Considering the values of **Table 3.2**, it is reasonable to expect that buoyancy will have a significant impact on the flow within the first section of the heat sink where the respective buoyancy forces overpower the inertial forces in all cases.

**Table 3.2** Non-dimensional numbers for each heat-sink section  $i$  characterizing the examined cases.

$q''$ [kW/m <sup>2</sup> ]	Re		Gr		Ar	
	$i=1$	$i=2$	$i=1$	$i=2$	$i=1$	$i=2$
28.3	559	359	4.11E+05	8.66E+03	1.32	0.07
60.0	605	389	1.14E+06	2.37E+04	3.12	0.16
100.0	667	429	2.59E+06	5.29E+04	5.82	0.29

Considering mixed convection conditions, **Fig. 3.31a** reveals that buoyancy-induced longitudinal rolls that tend to draw fluid from the upper adiabatic wall towards the lower heated wall are present in the first section of the heat sink even for the lowest value of the Archimedes number,  $Ar_1=1.32$ . In reference to the case of  $Ar_1=1.32$ , the roll intensity appears to obtain maximum values at approximately  $Z^*=-10$ . The streamwise distribution of the maximum vorticity magnitude in the channel first section (**Fig. 3.31b**), away from the influence of the flow contraction, indicates that the

intensity of the rolls gradually increases until a maximum intensity is reached and then decreases as the contraction location is approached. This behavior, which has also been reported by Cheng [3.59], is dictated by the initially high and subsequently decreasing bulk temperature difference between fluid and channel wall [3.59], which consequently determines the intensity of the secondary flow. The location of the maximum roll intensity is shifted towards the channel inlet as the Archimedes number increases, while for  $Ar_1=5.82$  a second (local), albeit much flatter, peak in the value of the roll maximum intensity can be detected at approximately  $Z^*=-9.0$

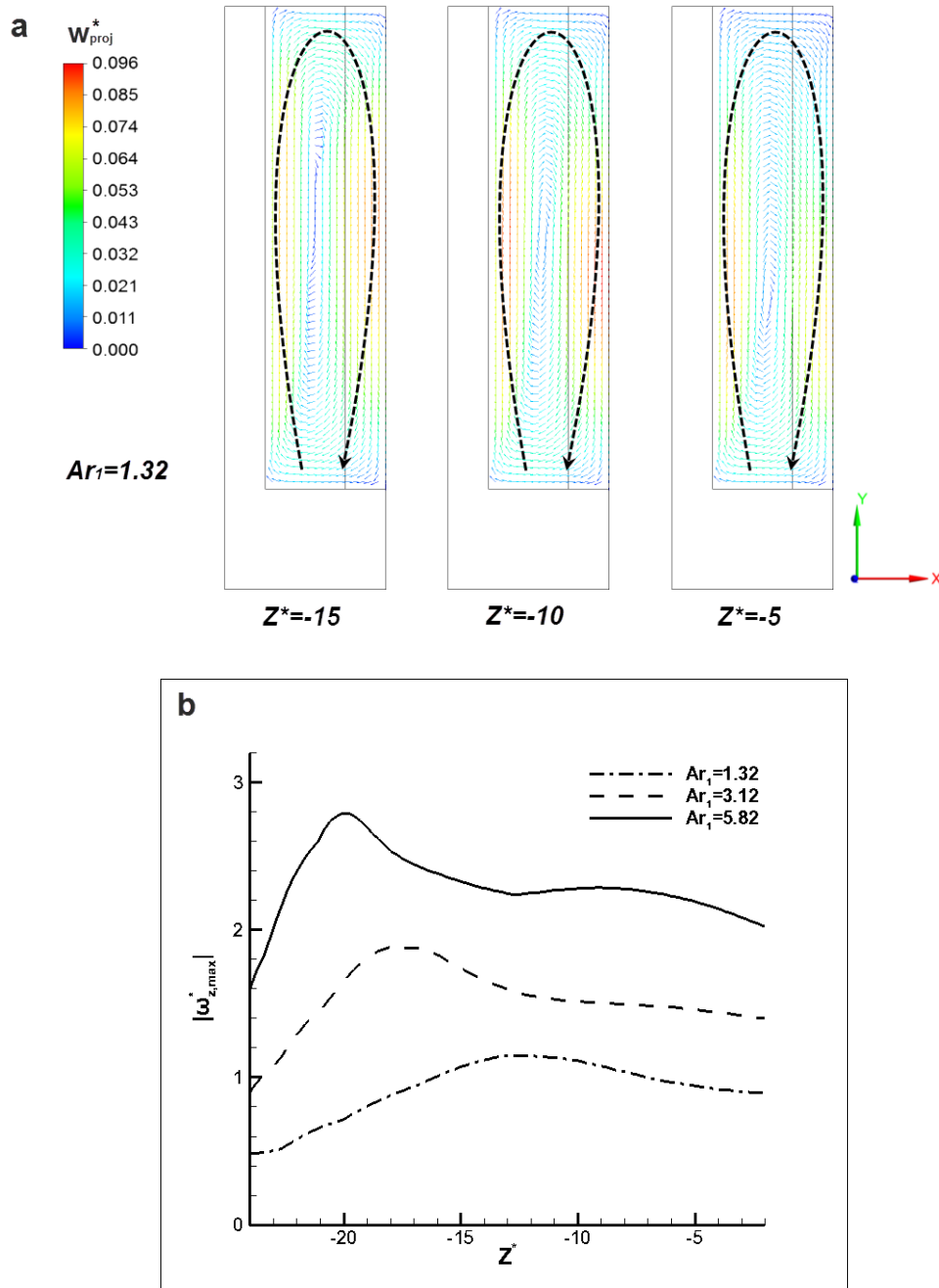


**Fig. 3.31** Buoyancy-induced secondary flow: (a) Velocity vector plot indicating the presence of a longitudinal roll in the half cross section of the first-section channel, (b) Distribution of the roll maximum vorticity magnitude in the first section of the heat sink.

As shown in **Fig. 3.31b** the longitudinal buoyancy rolls maintain a considerable magnitude as they approach the region of flow contraction and therefore, they interact with the contraction-induced vortical structures, as depicted in **Fig. 3.32a**. The interaction of the rolls with the longitudinal vortices produces a non-symmetrical flow field in the contraction region, as becomes evident from **Fig. 3.32b** where three pairs of  $\omega_z$ -vorticity iso-surfaces of equal magnitude ( $50-40-30\text{ s}^{-1}$ ) and opposite sign are plotted. The lower “modified” horseshoe vortex appears to be of considerably larger magnitude than the upper one, which is significantly shrunk in comparison to the non-buoyant case. **Fig. 3.32b** reveals that the topology of the hairpin-type vortex (see **Fig. 3.23c**) is affected by the buoyancy forces as well. The lower branch is much more localized than the upper one and furthermore it exhibits a higher intensity than its counterpart, as illustrated by the extent of the iso-surfaces of the highest  $\omega_z$ -vorticity absolute value. The asymmetric topology of the hairpin vortex is primarily influenced by the distortion of the upstream velocity profile and the shift of the maximum velocity location under the channel mid-height due to the effect of buoyancy forces.

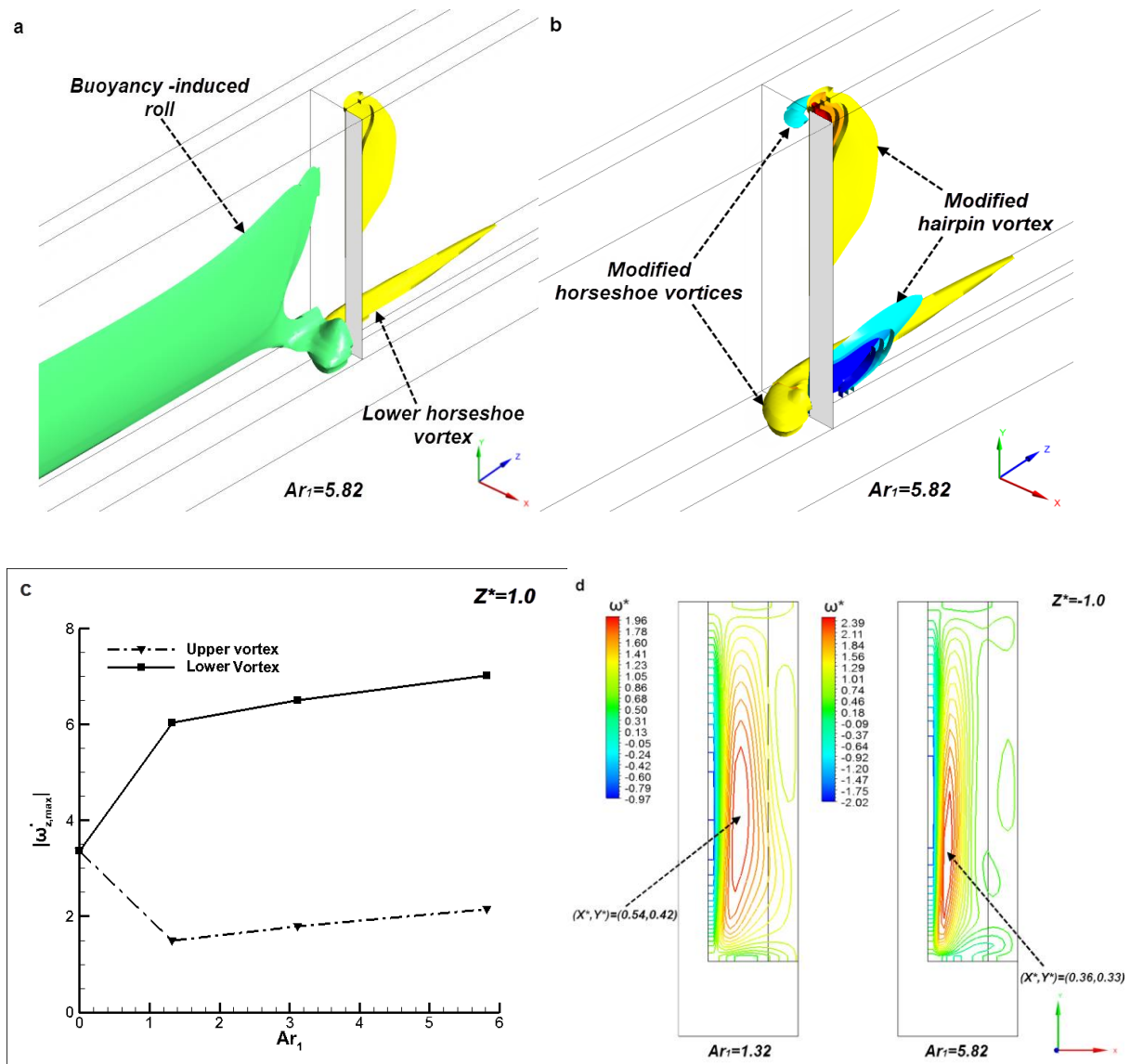


**Fig. 3.32** Vortical structures obtained for mixed convection at  $Re_1=559$ : (a)  $\omega_z$ -vorticity iso-surfaces ( $\omega_{z,vortex}=30\text{ s}^{-1}$ ,  $\omega_{z,roll}=8\text{ s}^{-1}$ ), (b)  $\omega_z$ -vorticity iso-surfaces in the contraction region, (c) maximum intensity of the longitudinal vortices at  $Z^*=1$  vs.  $Ar_1$ , (d)  $\omega_z$ -vorticity contours at  $Z^*=-1.0$ .

**Fig. 3.32c** presents the variation of the maximum vorticity magnitude values at a specified sampling location downstream of the contraction ( $Z^*=1.0$ ) with the Archimedes number. Both the buoyancy roll and the lower horseshoe vortex are of clockwise rotation and therefore their interaction leads to a significant enhancement of the lower longitudinal vortex, which subsequently leads to heavy fluid mixing in the vicinity of the heated bottom wall at the heat sink second section. The opposite is true for the upper vortex, as it is counter-rotating to the respective buoyancy roll. Regarding the mixed convection cases, both vortices tend to gain in magnitude which increases in a linear manner as the  $Ar_1$  number increases, albeit with the lower vortex exhibiting a relatively steeper increase with  $Ar_1$ . This magnitude enhancement of both vortices is, to some extent, also due to the change in thermophysical properties with the fluid mean temperature in each case. As the mean fluid temperature increases, the kinematic viscosity obtains lower values and the Reynolds number increases, consequently affecting the intensity of the longitudinal vortices (see **Table 3.2**). Nevertheless, regarding the upper vortex, the action of the buoyancy induced roll, which significantly increases in intensity with  $Ar_1$ , should counteract the effect of the increased Reynolds number. As depicted in **Fig. 3.32d**, the center of the roll moves toward the channel bottom wall as the Archimedes number increases and thus the influence of the roll on the upper vortex is mitigated to such an extent that it becomes inferior to the effect of the Reynolds number. On the other hand, the effect of the roll on the lower vortex becomes more significant for high values of the Archimedes number, a tendency that also explains the steeper increase in the magnitude of the lower vortex with  $Ar_1$ .

The topology of the fin tip separation bubble at the entrance to the second section of the heat sink is also significantly influenced by the combined secondary-flow pattern, as illustrated by the axial velocity contours on different horizontal planes, depicted in **Fig. 3.33a**. It is evident that the recirculation region has a three-dimensional non-symmetrical topology with its maximum size being located below the channel mid-height. Besides, the bubble does not occupy the entire width of the fin sidewall (e.g. see contour at  $Y^*=0.8$ ). **Fig. 3.33b** presents the distribution of the non-dimensionalized flow reattachment length  $L_z^*$  along the channel height for the three cases examined. An initial finding is that the streamwise and cross-stream extent of the recirculation region increases with  $Ar_1$ , although its characteristic shape remains invariable. It must be noted that the reattachment length downstream of the plate tip varies linearly with the Reynolds number [3.97]. In the present case, as explained earlier, an increase of the Archimedes number leads to an increase of the Reynolds number as well, up to approximately 19% for the case of  $Ar_1=5.82$ . Although, the shape of the separation bubble is significantly affected by the combined secondary flow, the reattachment length in the region around the fin mid-height is primarily influenced by the Reynolds number. Thus, the increased Reynolds number causes a more extensive recirculation region. Additionally, it can be seen that the recirculation bubble is completely absent for  $Y^*>0.77$  and  $Y^*<0.08$  in all cases. The upper part of the bubble is destroyed due to fluid stratification provoked by the buoyancy forces, while the lower part is destroyed by the lower horseshoe vortex which is of considerable size and draws high-velocity fluid towards the sidewall affecting this way the coherence of the bubble. The decay of the recirculation bubble in regions under the influence of longitudinal vortices has also been reported by Zhang et al. [3.82].

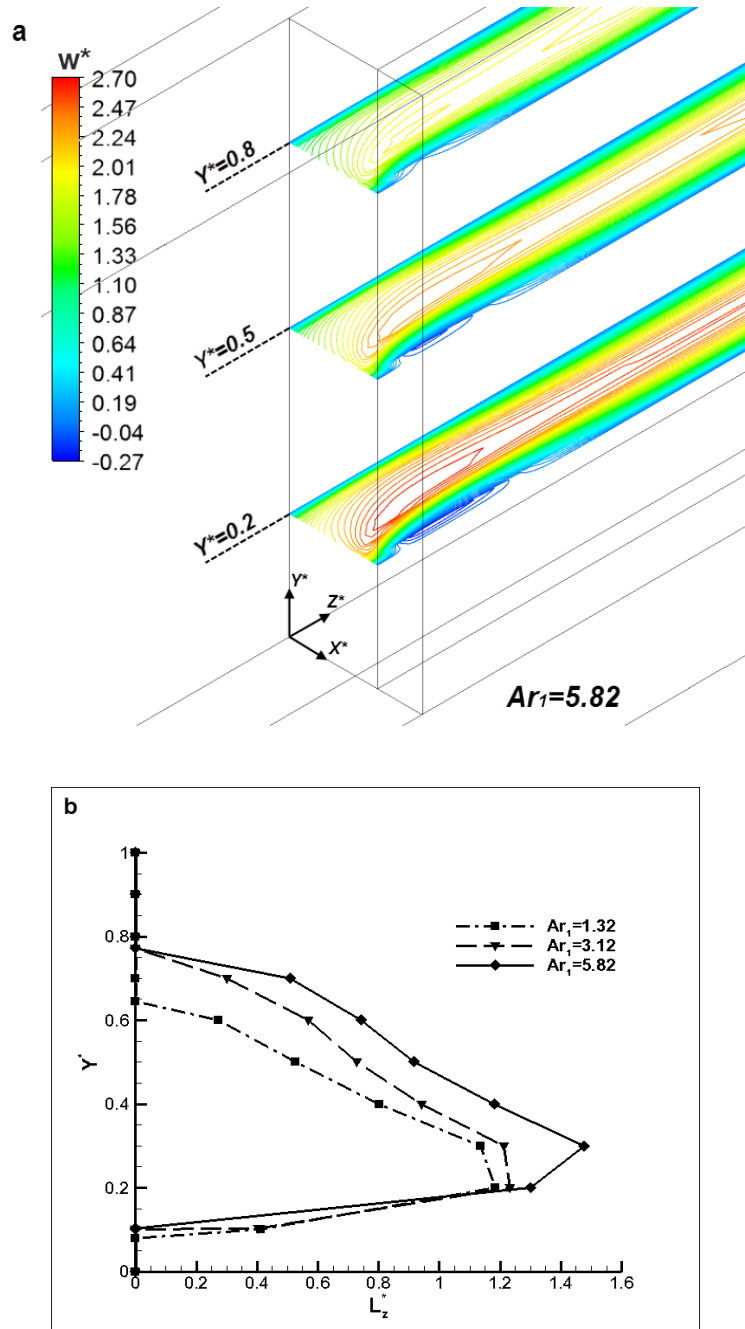
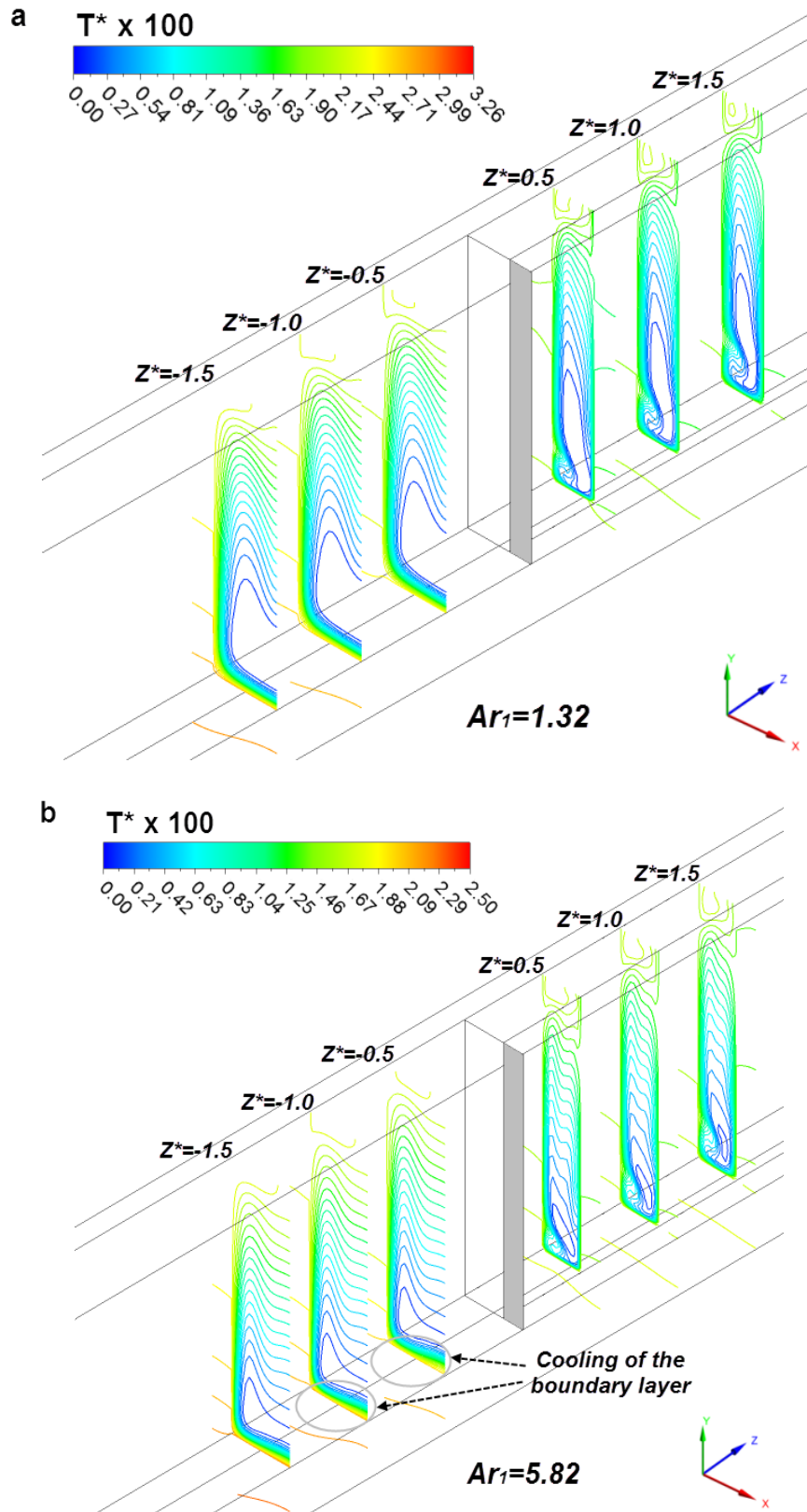


**Fig. 3.33** (a) Axial velocity contours at horizontal planes downstream of the flow contraction, (b) distribution of the reattachment length along the channel height.

### 3.4.3.10 Temperature field and heat transfer-Mixed convection conditions

The non-symmetrical recirculation pattern that arises within the heat sink due to the additional effect of buoyancy forces produces a modified temperature field in comparison to the forced convection case. **Fig. 3.34** illustrates the temperature distribution on several cross-flow planes in the vicinity of flow contraction for the cases of  $Ar_1 = 1.32$  (**Fig. 3.34a**) and 5.82 (**Fig. 3.34b**) respectively. Temperature stratification can be observed upstream of the contraction in both cases as warmer fluid is transferred towards the top of the channel due to the buoyancy forces; as expected, stratification is more intense for  $Ar_1 = 5.82$ . Contour plots at  $Z^* = -1.0$  and  $Z^* = 0.5$  reveal that the bottom wall boundary

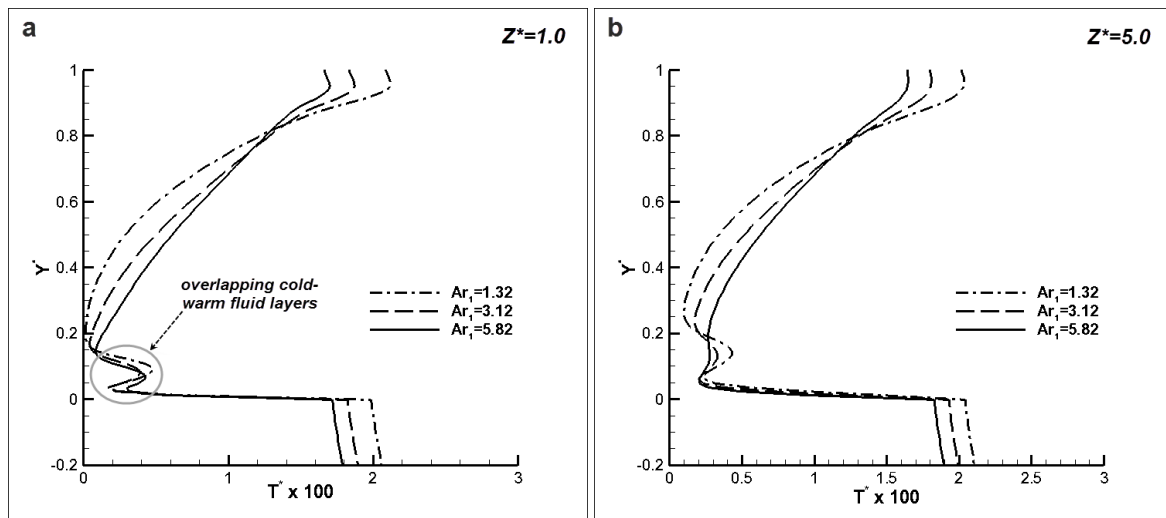
layer in the first channel section is subjected to cooling as the flow contraction is approached, in accordance to the forced convection case.



**Fig. 3.34** Temperature contour plots at cross-flow planes of increasing streamwise coordinate in the vicinity of the flow contraction: (a)  $Ar_1=1.32$ , (b)  $Ar_1=5.82$ .

Downstream of the contraction, the contour lines exhibit an intense distortion at the location of the strong lower vortex. This localized distortion is mainly due to the decreasing effect of buoyancy, which had a more global influence upstream, in the downstream section where the enhanced lower horseshoe vortex dominates. Regarding the case of  $Ar_1=5.82$  where the distortion is more pronounced, a high-temperature region is clearly visible at the “eye” of the lower vortex increasing in size downstream (**Fig. 3.34b**). In both cases, downstream of the contraction the unheated fluid core region is pushed toward the channel top wall causing thermal energy redistribution.

**Fig. 3.35** presents the development of the vertical temperature profiles at the center of the second-section channel ( $X^*=0.5$ ) for all the cases considered. The clearly discernible linear segment of the profiles near the bottom ( $Y^*<0$ ) accounts for the temperature distribution in the solid substrate. It is evident from **Fig. 3.35a** that downstream of the contraction ( $Z^*=1$ ) the temperature profiles exhibit substantial gradients in the fluid region right above the lower thermal boundary layer indicating the presence of overlapping layers of alternating cold and warm fluid in the lower channel region. These overlapping zones emerge due to heavy fluid mixing caused by the lower longitudinal vortex. A minor profile distortion is also evident at the symmetrical location near the top endwall. The distortion is of small scale due to the low magnitude of the upper vortex and primarily due to the imposed thermal boundary condition, as the top wall is kept adiabatic. **Figs. 3.35b** and **3.35c**, showing temperature profiles at further downstream locations ( $Z^*=5$  and  $Z^*=10$ ), illustrate the fact that the mixing zones extend to a considerable part into the second channel section, approximately equal to ten hydraulic diameters  $D_{h,1}$ .



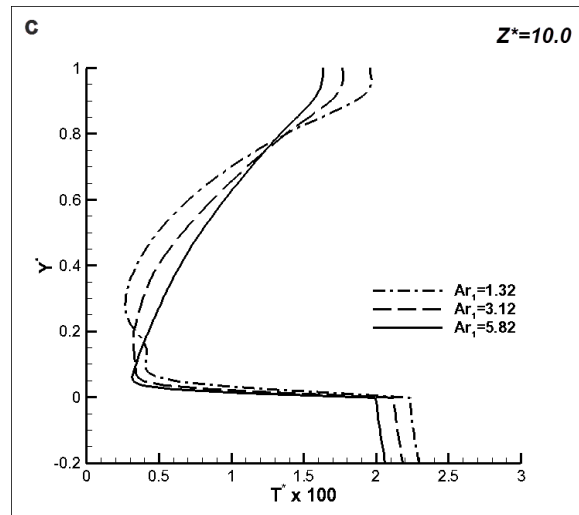


**Fig. 3.35** Temperature vertical profile development along the flow direction at  $X^*=0.5$ . Heat sink second section: (a)  $Z^*=1.0$ , (b)  $Z^*=5.0$  and (c)  $Z^*=10.0$

**Fig. 3.36a** presents the values of the average local Nusselt number along the flow direction for the three cases of increasing Archimedes number. The pure forced convection results ( $Ar_1=0$ ) are also presented for the sake of comparison. Regarding the first heat-sink section, heat transfer is significantly enhanced due to buoyancy as the local Nusselt values attained are much higher than the corresponding ones for forced convection and with a much flatter distribution. The enhanced heat transfer is explained, if the secondary flow pattern is considered, which is responsible for the continuous feeding of the heated bottom wall with cold fluid from the channel top layer. Downstream of the contraction ( $Z^*\geq 0$ ), the Nusselt number values obtained under mixed convection conditions are considerably higher than the respective ones for forced convection, despite the minor effect of buoyancy in the second section. It has been established that the lower longitudinal vortex gains in magnitude as the Archimedes number increases (see **Fig. 3.32c**) and this causes a more intense fluid mixing in the region of the bottom boundary layer, leading to increased heat transfer.

It is also evident from **Fig. 3.36a** that the distributions in the mixed convection cases exhibit a characteristic local minimum point at axial locations of the first section which tend to shift toward the channel inlet as the Archimedes number increases. This local minimum results from the combined effect of thermal entrance and buoyancy induced secondary flow [3.59, 3.62], manifesting the strong interrelation between heat transfer and secondary flow pattern, given that the buoyancy rolls obtain their maximum strength (see **Fig. 3.31b**) slightly downstream of the location of the minimum Nusselt number. Downstream of the latter location, a region of slightly increasing Nusselt number values is observed, which extends up to approximately  $Z^*=4$ . This increasing trend is due to the well-established recirculation pattern, which enhances heat transfer and hence, for a constant heat flux, decreases the wall-fluid temperature difference, as depicted in **Fig. 3.36b**. In the vicinity and immediately upstream of the flow contraction, a decrease in Nusselt number, attributed to flow separation upstream of the additional fin frontal surface, is observed, followed by a significant heat transfer rate augmentation at the location of the step-change reduction of the hydraulic diameter. **Fig. 3.36c** presents the local Nusselt number variation as a function of the non-dimensional “unwound” coordinate  $S^* = \frac{s - z_0}{D_{h,1}}$ , in the sense that the  $s$  coordinate describes the full unit cell outline at the

contraction region by also including the fin frontal surface. It is evident that the local Nusselt number exhibits its peak value exactly at the symmetry line of the fin and maintains very high values throughout the fin frontal surface. This abrupt heat transfer enhancement is due to the flow impingement on the leading surface of the additional fin, combined with the action of the lower horseshoe vortex which draws cold free-stream fluid toward the fin (heated) frontal surface.

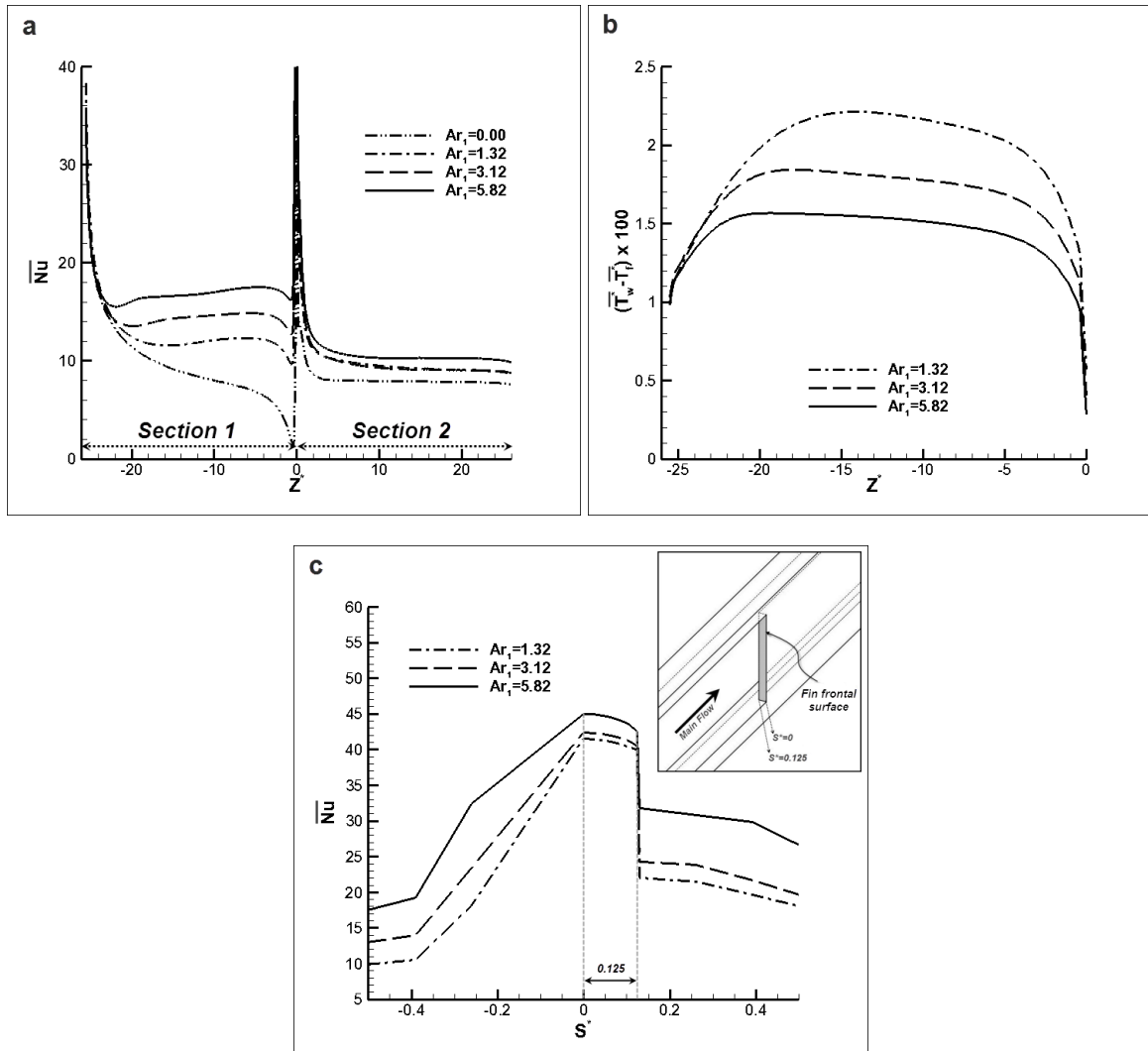


**Fig. 3.36** (a) Distribution of the circumferentially averaged Nusselt number in the streamwise direction, (b) average wall-fluid temperature difference in the first heat-sink section and (c) local Nusselt number variation in the vicinity of the flow contraction as a function of the unwound coordinate for various values of  $Ar_1$ .

It has been established that the buoyancy induced recirculation has a significant influence on heat transfer at the first heat-sink section, as fluid from the upper part of the channel is drawn towards the bottom wall. Consequently, it is of interest to examine the effect of the top wall boundary condition on the local heat transfer rate. Two kinds of heating conditions were considered, namely heating through three (3HS) or four surfaces (4HS). The computational domain representative of the latter case (four heated surfaces) includes an additional solid domain characterized by the same thermal conductivity ( $k_{al}=237 \text{ W/mK}$ ) as the rest of the heat sink body at the top part. **Fig. 3.37** depicts the ratio of the Nusselt number values for the two different heating conditions considered. As illustrated, the use of an insulating top cover enhances heat transfer throughout the heat sink and especially in the first section

where fluid from the top part of the channel is entrained into the lower thermal boundary layer. If the channel top surface is kept adiabatic, fluid of lower temperature is drawn toward the bottom wall due to the absence of a top thermal boundary layer, as illustrated by the inset of Fig. 3.37. Consequently, maintaining the upper part of the heat sink adiabatic is favorable in terms of thermal performance.

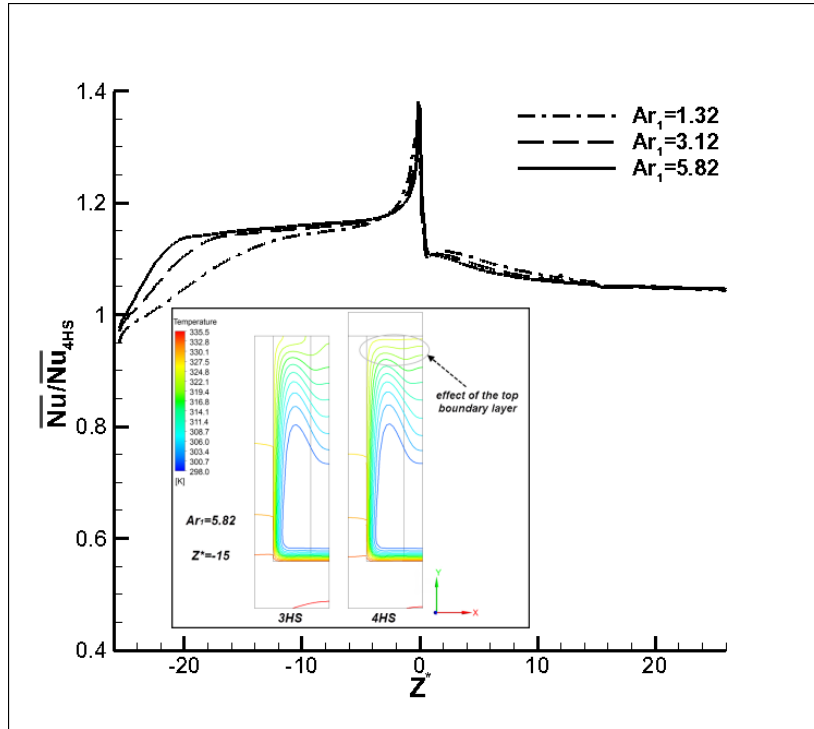


Fig. 3.37 Comparison of the Nusselt number values attained for heating through three vs. through four surfaces.

### 3.4.4 Heat transfer enhancement: cold-fluid injection in the channels

As can be deduced from the temperature distributions developing in the VW configurations, e.g. Fig. 3.30b, the first heat-sink section prior to the geometry contraction is expected to exhibit the maximum wall temperature due to the moderate thermal performance of the wide channels, regardless of the number of heat-sink sections. A variation of the VW heat-sink design has thus been conceived and presented in the present paragraph, with additional vertical inlets that feed cold fluid to the region of the heat sink with the least effective thermal performance, in order to cause local thinning of the thermal boundary layer and thus heat transfer enhancement. Besides, the longitudinal vortices that are expected to set in, act as additional heat transfer enhancement mechanisms. The arising configuration bears similarities to the problem known as “Jets in Cross-Flow” in the fluid-mechanics literature, thus the present investigation will seek valuable information among the findings of the prior relevant research. The additional inlets (cooling holes) are here being placed at the heat-sink top wall so that a portion of the overall flow rate enters the heat sink vertically through the cooling holes, while the remaining enters in parallel through the inlet. Thus, the liquid jets are submerged into the main flow under cross-flow conditions. Considering that the cooling holes are located at the channel top wall, a large jet penetration is required in order to achieve effective cooling of the bottom wall. It must be noted that the present configuration has been considered only for numerical evaluation, as the realization of a prototype, hybrid VW device with inlets at the top cover would also require the design

of an additional manifold system to feed the jets. The integration of such a manifold within the CPVT system receiver was considered as high risk, considering the manufacturing know-how at the time, in terms of reliable operation and successful sealing to prevent leaks of the cooling fluid.

#### 3.4.4.1 Jets In Cross-Flow (JICF) – Literature survey

The utilization of jets in cross-flow for cooling purposes is a common practice encountered in the field of turbomachinery in order to protect the turbine blade, which is exposed to gas of high temperature. This technique is referred to as film-cooling, as a film of air is interposed between the blade and the hot gas. The jet of the cooling fluid must remain close to the blade surface and thus the injection nozzles must be properly designed so as to induce low penetration of the jet into the main flow [3.98]. For this reason, special attention is given to the design and orientation of the cooling nozzles [3.99,3.100] which primarily affect the jet penetration. Liang and Kang [3.101] experimentally evaluated the cooling performance of jets in cross-flow to an unconfined air stream for different jet plenum shapes, namely a straight and a 90° curved plenum. The film cooling effectiveness of the jets exiting the curved plenum was found to be higher than those exiting the straight one regardless of the blowing ratio. The superior performance was attributed to the longitudinal (Dean) vortices induced by the plenum curvature that keep the jet attached to the wall, as they counterbalance the effect of the vortices that onset due to the interaction of the two streams. Increased blowing ratio was found to enable the thermal mixing between the streams and lower cooling effectiveness. The authors concluded that the optimum blowing ratio was in the range 0.2-0.4.

In a quite different field of application, cooling of electronics, Jubran and Al-Salaymeh [3.102] experimentally investigated turbulent heat transfer over an array of parallel rectangular blocks. They evaluated the thermal wake on subsequent blocks of the same column due to the heating of an upstream specified block. Layouts of secondary flow injection were inserted between the rows, in order to evaluate the potential cooling efficiency enhancement. It was concluded that the secondary flow injection was superior, in comparison to placing ribs to disrupt the development of the boundary layer, in terms of temperature attenuation and induced pressure drop. Larraona et al. [3.103] proposed the incorporation of jet-in-cross-flow configurations also for cooling electronic circuits. Their parametric study revealed that the cooling effectiveness is mainly influenced by the cross-flow velocity and the jet blowing ratio. In general, the overall Nusselt number obtained was found to be higher in comparison to parallel-flow configurations. It must be noted that the objective in the case of electronics cooling is the opposite combined to blade cooling as high jet penetration is sought, in order to instigate thermal mixing and heat transfer enhancement. Jubran and Al-Haroun [3.104] focused on the effect of various flow injection layouts on heat transfer and pressure drop using an experimental setup similar to that used in [3.102]. Their experimental results demonstrated that decreasing the flow injection angle has a beneficial impact on heat transfer and that the optimal hole pitch-to-diameter ratio was 2.5. Besides, the pressure drop was found to remain relatively unaffected by the blowing ratio.

Allauddin et al. [3.105] illustrated the heat transfer enhancement obtained through the use of jets in cross flow in conjunction with detached ribs protruding from the heated surface. For turbulent flow conditions, their numerical results showed that the heat transfer rate increases with the jet blowing ratio, while the axial location of maximum Nusselt number shifts further downstream from the jet

inlet, as the blowing ratio decreases. The use of detached ribs was found to be beneficial in terms of heat transfer, only in the case of multiple jet configurations. Wong [3.106] simulated the effect on heat transfer of a laminar jet in cross-flow inside a microchannel of hydraulic diameter equal to  $390\mu\text{m}$ . The numerical results showed that the overall Nusselt number increases as the jet Reynolds number and consequently the jet penetration increase. Furthermore, it was shown that it is beneficial in terms of heat transfer the jet inlet hole to be located close to the channel inlet.

The injection of a jet into parallel flow distorts the jet main axis and gives rise to various coherent vortical structures [3.107-3.113]. Along the streamwise direction, a counter rotating vortex pair (CVP), also referred to as kidney-shaped vortices, emerges in the near field, downstream of the jet due to the shear of the cross-flow and follows the jet trajectory, whereas a horseshoe vortex emerges upstream of the cooling hole due to the fact that the jet is perceived by the cross-flow as a bluff body. In addition, ring vortices have been observed to wrap around the CVP, as well as unstable wake vortices that form perpendicular to the cross-flow. In an early study, Chassaing et al. [3.107] managed to experimentally determine the central axis of a turbulent jet in cross flow for values of the blowing ratio in the range 2.37-6.35. The horizontal velocity profiles downstream of the jet were found to have a symmetric parabolic form for blowing ratio equal to 3.95. Sherif and Fletcher [3.108] measured the vertical velocity profile downstream of a jet in cross flow under turbulent conditions. For Reynolds number in the range of 17000 to 26000 and blowing ratio equal to four and six it was established that the profile exhibits two peaks, a prevalent one within the jet core and a minor one within the jet wake upstream of the jet near vertical part.

Huq and Dhanak [3.109] visualized the turbulent flow field emerging from a jet in cross-flow with the jet injection point being located above the cross-flow boundary layer. It was observed that the jet bifurcates, i.e. two clearly discernible coherent vortical structures exist along the cross-flow direction for values of the blowing ratio larger than four. The flow topology and the vortical structures emanating due to the interaction of a round jet and the oncoming parallel flow are illuminated in the experimental study of Kelso et al. [3.110]. It was illustrated in the study that the horseshoe vortices with opposite vorticity in reference to the wall vorticity detach from the wall and merge with the CVP pair. In addition, the form of the jet was observed to be asymmetrical for Reynolds number equal to 6200 and blowing ratio equal to 2.2. Shedding of the wake vortices was observed for values of the cross-flow Reynolds number greater than 500. As pointed out by Rivero et al. [3.111], the CVP pair is a prominent flow feature manifested at the interaction of a jet with a parallel flow stream, regardless of the Reynolds number and the blowing ratio. It was furthermore illustrated in [3.111] through plots of the instantaneous velocity field that the counter rotating vortices are in fact an unsteady feature of the flow and that their time-averaged topology for specified flow conditions ( $Re=6600$  and  $BR=3.8$ ) obtains a distorted, asymmetrical meandering form. Sau et al. [3.112] thoroughly elucidated the flow field emanating from a square jet in cross-flow by conducting unsteady direct numerical simulations. It was pointed out that the shear layer vortices upstream of the jet are induced due to a Kelvin-Helmholtz instability and that they do not form closed loops but instead their open tails eventually merge with the CVP. It was furthermore shown that the horseshoe-vortex branches downstream of the jet detach from the wall and they are entrained upwards and eventually merge with the CVP in an unsymmetrical manner. Bagheri et al. [3.113] conducted a linear stability analysis for a jet in cross-flow under laminar flow conditions for both flow streams and a blowing ratio equal to 3. The analysis

showed that the flow is globally unstable and that the instability is manifested through oscillating waves the wrapped around the CVP.

All the studies referenced above investigate the flow features of a round jet emerging in an unconfined parallel flow stream. Few studies have been found in the literature that examine additional factors, related to the geometry or the flow conditions, that could possibly have a significant influence on the emanating flow field in JICF configuration [3.114-3.118]. Fernandes et al. [3.114] focused on the effect of flow confinement, due to the presence of rigid walls, on the distinct flow features of a turbulent jet in turbulent cross flow. Their flow visualization studies revealed that the growth of the CVP is hindered by the confining walls and that the jet central axis exhibits a more significant bend in comparison to unconfined jets. Saha and Yaragani [3.115] conducted a numerical study on the immersion of a square jet in cross-flow for Reynolds number equal 100. It was shown that a three dimensional hairpin vortex, having its main axis perpendicular to the main axial flow, emanates from the shear layer at the side edges of the jet nozzle. It was furthermore proven that a jet immersing into the axial flow with a parabolic velocity profile has a greater penetration and is significantly detached from the wall in comparison to one having a uniform profile. Thus, it was deduced the film cooling effectiveness of a uniform-profile jet is higher.

Wang et al. [3.116] numerically verified, conducting both steady RANS and unsteady DES simulations, the existence of a bifurcation in the case of a square jet in cross-flow under turbulent flow conditions ( $Re_{jet}=4700$ ). The counter rotating vortex pair that emerges downstream of the cooling hole is found to be of asymmetrical topology when the velocity ratio surpasses a critical value of 0.7. Gungor and Roberts [3.117] visualized the flow topology of a turbulent jet entering a fluid cross-flow of lower density using laser induced fluorescence. The flow visualization revealed that for high values of the cross-flow the dense jet obtains an asymmetrical form and bifurcates completely after its interaction with the solid wall. Kishore et al. [3.118] focused on the interaction of two identical circular jets in cross-flow for a velocity ratio (jet to parallel flow) velocity equal to 5. Their numerical investigation revealed a different secondary flow topology in comparison to single-jet configurations and it was confirmed that neither the jet vertical center plane nor the plane at the mid-distance between the jets can serve as symmetry planes.

Given the beneficial effects on cooling found in previous studies, the incorporation of JICF in the VW configuration was considered and results of a numerical investigation are presented in this paragraph. The effect of flow confinement due to presence of the channel side walls is expected to be significant, thus new findings related to new fluid dynamical phenomena are expected to arise and offer an important contribution to the international literature. In this effort, both single and dual-jets systems will be evaluated and the influence of jet interaction on the secondary flow will be discussed as well. The main objective is to point out which of the distinct flow features that arise due to the interaction of the jets with the bottom channel wall and the main flow promote thermal mixing and increase the heat transfer rate.

#### 3.4.4.2 Geometry and computational domain

The geometry of the hybrid (JICF-VW) configuration is identical to the VW configuration with the only exception being the placement of cooling holes at the top part of the heat sink (**Fig. 3.1e**). Two jet configurations were considered, namely a single and a dual-jet system per channel. From a

manufacturing point of view, the implementation of the jets can be accomplished by drilling holes to the top heat-sink cover and connecting a manifold of tubes of small cross-section onto it. The lower limit for the cooling-hole diameter was selected equal to 1.0mm, which can be easily achieved by conventional drilling. In both the cases of single and dual-jet configurations, the overall area of the cooling holes was maintained roughly the same so as to ensure that the flow conditions are similar for the two jet configurations. Thus, the diameter of the cooling holes was equal to 1.0 mm and 1.4 mm for the single and dual-jet systems, respectively. Regarding the dual-jet configuration, the cooling holes had their centers transversally positioned, so as to coincide with the vertical symmetry plane of the second-section channels (**Figure 3.38a**). The cooling holes were placed at a location of the first-section of the heat sink (**Figure 3.38b**), where, for exclusively parallel flow, the wall average temperature is approximately equal to that at the heat sink outlet, as ideally the wall temperature values at the first section should not exceed those of the second section.

The computational domain of the configuration (**Figure 3.38**) comprises the fluid and solid regions that correspond to the full width of one first-section and two second-section channels, respectively, i.e. the computational domain used for the VW heat-sink cases analyzed in **paragraph 3.4.3** has been doubled. The use of the extended domain despite the fact that the geometry is perfectly symmetrical, is essential as the blowing ratio in the present investigation reaches values up to 7.3, which is well above the critical values for which breaking of symmetry has been reported [**3.111, 3.112, 3.118**]. Thus, a full domain is necessary to fully capture the flow topology. Additional internal cylindrical fluid sub-domains have been defined at the locations of the cooling holes, so that the mesh can be locally refined in the region in proximity to the cooling holes, being subject to the direct influence of the jets.

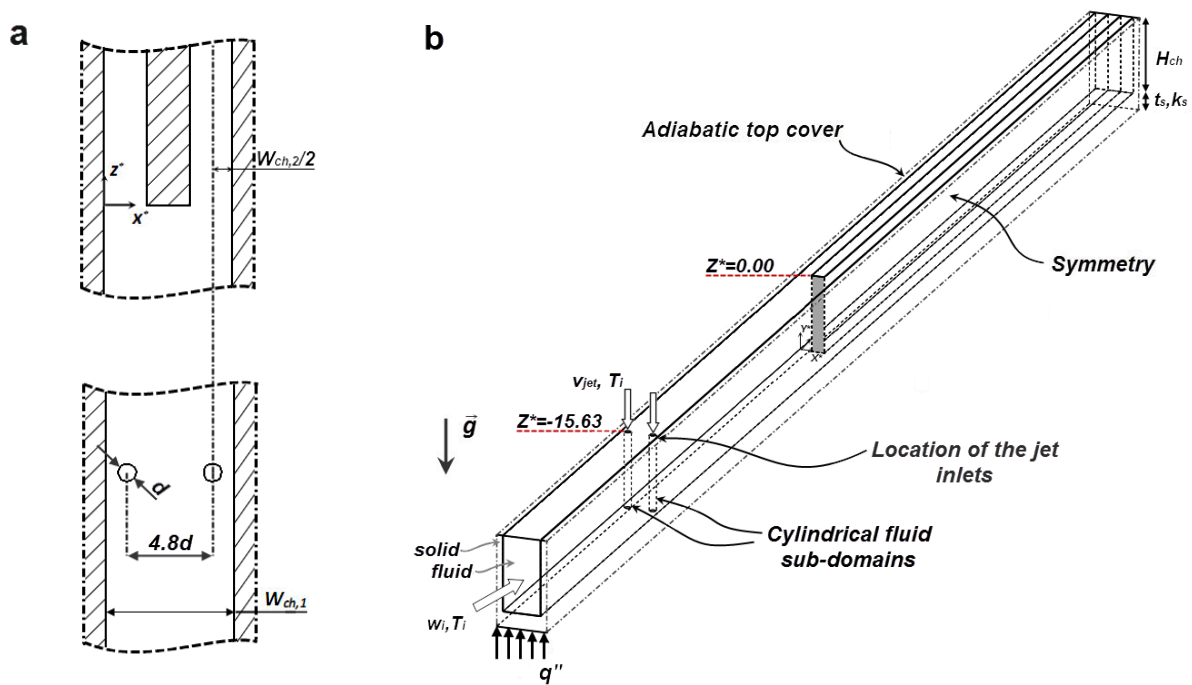


**Fig. 3.38** Computational domain for the JICF-VW configuration (dual-jet variation): (a) Top detailed view of the flow-contraction region, (b) perspective view.

In accordance to the cases referring to the conventional VW device, the hybrid configuration has been investigated under both forced and mixed convection conditions. The set of governing equations (3.1)-(3.4) or (3.1), (3.2)-(3.5) were considered for the forced-convection and mixed-convection cases, respectively. In regard to the originally imposed boundary conditions, apart from Eqs. (3.12)-(3.20), additional inlet conditions were imposed at the areas of the domain upper surface corresponding to the exit from the cooling holes. Both a uniform and a fully developed laminar velocity profile have been considered for the jet inlet, in order to illustrate the profile effect on jet penetration. The boundary conditions applied at the jet inlet in each case are, thus, the following:

At  $y = t_s + H_{ch}$ ,

$$u = 0, \quad v = -v_{jet}, \quad w = 0 \quad \text{(uniform profile)} \quad (3.33)$$

$$u = 0, \quad v = -2\bar{v}_{jet} \left( 1 - \left( \frac{r}{R_{jet}} \right)^2 \right), \quad w = 0 \quad \text{(fully-developed profile)} \quad (3.34)$$

where  $r = \sqrt{x^2 + y^2}$ ,  $\bar{v}_{jet} = \frac{\dot{V}_{jet}}{\pi R_{jet}^2}$  and  $R_{jet}$  is the cooling hole radius. The governing equations along

with the boundary conditions were solved on the computational domain with a convergence criterion of  $10^{-6}$  set for the root mean square (RMS) mass, momentum and energy residuals.

#### 3.4.4.3 Grid independency

The computational domain for the hybrid VW configuration was discretized with a grid similar to that depicted in **Fig. 3.17**, in the sense that smaller control volumes were placed in the vicinity of the geometry constriction, while the grid arrangement was cross-sectionally uniform. However, non-orthogonal elements were placed at the region enclosing the new internal fluid sub-domains, constituting by this way the grid unstructured. Furthermore, the grid was locally refined at the vicinity of the jets, as depicted in **Fig. 3.39**.

The grid independency study was conducted for the case of the dual jet system, where the most complex velocity field is expected to set in. Pure forced convection conditions were considered and the jets were assigned fully developed inlet velocity profiles. Three grids consisting of 9.39 (coarse), 16.48 (intermediate) and  $23.82 \cdot 10^6$  elements (dense) were successively tested to confirm that a grid independent solution had been obtained. The accuracy in the prediction of the flow field was evaluated by monitoring the vertical profile of the axial velocity at a location five hydraulic diameters downstream of the cooling holes ( $Z^* = -10.63$ ), which is expected to exhibit significant fluctuations as reported by Sherif [3.108]. As depicted in **Fig. 3.40**, the profile indeed exhibits one global and two local maxima, which are accurately captured only by the intermediate and the dense grid. In reference to heat transfer, the discrepancy in the values of the overall Nusselt number produced by the coarse and the dense grid is approximately equal to 0.2%. In order to predict both the flow and thermal fields accurately, the intermediate grid is selected for the production of the presented results.

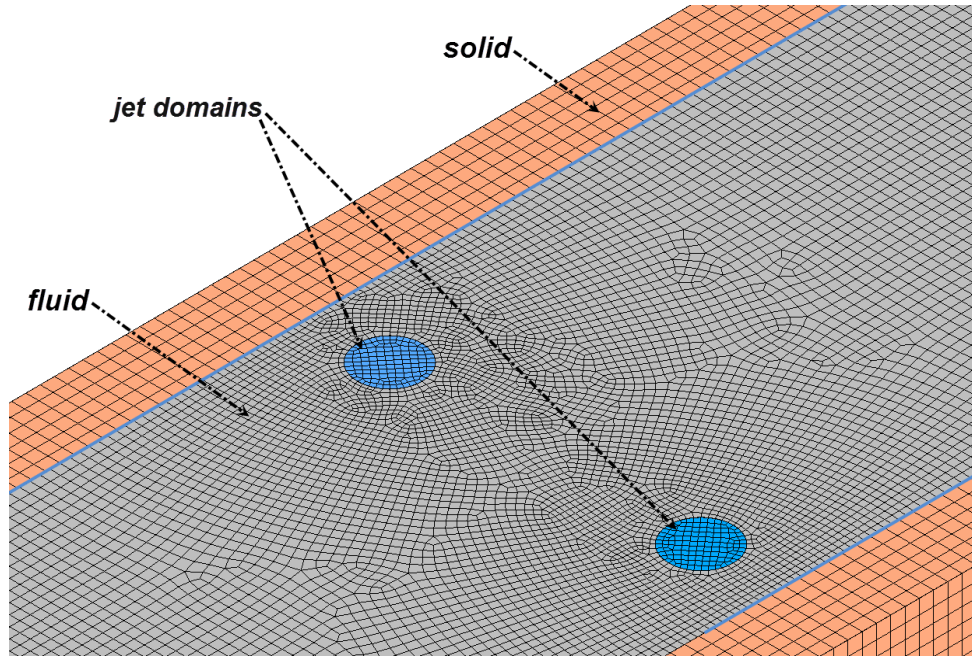


**Fig. 3.39** Local refinement of the computational grid in the vicinity of the “jet” injection and the specially defined internal sub-domains.

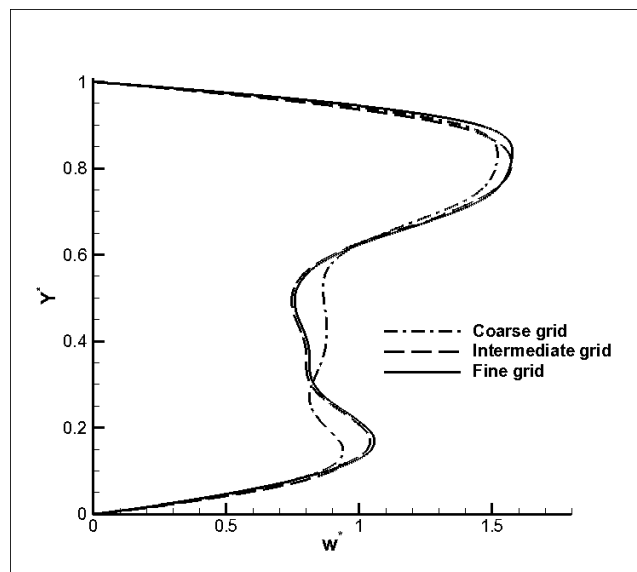


**Fig. 3.40** Vertical profiles of the axial velocity at the plane of the jet axis ( $X^* = 2.5$ ) downstream of the cooling holes ( $Z^* = -10.63$ ).

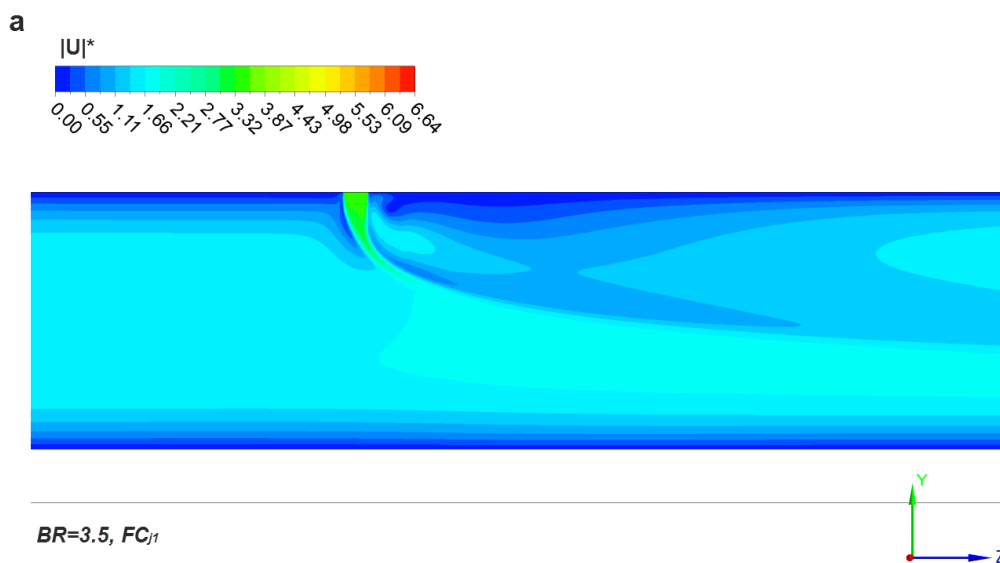
#### 3.4.4.4 Flow field

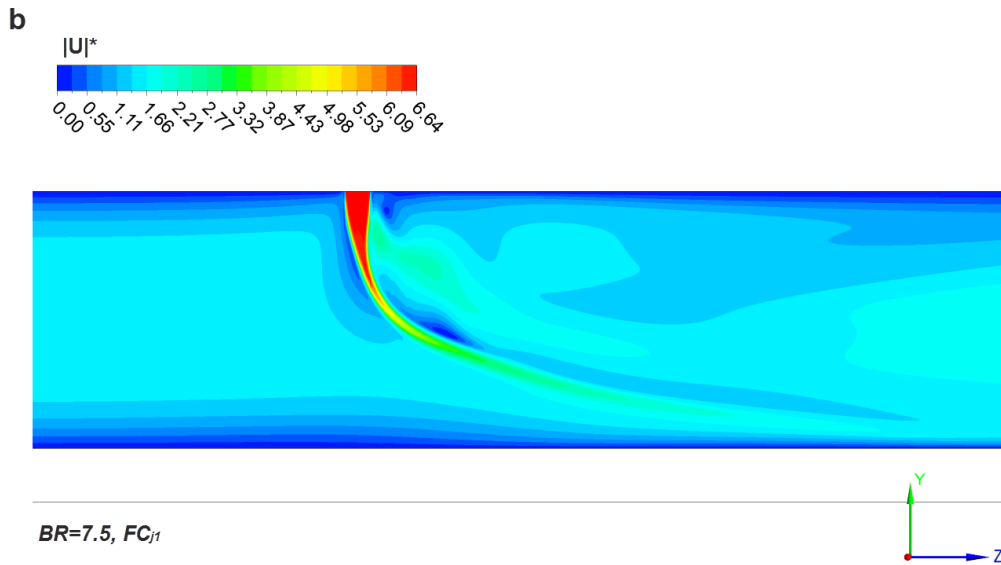
Twelve cases were examined in total regarding the hybrid VW configuration with the main objective being the identification of the combination of geometrical layout and flow conditions that provides the maximum heat transfer enhancement in the first heat sink-section. The different cases investigated for the two jet configurations are summarized in **Table 3.3**.

**Table 3.3** Cases examined regarding the hybrid VW configuration (where in the last column the subscripts ‘j1’, ‘j2’ refer to the single and dual-jet configurations, respectively).

Case	BR	Number of jets	Jet profile	Ar	Abbreviation
1	3.5	1	Uniform	0	FC <sub>j1</sub>
2	5.5	1	Uniform	0	FC <sub>j1</sub>
3	7.5	1	Uniform	0	FC <sub>j1</sub>
4	7.5	1	Fully Developed	0	FC-FD <sub>j1</sub>
5	7.5	1	Uniform	1.32	MC <sub>j1</sub>
6	7.5	1	Fully Developed	1.32	MC-FD <sub>j1</sub>
7	3.5	2	Uniform	0	FC <sub>j2</sub>
8	5.5	2	Uniform	0	FC <sub>j2</sub>
9	7.5	2	Uniform	0	FC <sub>j2</sub>
10	7.5	2	Fully Developed	0	FC-FD <sub>j2</sub>
11	7.5	2	Uniform	1.32	MC <sub>j2</sub>
12	7.5	2	Fully Developed	1.32	MC-FD <sub>j2</sub>

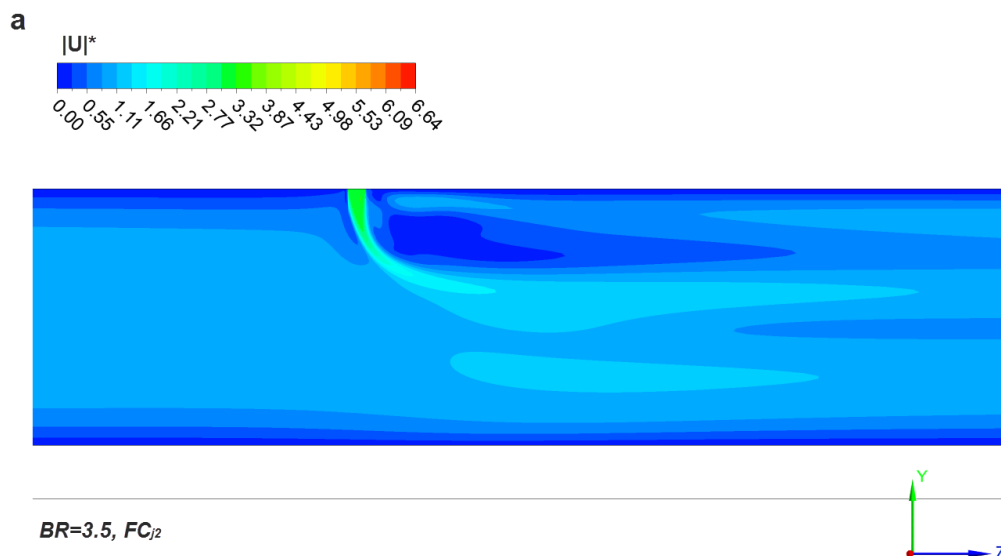
High jet penetration is of vital importance for the cooling effectiveness of the configuration, as the cold jet fluid must approach as close as possible the heated bottom wall. **Figs. 3.41-3.42** depict the interaction of the jet with the parallel flow through contour plots of the velocity magnitude. In reference to the single-jet configuration (**Fig. 3.41**), for BR=3.5 (**Fig. 3.41a**) the jet is almost immediately drifted away by the cross-flow and does not seem to have a considerable impact on the bottom boundary layer region. The jet of higher momentum, on the other hand, reaches the channel bottom wall and tends to reduce the thickness of the boundary layer, as depicted in **Fig. 3.41b**. It must be noted that even for the highest blowing ratio, BR=7.5, the jet central axis is considerably bent by the cross flow and the jet reaches the bottom wall approximately three hydraulic diameters downstream of the cooling hole.





**Fig. 3.41** Velocity magnitude contour plots at the channel vertical symmetry plane of the single-jet configuration: (a)  $BR=3.5$  and (b)  $BR=7.5$ .

The velocity contours of **Fig. 3.42** depict a higher jet penetration in the cases of dual-jets compared to the single jet configuration. Especially in the case of the high blowing ratio (**Fig. 3.42b**), the jet is observed to impinge on the bottom wall and subsequently ascend toward the channel mid-height. The higher jet penetration in the dual-jet configuration, despite the blowing ratio being equal in both single and dual-jet cases, is attributed to the velocity distribution of the cross-flow in conjunction with the location of the jet inlet holes. In the single-jet configuration, the cooling hole is located at the channel mid-width, where the axial velocity obtains its maximum value and thus has an appreciable impact on the streamwise evolution of the jet trajectory. The locations of jet submersion in the dual-jet configuration are close to the channel sidewalls, where the parallel flow velocity is lower due to the parabolic form of the horizontal profile. The lower cross-flow momentum is hence allowing the jets to achieve higher penetration in comparison to the single-jet case. The higher cross-flow velocity at the plane of the jet axis in the single-jet configuration is clearly illustrated if **Fig. 3.41** and **Fig. 3.42** are compared.



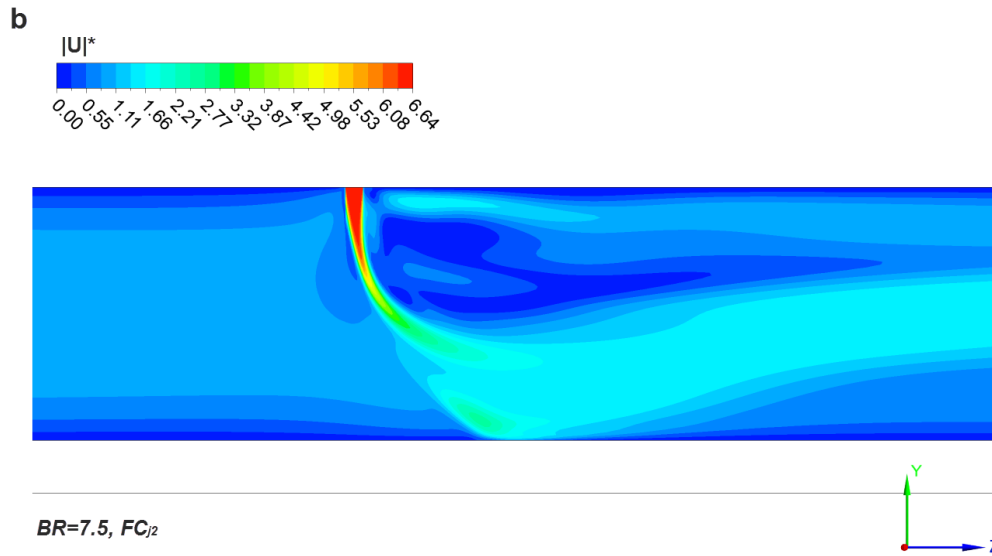


**Fig. 3.42** Velocity magnitude contour plots at the channel vertical symmetry plane of the dual-jet configuration: (a)  $BR=3.5$  and (b)  $BR=7.5$ .

The extent of jet penetration in each case can be better perceived by plotting the jet trajectory, which is defined as the streamline passing through the center of the jet inlet and lying on the channel longitudinal central plane [3.115]. **Figs. 3.43a-b** present the jet trajectories for the various flow conditions in the single and dual-jet configurations, respectively. In the single-jet configuration, as shown in **Fig. 3.43a**, the jet in all cases with uniform inlet-velocity profile achieves a maximum penetration and consequently ascends slightly prior to a new submersion to the channel lower part. Especially for  $BR=7.5$ , the trajectory is maintained below  $Y^*=0.2$  for the largest part of the heat-sink first section. Flow impingement on the bottom surface may also be observed, present only in the cases of fully-developed jet inlet velocity, whereby the jet is subsequently deflected toward the channel mid-height. **Fig. 3.43b** confirms that the jet penetration is generally deeper and the subsequent rise higher in the dual-jet configuration. The jet reaches the bottom wall for  $BR=7.5$  regardless of the jet inlet profile, while the jet impingement is more severe in the cases of fully-developed profile. In the latter case, the jet impinges almost vertically onto the channel bottom wall and is subsequently deflected toward the channel upper part. It must be noted that the jet trajectory is fully three dimensional in the cases where flow impingement occurs and so the trajectory presented in **Figs. 3.43a-b** is the projection of the actual trajectory on the plane of the jet axis.

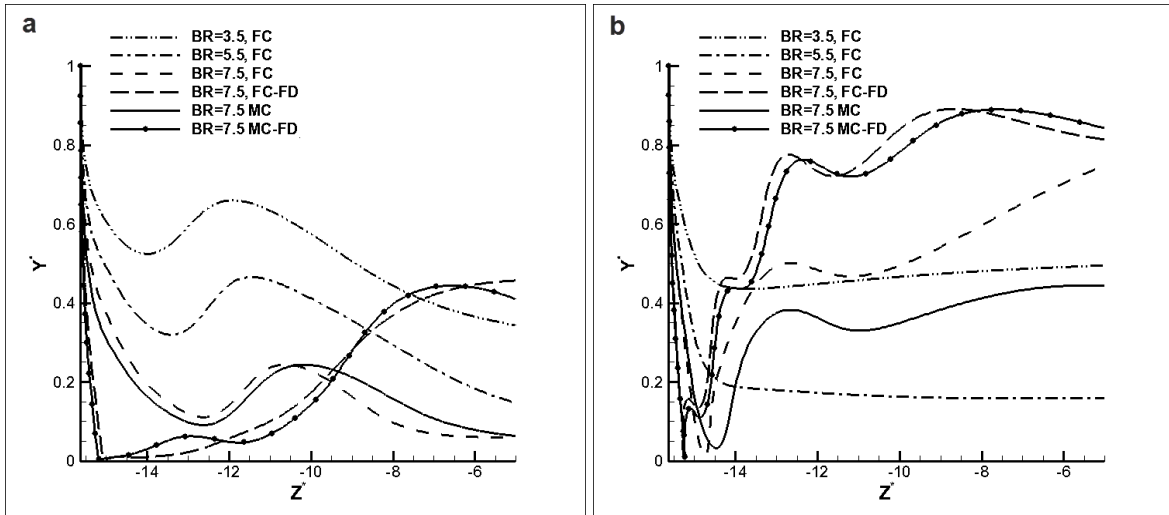


**Fig 3.43** Jet trajectory along the streamwise direction: (a) Single (j1 cases) and (b) dual-jet (j2 cases) configuration.

The flow topology emerging within the heat-sink first section due to the interaction of the jets with the parallel cross-flow is of considerable complexity and a number of vortical structures can be identified. **Figs. 3.44** and **3.45** illustrate the secondary flow pattern in the hybrid VW configurations through contour plots of the streamwise vorticity component  $\omega_z$ . In regard to the single jet configuration (**Fig. 3.44**), a pair of counter-rotating vortices is clearly discernible on either side of the cooling hole, which is identified as the CVP structure associated with JICF. The inset of **Fig. 3.44**, which depicts vorticity iso-surfaces, reveals that two symmetrical elongated vortical structures connect the CVP to the channel upper wall. It was established through additional contour plots not shown for brevity that these structures are in fact the two legs of the characteristic horseshoe vortex, which detach from the upper wall downstream of the cooling hole and merge with the CVP. An additional observation is that, although the secondary flow pattern is symmetrical for BR=5.5, breakdown of symmetry is evident for BR=7.5, as the left vortex (colored in red) is of increased sized compared to the right one (colored in blue). The asymmetrical topology is estimated to arise due to the flow confinement caused by the channel sidewalls. As the blowing ratio and thus the size of the CVP increases, the interaction of the two vortices becomes more intense and the left gains in size to the detriment of the right one.

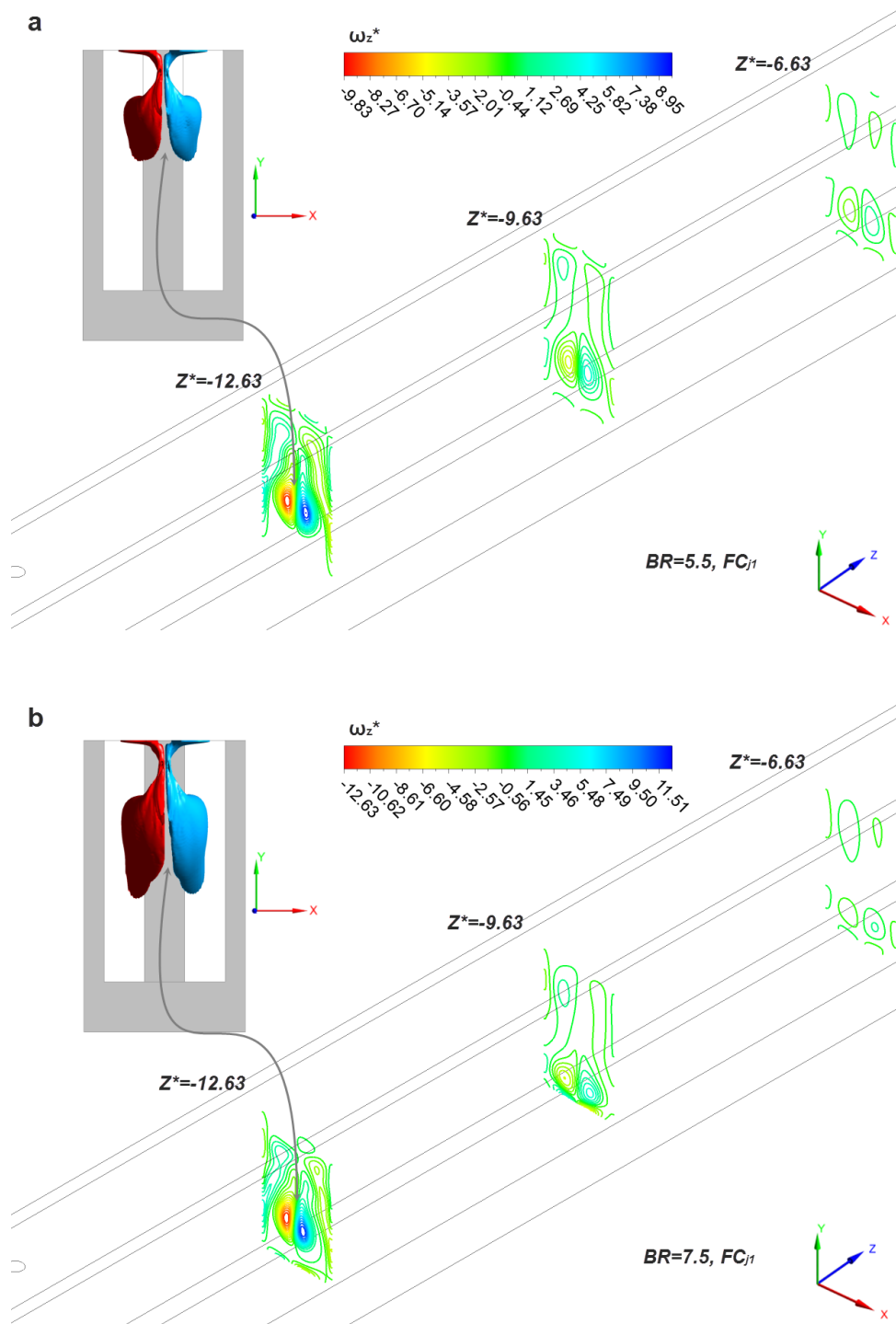


**Fig. 3.44**  $\omega_z$ -vorticity contour plots in the vicinity of the cooling hole (single-jet configuration): (a)  $BR=5.5$  and (b)  $BR=7.5$ . Inset:  $\omega_z$ -vorticity iso-surfaces ( $|\omega_z|=50\text{s}^{-1}$ ).

As shown in **Fig. 3.45**, the placement of the cooling holes close to the sidewalls in the dual-jet configuration gives rise to four coherent vortical structures. The lower vortex-pair of increased magnitude depicted in **Figs. 3.45a-b** corresponds to a vortex of each CVP that sets in downstream of each cooling hole. The coherence of the respective symmetrical vortices is destroyed due to the presence of the sidewalls. The vortex pair in the vicinity of the upper wall is in fact an after-effect of the two horseshoe vortices that form near the upper wall. As was mentioned in the discussion regarding the previous figure, the legs of the horseshoe vortices appear elongated in shape along the

dimension of the channel height. The outer legs close to the sidewalls decay shortly after their onset, while the inner legs constantly stretch toward the channel bottom wall until each of them eventually breaks up to two separate vortical structures. A vortical structure of elongated shape that connects each upper vortex to the respective lower one can be clearly discerned at the contour plot at  $Z^*=-12.63$  of **Fig. 3.45a**. Furthermore, the connection between each upper and lower vortex is elucidated by the vorticity iso-surfaces presented as insets in **Fig. 3.45**. The detached upper structures form the vortices close to the top wall evident in the contour plots, while the lower pair merges with the respective vortices that constitute the counter-rotating vortex pair. The vortical structures decrease in magnitude at further downstream locations yet increase in size due to viscous diffusion.

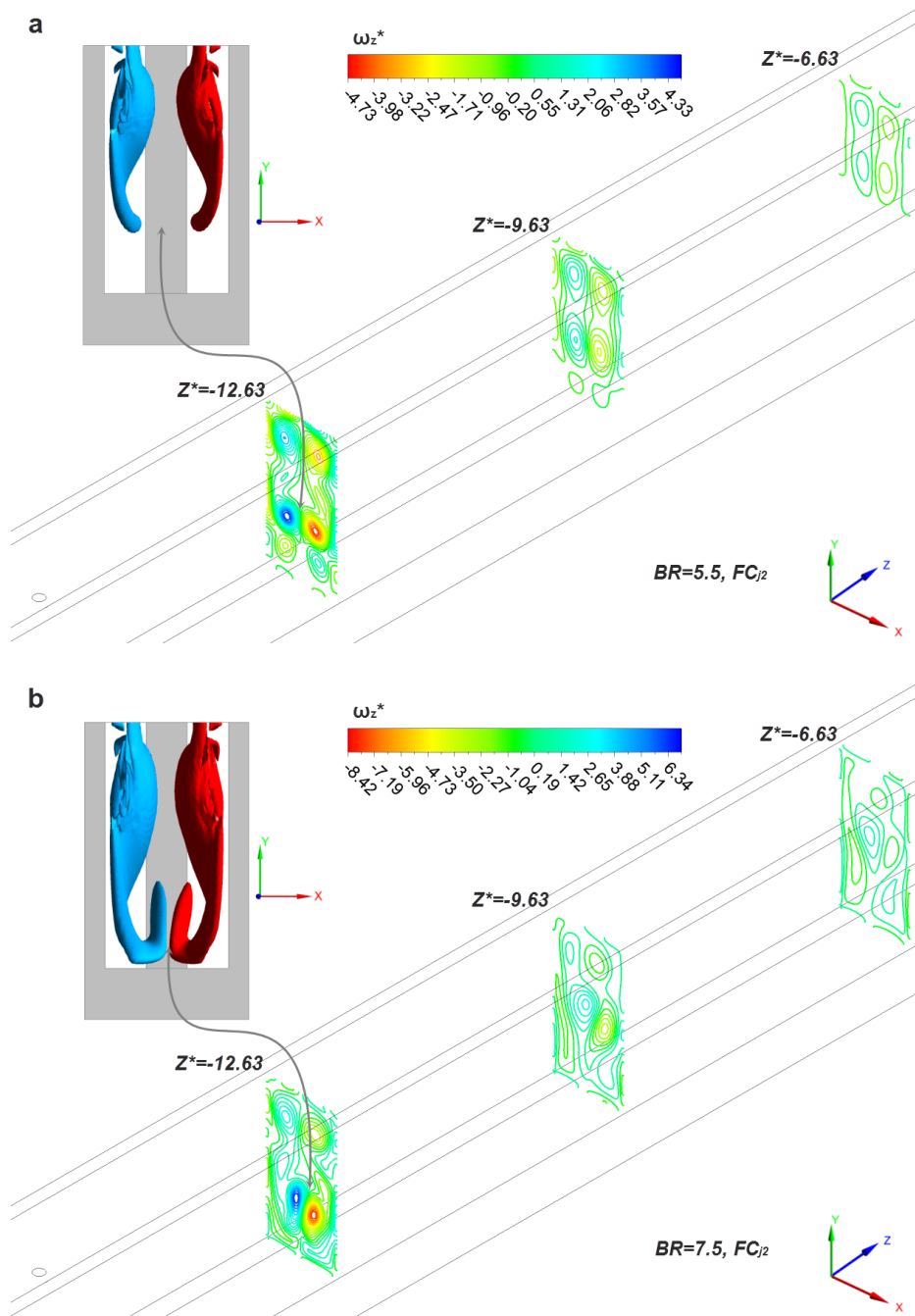


**Fig. 3.45**  $\omega_z$ -vorticity contour plots in the vicinity of the cooling hole (dual-jet configuration): (a)  $BR=5.5$  and (b)  $BR=7.5$ . Inset:  $\omega_z$ -vorticity iso-surfaces ( $|\omega_z|=50s^{-1}$ ).

For the highest value of the blowing ratio ( $BR=7.5$ ), an asymmetrical secondary-flow pattern is clearly evident in **Fig. 3.45b**. As can be seen from the  $\omega_z$ -vorticity iso-surfaces, the right vortex drifts along the parallel flow direction in an oblique trajectory. The breakdown of symmetry is attributed to the interaction of the vortices that form at the lower part of the channel after the jet impingement on the bottom wall. The stream lines originating from the two cooling holes depicted in **Fig. 3.46** elucidate that the two flow streams first interact with one another right after their impingement on the bottom channel wall. The subsequent whirling motion obtained by the fluid exhibits a different topology between the two streamline bundles. It is also interesting to notice that a number of streamlines originating from the right jet inlet hole are entrained toward the left second-section channel. In general, it was established that the jet interaction increases the complexity of the flow field, regardless of the prevailing flow conditions (forced or mixed convection), which do not have an appreciable effect on the evolution of the various vortical structures. Hence, the temperature field arising in the two configurations is also expected to exhibit different distinctive features.

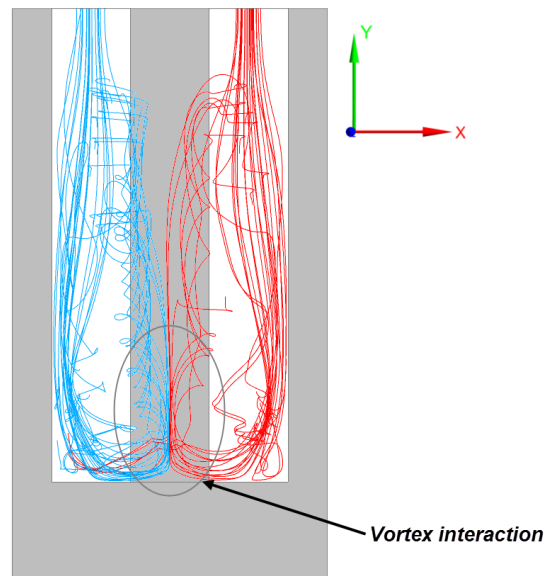


**Fig. 3.46** Velocity streamlines originating from the two jet inlet holes ( $BR=7.5$ ,  $FC_j$ ).

#### 3.4.4.5 Temperature field and heat transfer

As heat transfer is primarily taking place in the bottom channel wall, the effect of the jets on the cooling effectiveness of the device is expected to be more considerable if the injected cold fluid remains in the vicinity of the heated surface for an extensive part of the first heat-sink section. **Fig. 3.47** refers to the single jet configuration and presents temperature contour plots at three axial locations downstream of the cooling hole for  $BR=7.5$ . An initial observation is that the emerging temperature fields for forced (**Fig 3.47a**) and mixed-convection conditions (**Fig. 3.47b**) exhibit similar topology with a substantial cold-fluid core in both cases. Yet the asymmetry in the temperature profiles is more pronounced for mixed-convection conditions, e.g. in the temperature profile at  $Z^*=-6.63$  (**Fig. 3.47b**) a region of warm fluid is evident at the upper left part of the channel due to the buoyancy induced recirculation, while the cold fluid core is clearly shifted to the channel right-hand

side. The development of the bottom boundary layer is disrupted in both cases, as made evident by comparing its thickness at  $Z^*=-12.63$  and  $Z^*=-9.63$  in both **Figs. 3.47a** and **3.47b**. However, in the mixed-convection case more significant thermal mixing between core and boundary-layer fluid takes place as is illustrated by the plot at  $Z^*=-6.63$  of **Fig. 3.47b**. Furthermore, the wall temperature is lower in the mixed-convection case. It should be reminded that the temperature values were non-dimensionalized using the imposed value of the heat flux at the heat sink bottom surface and thus the results presented can be compared in a straightforward manner.

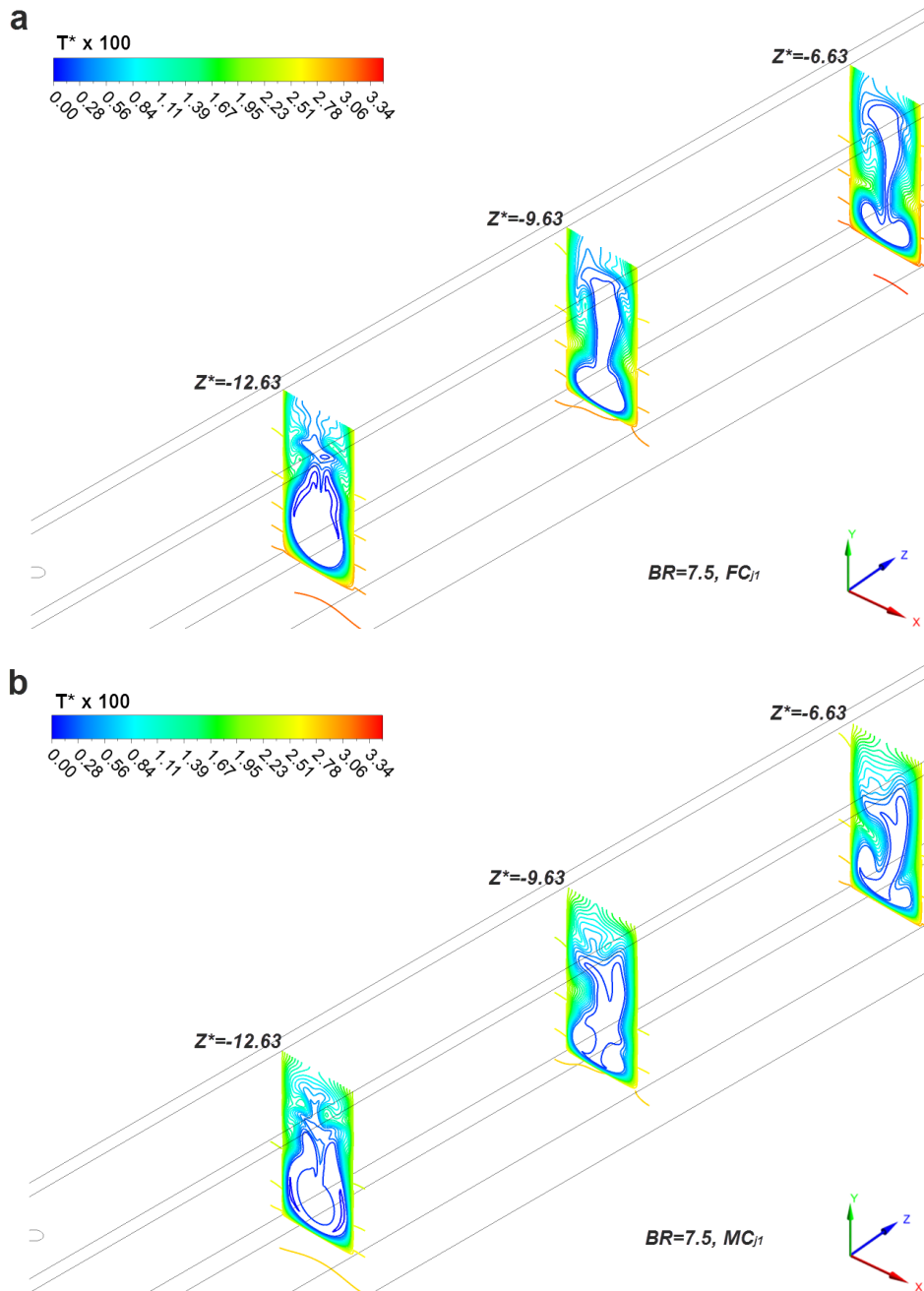


**Fig. 3.47** Temperature contour plots at axial locations downstream of the cooling hole for the single-jet configuration ( $BR=7.5$ ): (a) Forced convection ( $Ar_1=0.00$ ) and (b) mixed convection conditions ( $Ar_1=1.32$ ).

In correspondence to **Fig. 3.47**, **Fig 3.48** illustrates the development of the temperature field in the first-section of the dual-jet configuration. The strong interaction of the jets with the boundary-layer

fluid has as a result the drift of warm fluid toward the channel core, as depicted at the contour plots at  $Z^*=-12.63$  of both **Figs. 3.48a-b**. The two jets impinge on the bottom wall and consequently entrain fluid along their trajectory. The distinctive form of the temperature profile at the mid-lower part of the channel is also indicative of the mutual interaction of the lower vortices. Two additional isolated regions of warm fluid can be discerned in the vicinity of the upper wall due to the action of the additional vortex pair (see **Fig. 3.45**). Further downstream of the cooling holes thermal mixing occurs between the warm fluid of the isolated regions and the core fluid, with the thermal mixing being more intense for the mixed convection case; yet the bottom wall boundary layers appear to be of greater thickness in comparison to the respective single-jet cases.

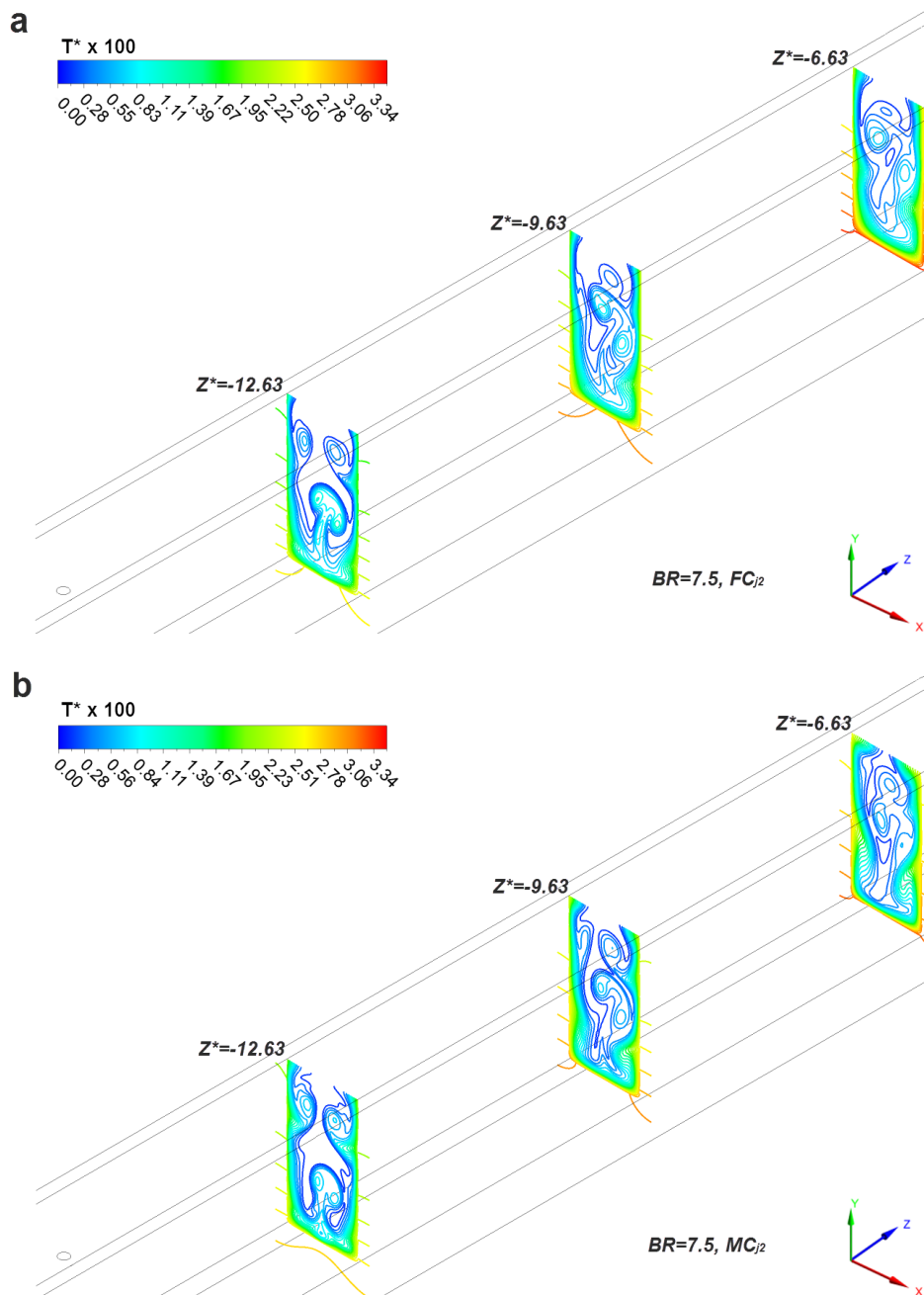


**Fig. 3.48** Temperature contour plots at axial locations downstream of the cooling holes for the dual-jet configuration ( $BR=7.5$ ): (a) Forced-convection ( $Ar_1=0.00$ ) and (b) mixed-convection conditions ( $Ar_1=1.32$ ).

**Fig. 3.49** depicts the average wall temperature distribution at the first heat–sink section for the single (**Fig. 3.49a**) and dual-jet (**Fig. 3.49b**) hybrid configurations. The respective distribution for purely parallel flow under forced and mixed-convection conditions is also depicted for comparison. In reference to forced-convection conditions, the incorporation of jets always leads to decrease of the wall average and maximum temperature, even in the case of the smallest blowing ratio considered. However the rate of temperature mitigation decreases as the blowing ratio increases. Especially for  $BR=7.5$ , the wall maximum temperature remains approximately the same regardless of the jet inlet-velocity profile, although the jets with a fully-developed inlet profile cause a larger temperature decrease at the axial location ( $Z^*\approx-14$ ) where they impinge onto the bottom wall. This trend, which is common for both configurations as shown in **Figs. 3.49a-b**, is justified by the fact that as the blowing ratio increases, the jets detach from the bottom wall toward the channel core after their impingent and thus fail to offer further enhancement of heat transfer at downstream locations.

In terms of hotspot temperature mitigation, the effect of the jets is less pronounced in mixed-convection conditions. For  $BR=7.5$ , the maximum wall temperature is slightly decreased in comparison to purely parallel flow in the single-jet configuration, while it is actually slightly increased in the dual-jet configuration. Nevertheless, the average wall temperature is decreased in both cases owing to the considerably lower temperature values at the wall region under the direct influence of the jets. The reduced heat-transfer enhancement at the channel part further downstream of the cooling holes must be attributed to a counteracting effect between the jet and the buoyancy-induced secondary flows. As was indicated by **Fig. 3.48b**, where temperature stratification is absent, the emergence of the jet-induced vortices disturbs the coherence of the buoyancy-induced longitudinal rolls, whose action has been also proven beneficial to heat transfer.

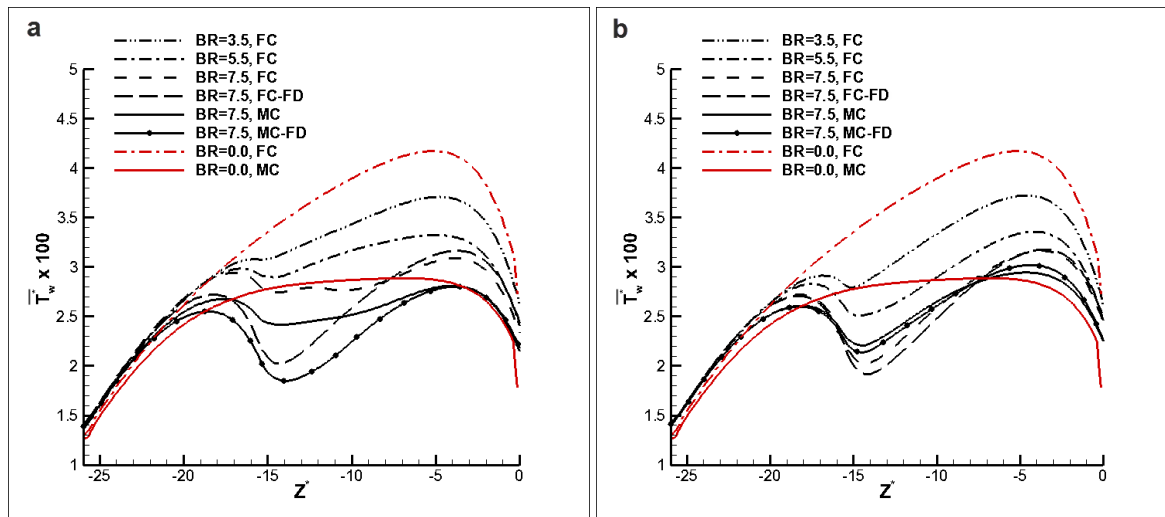


**Figure 3.49** Distribution of the average wall temperature at the first section of the VW-JICF heat sink: (a) single (j1 cases) and (b) dual-jet configuration (j2 cases).

To summarize, concerning the best performing, i.e. single-jet, configuration, the injection of a jet with blowing ratio of 7.5 under forced-convection conditions reduces the temperature difference between both the average and maximum wall temperature at the heat-sink first section and the fluid inlet temperature by the same percentage, approximately equal to 31%, compared to parallel flow. The respective temperature reductions in regard to mixed convection conditions were found equal to 16.4%

and 7.2% referring to the average and maximum wall temperature, respectively. It can be therefore deduced that the incorporation of cold fluid injection enhances the thermal performance of the VW device, with the enhancement being more pronounced for forced convection conditions.

**Fig. 3.50** presents the average Nusselt number distribution at the first section of the hybrid configurations. It is evident that the Nusselt number obtains peak values at approximately  $Z=-15$ , where the jets enter the channel. In the single-jet configuration (**Fig. 3.50a**), the Nusselt number increase is clearly steeper for the jets with fully-developed inlet profile, as flow impingement occurs only in these cases. Downstream of the jet submersion location, the Nusselt number decreases asymptotically up to the channel region where the influence of the geometry contraction becomes significant. A close look at the channel region downstream of  $Z^*=-5$  reveals that the highest Nusselt numbers are achieved for  $BR=7.5$  under mixed-convection conditions, justifying by this way the larger hotspot temperature mitigation for these cases, as shown in **Fig. 3.49**. It is interesting to notice that although the maximum Nusselt number values are obtained in the cases of impinging flow, the subsequent values obtained further downstream decrease rapidly. This trend is followed in both configurations and verifies the general remark that impinging flow offers high heat transfer enhancement, yet in a localized manner. In any case, the Nusselt number values obtained downstream of the jets submersion are higher than those obtained for purely parallel flow under the same conditions.

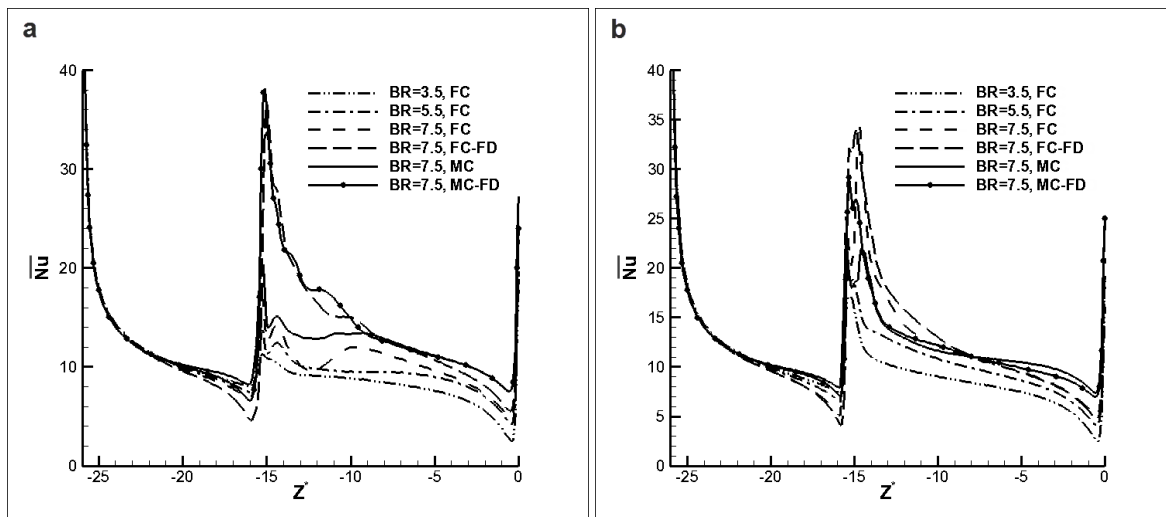


**Figure 3.50** Distribution of the circumferentially averaged Nusselt number at the first section of the VW-JICF heat sink: (a) single and (b) dual-jet configuration.

### 3.5 Tube-on-plate configuration with serpentine tube

In this section, a largely different concept of a cooling device is investigated, based on curved tubes. In the field of thermal engineering, such tubes are widely used, incorporated in heat exchanging devices and cooling configurations, as they offer increased heat transfer area per unit volume of the device. In addition, the effect of the centrifugal force on the flow due to the tube curvature induces a characteristic secondary flow, which promotes thermal mixing. Thus, the incorporation of curved tubes into heat exchanging applications can be regarded as a passive heat transfer enhancement technique [3.68]. The main features of the hydrodynamic and thermal behavior of fluid flow inside a number of coiled and horizontal curved-tube configurations widely used in industrial processes are

summarized in the comprehensive review articles of Vashisth et al. [3.119] and Naphon and Wongwises [3.120]. Apart from the traditional heat exchangers, curved tubes also find application in geothermal heat pumps. Referring to a borehole heat pump, Kobayashi et al. [3.121] numerically investigated the time dependent heat transfer in various serpentine tube configurations embedded in a conductive solid. The numerical results showed that serpentine tubes exhibit superior thermal performance in comparison to simple U-shaped tubes and, in addition, it is beneficial in terms of heat transfer for the conductive solid surrounding the tubes to have a large overall length to overall width ratio. Finally, the authors derived a relation for the optimal tube spacing.

Flow in curved tubes has been extensively investigated with the main focus on illustrating the effect of the centrifugal force on the flow field development and identifying the topology of the emerging secondary flow pattern. A thorough outline of the basic characteristics of flow in curved tubes can be found in [3.122]. It has been well established that the secondary flow is manifested through a pair of counter rotating vortices having their axes parallel to the main flow. The prime mechanism responsible for the emergence of the vortex pair is the interaction between the centrifugal force and the induced pressure gradient on the tube cross section [3.122, 3.123]. The experimental investigation of Fairbank and So [3.124] focused on the effect of a 180° bend on the upstream and downstream straight tube sections. The authors considered laminar flow and through the axial velocity distributions obtained it was demonstrated that the effect of the bend on the axial velocity distribution is more significant in the downstream section, where the velocity profiles appeared distorted for a distance up to seventeen tube diameters. Sugiyama and Hitomi [3.125] used a Reynolds stress model to predict turbulent flow in a tube with an 180° bend. They presented illustrative results regarding the flow field and the secondary flow intensity in the curved as well as the straight downstream section of the tube. In addition, the produced cross-sectional contour plots of the Reynolds stresses and their entire set of predicted results were compared against available experimental data.

However, the distinct features of the secondary-flow pattern on the tube cross section are strongly dependent on a similarity parameter that fully governs the flow inside curved ducts, namely the Dean number. Different systems of vortical structures may possibly develop depending on the value of the Dean number, as critical values exist that lead to dual solutions for the flow field. Dennis and Ng [3.126] numerically investigated the two-dimensional steady laminar flow in a slightly curved tube for the Dean number range of 96-5000. Above a critical value of  $De=956$ , they were able to obtain dual solutions that led to either a single or two pairs of symmetrical vortices on cross stream planes. The authors identified these vortices as being of the Taylor-Goertler type. The critical value of the Dean number ( $De = 956$ ) for the onset of a four vortex solution was also confirmed by the numerical study of Yanase et al. [3.127]. In the same study, the authors also conducted a linear stability analysis and concluded that the two-vortex solution is stable in response to both symmetrical and asymmetrical, with respect to the tube horizontal mid-plane, flow perturbations. On the other hand, the four-vortex solution was found to be conditionally unstable to all perturbations. Besides, it was stated that the four-vortex system could possibly appear at lower Dean number values, provided that the secondary flow is not fully developed, namely that the secondary flow topology does not remain invariant throughout the entire curved tube. Di Piazza and Ciofalo [3.128] considered the flow in two closed toroidal tubes of different curvature and characterized the regimes of flow transition from stationary to chaotic (turbulent) flow using direct numerical simulation. For Reynolds number values greater than the designated critical ones for each curvature, two distinct traveling waves were detected to emerge in

the torus. The first of these affected primarily the Dean vortices, while the second one manifested itself as an array of oblique vortices in the vicinity of the Dean vortex region. Cheng and Yuen [3.129] performed a flow visualization study in a  $180^\circ$  bent tube using smoke injection for fully developed laminar flow. Their observations revealed the existence of an additional pair of counter-rotating vortices in the vicinity of the outer wall for Dean numbers greater than 100. The authors attributed the emergence of the additional vortex pair to the centrifugal instability induced by the tube curvature. Furthermore, the authors showed that for Dean number equal to 200 and 370 two- or four-vortex systems are possible to emerge depending on the perturbation of the main flow.

Olson and Snyder [3.130] experimentally proved that the mean axial vorticity in a curved tube initially increases to a maximum value and then decreases asymptotically. They also observed a four-vortex system for  $De=510$  and they adopted the explanation for the onset of the additional vortex pair provided by Rowe [3.131]. In the experimental investigation conducted by Rowe [3.131], the existence of the additional pair of vortices was attributed to the interaction of the vortex filaments in the vicinity of the inner wall leading to an additional vortex roll-up, which is consequently pushed toward the outer wall by the secondary flow. After reviewing the research that has been conducted regarding the flow in weakly curved tubes, Siggers and Waters [3.132] came to the conclusion that the number of branches of the solution that may be inferred from the findings in the open literature is five. An initial branch of the solution appears even for creeping flows ( $De \ll 1$ ), while solution bifurcations leading to dual solutions occur at  $De=956$  and  $De=2494$ , respectively. The initial branch is manifested through a two-vortex system, while all other branches through four-vortex systems. The above mentioned authors, in their numerical investigation regarding tubes of finite curvature, also observed the dual solution, of two- and four-vortex systems respectively, appearing at  $De=2500$ . However, it must be noted that the critical Dean number values for flow bifurcation reported in theoretical studies are considerably higher than the values for which four vortex systems have been actually observed in experiments [3.129, 3.130]. Besides, according to the theoretical study of Yang and Ye [3.133], a branch of solutions leading to asymmetric recirculation pattern does also exist for Dean numbers exceeding a critical value equal to 12734.

There is also a number of studies that focus on the heat transfer characteristics for flow inside curved tubes. Mori and Nakayama [3.134, 3.135] theoretically and experimentally investigated heat transfer in a toroidal geometry under uniform heat flux conditions both in the laminar and the turbulent flow regime. They managed to obtain theoretical predictions that correlate the fully developed overall Nusselt number to the Dean and Prandtl numbers. Subsequently, they verified these correlations through an experimental investigation of air flow inside a toroidal tube. Jayanti et al. [3.136] numerically simulated the flow and heat transfer inside a curved tube of constant pitch (helical coil) by applying a spatially varying centrifugal force on the flow inside a straight tube. Their results illustrate the basic features of the flow and temperature fields under a wide range of heating conditions, both in laminar and turbulent flow.

Kalb and Seader [3.137] conducted a theoretical investigation on the fully developed heat transfer in curved circular tubes under the boundary condition of axially constant heat flux with circumferentially constant temperature. Their results revealed that the local Nusselt number at the tube outer wall always obtains larger values than the one at the inner wall and the value of their ratio increases with the Dean number. Furthermore, they managed to obtain correlations for the fully developed Nusselt number as a function of the Dean and Prandtl numbers for Dean numbers less than

1200. Besides, the numerical results of Tarbell and Samuels [3.138] referring to Dean numbers of up to 453 showed that the circumferentially averaged local Nusselt number exhibits oscillations as a function of the local Graetz number for moderate Prandtl numbers and under the condition of constant wall temperature. The effect of temperature-dependent viscosity on heat transfer, regarding laminar forced convection in a curved tube was numerically investigated by Andrade and Zapparoli [3.139]. It was reported that the overall Nusselt number values attained were slightly higher in comparison to a fluid of constant properties under the condition of constant wall heating. Di Liberto and Ciofalo [3.140] investigated turbulent heat transfer in curved tubes at Reynolds numbers in the range 12630-17530 using direct numerical simulation. They presented results regarding both the time-averaged and instantaneous velocity and temperature fields. Through their results, it was established that the temperature fluctuations and the turbulent heat flux obtained maximum values in the vicinity of the outer wall, where secondary flow impingement occurs. In addition, it was illustrated that the enhanced heat transfer observed in curved tubes is not related to turbulence, as the turbulence levels were in fact reduced in comparison to a straight pipe.

Ohadi and Sparrow [3.141] took advantage of the heat and mass transfer analogy and, through the use of the naphthalene sublimation technique, produced experimental values for the Sherwood number characterizing turbulent flow downstream of an 180° bent. The most interesting finding of the study was that the Sherwood number distribution, for Reynolds numbers having values less than 15000, presented an initial undershoot in the straight tube section downstream of the bent and subsequently redeveloped to a constant value. The undershoot was completely absent for Reynolds number values higher than 24000. The authors attributed this heat transfer reduction to flow relaminarization occurring at that region. The assumption of flow relaminarization has been confirmed by Noorani et al. [3.142] who performed direct numerical simulations of the turbulent flow in bent tube configurations. Partial relaminarization at the inner part of the tube was observed for Reynolds number equal to 11700 and curvature to tube radii ratio equal to 0.1. It was furthermore reported that the flow tendency to relaminarization becomes stronger as the curvature to tube radii ratio increases. In addition, the effects of buoyancy forces on the secondary flow topology and heat transfer have also been looked at by a few researchers [3.143-3.145]. Finally, from the second-law-of-thermodynamics point of view, Bahiraei et al. [3.146] analytically investigated laminar forced convection in a helically coiled tube. They obtained correlations for predicting the Dean number that leads to minimum entropy generation, as a function of the geometrical parameters and heat transfer conditions. By resolving the total exergy destruction to avoidable and unavoidable parts, they designated the potential of improvement of configurations having fixed operating parameters.

The turbulent flow and conjugate heat transfer inside a tube-on-plate heat-sink design is investigated in this paragraph. The heat sink incorporates a serpentine tube with 180° bends (U-turns) thermally bonded to a conductive substrate (see Fig. 3.2). The flow phenomena emerging inside the tubes are identified and their effect on heat transfer is analyzed. The effect of the tubing embedment depth on heat transfer is also studied. It must be noted that in such a configuration, the conjugate heat transfer effects, allowing for the various parallel branches of the tubes to thermally interact with one another in the lateral direction, give rise to a heat transfer problem fundamentally different than that of the aforementioned studies in the literature which considered the bent tube alone.

3.5.1 Geometry and computational domain

The tube-on-plate heat-sink design under investigation comprises a copper ( $k_{cu}=408 \text{ W/mK}$ ) serpentine tube thermally bonded to a rectangular aluminum ( $k_{al}=237 \text{ W/mK}$ ) substrate bearing parallel grooves. The concept of the design is based on a commercially available “cold plate” cooling configuration [3.147]. The serpentine tubing forces the cooling fluid inside it to divert its course by  $180^\circ$ , in order to pass multiple times through the solid substrate. It must be noted that the straight parts of the tube are partially imbedded in the substrate, whereas the curved bends lay outside of the plate area, as depicted in Fig. 3.2. Two variations of this type of heat-sink design are addressed in the present analysis having two (Fig. 3.2a) and four (Fig. 3.2b) equidistant straight tube segments on the substrate respectively (from now on called “two-pass” or 2P and “four-pass” or 4P configurations). The tube cross section is maintained the same for both configurations and thus the transversal distance between consecutive passages is smaller for the four-pass heat sink. The same applies to the radius of curvature of the bend.

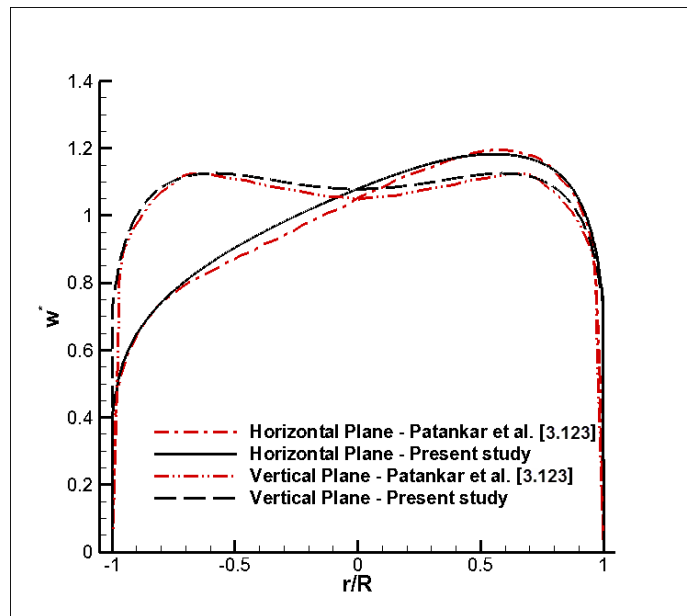
The entire heat sink configuration was included in the computational domain due to the lack of symmetry. The computational domain consists of two solid and one fluid sub-domains corresponding to the substrate, the tubing and to the cooling fluid, respectively. Pure forced convection conditions occur within the serpentine tubing as the Archimedes number for the prevailing flow and heating conditions is in the order of  $10^{-2}$ . Since here, unlike the case of the plate-fin heat sink type analyzed earlier, the overall flow rate, which is the same, is not distributed into many channels but remains within a single tube, the flow is characterized by a much higher Reynolds number and lies within the turbulent regime. Therefore, the set of governing equations (3.4), (3.8)-(3.10) along with the boundary conditions (3.12)-(3.20) were solved on the computational domain, using the Shear Stress Transport  $k-\omega$  model for the calculation of the Reynolds stresses and the turbulent heat flux. A convergence criterion of  $10^{-6}$  was set for the root mean square (RMS) mass, momentum and energy residuals, as well as for the turbulent kinetic energy and the turbulent frequency. Due to the specific layout of the serpentine tubing and the additional solid domain, the imposed boundary conditions, although qualitatively similar to Eqs. (3.12)-(3.20), are also summarized in Table 3.4.

Table 3.4 Imposed boundary conditions for the tube-on-plate configurations.

	Hydrodynamic BC	Thermal BC
Inlet	$w = w_i, u = 0, v = 0$	$T_f = T_i$
Outlet	$p_{ave} = 0$	$\frac{\partial^2 T_f}{\partial z^2} = 0$
Fluid-wall Interface	$u = v = w = 0$	-
Bottom surface	-	$-k_s \frac{\partial T_w}{\partial y} = q''$
Other outer surfaces	-	$-k_s \frac{\partial T_w}{\partial n} = 0$
Interface between successive domains D (D=1-3)	-	$T_D _{int} = T_{D+1} _{int}, -k_D \frac{\partial T_D}{\partial n} _{int} = -k_{D+1} \frac{\partial T_{D+1}}{\partial n} _{int}$

### 3.5.2 Validation of the numerical model

In order to verify that the formulated numerical model can adequately predict the effect of the centrifugal force on a curved-tube flow, numerical results were produced and compared against published data regarding flow in curved pipes [3.123, 3.124]. Patankar et al. [3.123] predicted the turbulent flow in a curved tube having a ratio of the tube radius  $R$  to the radius of curvature  $R_c$  equal to 0.025 using the standard  $k$ - $\epsilon$  turbulence model. The horizontal and vertical fully developed velocity profiles published in [3.123] for Reynolds number equal to 25000 are compared with the respective ones calculated in the present study using the SST  $k$ - $\omega$  model (Fig. 3.51). As can be seen, the predictions of the two models are in good agreement and the velocity overshoots are captured in both planes.



**Fig. 3.51** Comparison of the fully developed velocity profiles calculated in the present study against those available in Ref. [3.123] for turbulent flow at  $Re=25000$ .

Fairbank and So [3.124] obtained experimental velocity profiles at the horizontal symmetry plane of two U-shaped tubes characterized by different  $R/R_c$  ratios equal to 0.08 and 0.30, respectively. The Reynolds number was maintained the same in both cases and equal to 400, while the Dean number was equal to 110 and 220, respectively. The comparison between the present numerical results, which were produced using a computational domain similar to the experimental setup described in [3.124], and the experimental data is shown Fig. 3.52, where the velocity profiles at two dimensionless positions  $s/2a$  downstream of the bend and equal to 0.5 and 5.0 are compared. Good agreement is established with the root mean square deviation not exceeding 3%, while the uncertainty in the experimental velocity values being 2.5%. The shift of the maximum velocity toward the outer wall is also well captured.

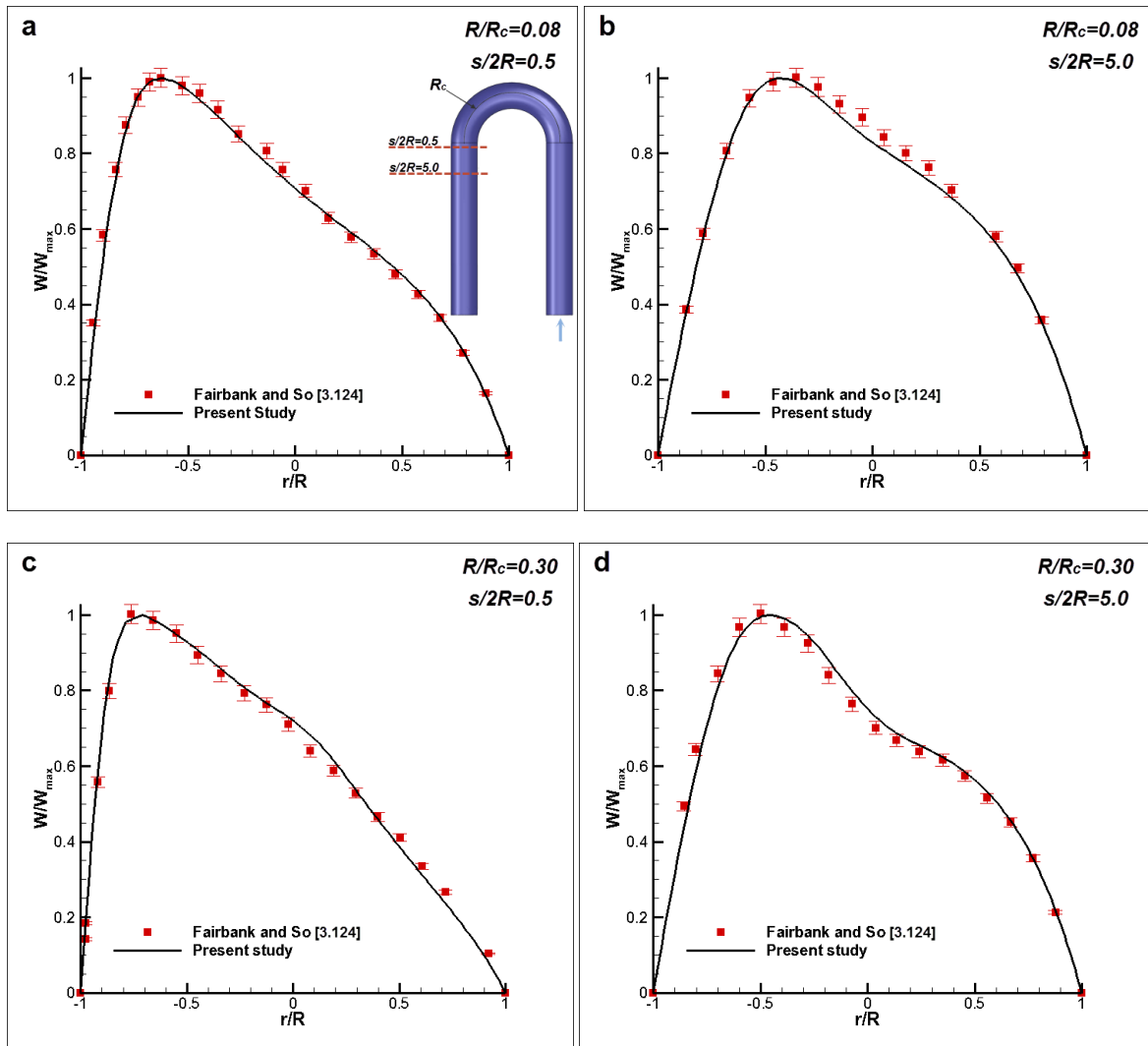


**Fig. 3.52** Validation of the numerical code with the experimental results of Ref. [3.124] for two bent tubes ( $R/R_c=0.08, 0.30$ ) in laminar flow with  $Re=400$ . Horizontal velocity profiles at two locations downstream of the bend: (a), (b)  $s/2R=0.5$  and (c), (d)  $s/2R=5.0$ .

### 3.5.3 Grid independence study

The computational domains for both cooling configurations were discretized using unstructured grids of hexahedral elements (**Fig. 3.53**). The grids had a non-uniform arrangement along the flow direction, as a fine grid was used along the curved sections of the domain (**Fig. 3.53a**), in order to fully capture the topology of the expected secondary flow. In addition, the grid nodes were closely positioned in the fluid cross section adjacent to the solid wall (**Fig. 3.53b**), in order to capture the steep gradients in the boundary layer region. A grid independence study was conducted in order to verify that the produced computational results remained unaffected from the grid density. For this reason, the 4P configuration was selected and simulations were performed using three grids of increasing density, namely of  $1.2, 2.6$  and  $4.0 \times 10^6$  elements, respectively.

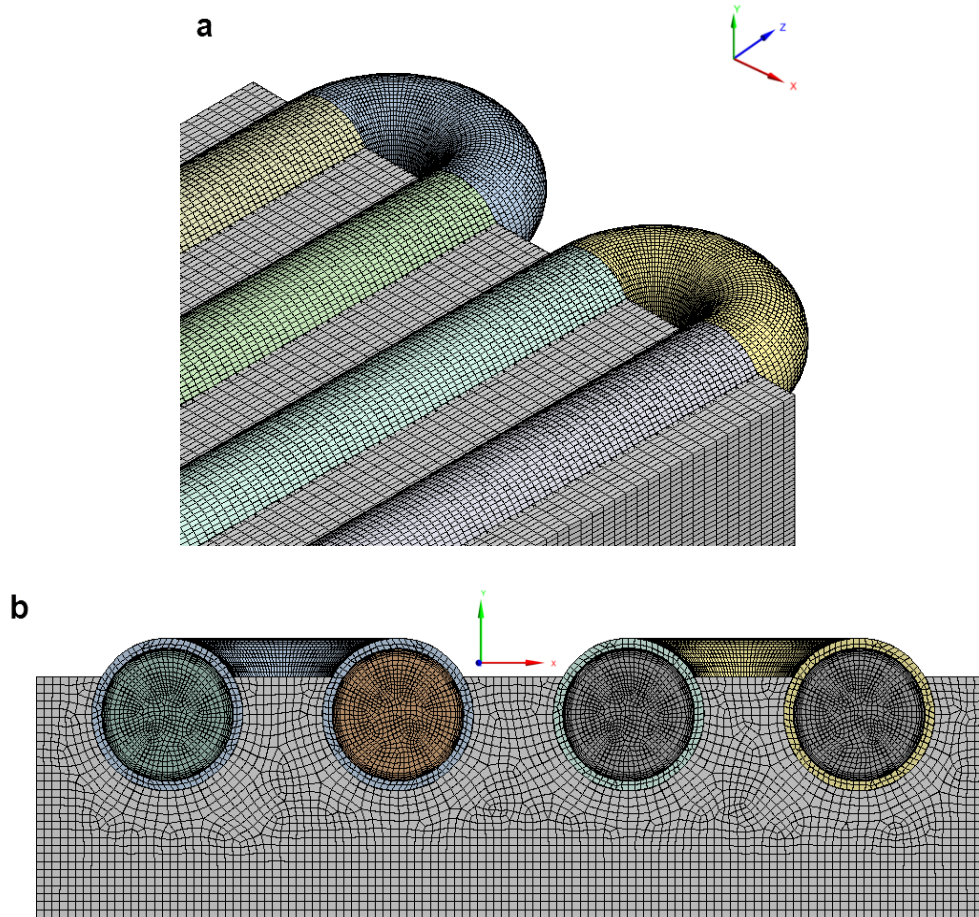


**Figure 3.53** Computational grid used for the simulations (4P configuration): (a) detail view of the bends area and (b) sectional view.

The cooling fluid pressure drop through the configuration, the substrate maximum temperature and the overall Nusselt number were considered as adequate quantities in order to ensure the grid independency of the solution. As it is evident from the values of **Table 3.5**, the computational grid consisting of  $2.6 \times 10^6$  elements is suitable for the production of the numerical results, as a further grid refinement to  $4.0 \times 10^6$  elements causes all the monitored quantities to deviate by less than 1%. Subsequently, the computational domain for the 2P configuration was discretized using elements of the same dimensions and topology, as those comprising the selected grid for the 4P configuration, and the final grid consisted of  $2.2 \cdot 10^6$  elements.

**Table 3.5** Grid independence study for the tube-on-plate configuration.

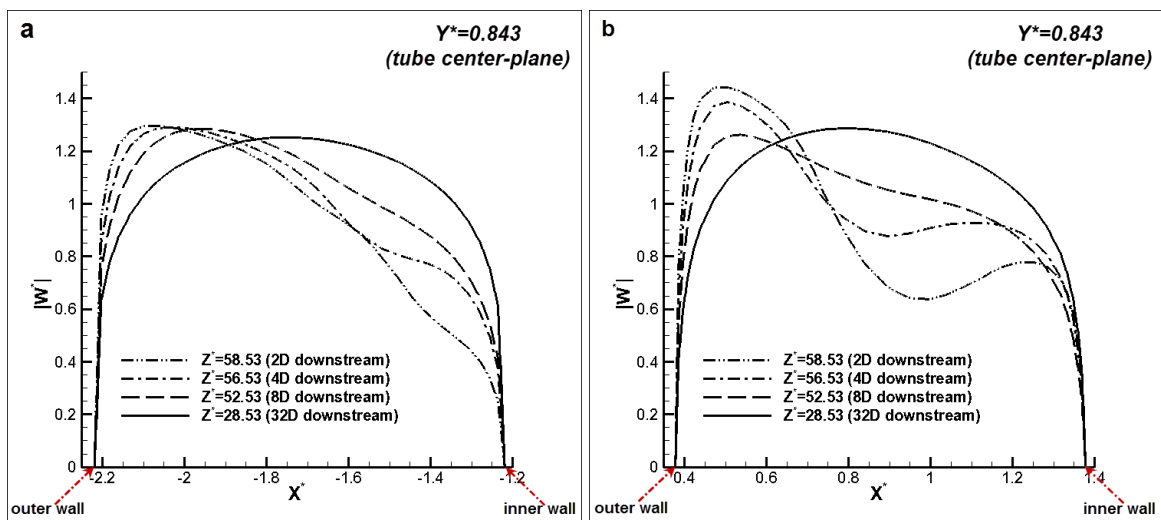
Grid	Coarse	Intermediate	Fine
Elements	$1.24 \cdot 10^6$	$2.61 \cdot 10^6$	$4.06 \cdot 10^6$
Pressure drop [Pa]	1804.75	1835.50	1847.05
$T_{\max}$ [K]	309.68	309.62	309.60
Nu [-]	50.12	50.88	51.35

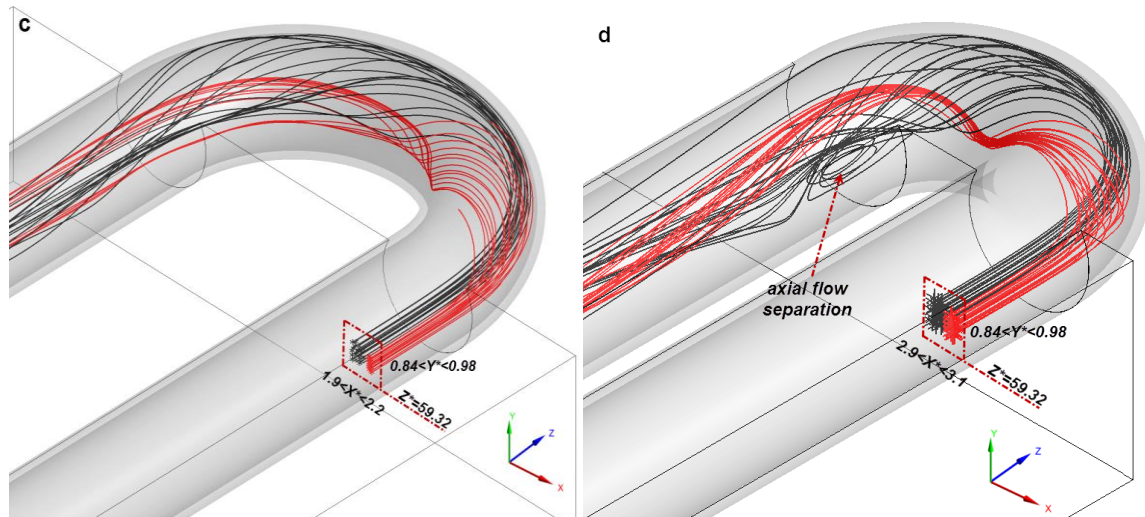
### 3.5.4 Flow Field

The flow inside the tubing of both configurations is characterized by the same Reynolds number equal to 5124, corresponding to a flow rate of 30 mL/s. However, the Dean number, which accounts

for the effect of the centrifugal force, varies due to the different ratio of the tube radius to the bend curvature radius  $\delta$ , obtaining the values of 2763 and 3867 for the 2P and 4P configurations respectively. **Figs. 3.54a-b** present non-dimensional axial velocity profiles (i.e. normal to the cross stream plane) at the horizontal symmetry plane of the tube for several streamwise positions downstream of the bend for the 2P and 4P configurations. Especially regarding the 4P configuration (**Fig. 3.54b**), the streamwise positions refer to the straight tube section downstream of the first bend encountered by the flow. As can be seen, the velocity profile appears distorted downstream of the bend for both configurations; the maximum velocity location is shifted toward the outer wall, with the maximum velocity being higher for the higher Dean number configuration (4P configuration). However, the velocity profiles at  $Z^*=58.53$  and  $Z^*=56.53$  for the 4P configuration exhibit off the wall minimum velocity and thus a second peak of the velocity value in the vicinity of the inner wall, a feature not present in the 2P configuration. The velocity minimum and thus this velocity peak for the 4P configuration is due to a strong recirculation zone which develops (as the result of the higher Dean number) and draws high-velocity fluid from the tube core toward the inner wall. In addition, the velocity profiles at  $Z^*=28.53$ , a location slightly downstream of the straight-section mid-length, appear almost fully developed and therefore it is obvious that the flow is recovering to a development state in the straight section of the tubes. Thus, with regard to the 4P configuration, the flow upstream of each bend has developed fully after recovering from the effects of the preceding bend and identical flow phenomena repeat themselves in each curved section and downstream of it.

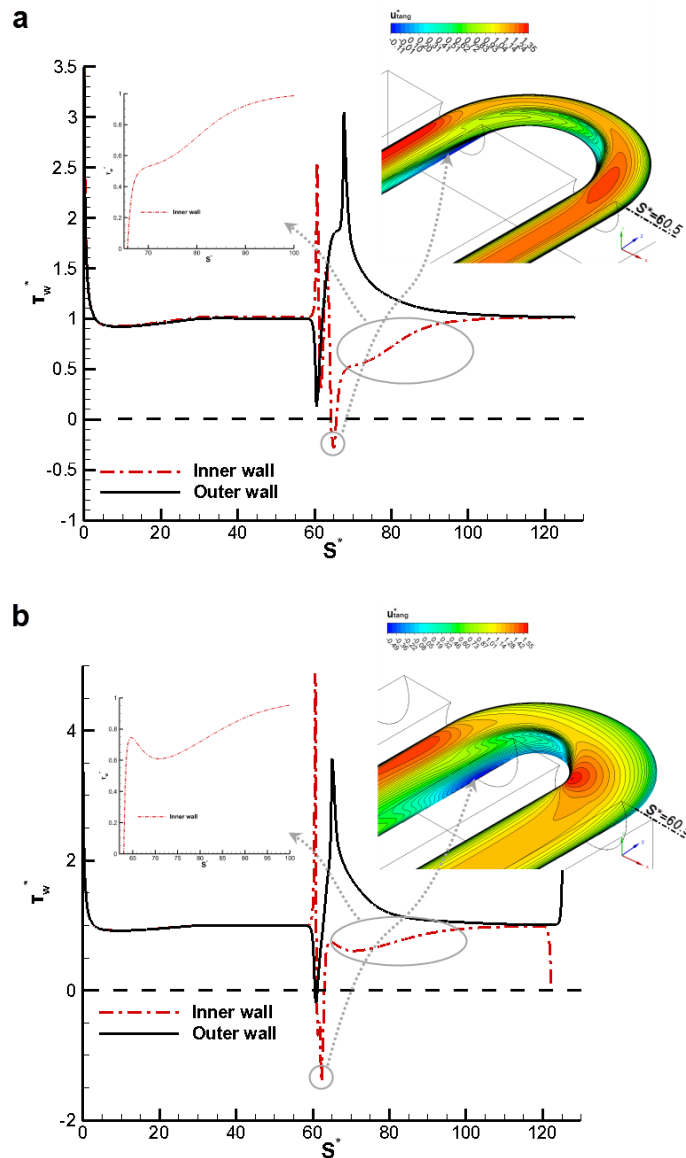
**Figs. 3.54c-d** illustrate some three-dimensional features of the developing flow field within the bends of the 2P (**Fig. 3.54c**) and 4P (**Fig. 3.54d**) configurations through streamlines. It must be noted that streamlines have been drawn only for the upper half of the tube cross-section as the flow field is symmetric about the horizontal plane. It is evident that a secondary flow pattern develops in both configurations, as the streamlines exhibit a whirling trajectory in both figures. Two bundles of streamlines have been highlighted with different colors, in order to point out the two distinct vortical structures that set in at the bend region. Black lines reproduce an extensive vortical cell that occupies the entire tube half cross section, while red lines reproduce a more localized cell in the vicinity of the inner wall. Regarding the 4P configuration (**Fig. 3.54d**), a horizontal recirculation bubble due to axial flow separation is also visible.





**Fig. 3.54** Non-dimensional axial velocity profiles at the tube horizontal symmetry plane downstream of the bend: (a) 2P and (b) 4P configuration. Three dimensional streamlines at the area of the bends: (c) 2P and (d) 4P configuration.

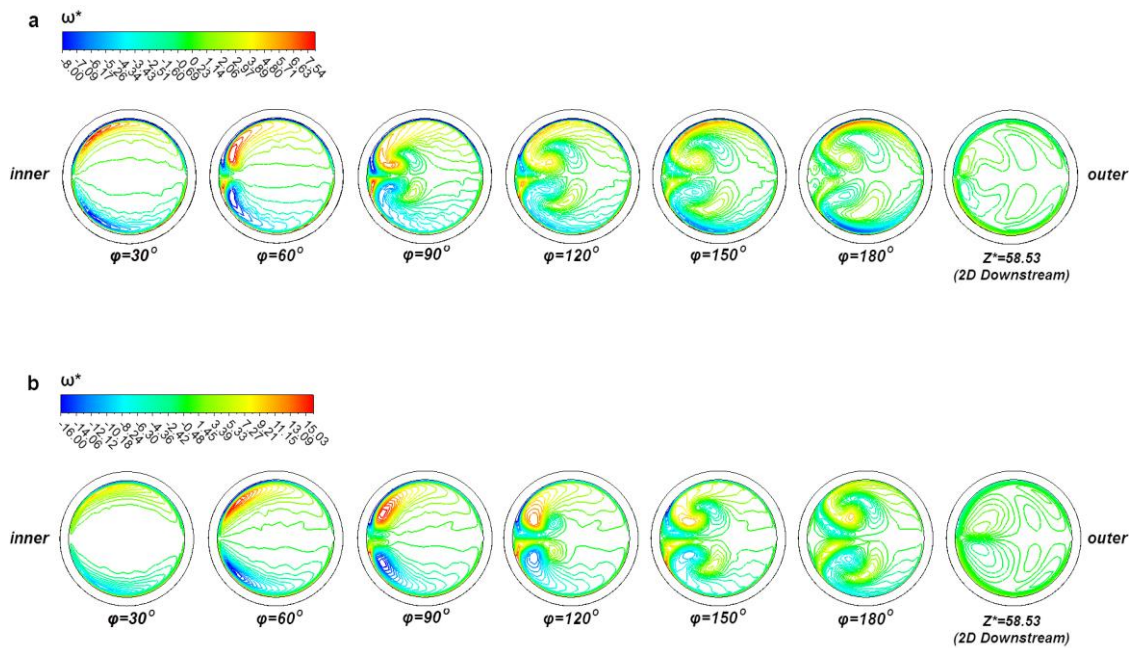
**Fig. 3.55** depicts the distribution of the non-dimensional wall shear stress at the intersections of the horizontal symmetry plane with the tube wall as a function of the non-dimensional “unwound” coordinate  $S^*$ . This is obtained from an  $s$  coordinate, which describes the full flow path, encompassing the curved section of the tube as well as the upstream and downstream straight ones. Consequently, the  $S^*$  coordinate obtains a slightly larger value for the outer wall due to the larger radius of curvature of the outer curved section. Regarding the 4P configuration, it must be noted that the wall shear stress values are plotted only for the two first passages, as the same behavior is expected to be repeated in the following two. Upstream of the bend, after an initial adjustment due to the uniform inlet velocity, the shear stress value remains constant and identical for both inner and outer walls in both configurations. In the curved section, the two walls are differentiated as the shear stress exhibits more rapid changes at the inner wall of both configurations (**Fig. 3.55a-b**). A characteristic change of the shear stress sign is observed in the distribution of the inner wall in both graphs, a clear indication of flow separation. It is interesting to notice that flow separation also occurs at the outer wall of the 4P configuration (**Fig. 3.55b**); however, it is of negligible magnitude and the shear stress regains positive values almost immediately. Indeed, as depicted on the inset of each graph a recirculation bubble develops on the horizontal (XZ) plane in the vicinity of the inner wall for both configurations. The insets depict contours of the tangential to the wall velocity in a local coordinate system, so that negative values indicate flow recirculation. The recirculation bubble is located at the downstream straight section in the 2P design ( $S^*=64.3-65.7$ , **Fig. 3.55a**), whereas a close look at the contours regarding the 4P design (**Fig. 3.55b**) reveals that, in fact, two connected bubbles exist having their centers at the straight section adjacent to the curve and slightly downstream of the inner curve apex respectively ( $S^*=61.0-63.0$ ). Besides, it is interesting to notice that the distributions of the inner and the outer wall in the straight section downstream of the bend are not identical, as in the upstream section. The inner-wall distribution of the 4P configuration exhibits a local minimum approximately at  $S^*=71$ , which could suggest a significant change in the flow conditions. However, the two lines coincide to a common value further downstream.



**Fig. 3.55** Wall shear stress distribution at the wall on the tube horizontal symmetry plane: (a) 2P and (b) 4P configuration.

**Fig. 3.56** illustrates clearly the sequence of the creation of the vortical structures that set in in the curved section of the tube through vorticity projection plots at several cross-stream planes along the curved ( $0^\circ < \varphi < 180^\circ$ ) as well as the downstream straight tube section. At  $\varphi=60^\circ$ , a pair of Dean vortices having their centers shifted toward the inner wall is already evident in both configurations (**Figs. 3.56a** and **3.56b**). The vortices have opposite vorticity sign with regard to the wall vorticity at the respective locations. In fact, the vertical distance between these locations of concentrated wall vorticity appears to be smaller in the 4P configuration. In addition, a second pair of vortices can be clearly seen at  $\varphi=90^\circ$  for the 2P configuration (**Fig. 3.56a**) but less developed for the four pass configuration which however is clearly seen at  $\varphi=120^\circ$  (**Fig. 3.56b**). It seems that the development of the secondary flow pattern is affected by the Dean number and the additional vortices emerge further downstream along the bend arc as the Dean number increases. This second pair of vortices is initially more localized in the vicinity of the Dean vortices, but as the flow travels further downstream in the bend (e.g. see plots at  $\varphi=150^\circ$ ), the vortices become oblique and elongated (kidney shape) with their

upper part moving toward the tube wall. These “middle” vortices interact with the Dean vortices and significantly distort their topology in both configurations. The onset of the middle vortices in the vicinity of the Dean vortices and subsequent drifting toward the tube core observed in the present investigation is in agreement with the findings of Rowe [3.131] who reports that the additional pair of vortices emanates at the boundaries of the Dean vortices and is then pushed toward the outer wall by the secondary flow. Another region of high vorticity can be detected near the inner tube wall in both configurations due to the secondary flow separation. This “inner” vortex pair gradually increases in size and coherence as  $\phi$  increases. Additional discussion on the secondary flow topology under different flow conditions is provided in the next **paragraph 3.5.5**. The vortex system persists in the downstream straight section, gradually reducing in magnitude and the additional pair of vortices decays completely at approximately a distance of eight hydraulic diameters downstream of the bend ( $Z^*=52.53$ ). **Fig. 3.56c** depicts the distribution of the average non-dimensional streamwise vorticity in the curved section. It can be seen that higher values are obtained in the 4P configuration due to the higher Dean number. Regarding the 2P configuration, the peak vorticity value is obtained at  $\phi=90^\circ$  and the distribution is approximately symmetrical about the center of curvature. On the contrary, the distribution is strongly asymmetrical in the 4P configuration with a peak value at  $\phi=135^\circ$ .



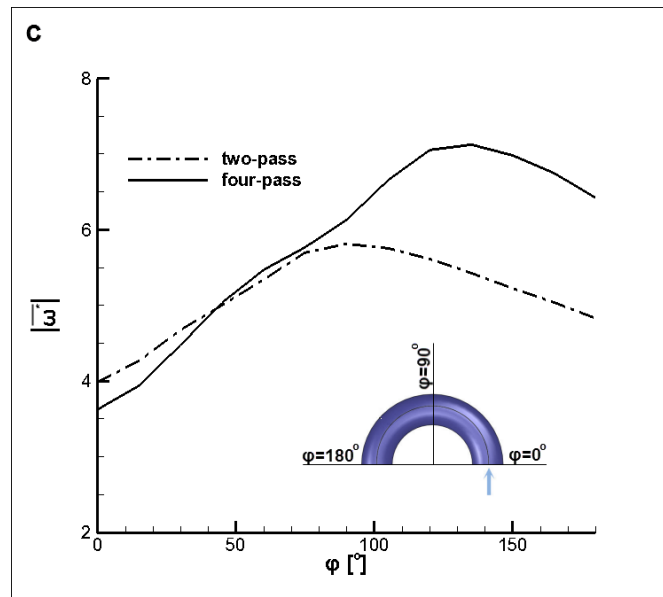


**Fig. 3.56** Contour plots of the vorticity projection normal to cross-stream planes in the curved and straight downstream section: (a) 2P configuration, (b) 4P configuration. (c) Cross-sectional averaged value of the total vorticity magnitude in the tube curved section.

**Fig. 3.57** presents contours of the non-dimensional turbulent kinetic energy  $k^*$  in the curved and the downstream sections of the two configurations. Regarding the curved section, the contour lines already appear distorted in the region close to the tube inner part at  $\varphi=60^\circ$ . The distortion becomes more intense as the flow travels through the curved section. For the 2P configuration (low Dean number) turbulence levels increase up to  $120^\circ$  to  $150^\circ$  in the bent and then start decreasing, whilst in the 4P configuration turbulence keeps increasing up to the exit of the bend; the maximum turbulence level attained is approximately three times higher compared to that for the 2P configuration. Turbulence maxima along the bend are found near the inner part of the bend and in proximity to the centers of the vortices on the cross stream planes. As depicted in **Figs. 3.57a** and **3.57b**, the turbulent kinetic energy values in the downstream section of both configurations appear significantly reduced in comparison to the ones in the respective curved sections. The profiles gradually redevelop to a fully developed, symmetrical form ( $Z^*=2.53$ ) and the mean turbulent kinetic energy in the tube cross-section obtains the expected value equal to that in the upstream section. It is of interest also to notice that the location of the maximum  $k^*$  is at different positions for the two configurations; for the 2P configuration the  $k^*$  maximum is near the wall, whilst in the 4P configuration the corresponding maximum is near the center of the tube. This can be explained by the fact that in the 4P configuration the locations from which the vortices appear to be shed are closer to the central plane and this coupled with the much stronger secondary flow due to higher Dean number transports the wall-generated turbulence towards the center plane. It must also be noted that the profiles are identical for both configurations. A close look at **Fig. 3.57b** reveals that, in the 4P configuration, the turbulent kinetic energy obtains a minimum value at  $Z^*=44.53$  and subsequently increases again.

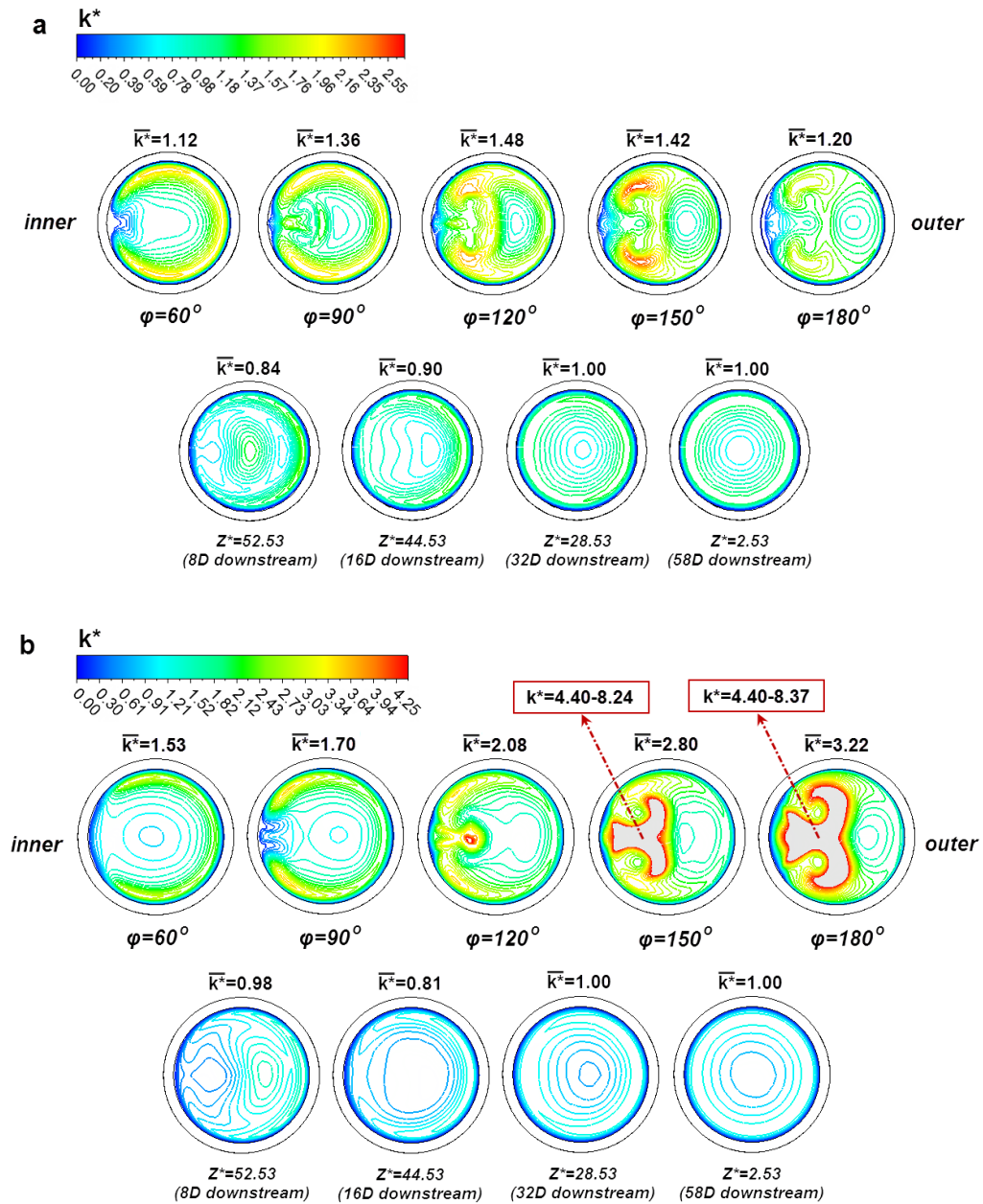


**Fig. 3.57** Contour plots of the turbulent kinetic energy in the tube cross section: (a) 2P configuration, (b) 4P configuration.

Further insight into this distinct behavior can be gained through **Fig. 3.58**, which presents values of the averaged over the cross section non-dimensional turbulent kinetic energy as a function of the “unwound” coordinate  $S^*$ . It is clear that the turbulent kinetic energy initially increases rapidly in the curved section of both configurations and then drops in the subsequent straight section. The peak value is attained within the curved section, at approximately  $\varphi=120^\circ$ , in the 2P configuration and slightly downstream of it, approximately half a hydraulic diameter, in the 4P configuration. The distribution subsequently exhibits a steep decreasing trend and minimum values are obtained at  $S^*=13$  for the 2P and  $S^*=17$  for the 4P configuration, respectively. This significant reduction of the turbulent kinetic energy in the straight section region slightly away from the influence of the longitudinal vortices is indicative of a flow tendency to transition to the laminar regime and it is attributed to the decelerated

flow in the tube core. This is a remaining consequence of the secondary flow which drew high-velocity fluid to the boundary layer region.

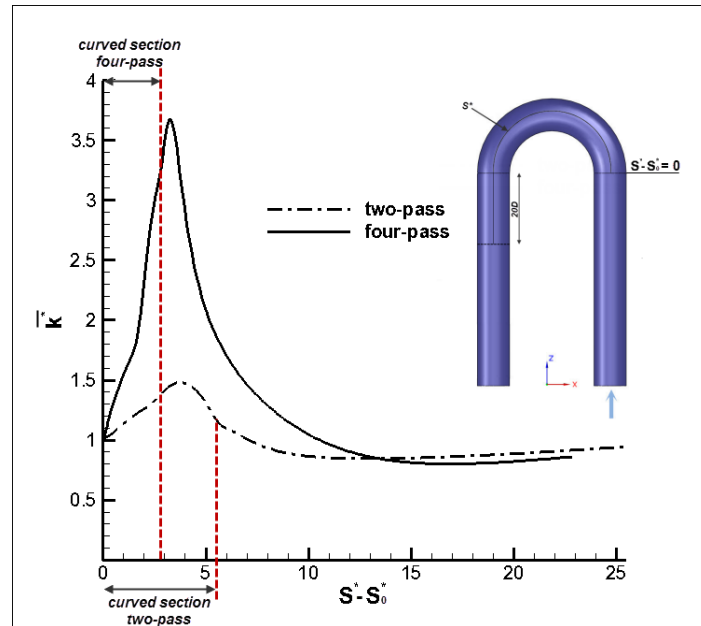


**Fig. 3.58** Distribution of the average turbulent kinetic energy as a function of the unwound coordinate  $S^*$ . The  $S^*$  coordinate in the present figure ranges from the entrance of the curved section up to 25 tube diameters downstream of the bend ( $S_0^* = 60.50$ ).

### 3.5.5 Effect of the Reynolds number - parametric analysis

The flow field in the curved tubes is significantly affected by the flow conditions and the tube geometry and thus different vortical structures are possible to arise. Yanase et al. [3.148] proposed that, regarding tubes of finite curvature, the effect of the Reynolds number and  $\delta$  should be treated as independent factors, as the appearance of additional vortices could be attributed to either the flow convective effect or the centrifugal effect due to curvature. They also determined the regions on the  $\delta$ -Re plane, where strictly two-vortex solutions and either two or four-vortex solutions should be expected. So et al. [3.149] investigated laminar flow in U-shaped tubes of small curvature and identified the Reynolds number, the  $\delta$  ratio and the flow profile at the entrance of the bend as the three main factors that determine the characteristics of the emerging secondary flow pattern. It was concluded that an additional pair of vortices symmetrical about the horizontal plane always emerges in the tube center under the condition that the velocity profile at the entrance of the bend is fully developed.

In order to further elucidate the topology of the vortex system that emerges under different flow conditions in the cooling configurations investigated, a parametric analysis has been carried out for lower values of the Reynolds number, covering a wide range within the laminar flow region (Re=100-1600). The 2P configuration has been selected for the parametric analysis, as it is more favorable in terms of computational cost in comparison to the respective 4P configuration. **Fig. 3.59** presents the cross-stream secondary flow patterns in the form of vorticity contour plots and normalized vector plots at a sample plane midway along the bend ( $\varphi=90^\circ$ ). For Reynolds number equal to 100, only a pair of

symmetrical Dean vortices can be detected, occupying the entire cross-sectional area and having their centers lying almost at the vertical symmetry plane of the tube cross-section. As the Reynolds number increases to 200, the vortices reduce in size, become skewed and their centers shift toward the tube inner wall, however, still a two-vortex solution is evident. On the contrary, a new distinct, weak pair of vortices becomes clearly discernible in the Reynolds number range 400-1600. This second pair of oblique vortices is located about the tube central axis. Yanase et al. [3.148] reported that for  $\delta=0.29$  as in the present case, the onset of the additional pair of vortices is possible at Reynolds number values higher than 270. An additional feature that can be observed is the secondary flow separation near the inner wall, which gains in coherence as the Reynolds number increases, and is clearly manifested at  $Re=1600$  in the form of a pair of localized vortices attached to the inner wall and in the vicinity of the horizontal symmetry plane. The resulting “three cell topology” is in agreement with the findings of So et al. [3.149] and also with the experimental observations of Agrawal et al. [3.150] and Choi et al. [3.151]. The distinct vortical structures detected in the laminar flow region clearly persist in the turbulent region as well, as revealed by comparing Figs. 3.56a-b and 3.59.

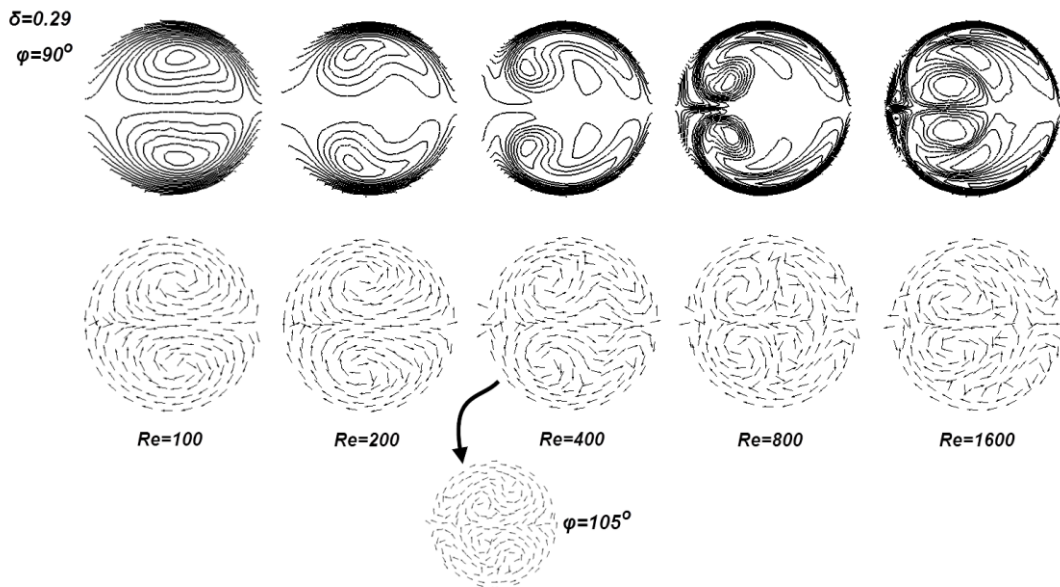


**Fig. 3.59** Secondary-flow patterns at a cross-stream plane ( $\varphi=90^\circ$ ) as a function of the Reynolds number (2P configuration).

**Figs. 3.60a-b** give a perception of the magnitude increase of the vortical structures with  $Re$ . As depicted in **Fig. 3.60a**, the location of the maximum non-dimensional vorticity at the tube cross-section slightly shifts toward the bend middle ( $\varphi=90^\circ$ ) as the Reynolds number increases. In all cases, the maximum averaged vorticity value has been obtained by  $\varphi=75^\circ$  and a decreasing trend clearly prevails after  $\varphi=90^\circ$ . By comparing **Fig. 3.60a** to **Fig. 3.56c**, it can be seen that higher values of the non-dimensional vorticity are obtained in the laminar flow region, thus the  $\bar{\omega} / \bar{w}$  ratio decreases as the Reynolds number increases. This is an indication that the magnitude of the combined secondary flow pattern increases at a lower rate with  $Re$  in the turbulent flow region. **Fig. 3.60b** shows the maximum vorticity magnitude of the Dean and middle vortices at the sample plane at  $\varphi=90^\circ$  as a function of the Reynolds number. As illustrated, the relative increase in the magnitude of the Dean vortices becomes smaller as the Reynolds number increases, a trend which confirms the remark made

regarding the vorticity magnitude in the turbulent flow region. The magnitude of the middle vortices, on the other hand, increases in a nearly linear manner with the Reynolds number. However, the maximum magnitude attained by the middle vortices (at  $Re=1600$ ) is approximately half the respective one of the Dean vortices.

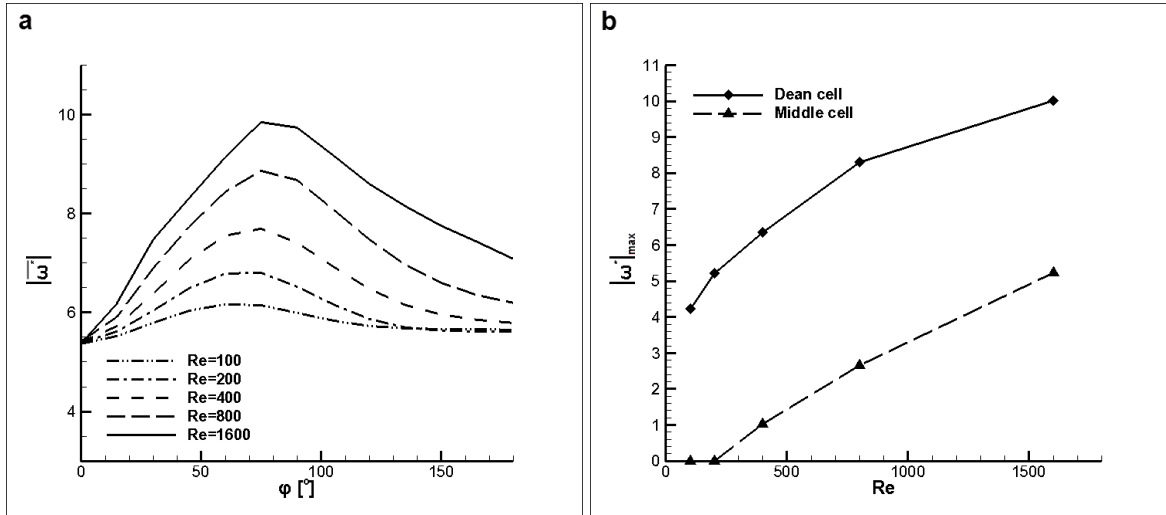


**Fig 3.60** 2P configuration: (a) Cross-sectional averaged values of the vorticity magnitude at the tube curved section for various Reynolds numbers values, (b) maximum vorticity magnitude of the distinct vortical structures at a sample plane ( $\phi=90^\circ$ ) vs. the Reynolds number.

Finally, two further simulations have been conducted in the turbulent flow regime ( $Re=10248$  and  $20496$  leading to  $De=5527$  and  $11053$  respectively) in order to illustrate the flow tendency to re-transition to the laminar regime in the straight tube section adjacent to the bend (see **Fig. 3.58**). **Fig. 3.61** presents the streamwise variation of the average turbulent kinetic energy with the Reynolds number as parameter. It can be observed that an increase of the Reynolds number shifts the undershoot of the turbulent kinetic energy to lower values and, in addition, towards axial positions further downstream of the bend. Nevertheless, as the Reynolds number increases from  $10248$  to  $20496$ , the variation of the turbulent kinetic energy distribution becomes smoother. It must be noted that by comparing **Figs. 3.58** and **3.61**, it is evident that, although the Dean number for the 4P configuration is lower ( $De=3867$ ), the higher value of  $\delta$  in comparison to the 2P configuration has a similar effect in the turbulent kinetic energy distribution, as in the case of  $Re=10248$  in **Fig. 3.61**. Thus, it can be concluded that the Reynolds number and  $\delta$  affect the turbulent kinetic energy distribution in an independent manner and thus should be rather treated as distinct parameters instead of combining their effect in the Dean number.

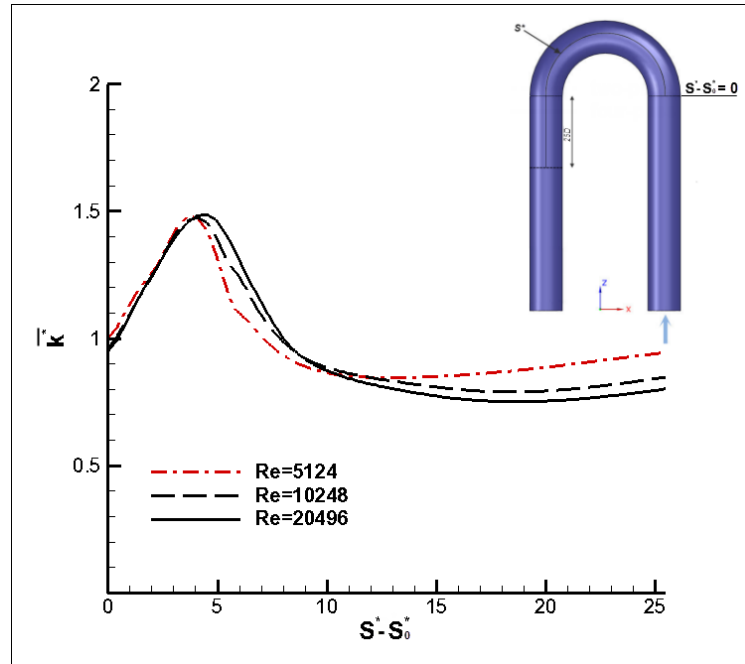


**Fig. 3.61** Distribution of the average turbulent kinetic energy on cross-stream planes as a function of the unwound coordinate  $S^*$  with Reynolds number as parameter (2P configuration). The  $S^*$  coordinate in the present figure ranges from the entrance of the curved section up to 25 tube diameters downstream of the bend ( $S_0^* = 60.50$ ).

### 3.5.6 Temperature field and heat transfer

As shown in **Fig. 3.62a** through contour plots of the non-dimensional temperature, the flow reaches full thermal development in the straight tube section upstream of the bend. It is interesting to notice that the thermal boundary layer in the lower part of the tube is thicker in comparison to the upper one. This is due to the non-uniform heating conditions, as the tube is mainly heated through the part of its circumference that is embedded in the substrate, which is approximately equal to three quarters of the total. The flow behavior upstream of the bend is identical for the 2P and 4P configurations and **Fig. 3.62a** indicatively contains results only for the 2P configuration.

The effects of the secondary-flow pattern are significant in the development of the temperature field downstream of the bend as intense thermal mixing takes place in both configurations (**Figs. 3.62b-c**). Cold fluid is deflected toward the outer tube wall causing the disruption of the boundary layer development in that region. On the contrary, the maximum fluid temperature values are detected in the inner tube wall and especially in the vicinity of the horizontal symmetry plane, where the thermal boundary layer is also locally thickened. This is due to the secondary flow, which, after impinging on the outer wall, is symmetrically diverted toward the lower and upper part of the tube circumference, where it draws fluid from the boundary layer region and guides it to the symmetry plane of the inner wall. The effect of the secondary flow gradually weakens in the straight section and the flow redevelops. As can be seen from the contour plot at  $Z^* = 28.53$ , the fully developed profile is slightly distorted toward the outer wall. It must be noted that **Fig. 3.62c** refers to the second pass of the 4P configuration. The temperature distribution in the respective regions of the other downstream passages is qualitatively identical. However, the absolute temperature values are higher as the fluid is constantly heated throughout the substrate area (**Fig. 3.62d**).

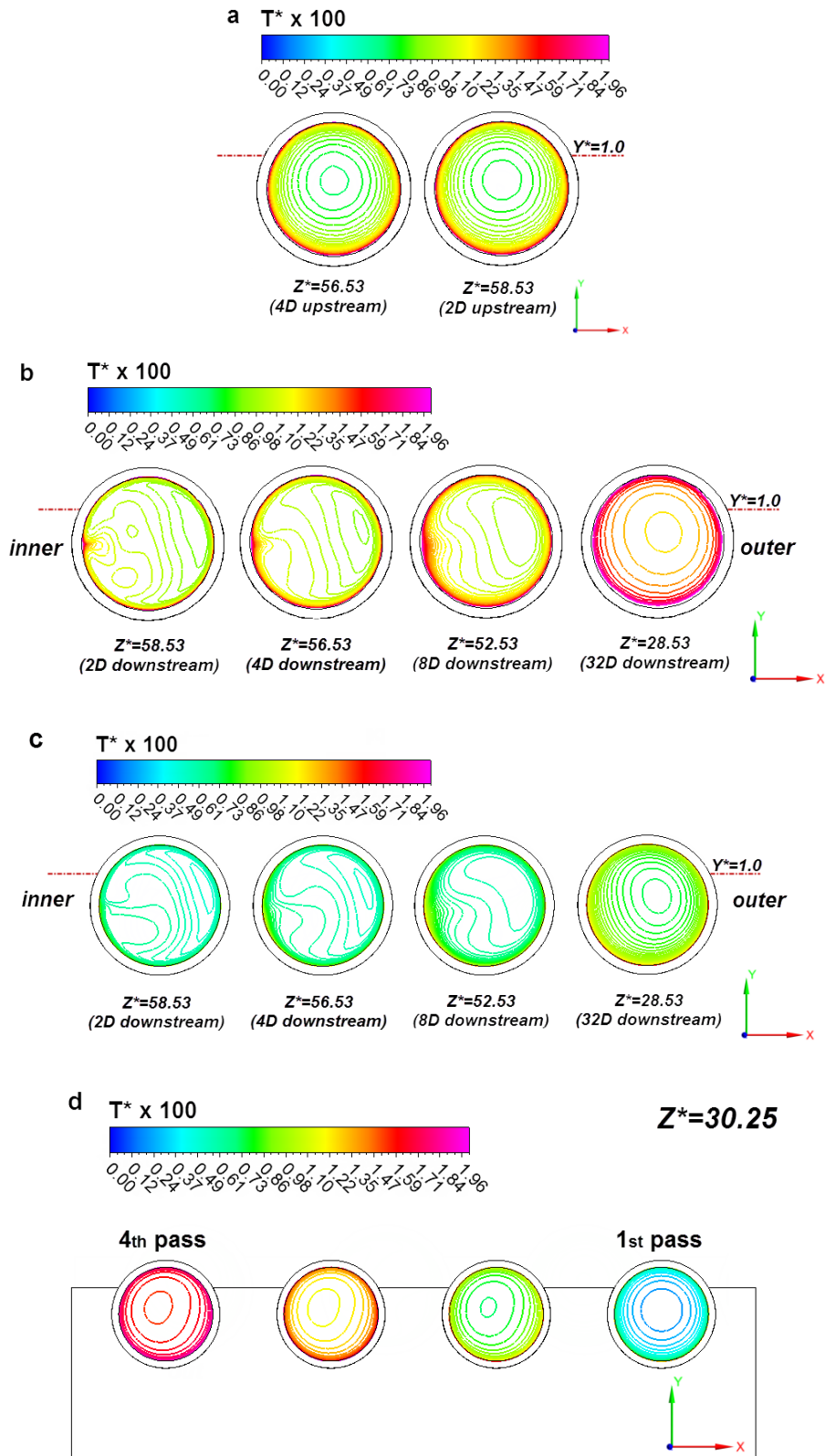


**Fig. 3.62** Temperature contour plots in the fluid region (solid top surface shown at  $Y^*=1$ ): (a) upstream tube section of the 2P configuration, (b) downstream tube section of the 2P configuration, (c) downstream tube section of the 4P configuration (second passage), (d) at the passages of the 4P configuration.

It is also of importance to illustrate the temperature distribution in the solid substrate as this is indicative of the thermal performance of the cooling device. As shown in **Fig. 3.63a**, the temperature

field is fully three-dimensional in both configurations due to the effect of axial conduction, enabled by the high thermal conductivity of the substrate material. It is clearly discernible that the substrate region of high temperatures is shifted in both configurations toward the section of the heat-sink close to the tubing outlet, with the maximum temperature located at the left vertical wall approximately ten hydraulic diameters upstream of the outlet; the maximum wall temperature is higher for the 2P configuration (Fig. 3.63a) due to the smaller area available for heat transfer between the substrate and the tubing. Besides, it is evident that the transversal temperature distribution of the substrate is primarily influenced by the fluid temperature inside the tubing, which is embedded by approximately three quarters of its circumference. Thus, the region of the heat sink closer to the inlet passage obtains lower temperatures. In fact, the effect of the fluid temperature on the substrate is manifested in a more regular manner in the 4P configuration (Fig. 3.63b).

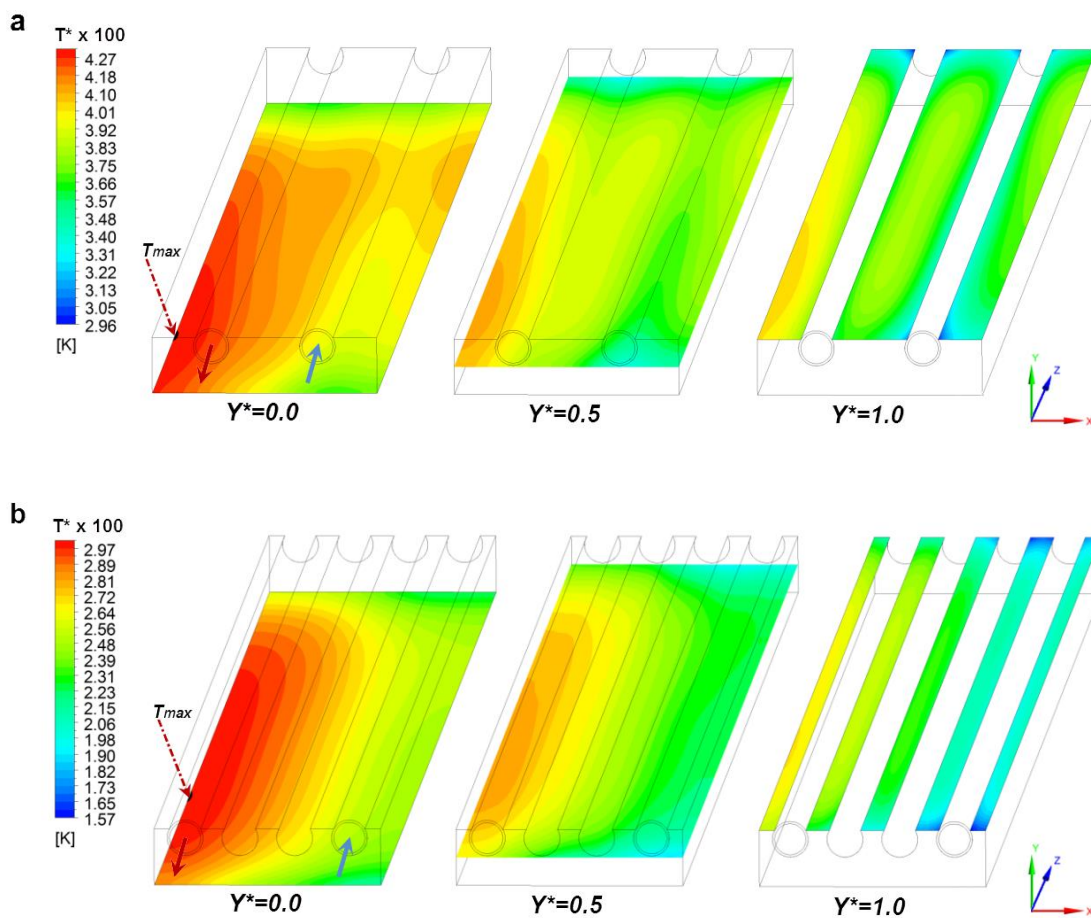
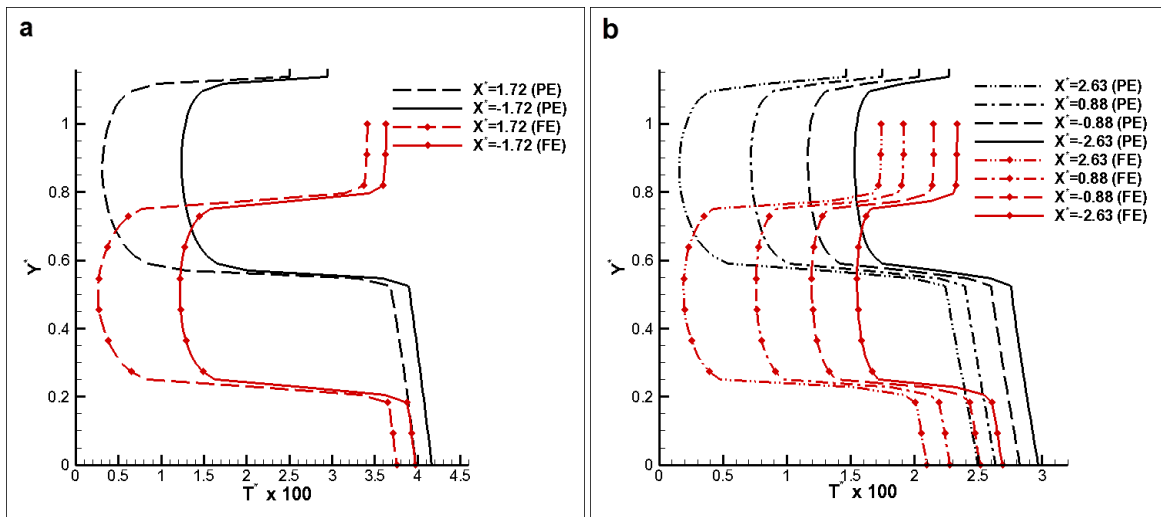


Fig. 3.63 Temperature contour plots at various heights within the substrate area of the heat sink: (a) 2P and (b) 4P configuration.

The relative position of the tube center to the heated surface ( $Y^*=0$ ) is a manufacturing parameter that can significantly differentiate the temperature field in the heat sink and is expected to have a significant effect on its thermal performance. In order to elucidate the effect of the tube embedment into the substrate, two additional variations of the cooling configuration have been examined, similar to the 2P and 4P configurations of Fig. 3.2, with the difference that the center of the tubing cross section is located exactly at the middle of the substrate ( $Y^*=0.5$ ). Fig. 3.64 depicts the vertical non-dimensional temperature profiles at two and four characteristic span-wise ( $X^*$ ) locations, respectively,

along the heat sink streamwise mid-length ( $Z^*=30.25$ ), in order to illustrate the temperature distribution in both the solid and the fluid regions of the heat sink. Heat is distributed through conduction in the lower and upper solid parts of the cooling device and through convection in the fluid section inside the tubing. Regarding the fluid region, it can be seen that the temperature profiles remain invariant regardless of the tubing position and, regarding the 4P configuration, the fluid is being heated at a higher rate in the two passages ( $X^*=2.63$  and  $X^*=0.88$ ) closer to tube inlet, as revealed by the temperature difference between consecutive profiles in **Fig. 3.64b**.

The discernible linear parts of the profiles clearly show that the substrate temperature also increases in the design employing fully embedded (FE) tubes, as the outer vertical side closer to the outlet is approached, i.e. the  $X^*$  coordinate decreases. Furthermore, it is evident that the fully embedded tubing leads to reduced temperature at the lower part of the substrate and consequently at the heated bottom side ( $Y^*=0$ ) as well, which is an indication of enhanced thermal performance. The transversal temperature distribution at the substrate, which is not presented for brevity, has a similar form to the designs employing partially embedded tubes (see **Fig. 3.64**). Nonetheless, the absolute temperature values are decreased in the configurations employing fully embedded tubes.



**Fig. 3.64** Vertical temperature profiles at the heat sink streamwise mid-length ( $Z^*=30.25$ ): (a) 2P and (b) 4P configuration.

The quantification of the heat transfer rate is limited to the straight sections of the serpentine tube, as the curved sections lay outside of the substrate active area. **Fig. 3.65** presents the local Nusselt number distribution in the considered heat-sink layouts. In the largest part of the straight sections of both configurations, the Nusselt number exhibits constant, fully developed values. The fully developed value is slightly different in each passage, a behavior that should be attributed to the non-uniform heating, as the temperature distribution in the substrate is fully three dimensional. Furthermore, the designs employing fully embedded tubes obtain higher Nusselt number values, as much as 5% in the 4P configuration. The temperature non-uniformity is higher in the substrate of the designs with fully embedded tubes and non-uniform heating conditions have been reported to enhance heat transfer [3.8].

**Fig. 3.65** also reveals that the Nusselt number distribution in the first passage of both configurations exhibits a minimum point right after the thermal entrance region and subsequently redevelops to a fully developed value. The reduced heat transfer is explained by taking into

consideration the low substrate temperature in the specific region (see also Fig. 3.63), which leads to a decreased temperature gradient and thus to low heat flux  $q'' = -k \frac{dT}{dy}$ . The local Nusselt number obtains high values in the tube section immediately downstream of the bend and more specifically at the range  $Z^*=50-60$  in the 2P (Fig. 3.65a) and  $Z^*=45-60$  in the 4P configuration (Fig. 3.65b), respectively. This heat transfer enhancement is due to the effect of the secondary flow, which constantly feeds the circumferential boundary layer area with colder fluid from the tube core. It is justifiable, that the high heat-transfer region has a greater extent in the 4P configuration due to the higher intensity of the recirculation (also see Fig. 3.56). A close look at Figs. 3.65a-c also reveals that the local Nusselt number distribution exhibits an undershoot in the subsequent tube section, where the longitudinal vortices have decayed completely. The region in question extends approximately to the streamwise distance  $Z^*=40-50$  in the 2P configuration and  $Z^*=35-45$  in the 4P configuration, respectively. A similar undershoot has also been observed by Ohadi and Sparrow [3.118] who attributed it to flow re-transition to the laminar regime. The findings of the present study support their assumption, as can be established by comparing Figs. 3.58 and 3.65. It is evident that the turbulent kinetic energy values are considerably reduced in the region of the Nusselt number undershoot.

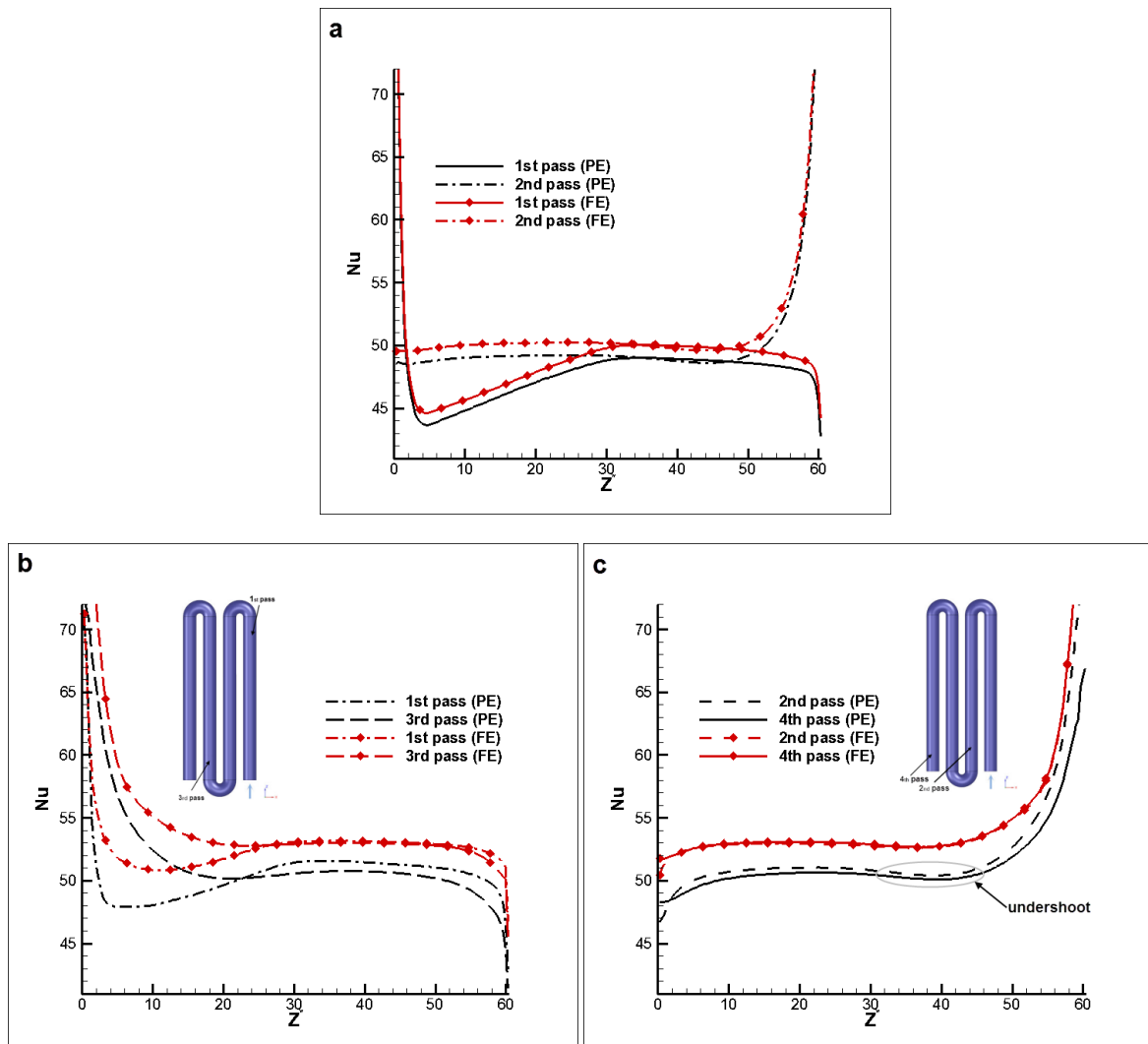


Fig. 3.65 Local Nusselt distribution in the substrate area: (a) 2P configuration, (b) 4P configuration, first and third passage (c) 4P configuration, second and fourth passage.

### 3.6 Comparative evaluation of the various configurations

In order to gain insight into the performance characteristics of the examined cooling devices, the various configurations are comparatively evaluated in terms of thermal and hydrodynamic performance, as well as exergetic performance. A number of criteria have been selected in order to elucidate each aspect of the heat-sink performance.

A suitable measure for the quantification of the thermal performance of a cooling device is the thermal resistance [3.152]. The overall thermal resistance is determined on the basis of an equivalent resistance circuit (**Fig. 3.66a**) [3.152]:

$$R_{th} = R_{cond} + R_{cal} + R_{conv} \quad (3.35)$$

The three terms on the right hand side of **Eq. (3.35)** correspond to the conductive, caloric and convective individual resistances:

$$R_{cond} = \frac{t_s}{k_s A} \quad (3.36)$$

$$R_{cal} = \frac{1}{\rho \dot{V}_{tot} c_p} \quad (3.37)$$

$$R_{conv} = \frac{1}{\overline{h_{ove}} A_{HTR}} \quad (3.38)$$

where  $\overline{h_{ove}}$  is the overall heat transfer coefficient and  $A_{HTR}$  is the total heat transfer area. In the case of plate-fin heat sinks, a heat transfer efficiency is assigned to the fins and thus **Eq. (3.35)** becomes:

$$R_{conv} = \frac{1}{\overline{h_{ove}} [N(2\eta_{fin} H_{ch} + W_{ch})L]} \quad (3.39)$$

where  $N$  is the number of channels and  $\eta_{fin}$  is the fin efficiency defined as:

$$\eta_{fin} = \frac{\tanh(mH_{ch})}{mH_{ch}} \quad \text{and} \quad m = \sqrt{\frac{2h}{k_s W_w}} \quad (3.40)$$

The total thermal resistance in regard to the VW heat-sink configuration can be determined by **Eq. (3.35)**, if a mean convective resistance is defined as for the case of parallel resistances:

$$\frac{1}{R_{conv,tot}} = \sum_{i=1}^{N_s} \frac{1}{R_{conv,i}} = \sum_{i=1}^{N_s} \frac{1}{\overline{h}_i A_{HTR,i}} \quad (3.41)$$

where  $N_s$  is the number of sections. Each section of the VW heat sink is characterized by a different number  $N_i$  of microchannels having width  $W_{ch,i}$  and therefore, according to Eq. (3.39), an individual convective thermal resistance should be assigned to each one. Eq. (3.41) is obtained if the equivalent thermal resistance network is considered (Fig. 3.66b), where the thermal resistances of the equal-length sections of different hydraulic diameters should be connected in parallel, as the total heat flux at the microchannel bottom wall branches to the three sections.

It should be noted that in the case of straight channels Eq. (3.35) reduces to the following expression [3.152]:

$$R_{th} = \frac{T_{w,max} - T_{f,i}}{Q} \quad (3.42)$$

where  $T_{w,max}$  and  $Q$  are the maximum wall temperature and the heat rate at the heated surface, respectively. However, in the case of variable-width channels, where the temperature increase at the solid wall is not linear, Eq. (3.42) is expected to overestimate the thermal resistance of the cooling device, yet will be included in the evaluation of the devices conducted in chapter 4, as it is a performance index widely used in the literature [3.16-3.24].

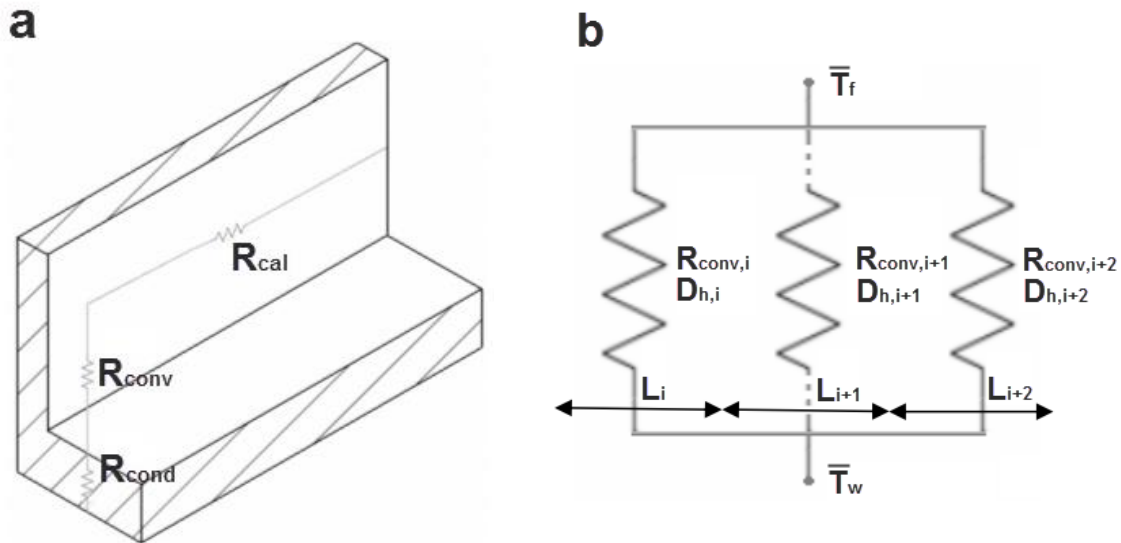


Fig. 3.66 Equivalent total thermal resistance network: (a) Configuration with ducts of constant cross-section, (b) configuration with ducts of stepwise varying cross-section

The temperature non-uniformity at the duct bottom wall, affects the efficiency of the solar-cell module (see paragraph 2.4) and is estimated through the standard deviation of temperature. Hydrodynamic performance can be adequately represented through the required pumping power  $P_{pump} = \dot{V} \cdot \Delta p$  which, for a constant flow rate, is determined by the pressure drop values. Besides, the heat transfer to pressure drop ratio has been proposed as an indication of the overall performance of a heat exchanging device [3.153, 3.154]. In the present study, this overall performance index ( $PI$ ) is calculated in a non-dimensional form as follows:

$$PI = \frac{\overline{Nu}_{ove}}{f} \quad (3.43)$$

where  $\overline{Nu}_{ove}$  is the overall mean Nusselt number and  $f$  is the friction factor calculated through  $f = \Delta p D_i / (2 \rho L \bar{w}^2)$ .

From the point of view of the second-law of thermodynamics, the cooling devices can be evaluated through the concept of the entropy generation rate, which is equivalent to the rate of destruction of available work. The entropy generation rate per unit length of a duct having an arbitrary cross-section can be calculated using averaged quantities regarding heat transfer and fluid friction [3.155]:

$$\dot{S}'_{gen} = \frac{q'^2}{4 \bar{T}_f^2 \dot{m} c_p} \frac{D_h}{\bar{St}} + \frac{2 \dot{m}^3}{\rho^2 \bar{T}_f} \frac{f}{D_h A_{cs}^2} \quad (3.44)$$

where  $q'$  is the heat rate per duct unit length and  $\bar{St} = \overline{Nu} / Re Pr$  is the mean overall Stanton number. The two terms on the right hand side of **Eq. (3.43)** correspond to the contribution of heat transfer and friction losses, respectively, to the entropy generation rate. The discrete contribution of each term to the total entropy generation rate can be designated through the Bejan number  $Be = \frac{\dot{S}'_{gen, \Delta T}}{\dot{S}'_{gen}}$ .

The comparative results of the cooling configurations considered with regard to the above mentioned criteria are summarized in **Table 3.6**. From the evaluation criteria presented in **Table 3.6**, thermal resistance  $R_{th}$  is expected to have the strongest influence on the overall efficiency of a CPVT system, as it affects both the thermal losses and the electrical efficiency of the solar cell module. The lowest thermal resistance value is achieved by the microchannel configuration primarily due to the multitude of the available heat transfer areas. It is interesting to notice that the VW configuration, despite the much smaller number of channels employed, achieve thermal resistance values 25% higher than the microchannel configuration, when mixed convection conditions are considered. The other devices are less effective in terms of heat transfer, with the poorest performance achieved by the FW<sub>1</sub> configuration due to the inadequate number of heat transfer surfaces and the low flow velocity.

The effect of the pressure drop penalty, and consequently the parasitic pumping power required, in the efficiency of the CPVT system can be significant if the system length is considerable, as is usually the case with linear concentrating systems. In terms of hydrodynamic performance, the minichannel heat-sinks (FW and VW) induce almost negligible pressure drop to the cooling fluid due to their relatively large hydraulic diameter and the relatively small flow velocity. The pressure drop induced by the tube-on-plate configurations is significantly larger, as the entire flow rate enters a single duct, opposed to flow branching in the channel configurations and furthermore the length of the employed serpentine tube is two and four times the channel length of the plate fin configurations. Besides, the recirculation developing in the tube bends also induces further pressure losses. However, the highest pressure drop is induced by far within the microchannel configuration due to the increased flow friction caused by the small channel hydraulic diameter and the high flow velocity. As has been

mentioned in the introduction section of **paragraph 3.4.1**, the pressure drop penalty is the major drawback associated with microchannel cooling devices.

The 2P tube-on-plate configuration exhibits the highest temperature uniformity in the substrate due to the three-dimensional temperature distribution and the considerable flux “smearing” caused by lateral conduction. As less substrate area is occupied by tubes in comparison to the 4P designs, the effect of the conductive substrate, which tends to homogenize the temperature distribution is more significant leading thus to greater uniformity. It must also be noted that full embedment of the tubing deteriorates temperature uniformity in both configurations. In reference to plate-fin configurations the values of the temperature standard deviation are somewhat higher due to the linear temperature gradient along the flow direction and the small substrate thickness, which has no effect on the wall heat flux distribution. It must be noted that the layout of the  $VW_t$  configuration enhances temperature uniformity in comparison to straight channels (e.g. compared to the  $FW_h$  configuration), in agreement to what is stated by Morega and Bejan [3.63]

The values of the performance index  $PI$  achieved by the tube-on-plate configurations are an order of magnitude larger than the respective ones achieved by the plate-fin configurations. This large discrepancy in the values is due to the different flow conditions, turbulent and laminar flow respectively, that occur in the two heat-sink designs, leading to much higher values of the Nusselt number in the case of turbulent flow. However, the  $PI$  values alone may be misleading in assessing the actual heat sink performance, as, for instance, the overall performance of the 4P (FE) configuration that achieves the highest  $PI$  value is inferior in comparison to the VW configuration, as illustrated by the values of the thermal resistance and the pressure drop. Hence, it can be deduced that this indicator alone is inappropriate for comparing fundamentally different cooling devices as it could lead to a misleading evaluation.

Regarding the exergetic performance, the 4P configurations achieve much lower values of the entropy generation rate in comparison to plate-fin configurations primarily due to the distribution of the same heat rate to greater duct length, 2.0 m instead of 0.5 m for the plate-fin configurations (see **Eq. (3.44)**). In other words, if the entropy generation rate was restricted to the CPVT system length, the values regarding the 4P configurations would have been four times higher. Especially for the cases of the plate-fin devices, the values of the entropy generation rate differ mainly according to the values of the Stanton number obtained in each configuration, which, in turn, are primarily determined by the values of the Reynolds number. Besides, the values of the Bejan number illustrate the fact that the values of the total entropy generation rate are primarily determined by the first term on the right hand side of **Eq. (3.43)**, i.e. the one corresponding to heat transfer.

The general conclusion that can be drawn is that there is no device that clearly outperforms the others regarding all the considered criteria. Hence, the significance of each criterion must be estimated, in order to designate the most attractive designs. Considering the integrated CPVT system, the cell efficiency, the thermal losses and the parasitic power all have a vital impact on the overall efficiency. Thus it is important to have an altogether efficient cooling, i.e. low thermal resistance of the heat sink, with low pressure drop penalty. The microchannel heat sink ( $FW_\mu$ ) is clearly the best performing configuration in terms of heat transfer, however with a considerable pressure drop penalty. On the other hand the VW configuration, especially under mixed convection conditions, appears as the most efficient trade-off exhibiting low values of both the thermal resistance and the pressure drop. Besides the temperature non-uniformity characterizing all the configurations, is remarkably low and

should not affect the cell efficiency. In conclusion, it is decided to construct two heat sink designs, employing fixed-width microchannels and channels of stepwise-varying width, respectively. The optimization, construction and evaluation procedure of the heat-sink designs is presented in the next chapter.

**Table 3.6** Comparative results for the performance of the evaluated cooling devices. The conductive thermal resistance for all the plate-fin configurations corresponds to a substrate thickness of 3mm.

- 1 The value for the temperature standard deviation was calculated from the temperature distribution at the bottom wall centerline, which is representative of the entire plane as there are no lateral gradients.
- 2 The values presented for  $R_{th}$  and  $\dot{S}'_{gen}$  are based on the averaged channel hydraulic diameter.
- 3 The values presented for  $\dot{S}'_{gen}$  are based on the averaged channel hydraulic diameter, calculated as the mean of the first and second section hydraulic diameters.

$\dot{V}_{tot} = 30 \text{ mL/s}$ $q'' = 28.3 \text{ kW/m}^2$ $T_{in} = 298 \text{ K}$						
<i>Reference Case</i>						
	$R_{th}$ [K/W]	$\Delta P$ [Pa]	StDev T [K]	PI [-]	$\dot{S}'_{gen}$ [W/mK]	Be [-]
FW <sub>h</sub>	0.0146	74.3	2.30	126	0.0755	0.971
FW <sub>1</sub>	0.0219	10.8	2.14	288	0.155	0.999
FW <sub><math>\mu</math></sub> <sup>1</sup>	0.0097	7789.5	2.08	111	0.0186	0.916
VW <sub>t</sub> <sup>2</sup>	0.0139	116.2	1.18	90	0.0694	0.952
VW (FC) <sup>3</sup>	0.0125	45.4	3.95	65	0.1255	0.996
VW (MC) <sup>3</sup>	0.0122	45.7	2.06	138	0.0872	0.995
2P (PE)	0.0232	859.6	0.52	4490	0.0808	0.966
2P (FE)	0.0196	859.6	0.68	4605	0.0788	0.965
4P (PE)	0.0158	1835.5	0.76	4378	0.0219	0.865
4P (FE)	0.0140	1835.5	0.93	4614	0.0209	0.858

### Chapter references

[3.1] S.V. Patankar, Numerical Heat Transfer and Fluid Flow, Taylor & Francis, USA, 1980, pp.11-22.

[3.2] H.K. Versteeg, W. Malalasekera, An introduction to computational fluid dynamics: The finite volume method, Longman Scientific & Technical, Essex, 1995, pp. 10-39.

[3.3] ANSYS Inc., ANSYS CFX-Solver Theory Guide, Release 13.0, Canonsburg, PA, 2010.

[3.4] B.E. Launder, D.B. Spalding, The numerical computation of turbulent flows, Comp. Meth. Appl. Mech. Energy 3 (1974) 269-289.

- [3.5] F.R. Menter, Two-Equation Eddy-Viscosity Turbulence Models for Engineering Applications, *AIAA J.* 32 (1994) 1598–1605.
- [3.6] D.C. Wilcox, Re-assessment of the scale-determining equation for advanced turbulence models, *AIAA J.* 26 (1988) 1299-1310.
- [3.7] ANSYS Inc., ANSYS CFX-Solver Manager User's guide, Release 13.0, Canonsburg, PA 2010.
- [3.8] R.K. Shah, A.L. London, *Laminar Flow Forced Convection in Ducts: a Source Book for Compact Heat Exchanger*, Academic press, New York, 1978, pp. 196-222.
- [3.9] J.P. Holman, *Heat Transfer*, tenth ed., McGraw-Hill, New York, 2010, pp. 331,360.
- [3.10] J.A. Duffie, W.A. Beckman, *Solar Engineering of Thermal Processes*, second ed., Wiley, New York, 1991, pp. 358-367.
- [3.11] K. Foli, T. Okabe, M. Olhofer, Y. Jin, B. Sendhoff, Optimization of micro heat exchanger: CFD, analytical approach and multi-objective evolutionary algorithms, *Int. J. Heat Mass Transf.* 49 (2006) 1090-1099.
- [3.12] A. Bejan, *Shape and Structure, from Engineering to Nature*, first ed. Cambridge University Press, Cambridge, 2000, pp. 29-41.
- [3.13] EN12975-2:2006 Standard, Thermal solar systems and components - Solar Collectors - Part 2: Test methods.
- [3.14] A. Mohammed Adham, N. Mohd-Ghazali, R. Ahmad, Thermal and hydrodynamic analysis of microchannel heat sinks: A review, *Renew. Sustain. Energy Rev.* 21 (2013) 614-622.
- [3.15] I. Hassan, P. Phutthavong, M. Abdelgawad, Microchannel Heat Sinks: an Overview of the State-of-the-Art, *Microscale Thermophys. Eng.* 8 (2004) 183–205.
- [3.16] D.B. Tuckerman, R.F.W. Pease, High-performance heat sinking for VLSI. *IEEE Electron Device Let.* 2 (1981) 126–129.
- [3.17] T. M. Harms, M. J. Kazmierczak, F. M. Gerner, Developing convective heat transfer in deep rectangular microchannels. *Int. J. Heat Fluid Flow* 20 (1999) 149-157.
- [3.18] B. Lu, F. Mei, W.J. Meng, S. Guo, Fabrication of Metal-Based Microchannel Heat Exchangers and Quantification of Their Liquid Flow and Heat Transfer Characteristics, *Heat Transf. Eng.* 34 (2013) 15–28.
- [3.19] H.S. Park, J. Punch, Friction factor and heat transfer in multiple microchannels with uniform flow distribution, *Int. J. Heat Mass Transf.* 51 (2008) 4535–4543.

- [3.20] B.X. Wang, X.F. Feng, Experimental investigation on liquid forced-convection heat transfer through microchannels, *Int. J. Heat Mass Transf.* 37 (1994) 73-82.
- [3.21] P.S. Lee, S. V. Garimella, D. Liu, Investigation of heat transfer in rectangular microchannels, *Int. J. Heat Mass Transf.* 48 (2005) 1688–1704.
- [3.22] P.S. Lee, S. V. Garimella, Thermally developing flow and heat transfer in rectangular microchannels of different aspect ratios, *Int. J. Heat Mass Transf.* 49 (2006) 3060–3067.
- [3.23] X.F. Peng, G.P. Peterson, Convective heat transfer and flow friction for water flow in microchannel structures, *Int. J. Heat Mass Transf.* 39 (1996) 2599–2608.
- [3.24] S.A. Jajja, W. Ali, H.M. Ali, A.M. Ali, Water cooled minichannel heat sinks for microprocessor cooling: Effect of fin spacing, *Appl. Therm. Eng.* 64 (2014) 76–82.
- [3.25] C.K. Loh, D.J. Chou, Comparative analysis of heat sink pressure drop using different methodologies, In *Proceeding of: Thermal and Thermomechanical Phenomena in Electronic Systems*, 2004.
- [3.26] H.L. Wang, H.C. Wu, S. Kong Wang, T.-C. Hung, R.-J. Yang, A study of mini-channel thermal module design for achieving high stability and high capability in electronic cooling, *Appl. Therm. Eng.* 51 (2013) 1144–1153.
- [3.27] J. Zhang, T. Zhang, S. Prakash, Y. Jaluria, Experimental and Numerical Study of Transient Electronic Chip Cooling by Liquid Flow in Microchannel Heat Sinks, *Numer. Heat Transf. Part A Appl.* 65 (2014) 627–643.
- [3.28] A.G. Fedorov, R. Viskanta, Three-dimensional conjugate heat transfer in the microchannel heat sink for electronic packaging, *Int. J. Heat Mass Transf.* 43 (2000) 399–415.
- [3.29] K. Toh, X. Chen, J. Chai, Numerical computation of fluid flow and heat transfer in microchannels, *Int. J. Heat Mass Transf.* 45 (2002) 5133–5141.
- [3.30] Y. Chen, C. Zhang, M. Shi, J. Wu, Three-dimensional numerical simulation of heat and fluid flow in noncircular microchannel heat sinks, *Int. Commun. Heat Mass Transf.* 36 (2009) 917–920.
- [3.31] Z. Li, W.Q. Tao, Y.L. He, A numerical study of laminar convective heat transfer in microchannel with non-circular cross-section, *Int. J. Therm. Sci.* 45 (2006) 1140–1148.
- [3.32] P. Gunnasegaran, H.A. Mohammed, N.H. Shuaib, R. Saidur, The effect of geometrical parameters on heat transfer characteristics of microchannels heat sink with different shapes, *Int. Commun. Heat Mass Transf.* 37 (2010) 1078–1086.

- [3.33] W. Qu, I. Mudawar, Analysis of three-dimensional heat transfer in micro-channel heat sinks, *Int. J. Heat Mass Transf.* 45 (2002) 3973–3985.
- [3.34] W. Qu, I. Mudawar, Experimental and numerical study of pressure drop and heat transfer in a single-phase micro-channel heat sink, *Int. J. Heat Mass Transf.* 45 (2008) 2549–2565.
- [3.35] Z. Li, X. Huai, Y. Tao, H. Chen, Effects of thermal property variations on the liquid flow and heat transfer in microchannel heat sinks, *Appl. Therm. Eng.* 27 (2007) 2803–2814.
- [3.36] J.T. Choi, O.K. Kwon, D.A. Cha, A numerical study of the heat transfer and fluid flow of micro-channelled water block for computer CPU cooling, *J. Mech. Sci. Technol.* 25 (2011) 2657–2663.
- [3.37] J.H. Ryu, D.H. Choi, S.J. Kim, Numerical optimization of the thermal performance of a microchannel heat sink, *Int. J. Heat Mass Transf.* 45 (2002) 2823–2827.
- [3.38] D. Farnam, B. Sammakia, H. Ackler, K. Ghose, Comparative Analysis of Microchannel Heat Sink Configurations Subject to a Pressure Constraint, *Heat Transf. Eng.* 30 (2009) 43–53.
- [3.39] J. Li, G.P. Peterson, 3-Dimensional numerical optimization of silicon-based high performance parallel microchannel heat sink with liquid flow, *Int. J. Heat Mass Transf.* 50 (2007) 2895–2904.
- [3.40] A. Koşar, Effect of substrate thickness and material on heat transfer in microchannel heat sinks, *Int. J. Therm. Sci.* 49 (2010) 635–642.
- [3.41] X. Wei, Y. Joshi, Experimental and numerical study of sidewall profile effects on flow and heat transfer inside microchannels, *Int. J. Heat Mass Transf.* 50 (2007) 4640–4651.
- [3.42] K. Vafai, L. Zhu, Analysis of two-layered micro-channel heat sink concept in electronic cooling, *Int. J. Heat Mass Transf.* 42 (1999) 2287–2297
- [3.43] M.L.J. Levac, H.M. Soliman, S.J. Ormiston, Three-dimensional analysis of fluid flow and heat transfer in single- and two-layered micro-channel heat sinks, *Heat Mass Transf.* 47 (2011) 1375–1383.
- [3.44] T.H. Tsai, R. Chein, Simple model for predicting microchannel heat sink performance and optimization, *Heat Mass Transf.* 48 (2011) 789–798.
- [3.45] T.S. Fisher, K.E. Torrance, Optimal Shapes of Fully Embedded Channels for Conjugate Cooling, 24 (2008) 2005–2008.
- [3.46] C.Y. Zhao, T.J. Lu, Analysis of microchannel heat sinks for electronics cooling, *Int J. Heat Mass Transfer* 45 (2008) 4857–4869.

- [3.47] S.J. Kim, D. Kim, D.Y. Lee, On the local thermal equilibrium in microchannel heat sinks, *Int. J. Heat Mass Transf.* 43 (2000) 1735–1748.
- [3.48] B. Agostini, M. Fabbri, J.E. Park, L. Wojtan, J.R. Thome, B. Michel, State of the Art of High Heat Flux Cooling Technologies, *Heat Transf. Eng.* 28 (2007) 258–281.
- [3.49] M.A. Ebdian, C.X. Lin, A Review of High-Heat-Flux Heat Removal Technologies, *J. Heat Transfer.* 133 (2011) 110801.
- [3.50] S.G. Kandlikar, A. V. Bapat, Evaluation of Jet Impingement, Spray and Microchannel Chip Cooling Options for High Heat Flux Removal, *Heat Transf. Eng.* 28 (2007) 911–923.
- [3.51] N. Nagarani, K. Mayilsamy, a. Murugesan, G.S. Kumar, Review of utilization of extended surfaces in heat transfer problems, *Renew. Sustain. Energy Rev.* 29 (2014) 604–613.
- [3.52] S.S. Mehendale, A.M. Jacob, Fluid flow and heat transfer at micro- and meso-scales with application to heat exchanger design, *Appl. Mech. Rev.* 53 (2013) 175-193
- [3.53] R. Dey, T. Das, S. Chakraborty, Frictional and Heat Transfer Characteristics of Single-Phase Microchannel Liquid Flows, *Heat Transf. Eng.* 33 (2012) 425–446.
- [3.54] R.N. Wagner, S.G. Kandlikar, Effects of Structured Roughness on Fluid Flow at the Microscale Level, *Heat Transf. Eng.* 33 (2012) 483–493.
- [3.55] S. Shen, J.L. Xu, J.J. Zhou, Y. Chen, Flow and heat transfer in microchannels with rough wall surface, *Energy Convers. Manag.* 47 (2006) 1311–1325.
- [3.56] M.G. Khan, A.F. Fartaj, A review on microchannel heat exchangers and potential applications, *Int J. Energy Res.* 35 (2011) 553–582.
- [3.57] K.D. Cole, B. Çetin, The effect of axial conduction on heat transfer in a liquid microchannel flow, *Int. J. Heat Mass Transf.* 54 (2011) 2542–2549.
- [3.58] P. Rosa, T.G. Karayiannis, M.W. Collins, Single-phase heat transfer in microchannels: The importance of scaling effects, *Appl. Therm. Eng.* 29 (2009) 3447–3468.
- [3.59] K.C. Cheng, S.W Hong, G.J. Hwang, Buoyancy effects on laminar heat transfer in the thermal entrance region of horizontal rectangular channels with uniform heat flux for large Prandtl number fluid, *Int. J. Heat Mass Transfer* 15 (1972) 1819-1836.
- [3.60] C. Nonino, S. Del Giudice, Laminar mixed convection in the entrance region of horizontal rectangular ducts, *Int. J. Num. Meth. Fluids* 13 (1991) 33-48.

- [3.61] F.C. Chou, Effect of non-uniform heating on laminar mixed convection in the entrance region of horizontal ducts, *Comp. Fluids* 17 (1989) 487-496.
- [3.62] F.C. Chou, Laminar mixed convection in the thermal entrance region of horizontal rectangular channels with uniform heat input axially and uniform wall temperature circumferentially, *Can. J. Chem. Eng.* 68 (1990) 577-584.
- [3.63] M. Morega, A. Bejan, Plate fins with variable thickness and height for air-cooled electronic modules, *Int. J. Heat Mass Transfer* 37 (1994) 433-445.
- [3.64] T.C. Hung, W.-M. Yan, Effects of tapered-channel design on thermal performance of microchannel heat sink, *Int. Commun. Heat Mass Transf.* 39 (2012) 1342–1347.
- [3.65] T.C. Hung, W.-M. Yan, Optimization of a Microchannel Heat Sink with Varying Channel Heights and Widths, *Numer. Heat Transf. Part A Appl.* 62 (2012) 722–741.
- [3.66] L. Léal, M. Miscevic, P. Lavieille, M. Amokrane, F. Pigache, F. Topin, et al., An overview of heat transfer enhancement methods and new perspectives: Focus on active methods using electroactive materials, *Int. J. Heat Mass Transf.* 61 (2013) 505–524.
- [3.67] T. Ota, A survey of heat transfer in separated and reattached flows, *Appl. Mech. Rev.* 35 (2000) 219-235.
- [3.68] A.M. Jacobi, R.K. Shah, Heat transfer surface enhancement through the use of longitudinal vortices: A review of recent progress, *Exp. Therm. Fluid Sci.* 11 (1995) 295-309.
- [3.69] R.M. Manglik, Heat transfer enhancement, in: A. Bejan, A.D. Kraus (Eds.), *Heat Transfer Handbook*, Wiley, New Jersey, 2003, pp. 1059-1067
- [3.70] R.L. Webb, N.H. Kim, *Principles of Enhanced Heat Transfer*, second ed., Taylor & Francis, New York, pp. 89-129.
- [3.71] A.E. Bergles, Heat transfer enhancement-The encouragement and accommodation of high heat fluxes, *J. Heat Transfer* 119 (1997) 8-19.
- [3.72] H. Stür, A. Gyr, W. Kinzelbach, Laminar separation on forward facing step, *Eur. J. Mech. B/Fluids* 18 (1999) 675-692.
- [3.73] N. Djilali, Forced laminar convection in an array of stacked plates, *Num. Heat Transfer, Part A*, 25 (1994) 393-408.
- [3.74] M. Rahnema, M.A. Yaghoubi, H. Kazeminejad, A numerical study of convective heat transfer from an array of parallel blunt plates, *Int. J. Heat Fluid Flow* 18 (1997) 430-436.

- [3.75] M. Yaghoubi, E. Velayati, Conjugate heat transfer from surface-mounted finite blunt plates, *Proc. I. Mech. Eng. Part C: J. Mech. Eng. Sci.* 220 (2006) 83-94.
- [3.76] S.C.R. Dennis, F.T. Smith, Steady flow through a channel with a symmetrical constriction in the form of a step, *Proc. R. Soc. Lond.* 372 (1980) 393-414.
- [3.77] D.M. Hawken, P. Townsend, M.F. Webster, Numerical simulation of viscous flows in channels with a step, *Comp. Fluids* 20 (1991) 59-75.
- [3.78] P. Marty, F. Michel, P. Tochon, Experimental and numerical study of the heat transfer along a blunt flat plate, *Int. J. Heat Mass Transfer* 51 (2008) 13-23.
- [3.79] J.F. Largeau, V. Moriniere, Wall pressure fluctuations and topology in separated flows over a forward facing step, *Exp. Fluids* 42 (2007) 21-40.
- [3.80] D. Wilhelm, C. Härtel, L. Kleiser, Computational analysis of the two-dimensional-three-dimensional transition in forward-facing step flow, *J. Fluid Mech.* 489 (2003) 1-27.
- [3.81] J.G. Barbosa-Saldaña, N.K. Anand, Flow over a three-dimensional horizontal forward-facing step, *Num. Heat Transfer Part A* 53 (2008) 1-17.
- [3.82] L.W. Zhang, S. Balachandar, D.K. Tafti, Effects of intrinsic three dimensionality on heat transfer and friction loss in a periodic array of parallel plates, *Num. Heat Transfer: Part A* 31 (1997) 327-353.
- [3.83] H. Yanaoka, H. Yoshikawa, T. Ota, Numerical simulation of laminar flow and heat transfer over a blunt flat plate in square channel, *Trans. ASME J. Heat Transfer* 124 (2002) 8-16.
- [3.84] H. Nakamura, T. Igarashi, T. Tsutsui, Local heat transfer around a wall-mounted cube in the turbulent boundary layer, *Int. J. Heat Mass Transfer* 44 (2001) 3385-3395.
- [3.85] E.R. Meinders, K. Hanjalić, Vortex structure and heat transfer in turbulent flow over a wall-mounted matrix of cubes, *Int. J. Heat Mass Transfer* 20 (1999) 255-267.
- [3.86] H.I. Abu-Mulaweh, A review of research on laminar mixed convection flow over backward- and forward facing steps, *Int. J. Therm. Sci.* 42 (2003) 897-909.
- [3.87] J.R. Maughan, F.P. Incropera, Mixed convection heat transfer with longitudinal fins in a horizontal parallel plate channel: Part II-Experimental results, *J. Heat Transfer* 112 (1990) 619-624.
- [3.88] D. Chong, J. Liu, J. Yan, Z. Zhou, Experimental investigation of mixed convection in a rectangular duct with a heated plate in the middle of cross section., *Heat Mass Transfer* 43 (2007) 1283-1291.

- [3.89] M. Dogan, M. Sivrioglu, Experimental and numerical investigation of clearance gap effects on laminar mixed convection heat transfer from fin array in a horizontal channel- A conjugate analysis, *Appl. Therm. Eng.* 40 (2012) 102-113.
- [3.90] J. Barrau, D. Chemisana, J. Rosell, L. Tadriss, M. Ibañez, An experimental study of a new hybrid jet impingement/micro-channel cooling scheme, *Appl. Therm. Eng.* 30 (2010) 2058-2066.
- [3.91] T.P. Chiang, A. Sau, R.R. Hwang, Asymmetry and bifurcations in three-dimensional sudden-contraction channel flows, *Phys. Rev. E* 83 (2011) art. no. 046313.
- [3.92] A. Benderradji, A. Haddad, R. Taher, M. Médale, C. Abid, F. Papini, Characterization of fluid flow patterns and heat transfer in horizontal channel mixed convection, *Heat Mass Transfer* 44 (2008) 1465-1476.
- [3.93] C.J. Baker, The laminar horseshoe vortex, *J. Fluid Mech.* 95 (1979) 347-367.
- [3.94] R.L. Simpson, Junction flows, *Annu. Rev. Fluid Mech.* 33 (2001) 415-443.
- [3.95] T. Ota, Y. Asano, J. Okawa, Reattachment length and transition of the separated flow over blunt flat plates, *Bull. JSME* 24 (1981) 941-947.
- [3.96] D. Chemisana, Building integrated concentrating photovoltaics: A review, *Ren. Sust. Energy Rev.* 15 (2011) 603-611.
- [3.97] J.C. Lane, R.I. Loehrke, Leading edge separation from a blunt plate at low Reynolds number, *J. Fluids Eng.* 102 (1980) 494-496.
- [3.98] R.J. Goldstein, Film cooling, in: T.F. Irvine, J.P. Hartnett (Eds.), *Advances in Heat Transfer*, Vol. 7, Elsevier, 1971, pp. 321-330.
- [3.99] S.M. Kim, K.D. Lee, K.Y. Kim, A comparative analysis of various shaped film-cooling holes, *Heat Mass Transfer* 48 (2012) 1929-1939.
- [3.100] K. Lee, S. Kim, K. Kim, Multi-Objective Optimization of a Row of Film Cooling Holes Using an Evolutionary Algorithm and Surrogate Modeling, *Num. Heat Transfer: Part A* 63 (2013) 623-641.
- [3.101] J.Y. Liang, S. Kang, Experimental and numerical investigation of cooling effectiveness and heat transfer coefficient for straight and curved holes, *Int. J. Heat Mass Transf.* 56 (2013) 158-171.
- [3.102] B.A. Jubran, A.S. Al-Salaymeh, Thermal wakes measurement in electronic modules in the presence of heat transfer enhancement devices, *Appl. Therm. Eng.* 19 (1999) 1081-1096.

- [3.103] G.S. Larraona, A. Rivas, R. Antón, J.C. Ramos, I. Pastor, B. Moshfegh, Computational parametric study of an impinging jet in a cross-flow configuration for electronics cooling applications, *Appl. Therm. Eng.* 52 (2013) 428–438.
- [3.104] B.A. Jubran, M.S. Al-Haroun, Heat transfer enhancement in electronic modules using various secondary air injection hole arrangements, *J. Heat Transf.* 120 (1998) 342-347.
- [3.105] U. Allauddin, N. Uddin, B. Weigand, Heat Transfer Enhancement by Jet Impingement on a Flat Surface with Detached-Ribs under Cross-flow Conditions, *Numer. Heat Transf. Part A Appl.* 63 (2013) 921–940.
- [3.106] K. Wong, Numerical investigation of a crossflow jet in a rectangular microchannel, *Appl. Mech. Matl.* 287 (2013) 849–853.
- [3.107] P. Chassaing, J. George, A. Claria, F. Sananes, Physical characteristics of subsonic jets in a cross-stream, *J. Fluid Mech.* 62 (2006) 41-64.
- [3.108] S.A. Sherif, R.H. Fletcher, Measurements of the flow and turbulence characteristics of round jets in crossflow, *J. Fluids Eng.* 111 (1989) 165-171.
- [3.109] P. Huq, M.R. Dhanak, The bifurcation of circular jets in crossflow, *Phys. Fluids* 8 (1996) 754-763.
- [3.110] R.M. Kelso, T.T. Lim, A.E. Perry, An experimental study of round jets in cross-flow, *J. Fluid Mech.* 306 (1996) 111-144.
- [3.111] A. Rivero, J.A. Ferré, F. Giralt, Organized motions in a jet in crossflow, *J. Fluid Mech.* 444 (2001) 117–149.
- [3.112] A. Sau, T.W.H. Sheu, R.R. Hwang, W.C. Yang, Three-dimensional simulation of square jets in cross-flow, *Phys. Rev. E* 69 (2004) 066302-1-20.
- [3.113] S. Bagheri, P. Schlatter, P.J. Schmid, D.S. Henningson, Global stability of a jet in crossflow, *J. Fluid Mech.* 624 (2009) 33–44.
- [3.114] R.L.J. Fernandes, A. Sobiesiak, A. Pollard, Opposed round jets issuing into a small aspect ratio channel cross flow, *Exp. Therm. Fluid Sci.* 13 (1996) 374–394.
- [3.115] A.K. Saha, C.B. Yaragani, Three-dimensional numerical study of jet-in-crossflow characteristics at low Reynolds number, *Heat Mass Transf.* (2012) 391–411.
- [3.116] X.D. Wang, Z. Li, J.Y. Liang, S. Kang, Numerical simulations of imperfect bifurcation of jet in crossflow, 6 (2012) 595–607.

- [3.117] E. Gungor, P.J.W. Roberts, Experimental studies on vertical dense jets in a flowing current, *J. Hydraulic Eng.* (2009) 935–948.
- [3.118] A. Kishore, U. Ghia, K.N. Ghia, Numerical simulation of dual-Jet system in cross flow, *Proceedings of the 5<sup>th</sup> Joint ASME/JSME Fluids Engineering Conference*, San Diego , CA, 2007.
- [3.119] S. Vashisth, V. Kumar, K.D.P. Nigam, A Review on the potential applications of curved geometries in process industry, *Ind. Eng. Chem. Res.* 47 (2008) 3291-3337.
- [3.120] P. Naphon, S. Wongwises, A review of flow and heat transfer characteristics in curved tubes, *Ren. Sust. En. Rev.* 10 (2006) 463-490.
- [3.121] H. Kobayashi, S. Lorente, R. Anderson, A. Bejan, Serpentine thermal coupling between a stream and a conducting body, *J. Appl. Phys.* 111 (2012) 044911.
- [3.122] S.A. Berger, L. Talbot, L.S. Yao, Flow in curved pipes, *Ann. Rev. Fluid Mech.* 15 (1983) 461-512.
- [3.123] S.V. Patankar, V.S. Prapat, D.B. Spalding, Prediction of turbulent flow in curved pipes, *J. Fluid. Mech.* 67 (1975) 583-595.
- [3.124] J.A. Fairbank, R.M.C. So, Upstream and downstream influence of pipe curvature on the flow through a bend, *Int. J. Heat Fluid Flow* 8 (1987) 211-217.
- [3.125] H. Sugiyama, D. Hitomi, Numerical analysis of developing turbulent flow in a 180° bend tube by an algebraic Reynolds stress model, *Int. J. Numer. Meth. Fluids* 47 (2005) 1431-1449.
- [3.126] S.C.R. Dennis., M. Ng, Dual solutions for steady laminar flow through a curved tube, *Quart. J. Mech. Appl. Math.* 35 (1982) 305-324.
- [3.127] S. Yanase, N. Goto and K. Yamamoto, Dual solutions of the flow through a curved tube, *Fluid Dyn. Res.* 5 (1989) 191-201.
- [3.128] I. Di Piazza, M. Ciofalo, Transition to turbulence in toroidal pipes, *J. Fluid Mech.* 687 (2011) 72-117.
- [3.129] K.C. Cheng, F.P. Yuen, Flow visualization studies on secondary flow patterns in straight tubes downstream of a 180 deg bend and in isothermally heated horizontal tubes, *J. Heat Transfer* 109 (1987) 49-54.
- [3.130] D.E. Olson, B. Snyder, Upstream scale of flow development in curved circular pipes, *J. Fluid. Mech.* 150 (1985) 139-158.
- [3.131] M. Rowe, Measurements and computations of flow in pipe bends, *J. Fluid. Mech.* 43 (1970) 771-783.

- [3.132] J.H. Siggers, S.L. Waters, Steady flows in pipes with finite curvature, *Phys. Fluids*, 17 (2005) 077102 1-18.
- [3.133] Z.H. Yang, R.S. Ye, Symmetry-breaking and bifurcation study on the laminar flows through curved pipes with a circular cross section, *J. Comp. Phys.* 127 (1996) 73-87.
- [3.134] Y. Mori, W. Nakayama, Study on forced convective heat transfer in curved pipes (1st report, laminar region), *Int. J. Heat Mass Transfer* 8 (1965) 67-82.
- [3.135] Y. Mori, W. Nakayama, Study on forced convective heat transfer in curved pipes (2nd report, turbulent region), *Int. J. Heat Mass Transfer* 10 (1967) 37-59.
- [3.136] S. Jayanti, G.F. Hewitt, J.R. Knightley, Fluid flow in curved ducts, *Int. J. Num. Meth. Fluids* 10 (1990) 253-266.
- [3.137] C.E. Kalb, J.D. Seader, Heat and mass transfer phenomena for viscous flow in curved circular tubes, *Int. J. Heat Mass Transfer* 15 (1972) 801-817.
- [3.138] J.M. Tarbell, M.R. Samuels, Momentum and heat transfer in helical coils, *Chem. Eng. J.* 5 (1973) 117-127.
- [3.139] C.R. Andrade, E.L. Zaporoli, Effects of temperature-dependent viscosity on fully developed laminar forced convection in a curved duct, *Int. Comm. Heat Mass Transfer* 28 (2001) 211-220.
- [3.140] M. Di Liberto, M. Ciofalo, A study of turbulent heat transfer in curved pipes by numerical simulation, *Int. J. Heat Mass Transfer* 59 (2013) 112-125.
- [3.141] M.M. Ohadi, E.M. Sparrow, Effect of a 180° bend on heat transfer in a downstream positioned straight tube, *Int. J. Heat Mass Transfer* 33(1990) 1359-1362.
- [3.142] A. Noorani, G.K. El Khoury, P. Schlatter, International Journal of Heat and Fluid Flow Evolution of turbulence characteristics from straight to curved pipes, *Int. J. Heat Fluid Flow*, In press
- [3.143] J. Prusa, L.S. Yao, Numerical solution for fully developed flow in heated curved tubes, *J. Fluid. Mech.* 123 (1982) 503-522.
- [3.144] L.J. Li, C.X. Lin, M.A. Ebdian, Turbulent mixed convective heat transfer in the entrance region of a curved pipe with uniform wall temperature, *Int. J. Heat Mass Transfer* 41 (1998) 3793-3805.
- [3.145] R. Yang, S.F. Chang, Combined free and forced convection for developed flow in curved pipes with finite curvature ratio, *Int. J. Heat Fluid Flow* 15 (1994) 470-476.

- [3.146] F. Bahiraei, R.K. Saray, A. Salezadeh, Investigation of potential of improvement of helical coils based on avoidable and unavoidable exergy destruction concepts, *Energy* 36 (2011) 3113-3119.
- [3.147] Aavid Thermalloy, LLC, "High Contact Liquid Cold Plates" Datasheet, NH, USA.
- [3.148] S. Yanase, K. Yamamoto, T. Yoshida, Effect of curvature on dual solutions of flow through a curved circular tube, *Fluid Dyn. Res.* 13 (1994) 217-228.
- [3.149] R.M.C. So, H.S. Zhang, Y.G. Lai, Secondary cells and separation in developing laminar curved-pipe flows, *Theoret. Comput. Fluid Dyn.* 3 (1991) 141-162.
- [3.150] Y. Agrawal, L. Talbot, K. Gong, Laser anemometer study of flow development in curved circular pipes, *J. Fluid. Mech.* 85 (1978) 497-518.
- [3.151] U.S. Choi, L. Talbot, I. Cornet, Experimental study of wall shear rates in the entry region of a curved tube, *J. Fluid. Mech.* 93 (1979) 465-489.
- [3.152] A. Bar-Cohen, A.A. Watwe, R.S. Rasher, Heat Transfer in Electronic Equipment, in: A. Bejan, A.D. Kraus (Eds.), *Heat Transfer Handbook*, Wiley, New Jersey, pp. 956-964, 2003.
- [3.153] M.I. Hasan, A.A. Rageb, M. Yaghoubi, H. Homayoni, Influence of channel geometry on the performance of a counter flow microchannel heat exchanger, *Int. J. Therm. Sci.*, 48 (2009) 1607-1618.
- [3.154] D.W. Kim, Convection and flow boiling in microgaps and porous foam coolers, PhD Thesis, University of Maryland, College Park, MD, 2007.
- [3.155] A. Bejan, *Entropy Generation Minimization*, first ed., CRC Press, New York, 1996.

### 4.1 Introduction

In this chapter, and after the most suitable type of cooling device for the CPVT system has been selected, the design and optimization methodology is outlined, along with the evaluation procedure. A critical stage in the design procedure of a cooling device is the determination of the optimal geometric parameters that maximize overall performance. For the case of plate-fin heat sinks in particular, which is the configuration of interest in this chapter, the main geometrical parameters correspond to the channel width, aspect ratio and channel wall thickness (see **Fig. 3.1**). A number of researchers [4.1-4.6] have utilized analytical thermal-resistance models and pressure-drop correlations in order to highlight the effect of the geometrical layout on the heat sink thermal and hydrodynamic performance. Investigations have historically focused first on conventional heat sinks ( $D_h \gg 1.0$  mm) but, over the past couple of decades, an ever increasing number of studies is being devoted to microchannels ( $D_h \leq 1.0$  mm). Liu and Garimella [4.5] compared five analytical models for the prediction of the thermal performance of a microchannel heat sink (MCHS). It was concluded that the one-dimensional thermal resistance model offers comparable precision with the other more complex models and it was suggested as adequate for optimization procedures. Türkalar and Okutucu [4.6] used a one-dimensional model to optimize the geometry of a heat sink considering heating from discrete heat sources, corresponding to the cores of a CPU unit. The configurations were optimized in terms of thermal resistance with pumping power as a constrain and it was concluded that the optimal geometry comprised high aspect-ratio microchannels and slender fins. A general analytical procedure based on the *constructal technique* proposed by Bejan [4.7], has also been proposed for the optimization of heat sinks comprising of duct-arrays [4.8, 4.9]. The objective of the procedure is to determine the heat sink hydraulic diameter that maximizes heat transfer for a constrained overall heat-sink volume and specified pressure drop penalty. According to the procedure, two distinct limits of the flow geometry are considered where the flow can be characterized as either Poiseuille or boundary-layer flow in each limiting case, respectively. A relation between the duct characteristic length scale (i.e. the hydraulic diameter) and the heat transfer rate is formulated for the two limiting cases and the optimal duct-cross section is determined by means of a graphical method

*Multi-objective optimization techniques* in combination with *genetic algorithms* have also been proven to be suitable solution methods for problems where multiple criteria must be satisfied, as they result to concurrent optimization of all the objectives and offer alternative options regarding the optimal solution [4.10, 4.11]. Furthermore, genetic algorithms constitute a robust optimization method as the initial guess has a low influence on the final result. In regard to the optimization of cooling devices, thermal resistance and required pumping power are two widely used objectives that are sought to be minimized [4.11], while characteristic geometrical parameters are usually selected as design (free) variables. Bureerat and Srisomporn [4.12] coupled a three-dimensional numerical model to an evolutionary algorithm for the optimization of air cooled plate fin-heat sinks. Heat-sink configurations with vertical as well as oblique fins were considered, while the fin height was non-

uniform in a specified design but its distribution was determined through an approximation curve derived by the results of the optimization procedure. Copiello and Fabbri [4.13] coupled a simplified numerical procedure with a multi-objective optimization technique in order to determine the optimal geometry of a wavy finned heat sink. They stated that the use of a detailed three-dimensional numerical model would lead to excessively time consuming computations. Hilbert et al. [4.14] coupled a two-dimensional numerical model to a genetic algorithm using an in-house developed software that allowed for parallel computations. The objective of the optimization procedure was to determine the optimal cross section of a bundle of tubes that were cooled by an air stream. The tube cross-section was approximated by splines with control points that derived from the optimization procedure.

Husain and Kim [4.15] used a full three-dimensional numerical model of a parallel microchannel heat sink, in order to produce an initial number of objective function values required for the multi-objective optimization. Simple surrogate models representing the numerical solutions were used to perform the multi-objective optimization in order to accelerate the procedure. In a subsequent study Husain et al. [4.16] used a procedure similar to that in [4.15] for the optimization of a jet-impingement heat sink. The optimization goal was to determine the nozzle diameter and nozzle-array arrangement that result to maximum overall performance. Li et al. [4.17] coupled an analytical model, which predicts the heat sink thermal resistance and pressure drop, to a genetic algorithm in order to optimize the layout of a cooling configuration employing a serpentine rectangular duct with steep 180° bends. Their investigation revealed that the optimal channel height obtains the maximum allowed value, regardless of the values of the other design variables. Shao et al. [4.18] presented a similar procedure for the optimization of a microchannel heat sink. Ndao et al. [4.19] performed a comparative analysis and multi-objective optimization of different cooling technologies, namely microchannel, pin fin, offset strip fin and jet-impingement heat sinks using air as coolant. The investigation was performed using genetic algorithms coupled with one-dimensional models and correlations that approximate the overall behavior of the different configurations. It was concluded that the offset strip fin configuration exhibits superior overall performance.

It must be noted that additional multi-objective methods such as Sequential Quadratic Programming (SQP) and the Broydon-Fletcher-Goldfarb-Shanno (BFGS) method have been reported in the open literature for the optimization of the geometrical layout of plate fin heat sinks [4.20,4.21].

### 4.2 Heat-sink theoretical model

The thermal and hydrodynamic behaviour of the FW and VW heat sink designs that were selected for optimization, as discussed in **chapter 3**, were predicted by means of a one-dimensional thermal resistance model and pressure drop correlations. The thermal resistance model has been reported as adequate to fully represent the thermal performance of a heat-sink configuration [4.1, 4.5] and furthermore its simplicity makes it suitable for optimization purposes [4.5]. As was illustrated in **paragraph 3.6**, the total thermal resistance of a heat sink is given in a general form by **Eq. (3.35)**. The term corresponding to the convective thermal resistance is calculated by **Eqs. (3.39)** and **(3.41)** for the FW and the VW configurations, respectively. In addition, appropriate Nusselt number values are required for the determination of the overall heat transfer coefficient and consequently of the convective thermal resistance in each case. The thermal boundary condition realized in various practical heat dissipating applications, such as electronics cooling devices, or solar receivers is that of

constant heat rate per unit duct length [4.22]. In such applications, the heating is usually cross-sectionally non symmetrical due to either the imposed heating conditions or the geometrical layout of the duct. Especially due to the high thermal conductivity of the manufacturing materials, which enables heat conduction, it is widely accepted that the boundary condition that best suits the specified heating conditions is that of axially constant heat flux with peripherally constant temperature yet variable heat flux [4.22]. Correlations for the calculation of the fully developed Nusselt number value for the specified boundary condition, usually abbreviated as the H1 boundary condition are available in heat transfer handbooks [4.22, 4.23]. Regarding ducts of orthogonal cross-section under laminar flow conditions, the fully developed Nusselt number is dependant only on the aspect ratio and is calculated as follows:

$$Nu_{H1} = 8.235 \left[ 1 - 2.0421 \left( \frac{W_{ch}}{H_{ch}} \right) + 3.0853 \left( \frac{W_{ch}}{H_{ch}} \right)^2 - 2.4765 \left( \frac{W_{ch}}{H_{ch}} \right)^3 + 1.0578 \left( \frac{W_{ch}}{H_{ch}} \right)^4 - 0.1861 \left( \frac{W_{ch}}{H_{ch}} \right)^5 \right] \quad (4.1)$$

It must be noted that heat transfer is strongly dependant on the thermal boundary condition in laminar flows. However, it is by no means guaranteed that fully developed conditions occur in the entire heat sink length, especially in the VW configuration due to the relatively large hydraulic diameter of the first section. The thermal development length must be therefore calculated and an appropriate value of the Nusselt number must be assigned in the part of the channel where the flow is thermally developing. It is important to note that this procedure must be followed for each section of the VW heat sink characterized by a different hydraulic diameter. The assumption that the flow enters each section with a uniform profile is made. The thermal entrance length is calculated by the relation:

$$L_{th} = L_{th}^* Re Pr D_h \quad (4.2)$$

where values of the non-dimensional thermal entrance length  $L_{th}^*$  can be found for rectangular ducts in [4.23]. A polynomial fitting of the tabulated values produces the following relation:

$$L_{th}^* = 0.0004 \left( \frac{W_{ch}}{H_{ch}} \right)^2 - 0.0101 \left( \frac{W_{ch}}{H_{ch}} \right) + 0.0756 \quad (4.3)$$

Regarding thermally developing flow in a duct of specified cross-section, the Nusselt number value is dependent on the axial distance from the duct inlet. Tabulated values for various channel aspect ratios can be found in [4.22]. An average value is calculated for the entire developing flow region for each aspect ratio and these values are fitted using a second-order polynomial to produce a representative value of the Nusselt number:

$$Nu_{H1} = -9.3716 \left( \frac{W_{ch}}{H_{ch}} \right)^3 + 20.891 \left( \frac{W_{ch}}{H_{ch}} \right)^2 - 15.737 \left( \frac{W_{ch}}{H_{ch}} \right) + 9.5012 \quad (4.4)$$

The total induced pressure loss by the heat sink can be described by a relation of the general form:

$$\Delta p_{tot} = \Delta p_c + \Delta p_d + \Delta p_{fd} + \Delta p_e \quad (4.5)$$

The four terms on the right-hand side of **Eq. (4.5)** refer to the pressure drop due to contraction, fluid friction in the developing-flow and the fully-developed regions, respectively, and pressure recovery due to flow expansion at the channel exit. The pressure drop due to contraction can be calculated from an analytical correlation given by Blevins [4.24] and accounts for the additional pressure losses due to flow impingement on the fins (walls) leading surfaces and consequent separation downstream of the fin edge.

$$\Delta p_c = \left[ 1 - \left( \frac{A_2}{A_1} \right)^2 + K \right] \frac{1}{2} \rho \bar{w}_2^2 \quad (4.6)$$

where the subscripts 1,2 refer to the flow regions before and after the contraction location, respectively. Likewise, pressure recovery due to expansion is given by a similar expression:

$$\Delta p_c = \left[ \left( \frac{A_1}{A_2} \right)^2 - 1 + K \right] \frac{1}{2} \rho \bar{w}_1^2 \quad (4.7)$$

where the subscripts 1,2 refer to the flow regions before and after the expansion location. Values for the dimensionless loss coefficient  $K$  for rectangular ducts under for laminar flow conditions are available in [4.24]. The pressure drop in the developing and the fully-developed regions is expressed by a relation of the general form:

$$\Delta p = \frac{2\rho f L \bar{w}^2}{D_h} \quad (4.8)$$

where  $f$  is the apparent friction factor or the Fanning friction factor and  $L$  is the hydrodynamic entrance or the fully developed length in each case. A correlation that relates the apparent friction factor for developing flow to the Fanning friction factor and the hydrodynamic entry length has been proposed by Shah [4.25]. The Fanning friction factor is dependent only on the channel aspect ratio [4.22]:

$$f_F Re = 24 \left[ 1 - 1.3553 \left( \frac{W_{ch}}{H_{ch}} \right) + 1.9467 \left( \frac{W_{ch}}{H_{ch}} \right)^2 - 1.7012 \left( \frac{W_{ch}}{H_{ch}} \right)^3 + 0.9564 \left( \frac{W_{ch}}{H_{ch}} \right)^4 - 0.2537 \left( \frac{W_{ch}}{H_{ch}} \right)^5 \right] \quad (4.9)$$

The hydrodynamic entrance length is:

$$L_{hy} = L_{hy}^+ \text{Re} D_h \quad (4.10)$$

where tabulated values of the non-dimensional hydrodynamic entrance length  $L_{hy}^+$  for rectangular ducts are available in [4.23]. A polynomial fitting of the values produces the following relation:

$$L^+ = -0.04 \left( \frac{W_{ch}}{H_{ch}} \right)^2 + 0.07 \left( \frac{W_{ch}}{H_{ch}} \right) + 0.06 \quad (4.11)$$

In the case of small hydraulic diameters, where the hydrodynamic entry length is also small, the overall pressure drop through the heat sink is predominantly influenced by the term  $\Delta p_{fd}$  of Eq. 4.5 that corresponds to fluid friction under fully developed flow conditions. In correspondence to heat transfer, the procedure for the calculation of pressure drop must be followed for each section of the VW heat sink by also taking into account the effect of contraction at each section step-change.

### 4.3 Model validation

The results of the developed thermal-resistance model for heat transfer were compared against the experimental values published by Tuckerman and Pease [4.26], who investigated the performance of a silicon ( $k_{si}=148 \text{ W/mK}$ ) microchannel heat sink of total area equal to  $1.0 \text{ cm}^2$ , cooled by water with an initial temperature of 296 K. According to Table 4.1, the experimental values regarding the overall heat-sink thermal resistance agree well with the analytically predicted ones. The maximum discrepancy detected is less than 9% (for the second point of Table 4.1), which is acceptable for such small length scales, as the effect of the uncertainty in the channel dimensions due to manufacturing precision is probable to cause such a discrepancy in the thermal resistance values. For example, a microchannel wider by only  $4.0 \mu\text{m}$ , would cause an increase of approximately 9% in the values of the thermal resistance for the parameters specified in the second row of Table 4.1. In conclusion, the analytical model is considered reliable to be used in the optimization procedure.

**Table 4.1** Validation of the thermal-resistance model against the experimental results of Tuckerman and Pease [4.27].

$W_{ch}$ ( $\mu\text{m}$ )	$W_w$ ( $\mu\text{m}$ )	$H_{ch}$ ( $\mu\text{m}$ )	$q''$ ( $\text{W}/\text{cm}^2$ )	$\dot{V}_{tot}$ ( $\text{mL}/\text{s}$ )	$R_{th}$ (K/W)	
					Experimental	1-D model
56	44	320	181	4.7	0.110	0.112
55	45	287	277	6.5	0.113	0.104
50	50	302	790	8.6	0.090	0.085

### 4.4 Optimization procedure

#### 4.4.1 Determination of the objective functions and the design variables

The thermal and hydraulic behaviour of the heat sink can be fully described by the sum of the convective and caloric thermal resistances, Eqs. (3.37)-(3.38), as well as the required pumping

power  $P_{pump} = \dot{V}_{tot} \Delta p$ . These two quantities are selected as the objective functions for the optimization process. The two objective functions are correlated by no means, as this would require the undesired use of scaling or weighting factors [4.10], and thus the optimization problem is treated as multi-objective. The total width and length of the device are fixed and therefore the design parameters, which determine its performance, and can be generally included in the optimization process are the channel width  $W_{ch}$  and aspect ratio  $AR$ , along with the fin thickness  $W_w$ . It is evident from the analytical correlations for the thermal resistance and pressure drop, Eqs. (3.38) and (4.8), that, for a constant channel width, an increase in the channel aspect ratio has a beneficial impact on both the objective functions, due to the increase of the available heat transfer area and the decrease of the flow velocity. Therefore, the height is fixed at the “maximum” structurally feasible value. Consequently, two independent design variables are selected for optimization, namely the microchannel width  $W_{ch}$  and the fin thickness  $W_w$ .

For the VW heat sink in particular, the fin thickness  $W_w$  must also be constrained by the minimum structurally feasible value. This constraint is posed by structural limitations that dictate that the thickness of the fins through all the sections of the heat sink be maintained constant. In addition, regarding the first heat-sink section, the fin thickness cannot be a very small fraction of the channel initial width, as this would lead to rupture of the fins during the machining process. The  $a (=W_w/W_{ch})$  ratio, consequently will inevitably increase along consecutive sections (as the channel width decreases) and within the third section in particular, it obtains values significantly larger than unity, which is undesirable from a thermal performance point of view.

Nevertheless, if the fin thickness leading to optimal performance, e.g., of the third-section microchannels, were to be included in the optimization procedure as one of the free variables, it would have led to non-feasible designs, as the fins in the first section would have come out too slender, rendering their manufacture impossible. Thus, the only design variable that can be varied in this case (VW configuration) is the width of the channel of the initial section  $W_{ch,init}$ , while the channel widths in the following sections are consequently determined in an unambiguous manner.

### 4.4.2 Surrogate functions

A pair of design variables ( $W_{ch}$ ,  $W_w$ ) produces an output value of both the objective functions. The purpose of surrogate modelling is to formulate continuous functions that correlate the design variables with the output (response) of the objective functions. By this way, the optimization procedure is decoupled by the model that describes the actual device and consequently it becomes quicker and more versatile, as it only needs to manage explicitly defined functions. A number of surrogate models suitable for optimization purposes have been proposed in the open literature including response surface approximation (polynomial regression), kriging and radial basis functions [4.11, 4.27].

The response surface approximation was selected as appropriate to model the objective functions in the present case, as it was verified that excellent fitting of the objective responses could be achieved. A number of polynomial and power functions were evaluated for the fitting of the data produced by the analytical model. The adjusted coefficient of multiple determination  $R_{adj}^2$ , which quantifies the quality of the fitting, was used as the evaluation criterion with a value equal to unity indicating an excellent fitting. A third order polynomial was finally chosen to approximate the thermal resistance response of the FW configuration:

$$\begin{aligned}
 R_{th}(W_{ch}, W_w) = & P_{00} + P_{10}W_{ch} + P_{01}W_w + P_{20}W_{ch}^2 \\
 & + P_{11}W_{ch}W_w + P_{02}W_w^2 + P_{30}W_{ch}^3 \\
 & + P_{21}W_{ch}^2W_w + P_{12}W_{ch}W_w^2 + P_{03}W_w^3
 \end{aligned} \tag{4.12}$$

Likewise, a power function was selected to approximate the pumping power response, considering the decaying trend that it exhibits:

$$P_{pump}(W_{ch}, W_w) = b_1 \cdot W_{ch}^{b_2} \cdot W_w^{b_3} \tag{4.13}$$

Referring to the VW design, single-variable surrogate functions were used, as the ratio of the fin thickness to the initial channel width is kept constant to 0.2. Hence, the surrogate functions reduced to the forms:

$$R_{th}(W_{ch,init}) = r_0 + r_1W_{ch,init} \tag{4.14}$$

$$P_{pump}(W_{ch,init}) = c_1W_{ch,init}^{c_2} \tag{4.15}$$

#### 4.4.3 Multi-objective optimization using the genetic algorithm

The heat sink optimization constitutes a multi-objective optimization problem, which can be mathematically formulated as follows:

$$\begin{aligned}
 \min \vec{f}(\vec{x}) = & [f_1(\vec{x}), f_2(\vec{x}), \dots, f_i(\vec{x})] \\
 \text{subject to } & \vec{g}(\vec{x}) \leq 0 \text{ and } \vec{h}(\vec{x}) = 0
 \end{aligned} \tag{4.16}$$

where  $\vec{x}$  is the vector that contains the design variables and  $\vec{f}(\vec{x}), \vec{g}(\vec{x}), \vec{h}(\vec{x})$  are the vector functions that contain the objective, inequality and equality constraints functions, respectively. The multi-objective optimization process converges to a set of non-dominated solutions, referred to as the *Pareto front* [4.28].

In order to locate the Pareto front, a variation of the Non-dominated Sorting Genetic Algorithm (NSGA-II) is used [4.28]. A fixed population [4.29] of design-variable vectors  $\vec{x}_i$  or *individuals* is repeatedly modified over a number of successive iterations or *generations*. The general iterative procedure performed by the algorithm is as follows:

**Step 1:** Creation of an initial population.

**Step 2:** Division of the general population into sub-populations.

**Step 3:** Evaluation of the population in terms of the objective functions.

**Step 4:** Sorting of the individuals and assignment of fitness ranks.

**Step 5:** Creation/Modification of the set of elite individuals (Pareto fraction).

**Step 6:** Selection of the individuals suitable for reproduction (creation of mating pool).

**Step 7:** Application of the reproduction operators in the members of the mating pool.

**Step 8:** Creation of the offspring generation-increase of the generation number by one.

**Step 9:** Verification whether one of the algorithm termination criteria has been met or not.

It is obvious that after the creation of the new generation (step 8), the individuals created are treated as the potential (initial) parent population and the algorithm is repeated from step 2 onward. The initial population required for the algorithm to commence is generated randomly in the design space designated for the free variables. The population of individuals is real-coded in the present algorithm. At each step, individuals of the current population are selected to produce offsprings of the next generation. The selection procedure is based on the objective function values that each individual produces, leading to the designation of a *fitness score*  $F_i(\vec{x})$ , which is a measure of each individual's performance, regarding an objective function, relative to the whole population of individuals:

$$F_i(\vec{x}) = \frac{f_i(\vec{x})}{\sum_{j=1}^{N_{nd}} f_j(\vec{x})} \quad (4.17)$$

The individuals of each generation are sorted based on the solution *non-domination*, with the best-performing individual obtaining the first rank. An individual A ( $\vec{x}$ ) is characterized as a non-dominated solution when there is no other individual B that achieves a better fitness for a single objective  $f_i(\vec{x})$  without deteriorating the other objectives. The selection of individuals as parents for the next generation takes place by a *tournament* of a specified number of randomly picked individuals, which compete in terms of their non-domination rank. For individuals of equal rank, an additional criterion, the *distance measure* is applied to designate the prevailing individual. The distance measure indicates how far an individual from other individuals of the same rank is. Individuals that enhance the population diversity are selected for reproduction.

The prevailing individuals are placed in a mating pool, where a reproduction operator (crossover) is applied in order to produce offsprings. The crossover operator in the present algorithm produces the offspring as a weighted average of the two parents:

$$off = p_1 + rand \cdot w \cdot (p_2 - p_1) \quad (4.18)$$

where  $p_1, p_2$  are the parent individuals, *rand* is a random number between zero and one, and  $w$  is the weighting factor. The children of the next generation are created either by combination of two parent individuals (*crossover children*) or random changes introduced to a single individual (*mutation children*). The mutation operator performs a small random change to single individuals and in that way enhances the diversity of the population. The algorithm was properly modified, so that every part of the design-variable vector has the same, specified probability of being mutated, i.e. replaced by a random number within the specified bounds of the variables.

*Elitism* is introduced in the algorithm through the concept of migration of fit individuals within different sub-populations prior to the selection of potential parents. More specifically a specified fraction of the worst-performing individuals of a sub-population is substituted by the best-performing individuals of another sub-population. The substitution takes place in a serial manner, meaning that

individuals of the n-th sub-population migrate to the (n+1)-th sub-population. In addition, the set of elite individuals (*Pareto fraction*) is a specified fraction of the entire population that is maintained constant as the generations progress. As the individuals with high fitness score become more frequent in the population, while less fit individuals are excluded from reproduction, the algorithm gradually evolves to the optimal or, in the case of multi-objective optimization, *non-dominated* solutions. As the algorithm reaches the imposed termination criteria, the non-dominated individuals over all generations lead to the formation of the Pareto front [4.30].

### 4.5 Optimal designs

The design variables for the optimization of the selected FW and VW heat-sink configurations were allowed to vary within the following range:

$$\begin{aligned}
 0.25 \cdot 10^{-3} \text{ m} &\leq W_{ch} \leq 1.00 \cdot 10^{-3} \text{ m} \\
 0.25 \cdot 10^{-3} \text{ m} &\leq W_w \leq 1.00 \cdot 10^{-3} \text{ m} \\
 1.25 \cdot 10^{-3} \text{ m} &\leq W_{ch,1} \leq 7.5 \cdot 10^{-3} \text{ m}
 \end{aligned}
 \tag{4.19}$$

where  $W_{ch,1}$  refers to the channel width of the initial section of the three-section VW heat sink. The channel height was chosen to be six times the channel width in the FW heat sink and two times the initial channel width in the VW heat sink, as these are the maximum values that can be attained using conventional machining techniques. The responses of the analytical models, depicted in **Fig. 4.1** clearly show the conflicting nature of the two objective functions as an increase in the thermal resistance leads to a decrease of the pumping power required and vice versa. **Figs. 4.1a-b** illustrate the variation of the objective functions for the FW heat sink, while the three-section VW heat sink exhibits the same behavior (**Fig. 4.1c-d**), but in the two dimensional space, as the fin width is considered a constraint. Subsequently, appropriate fitting functions were constructed in order to surrogate the analytical values. The coefficients used by the surrogates for the objective functions of both heat sink configurations along with the constraints that were taken into account for their construction are summarized in **Table 4.2**. The quality of the fitting is confirmed by the  $R_{adj}^2$  value, which is above 0.99 for all the surrogate functions.

**Table 4.2** Design constraints and coefficients of the surrogate functions.  $R_{adj}^2 > 0.99$  in all fittings.

FW			VW		
$\dot{V}_{tot} = 30.0 \text{ mL/s}$			$\dot{V}_{tot} = 30.0 \text{ mL/s}$		
$H_{ch} = 6 \cdot W_{ch}$			$H_{ch} = 2 \cdot W_{ch,init}$		
			$W_{ch,i+1} = \frac{W_{ch,i}}{2} - \frac{W_w}{2}$		
			$W_w = 0.2 \cdot W_{ch,init}$		
Surrogates coefficients					
p00	0.008033	p30	$-3.681 \cdot 10^4$	r0	0.1707
p10	1.942	p21	$-5.185 \cdot 10^4$	r1	0.008
p01	0.7333	p12	$1.276 \cdot 10^6$	c1	$5.000 \cdot 10^{-9}$
p20	751.0	p03	$-8.141 \cdot 10^5$	c2	-2.963
p11	-1652	b1	$1.658 \cdot 10^{-10}$		
p02	1233	b2	-3.420		
		b3	0.6472		

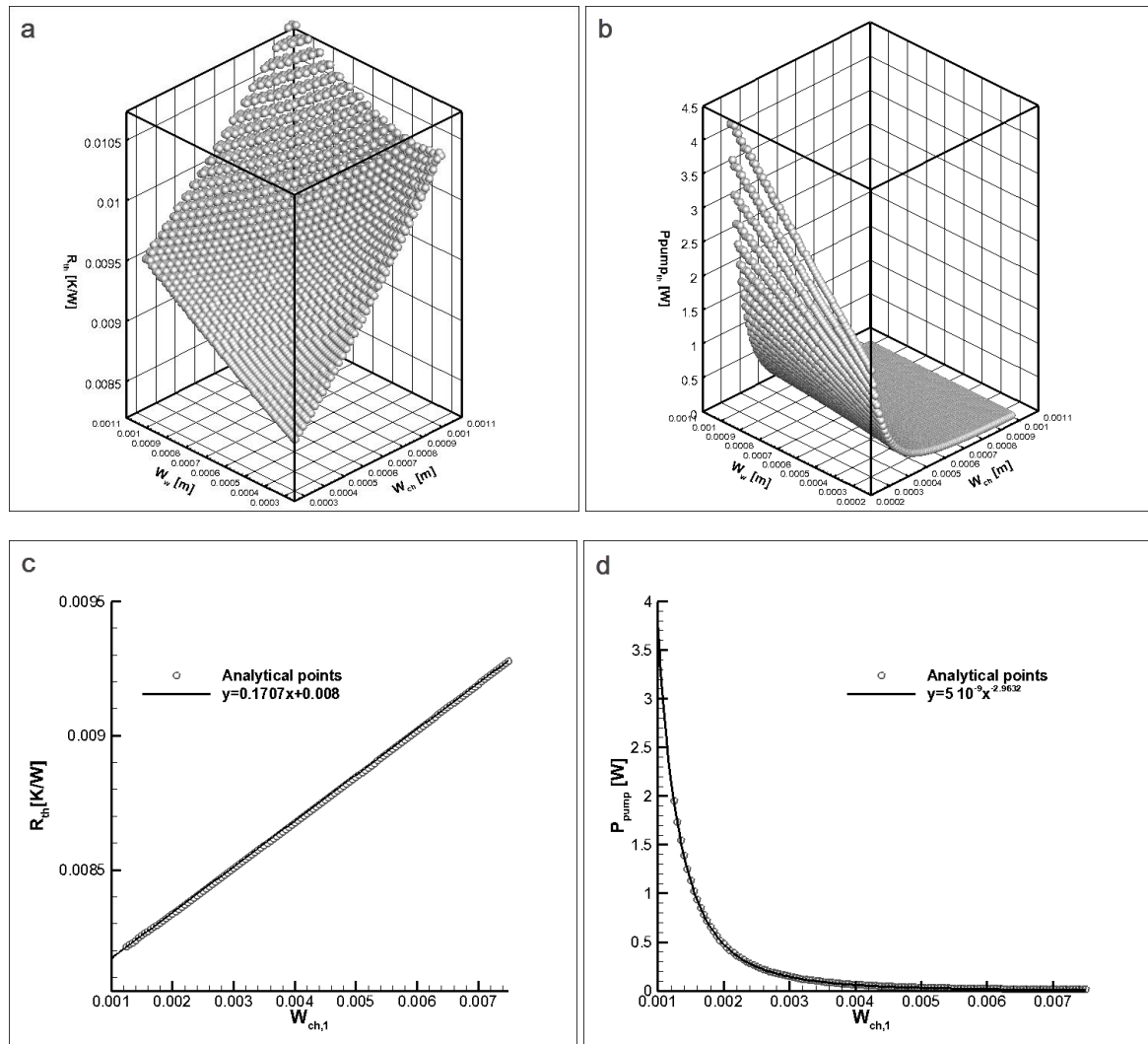


**Fig. 4.1** Response values: (a) thermal resistance-FW heat sink, (b) pressure drop-FW heat sink, (c) thermal resistance-VW heat sink and (d) pressure drop-VW heat sink.

The multi-objective optimization problem was solved using the Matlab Optimization Toolbox [4.30], along with the parameters and constraints shown in **Table 4.3**. There is no clear guideline for the selection of the population size for a specified optimization problem [4.11, 4.27]. Consequently, a relatively large population was selected, so as to cover a wide part of the design space and to ensure that optimal solutions have been reached [4.31]. The algorithm terminates either if a maximum number of generations equal to 500 is reached or if the Pareto front remains unaffected for 200 consecutive generations. The crossover fraction designates the percentage of individuals within the population that originate as cross-over children, whereas the remaining of the individuals are created by applying the mutation operator. The fraction of individuals to be replaced in a sub-population due to low fitness is designated by the migration fraction, while the migration interval sets the number of generations that intercede between consecutive migrations of individuals.

**Table 4.3** Parameters of the genetic algorithm. Multiple Pareto fronts were obtained for different values of the reproduction parameters.

Population of individuals		500
Generations		1000
Stall generations		200
Tournament size		2
Percentage of population in the Pareto front		20%
Crossover fraction		0.75-0.80-0.85-0.90
Crossover weighting factor		1.0
Migration interval		20
Migration fraction		0.15-0.20-0.25
Mutation probability		0.01-0.10
Constraints	<b>FW</b>	$0.25 \cdot 10^{-3} \leq x_1 \leq 1.00 \cdot 10^{-3}$ & $0.25 \cdot 10^{-3} \leq x_2 \leq 1 \cdot 10^{-3}$
	<b>VW</b>	$1.25 \cdot 10^{-3} \leq x_1 \leq 7.5 \cdot 10^{-3}$

The Pareto front of non-inferior solutions for the two heat sink configurations is illustrated in **Fig. 4.2**. It is interesting to notice that the Pareto front has the characteristic convex form expected for a double-minimization problem [4.32]. The vast majority of optimal solutions for the FW heat sink (**Fig. 4.2a**) are shifted towards channels with small hydraulic diameter and thin walls resulting in a configuration with low thermal resistance and high pressure drop. A similar pattern, regarding the channel width, is also followed by the optimal solutions of the VW heat sink (**Fig. 4.2b**). As is evident in **Fig. 4.2**, the VW configuration can achieve lower thermal resistance values than the respective obtained by the FW one. The utilization of microchannels only in the last part of the heat sink does not deteriorate the total thermal performance of the heat sink, due to the considerably increased microchannel aspect ratio ( $AR=20$ ) in the part of the heat sink where the cooling fluid has attained a high temperature. Such a high aspect ratio can be fabricated by mechanical machining provided that the fin thickness has a sufficiently high value. It has also been reported in [4.15] that a microchannel aspect ratio of twenty can be attained using the Deep Reactive-Ion Etching (DRIE) technique.

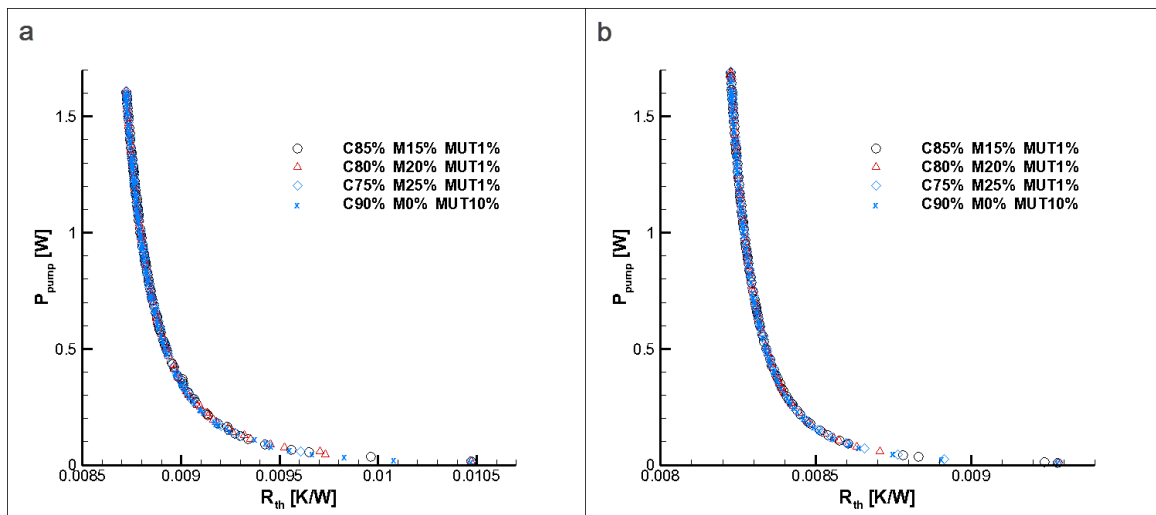


**Fig. 4.2** Pareto front of non-inferior solutions: (a) FW configuration and (b) VW configuration.

To allow for a more straightforward assessment of the produced optimal solutions, the points of the Pareto front that are derived from individuals that would be considered “identical” from a practical point of view (e.g. due to the precision of the manufacturing procedure) can be grouped into sets

represented by a single value. For this reason, a method referred to as *k-means clustering* [4.33] was used and a representative point (centroid) of each set was found. The scope of the *k-means clustering* method is to divide a number of data points  $x_j$  into a number  $k$  of representative clusters  $S_i$ , so that the following sum of squares within each cluster is minimum:

$$\sum_{x_j} \|x_j - \mu_i\|^2, \text{ where } \mu_i \text{ is the mean of points within the cluster } S_i.$$

**Fig. 4.3** presents the centroids of the assigned clusters for the FW (**Fig. 4.3a**) and the VW (**Fig. 4.3b**) configurations, respectively. As can be seen eight clusters were regarded as adequate to cover the entire value range of the Pareto front.

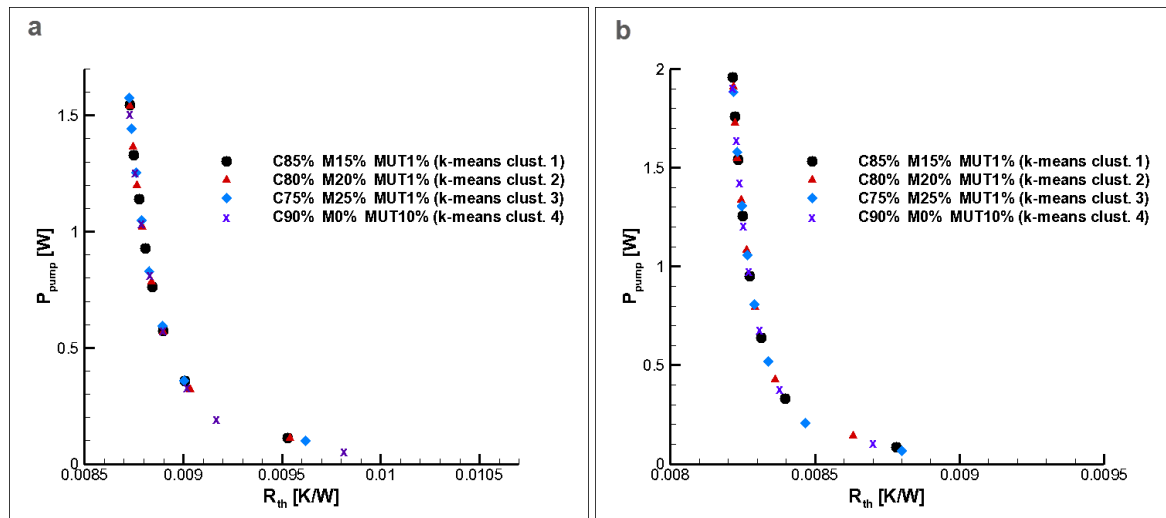


**Fig. 4.3** Representative points of the Pareto front as resulted through k-means clustering: (a) FW configuration and (b) VW configuration.

All the solutions that constitute the Pareto front are considered optimal from an overall –thermal and hydrodynamic- performance point of view. However, a single design point must be finally designated for the construction of the heat sink. For this reason, additional criteria must be considered in order to further evaluate the optimal solutions that comprise the Pareto front. These criteria can be dictated by an appropriate combination of additional thermodynamic aspects of the application, such as the exergetic efficiency and the overall efficiency of the CPVT system, and practical limitations posed by the available manufacturing techniques and underlying cost. In the present study, the ideal design point for each device is selected considering the minimization of the entropy generation rate.

The use of the entropy generation rate as the optimization criterion for cooling devices has been reported in a number of studies [4.34-4.38]. Jianhui et al. [4.34] imposed the minimization of the entropy generation rate as a global optimization criterion for a genetic algorithm, in order to obtain the optimal geometry and flow rate for an air-cooled plate-fin heat sink. Khan et al. [4.35] followed a similar optimization procedure as in [4.34], for a microchannel heat sink. Abbassi [4.36] conducted a parametric analysis that illustrated the effect of the various geometrical and operational parameters of a microchannel heat sink on the entropy generation rate due to heat transfer and fluid friction, respectively. It must be noted that the heat sink was modeled as a porous medium in [4.36]. Parlak et

al. [4.37] conducted an experimental evaluation regarding the entropy generation rate due to laminar flow through silica micro-tubes. The flow was isothermal and the entropy generation rate due to viscous dissipation and fluid friction were elucidated. Yang et al. [4.38] utilized the local and global generation rates to optimize the layout of a printed-circuit stack cooled by an air stream.

The entropy generation rate is calculated using a formulation proposed by Khan et al. [4.35], in which the contribution of both the thermal resistance and fluid friction are clearly illustrated:

$$\dot{S}_{gen} = \frac{Q^2 R_{th}}{T_{f,i} T_{w,max}} + \frac{\dot{m} \Delta p}{\rho T_{f,i}} \quad (4.20)$$

where  $Q$  is the heat rate equal to 850.0 W. Fig. 4.4 shows the production of entropy generation rate associated with each characteristic centroid of the Pareto front. Minimum points are evident in both graphs corresponding to the FW (Fig. 4.4a) and VW (Fig. 4.4b) configurations respectively. Due to the conflicting nature of the objective functions, their relative influence on the entropy generation rate varies, i.e. as the magnitude of the term referring to heat transfer decreases, the magnitude of the respective term for pumping power increases and therefore an optimal trade-off between the two exists. It is also interesting to notice that the VW configuration exhibits superior performance from an exergetic point of view.

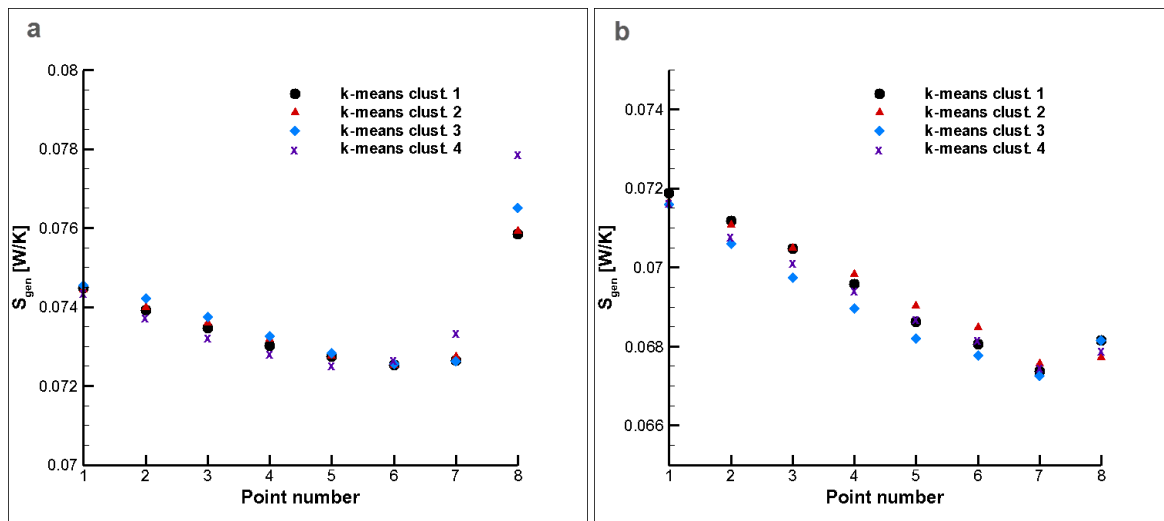


Fig. 4.4 Entropy generation rate associated with the representative optimal geometries: (a) FW configuration and (b) VW configuration.

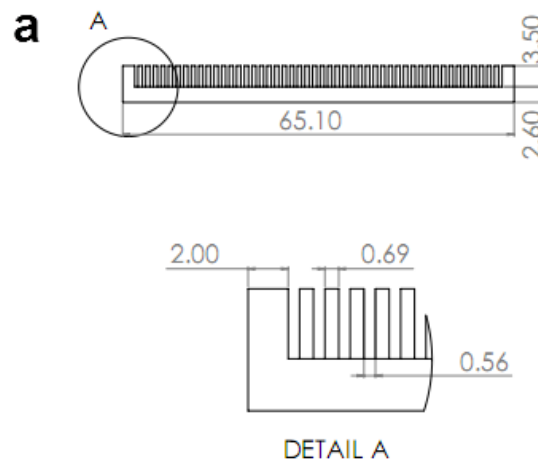
Table 4.4 summarizes the optimal geometrical parameters of the two heat sinks as were determined from the optimization procedure. The final geometrical parameters of the constructed heat sinks were determined by the constraints posed by the manufacturing procedure and are presented in the next paragraph. The layout of the two heat sink designs that were constructed is discussed in detail in the following paragraph, as well.

**Table 4.4** Geometrical parameters of the optimal heat-sink configurations.

	$W_{ch}$			$W_w$	$H_{ch}$
<b>FW</b>		0.00035		0.00025	0.00210
	<i>i=1</i>	<i>i=2</i>	<i>i=3</i>		
<b>VW</b>	0.00234	0.00094	0.00023	0.00047	0.00468

#### 4.6 Fabrication of the optimized heat sinks

The heat sinks were manufactured out of 5083 aluminum alloy. The specific material was selected, on the one hand, due to its corrosion resistance and, on the other hand, due to its high durability that allows the microchannels to be machined of aluminum rods using a conventional milling machine. In addition, the material mechanical properties enabled the welding of the top cover, which is necessary for sealing the heat sink, onto the two outer channel walls without causing any deformation to the parts. The drawings for the two manufactured heat sinks are shown in **Fig. 4.5**. It must be noted that the actual dimensions are the best approximations of the respective ideal ones, which resulted from the optimization procedure, that could be achieved by the milling machine used for manufacturing. Both configurations have the same overall area 65mm x 500mm, however, the VW configuration has a significantly larger height in comparison to the FW one (10.60mm instead of 3.50mm). Consequently, the channels at the third section of the VW configuration obtain a very high aspect ratio ( $AR \approx 19$ ). To the author's knowledge it is first time reported in the open literature that it has been made possible to manufacture a plate-fin heat sink of large length-to-width ratio ( $L/W \approx 9$ ), which employs microchannels of such high aspect ratio. Inflow and outflow chambers of length 50mm were created upstream and downstream of the channel region, respectively, in order to avoid any perturbations, caused by the hydraulic circuit and the fittings, being transported to the flow within the channel region.



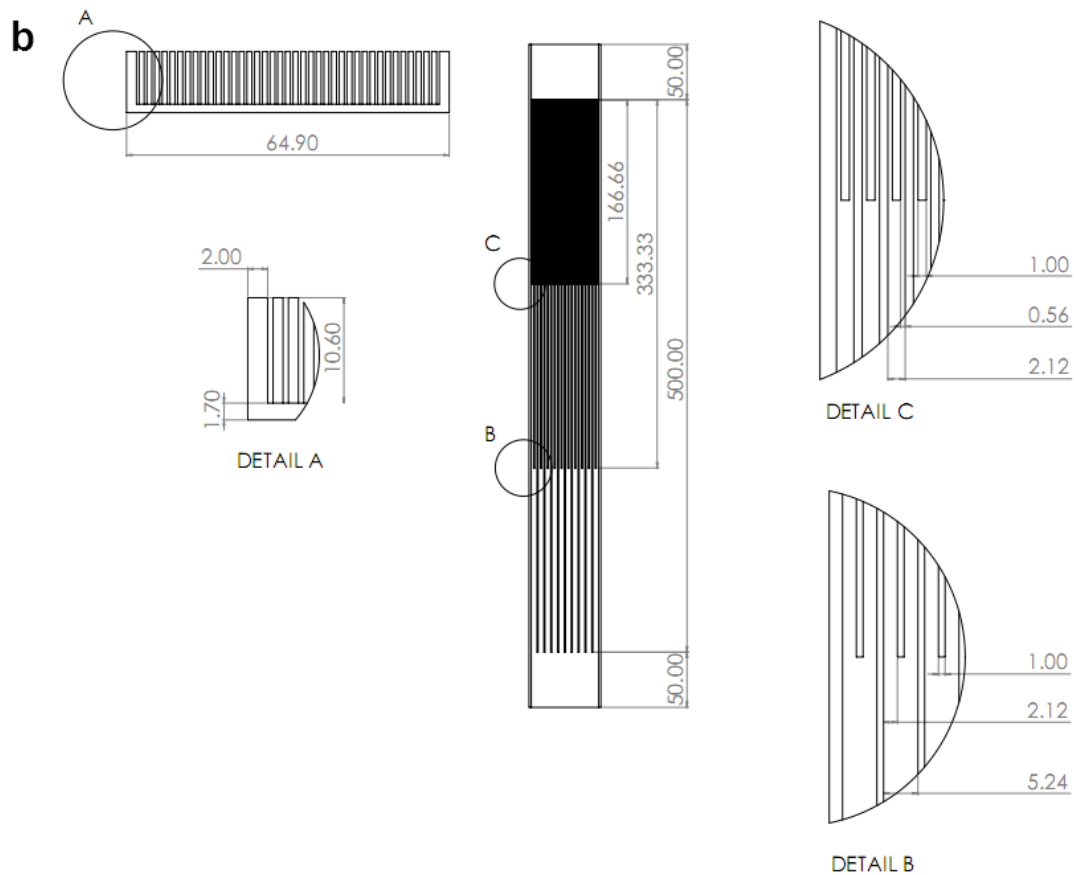


**Figure 4.5** Manufacturing drawings of the two heat-sink configurations: (a) FW and (b) three-section VW.

## 4.7 Inlet-outlet manifold

### 4.7.1 Design concept

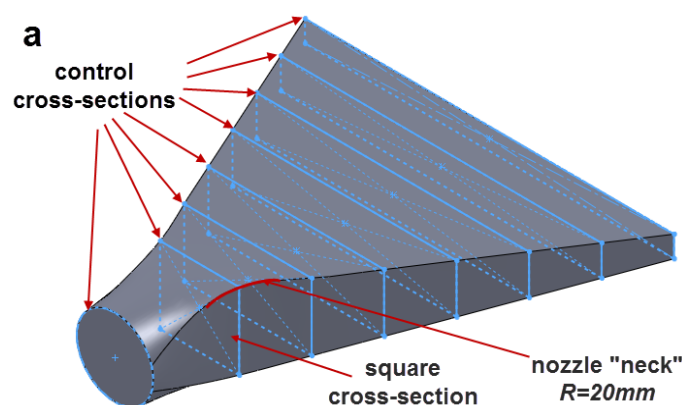
Few studies have focused on the influence of the inlet/outlet manifold on the performance of cooling devices [4.39,4.42] despite the fact that these are key components, particularly in the case of plate-fin heat sinks, in ensuring the uniformity of the flow distribution in the channels. Chein and Chen [4.39], through a numerical evaluation of simple rectangular slot arrangements, concluded that it is beneficial in terms of flow and temperature uniformity, as well as thermal resistance and pressure drop penalty, the cooling fluid to be distributed and collected by the microchannels by a vertical inlet/outlet arrangement rather than a horizontal. The experimental study of Sehgal et al. [4.40] showed that vertical cooling fluid distribution and collection offers a superior hydrodynamic performance in comparison to horizontal configurations. However, the cooling configuration employing a horizontal manifold where the fluid enters and exits the heat sink from the same side, was found to have the highest thermal performance. For vertical inlet/outlet round ports, Kim et al. [4.41] introduced a geometrical parameter that takes into account the manifold length and width and the relative transversal port distance. The optimum value of this parameter was determined, for which the flow distribution uniformity is maximized. Kumaraguruparan et al. [4.42] experimentally and numerically examined the flow maldistribution to the microchannel core induced by a horizontal

manifold where the flow enters from the side. It was found that depending on the geometrical parameters of the microchannels, recirculation may emerge in the inlet region and that increased flow resistance, e.g. by high fin density in the entrance is beneficial in terms of flow distribution.

In order to distribute the coolant to the microchannels and subsequently re-collect it to a single flow stream that flows through the closed-circuit tubing, manifold nozzles that geometrically match each constructed heat-sink design were designed and manufactured. The nozzles, apart from the practical fact that their cross-section must gradually vary from circular to rectangular, are required to allow for even distribution of the coolant to the channels and to induce a minor pressure loss penalty. The design was based on the concept that the shape of the fluid-flow layout can be determined by a number of characteristic cross-sections that guide splines, as depicted in **Fig. 4.6a**, and subsequently the nozzle final shape results as a “shell” by adding the necessary wall thickness (**Fig. 4.6b**). It must be noted that the nozzle rectangular cross sectional area must exactly match that of the heat-sink configuration and thus nozzles of different dimensions had to be designed corresponding to each of the heat-sink designs. Nevertheless, both nozzle designs should comply with the criteria of low pressure drop and even distribution.

A parametric analysis based on numerical three-dimensional models of the nozzles was conducted in order to designate acceptable designs suitable for the constructed heat sinks. The analysis was limited to the inlet nozzles, as possible perturbations to the flow prior to the channels entrance could affect the performance of the heat sinks as well. The outlet nozzles were manufactured identical to the respective inlet ones.

Flow separation is possible to occur owing to the cross-sectional expansion, as the circular inlet of the nozzle changes to a rectangular cross section. The nozzle design exhibits a characteristic “throat” in that region, as depicted in **Fig. 4.6**. It was established through the numerical models that if the first control cross-section downstream of the circular inlet is a square with side length equal to the inlet diameter, then flow separation does not occur at the nozzle “throat”. Furthermore, the radius of curvature at the throat region should be approximately equal to 20mm. The diameter of the circular inlet was selected to approximately match that of standardized tubes in order to facilitate the interconnection to the flow loop. In order to render the manufacturing of the nozzles feasible, the gradual decrease of the nozzle height as the outlet is approached must occur in a linear manner. The same applies for the increase in the nozzle width. In addition, the height gradient should be kept close to  $5^\circ$ . Considering the specified gradient, the length between the square control cross section and the nozzle outlet can be explicitly specified. In order to manufacture the two nozzle designs of equal length, the height gradient was equal to  $4.53^\circ$  for the FW and  $5.06^\circ$  for the VW design, respectively.



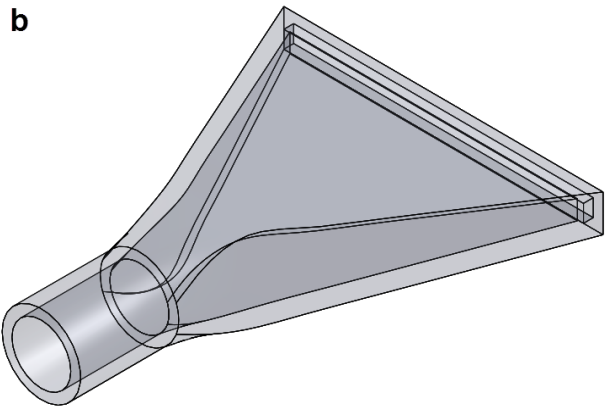


Fig. 4.6 (a) Formation of the fluid-flow arrangement and (b) the shape of the nozzle.

4.7.2 Fabrication of the inlet/outlet nozzles

The inlet/outlet nozzles for the two cooling configurations were machined out of aluminum rods according to the manufacturing drawings shown in Figs. 4.7a-b. Each nozzle was manufactured as two symmetrical, separate parts in a CNC milling machine, as shown in Fig. 4.7c. Guides were placed at the top faces of the parts, so that they can be precisely aligned, and the parts were bonded using an epoxy adhesive resin (Araldite 2014-1), as the alternative option of welding was not feasible due to the small thickness of the nozzle walls. The final part (for the FW configuration) is shown in Fig. 4.7d.

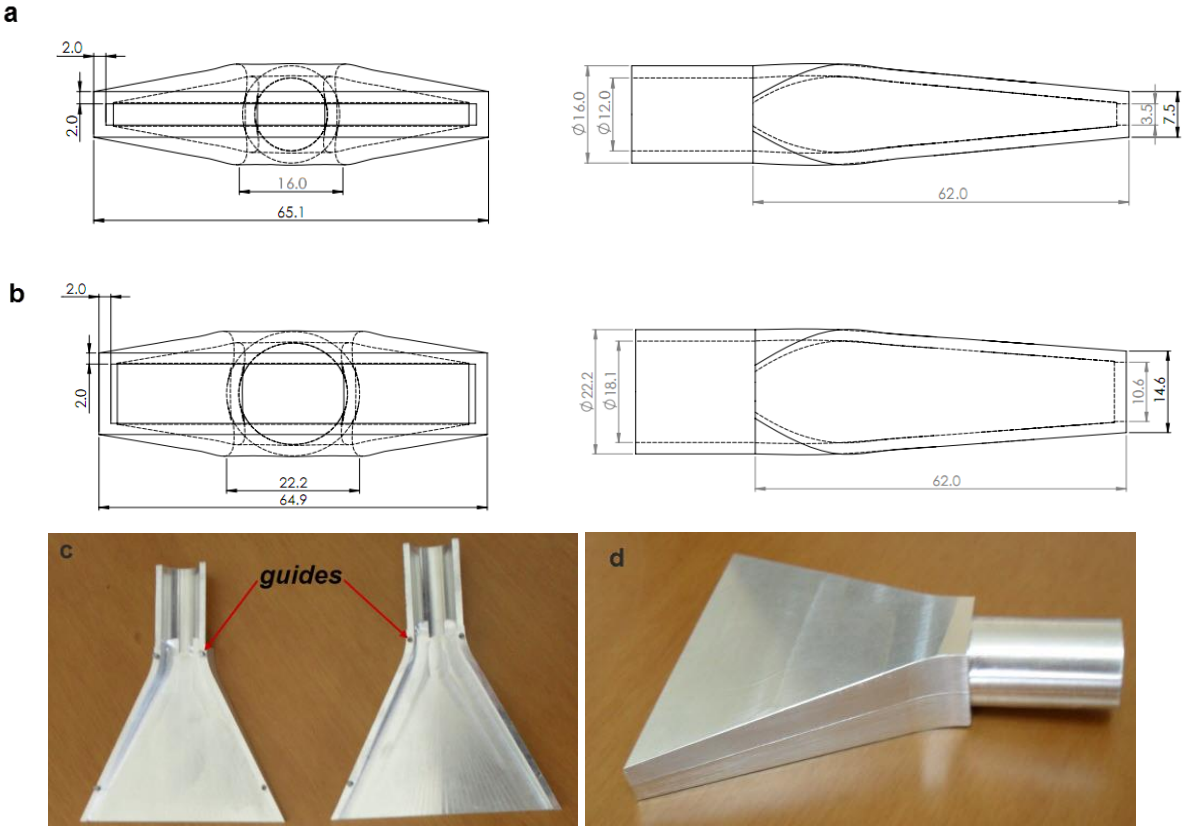
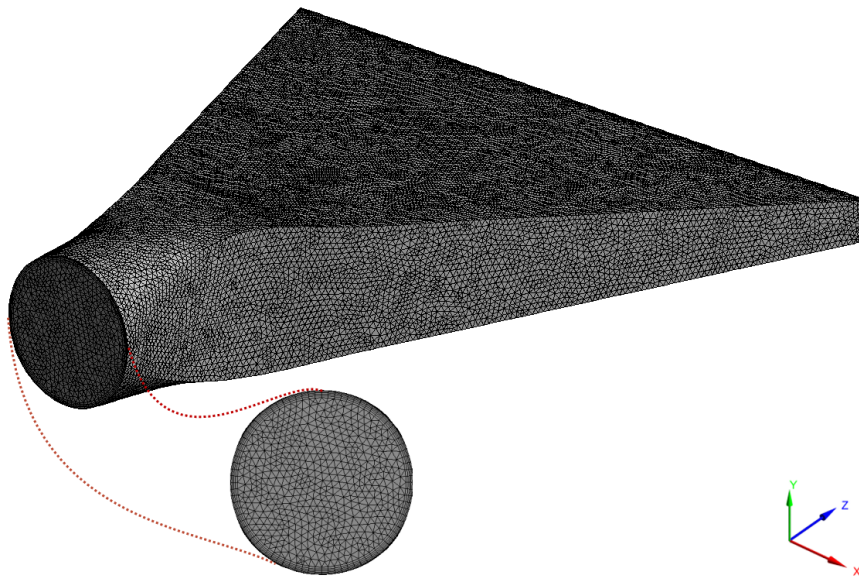


Fig. 4.7 Manufacturing drawings for the inlet-outlet nozzles: (a) FW and (b) configuration. Manufactured nozzle (FW configuration: (a) machined symmetrical parts and (d) final assembled part.

**4.7.3 Numerical investigation of the manifold system**

Numerical models were formulated for the inlet-outlet nozzles that match each cooling configuration. The computational domains for the inlet-outlet nozzles in both cases comprised the entire geometry due to the lack of any symmetry. The flow was considered to be isothermal, steady and turbulent for the range of flow rates considered, with the thermophysical properties of water evaluated at 25°C. The Reynolds number characterizing the flow was based on the velocity and geometry of the circular inner cross-section of the nozzle. The three-dimensional transport equations of mass, momentum obtain a common form which can be found, e.g. in [4.43]. The standard k- $\epsilon$  model [4.44] was used for the calculation of the Reynolds stresses that appear in the Reynolds Averaged Navier-Stokes (RANS) equations. A uniform velocity profile was imposed at the nozzle inlet, while a zero static pressure condition was imposed at the channel outlet. The governing equations were solved using ANSYS CFX with a convergence criterion of  $10^{-6}$  for the mass and momentum root mean square (RMS) residuals.

The computational domains were discretized using unstructured grids of tetrahedral elements, as depicted in **Fig. 4.8**. The grid had a non-uniform density as smaller elements were placed at the rectangular cross section of the nozzles. In addition, layers of prismatic elements were placed in the boundary-layer region in order to capture the velocity gradients. A grid independence analysis was conducted for the highest value of coolant flow rate considered throughout the present analysis, equal to 40 mL/s, corresponding to Reynolds numbers equal to 4456 and 3059. It was established through examining the overall pressure drop values and the outlet velocity profiles produced by denser grids that  $1.29 \cdot 10^6$  and  $2.38 \cdot 10^6$  elements for the FW and the VW manifold grids, respectively, suffice to obtain grid independent solutions.

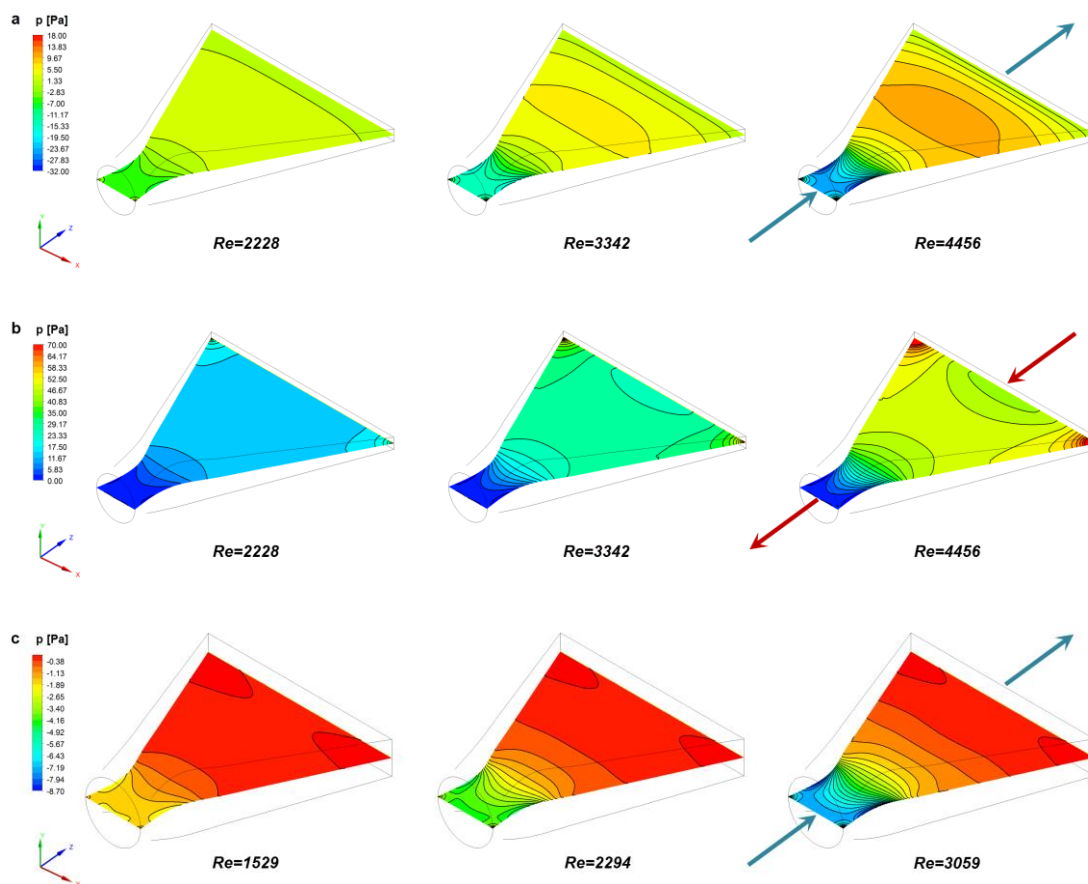


**Fig. 4.8** Grid topology used for the discretization of the nozzle geometry.

## 4.7.4 Flow field in the manifold system

Due to the geometrical form of the nozzles, the flow is forced to sustain both gradual expansion and contraction, which lead to pressure recovery and loss, respectively [4.25]. As can be seen in **Figs. 4.9a** and **4.9c**, flow through the inlet nozzle results to a pressure recovery, due to the rapid recovery rate at the nozzle “throat” where the geometry is gradually expanding. Especially, in the case of the inlet nozzle for the FW configuration (**Fig. 4.9a**), it is clearly discernible that the pressure initially increases to a maximum pressure value at the location, where the nozzle obtains its largest cross-sectional area. Subsequently, the pressure decreases as the flow is subject to constriction due to the gradual decrease of the nozzle height to a final value of only 3.5 mm. This behavior is less evident in the nozzle for the VW design (**Fig. 4.9c**), as the flow velocity within the nozzle is in general lower than that in the FW design and the gradual geometry contraction up to the nozzle outlet has a much less steeper gradient, as the outlet height is equal to 10.6 mm.

On the other hand, the outlet nozzle induces a fluid pressure loss, as depicted in **Figs. 4.9b** and **4.9d**. As can be deduced from the contour plots, once again the pressure change rate is becoming rapid in the “throat” region where the flow experiences a gradual contraction. As expected, the induced pressure loss has a more significant magnitude in the outlet nozzle of the FW configuration and furthermore the pressure loss/recovery at the outlet/inlet nozzle becomes more considerable as the Reynolds number increases. Nevertheless, the overall effect of the manifold on the induced pressure drop is negligible, as will be shown in the next paragraph.



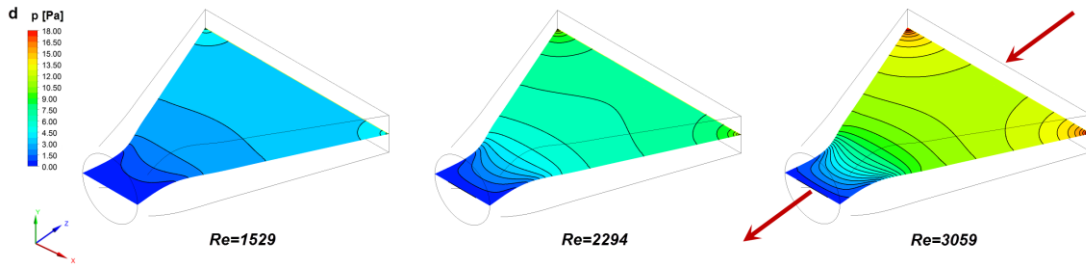


**Fig. 4.9** Pressure distribution at the horizontal symmetry plane of the manifold: (a) inlet nozzle-FW, (b) outlet nozzle-FW, (c) inlet nozzle-VW, (d) outlet nozzle-VW.

**Fig. 4.10** depicts the outlet velocity profiles of the two inflow-nozzle designs. The insets of **Fig. 4.10** depict the horizontal velocity distribution at the nozzle horizontal symmetry plane in conjunction to a vector plot. It is evident for both designs, that flow separation does not occur at the critical “throat” region, where the geometry expands, and the flow remains parallel throughout the nozzle. The velocity profile obtains a flatter form in the FW design as the flow is in a less developed stage than the VW design due to the higher flow velocity. It must be taken in mind that both nozzle designs are of equal length. Besides, in both cases the flow exits the nozzles unperturbed and no secondary flow occurs as aspired. The smooth outflow from the nozzle in conjunction to the effect of the rectangular heat-sink inlet chamber, which tends to produce an even flatter velocity profile typical of rectangular geometries with high aspect ratios, enable the even flow distribution in the channels.

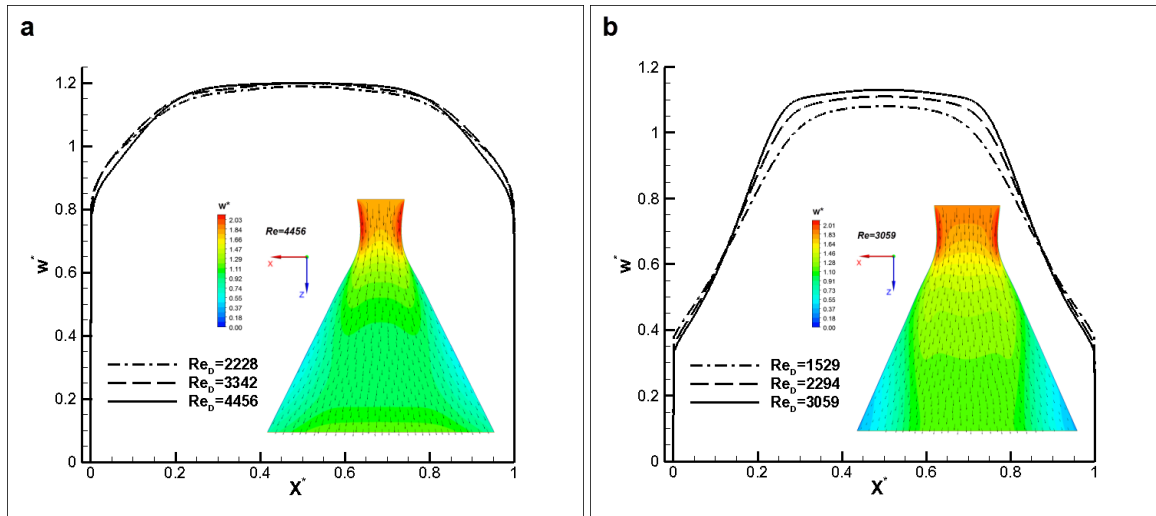


**Fig. 4.10** Axial velocity horizontal profile at the exit of the inflow nozzle. The velocity was non-dimensionalized using the mean flow velocity within the nozzle. (a) FW and (b) VW configuration.

## 4.8 Evaluation of the implemented heat-sink designs

### 4.8.1 Experimental evaluation

#### 4.8.1.1 Flow loop and test rigs

The cooling devices were evaluated in a closed flow loop (**Fig. 4.11a**), where the working fluid, which is water in the present case, was circulated with the use of a gear pump manufactured by *Speck*

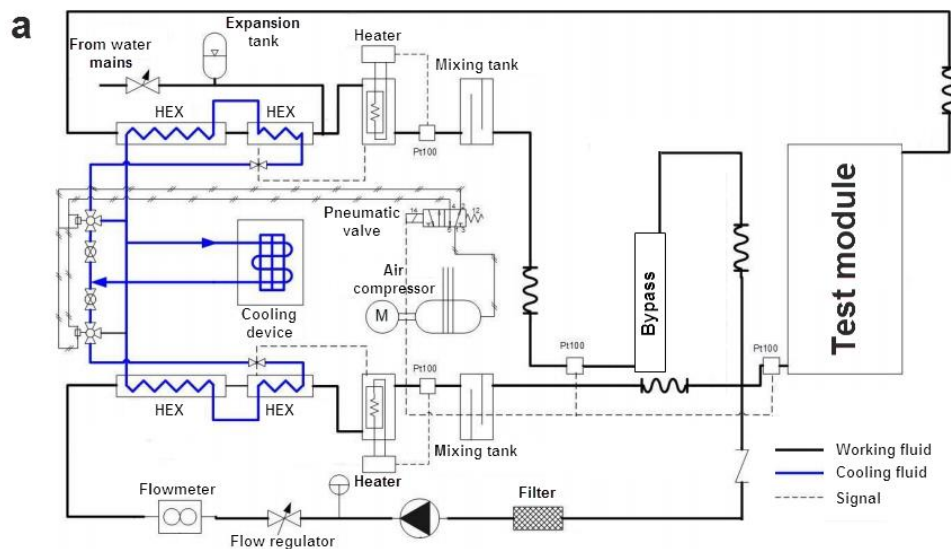
*GmbH*. The water flow rate was measured with a ring piston flow meter manufactured by *Aqua Metro AG* and could be properly adjusted through a flow regulator. A 50  $\mu\text{m}$  filter was also inserted in the tubing prior to the test device, in order to prevent the possible clogging of the channels from impurities. The temperature of the fluid that enters the test-device was adjusted to a specified set-point, with the use of a water-conditioning unit that housed a number of resistors and mantle heat exchangers. A separate cooling unit was hydraulically connected to the water-conditioning unit through an additional closed flow loop that provides the “cold stream” of the heat exchanger (tap water). The flow in the “cooling” flow loop is regulated through pneumatic valves and the control signal for the valves is provided by a PLC where the temperature set-point is specified. As depicted in **Fig. 4.11a**, the experimental setup allows the simultaneous evaluation of two test devices; however a bypass tube was placed at the second spot, in order to evaluate a single test-device.

The induced pressure drop by the heat sinks was measured using a diaphragm differential pressure transducer manufactured by *Endress+Hauzer AG*. In order to obtain a measurement, two probe fittings were inserted to the hydraulic circuit in proximity to the heat-sink inlet and outlet and the pressure transducer was connected to the circuit through flexible tubes. Inevitably, a number of fittings and connectors interceded between the probe and the heat-sink inlet (or outlet) manifold and consequently the pressure drop in these sections was also measured separately, in order to be able to determine the pressure drop that accounts for the heat sink length and the manifold system alone. However, in order to have a straightforward comparison to the numerical predictions the pressure losses due to the flow entrance into the multi-channel core (and respectively the pressure recovery due to the exit into the outlet chamber) must also be determined. As it was not possible to directly measure the pressure in these specific regions, theoretical predictions were used and the experimental data were appropriately retrofitted. Besides, the contribution of the inlet-outlet regions to the overall induced pressure drop is much smaller in comparison to that of the channel core region. The correlations used for the calculation of the pressure loss (or recovery) due to the flow transition into and out of the channel core are of the general form regarding flow contraction or expansion, using the total cross-sectional area of the channels and the inlet (outlet) chamber cross-sectional as  $A_1$ ,  $A_2$  respectively (see **Eqs. (4.6-4.7)**). Besides, the pressure losses in the manifold system were numerically predicted.

The heat-sink thermal performance was evaluated under constant heat flux conditions with the imposition of negligible heat losses. In order to impose the uniform and constant heat flux at the bottom surface of the heat sink, a heating device was constructed, which comprises two symmetrical aluminum plates of total dimensions equal to (L x W) 500mm x 65mm so as to exactly match the active area of the heat sink. The two plates, which bear four equidistant parallel grooves, were bolted together and rod resistors having a nominal diameter of 6mm were housed in the through holes that were created. The nominal resistance value and the active length of the resistors were equal to 96 $\Omega$  and 500mm, respectively. Thermally conductive paste was applied at the interface between the resistors and the aluminum plate in order to facilitate heat transfer. The heat sink and the heating device were clamped together using bolts and placed inside an insulating container made of bakelite with an additional interior insulating layer of Armaflex with thickness greater than 4cm. A cut-view of the test section is depicted in **Fig. 4.11b**. The resistors were connected in parallel and a voltage divider was used in order to adjust the input power. The input power was set approximately equal to 850W, which is close to the expected heat rate in the actual CPVT system.

Two four-wire Pt100 thermometers were used for the measurement of the fluid temperature at the inlet and the outlet of the heat sink. Each sensor was housed in a configuration which allows the insertion of the probe opposite to the incoming flow and furthermore enables fluid mixing prior to the measurement. In order to illustrate the temperature distribution at the heat sink bottom wall, holes of diameter 0.9mm were drilled into the substrate and series of Type T thermocouples were placed along the heat sink length. **Fig. 4.11c** depicts the thermocouple locations for the two heat-sink configurations. The voltage and current in the electrical circuit were measured using a volt-meter and a shunt resistor ( $R=1\text{m}\Omega$ ) respectively and thus the input power was determined. A more thorough discussion on the instrumentation used for the various experimental investigations and the accuracy of measurements is made in **paragraphs 6.1 and 6.2**.

The experimental results presented in the following sections were obtained by following the procedure as discussed here. A constant flow rate and fluid inlet temperature were assigned and once these values remained constant for a time interval of at least 5 min, the resistors were turned on. With the resistors on, values of the bottom-wall temperature, the fluid temperature at the heat sink inlet and outlet and the volumetric flow rate were recorded every 5s. The recording of the wall-temperature values, from which the experimental points result, commenced, once the fluid thermal balance was verified and the fluid maintained a constant inlet-outlet temperature difference. The experimental data resulted as averaged values for time intervals of at least 5 min under steady-state conditions, namely provided that the temperature values varied less than  $\pm 0.2\text{K}$ . The sensors signals were directly measured using an Agilent data logger. Measured values were being processed and stored to a computer using the Agilent VEE software.



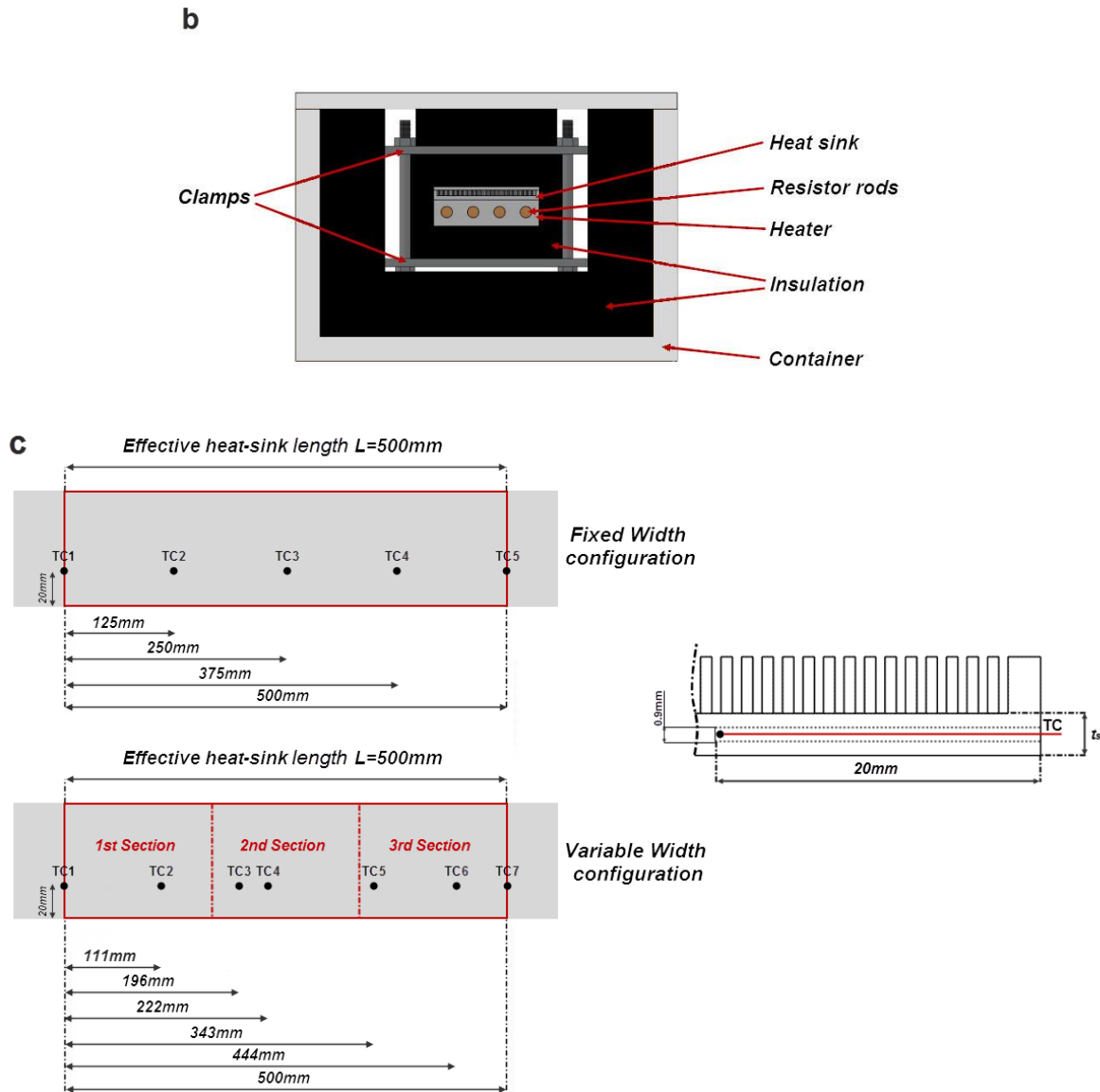


**Fig. 4.11** Schematics of the experimental rig: (a) water conditioning unit and flow loop, (b) cross-section of the test module and heating elements. (c) Locations of the thermocouples.

#### 4.8.1.2 Uncertainty of the experimental data

The uncertainties in the values of all the measured quantities are given for a confidence level equal to 95% and summarized in **Table 4.5**. An uncertainty analysis based on propagation of errors has been conducted in order to determine the resulting uncertainty of the calculated quantities. The topic of experimental uncertainties and the procedure followed to determine the uncertainty associated with calculated values are discussed in detail in **paragraph 6.2**. It is interesting to notice the relatively large uncertainties associated with the parameters of the FW heat sink, due to the fact that the manufacturing precision remains constant, although the channel dimensions are significantly reduced and lie in the microscale.

**Table 4.5** Uncertainty in measured quantities.

Measured quantity	U
$\dot{V}_{\text{tot}}$ [m <sup>3</sup> /s]	1.76%
$T_f$ [K]	0.054 K
$T_w$ [K]	0.5 K
$V_{\text{mult}}$ [volts]	0.66%
$I_{\text{shunt}}$ [amps]	0.00%
$\Delta p$ [Pa]	0.02%
$W_{\text{ch,FW}}$ [m]	3.57%
$W_{\text{ch,VW,1}}$ [m]	0.38%
$W_{\text{ch,VW,2}}$ [m]	0.94%
$W_{\text{ch,VW,3}}$ [m]	3.57%
$W_{\text{w,FW}}$ [m]	2.90
$W_{\text{w,VW}}$ [m]	2.00%
$H_{\text{ch,FW}}$ [m]	0.57%
$H_{\text{ch,VW}}$ [m]	0.19%
$W_{\text{hs}}$ [m]	1.67%
$L_{\text{hs}}$ [m]	0.20%

**Table 4.6** Uncertainty in calculated quantities.

Calculated quantity	U
$D_{\text{h,FW}}$ [m]	3.08%
$D_{\text{h,VW,1}}$ [m]	0.26%
$D_{\text{h,VW,2}}$ [m]	0.79%
$D_{\text{h,VW,3}}$ [m]	3.39%
$A_{\text{ch,FW}}$ [m <sup>2</sup> ]	3.62%
$A_{\text{ch,VW,1}}$ [m <sup>2</sup> ]	0.43%
$A_{\text{ch,VW,2}}$ [m <sup>2</sup> ]	0.96%
$A_{\text{ch,VW,3}}$ [m <sup>2</sup> ]	3.58%
$A_{\text{rec,active}}$ [m <sup>2</sup> ]	1.68%
$Z^*$	0.33%
$u_{\text{FW}}$ [m/s]	4.02%
$u_{\text{VW,1}}$ [m/s]	1.81%
$u_{\text{VW,2}}$ [m/s]	2.01%
$u_{\text{VW,3}}$ [m/s]	3.99%
$Re_{\text{FW}}$	5.07%
$Re_{\text{VW,1}}$	1.83%
$Re_{\text{VW,2}}$	2.15%
$Re_{\text{VW,3}}$	5.23%
$Q_{\text{el}}$ [W]	0.66%
$q''$ [W/m <sup>2</sup> ]	1.81%
$T_{\text{FW}}^* \times 100$	1.123-1.374
$T_{\text{VW}}^* \times 100$	0.168-0.181
$\Delta T_{\text{f,therm.bal.}}$	1.88%
$f_{\text{FW}}$	8.62%
$f_{\text{VW}}$	3.64%

## 4.8.2 Numerical analysis

### 4.8.2.1 Formulation of the numerical model

The numerical models representing the actual heat sink configurations were decreased to appropriate unit cells in order to reduce computational time. Both models were applied on a composite fluid and solid domain. The computational domain for the FW configuration was similar to that depicted in **Fig. 3.3** and it was truncated to  $Z^*=172$  along the streamwise direction, which is a length far exceeding the flow development length. The domain for the VW heat sink included channels of three different hydraulic diameters and thus its lateral extent was such as to include half a first-section, one full second-section and two full third-section channels respectively, as depicted in **Fig. 4.12**. Just as in the cases presented in the second chapter, heat transfer was again treated as conjugate with simultaneous heat conduction in the solid and convection in the fluid domains, respectively. The thermophysical properties of the cooling fluid were evaluated at the fluid overall mean temperature, which was estimated through a global thermal balance for each value of the volumetric flow rates considered for the simulations. The effect of buoyancy was taken into account through the Boussinesq approximation

and the flow and temperature fields were considered coupled in all cases. The assumptions stated in **paragraph 3.2.1** were adopted and **Eqs. (3.1)** and **(3.3)-(3.5)** were solved. A convergence criterion of  $10^{-6}$  was set for the root mean square (RMS) mass, momentum and energy residuals.

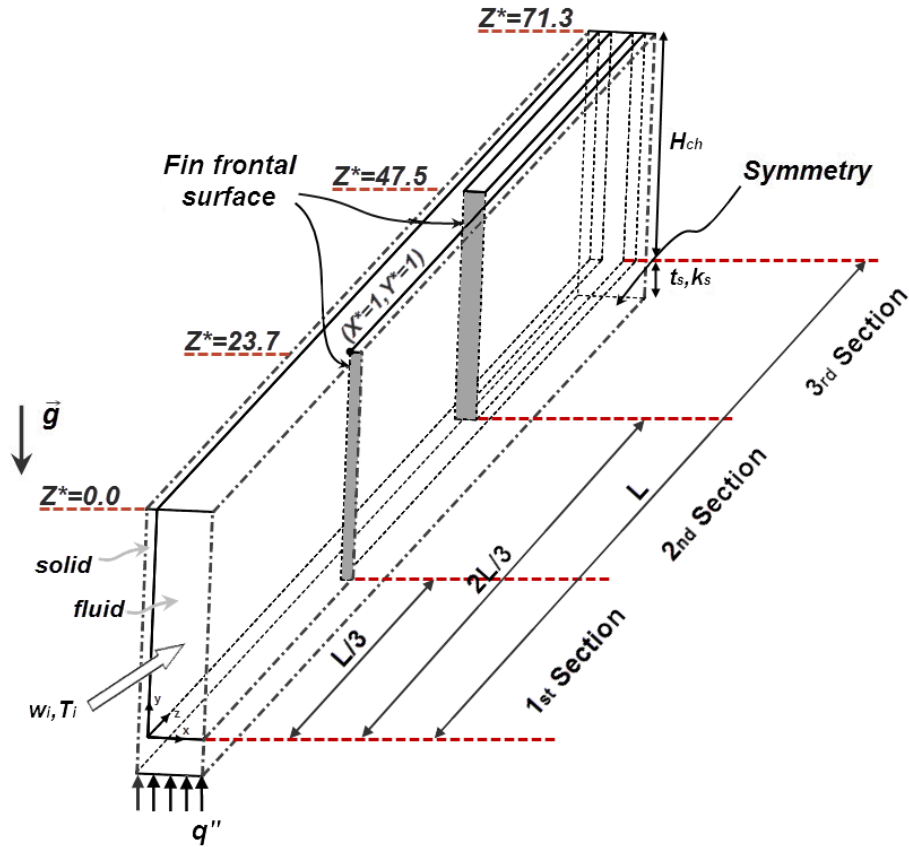


**Fig. 4.12** Computational domain for the three-section VW configuration.

#### 4.8.2.2 Grid independence

The computational domains of the two configurations were discretized using hexahedral elements in a non-uniform arrangement along the streamwise direction. In the case of the FW configuration, the grid was denser in the developing flow region, whereas, in regard to the VW configuration, the grid was refined in the locations of geometry contraction. Across the channel cross-section, the grid was refined in the near-wall regions of the FW-configuration unit cell, while the grid density was kept uniform in the VW-configuration unit cell.

The grid-independence study for both heat sink configurations was conducted assuming the highest value of the flow rate considered throughout the evaluation, i.e.  $\dot{V}_{tot} = 40 \text{ mL/s}$ , which corresponds to  $\text{Re} = 476$  for the FW configurations and  $\text{Re}_1 = 598$  for the VW configuration respectively. Three grids consisting of  $1.91$ ,  $3.35$  and  $4.92 \cdot 10^6$  elements respectively were considered for the FW configuration. The comparison among the values of the coolant pressure drop obtained for the consecutive grids of increasing density showed deviations of  $0.5\%$  and  $0.3\%$  respectively. Besides, the discrepancy in the values of the overall Nusselt number produced by the first two grids was equal to  $2.6\%$ , whereas the

refinement to the third, finer grid caused a deviation of 1.0%. The intermediate grid was therefore selected for producing the presented results.

In regard to the VW configuration the computational grid was consecutively refined from  $15.9 \cdot 10^6$  to  $20.6 \cdot 10^6$  and finally to  $24.9 \cdot 10^6$  elements. The relative discrepancy in the overall pressure drop of the cooling fluid flow was equal to 1.0% between the coarse and the intermediate grid and equal to 0.4% between the intermediate and the dense grid, respectively. In addition, as depicted in **Fig. 4.13a**, the horizontal axial velocity profiles slightly downstream of the first step-change in the channel hydraulic diameter ( $Z^*=28.9$ ) produced by the three grids are similar and the extent of the expected flow recirculation adjacent to the fin sidewall is well captured. The root mean square discrepancy between the values of the intermediate and dense grid is equal to 0.69%. Besides, the vertical temperature profiles at the same location (**Fig. 4.13b**) are identical for the three grids tested and the expected mixing zones in the upper and lower boundary layer regions are also well captured.

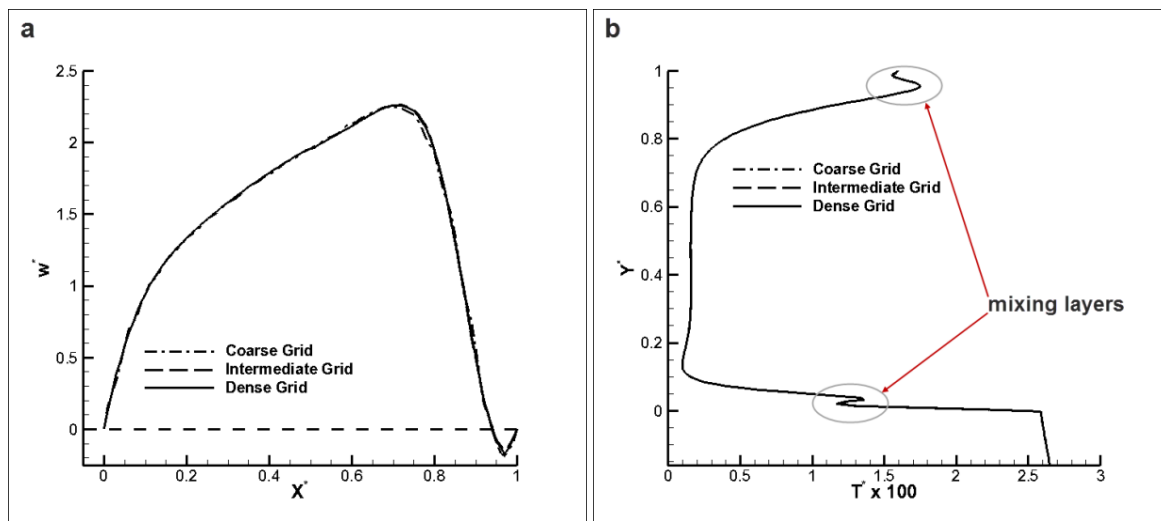


**Fig. 4.13** Grid independency study for  $Re_1=598$ : (a) Horizontal velocity profile ( $Y^*=0.5$ ) at  $Z^*=23.9$ , (b) Vertical temperature profile ( $X^*=0.5$ ) at  $Z^*=23.9$ .

## 4.9 Results

The results presented in the following sections were non-dimensionalized using appropriate quantities. It must be noted that regarding the comparison of the experimental data to the numerical predictions, the non-dimensional quantities ( $f, T^*$ ) introduced allow for a more clear illustration of the experimental uncertainties, as the uncertainty associated to the geometrical parameters, which has an effect on heat sink performance, is also included. In the case of the VW heat sink, quantities associated with the first heat-sink section were selected for the non-dimensionalization. This constitutes a conservative choice as the uncertainties associated with the characteristic flow quantities in the third heat-sink section are considerably larger, as can be seen in **Table 4.5**.

It must be pointed out that the non-dimensional numbers that characterize the flow are defined using the channel hydraulic diameter and are thus different for the two configurations, as well as for each section of the VW configuration, as presented in **Tables 4.7-4.8**. The nominal values of the Reynolds number shown in the second column of the tables result by evaluating the thermophysical properties of water at  $25^\circ\text{C}$  and refer to the pressure drop tests. Nevertheless, in order to have a

uniform representation of the results, the values of  $Re$  from the third column of the tables will be used in the following sections.

**Table 4.7** Non-dimensional numbers characterizing the flow conditions in the FW configuration.

$\dot{V}_{tot}$ [mL/s]	$Re(nom)$	$Re$	$Gr$	$Ar$
15.0	168	196	<i>Hydrodynamic evaluation only</i>	
20.0	223	252	3.11E+01	4.91E-04
25.0	279	308	2.89E+01	3.05E-04
30.0	335	364	2.75E+01	2.07E-04
35.0	391	420	2.65E+01	1.50E-04
40.0	447	476	2.58E+01	1.14E-04

**Table 4.8** Non-dimensional numbers characterizing the flow conditions within each section  $i$  of the VW configuration.

$\dot{V}_{tot}$ [mL/s]	$Re$				$Gr$			$Ar$		
	i=1(nom)	i=1	i=2	i=3	i=1	i=2	i=3	i=1	i=2	i=3
15.0	210	246	153	87	<i>Hydrodynamic evaluation only</i>					
20.0	281	316	197	112	1.18E+05	4.49E+03	2.06E+01	1.18	0.12	0.18
25.0	351	387	241	137	1.09E+05	4.16E+03	1.92E+01	0.73	0.07	0.14
30.0	421	457	285	162	1.03E+05	3.96E+03	1.83E+01	0.49	0.05	0.11
35.0	491	528	329	187	9.94E+04	3.82E+03	1.77E+01	0.36	0.04	0.09
40.0	561	598	373	212	9.67E+04	3.72E+03	1.72E+01	0.27	0.03	0.08

#### 4.9.1 Flow fields

The induced pressure drop was evaluated in cold flow conditions, so as to exclude possible effects of the variable water thermophysical properties due to heating. A constant temperature of 25°C was set in the flow loop. **Fig. 4.14** presents the obtained values of the friction factor as a function of  $Re$  for the two heat-sink configurations, indicative of the pressure drop, and the respective numerical and theoretical predictions. The numerical predictions were produced by “cold flow” models using only the fluid computational domains of the FW and VW unit cells, while the theoretical values were produced by considering the fluid friction in the channels region. In the case of the VW design, an additional pressure drop component arose due to flow constrictions. The pressure drop in the contraction locations was calculated using equation **Eq. 4.6**, whereas in the straight channel sections equations similar to **Eq. 4.8** were used by also considering the hydrodynamic development length. Besides, the appropriate Fanning friction factor  $f_F$  values were chosen corresponding to the aspect ratio of each channel. As can be seen, the experimental values exhibit very good agreement with the predictions. The discrepancy in the case of the FW configuration lies within the range of experimental uncertainty, whereas, regarding the VW configuration, the maximum discrepancy detected is between the theoretical predictions and the experimental data for the lowest Reynolds number, which is in the order of 10%. This small deviation is probably due to the fact that the values used for the development length in the channels of the third section ( $AR=18.9$ ), not being readily available, had to be extrapolated from available theoretical values of channels with a lower aspect ratio. In addition the effect of the geometrical constrictions along the heat sink length is possible to have been overestimated, as the frontal surface of the actual fins is not perfectly rectangular due to manufacturing limitations, and thus a smoother flow transition between sections is plausible to be assumed.

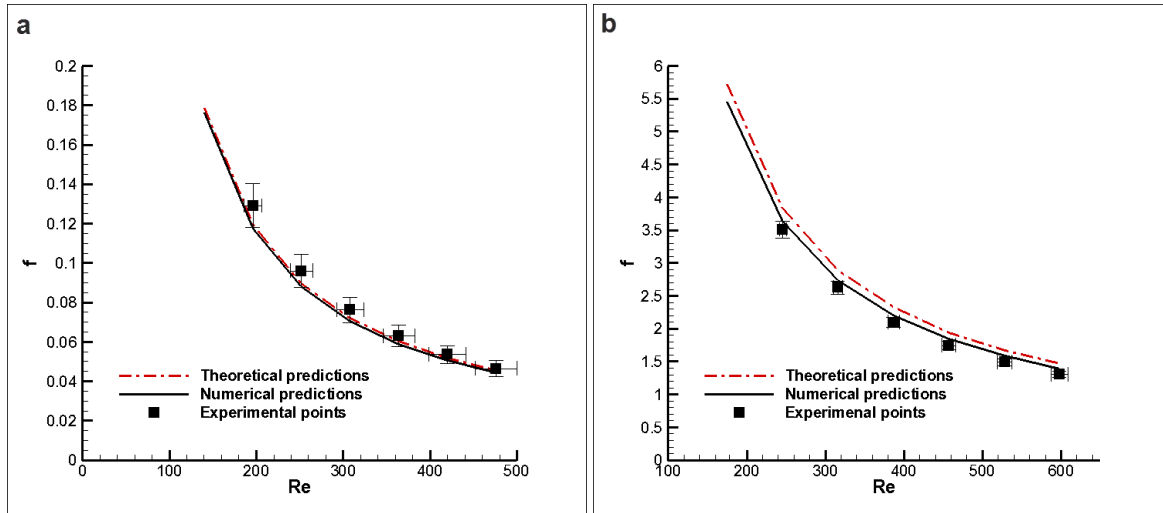
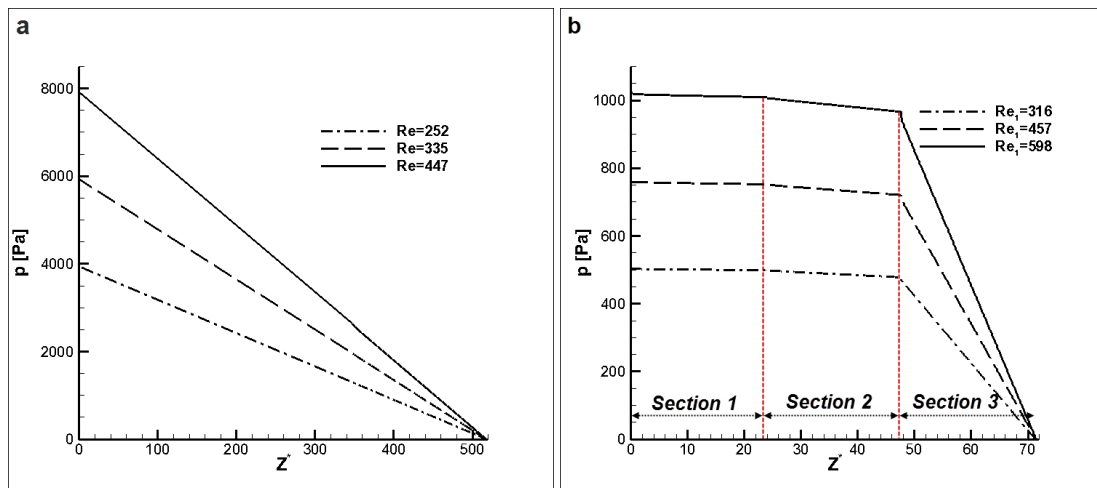
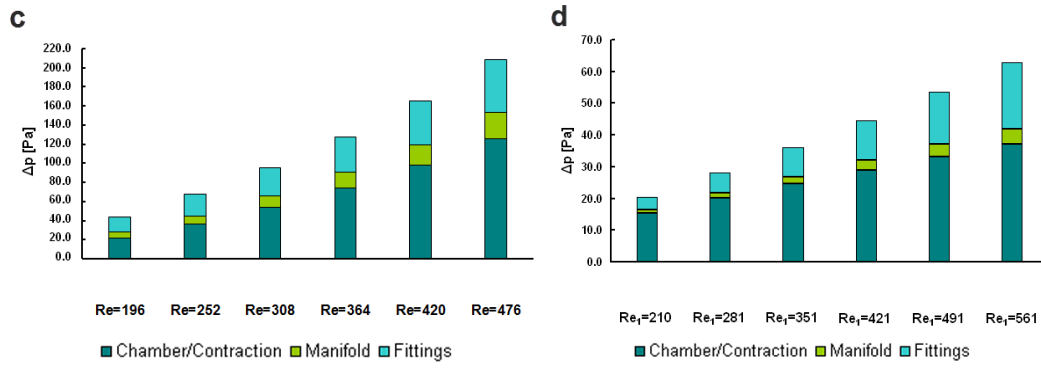


Fig. 4.14 Friction factor vs. Re through the (a) FW and (b) VW configuration.

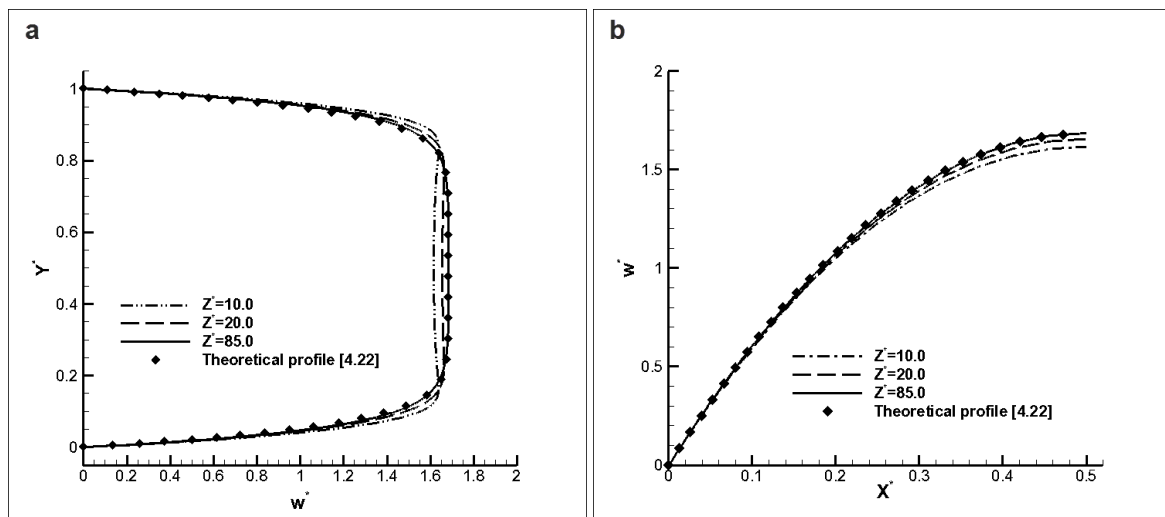
**Figs. 4.15a-b** depict the pressure distribution along the heat-sink length for the two configurations. The pressure in the FW channel decreases linearly with the axial coordinate, as expected (**Fig. 4.15a**). On the other hand, as can be seen in **Fig. 4.15b**, the friction losses in the third, high-fin density section of the VW heat sink account for approximately 95% of the overall induced pressure drop, while the linear pressure decrease has a much less steep gradient in the first two sections. By comparing the two figures, it is evident that the removal of fins in the first two sections reduces the pressure drop penalty considerably and enhances the hydrodynamic performance of the configuration. It is also interesting to notice that the effect of the flow impingement on the fin front surfaces of consecutive sections is very small. As made evident by **Figs. 4.15c-d** the pressure losses induced outside of the heat sink active area have a very small effect on the overall pressure drop. Especially regarding the pressure drop in the manifold system, which was determined numerically, the reduction of the experimental data verifies that its contribution to the overall pressure drop is negligible corresponding to less than 0.3% and 0.5% of the overall pressure drop for the FW and the VW configuration, respectively. In fact the pressure loss induced as the flow enters the channels from the inlet chamber has the most significant contribution to these minor losses. For the sake of thoroughness, it must be stated that the flow pressure recovery at the channels exit is subtracted during the calculation of the aforementioned term.





**Fig. 4.15** Longitudinal pressure drop distribution: (a) FW and (b) VW configuration. Pressure drop induced in regions outside the heat-sink active length: (c) FW configuration and (d) VW configuration.

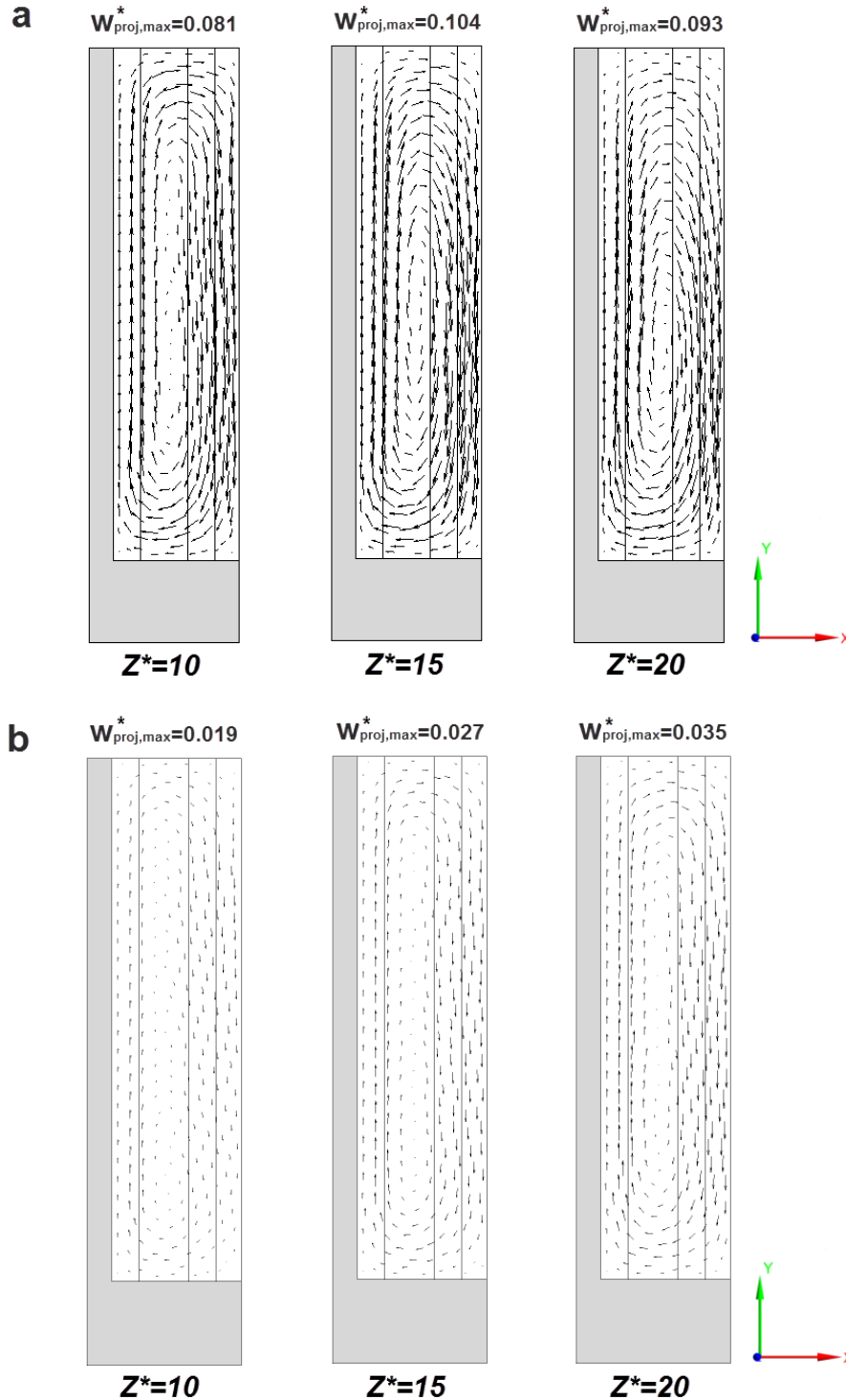
In reference to the flow field that emerges in the FW configuration, the velocity is expected to remain parallel throughout the heat-sink length, as the values of the Archimedes number (**Table 4.7**) indicate that the effect of natural convection is negligible. As illustrated in **Fig. 4.16** for the highest Reynolds number considered  $Re=476$ , the axial velocity profile is already fully developed at a length roughly equal to 85 hydraulic diameters downstream of the inlet. The extent of the hydrodynamic entry length is limited due to the small hydraulic diameter of the microchannels and fully developed conditions occur along the larger part of the microchannel (approximately 84% of the total channel length for  $Re=476$ ). The fully developed vertical velocity profile (**Fig. 4.16a**) obtains a flat form due to the high aspect ratio ( $AR=6.25$ ) of the microchannel, whereas the respective horizontal profile obtains the typical parabolic form (**Fig. 4.16b**). Both profiles are in agreement with the analytical solution for the specified channel aspect ratio.



**Fig 4.16** Axial velocity profiles at various streamwise locations of the FW configuration ( $Re=476$ ): (a) horizontal profile at the channel mid-height, (b) vertical velocity profile at the channel mid-width.

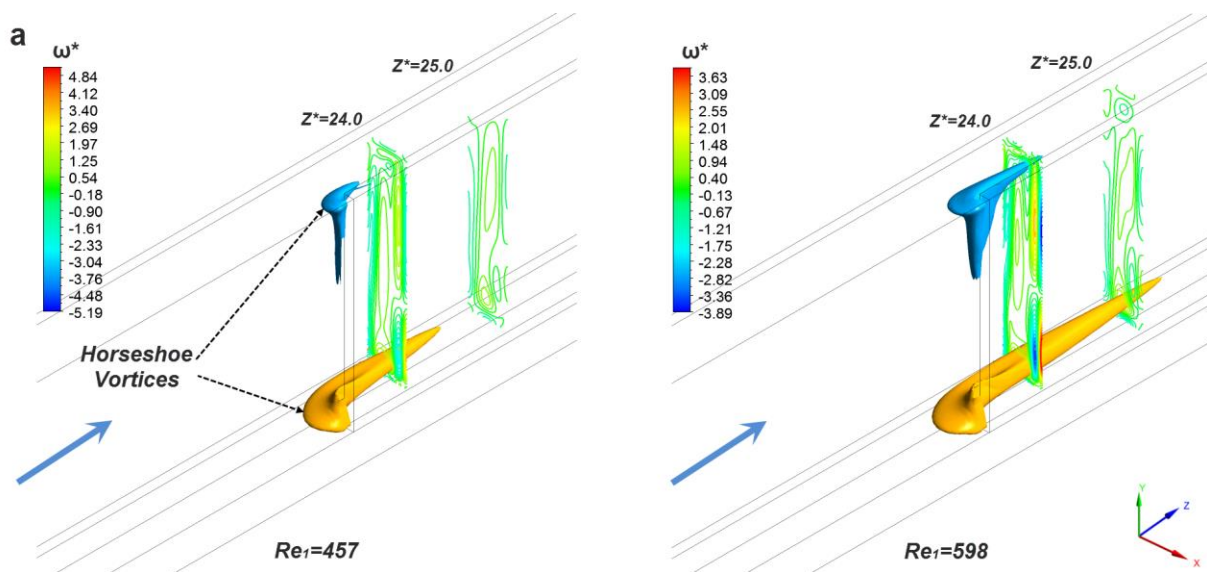
On the other hand, the flow field emerging in the VW configuration is much more complex. As can be deduced from the Archimedes number values of **Table 4.8**, buoyancy forces attain a significant magnitude than inertial forces only in the first heat-sink section and it is thus expected that longitudinal buoyancy rolls will emerge in that region. Indeed, as depicted in **Fig. 4.17**, a secondary

flow pattern is discernible even for the highest number of the Reynolds number considered. The rolls draw fluid from the upper wall to the lower heated wall and have an enhancing effect on heat transfer, as will be shown in the next paragraph. As expected, the magnitude of the rolls diminishes as the Reynolds number increases and furthermore the roll intensity maximum is shifted to downstream locations, as is evident by comparing **Fig. 4.17a** to **Fig. 4.17b**. This distinct behavior was elucidated in **paragraph 3.4.3**, where the flow and thermal behavior of a two-section VW heat sink was discussed.



**Fig. 4.17** Velocity vector plots indicative of the magnitude of the buoyancy induced rolls in the heat-sink first section: (a)  $Re_1=316$ , (b)  $Re_1=598$ .

A three-dimensional secondary flow pattern emerges due to the effect of the geometrical constriction, as has been illustrated in **paragraph 3.4.3.6**. The most distinctive feature is a pair of horseshoe vortices that develop in the upper and lower boundary layer regions. Under mixed convection conditions, the vortices become asymmetric due to the effect of the upstream established buoyancy rolls (see **paragraph 3.4.3.9**). **Fig. 4.18a** depicts the topology of the longitudinal vortices in the first section of the VW heat sink. The vortices set in transversally to the main flow due to the impingement of the oncoming flow on the frontal surface of the additional, second-section fin and persist in the consecutive section. As can be seen, the vortices remain asymmetrical even for the largest value of the Reynolds number, with the lower vortex being enhanced. It can be therefore deduced that the secondary flow topology considerably deviates from the respective one for purely forced convection conditions, already at a value of the Archimedes number as low as 0.27. Of course, as the Reynolds number increases the absolute magnitude of the vortices increases as well. As is evident from **Fig. 4.18b**, the flow confinement also influences the development of the secondary flow. The longitudinal vortices, which emerge in the vicinity of the second geometrical contraction (**Fig. 4.18b**), decay almost immediately and the flow changes into a pure parallel one. It must be noted that the upper and lower vortices are of equal magnitude, as the effect of buoyancy is negligible in the second and third heat sink sections. The small width of the third-section channels ( $W_{ch,3}=0.56mm$ ) renders the interaction of the secondary flow with the channel sidewalls more intense than in the second section. As it appears, this interaction destroys the coherence of the longitudinal vortices.



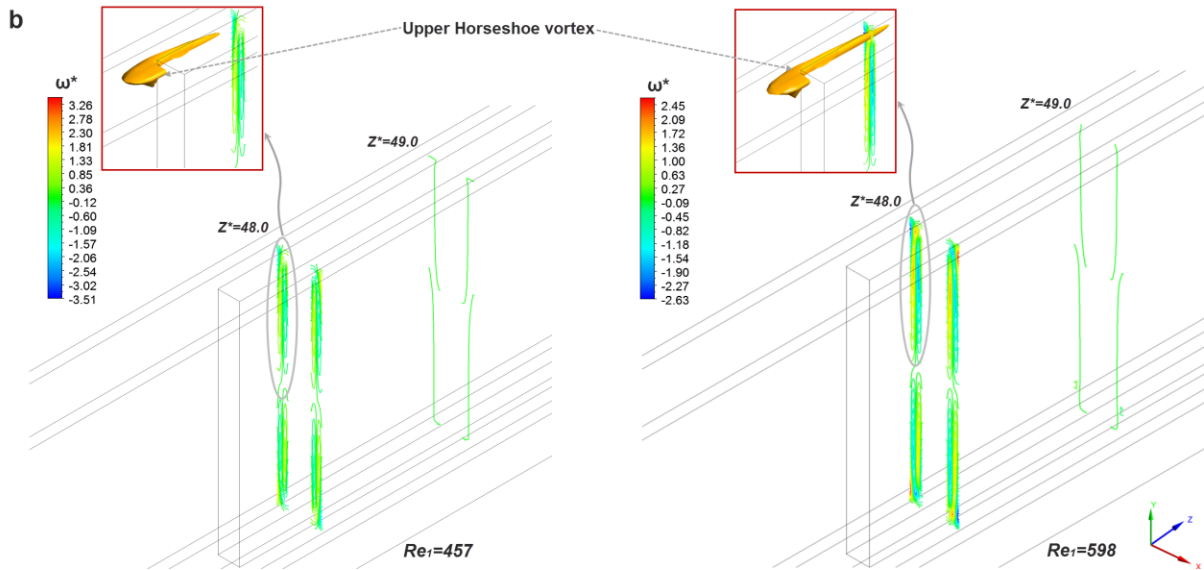


**Fig. 4.18** Contraction induced secondary flow pattern. Contour iso-surfaces ( $\omega=12s^{-1}$ ) and plots illustrating the topology of the horseshoe vortices: (a) First and (b) second geometrical contraction.

#### 4.9.2 Temperature fields and heat transfer

First of all, in order to verify the soundness of the experimental data regarding heat transfer, it is essential to ensure that all the heat provided by the rod resistors is extracted by the cooling fluid. The measured water temperature rise  $\Delta T$  through the heat sink for various flow and heat rates was compared to the theoretical values, as they result from a global thermal balance. As depicted in **Fig. 4.19**, the predictions agree very well with the experimental data and it is thus verified that heat losses are negligible.

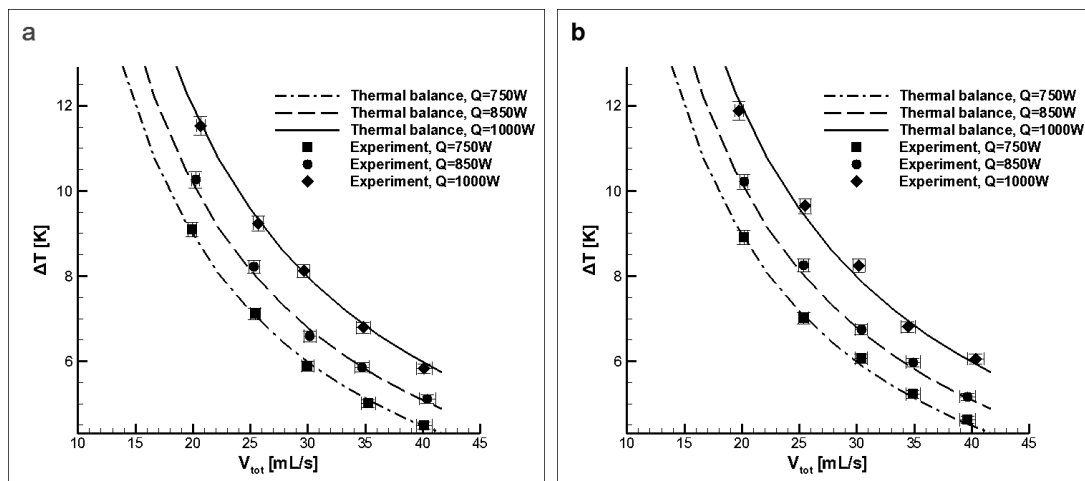


**Fig. 4.19** Comparison of the experimental data to thermal balance predictions for various flow and heat rates: (a) FW and (b) VW configuration.

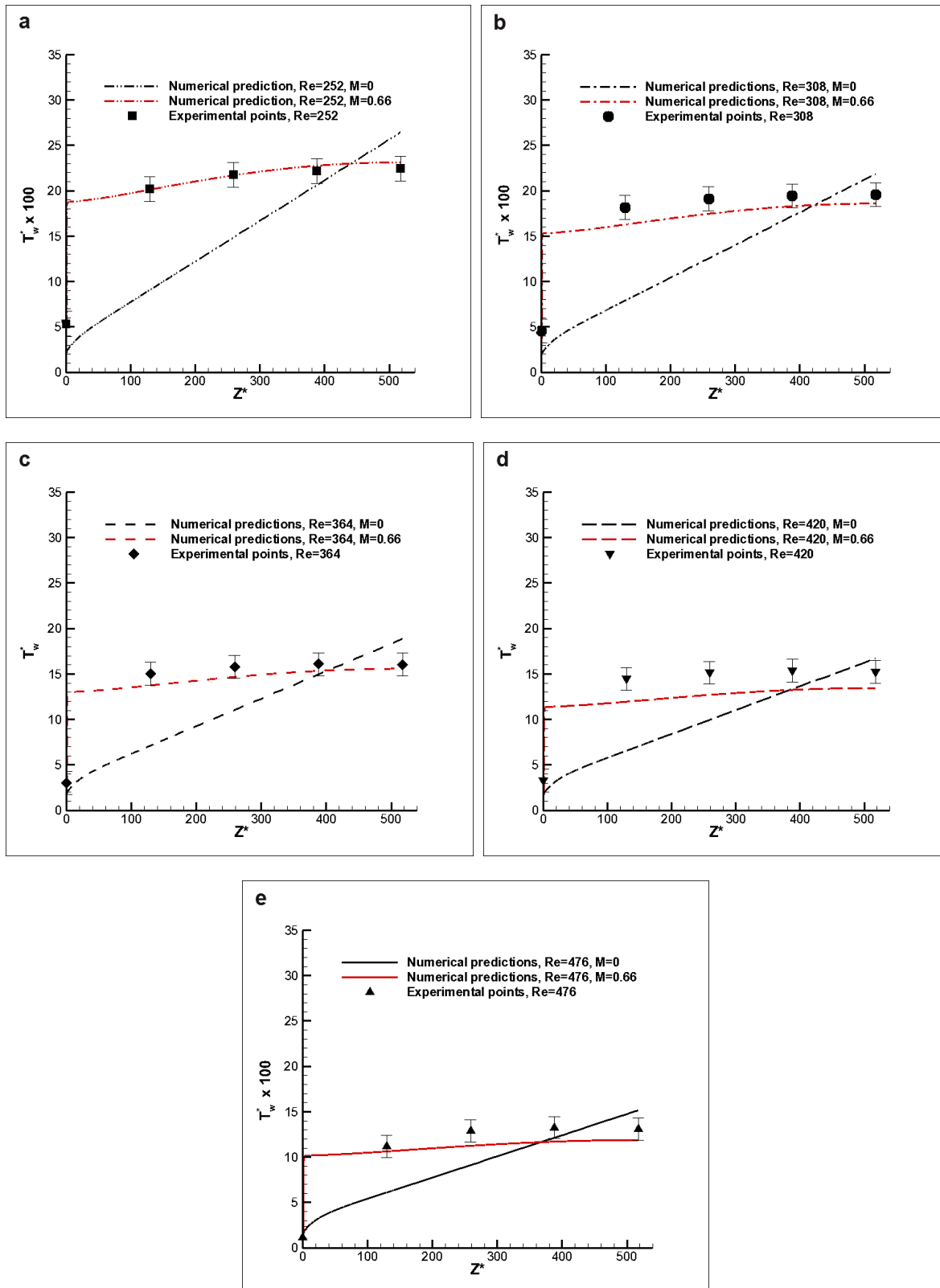
**Figs. 4.20 and 4.21** show the bottom wall streamwise temperature distribution of the two configurations for the flow rates considered (20-40 mL/s). The numerically predicted distribution for the FW configuration (**Fig. 4.20**) is typical for fully developed forced convection under constant heat

flux, as the solid temperature increases linearly along the streamwise direction. On the contrary, the experimental data illustrate a distribution that resembles that of constant temperature heating, with the exception of the experimental point at the heat-sink inlet. Nevertheless, the experimental values for the maximum temperature at the heat-sink outlet, which is directly related to the heat sink thermal resistance, are in agreement with the predictions. The deviation of the heat sink thermal behavior in the part prior to the channel mid-length is probably due to the heat flux “smearing” by axial conduction in the solid substrate. Some aspects of manufacturing imperfections were identified as possible causes. On the one hand, the overall width of the manufactured device is larger by 0.54 mm than the theoretical one, calculated for 49 channels with dimensions depicted in **Fig. 4.5a**. It is therefore possible that some microchannels have a larger width than others. On the other hand and more importantly, the microchannels could not be fabricated in a single passage of the milling machine due to the limited length of the milling table. For this reason, microchannels were machined at approximately three-quarters of the heat sink active length, the device was rotated and the machining along the remaining channel length continued with a second passage. Vibrations were detected at the end of the first passage, as the milling table reached its limit, which could lead to non-uniform machining of the channels. It is thus possible that the channels have a non-uniform cross section in that specified region due to vibration and, in addition, a slight misalignment of the device for the second passage could also distort the channel cross-section. The emergence of axial conduction in the substrate due to the non-ideal geometry would result to heat transfer from the “hot” part of the device closer to the outlet to the respective cold one closer to the inlet, as is the case actually observed.

The effect of axial conduction can be quantified with the use of a non-dimensional number [4.45], defined as:

$$M = \frac{k_s t_s / L_{hs}}{\rho c_p H_{ch} \bar{w}} \quad (4.21)$$

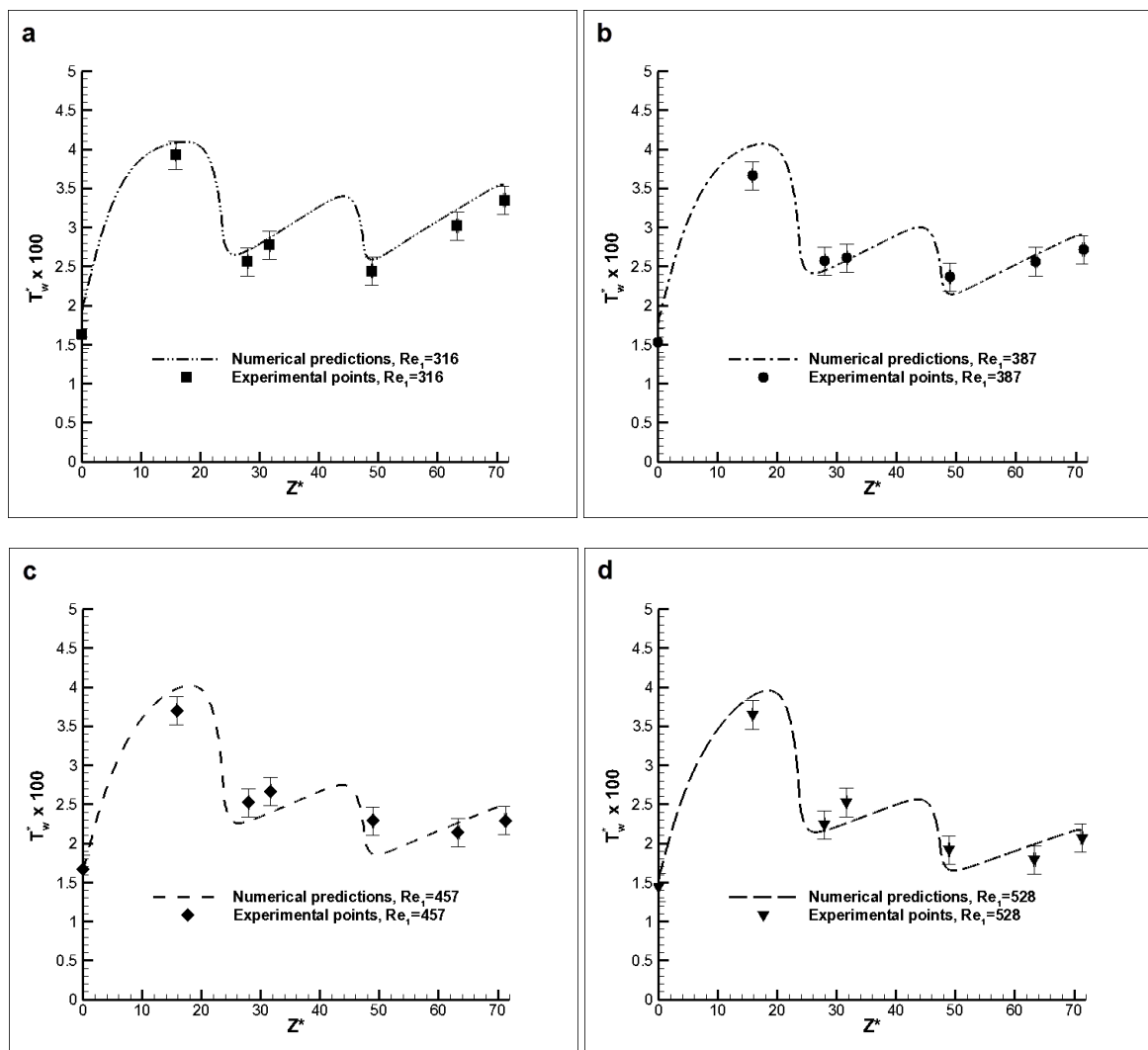
where  $k_s$ ,  $t_s$  are the substrate thermal conductivity and thickness, respectively, and  $\bar{w}$  is the mean axial flow velocity within the heat sink. Additional numerical simulations were conducted with gradually increased values of the  $M$  parameter, in order to illustrate the effect of axial conduction on the temperature distribution of the bottom wall. In agreement to the findings of Davis [4.46], it was found that the temperature of the bottom wall becomes more uniform along the streamwise coordinate as  $M$  increases. The temperature distributions for  $M=0.66$  are also depicted with a red line in **Figs. 4.20a-e**. It is evident that the numerical results are in good agreement with the experimental data, justifying by this way the assumption that axial conduction is the cause for the temperature uniformity of the heat sink substrate.

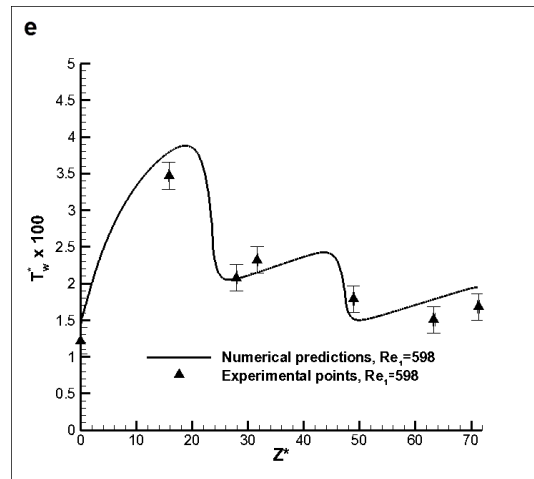


**Fig. 4.20** Streamwise temperature distribution at the channel bottom wall of the FW configuration for: (a)  $Re=252$ , (b)  $Re=308$ , (c)  $Re=364$ , (d)  $Re=420$ , (e)  $Re=476$ .

In reference to Fig. 4.21, the experimental values and the numerical predictions for the VW configuration follow the same trend, with the maximum temperature point being located, in all cases,

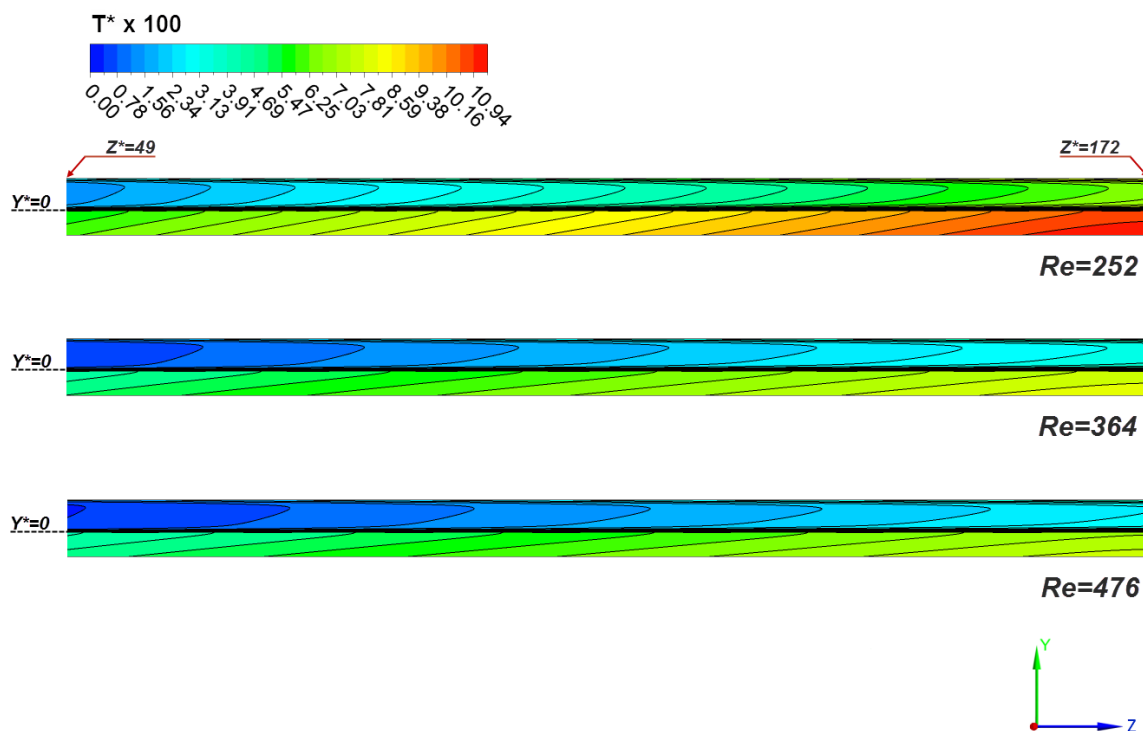
at the part of the first heat-sink section upstream of the effect of the first contraction. This trend is justifiable as the first section of low-fin density is expected to have high thermal resistance due to the smaller heat transfer area. In general, good agreement is evident between the predictions and the experimental data. As also revealed by **Fig. 4.21**, the maximum wall temperature remains relatively unaffected by the variation of the Reynolds number. The mitigation of the hotspot temperature as the value of the Reynolds number decreases is due to the increasing effect of free convection within the first heat sink section. As depicted in **Fig. 4.17**, the magnitude of the buoyancy induced rolls increases as the Reynolds number decreases and thus the Archimedes increases compensating for the hindering effect of the lower flow velocity on heat transfer. In comparison, the difference in the maximum temperatures obtained, e.g. for  $Re_1=316$  and  $Re_1=598$ , in the following heat sink sections, where forced convection conditions dominate, is substantially larger.





**Fig. 4.21** Streamwise temperature distribution at the channel bottom wall of the VW configuration for: (a)  $Re_1=316$ , (b)  $Re_1=387$ , (c)  $Re_1=457$ , (d)  $Re_1=528$ , (e)  $Re_1=596$ .

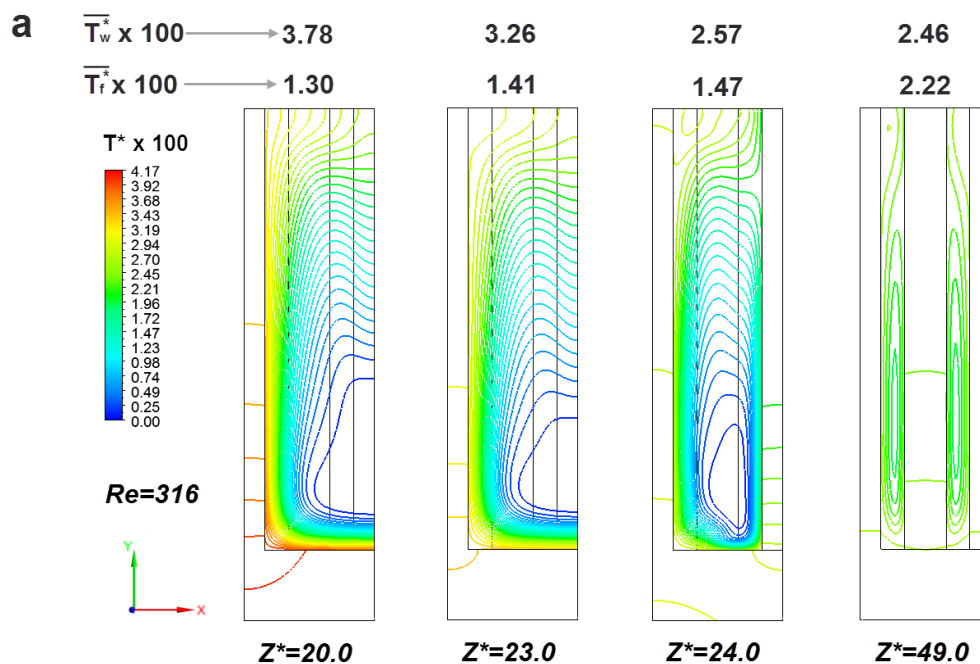
The temperature field in the FW configuration is elucidated through contour plots on the channel longitudinal symmetry plane, as shown in **Fig. 4.22**. The contours clearly indicate pure forced convection conditions as temperature stratification is absent. Besides, it is interesting to notice that the peaks of the contours are shifted toward the upper wall due to the non-uniform heating, as the fluid is primarily heated from the channel bottom wall, whereas the top wall is considered adiabatic. It is also evident that the flow reaches full thermal development in all cases, indicated by the identical form of the contours that appear prior to the channel outlet. Thus, it is justified that the truncation of the unit cell length had no effect on the produced numerical solution.



**Fig.4.22** Contour plots of the longitudinal temperature distribution along the channel vertical symmetry plane in the FW configuration.

In regard to the temperature field of the VW configuration, the effect of natural convection in the first section ( $Z^*=20.0$  and  $23.0$ ) is evident for  $Re_i=316$  (Fig. 4.23a), as significant temperature stratification exists with warmer fluid having been transferred to the channel upper part. A low temperature core is shown to develop near the bottom of the channel. As the Reynolds number increases, temperature stratification becomes less pronounced and the temperature profile obtains a form typical of forced convection conditions. A comparison between the locations  $Z^*=20.0$  and  $Z^*=23.0$  reveals that the bottom boundary layer is subject to cooling due to the flow separation slightly upstream of the contraction (see paragraph 3.4.3.6). Downstream of the flow constrictions (at  $Z^*=24.0$  and  $Z^*=49.0$ ), the contour lines at the lower and upper parts of the channel are skewed due to the effect of the horseshoe vortices. Especially regarding the second section channel ( $Z^*=24.0$ ) the bottom boundary layer is cooled as cold fluid from the channel core is drawn to that region, and thus heat transfer is enhanced.

The length of the second section was found to be adequate for any disturbances in the flow and temperature fields to decay and the flow to recover its purely parallel form prior to the next contraction. In any case the fluid core region is pushed toward the channel top causing redistribution of thermal energy. In reference to the lateral thermal boundary layers, their thickness decreases along consecutive sections, as the flow cross-section decreases and the fluid accelerates. The temperature contours also verify that the heat-sink solid part is cooled after each step-change of the channel hydraulic diameter, as additional heat transfer areas are added. A close look at the temperature contours within the third section ( $Z^*=49.0$ ) reveals that these are slightly asymmetrical. This is justifiable if we consider that the development of the thermal boundary layers at the channel sidewalls is not symmetrical as well. The development of the boundary layer of the left fin wall commences at the channel inlet and remains uninterrupted, whereas regarding the right side-fin wall the thermal boundary layer originates at the entrance to the second heat-sink section, where the additional fin intercepts the oncoming fluid free stream. Thus, for a specified location, the left sidewall boundary layer is of larger thickness in comparison to the respective right one.



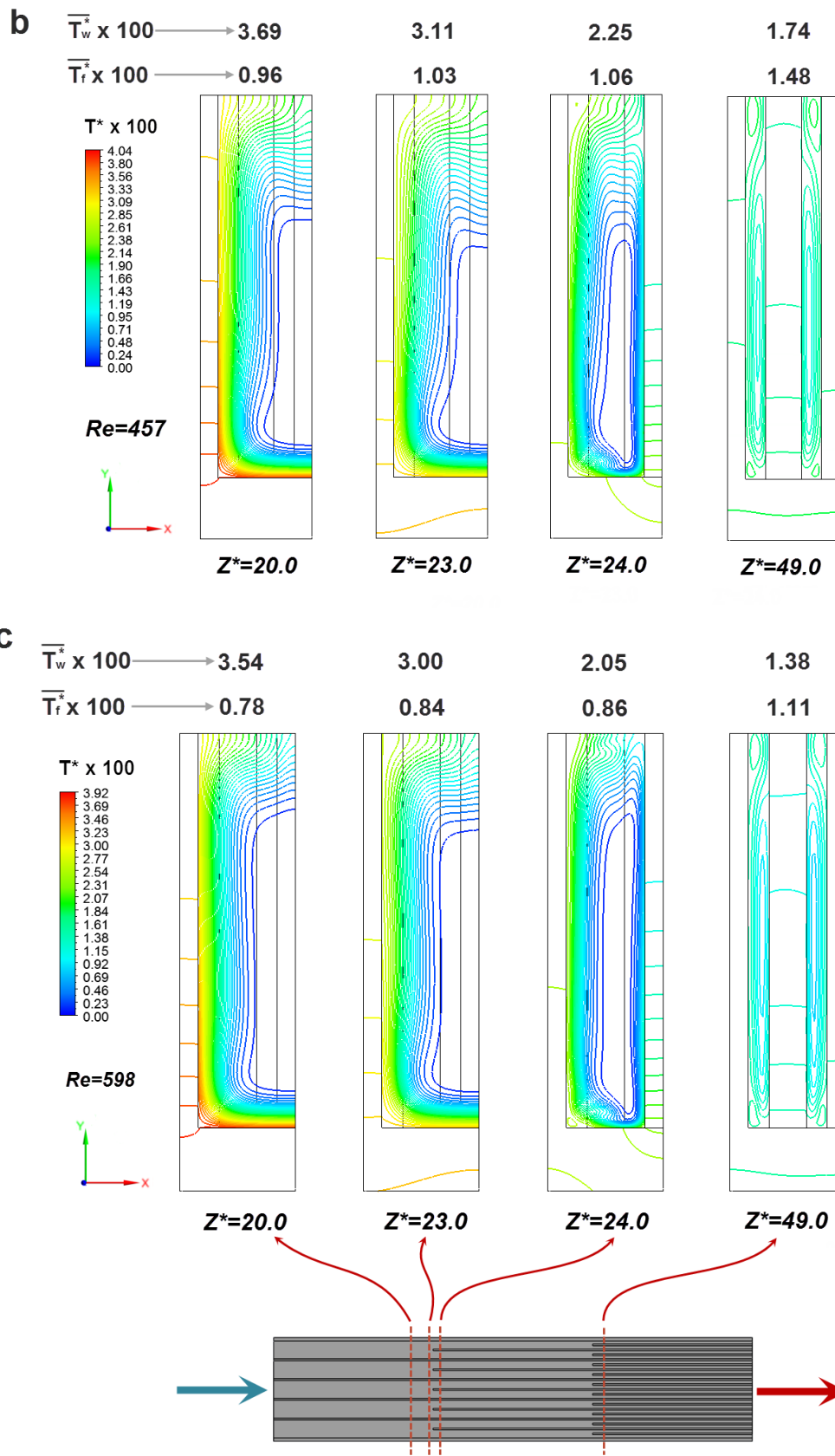


**Fig. 4.23** Temperature contour plots at cross-flow planes of increasing streamwise coordinate: (a)  $Re_1=316$ , (b)  $Re_1=457$  and (c)  $Re_1=598$ .

In order to quantify the local heat transfer rate, the circumferentially averaged Nusselt number distribution calculated by using the values of the local heat flux and the temperature distributions available from the numerical simulations. As depicted in Fig. 4.24a, the Nusselt number distribution in respect to the FW design exhibits the expected asymptotic behavior to a fully developed value, which is independent of the flow rate. The extent of the thermally developing flow region increases with the Reynolds number, as also do the values of the Reynolds in that region. However, the flow reaches full thermal development approximately at  $Z^*=80.0$  even for the highest value of the Reynolds number,  $Re=476$  and consequently fully developed conditions occur along the largest portion of the microchannel (at least 85% of the total length).

The form of the Nusselt number distribution in the first section ( $Z^*<23.6$ ) of the VW configuration varies depending on the value of the Reynolds number (Fig 4.24b). For the lowest considered value,  $Re_1=316$ , the distribution exhibits a minimum point at approximately  $Z^*=12.0$ , a behavior typical of mixed convection conditions that prevail due to the large channel hydraulic diameter in the specific section. As the Reynolds number increases, the Archimedes number decreases and thus the distribution shifts to a monotonical behavior. It is interesting to note that the overall Nusselt number is higher for the lowest Reynolds number value due exactly to the beneficial effect of the buoyancy rolls on heat transfer.

The Nusselt number retains almost constant and relatively high values through the larger part of the second heat-sink section due to the action of the longitudinal vortices that cause redistribution of thermal energy. The distribution for  $Re_1=316$  exhibits a slightly increasing plateau, which indicates that the effect of free convection is non-negligible. For the other two Reynolds numbers, the constant Nusselt number values obtained exceed the theoretical one by 46-49% [4.23].

Regarding the third heat sink section, an undershoot in the distribution is clearly discernible in the initial part of the channel. The Nusselt number subsequently recovers to a fully developed value, which is independent of the Reynolds number and is in agreement with the theoretical value ( $Nu_{FD}=7.24$ ) [4.23]. As discussed in paragraph 5.2 the effect of the secondary flow in the third section is negligible and it is thus expected the Nusselt number to obtain the value of fully developed parallel flow.

As illustrated in Fig. 4.24c, a significant flux reversal occurs at the entrance of the third section of the heat sink (regions A' in Fig. 4.24c) due to the step change of the channel hydraulic diameter and this is the cause for the observed undershoot of the Nusselt number values. It is evident that the flux reversal becomes more pronounced for increasing values of the Reynolds number. The fluid within the heat-sink is constantly heated, whereas the solid bottom wall experiences a rapid cooling in the locations of flow contraction. Therefore, in the boundary layer regions, the elevated fluid temperature can locally exceed the respective wall temperature and consequently the heat flow direction is reversed. On the other hand, in the regions under the influence of the horseshoe vortex (regions A in Fig. 4.24c) the local heat flux obtains very high values, over 4.5 times higher than the average flux value in the specific section.

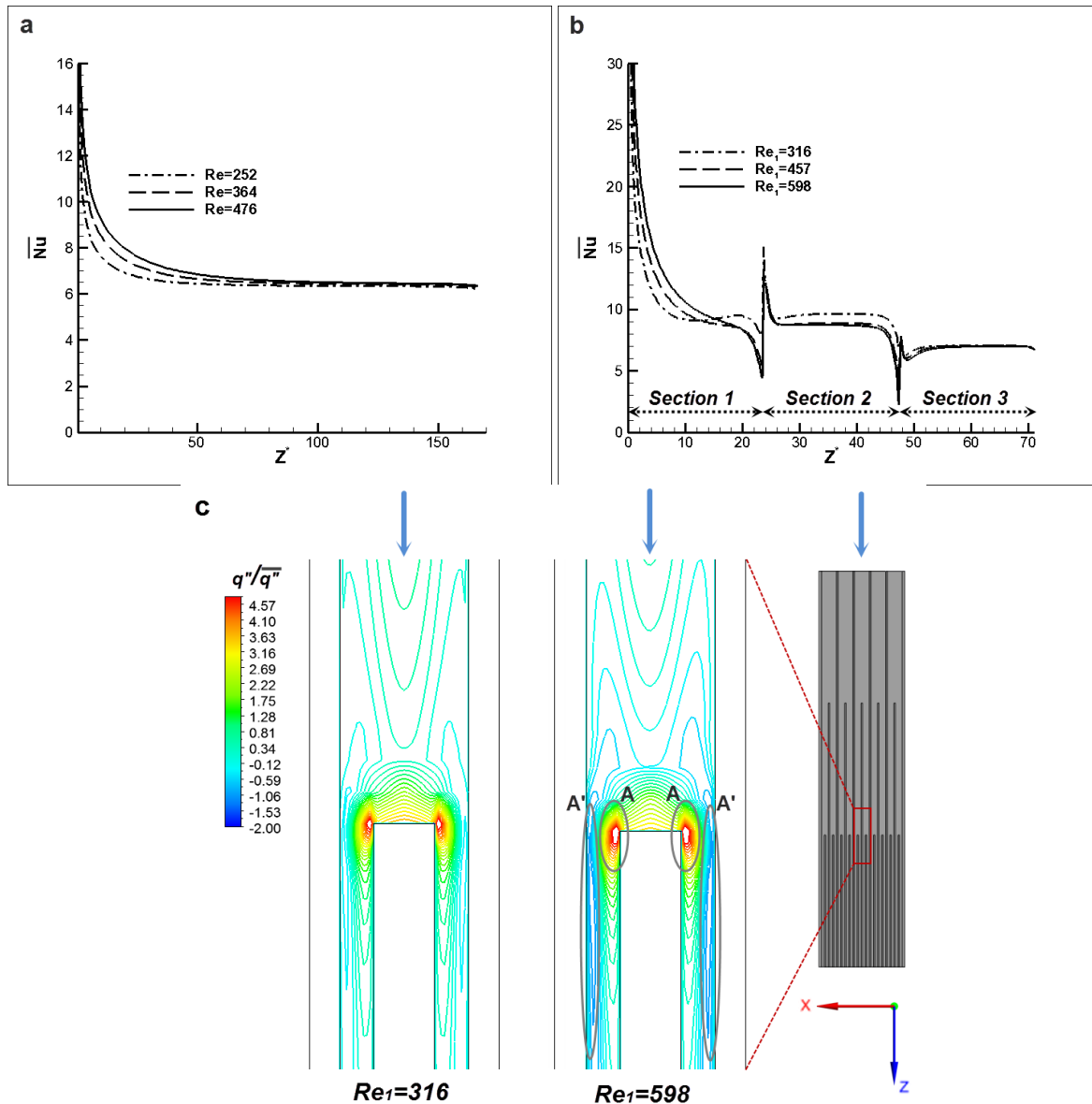


**Fig. 4.24** Distribution of the circumferentially averaged local Nusselt number for (a) the FW and (b) the VW configuration. (c) Contour plots of the wall heat flux at the region of the second flow contraction.

#### 4.9.3 Comparative evaluation of the FW and VW designs.

The two cooling configurations were comparatively evaluated, in terms of energetic and exergetic performance, in order to point out the merits and drawbacks of each design. The values of the heat sink thermal resistance for the two devices are presented in **Fig. 4.25a**. It must be noted that the thermal resistance for the VW design was calculated using both **Eqs. (3.35)** and **(3.42)**, which are based on the wall average and maximum (hotspot) temperatures, respectively. In general the FW configuration achieves lower thermal resistance values primarily due to the larger available heat transfer area and additionally due to the higher channel flow velocity, in comparison to the respective VW one. As can be seen,  $R_{th,eq.(3.42)}$  remains relatively unaffected by the Reynolds number at a value of 0.015-0.016 K/W, whereas  $R_{th,eq.(3.35)}$  decreases with the Reynolds number due to the fact that the wall average temperature decreases as well. The thermal resistance values based on **Eq. (3.35)** indicate

that, from a conservative point of view, the VW configuration achieves a heat transfer performance equivalent to the respective FW.

As depicted in **Fig. 4.25b**, the required pumping power for the FW device increases exponentially with the Reynolds number; on the other hand, the increase in the values regarding the VW device appears to occur in a nearly linear fashion. In any case, the pumping power values in the latter case are lower by as much as an order of magnitude due to the negligible pressure drop in the first two, reduced-fin-density sections of the VW device. This difference could have a vital impact on the parasitic power losses of applications, where long heat sink arrays are required, such as in the case of linear CPVT systems.

For the geometrical parameters of the manufactured heat sinks (channel hydraulic diameter and length), the entropy generation rate and thus the exergetic performance of the devices is determined mainly by the thermal resistance, as the effect of pumping power is minor. As depicted in **Fig. 4.25c**, the entropy generation rate follows the same trend as the thermal resistance. The Bejan number (see **paragraph 3.6**), in the case of the VW device is practically equal to 1.0 regardless of the flow rate, while it ranges between 0.982 and 0.997 for the FW device.

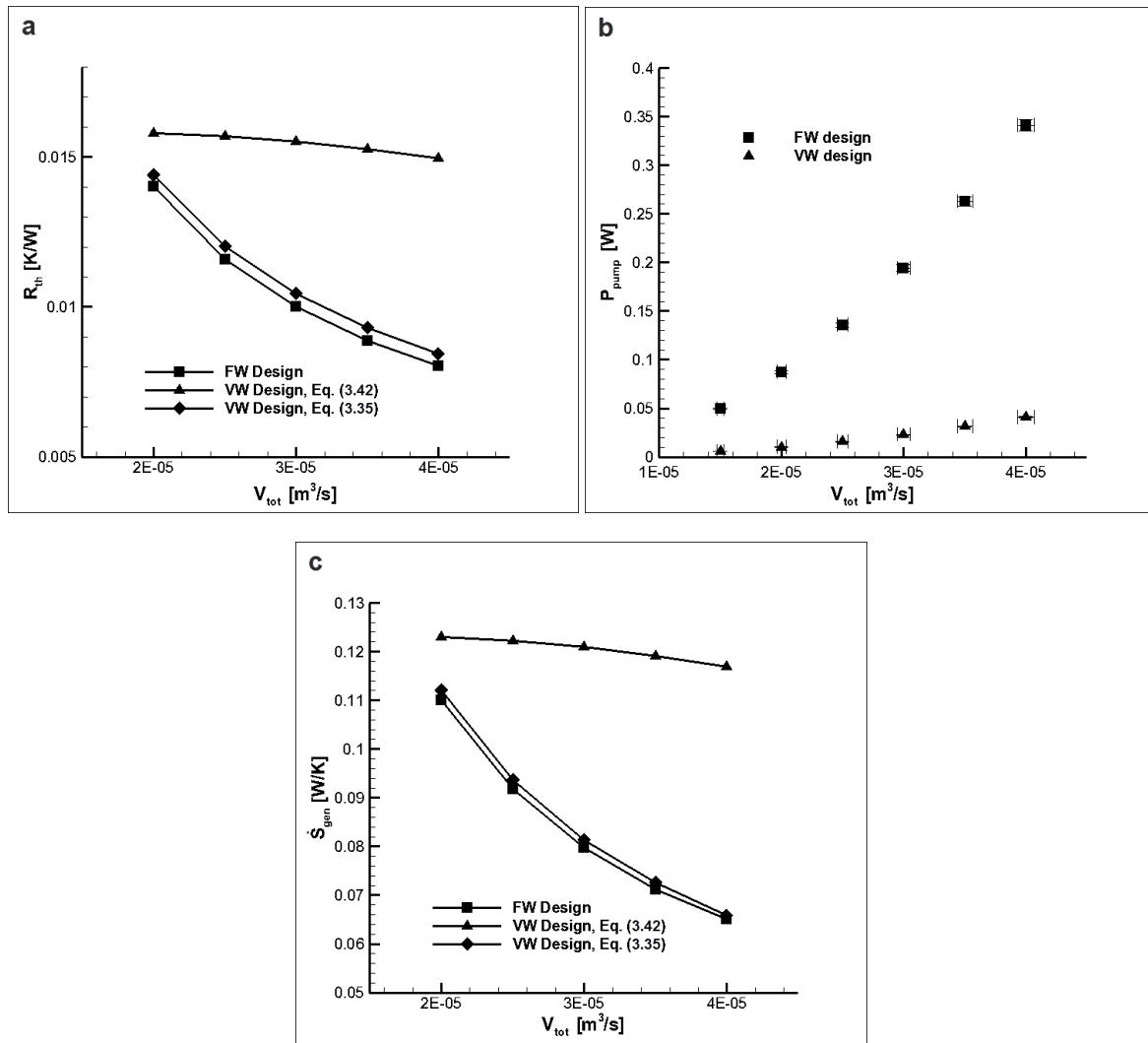


**Fig. 4.25** Comparative evaluation of the two heat sinks: (a) Thermal resistance, (b) required pumping power, (c) entropy generation rate.

In conclusion, it is essential to point out that the thermal behavior of the VW cooling device is particularly attractive as the hotspot temperature can be specified by a proper optimization procedure and it can be unconditionally controlled for a wide range of flow conditions. In applications such as electronics' cooling where the effectiveness of cooling is determined by the hotspot temperature, the incorporation of such a device can greatly reduce the parasitic power required for pumping.

#### 4.10 Effect of fouling on the heat-sink performance.

Fouling, i.e. the accumulation of impurities on the surface of the heat-sink channels can alter the flow geometry and increase the surface roughness thus affecting the hydrodynamic and thermal behavior of the heat sink in a significant manner. Referring to heat transfer, fouling adds a layer of poor thermal conductivity material (deposits) to the heat transfer area. Consequently, an additional thermal resistance accounting for the heat conduction in the fouling layer must be taken into account. The effect of fouling on pressure drop stems from the decrease of the duct internal diameter, which can be reduced to a value  $D_{h,f}$ , due to the fouling layer:

$$D_{h,f} = D_h \cdot \exp\left(-\frac{2\pi k_f R_f}{D_h}\right) \quad (4.22)$$

where  $k_f$  and  $R_f$  are the fouling thermal conductivity and fouling resistance, respectively. Typical values of the fouling resistance for various industrial applications are available in [4.47]. The decreased hydraulic diameter leads to increased flow velocity in the duct, in comparison to the nominal one for a specified flow rate, and thus to increased pressure drop. The values of the Fanning friction factor could also be affected by the fouling deposits [4.47]. Fouling was detected in both heat sink configurations after the conclusion of the experimental evaluation (Fig. 4.26). Since tap and not ionized water flowed within the heat sinks during the evaluation procedure, the occurrence of fouling could not be impeded as the channels of both configurations are of small cross-sectional area and furthermore the maximum fluid velocity obtained was less than 0.7 m/s, whereas for cooling water the minimum flow velocity to prevent fouling has been proposed to be over 1.2 m/s [4.48]. Nevertheless, no signs of any significant thermal or hydrodynamic performance deterioration were detected during the experimental tests.

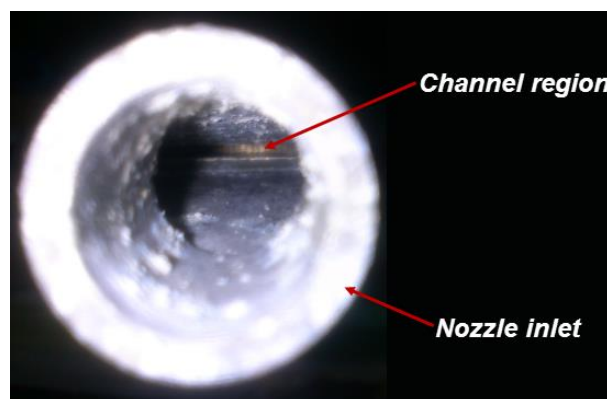


**Fig. 4.26** Fouling evident at the inlet of the FW configuration after the completion of the experimental evaluation.

### Chapter references

- [4.1] T. M. Harms, M. J. Kazmierczak, F. M. Gerner, Developing convective heat transfer in deep rectangular microchannels, *Int. J. of Heat and Fluid Flow* 20 (1999) 149-157.
- [4.2] N. Goldberg, Narrow channel forced air heat sink. *IEEE Transactions on Components Hybrids and Manufacturing Technology CHMT-7* (1984) 154-159.
- [4.3] R.W. Knight, J.S. Goodling, D.J. Hall, Optimal thermal design of forced convection heat sinks- Analytical. *J. Electron. Packag.* 113 (1991), pp. 313-321.
- [4.4] S. Lee, W. Qu, Thermal design methodology for low flow rate single phase and two-phase micro channel heat sinks, *IEEE Trans. Comp. Packag. Tech.* 30 (2007), pp. 830-841.
- [4.5] D. Liu, S.V. Garimella, Analysis and optimization of the thermal performance of microchannel heat sinks, *Int. J. Num. Methods Heat Fluid Flow* 15 (2005) 7-26.
- [4.6] G. Türkalar, T. Okutucu-Özyurt, Dimensional optimization of microchannel heat sinks with multiple heat sources, *Int. J. Therm. Sci.* 62 (2012) 85-92.
- [4.7] A. Bejan, *Shape and Structure, from Engineering to Nature*, Cambridge University Press, New York, 2000, pp. 29-41.
- [4.8] T. Bello-Ochende, L. Liebenberg, J.P. Meyer, Constructal cooling channels for micro-channel heat sinks, *Int. J. Heat Mass Transf.* 50 (2007) 4141–4150.
- [4.9] Y.S. Muzychka, Constructal design of forced convection cooled microchannel heat sinks and heat exchangers, *Int. J. Heat Mass Transf.* 48 (2005) 3119–3127.
- [4.10] Y. Jaluria, Simulation-based optimization of thermal systems, *Appl. Therm. Eng.* 29 (2009) 1346–1355.
- [4.11] L. Gosselin, M. Tye-gingras, F. Mathieu-potvin, International Journal of Heat and Mass Transfer Review of utilization of genetic algorithms in heat transfer problems, *Int. J. Heat Mass Transf.* 52 (2009) 2169–2188.
- [4.12] S. Bureerat, S. Srisomporn, Optimum plate-fin heat sinks by using a multi-objective evolutionary algorithm, *Eng. Optim.* 42 (2010) 305-323.
- [4.13] D. Copiello, G. Fabbri, Multi-objective genetic optimization of the heat transfer from longitudinal wavy fins, *Int. J. Heat Mass Transf.* 52 (2009) 1167–1176.
- [4.14] R. Hilbert, G. Janiga, R. Baron, D. Thévenin, Multi-objective shape optimization of a heat exchanger using parallel genetic algorithms, *Int. J. Heat Mass Transf.* 49 (2006) 2567–2577.

- [4.15] A. Husain, K. Kim, Enhanced multi-objective optimization of a microchannel heat sink through evolutionary algorithm coupled with multiple surrogate models, *Appl. Therm. Eng.* 30 (2010) 1683–1691.
- [4.16] A. Husain, S.M. Kim, K.Y. Kim, Performance analysis and design optimization of micro-jet impingement heat sink, *Heat Mass Transf.* 49 (2013) 1613–1624.
- [4.17] X. Li, X. Hao, Y. Chen, M. Zhang, B. Peng, Multi-objective optimizations of structural parameter determination for serpentine channel heat sink, in: A.I. Esparcia-Alcázar et al. (Eds.) *Applications of Evolutionary Computation*, Springer Verlag, Heidelberg, 2013, pp. 449-458.
- [4.18] S. Baodong, W. Lifeng, L. Jianyun, C. Heming, Multi-objective optimization design of a micro-channel heat sink using adaptive genetic algorithm, *Int. J. Num. Methods Heat Fluid Flow* 21 (2011) 353–364.
- [4.19] S. Ndao, Y. Peles, M.K. Jensen, Multi-objective thermal design optimization and comparative analysis of electronics cooling technologies, *Int. J. Heat Mass Transf.* 52 (2009) 4317–4326.
- [4.20] L. Wang, B. Shao, H. Cheng, Multi-objective optimization design of multi-layer rectangle micro-channel heat sink for single-phase flow and heat transfer, *Adv. Mat. Res.* 709 (2013) 286–291.
- [4.21] K. Park, D. Choi, K. Lee, Numerical shape optimization for high performance of a heat sink with pin-fins, *Num. Heat Transf., Part A* 46 (2004) 909–927.
- [4.22] R.K. Shah, A.L. London, *Laminar Flow Forced Convection in Ducts: a Source Book for Compact Heat Exchanger Analytical Data*, first ed., Academic press, New York, 1978, pp. 196-222.
- [4.23] R.K. Shah, M.S. Bhatti, Laminar convective heat transfer in ducts, in: S. Kakac, R.K Shah, W. Aung (Eds.), *Handbook of Single Phase Convective Heat Transfer*, first ed., Wiley, New York, 1987, pp 3.31-3.52.
- [4.24] R.D. Blevins, *Applied Fluid Dynamics Handbook*, first ed., Van Nostrand Reinhold Company, New York, 1984, pp. 71-80.
- [4.25] R.K. Shah, A correlation for laminar hydrodynamic entry length solutions for circular and noncircular ducts, *J. Fluids Eng.* 100 (1978), 177-179.
- [4.26] D.B. Tuckerman, R.F.W. Pease, High-performance heat sinking for VLSI, *IEEE Electron. Dev. Letters* 2 (1981), 126–129.
- [4.27] N. V Queipo, R.T. Haftka, W. Shyy, T. Goel, R. Vaidyanathan, P.K. Tucker, Surrogate-based analysis and optimization, *Progr. Aerospace Sci.* 41 (2005) 1–28.
- [4.28] K. Deb, A fast and elitist multiobjective genetic algorithm: NSGA-II, *IEEE Trans. Evol. Comp.* 6 (2002), 182-197.

- [4.29] A. Konak, D.W. Coit, A.E. Smith, Multi-objective optimization using genetic algorithms : A tutorial, *Reliab. Eng. Syst. Safety* 91 (2006) 992–1007.
- [4.30] The Mathworks Inc., Genetic Algorithm and Direct Search Toolbox for use with MATLAB, User's Guide, Version 1, 2004, pp. 2.1-2.24.
- [4.31] E. Zitzler, K. Deb, Comparison of Multiobjective Evolutionary Algorithms : Empirical Results, *Evol. Comp.* 8 (1994), 173–195.
- [4.32] K. Amouzgar, Multi-objective optimization using genetic algorithms, Master Thesis, KTH University, Sweden, 2012.
- [4.33] The Mathworks Inc., Matlab online documentation, 2014 available at <http://www.mathworks.com/help/stats/kmeans.html>.
- [4.34] Z. Jian-hui, Y. Chun-xin, Z. Li-na, Minimizing the entropy generation rate of the plate-finned heat sinks using computational fluid dynamics and combined optimization, *Appl. Therm. Eng.* 29 (2009) 1872–1879.
- [4.35] W.A. Khan, M.B. Kadri, Q. Ali, Optimization of Microchannel Heat Sinks Using Genetic Algorithm, *Heat Transf. Eng.* 34 (2013) 279–287.
- [4.36] H. Abbassi, Entropy generation analysis in a uniformly heated microchannel heat sink, *Energy.* 32 (2007) 1932–1947.
- [4.37] N. Parlak, M. Gür, V. Arı, H. Küçük, T. Engin, Second law analysis of water flow through smooth microtubes under adiabatic conditions, *Exp. Therm. Fluid Sci.* 35 (2011) 60–67.
- [4.38] W.-J. Yang, T. Furukawa, S. Torii, Optimal package design of stacks of convection-cooled printed circuit boards using entropy generation minimization method, *Int. J. Heat Mass Transf.* 51 (2008) 4038–4046.
- [4.39] R. Chein, J. Chen, Numerical study of the inlet/outlet arrangement effect on microchannel heat sink performance, *Int. J. Therm. Sci.* 48 (2009) 1627–1638.
- [4.40] S.S. Sehgal, K. Murugesan, S.K. Mohapatra, Experimental Investigation of the Effect of Flow Arrangements on the Performance of a Micro-Channel Heat Sink, *Exp. Heat Transf.* 24 (2011) 215–233.
- [4.41] D. Kim, C.-H. Yu, S.H. Yoon, J.S. Choi, Effects of manifold geometries on flow distribution to parallel microchannels, *J. Mech. Sci. Technol.* 25 (2012) 3069–3074.
- [4.42] G. Kumaraguruparan, R.M. Kumaran, T. Sornakumar, T. Sundararajan, A numerical and experimental investigation of flow maldistribution in a micro-channel heat sink, *Int. Commun. Heat Mass Transf.* 38 (2011) 1349–1353.

[4.43] ANSYS Inc., ANSYS CFX-Solver theory guide, Release 13.0, Canonsburg, PA 2010.

[4.44] B.E. Launder, D.B. Spalding, The numerical computation of turbulent flows, *Comp. Meth. Appl. Mech. Energy* 3 (1974) 269-289.

[4.45] G. Maranzana, I. Perry, D. Maillet, Mini- and micro-channels: influence of axial conduction in the walls, *Int. J. Heat Mass Transf.* 47 (2004) 3993-4004.

[4.46] E.J. Davis, W. N. Gill, The effects of axial conduction in the wall on heat transfer with laminar flow, *Int. J. Heat Mass Transf.* 13 (1969) 459-470.

[4.47] S.Kakac, H. Liu, *Heat Exchangers: Selection, Rating and Thermal Design*, second ed., CRC Press, Boca Raton, 2002, pp. 159-165.

[4.48] K. Thulukkanam, *Heat Exchanger Design Handbook*, second ed., CRC Press, Boca Raton, 2013, pp. 483-484.

The design procedure followed and the materials and manufacturing processes selected for the realization of the CPVT system, a schematic of the main constituents and geometrical parameters of which is presented in **Fig. 5.1**, are thoroughly discussed in the present chapter. As was mentioned in the previous two chapters, the cooling system was designed assuming that the system module aperture area was equal to  $1.0\text{m}^2$ . Hence, the integrated CPVT system module was designed having this specified design variable as a basis. The rationale behind the selection of the main design parameters of the system, such as the aperture width and length, parabola rim angle, focal length, and the concentration ratio  $CR$  is illustrated below. The manufacturing materials for the system components were selected bearing in mind the module structural rigidity, reliable operation under varying environmental conditions and high optical quality, while also maintaining the overall cost moderate. The influence of the properties of the materials and the precision of manufacturing processes on the system performance is also elucidated.

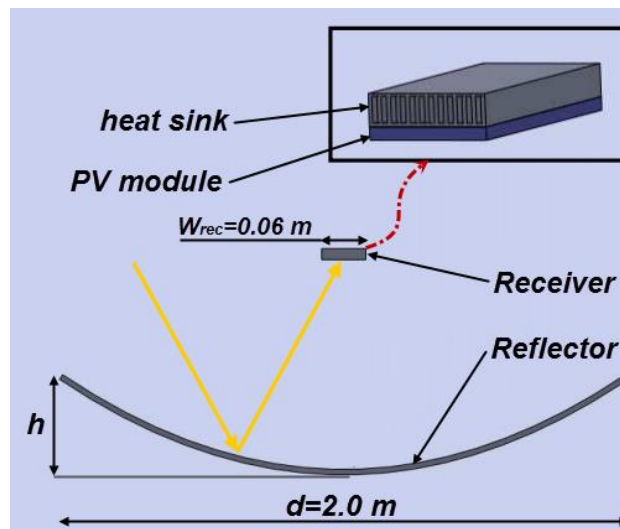


**Fig. 5.1** Schematic of the CPVT system

### 5.1 Selection of the parabola

The initial step of the design procedure was to determine the geometrical form of the parabolic optical device. Taking into account that the module aperture area and the receiver active length were constrained at  $1.0\text{m}^2$  and  $0.5\text{m}$ , respectively, the parabola width  $d$  must be equal to  $2.0\text{m}$  (see **Fig. 5.1**) and consequently the geometrical concentration ratio  $CR$  results equal to  $(d/W_{rec}) = 33.3$ . Thus, the geometrical shape can be fully defined if the focal length of the parabola is determined, which also designates the parabola height  $h$  and rim angle  $\psi_{rim}$ , as depicted in **Fig. 5.2** [5.1]:

$$h = \frac{d^2}{16f} \quad \tan \psi_{rim} = \frac{1}{(d/8h) - (2h/d)} \quad (5.1)$$

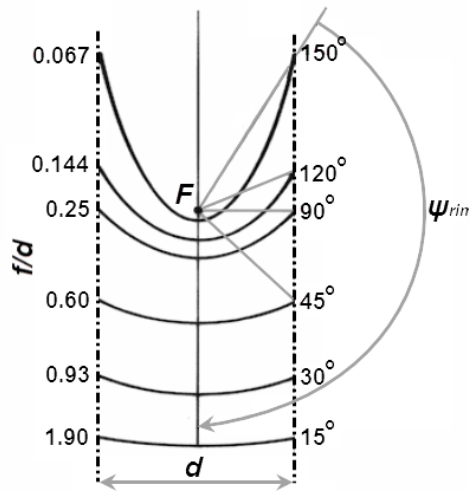
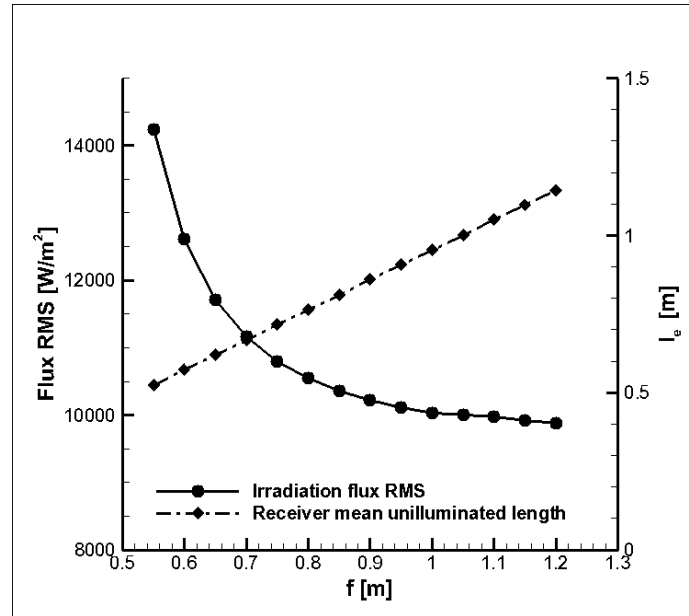


Fig. 5.2 Effect of the focal length on the shape of the parabola [5.1].

An initial limitation for the selection of the focal length  $f$  is posed by the receiver cross-section. The solar irradiation must be concentrated at the bottom surface of a flat receiver, i.e. the PV module, and therefore the ratio of the focal length to the aperture (parabola) width ratio  $d$  must be larger than 0.25 and consequently the rim angle smaller than  $90^\circ$ , according to Fig. 5.2. Evans [5.2], using a theoretical model, showed that the peak concentration ratio achieved at the receiver center line increases as the rim angle increases. In fact, as was shown by Hassan and El-Refaie [5.3], an increase of the trough rim angle from  $30^\circ$  to  $90^\circ$  leads to a twofold value of the maximum local concentration ratio. Thus, parabolic concentrators with a “flatter” form produce a more uniform irradiation distribution across the receiver width, which is beneficial in terms of solar cell efficiency. However, selecting a large focal length would result to increased end losses under non-perpendicular irradiation incidence and, from a structural point of view, increased height of the supporting brackets that would require additional material, in order for the brackets to be able to withstand the bending stress due to the receiver weight and possible wind loads.

A ray tracing simulation was conducted in order to elucidate the effect of the parabola focal length on the irradiation distribution on the receiver. The ray-tracing method is further discussed in paragraph 5.7.1. A parabolic trough of perfect shape was considered with aperture area equal to  $1.0\text{m}^2$ , while the reflectivity of the reflector was set equal to 0.95. Typical one-sun irradiation was considered ( $1.0\text{ kW/m}^2$ ), while the values of the focal length lied in the range  $0.55\text{-}1.2$  ( $f/d=0.275\text{-}0.6$ ). The irradiation non-uniformity was evaluated in terms of the root mean square (RMS) of the irradiation flux on the system receiver. As can be seen in Fig. 5.3, the decrease rate of the flux RMS becomes less steep as the focal length increases. It must be noted that the irradiation non-uniformity was evaluated for an axial displacement of the receiver that offers the most uniform profile attainable, as will be discussed in the following paragraph. The average non-illuminated length of the receiver for incidence angles between  $0\text{-}70^\circ$ , considering single axis tracking, is also presented in Fig. 5.3 and it is clearly shown to increase in a linear manner with the focal length between the values of  $0.48$  and  $1.14\text{m}$ .



**Fig. 5.3** Effect of the parabola focal length on the irradiation uniformity and the end losses.

Following the procedure proposed by Foli and Okabe [5.4], which was also discussed in paragraph 3.4 regarding the selection of the cooling fluid flow rate, the optimal value of the focal length taking into account only the flux uniformity criterion results equal to 0.73m; the actual focal length, however, was selected slightly smaller and equal to 0.69m for clearly practical reasons associated with the receiver axial displacement that produces uniform flux (see **paragraph 5.2**) and the manufacturing precision.

## 5.2 Position of the receiver

Smoothing the illumination distribution is an important objective for the design of concentrated solar power devices, as it benefits the cell performance [5.5] and deters the occurrence of hotspots on the receiver surface, especially if it is manufactured by a material of low thermal conductivity (e.g. stainless steel). Optical devices such as segmented parabolic or Fresnel reflectors and secondary optical devices, e.g. refractive prisms, have been proposed in order to smooth the irradiation distribution [5.6]. For a parabolic trough of specified geometry, it has been shown by Evans [5.2] that the illumination distribution profile becomes more uniform and the peak concentration ratio decreases as the receiver is shifted closer to the trough apex and thus the actual focal length is lower than the geometrical one. A similar trend is also followed in the case of a parabolic trough with vertical flat receiver, when the receiver is laterally shifted away from the focal point [5.7]. Therefore, the simplest way to enhance irradiation uniformity is to shift the receiver toward the parabola slightly off the focal line.

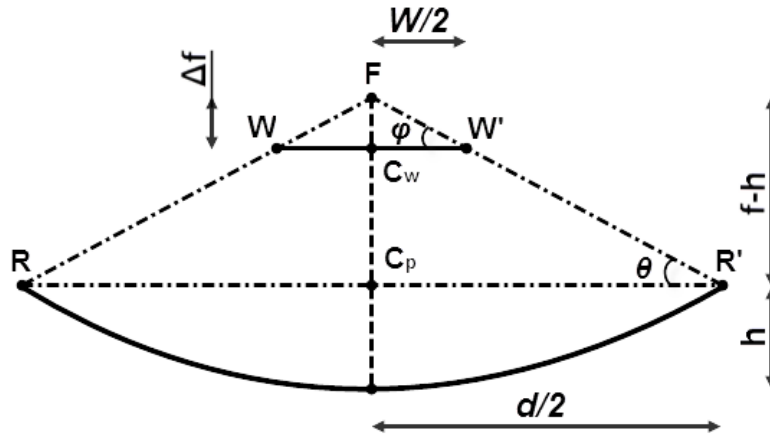


Fig. 5.4 Geometry of the parabola

For a perfect parabolic concentrator, if the receiver of width  $W$  is placed exactly at the focal spot  $F$  of the parabola, the focal line is considered to be of infinitesimal small width. The maximum receiver displacement  $\Delta f$ , **Fig. 5.4**, for which the solar band will be equal to the receiver width and thus the most uniform profile for an intercept factor equal to one will be produced, can be calculated based on the following relations:

$$\left. \begin{array}{l} \tan \theta = \frac{f-h}{d/2} \\ \tan \phi = \frac{\Delta f}{W/2} \end{array} \right\} \begin{array}{l} \hat{\phi} = \hat{\theta} \\ FC_p R' \sim FC_w W' \end{array} \rightarrow \boxed{\frac{\Delta f}{W/2} = \frac{f-h}{d/2}} \quad (5.2)$$

For a parabola of specified aperture  $d$  and focal length  $f$ , the maximum displacement for which the receiver of width  $W$  intercepts the entire solar irradiation band can be explicitly determined.

### 5.3 Supporting frame

A rigid metallic structure that realizes the parabolic shape of the reflector and supports the receiver at the focal spot has been designed and manufactured (**Fig. 5.5**). The structure comprises the frame, onto which the reflecting sheet and the receiver are seated, and the supporting arrangement, consisting of pillars and a circular base that is bolted to the ground. The reflector sheet is bolted on the parabolic profile of the frame, whereas the receiver container is allowed to be translationally displaced along the frame brackets and its final position can be fixed using screw-nut assemblies. The parabolic profile is supported through metallic ribs mounted on the frame main axle. The supporting arrangement also comprises two axle joints, which allow the frame to rotate around both the horizontal and vertical axes and thus two-axis tracking of the solar movement is possible. The parabolic frame was constructed of aluminum in order to be lightweight and hence facilitate the collector tracking, whereas the supporting base and pillars were constructed of steel in order to enforce the construction rigidity and furthermore to reduce the overall cost.

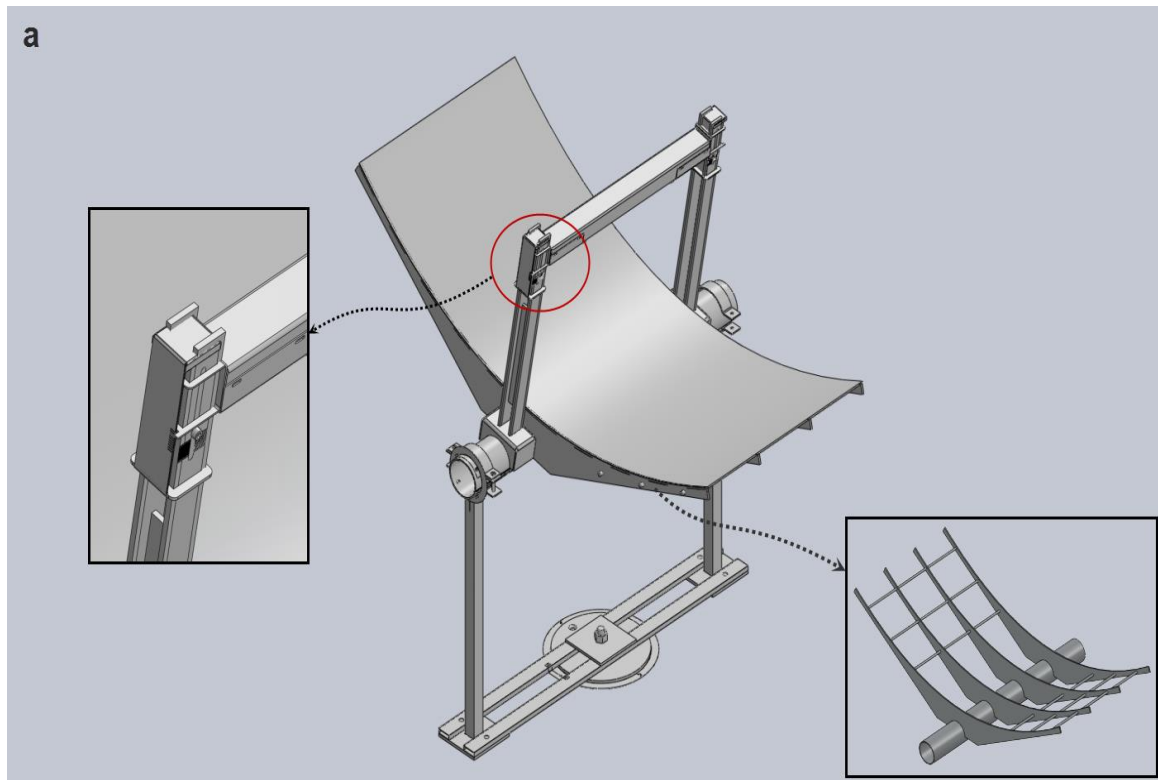


**Fig. 5.5** Metallic structure of the CPVT system: (a) CAD drawing and (b) photograph showing the frame constructed along with the main hydraulic and electrical connections.

The supporting pillars and base, apart from being capable of supporting the weight of the metallic frame, are also required to withstand stresses experienced due to wind loads. The Sandia Laboratory of the U.S.A. has specified that a parabolic trough collector structure should be able to survive 120 km/h wind in any position and operate in 40 km/h average wind [5.8]. A structural analysis was performed using the *Solidworks FE* solver [5.9], in order to obtain an estimation of the deformation and factor of safety (FOS) of the metallic frame and pillars under extreme loading conditions. The worst scenario, where the wind direction is perpendicular to the trough aperture, was considered, while also the wind pressure was calculated for a fairly high value of the drag coefficient equal to two. As depicted in Fig. 5.6, the frame sizing is clearly adequate for such a high level of wind loading, as the maximum deformation is less than 0.7mm and, in fact, is located at the thin aluminum plate, which can easily be replaced by a thicker one. In addition, the minimum factor of safety (Fig. 5.6b) is equal to 16.2, much higher than the commonly used values, and located at the two middle ribs.

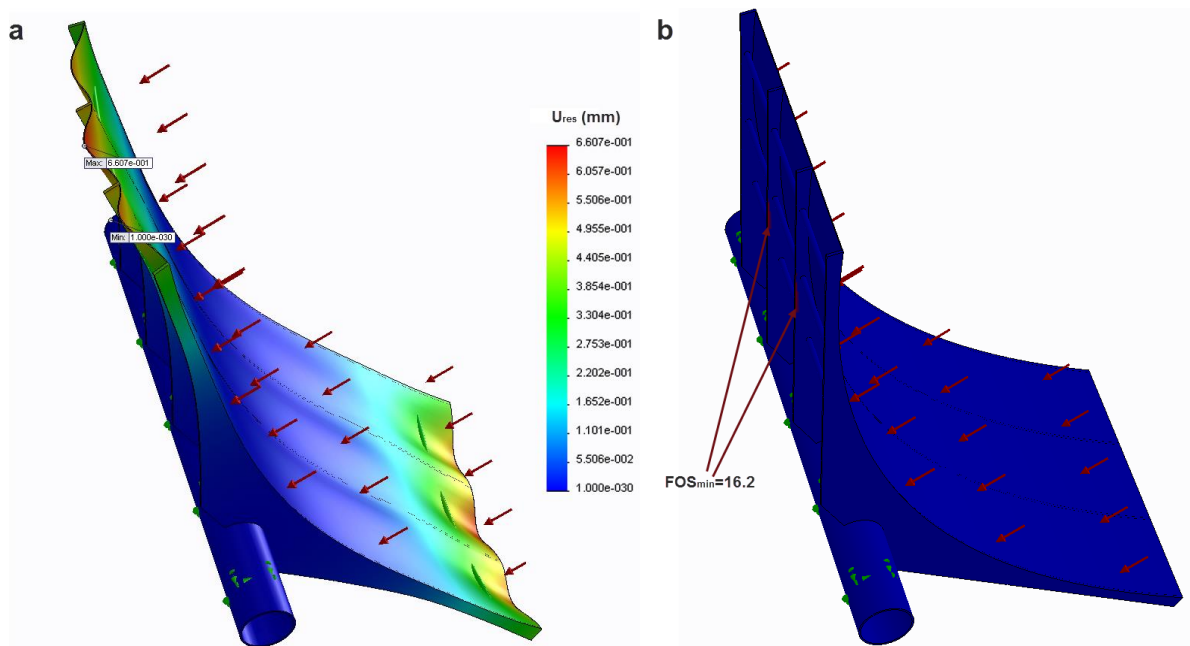


**Fig. 5.6** (a) Deformation and (b) Factor of Safety (FOS) of the metallic frame for wind load corresponding to velocity of 120 km/h (wind pressure equal to 1361 N/m<sup>2</sup>).

However, the bending stresses due to wind load experienced by the supporting pillars are much more dangerous for the integrity of the system. The pillars have a hollow, square cross section of thickness 10mm, in order to reduce the raw material used, height approximately equal to 1.0m and are constructed of plain steel. The force imposed by the wind load on the frame aperture is divided between the two pillars and is considered to produce a bending moment only. Fig. 5.7 illustrates the pillar deformation and factor of safety for wind load corresponding to velocity of 120 km/h. As can be seen the pillar deformation (Fig. 5.7a) is an order of magnitude higher in comparison to the frame and the structure is marginally safe with a factor of safety equal to 1.7. However, for wind velocity of 40km/h the minimum factor of safety was calculated equal to 14.7. The pillars were constructed with the aforementioned height so that the trough could be turned into “stow” position on windy days and

thus eliminating any hazard due to extreme wind load. In any case the structural rigidity of the pillars can be increased by increasing their cross-sectional thickness or decreasing their height.

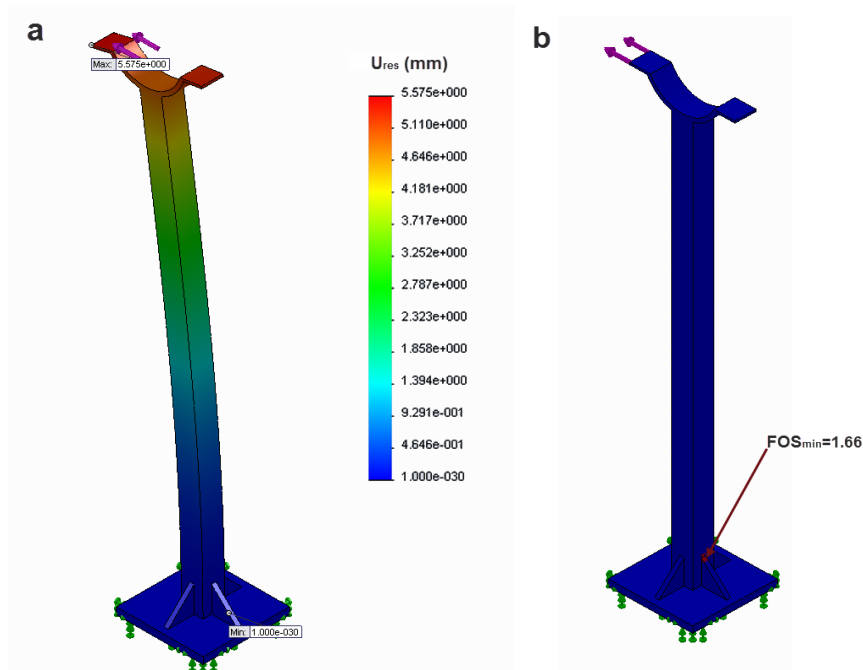


**Fig. 5.7** (a) Deformation and (b) Factor of Safety (FOS) of the supporting pillar for wind load corresponding to velocity of 120 km/h (force at the upper pillar edge equal to 1375 N).

#### 5.4 Reflector sheet

Commercially available anodized aluminum sheets (Miro95) by *Alanod Solar* were used as reflectors [5.10]. The sheets have an additional coating, applied through a Physical Vapor Deposition (PVD) process on the aluminum surface. This additional coating increases the sheet total reflectivity in comparison to plain anodized aluminum and also allows it to maintain an approximately constant value for the entire visible light spectrum, as depicted in **Fig. 5.8**. The sheets average total reflectance is equal to 95%, while their specular reflectance is approximately equal to 92% [5.10]. The reflectors parabolic shape is imposed by the supporting frame, as the sheet is flexible due to its small thickness ( $t=0.5mm$ ) and can be easily clamped on the parabolic surface of the aluminum frame, using two aluminum strips that run the entire reflector length to ensure that the sheet obtains the correct parabolic form.

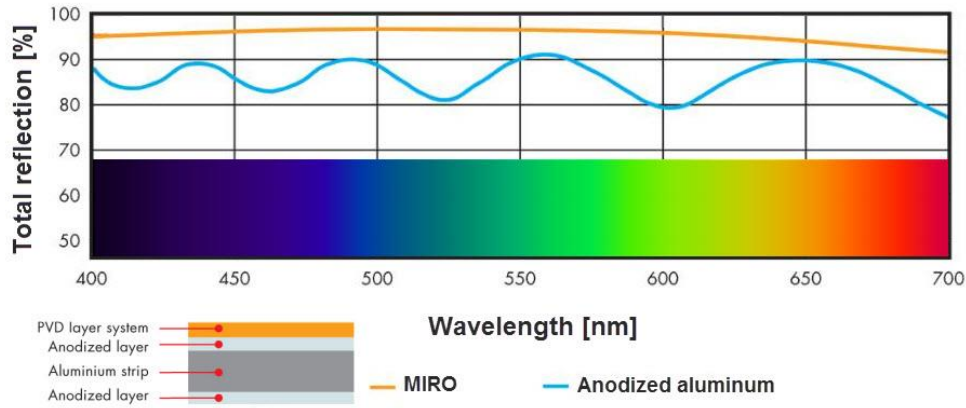


Fig. 5.8 Miro95 sheet reflectance with irradiation wavelength.

### 5.5 Optical losses and slope error

The optical efficiency of the CPVT system is primarily influenced by the properties of the materials used, such as the reflectivity of the mirror, the transmissivity of the glass cover and the reflectivity of the solar-cell front contact, and the optical errors associated with the system. The optical errors are due to the manufacturing precision of the reflector material sheets (percentage of non-specular reflection) and the parabolic frame, the misalignment of the receiver with respect to the focal line and the misalignment of the system aperture with respect to the sun caused by tracking errors. In general, these errors are assumed to be random and are reported in standard deviation units. Their combined effect is represented by normal probability (Gaussian) distributions with zero mean [5.1].

The characterization of the concentrator surface shape and optical quality is a complicated task that can be accomplished only experimentally and requires imaging systems of high resolution and especially developed test rigs. The most commonly used methods of surface characterization are the VSHOT method, photogrammetry and deflectometry [5.11]. An additional method reported by Stynes [5.12] that also makes use of high resolution photography is the distant observer method.

The non-ideal shape of the reflector and misalignment errors lead to a distorted flux distribution on the receiver, spreading of the reflected light beam and possible solar radiation spillage, as the solar rays could be reflected outside of the receiver overall width. These optical losses determine an optical quality parameter referred to as the intercept factor  $\gamma$ , which is defined as the percentage of the irradiation on the reflector aperture that is incident on the receiver active area. Optical losses are expected to be more significant than thermal losses for concentrating systems operating in low temperatures, under 100°C. Although the intercept factor is important for the evaluation of the performance of a concentrating collector, its direct determination is a rather complex procedure due to the many contributing factors. Of these factors, the greatest influence is attributed to the reflector profile, characterized by surface slope error [5.12]. The surface slope error of a parabolic profile is defined as the angular difference between the measured surface normal and the surface normal for an ideal parabolic shape [5.12] (Fig. 5.9). The effect of the reflector slope error on the achieved peak concentration was elucidated by Evans [5.2], who showed that an imperfect mirror with slope error standard deviation equal to 0.25° achieves a maximum concentration that is approximately 66% lower compared to a perfect mirror. However, the irradiation distribution becomes more uniform. The

existence of slope errors on the concentrator surface gives rise to focal errors defined as the vertical distance of the vector of a reflected ray from the geometrical focal point (distance  $\varepsilon$  in **Fig. 5.9**) [5.13]. Focal errors are the true cause for the widening of the focal band and consequently a more accurate estimate of the system geometrical concentration ratio, compared to the simple  $d/W$  ratio is provided by the following expression:

$$CR = \frac{d}{d_{band}} \quad (5.3)$$

where  $d_{band}$  is the width of the light band at the focal line.

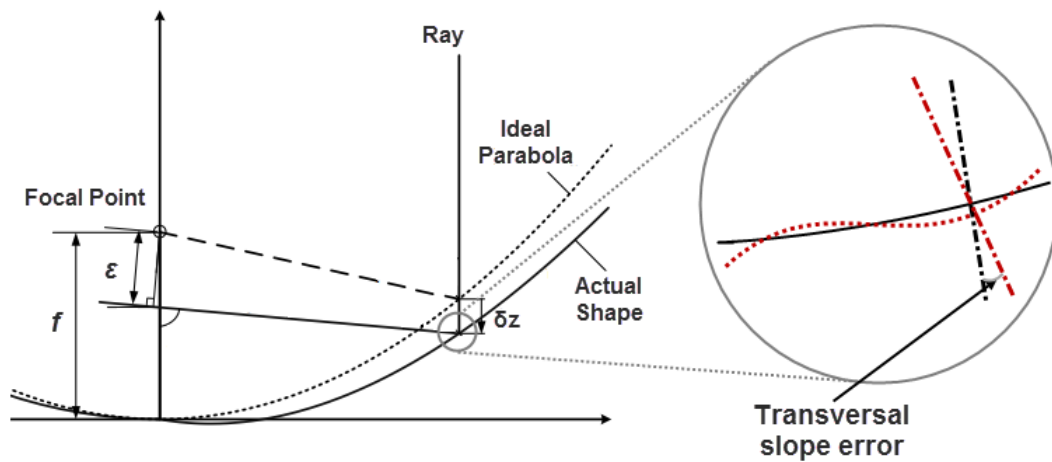


**Fig. 5.9** Slope and focal errors of a parabolic concentrator.

## 5.6 Solar Tracking mechanism

### 5.6.1 Obtaining normal incidence

Since sun tracking is performed manually it is of vital importance to make certain that the sunlight is properly focused on the system receiver. For this reason three separate configurations have been employed to adjust the rotating-base (longitudinal) and fame-axis (transversal) angles, so that normal incidence is obtained. Firstly, scales have been placed on the system circular base and the frame longitudinal shaft to facilitate the adjustment of the longitudinal and transversal angles. In addition, a device resembling a sundial, comprising a cylindrical rod vertically mounted on an aluminum disc, has been placed on a steel bar protruding from the frame shaft that follows the frame movement (see **Fig. 5.5b**). The device has been properly calibrated and circles have been engraved on the disc in such a way that the intersection of the shade of the rod with a circle reveals the angle of incidence. Besides, a photodiode (Vishay BPW34) of small aperture and high resolution, so that even small variations in the solar irradiation intensity can be detected, was placed at the top surface of one of the frame brackets. The procedure to obtain normal incidence at a specified time commenced by setting the main shaft and base angles at appropriate values corresponding to the sun azimuth and altitude, which can be calculated using simple equations, available in [5.14]. The reading of the mechanical device was consulted to verify the absence of any shade on the disc and thus normal incidence. Finally, small

adjustments on the transversal angle were made when necessary, based on the photodiode signal. It must be noted that the tracking procedure was carried out with the reflecting area being covered, in order to protect the receiver and wiring and tubing from misaligned concentrated irradiation

### 5.6.2 System orientation

It is common practice in the case of linear parabolic thermal collectors to perform single axis tracking, along their main axis, as the integrated system length can be much larger than the respective width and hence two-axis tracking would require massive rotating bases accompanied by high parasitic power for tracking. Consequently, orientation is an additional factor that affects the system performance. Two options for the system orientation are usually considered with the system having its main axis either along the east-west (E-W) or the North-South (N-S) axis. The system orientation that leads to higher annual yield depends on the geometrical layout of the system, e.g. system length to width ratio and focal length to width ratio, and primarily on the latitude of the location site [5.15, 5.16]. As was discussed in **paragraph 2.7**, the collecting efficiency of single-axis tracking systems is decreased due to the effect of cosine and end losses. It has been established through the theoretical model of Hegazy et al. [5.16] that a parabolic trough collector having its longitudinal axis oriented along the East-West axis achieves slightly higher annual collecting efficiency in comparison to having a North-South orientation for locations with latitude higher than 30°. In addition, the collecting efficiency for a trough oriented along the East-West axis is relatively uniform throughout the year and obtains its higher values during the winter months, where the demand for hot water is also higher. On the contrary, in the case of North-South orientation, the collecting efficiency obtains its higher and lower values in the summer and winter months respectively.

A ray-tracing analysis (see **paragraph 5.5.1**) was conducted for a (0.5 x 2.0) m<sup>2</sup> concentrating system considering three characteristic days of the year, namely the spring equinox, winter and summer solstices, in order to illustrate the daily yield for each (E-W or N-S) orientation. A time period from 08:00 to 17:00 (solar time) was considered in all cases and values for the direct irradiation were obtained from meteorological data available for Athens (latitude 38°). The results for the daily collected energy are presented in **Fig. 5.10a**. As can be seen, a collector having its main axis oriented along the E-W axis, achieves larger daily energy output in the spring equinox and the winter solstice, whereas the N-S oriented collector significantly outperforms the respective E-W oriented one in the summer solstice. It is interesting to notice that the output of the N-S oriented collector is almost zero in the winter solstice. In general, the output for E-W orientation exhibits much less variation in the three days considered compared to the N-S orientation.

The ray-tracing results can be explained by considering the variation of the irradiation incidence angle (**Eq. 2.13**) on the collector throughout the day for the two orientations, as depicted in **Fig. 5.10b**. An initial observation is that the incidence angle variation for the E-W orientation remains relatively constant regardless of the day considered, which is not the case for the N-S orientation. In addition, for the E-W orientation, the incidence angle is equal to zero at solar noon throughout the year, while it obtains large values in the morning and evening hours. On the contrary, the incidence angle for the N-S orientation has a yearly variation and obtains its minimum and maximum values in the summer and winter solstices, respectively; nevertheless the maximum incidence angle of the day occurs at solar noon. Hence, an E-W oriented collector operates well in the hours around the solar noon, while its

performance drops significantly in the morning and evening hours; a trend which is maintained throughout the year. A N-S oriented collector instead, operates better in the morning and evening hours. Especially in the summer, where the irradiation intensity is high throughout the day, the N-S orientation is justified to be preferable, as the incidence angle maintains low values throughout the day as well. The opposite is true for winter months, where the solar intensity is significant only in the hours around solar noon and therefore the E-W orientation, which leads to small incidence angles in the hours 11-13, is a far more attractive option as a N-S oriented receiver has a negligibly small daily output. The annual output for latitudes  $30^{\circ}$ - $40^{\circ}$  is approximately the same for the two orientations [5.16] and consequently the E-W orientation appears as a more attractive choice due to the increased performance in periods of the year with low insolation and ambient temperature. Moreover, the daily angular displacement of the reflector trough for tracking is much smaller for the E-W orientation, which could have a considerable effect on maintenance cost.

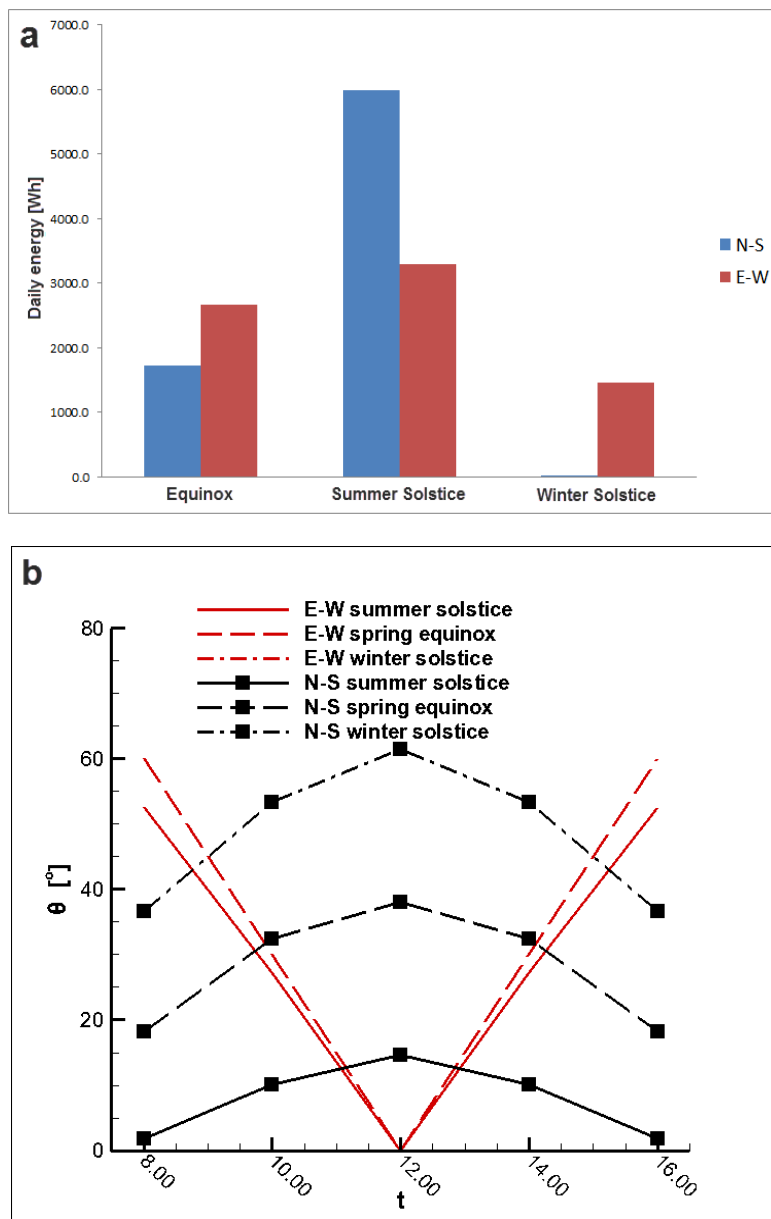


**Fig. 5.10** (a) Daily collected energy for a  $1.0 \text{ m}^2$  system. (b) Variation of the irradiation incidence angle throughout the day.

## **5.7 System optical analysis**

### **5.7.1 Ray-tracing**

Ray-tracing is a numerical approach widely used for the prediction of the optical behavior of concentrating devices having various geometrical layouts. Gregory and Koshel [5.17] used the ray-tracing technique in order to simulate the operation of two CPV systems utilizing a Fresnel lens and a compound parabolic concentrator, respectively, for different irradiation intensities. Solar irradiation was modeled as monochromatic, considering that the optical devices do not alter the solar light spectrum. Hongfei et al. [5.18] used ray-tracing to evaluate the optical efficiency of a novel trough reflector with a cross-section that comprises a paraboloid and a linear part. The percentage of rays reaching the receiver for various irradiation incidence angles was determined for two receiver designs, viz. flat or cylindrical. Hernandez et al. [5.19] conducted a parametric study and obtained the optimal geometrical parameters for a cavity receiver of conical shape by means of ray-tracing simulations. The average flux on the receiver and the receiver intercept factor were selected as the optimization objectives. Jiang et al. [5.20] developed a ray-tracing code in order to evaluate the optical performance of a parabolic trough CPVT system with an additional spectral splitting optical device. The system thermal receiver was placed at the parabola focal spot, while a solar cell array was placed at the parabola apex. The irradiation flux distribution on the receiver, the cell array and the beam splitting filter was determined and a parametric study was conducted in order to maximize the system optical efficiency. Dye [5.21] performed a ray-tracing analysis in order to design a refractive secondary optical device intended for incorporation in a paraboloid concentrating CPV system in order to split the infrared irradiation part from the solar spectrum. Besides, Dai et al. [5.22] developed a Monte Carlo ray-tracing code in order to evaluate the optical efficiency and the intercept factor of a three-dimensional CPC reflector, which is formed if the typical cross-section of a CPC reflector is rotated along its main axis, for various irradiation angles of incidence.

A ray-tracing analysis was conducted in reference to the designed CPVT system, in order to predict the irradiation profile on the receiver for both ideal and imperfect concentrators. The effect of the receiver axial displacement on the flux distribution has also been taken into account. The analysis was performed with the ray-tracing software TracePro [5.23], which utilizes the Monte Carlo method to predict the propagation of solar rays. In Monte Carlo ray tracing, discrete samples of the light distribution, in the form of rays, are propagated instead of an integrated distribution. At each intersection of the rays with a solid object, individual rays can be subject to absorption, reflection, refraction, diffraction and scattering, with scattering and diffraction being treated as random processes. The samples are randomly chosen and hence a reliable solution is obtained by tracing a large number of rays. As the rays propagate along different paths throughout the solid model, the irradiation flux associated with each ray is recorded by the software in each intersecting surface [5.23].

A simplified geometrical model of the CPVT system was created, by omitting the supporting frame and base, and appropriate material properties were assigned to the system reflector and receiver, respectively. The solar irradiation was modeled as a circular sun source where all the radiation originates within a disc of radius 1.25m, so that the flux density will be uniform in the reflector aperture for a large number of rays. A proper flux value was assigned to each ray so that the overall emitted irradiation flux is maintained equal to  $1.0 \text{ kW/m}^2$ . The system receiver was modeled as a

perfect absorber ( $a=1.0$ ), as the focus is on the optical quality of the concentrator. In reference to the parabolic concentrator, two cases were considered, i.e. a perfectly specular mirror and an imperfect mirror that also induces light scattering (non-specular reflectance) due to surface and shape irregularities. In general, both specular and non-specular reflections occur simultaneously to some extent and the term “reflectance” is used for the ability of a material to reflect light in any manner [5.1].

Light scattering by a surface can be quantified using the Bidirectional Scattering Distribution Function (BSDF), which is defined as the scatter radiance per unit incident irradiance [5.23]:

$$BSDF = \frac{G_{scat} / \Omega}{G \cos \theta} \quad (5.4)$$

where  $G_{scat}$  is the scattered irradiation within a solid angle  $\Omega$ , and  $\theta$  is the angle between the normal and a scattered ray (see Fig. 5.11).

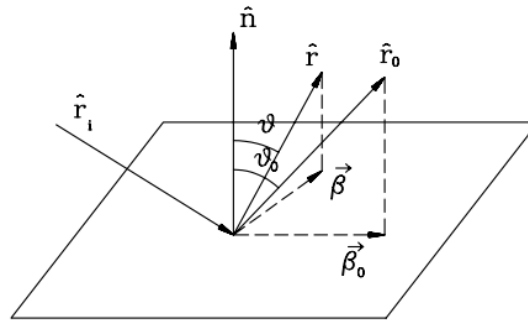


**Fig. 5.11** Geometrical representation of light scattering ( $\hat{r}_i, \hat{r}_0, \hat{r}$ : unit vectors of an incident, specularly reflected and scattered ray, respectively.  $\vec{\beta}, \vec{\beta}_0$  projections of  $\hat{r}$  and  $\hat{r}_0$  on the tangent plane).

The ABg model [5.23] is used by TracePro in order to approximate BSDF, as follows:

$$BSDF(\vec{\beta} - \vec{\beta}_0) = \frac{A}{B + |\vec{\beta} - \vec{\beta}_0|^g} \quad (5.5)$$

where  $\vec{\beta}, \vec{\beta}_0$  are the projections on the tangent plane of the unit vectors along the scattering ( $\hat{r}$ ) and the specular directions ( $\hat{r}_0$ ) respectively (Fig. 5.11). A, B, and g are coefficients to fit the produced formula values to specified scattering data. As depicted in Fig. 5.12a, for a BSDF value equal to zero all the rays are reflected to the focal line and there is no flux spillage; on the contrary when the reflector induces non-specular reflection as well ( $BSDF > 0$ ), depicted as blue rays in Fig. 5.12b, a part of the incoming radiation misses the receiver and thus the intercept factor and the optical efficiency of the system decreases.

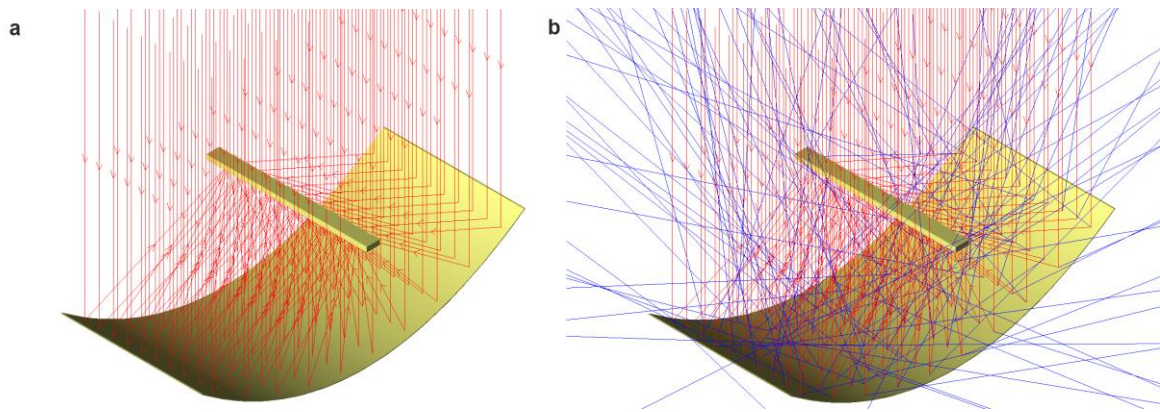


**Fig. 5.12** Pattern of reflected rays from the parabolic concentrator: (a) BSRDF=0, (b) BSRDF>0 (red rays: specular reflection, blue rays: light scattering)

### 5.7.2 Measurement of the heat flux on the receiver

There are few studies in the literature that present sensor devices suitable for measuring the irradiation distribution on the receiver of concentrated solar power systems. Coventry [5.24] used a custom-built device to measure the longitudinal irradiation profile along the receiver of a parabolic trough CPVT system. The device comprised a concentrating solar cell bonded to a fin heat sink and mounted on a moving carriage. Localized flux non-uniformity was detected in the focal-line sections affected by the shading of the support posts and the gap between mirrors. In general, the flux measurements in conjunction to slope error measurements using the photogrammetry method demonstrated that small deviations from the parabolic shape cause significant non-uniformity in the irradiation distribution. Riffelmann et al. [5.25] managed to measure the intercept factor and the optical losses of the EUROTROUGH solar thermal collector prototype using a grid of photodiodes with translucent filters mounted on a carriage that was positioned along the receiver length with the use of a linear actuator. Pihl and Thapper [5.26] measured the transversal irradiation distribution on the receiver of a low-concentrating CPVT system using a device comprising a photodiode mounted on a rotating base. The test device was custom-made at the University of Lund. Chong and Yew [5.27] illustrated the manufacturing procedure of a novel flux scanner employing photodiodes. An array of 25 photodiodes was mounted on a metallic frame that was able to move along two dimensions, producing thus a grid of measuring points. The frame was moved by a stepper motor that received a control signal to proceed to the next position, after the photodiode array signal was recorded. The produced irradiation maps showed good agreement with actual CCD camera depictions for both artificial and solar light.

In order to measure the transversal and longitudinal irradiation flux distribution on the receiver, a measuring device has been developed comprising an array of photodiodes properly mounted on the bottom surface of a rectangular hollow beam, as depicted in Fig. 5.13. The sensors are unable to detect the spatial non-uniformity of light irradiance within their active area; consequently a sensor of small size is required, especially when measuring the transversal distribution, which exhibits high variation within a short length. Photodiodes with rectangular aperture ( $5.4 \times 4.3$ ) mm<sup>2</sup> were used with tinted glasses as filters in order to prevent overheating under concentrated sunlight. The tinted glasses also served as light attenuators in order to ensure that the photodiode response was well below the saturation region. Light collimators were placed on the tinted glasses to cut out the diffuse part of the

irradiation so that the photodiode mainly detects the beam component of the light and also to prevent the filters from overheating and rupture. A highly reflective Mylar tape was adhered on the collimators in order to further reduce the heat absorbed by the filters. It was verified that the filters could remain up to three minutes under concentrated sunlight prior to rupture, which is an adequate time interval to obtain meaningful results regarding the concentration. It must be noted that two variations of the measuring device were developed for measuring the longitudinal and transversal irradiation distributions, respectively. In regard to the longitudinal-measurement configuration, the distance between consecutive sensors was equal to 0.125 m and five photodiodes were placed to cover the entire receiver active length. Filters of circular aperture with diameter of 5.0 cm were placed over the photodiodes. In order to measure the transversal irradiation flux profile, five photodiodes were housed in holes drilled into an aluminum plate of dimensions 124 x 62 x 5 mm, which was subsequently mounted at the bottom face of the beam. The intermediate distance between sensors was equal to 15.0 mm, with the middle sensor being located exactly and the receiver mid-width. The plate was able to slide along the beam length allowing the measurement of the transversal profile at different longitudinal locations. A rectangular tinted glass was placed on the plate to serve as filter, while the collimator had a narrow slit with width of 8 mm midway along its length.

The signal of the photodiodes can be measured either as voltage or current. However current output is linearly proportional to the incident light power per unit area and hence is selected as output signal. The concentration ratio values were calculated by dividing the output of the photodiodes under concentrated sunlight by the output of a photodiode placed at the upper surface of the device and therefore measuring the direct, one-sun irradiation, as shown in **Fig. 5.13**.

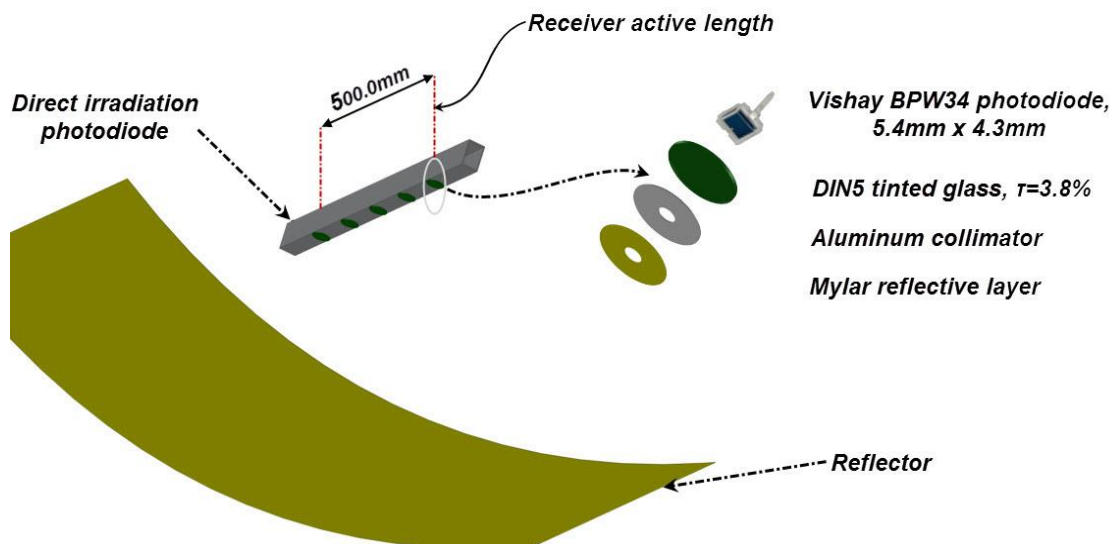


**Fig. 5.13** Schematic of the device used for measuring the incident radiation on the system receiver.

Prior to the concentration measurements, the linearity and signal uniformity of the sensors were tested. The photodiodes were left under direct sunlight without filters so that high values of the output signal can be obtained. As depicted in **Fig. 5.14a**, the photodiode response remains linear in a wider

irradiation range than the expected operating range and thus the output values can be directly used to determine the local concentration ratio.

In addition the device was assessed under natural radiation with the filters on, in order to verify that all the sensors produce the same output current and that there is no significant systematic error in the measurement due to e.g. misalignment of the sensors or partial blockage due to the collimator. An overcast day was selected for the testing so that the sensor resolution and response time in rapid variations of the irradiation intensity can also be examined. The sensor output for the device configuration used for the measurement of the transversal distribution is depicted in **Fig. 5.14b** for a time interval with sunlight fluctuations. It is evident that the signals of all photodiodes follow the same trend and considerable light fluctuations can be captured. The signals of the sensors showed general agreement with the maximum discrepancy detected in both the transversal and longitudinal-measurement configurations (not shown for brevity) being approximately equal to 8%. This value (8%) will be used as the experimental uncertainty in the values of the concentration ratio presented in **paragraph 5.7.3**.

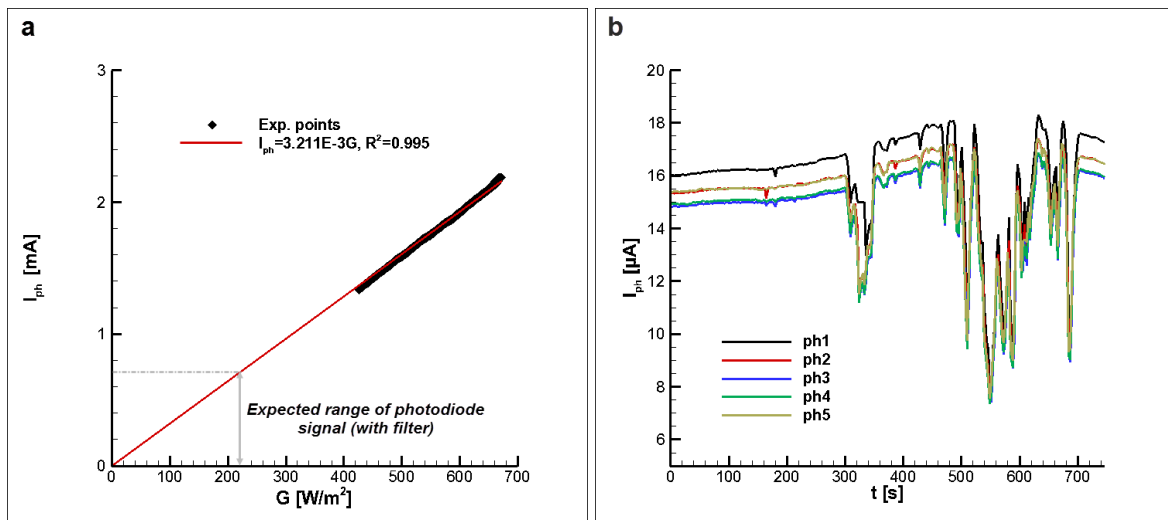


**Fig 5.14** (a) Sensor response for increasing values of solar irradiation. (b) Photodiodes signals (transversal-measurement configuration) for fluctuating solar radiation.

### 5.7.3 Irradiation flux distribution

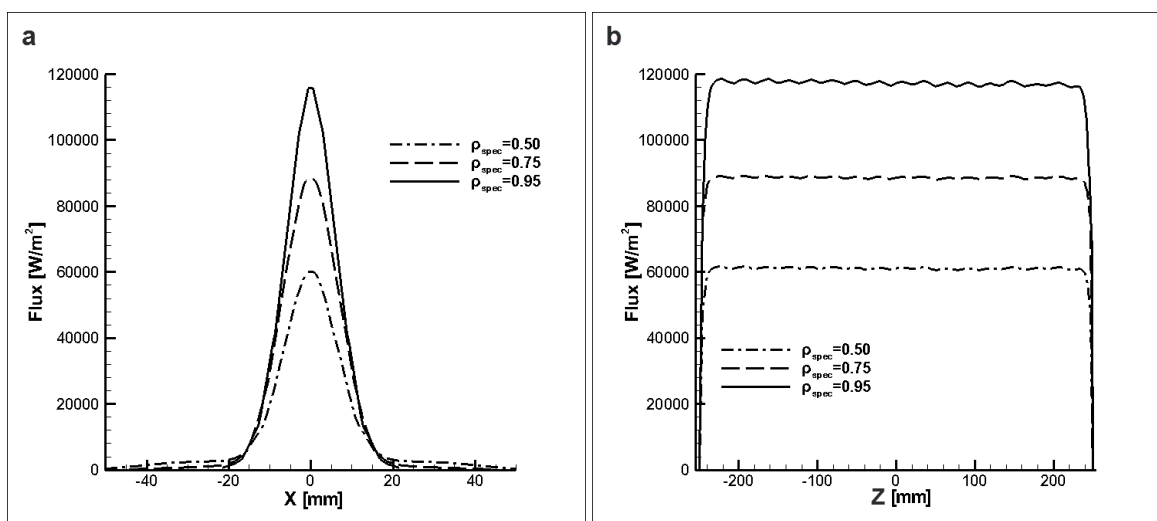
Ray-tracing simulations and measurements were conducted to elucidate the transversal and longitudinal irradiation distributions on the receiver active area. The receiver was treated as a perfect absorber ( $a=1.0$ ) in the simulations, while the total reflectivity of the concentrator was selected equal to 95 % ( $\rho=0.95$ ,  $\alpha=0.05$ ). Numerical tests were conducted to confirm that the produced results are independent of the number of rays simulated. For this reason, Two benchmark cases were selected, for high ( $\rho_{spec}=\rho=0.95$ ) and low ( $\rho_{spec}=0.50$ ,  $\rho=0.95$ ) optical quality of the reflector, respectively. The number of simulated rays was gradually increased from  $0.5 \cdot 10^6$  to  $6 \cdot 10^6$  and the variation in the values of maximum and average concentration ratio  $CR$  on the receiver, as well as in the width of the solar band were monitored. The overall emitted irradiation flux was maintained equal to  $1.0 \text{ kW/m}^2$  in all cases. **Table 5.1** summarizes the variation of the quantities in question for the two cases considered and increasing number of rays. As can be seen from the values of **Table 5.1**, the only quantity that

exhibits some discrepancy with the number of rays is the maximum concentration ratio. It was decided to produce the results using  $2 \cdot 10^6$  rays, in order to obtain high accuracy and smooth irradiation profiles, as the simulation time was approximately four minutes on an eight-core CPU.

**Table 5.1** Effect of the number of simulated rays on the produced irradiation profiles.

Rays ( $\cdot 10^6$ )	$\rho_{spec}=0.95$			$\rho_{spec}=0.50$		
	CR <sub>max</sub>	CR <sub>ave</sub>	W <sub>band</sub> [mm]	CR <sub>max</sub>	CR <sub>ave</sub>	W <sub>band</sub> [mm]
0.5	113.4	22.5	62	62.2	14.2	123
1	112.6	22.5	62	61.8	14.3	123
2	112.5	22.5	62	61.7	14.3	123
4	112.4	22.5	62	61.7	14.3	123

**Fig. 5.15** depicts the irradiation distribution on the receiver for concentrators of different optical quality with three values (0.95, 0.75, 0.50) being considered for the specular reflectance  $\rho_{spec}$ . The transversal profile shown in **Fig. 5.15a** exhibits a normal distribution for fully specular reflection ( $\rho_{spec}=0.95$ ). As the percentage of specular reflection decreases, i.e. the concentrator optical quality decreases, on the one hand, the peak value of irradiation flux achieved decreases and, on the other hand, the form of the transversal distribution deviates from the normal distribution. The solar band becomes wider and the profile exhibits plateaus of low concentration values at a distance spanning approximately between 20mm and 50mm from the receiver mid-width. The form of the flux longitudinal profile, depicted in **Fig. 5.15b**, remains qualitatively unaltered regardless of the value of specular reflectivity. However, as can be clearly seen the concentration achieved at the focal line is approximately reduced by half as the specular reflectivity reduces from 0.95 to 0.50, in accordance to the peak value of the transversal profile. The receiver intercept factor decreases in a linear manner with specular reflectivity (**Fig. 5.15c**) meaning that a significant portion of the incoming sunlight on the collector aperture completely misses the receiver in the cases of non-specular reflectance and hence the CPVT system performance is degraded.



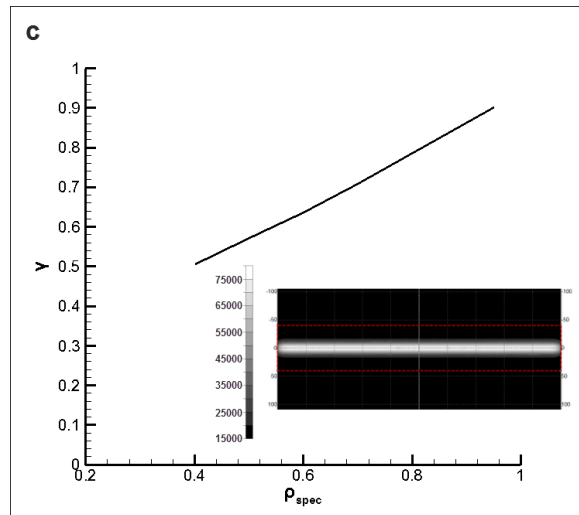


**Fig. 5.15** (a) Transversal and (b) longitudinal profiles of the irradiation distribution for concentrators of different optical quality. (c) Receiver intercept factor vs. specular reflectance (total reflectance equal to 95%).

It was made clear from **Fig. 5.15a** that the transversal irradiation distribution exhibits a clearly discernible peak at the receiver mid-width, regardless of the optical quality of the concentrator. However, the irradiation measurements revealed a different transversal profile with two regions of high irradiation intensity located on either side of the receiver centerline, while the irradiation at the location where maximum irradiation was expected (receiver mid-width), actually exhibited low concentration values. The fact that the profile exhibited (relative) symmetry led to the conclusion that the characteristic, dual-peak distribution did not occur due to tracking error but due to manufacturing flaws. It was postulated that the shape of the parabola was distorted in the sense that the parabola apex was not in reality a single point but instead a straight section, denoted as  $S$  in **Fig. 5.16**, resulting in the presence of two focal points. This assumption can be supported by the procedure followed for the construction of the parabolic frame, as the metallic ribs that realize the parabolic shape were manufactured as two symmetrical parts that were subsequently welded on the frame main shaft. The thickness of the welding joints, which are visible at the inset of **Fig. 5.16**, is small yet inevitably displaces the symmetrical ribs and distorts the shape of the parabola. Ray-tracing simulations were conducted to illustrate the effect of the distorted parabolic shape on the irradiation profile on the receiver. As was already mentioned, the displacement of the ribs must be small and thus values between 10.0 mm and 40.0 mm were considered as length for the segment  $S$ .

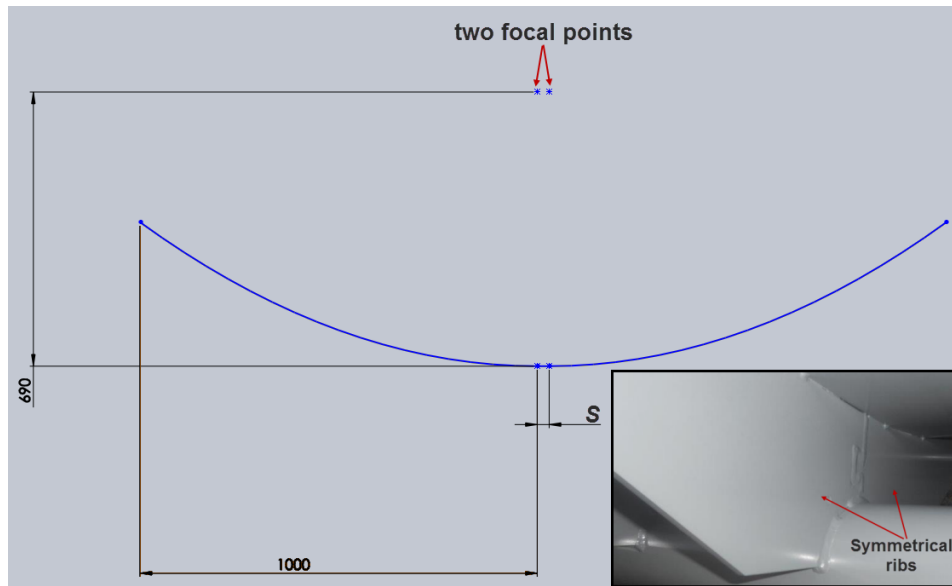


**Fig. 5.16** Distorted form of the parabola due to manufacturing imperfections.

**Fig 5.17** presents the solar bands incident on the receiver for increasingly distorted parabolic concentrators. It can be observed that two illuminated regions on either side of a dark region appear for values of the  $S$  segment length equal or larger than 20mm. As the distorting length increases the two peaks shift away from the receiver center-line and the middle dark area becomes more extended. In addition, the maximum irradiation intensity is significantly decreased for  $S=20.0$  compared to that for  $S=10.0$  mm. It is therefore made evident that small errors in the shape of the parabola can have a remarkable effect on the reflected radiation distribution.

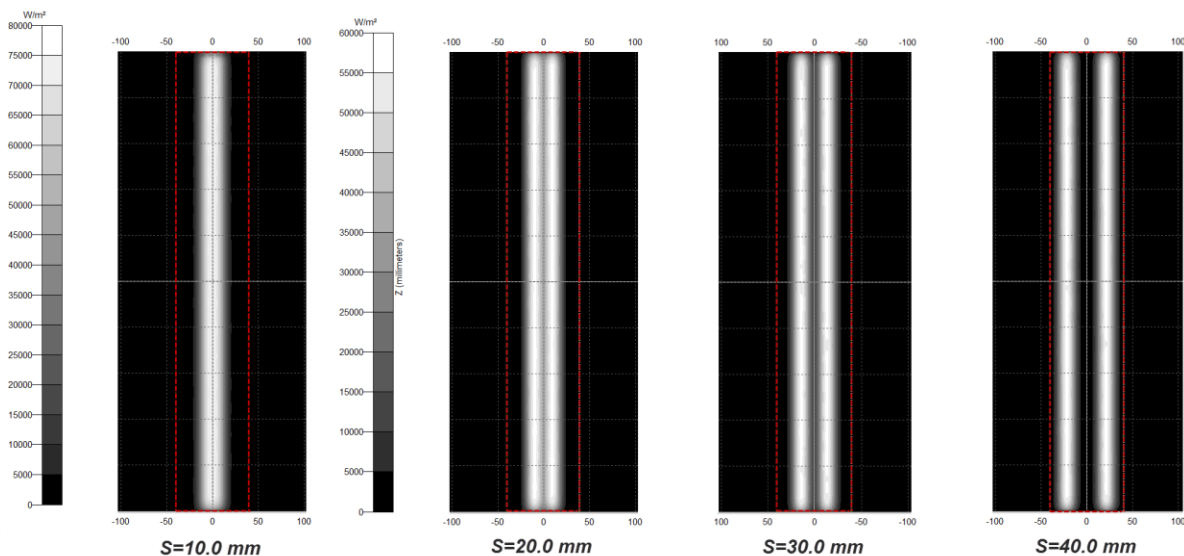


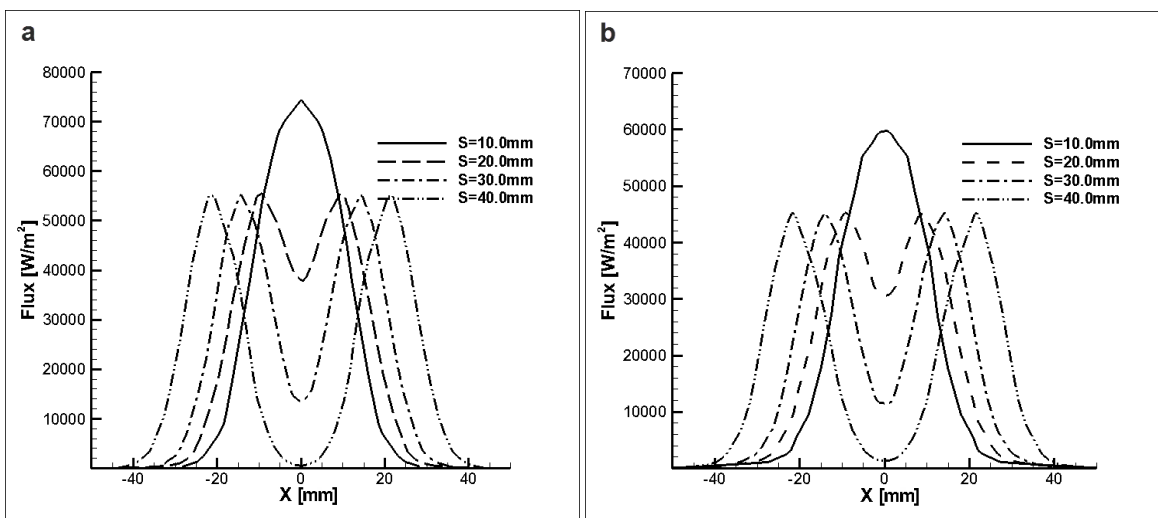
**Fig. 5.17** Solar bands incident on the receiver for different lengths of the  $S$  segment ( $\rho_{\text{spec}}=0.95$ ).

The “twin-peak” profiles are clearly evident also in **Fig. 5.18** for  $S \geq 20.0$ mm. Even though the profile maintains a single peak for  $S=10.0$ , the maximum concentration is reduced compared to a perfect parabola. An additional observation, which applies for all two-peak cases regardless of the value of specular reflectivity, is that the maximum flux value obtained remains constant and

unaffected by the length of the segment  $S$ . By comparing **Fig. 5.18** to **Fig. 5.15a**, it is made clear that the maximum concentration achieved by a pseudo-parabolic shape having two focal points is approximately half of that achieved by a geometrically ideal parabola. It must also be mentioned that the profiles for each value of  $S$  exhibit a similar qualitative form for the three values of specular reflectance considered. Besides, the receiver intercept factor variation with specular reflectivity remains unaffected by the shape distortion, for the values of  $S$  considered, and coincides with the variation regarding the precise parabolic shape, depicted in **Fig. 5.15c**.

Special attention must be given to **Fig. 5.18c**, where the concentration values measured across the receiver width at three locations along the receiver active length ( $Z=0.125, 0.250, 0.375$  m) are also presented. As can be seen, the experimental points lie between the predicted profiles for  $S=30.0$  mm and  $S=40.0$  mm, however they do clearly follow the same trend with alternating regions of low and high concentration. The asymmetry that can be discerned at the points at  $X=\pm 15.0$  mm could be either due to error in the location of the sensor or actual displacement of the rib as it is not guaranteed that the parabolic frame is perfectly symmetrical. It must be pointed out that small errors, in the order of 1 mm, associated with the sensor location can have a significant impact on the measured irradiation, as the flux intensity exhibits rapid changes within a small length of 60.0 mm. Besides, the measurements at the three longitudinal positions do not coincide, indicating that the parabolic frame is imperfect in a three-dimensional sense.

The error in the receiver vertical displacement relative to the exact focal line can also have a considerable effect on the flux distribution. The profile depicted with a red line in **Fig. 5.18c** corresponds to a displacement error of 0.73% ( $f^*=685$  mm) in the receiver position and a concentrator with distortion  $S=30.0$  mm. It is evident that the profile is noticeably different from the respective case with no displacement error. The profile is in fair agreement with the experimental measurements and it is regarded as the best approximation of the flux profile on the receiver. It must be highlighted that the complete elimination of displacement error could not be achieved, as the measuring device was placed on the focal line manually and thus the receiver vertical adjustment was associated with a certain error. In addition to that, it is possible that the aperture of the sensor was slightly offset from the bottom surface of the device, which was taken as reference for the adjustment of the receiver, hence adding to the displacement error.



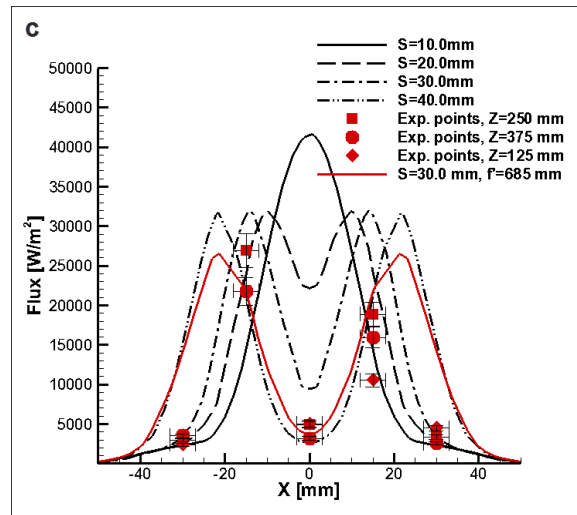


**Fig. 5.18** Transversal profiles of the irradiation distribution for “distorted” concentrators of different optical quality: (a)  $\rho_{\text{spec}}=95\%$ , (b)  $\rho_{\text{spec}}=75\%$ , (c)  $\rho_{\text{spec}}=50\%$ .

**Fig. 5.19** presents the longitudinal flux profiles for concentrators of different quality and distortion. The length of the segment  $S$  has no effect on the qualitative form of the longitudinal profiles but only affects the flux intensity. The profiles for  $S \geq 20.0$  mm correspond to the transversal locations on the receiver, where peak concentration is obtained. The experimental values of the flux intensity measured along the receiver active length are also included in **Fig. 5.19b**. The experimental values were obtained by gradually rotating the main axis of the parabolic frame by a few degrees about the position of sunlight normal incidence, while constantly recording the concentration values. The profiles comprising the highest recorded values were identified as the two irradiation peaks evident in **Fig. 5.18**. The length-wise distribution of the flux intensity clearly reveals that the parabolic frame is imperfect in a three-dimensional manner, as the concentration varies along the receiver length. The experimental values regarding the first peak are in good agreement with the ray-tracing prediction for  $\rho_{\text{spec}}=0.50$ ,  $S=30.0$  mm and  $f=685.0$  mm, which, as was also mentioned for the transversal profile, appears to be the most reliable approximation of the actual distribution. On the other hand, the measured flux values corresponding to the second peak are lower than the predicted ones. This discrepancy, which is also evident in **Fig. 5.18c**, could be attributed to increased slope error associated only with the one of the two symmetrical ribs that tends to widen the specific solar band. The slope error could be a result of imprecise manufacturing of the specific rib, but it is far more plausible to assume that the error occurs due to the uneven thickness of the welding joints that bond the aluminum sheet that realizes the parabola onto the ribs. Given that these joints are distributed along all the ribs and, in addition, there are several of them along the length of each rib, they are identified as the main cause of the three-dimensional distortion of the parabolic surface.

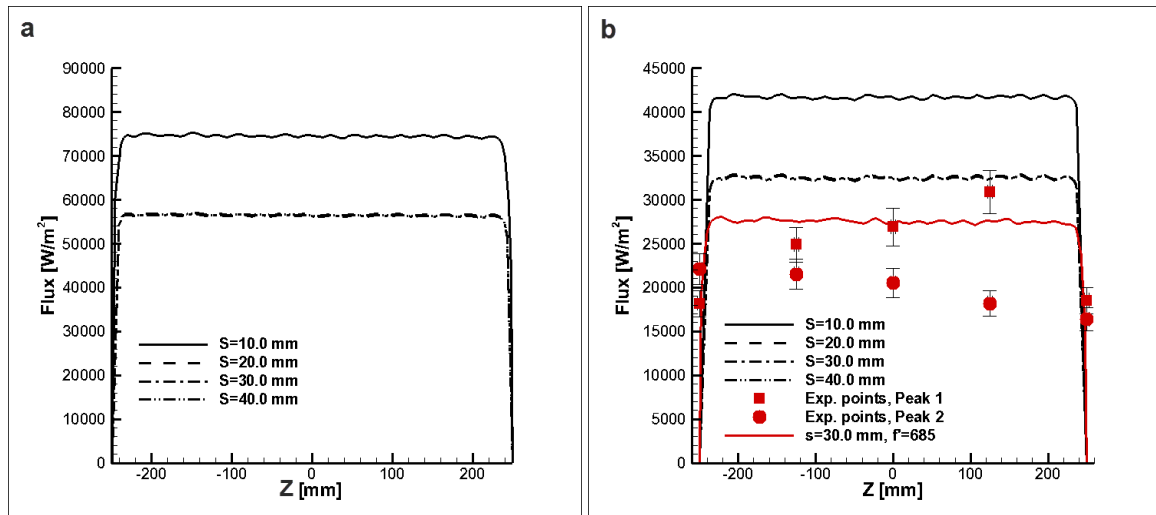


**Fig. 5.19** Longitudinal profiles of the irradiation distribution for “distorted” concentrators of different optical quality: (a)  $\rho_{\text{spec}}=95\%$ , (b)  $\rho_{\text{spec}}=50\%$ .

## 5.8 Solar-cell module

The main concern in manufacturing solar cells for concentrating applications is the increased current density due to the concentrated sunlight, as was discussed in **paragraph 2.4**. For this reason custom solar cells were developed by *Narec Ltd.* that specializes in the design of concentrating cells. The cells were manufactured by monocrystalline silicon wafers of thickness equal to 150  $\mu\text{m}$  and the most profound difference in their design, compared to conventional cells, is the much higher finger density, as depicted in **Fig. 5.20**. Two cell designs were considered having widths of 40.0mm (“narrow” cells) and 60.0mm (“wide” cells), respectively, in order to examine the effect on electrical performance of the mismatch between the solar band and the cell widths. The cell busbars, where the current is collected, have a width of 2.0 mm and the cell length is equal to 48.2mm for both designs. The basic dimensions of the solar cells are shown in **Fig. 5.20a**.

Ten cells were interconnected in series to fabricate a PV module and therefore the output voltage of the module is the sum of the individual cell voltages, while the same current flows through all the cells and therefore partial shading of the module can have a significant effect on the electrical performance. 2.0 mm wide tin-coated copper ribbons were used for the interconnection of the cells. Each module comprises a front cover made of low-iron glass, so that light reflection is limited, the PV laminate (EVA and solar cells) and a back aluminum substrate. The cells were thermally bonded to the substrate using a thermally conductive, yet electrically insulating, adhesive tape ( $k_t=0.6\text{W/mK}$ ). The power produced by the module is received through metallic terminals located at the side of the module. The layout and basic dimensions of the PV modules are depicted in **Fig. 5.20b**, while their basic performance characteristics are summarized in **Table 5.2**. Wires (*Ölflex SOLAR XLS*) of relatively large cross section were soldered on the terminals, capable of delivering the current of high amperage to the load with minimal losses and without overheating.

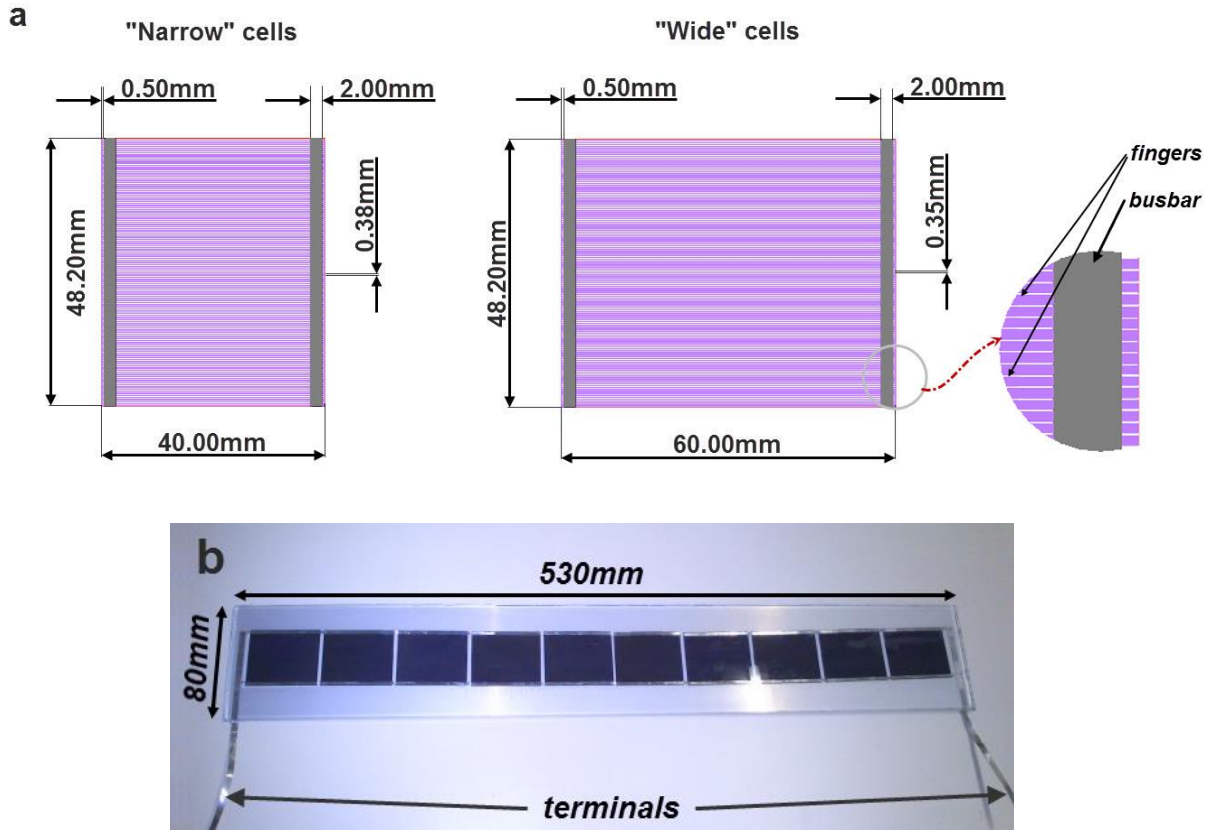


Fig. 5.20 Layout and dimensions: (a) of the two cell designs, (b) of the manufactured modules.

Table 5.2 Efficiency parameters of the PV modules for one-sun illumination.

	$R_s$ [ $\Omega$ ]	$R_{sh}$ [ $\Omega$ ]	$V_{oc}$ [V]	$I_{sc}$ [A]	$V_{MPP}$ [V]	$I_{MPP}$ [A]	FF
Module 1 (narrow cells)	0.700	230.3	6.157	0.549	5.423	0.498	0.799
Module 2 (narrow cells)	0.698	306.7	6.137	0.552	5.380	0.513	0.814
Module 3 (wide cells)	0.486	212.6	6.123	0.851	5.284	0.771	0.782
Module 4 (wide cells)	0.609	226.5	6.099	0.827	5.225	0.748	0.775

### 5.9 Receiver

The receiver of the system, i.e. the solar-cell module bonded to the heat sink, was housed in an aluminum container (Fig. 5.21) for protection against the environmental conditions, along with the required tubing, wiring and temperature sensors. It must be noted that the PV module substrate is of the same material as the heat sink, in order to ensure a common thermal expansion coefficient, which is desirable for the integrity of the thermal bond. The back and sides of the receiver were heavily insulated using Armaflex ( $k=0.037$  W/mK), which can withstand temperatures up to  $105^\circ\text{C}$ , to prevent heat losses. The insulation thickness was 5.0cm at the receiver back surface and 0.5cm at the receiver side surfaces. Flexible tubes were fitted to the cylindrical ends of the manifold that connected the heat sink to the hydraulic circuit of the test rig, while the wires that connected the PV module to the external load were also secured at the upper part of the container. The container was sealed with the use of two rectangular covers, which also bear characteristic metallic profiles in the form of “fingers” to secure the PV module into the proper position. The covers were bolted to the main body of the

container, while Mylar tape was placed at their bottom surfaces to reflect concentrated sunlight. Silicone able to withstand high temperature was used to seal the small gaps between the PV module and the edges of the container.

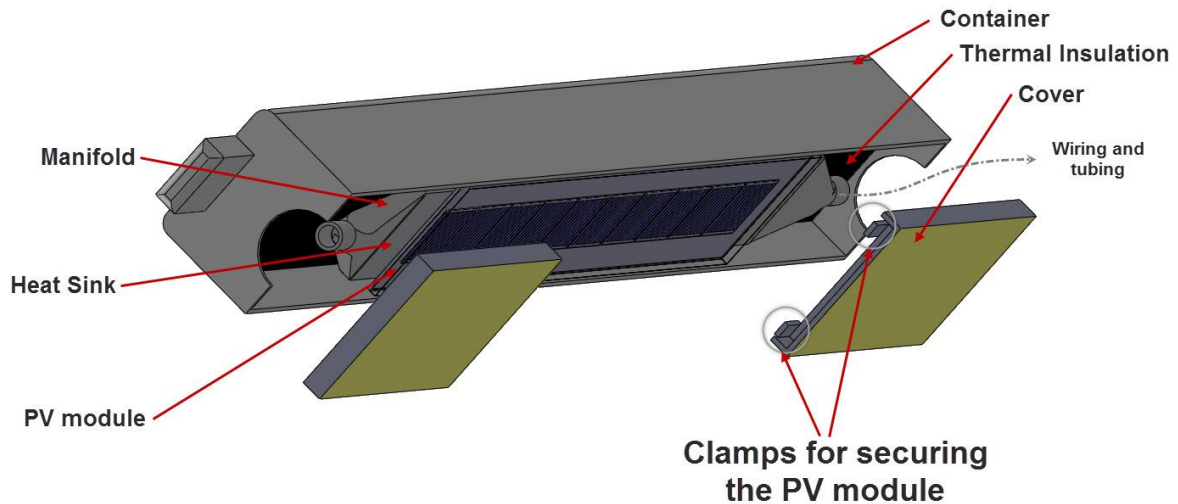


**Fig. 5.21** “Exploded” view of the system receiver.

### **5.10 Thermally conductive adhesive materials**

Achieving a good thermal bond between the heat sink and the heat source is of vital importance for effective cooling. The most common practice employed in the electronics industry is the use of solder Thermal Interface Materials (TIMs). However, the use of soldering materials is not feasible in the present case as they require heating to temperatures in the range of 120-250°C [5.28], a process that would certainly damage the solar-cell module. Consequently, only chemical adhesive materials with appropriate mechanical properties and high thermal conductivity were considered for bonding the module to the heat sink with two main categories of products being commercially available, namely adhesive tapes and adhesive resins. Increased thermal conductivity in these materials is achieved by filling the adhesive with conductive materials such as graphite, copper, aluminum, zinc oxide, aluminum nitride, diamond and silver powders [5.29].

An extensive market overview was conducted to specify the most suitable adhesive materials having the material thermal conductivity and curing temperature as main criteria but also taking into account the cost and the required lead time. The adhesives with the most attractive characteristics are summarized in **Table 5.3**. It must be noted that a practical problem associated with the procurement of conductive adhesives is the high lead time that can reach up, e.g., to 14 weeks for the Henkel Hysol product, due to the short shelf life of the materials that forces the manufactures to produce them “upon request”.

## Chapter 5. Design and manufacturing of the CPVT system

**Table 5.3** Suitable adhesive materials considered for bonding the PV module to the heat sink. All prices and quantities reported are for minimum orders.

Product	Description	k [W/mK]	Hardness	Quantity	Price
<b>AAVID ThermalBond</b>	2 component epoxy	1.34	86	20 pcs of 25 gr	15.9 €/pc
<b>Cast Coat CC3-450</b>	2 component epoxy	4.54	"resilient"	1.34 kg/0.17 kg H7	126.6 €
<b>EPO-TEK T7109-19</b>	2 component epoxy	1.30	41	85 g kit	271.6 €
<b>EPO-TEK T905BN-4</b>	2 component epoxy	1.78	79	85 g kit	293.4 €
<b>EPOXIES 50-3100R</b>	2 component epoxy	2.16	90	1.34 kg/0.44 kg Cat	74 \$
<b>EPOXIES 50-3150RFR</b>	2 component epoxy	2.16	90	1.34 kg/0.44 kg Cat	73\$
<b>Master Bond EP21AN</b>	2 component epoxy	3.17	85	130gr/130gr	750\$
<b>Henkel Hysol 9497</b>	2 component epoxy	1.40	83	10 pcs of 50mL	14.85 €/pc
<b>Saint Gobain C675</b>	Thermal Tape	2.00	-	122m roll	2762 €
<b>AIT CB7208-A</b>	Thermal Tape	3.60	40	6"X6"(in.) sheets	40.3\$/sheet
<b>Chomerics T412</b>	Thermal Tape	1.40	-	100m roll	~3000€

Finally, two products were procured, namely the epoxy resin and the tape with the highest thermal conductivity values, based on the information reported by the manufacturers. The basic properties of the two materials are stated in **Table 5.4**. As revealed by the values of **Table 5.4**, an attractive feature of the epoxy resin is that it has a coefficient of thermal expansion similar to aluminum ( $\approx 22$ ). In addition, the epoxy offers a much stronger bond, as can be ducted by comparing the values of the tensile strength. Regarding the material texture, the epoxy becomes rigid after curing, while the tape maintains a flexible form. The thermal resistance imposed by each material is evaluated in the next paragraph.

**Table 5.4** Properties of the procured adhesive materials

	<b>AIT CB7208-A</b>	<b>Cast Coat CC3-450</b>
Description	Aluminum nitride filled film adhesive	Aluminum filled two-component epoxy resin
State	Solid	Fluid
Density [kg/m <sup>3</sup> ]	2200	1785
Viscosity [Pa s]	-	6.5-7.0
Thermal conductivity [W/mK]	3.60	4.54
Tensile strength [MPa]	0.42	61
Coefficient of thermal expansion (10 <sup>-6</sup> /K)	110	28
Maximum operation temperature [K]	423	468

### 5.10.1 Thermal resistance of the adhesive materials

A simple test device was set up, in order to evaluate the conductive thermal resistance induced by the adhesive material. Two sets of aluminum plates were bonded together using the epoxy and the resin in each case. The overall dimensions of the plates were 0.5 m x 0.06 m x 0.003 m. The plates were clamped on a rod-resistor heater (see **paragraph 4.8.1.1**) and placed in a heavily insulated container. Provided that heat losses to the environment are made negligible, heat transfer to the bonded plates can be considered one-dimensional. Thus, the temperature of each plate is expected to increase in a linear manner and the system can reach a pseudo-steady state, where the temperature difference between the plates is maintained constant. By measuring this temperature difference  $\Delta T_{meas}$  and the heat input  $Q$ , the overall thermal resistance of the joint can be calculated as follows:

$$R_{th} = \frac{\Delta T_{meas}}{Q} = \frac{t_{pl}}{k_{al}A_{HTR}} + \frac{t_{adh}}{k_{adh}A_{HTR}} + \frac{t_{pl}}{k_{al}A_{HTR}} \quad (5.6)$$

where  $t_{pl}$  and  $t_{adh}$  are the plate and adhesive thicknesses, respectively. In order to measure the plate temperature, three holes of diameter 1mm were drilled at the side-face of each plate, along the plate length, and type T thermocouples were inserted approximately 20mm inside the plate. The holes were drilled approximately at the plate mid-thickness and the distance between the measuring point and the plate edge was roughly taken equal to  $t_{pl}=1mm$ . Each test commenced with the plates at room temperature and the container sealed. A heat input was specified and the resistors were turned on and values of the plate temperatures and the heat rate were recorded every 5 seconds.

Tests for each adhesive were conducted for two heat-rate values, 400W and 650W, in order to verify the independence of the measured thermal resistance.

**Fig. 5.22a** depicts the temperature rise with time for a set of plates bonded using the epoxy resin. It is evident that temperature increases in a linear manner and thus the assumption of one-dimensional heat transfer is justified. A similar heating pattern was observed for the plates bonded using the thermal tape. In addition, it can be noticed that the curves have the same gradient after  $t=300s$ . **Fig. 5.22b** presents the thermal resistance values measured for the two adhesive materials. The measurement uncertainty associated with the thermal resistance values was calculated according to the procedure discussed in paragraph 6.1.3 and is primarily influenced by the uncertainty in the temperature measurement, which is equal to 0.5 K for the employed thermocouples. Regarding the epoxy resin, the repeatability of the measurements was very good and the obtained values of the thermal resistance were found to be constant for different heat rates. However, the measured thermal resistance is approximately an order of magnitude higher than the theoretical value ( $R_{th,theory}=1.05 \cdot 10^{-3}$ ) calculated using the thermal conductivity as stated by the manufacturer. Common causes for the deterioration of the thermal bond are the adherence of the material on the metallic surfaces, the existence of voids and air pockets, the pressure on the joint and the effect of humidity on the material properties.

The thermal resistance values in regard to the thermal tape were measured in the range  $4.11 \cdot 10^{-5}$ - $3.0 \cdot 10^{-3}$  K/W with the theoretical value being equal to  $1.30 \cdot 10^{-3}$ . Measurement repeatability could not be obtained, as the values obtained after the first measurement were negligibly small. A visual check after the end of the measurements revealed that the tape had been heavily compressed due to the thermal cycling in conjunction with mechanical clamping and excess material was clearly visible beyond the edges of the plates. Nevertheless, in the actual application the tape will not be under pressure and the operating temperature will be lower (up to 70° C). Hence, it is presumed that the initial value obtained, equal to  $3.0 \cdot 10^{-3}$  K/W is representative of the actual thermal resistance imposed by the tape. It must be noted that a heating test was conducted for the epoxy resin as well to examine its behavior to temperatures up to its operating limit. For temperatures up to 120°C, the resin maintained its rigidity, no cracks appeared and the plates remained perfectly bonded. Furthermore, no deviation from the values of the thermal resistance shown in **Fig. 5.22b** was detected.

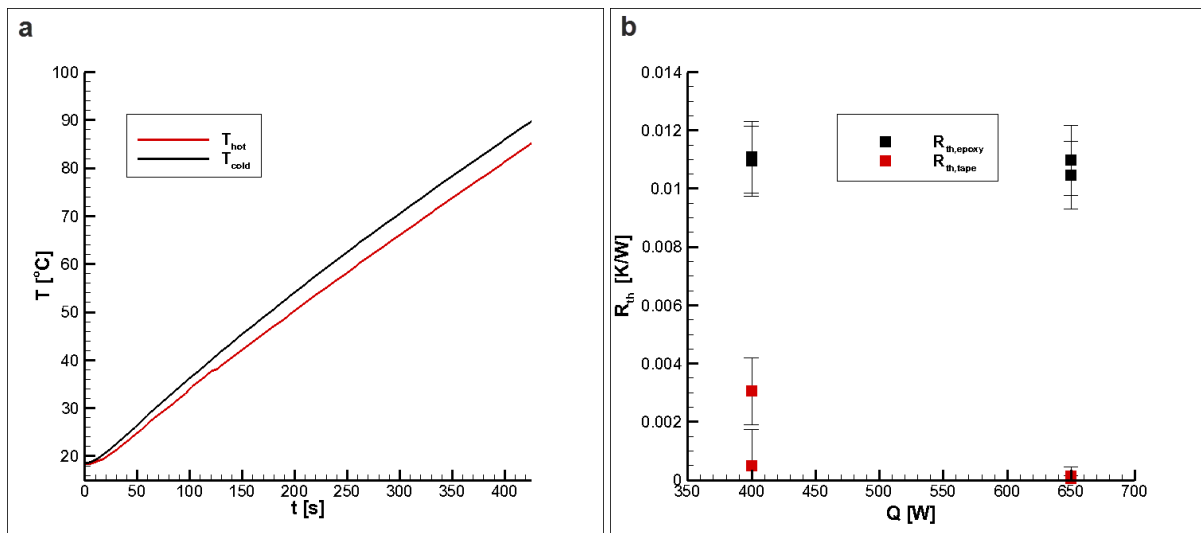


**Fig. 5.22** Results of the adhesive thermal-resistance evaluation: (a) Evolution of the plates temperature with time. (b) Measured values of the adhesives thermal resistances.

## Chapter references

- [5.1] W.B.Stine, R.W.Harrigan, Power from the sun, Wiley, New York, 1986, Chapter 8.
- [5.2] D.L. Evans, On the performance of cylindrical parabolic solar concentrators with flat absorbers, Sol. Energy 19 (1977) 379-385.
- [5.3] K.E. Hassan, M.F. El-Refaie, Theoretical performance of cylindrical parabolic solar concentrators, 15 (1973) 219-244, Sol. Energy 15 (1973) 219-244.
- [5.4] K. Foli, T. Okabe, M. Olhofer, Y. Jin, B. Sendhoff, Optimization of micro heat exchanger: CFD, analytical approach and multi-objective evolutionary algorithms, Int. J. Heat Mass Transf. 49 (2006) 1090-1099.
- [5.5] J.S. Coventry, A solar concentrating photovoltaic/thermal collector, PhD thesis, Australian National University, Canberra, 2004.
- [5.6] P. Singh, J.A. Liburdy, A solar concentrator design for uniform flux on a flat receiver, Energy Convers. Manag. 34 (1993) 533-543.
- [5.7] R.N. Singh, A.K. Singhal, S.S. Mathur, T.C. Kandpal, Performance of a cylindrical parabolic trough using a fin receiver: Limb darkening effects, Energy. Res. 6 (1982) 271-282.

- [5.8] A. Thomas, H.M. Guven, Effect of optical errors on flux distribution around the absorber tube of a parabolic trough concentrator, *Energy Convers. Manag.* 34 (1994) 575–582.
- [5.9] Dassault Systemes, Solidworks Simulation, available at:  
<http://www.solidworks.com/sw/products/simulation/simulation-xpress.htm>.
- [5.10] Alanod GmbH., Miro Reflective Surface Technical Specification Brochure, Ennepetal, Germany. Available at: <http://alanod.com/opencms/opencms/en/products/pvd/miro/>.
- [5.11] J. Xiao, X. Wei, Z. Lu, W. Yu, H. Wu, A review of available methods for surface shape measurement of solar concentrator in solar thermal power applications, *Renew. Sustain. Energy Rev.* 16 (2012) 2539–2544.
- [5.12] J.K. Stynes, B. Ihas, Slope error measurement tool for solar parabolic trough collectors, Proceedings 2012 World Renewable Energy Forum, Denver, CO, 2012.
- [5.13] L. Li, A. Kecskemethy, A.F.M. Arif, S. Dubowsky, A novel approach for designing parabolic mirrors using optimized compliant bands, Proceedings of the ASME 2011 International Design Engineering Technical Conferences & Computers and Information in Engineering Conference, ASME, Washington, DC, US, 2011, DETC2011-47096.
- [5.14] J.A. Duffie, W.A. Beckman, *Solar Engineering of Thermal Processes*, second ed., Wiley, New York, 1991 pp.10-31.
- [5.15] M.M. El-Kassaby, Rotation and incidence angles for parabolic trough, *Ren. Energy* 4 (1994) 59-68.
- [5.16] A. S. Hegazy, M.M. El-Kassaby, M.A. Hassab, Effect of Parabolic Trough Solar Collector Orientation on Its Collection Efficiency, *Int. J. Sol. Energy.* 16 (1995) 173–183.
- [5.17] G.G. Gregory, R.J Koshel, Modeling the operating conditions of solar concentrator systems, in: A. Gombert (Ed.), Proceedings of SPIE: Photonics for Solar Energy Systems, 6197 (2006) 61970J-1-11.
- [5.18] H. Zheng, T. Tao, J. Dai, H. Kang, Light tracing analysis of a new kind of trough solar concentrator, *Energy Convers. Manag.* 52 (2011) 2373–2377.
- [5.19] N. Hernández, D. Riveros-Rosas, E. Venegas, R.J. Dorantes, A. Rojas-Morín, O. a. Jaramillo, et al., Conical receiver for a paraboloidal concentrator with large rim angle, *Sol. Energy.* 86 (2012) 1053–1062.
- [5.20] S. Jiang, P. Hu, S. Mo, Z. Chen, Optical modeling for a two-stage parabolic trough concentrating photovoltaic/thermal system using spectral beam splitting technology, *Sol. Energy Mater. Sol. Cells.* 94 (2010) 1686–1696.
- [5.21] D.J. Dye, *Infrared non-imaging device for a full-spectrum solar energy system*, MSc Thesis, University of Nevada, Reno, LV, 2003

- [5.22] G.L. Dai, X.L. Xia, C. Sun, H.C. Zhang, Numerical investigation of the solar concentrating characteristics of 3D CPC and CPC-DC, *Sol. Energy* 85 (2011) 2833-2842.
- [5.23] Lambda Research Corp., *TracePro User's Manual*, Release 5.0, Littleton, MA, 2009.
- [5.24] J.S. Coventry, Performance of a concentrating photovoltaic/thermal solar collector, *Sol. Energy*. 78 (2005) 211–222.
- [5.25] K.-J. Riffelmann, A. Neumann, S. Ulmer, Performance enhancement of parabolic trough collectors by solar flux measurement in the focal region, *Sol. Energy*. 80 (2006) 1303–1313.
- [5.26] E. Pihl, C. Thapper, Evaluation of the concentrating PVT systems MaReCo and Solar8, MSc Thesis, Lund University, Lund, 2006.
- [5.27] K.K. Chong, T.K. Yew, Novel Optical Scanner Using Photodiodes Array for Two-Dimensional Measurement of Light Flux Distribution, *IEEE Trans. Instrum. Meas.* 60 (2011) 2918–2925.
- [5.28] S-Bond Technologies, <http://www.s-bond.com/solutions-and-service/aluminum-bonding/>.
- [5.29] Y.X. Fu, Z.X. He, D.C. Mo, S.S. Lu, Thermal conductivity enhancement with different fillers for epoxy resin adhesives, *Appl. Therm. Eng.*, In press.



### 6.1 Experimental rig and instrumentation

The electrical and thermal performance of the CPVT system was evaluated in an outdoor testing rig specially developed for this purpose. The experimental setup comprised the electrical and hydraulic circuits, as well as the necessary instrumentation for the measurement of the quantities needed for the characterization of the system overall performance. The test rig constituents as well as the instrumentation employed for the measurement of the quantities of interest, as depicted in **Fig. 6.1**, are presented in the following sections. It must be reminded that the hydraulic circuit used for the assessment of the CPVT system performance was also used for the evaluation of the cooling devices and has been described in detail in **paragraph 4.8.1.1**.

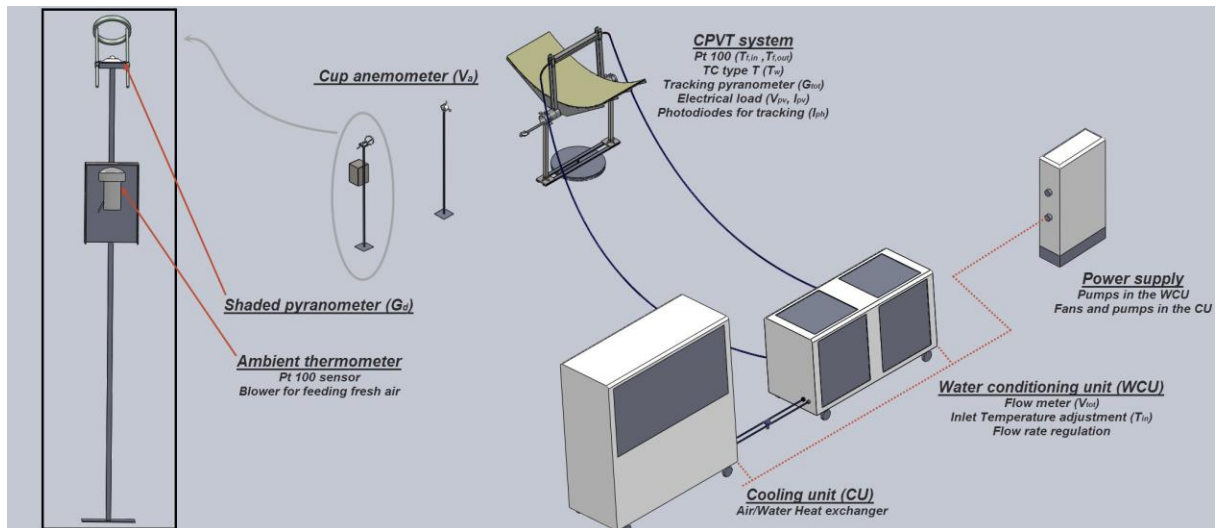


**Fig. 6.1** Layout of the test rig developed for the evaluation of the system.

#### 6.1.1 Direct (beam) solar radiation

Direct radiation  $G_b$  was calculated as the subtraction of the diffuse radiation  $G_d$  from the total radiation  $G_r$ . For this purpose, two *Kipp & Zonen* pyranometers of “secondary-standard” accuracy according to the ISO 9060 standard [6.1] were used. One instrument was mounted on the collector frame and tracked the movement of the sun in order to measure the total radiation perpendicularly incident on the collector, while the second was mounted on a static pillar beside the collector and was properly shaded using an appropriate ring manufactured by *Kipp & Zonen*, so as to detect only the diffuse part of the solar radiation. The uncertainty in the measurement of both instruments was estimated through a calibration procedure performed in the laboratory.

### 6.1.2 Ambient temperature

A properly shaded four-wire Pt100 temperature sensor manufactured by *Thies Klima* was used for the measurement of ambient temperature. The sensor was mounted on a probe approximately 1.0 m from the ground and constantly fed with fresh air by a blower. The measurement uncertainty is 0.054K in the temperature range 278-353K.

### 6.1.3 Wind velocity

A cup anemometer manufactured by *Thies Klima* was used for the measurement of the wind velocity. The instrument was mounted adjacent to the collector, approximately 1.5m from the ground. The instrument accuracy is equal to  $\pm 2\%$  of the measured value in the range 0.3-40m/s.

### 6.1.4 Volumetric flow rate

Water flow rate in the hydraulic circuit was measured with a ring piston flow meter manufactured by Aqua Metro. The instrument accuracy is equal to  $\pm 2\%$  of the measured value for flow rates in the range 60-1500L/h.

### 6.1.5 Fluid temperature

Two four-wire Pt100 temperature sensors were used for the measurement of the fluid temperature at the inlet and the outlet of the collector. The sensors are of accuracy 1/10 DIN according to the DIN EN 60751 standard [6.2] and were properly calibrated so that the uncertainty in the fluid inlet and outlet temperature is equal to 0.054K for the entire range of testing temperatures. Each sensor was housed in an appropriate fitting, which allows the insertion of the probe opposite to the main flow and enables fluid mixing, so that accurate measurements are ensured (Figure 6.2).

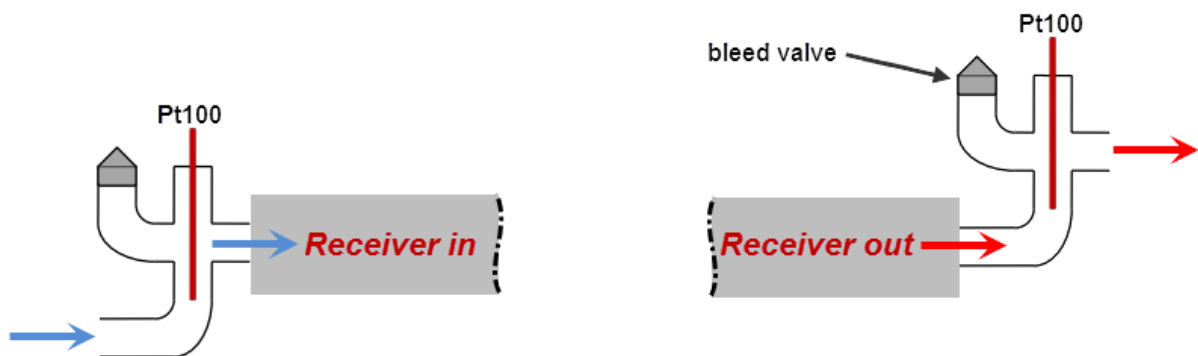


**Fig. 6.2** Housing of the sensors used for measuring the cooling fluid inlet-outlet temperature.

### 6.1.6 Solid temperature

The temperature at the solid substrate of the PV modules and the heat sinks was measured with the use of type T (copper-constantan) thermocouples manufactured by OMEGA with a measurement

uncertainty of 0.5K. As the thermocouple measurement is dependent on the temperature of its junction, special care was given to establish that the same conditions occur at the junctions of all sensors ensuring by this way the accuracy of the temperature measurements. The thermocouples were connected in a separate wire terminal in such a manner as to reduce the length of the terminal, as depicted in **Fig. 6.3**, and their signal was transferred to the data logger through copper wires. A Pt100 sensor was bonded on the terminal to measure the reference (junction) temperature  $T_{ref}$ . The absolute value of the solid material temperature was finally measured as:

$$T_{TC} = T_{ref} + (T_{probe} - T_{ref}) \quad (6.1)$$

where  $T_{probe}$  is the temperature at the thermocouple tip, which has a diameter approximately equal to 0.9 mm, i.e. the temperature at the solid material. The terminal along with the reference sensor was placed in a heavily insulated and shaded container, in order to maintain a constant temperature.

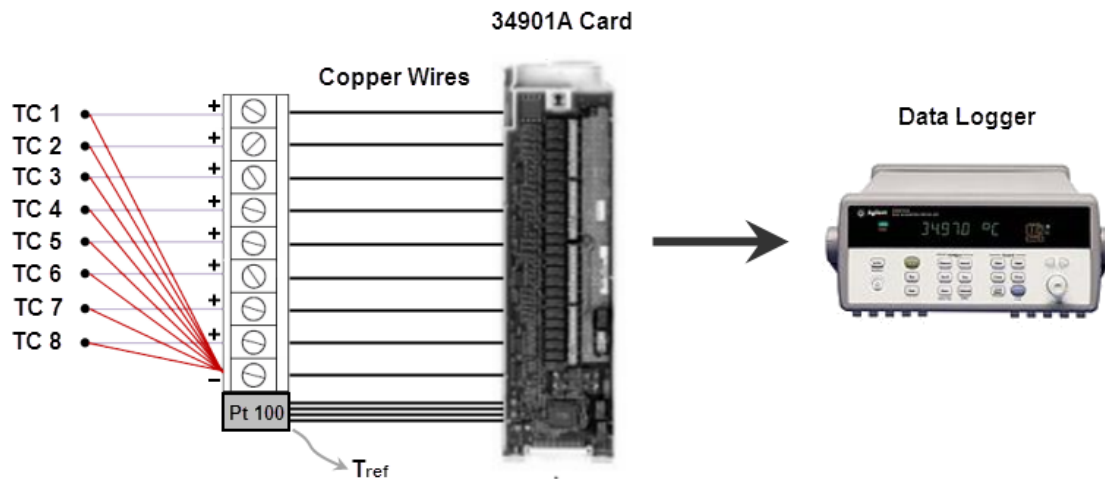


**Fig. 6.3** Wire terminal connection for the thermocouples.

### **6.1.7 Glass temperature**

A portable thermal camera manufactured by FLIR was used to visualize the temperature field on the glass cover of the PV model. The camera has an accuracy of 2°C for measured temperatures in the range -20°C to 250°C and it allows for a correction of the recorded values according to the emissivity of the material being measured. The thermal images taken had a resolution of 320x240 pixels and were processed using an appropriate software (FLIR Tools), in order to export the minimum and maximum temperature values in ASCII format.

### **6.1.8 Photovoltaic module voltage and current**

A variable resistor (0-6Ω) capable of dissipating up to 200W to the environment was used as electric load, in order to operate the solar cell model at the point of maximum power production. The voltage across the module was directly measured by the data logger through additional copper wires

soldered to the module leads, so as to avoid any voltage drop in the high current cables. The produced current was converted to voltage through a 1 mΩ shunt resistor and consequently measured by the data logger. Since both quantities were directly measured by the data logger, the uncertainty in their values is considered to be negligible in comparison to uncertainty associated with the other measured quantities used for the determination of the system total efficiency.

### 6.1.9 Data taking procedure

The cables carrying the signal of the various instruments were concentrated at a terminal-block board mounted at the base of the supporting frame. The signals were consequently carried to an Agilent 34901A data logger through a multicore copper wire. Measured values were being processed and stored to a computer using the Agilent VEE software [6.3]. Data were logged and stored in a file every five seconds.

## 6.2 Experimental uncertainty analysis

An uncertainty analysis based on propagation of errors, as described in [6.4, 6.5], has been conducted in order to determine the resulting uncertainty of the calculated quantities due to the error associated with the direct measurement of primary quantities. Considering that a result  $R$  is calculated from a set of measured quantities  $x_i$ ,  $R = R(x_1, x_2, x_3, \dots, x_i)$ ; then the uncertainty in the calculated value is equal to:

$$U_R = \left[ \sum_{i=1}^N \left( \left( \frac{\partial R}{\partial x_i} \right) U_{x_i} \right)^2 \right]^{1/2} \quad (6.2)$$

where  $U_{x_i}$  is the uncertainty associated with the measurement of the values  $x_i$ . **Eq. (6.2)** is valid regardless of whether the measurement uncertainty is given in absolute or relative values. The uncertainty in the values of the measured quantities required for the system characterization are given for a confidence level equal to 95% and summarized in **Table 6.1**. It must be noted that, in the cases where only the instrument accuracy  $acc$  was available the typical uncertainty of the measurement was calculated as  $u_{x_i} = \frac{acc}{\sqrt{3}}$  [6.5]. The uncertainty for a confidence level of 95% considering uniform error distribution is then equal to:

$$U_{x_i} = 1.645 \frac{acc}{\sqrt{3}} \quad (6.3)$$

In addition, it must be pointed out that the error in the electrical signals directly measured by the data logger was considered negligible, while the uncertainty in the measurements of the solar radiation, the volumetric flow rate and the fluid temperature presented in **Table 6.1** have been determined by calibration procedures performed in the laboratory.

**Table 6.1** Uncertainty in measured quantities.

Measured quantity	Uncertainty U
$V_{\text{air}}$ [m/s]	1.90%
$T_{\text{amb}}$ [K]	0.054
$G_{\text{tot}}$ [W/m <sup>2</sup> ]	1.41%
$G_{\text{d}}$ [W/m <sup>2</sup> ]	1.41%
$\dot{V}_{\text{tot}}$ [m <sup>3</sup> /s]	1.76%
$T_{\text{f}}$ [K]	0.054 K
$T_{\text{w}}$ [K]	0.5 K
$T_{\text{gl}}$ [K]	1.9K
$V_{\text{pv}}$ [V]	-
$I_{\text{pv}}$ [A]	-
$W$ [m]	0.025%
$L$ [m]	0.1%

The uncertainty associated with quantities deriving from the directly measured ones was calculated by making use of **Eq. (6.2)** and are presented in **Table 6.2**. The uncertainty in the values of the thermal gain  $Q_{\text{th}}$ , the thermal efficiency  $\eta_{\text{th}}$  and the total efficiency  $\eta_{\text{tot}}$  were calculated for the three different water flow-rates (20.0-30.0-40.0 mL/s) considered for the evaluation of the CPVT system.

**Table 6.2** Uncertainty in calculated quantities.<sup>1</sup> The uncertainty in the calculated values is dependent on the coolant flow rate. The values correspond to flow rates equal to 20, 30 and 40 mL/s, respectively.

Calculated quantity	Uncertainty U
$A_{\text{a}}$ [m <sup>2</sup> ]	0.10%
$G_{\text{b}}$ [W/m <sup>2</sup> ]	1.99%
$Q_{\text{th}}$ [W]	2.29%-2.90%-3.46%
$P_{\text{el}}$ [W]	-
$\eta_{\text{th}}$ [-]	3.04%-3.52%-4.00% <sup>1</sup>
$\eta_{\text{el}}$ [-]	2.05%
$\eta_{\text{tot}}$ [-]	3.64%-4.06-4.48% <sup>1</sup>

### 6.3 CPVT system performance

The performance of the integrated CPVT system was assessed for three variations of the system receiver comprising different PV module-heat sink combinations aiming at clearly illustrating the influence of the receiver component performance characteristics on the overall efficiency and possibly designate the most attractive configuration. The efficiency measurements presented in the following paragraphs were performed in the summer and autumn period of 2014 at latitude of 38°. The direct beam radiation, wind velocity and ambient temperature varied within the ranges 760-970 W/m<sup>2</sup>, 0-2 m/s and 288-308K for all the testing sequences. It is essential to note that although the system electrical and thermal output are of different “energy value”, their behavior is interdependent and, hence, they are treated as equal for the estimation of the total amount of incoming sunlight that is utilized by the system.

6.3.1 System electrical performance

6.3.1.1 Efficiency of the PV modules

An initial stage for the assessment of the modules electrical performance was to determine the current-voltage (IV) curves that characterize their operation under concentrated sunlight. For a specified flow rate of the cooling fluid, the system was allowed to reach steady-state conditions and then the value of the external load was gradually varied between its minimum and maximum values, so as to cover the entire operating range of the modules. **Fig. 6.4** presents the experimental points obtained for two PV modules assembled with narrow (**Fig. 6.4a**) and wide (**Fig. 6.4b**) cells, respectively. The IV curves for one-sun irradiation as resulted from a flash-tester measurement (at  $T_{ref}=25^{\circ}C$ ) are also included in the figures for comparison. It can be observed that the modules regardless of the cell design obtained an open circuit voltage  $V_{OC}$  approximately equal to 6.2V. However, the module with the wide (60.0mm) cells produced a short circuit current  $I_{SC}$  approximately equal to 12A, considerably higher compared to the approximately 9A produced by the module comprising narrow (40.0mm) cells. The enhanced electrical output of the wide-cell module should be primarily attributed to its larger active area.

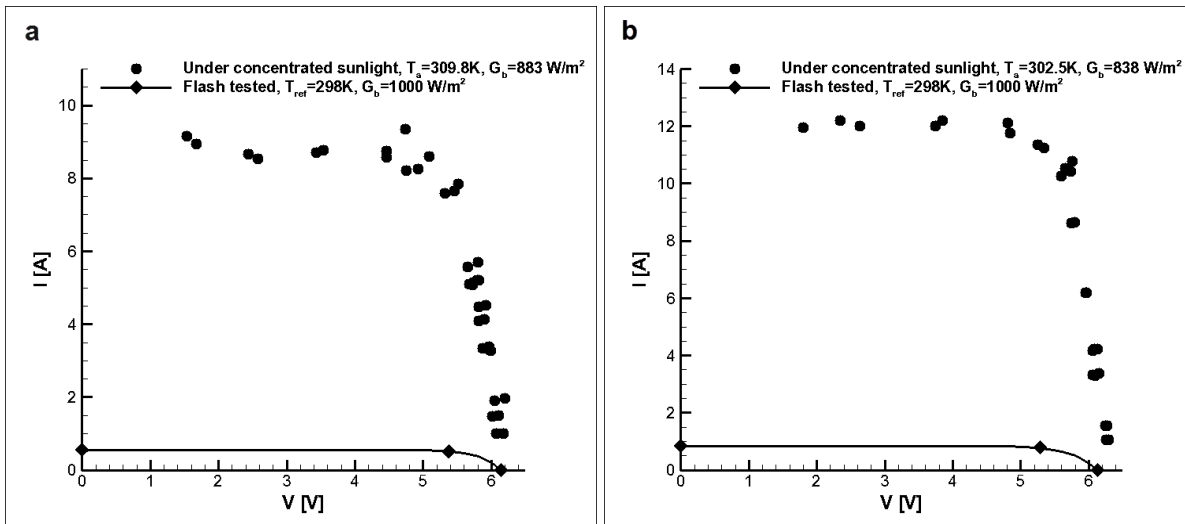


**Fig. 6.4** IV Curves measured for (a) the narrow-cell module (Module 2) and (b) the wide-cell module (Module 3).

The maximum electrical output that can be extracted from the PV module is equal to  $P_{el}=V_{MPP}I_{MPP}$ , where  $V_{MPP}$  and  $I_{MPP}$  are the voltage and current produced by the module when operating at the maximum power point. Consequently the system electrical efficiency can be defined as:

$$\eta_{el} = \frac{V_{MPP}I_{MPP}}{A_a G_b} \tag{6.4}$$

where  $G_b$  is the direct irradiation and  $A_a$  is the reflector active aperture. **Fig. 6.5** presents the variation of electrical efficiency of the three solar-cell modules examined with the substrate temperature. The

presented experimental points, albeit recorded during various testing sequences of the integrated CPVT system, can be compared in a straightforward manner as they are reduced to similar conditions through the variable  $(T_{PV} - T_a) / G_b$ . An initial observation is that the maximum electrical efficiency is in the order of 7.0% and is achieved by a wide-cell module (Module 3-**Fig. 6.5b**). On the contrary, the maximum efficiency achieved by the narrow-cell module is lower and approximately equal to 5.0% (**Fig. 6.5a**). The discrepancy in the efficiency of the two module designs is primarily attributed to the extent of their active area, as the width of the solar band is even wider than the 60mm-wide cells and thus the irradiation spillage outside the cell active area is significant especially for the narrow, 40mm-wide cells. Besides, the significant irradiation non-uniformity is the reason for the low efficiency of all the PV modules as, besides the significant irradiation spillage, the cells are primarily illuminated in the regions close to the busbar, while the bulk material at cell mid-width receives irradiation of much lower intensity (see **Fig. 5.18**). It is necessary to point out that the efficiency of Module 4 that comprises wide cells is lower by 2% absolute than the one obtained by the identical Module 3. The decline in the performance of Module 4 occurred on grounds of improper connection to the electrical load, as was identified after the testing completion and not on the module manufacturing quality. However, the overall system efficiency could be reliably evaluated, as will be shown in the next paragraph, due to the interdependent nature of the system electrical and thermal output. Hence, the experimental data obtained were reckoned as useful for the characterization of the overall system performance.

The narrow-cell modules exhibited a strong sensitivity to sun-tracking, as a minor misalignment between the system aperture and the normal irradiation lead to considerably lower electrical efficiency and this behavior partially obscured the effect of operating temperature on the efficiency. This behavior was absent in the cases of the wide-cell modules, which maintained essentially constant performance for minor tracking errors, and clearly exhibited a decreasing trend as a function of operating temperature. The effect of operating temperature on the solar-cell performance is further discussed in the next paragraph.

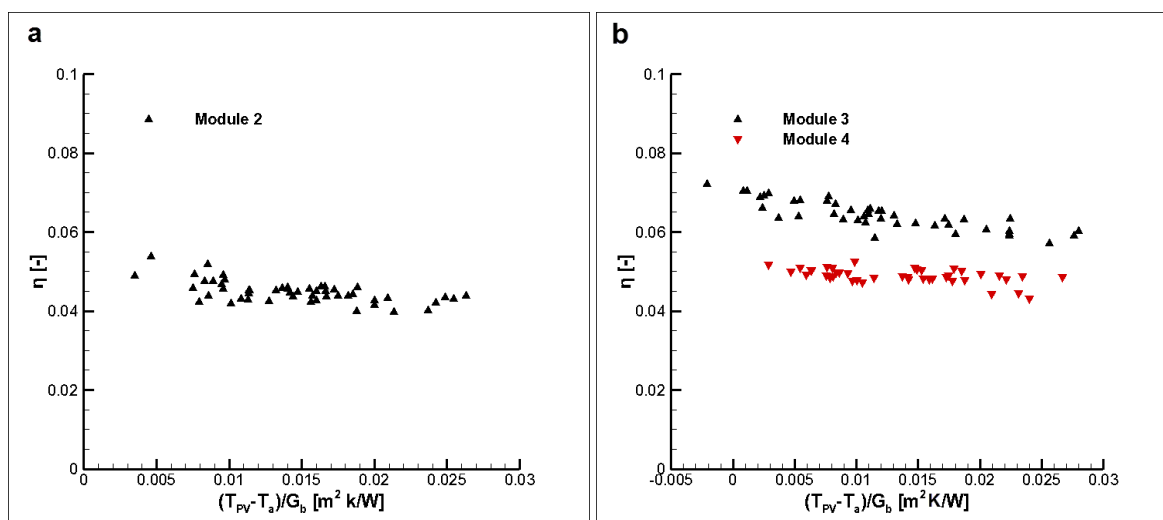


**Fig. 6.5** System electrical efficiency vs. normalized substrate temperature: (a) narrow-cell modules and (b) wide-cell modules.

6.3.1.2 Effect of temperature on PV module performance

The solar-cell modules were operated under concentrated sunlight without the presence of a heat sink, in order to evaluate the deterioration in their performance due to the elevated temperature. The resistive load was appropriately fixed so that the modules operated close to their maximum power point. The produced electrical power, the module temperature along with the direct solar irradiation and the ambient temperature were recorded at intervals of 3s, in order to keep the overall time period of each testing sequence as short as possible and thus minimize any effect on the results of a possible fluctuation of the environmental conditions or temporary loss of normal incidence. Two type-T thermocouples symmetrically attached to the mid-width of the back substrate were used for the measurement of the module temperature.

Fig. 6.6 shows the relative change in the module performance as a function of the temperature difference to ambient. The results were taken on consecutive clear days under slightly different environmental conditions and good repeatability of the measurements was achieved. As becomes evident by Figs. 6.6a-b, the expected linear decrease in performance is verified. However, the rate of decrease is steeper in the case of the “narrow” solar cells, which is a clear indication that the “wide” cells are better suited for operation at elevated temperature.

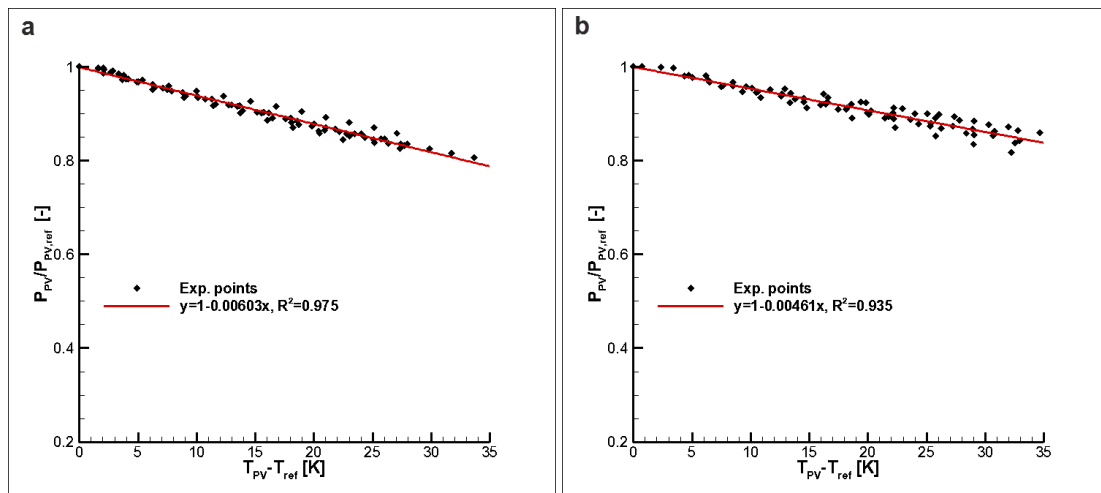


Fig. 6.6 Effect of temperature on the solar-cell module performance: (a) narrow cells, (b) wide cells.

The difference in the behavior of the two cell designs can be attributed to the series-resistance value that characterizes each design. According to the values of Table 5.2, the series-resistance value is higher for the narrow-cell module and by taking in mind that the series-resistance increases linearly with temperature [6.6], the power dissipation within the module and thus the performance deterioration is more profound for the narrow cells.

6.3.2 System overall performance

At the time being there is no official standard available for the performance characterization of CPVT systems [6.7]. Especially regarding the system thermal performance, the quasi steady-state method [6.8, 6.9], which applies for concentrating solar thermal collectors, was employed. According

to the method, the system efficiency is determined for a set of prescribed operating conditions, while requirements are also posed for the prevailing environmental conditions. The limits regarding the prevailing environmental conditions, as well as the restrictions posed to the variation of various quantities, in order for the experimental test to be considered valid are shown in **Table 6.3**. As stated by the standards [6.8-6.10], 16 experimental points for four different values of the cooling fluid inlet temperature suffice for the characterization of the system efficiency.

The flow rates selected for the measurement of the system thermal efficiency should represent actual operating conditions, while the PV module should be operated at the maximum power point. In addition, the CPVT system should be evaluated for inlet temperature values of the cooling fluid that span the entire range of achievable operating conditions. The time interval required for obtaining an experimental point must be in the order of 3-5 minutes and thus the rotating base of the CPVT system allows the acquisition of a large number of experimental points in each testing sequence, as near-normal incidence can be achieved throughout the entire daylight period, reducing this way the evaluation time period.

**Table 6.3** Requirements of the quasi steady-state method.

<b>Absolute restrictions</b>	
$V_a$	$<4.5$ m/s
$G_b$	$>630$ W/m <sup>2</sup>
$G_{b,max} - G_{b,min}$	$>200$ W/m <sup>2</sup>
$\theta$	$\approx 0^\circ$
<b>Restrictions in variance</b>	
$T_{in}$	1% or 0.2°C
$T_{f,out} - T_{f,in}$	4% or 0.4°C
$\dot{m} C_p$	1%
$G_b$	4%
$T_a$	2°C

Provided that the system has reached steady-state operating conditions, the thermal efficiency can be calculated as follows:

$$\eta_{th} = \frac{\dot{m} c_p (T_{f,out} - T_{f,in})}{A_a G_b} \quad (6.5)$$

where  $\dot{m}$ ,  $T_{f,in}$ ,  $T_{f,out}$  are the specified coolant mass flow rate and temperature at the receiver inlet and outlet, respectively. A linear model is commonly employed for the approximation of the system thermal efficiency as follows:

$$\eta_{th} = \eta_0 - U_0 \frac{\overline{T_w} - T_a}{G_b} \quad (6.6)$$

where  $\eta_0$  is the optical efficiency, namely the efficiency achieved by the system for negligible thermal losses to the environment and  $U_0$  is the thermal-loss coefficient. The optical efficiency is correlated to the receiver intercept factor and the properties of the reflector and the receiver materials as follows:

$$\eta_0 = \rho\tau\alpha\gamma \quad (6.7)$$

where  $\rho$  is the total reflectance of the reflective surface,  $\tau$  is the transmittance of the glass cover,  $\alpha$  the absorptance of the receiver active area and  $\gamma$  is the intercept factor of the receiver. The system overall efficiency was calculated by the simple summation of the respective thermal and electrical efficiencies, namely  $\eta_{tot}=\eta_{th}+\eta_{el}$ .

The system efficiency for the different receiver configurations considered (distinguished in terms of cell-width and heat-sink type) is illustrated in **Fig. 6.7** with the water volumetric flow rate being equal to 30mL/s. An initial observation can be made that the system optical efficiency is in the order of 50%, which implies that half of the radiation incident on the system aperture is lost due to the system optical quality. As was discussed in **paragraph 5.7.3**, the intercept factor of the receiver was estimated equal to 0.57 and thus the additional 7% of irradiation lost must be attributed to the transmittance-absorptance product  $\tau\alpha$  of the PV module. It is interesting to notice that the optical efficiency is approximately 2% higher in the systems employing PV modules with 60mm-wide cells (**Figs. 6.7a-b**). The enhanced optical efficiency is justified considering that the cell material, which has an anti-reflective coating, occupies a larger module area in the case of wide cells, while a portion of that area is substituted by reflective anodized aluminum in the narrow-cell modules. The comparison of **Figs. 6.7a-b** also reveals that the receiver employing the worse performing wide-cell module (Module 4-**Fig. 6.7b**) achieves higher thermal performance compared to the receiver corresponding to **Fig. 6.7a** due to the additional power available to be extracted as heat.

It is also made evident by **Fig. 6.7** that the system thermal efficiency exhibits a weak dependence on the operating temperature, i.e. heat losses are relatively insignificant and the heat-loss coefficient  $U_0$  lies in the range 0.5-1.1 W/m<sup>2</sup>K. This is due to the compact receiver configuration and the use of heavy insulation, which lead to minimal convection, radiation and conduction losses. It must be noted that the receiver configuration employing the narrow-cell module and the VW cooling device (**Fig. 6.7c**) was insulated using expanded polystyrene ( $k=0.033$  W/mK), which seems to be a more appropriate material in comparison to Armaflex that was used for the other configurations. This is made evident by the heat-loss coefficient of the specific configuration ( $U_0\approx 0.5$  W/m<sup>2</sup>K), whose value is approximately half of the respective one obtained by the other configurations. Nevertheless, the heat loss coefficients achieved by the CPVT system are significantly lower to those characterizing the thermal performance of flat-plate collectors, as will be illustrated in a subsequent paragraph.

A finding of significant importance that derives from the comparison of **Figs. 6.7a-c** is that the system achieves similar overall performance regardless of the employed cooling system (FW or VW device). It is rational to expect that heat spreading is significant within the receiver material layers with high thermal conductivity (aluminum substrates) as the irradiation non-uniformity on the receiver surface and the varying quality of the thermal bonding between the module and the heat sink should create a fully three-dimensional temperature field within each layer. Thus, it is plausible to claim that heat losses are designated by the average heat-sink temperature. As was discussed in **paragraph 4.9.3**, the values of the thermal resistance based on the average wall temperature were found to be approximately equal for the two cooling devices (see **Fig. 4.25**), a fact that gives grounds for the respective similar thermal performance of the CPVT system variations. Therefore, the VW heat-sink design appears to be a more attractive choice for incorporation in large-scale systems, where the system efficiency will be affected by parasitic pumping power, as it induces a much lower pressure

drop penalty in comparison to the FW design. In addition, the VW configuration achieves a more uniform cooling of the solar cells, which could also enhance the electrical production of large-scale systems.

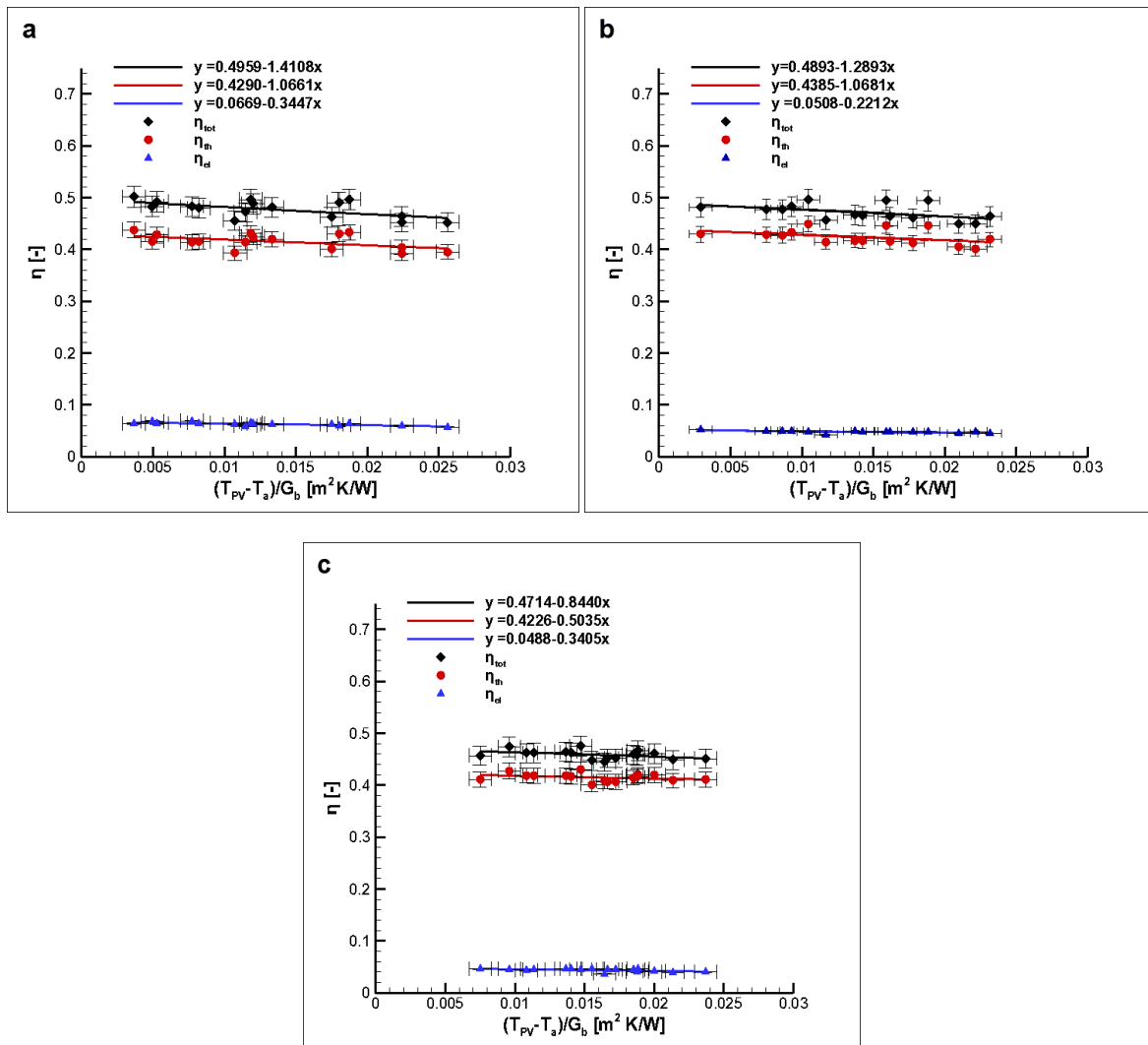
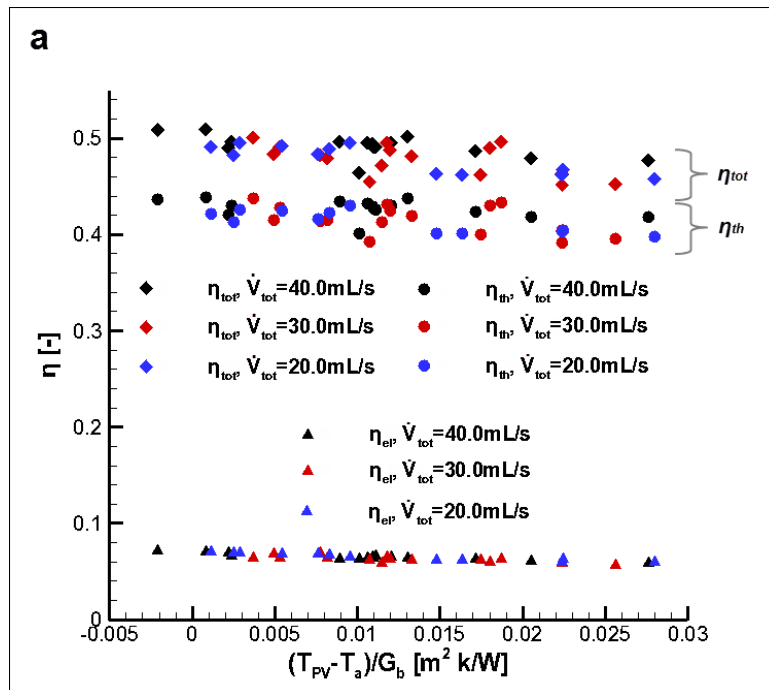


**Fig 6.7** Thermal and overall efficiency of the CPVT system for flow rate 30mL/s: (a) wide cells-FW heat sink, (b) wide cells-VW heat sink, (c) narrow cells-VW heat sink.

Several distinct nominal values of the cooling fluid flow rate equal to 20, 30 and 40 mL/s were also considered during the system experimental evaluation, in order to designate the flow-rate effect on the overall efficiency. **Fig. 6.8** depicts the experimental points obtained by the evaluation of three receiver layouts for the three values of the water flow rate considered. As regards to the receiver configuration employing the FW cooling device (**Fig. 6.8a**), increase of the fluid flow rate from 20.0 to 40.0 mL/s retains the same optical efficiency yet leads to a decrease of the heat-loss coefficient (i.e. the slope of the corresponding curve as results from a least-squares fitting of the experimental points) from 1.0 to 0.5 W/m<sup>2</sup>K. However, in the other configurations employing VW devices the heat-loss coefficient remains relatively invariant to the water flow rate with values approximately equal to 1.0 W/m<sup>2</sup>K and 0.5 W/m<sup>2</sup>K for the receiver configurations referring to **Figs. 6.8b** and **6.8c**, respectively. The low heat-loss coefficient of the narrow cells-VW heat sink configuration (**Figs. 6.8c**), obtained regardless of the

flow rate is a strong indication of the better thermal insulation provided by the expanded polystyrene in comparison to Armaflex.

In any case, the discrepancy in the system overall efficiency caused by the variation of the water flow rate, even for the receiver employing the FW device, is of comparable magnitude to the experimental uncertainty and hence it is justifiable to deduce that, at least for systems of small overall length, the system achieves a relatively constant efficiency regardless of the cooling fluid flow rate. Increase of the cooling fluid flow rate lowers the convective thermal resistance of the heat sink. However, the conductive resistances between the solid materials and especially that at the thermal bond between the module and the heat sink probably have a more significant contribution to the receiver overall thermal resistance and thus the effect of convective resistance cannot be clearly illustrated. Furthermore, as will be shown in a subsequent paragraph, the magnitude of conduction losses through the receiver insulation is negligible for the evaluated system and thus the system heat losses are designated by convection and radiation losses from the front cover. In reference to the CPVT prototype system, thermal losses from the front cover are inevitably small due to its limited area (0.04 m<sup>2</sup>). Furthermore, apart from the cover temperature, the thermal losses depend on the environmental conditions (ambient temperature and wind velocity). Especially the convective losses, which depend on the wind velocity and magnitude, are expected to exhibit considerable fluctuations between different testing sequences. On grounds of the aforementioned reasons, the effect of coolant flow rate on the system efficiency cannot be clearly illustrated, although there is an indication that increased flow rate tends to enhance the thermal performance of the system employing the FW heat sink. The evaluation of a large-scale system under specified environmental conditions would produce more illustrative results regarding the effect of the coolant flow rate on the system efficiency.



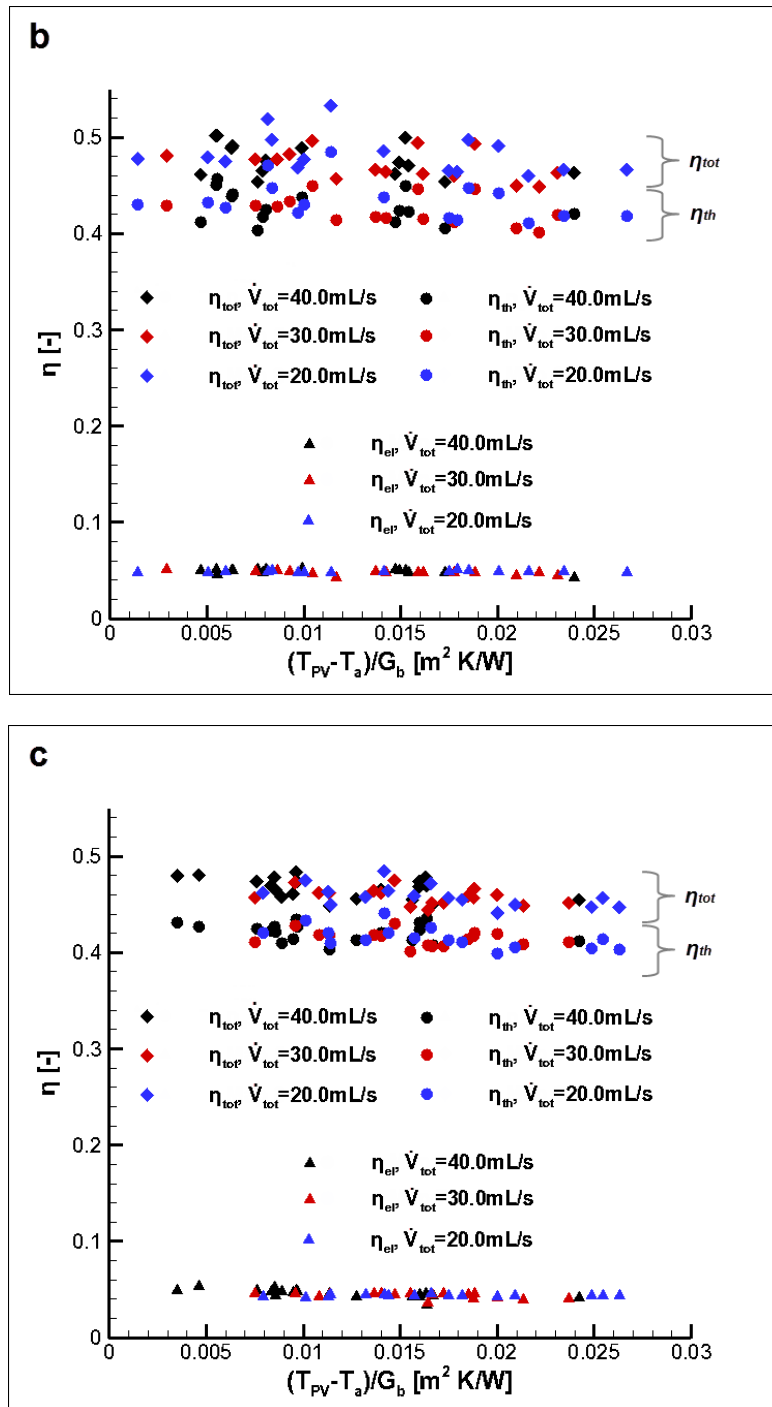


**Fig. 6.8** Effect of the water flow rate on the system efficiency: (a) wide cells-FW heat sink, (b) wide cells-VW heat sink, (c) narrow cells-VW heat sink. Error bars have been omitted to enhance the figure clarity.

### 6.3.3 Incidence angle modifier (IAM)

In the case of single-axis tracking, which is typical for linear concentrating collectors, the longitudinal angle of incidence and consequent cosine and end losses can have a significant effect on the collector daily performance since normal-incidence conditions apply only in the time interval around solar noon. The effect of non-perpendicular irradiation incidence on the system performance

can be quantified using the Incidence Angle Modifier (IAM)  $K(\theta_{long})$ , which defines how the optical efficiency decreases with incidence angle, relative to the trough's normal incidence:

$$K(\theta_{long}) = \frac{\eta_0|_{\theta_{long}=0}}{\eta_0|_{\theta_{long}}} \quad (6.8)$$

where  $\eta_0|_{\theta_{long}=0}$  is the collector thermal efficiency for normal incidence. It must be noted that the IAM is only dependant on the longitudinal angle of incidence  $\theta_{long}$ , as the respective transversal angle  $\theta_{trans}$  is always equal to zero provided the sun movement is properly tracked. The performance of the CPVT system was evaluated under non-perpendicular radiation incidence with the cooling fluid inlet temperature being kept within 2.5 °C of the ambient temperature in order to minimize heat losses, as dictated by the ASTM E905-87 standard [6.7].

**Fig. 6.9** shows the variation of the IAM with the incidence angle  $\theta_{long}$  for three receiver layouts. The best performing PV module (Module 3), showed the most significant decrease in the electrical IAM for an incidence angle of 10°, as depicted in **Fig. 6.9a**. The  $IAM_{el}$  for the specified module obtained a value close to 0.2, while the  $IAM_{el}$  of the other two modules obtained values in the range of 0.40-0.45 (**Figs 6.9b-c**). However, it was confirmed during the testing sequence that the electrical efficiency of the PV modules exhibited an intense sensitivity on the incidence angle for low angle values and the discrepancy in the  $IAM_{el}$  values detected between **Fig. 6.9a** and **Figs. 6.9b-c** could be due to small errors in the receiver manual positioning as the proper incidence angle. For an incidence angle of 30° the electrical output of the modules was nullified, although a part of the modules was still illuminated, and thus it was clearly demonstrated that the use of bypass diodes in concentrating photovoltaic applications is necessary.

The thermal efficiency of the system dropped only slightly for  $\theta_{long}=10^\circ$ , as the  $IAM_{th}$  obtained values in the range 0.85-0.95 depending on the receiver configuration. As the reflector length exceeds the receiver active length by approximately 15.0 cm on each side, it compensates for a large part of end losses and only a small part of the receiver remains unilluminated for  $\theta_{long}=10^\circ$  resulting to a small decrease of the thermal efficiency as well. For  $\theta_{long}=30^\circ$  the thermal efficiency decreased to almost half its value at normal incidence for all system variations. Besides, the IAM in reference to the overall system efficiency exhibited an approximately linear decrease with incidence angle, down to a value in the range of 0.45-0.50 depending on the receiver layout.

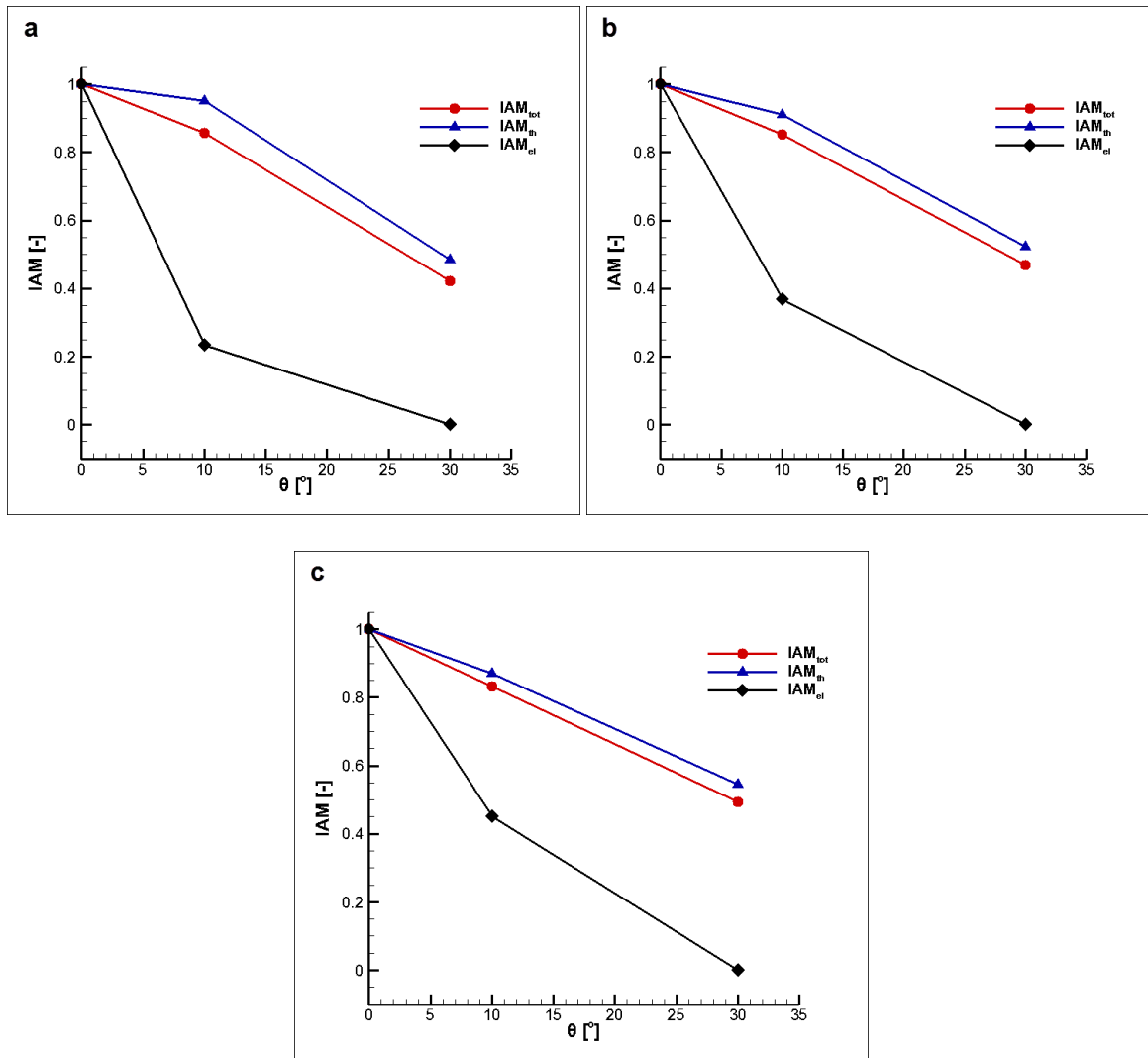


**Fig. 6.9** Incidence Angle Modifier (IAM) for the CPVT system: (a) wide cells-FW heat sink, (b) wide cells-VW heat sink, (c) narrow cells-VW heat sink

### 6.4 Temperature distribution on the glass cover

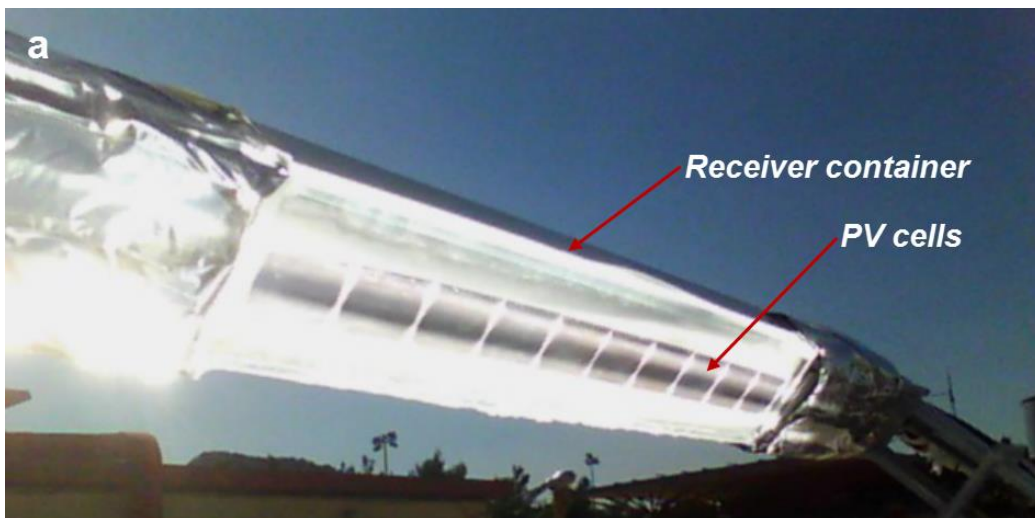
The temperature distribution of the glass cover gives an indication of the heat transfer within the various receiver materials. Furthermore, the system receiver primarily dissipates heat to the surrounding through its front cover, as will be discussed in detail in the next paragraph. It is therefore of interest to have an estimation of the temperature field that emerges on the glass cover under concentrated illumination. As was stated in **paragraph 6.1.7**, contours plots of the cover temperature field were captured with the use of a thermal camera. In order for the absolute temperature values in the captured thermal images to be accurate, the emissivity of low-iron glass cover was set equal to 0.88.

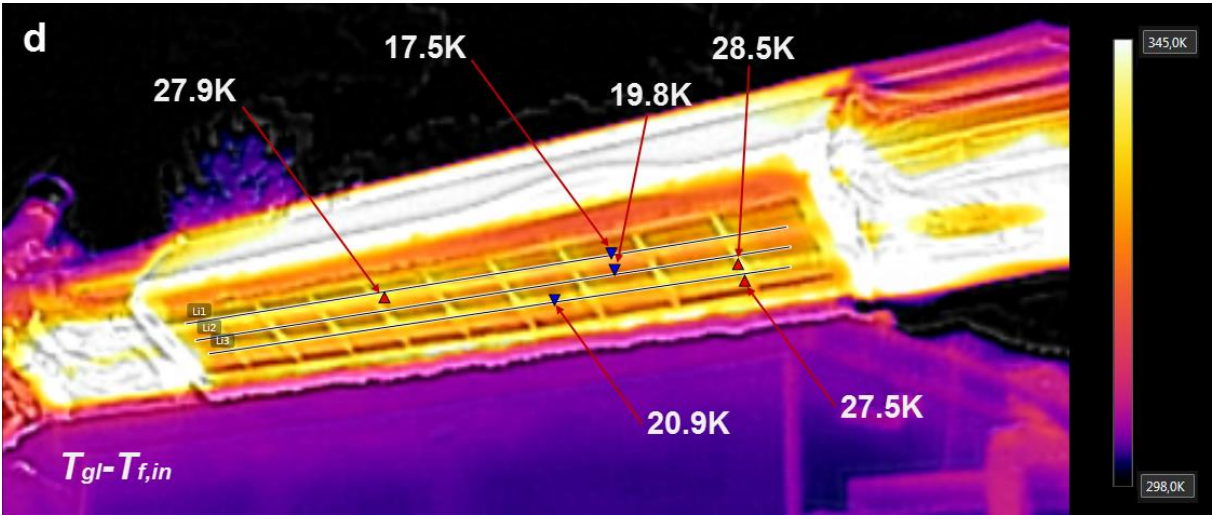
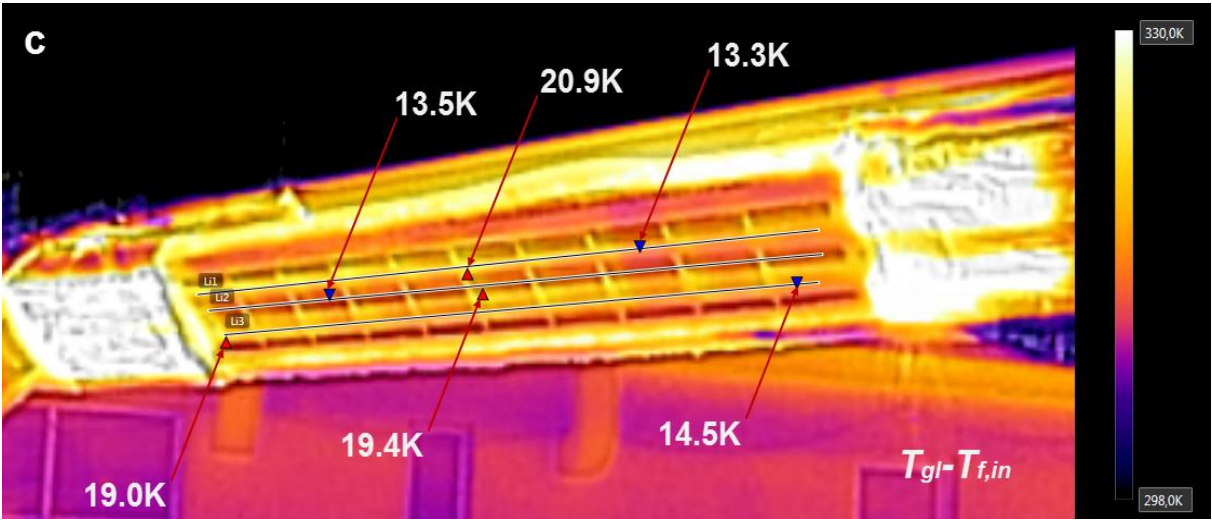
**Figs. 6.10a-b** are actual photographs of the system receiver under solar concentration. A dark region is clearly discernible at the central part of the modules, while regarding the wide-cell in particular, alternating dark and bright regions are clearly visible across the cell width. The irradiation pattern on the receiver active area, which is in compliance with the measurements presented in **paragraph 5.7.3**, must certainly have an effect on the temperature distribution as well. It is also

interesting to observe that the side walls of the receiver container are illuminated as well, revealing the irradiation spillage beyond the receiver active area.

**Figs. 6.10c-e** depict thermal images of the system receiver for the various designs of the PV module and the cooling system. An observation that applies to all the figures is that the temperature distribution on the surface of the glass cover is considerably non-uniform. Two lines of elevated temperature exist that correspond to the bright lines of **Figs. 6.10a-b**; however, there is a longitudinal temperature distribution on the lines as well.

Sampling lines (Li1, Li2, Li3) were placed on the thermal images using a processing software (FLIR Tools), with the objective to obtain a quantitative representation of the temperature distribution in characteristic regions of the glass cover. The maximum and minimum temperature points are depicted along each line (as red or blue triangles respectively) and, as can be seen, a substantial temperature difference as much as 10K exists in the glass cover e.g. see **Figs. 6.10d** and **6.10e**. In addition, points of maximum and minimum temperature occur at different locations in each receiver implying that the thermal bonding between the module and the heat sink is not uniform. The reason for the existence of hotspots on the glass cover, apart from the local irradiation intensity, is the locally poor quality of the thermal bond, i.e. the absence of conductive resin between the module and heat-sink substrates due to the manual resin spreading. Besides, it must be reminded that the solar cells are bonded onto the module substrate using a thermal adhesive tape and it is therefore plausible imperfections also to exist in the thermal bond within the PV module, e.g. due to air pockets trapped between the bonded surfaces, enabling thus the formation of hotspots.





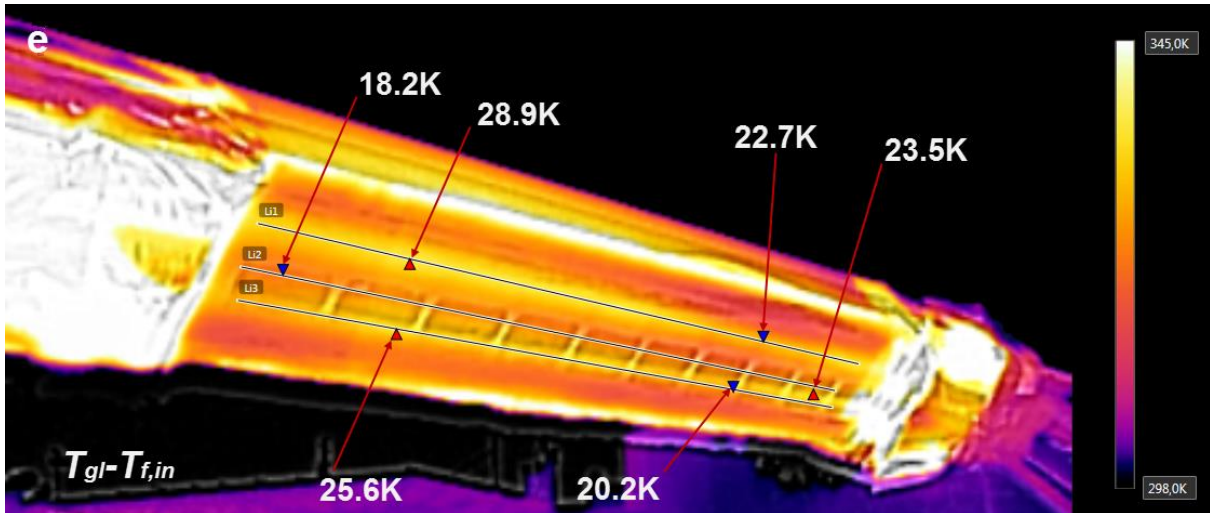


**Fig. 6.10** Photographs of the system receiver: (a) narrow (40mm) PV cells, (b) wide (60mm) PV cells. Thermal images of the system receiver: (c) wide cells-FW heat sink, (d) wide cells-VW heat sink, (e) narrow cells-FW heat sink, (e) narrow cells-VW heat sink.

## 6.5 Thermal losses

Heat is dissipated from the receiver of the CPVT system to the surroundings through three mechanisms: convection and radiation through the glass cover and conduction through the insulation of the receiver container, i.e.  $Q_{loss} = Q_{loss,conv} + Q_{loss,rad} + Q_{loss,cond}$ . The quantification of the radiation and conduction losses relies primarily on the glass cover and the heat sink temperatures, respectively, whereas the characterization of the convective thermal losses constitutes a complex task, in the sense that highly fluctuating environmental conditions such as the wind magnitude and orientation must be estimated. Additionally, the proper flow and heat transfer conditions must be assigned depending on the receiver operating temperature and relative position relative to the wind stream. An analytical approach is presented in this paragraph that enables the calculation of the total amount of heat dissipated from the receiver considering external fluid flow over a heated plate for the determination of the convective thermal losses.

The Reynolds number that characterizes the flow is defined in terms of the plate active length  $L_{pl,active}$ , according to the following expression:

$$Re_L = \frac{u_{wind} L_{plate}}{\nu_{air}} \quad (6.9)$$

where  $\nu_{air}$  is the air kinematic viscosity. In reference to forced convection conditions, the Nusselt number can be obtained from the following correlations for laminar and turbulent flow, respectively [6.11]:

$$\overline{Nu}_{FC,lam} = 0.664 Re_L^{1/2} Pr^{1/3} \quad (\text{laminar flow, } Re_L < 5 \cdot 10^5) \quad (6.10)$$

$$\overline{Nu}_{FC,turb} = (0.037 Re_L^{4/5} - 871) Pr^{1/3} \quad (\text{turbulent flow, } 5 \cdot 10^5 \leq Re_L < 10^8) \quad (6.11)$$

where the Prandtl number for air has a nominal value of 0.71 for the temperature range considered. Considering that even for a temperature difference of 5.0 K between the glass cover and the ambient, the Grashof number obtains a value in the order of  $10^8$ , the effect of natural convection on heat transfer is non-negligible. The Nusselt number for purely natural convection conditions can be approximated for a wide range of the Rayleigh number ( $10^{-1} < Ra < 10^{12}$ ) values by the following relation [6.12]:

$$Nu_{NC} = 0.56Ra^{1/4} \quad (6.12)$$

where  $Ra = GrPr$  is the Rayleigh number based on the Grashof number  $Gr = g\beta(T_{gl} - T_a) \frac{L^{pl,active}}{v_{air}^2}$ .

Given that a correlation for mixed convection over a flat surface for these conditions is not available in the literature, the Nusselt number for mixed convection conditions can be estimated with adequate accuracy [6.13, 6.14] from the respective values for pure forced (FC) and natural convection (NC), as follows:

$$Nu_{MC}^n = Nu_{FC}^n + Nu_{NC}^n \quad (6.13)$$

where the value of  $n=3$  has been proposed in the literature [6.13]. Fig. 6.11 shows the overall Nusselt number for mixed convection based on the assumption that the wind direction coincides with the system main axis ( $\theta_{wind}=0^\circ$ ) and thus the entire plate length is considered as active. Two system (plate) lengths have been considered, equal to 0.53m, which is the length of the actual module, and 5.3m, respectively, to clearly demonstrate the effect of the flow conditions on heat transfer. The heat transfer between the cover and the wind stream is forced-convection dominated, as the values of the overall Nusselt number exhibit a weak dependency on the cover temperature and are primarily influence by the wind velocity magnitude. The Nusselt number values for the 5.3m long system (Fig. 6.11b) are significantly higher as the flow transitions to turbulence at a certain location over the plate.

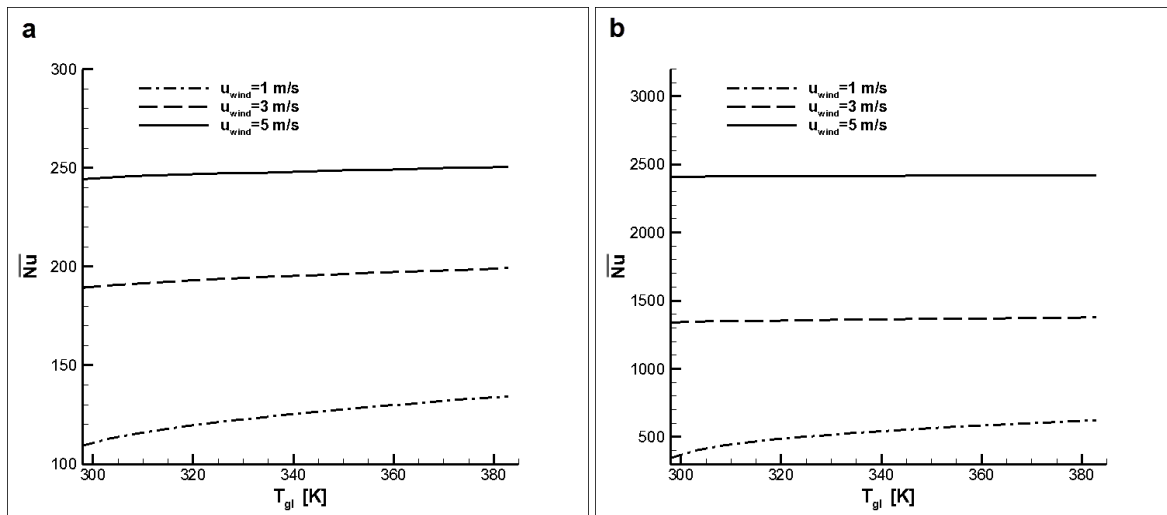


Fig. 6.11 Overall Nusselt for external flow over the glass cover considering mixed convection conditions: (a) laminar (short system) and (b) turbulent flow (long system), as a function of glass temperature and at different wind speeds.

The respective heat transfer coefficient calculated in terms of the previously formulated Nusselt number correlations is  $h_{conv,ext} = Nu_{MC} \frac{k_{air}}{L_{pl,active}}$ , where  $k_{air}$  is the air thermal conductivity. Consequently, the thermal losses from the glass cover due to convection are calculated as:

$$Q_{loss,conv} = h_{conv,ext} A_{gl} (\bar{T}_{gl} - T_a) \quad (6.14)$$

where  $A_{gl}$  is the glass cover area and  $\bar{T}_{gl}$  is the average glass temperature. It should be mentioned that in typical CPVT applications the glass cover temperature is not expected to be uniform and hence the use of the average wall temperature is a convention. However, as reported by Coventry [6.15], the use of the average cover temperature introduces a minor error less than 2% in the calculation of the thermal losses.

The radiative losses from the cover are calculated as gray-body radiation:

$$Q_{loss,rad} = \sigma \epsilon_{gl} A_{gl} (\bar{T}_{gl}^4 - T_a^4) \quad (6.15)$$

where  $\sigma$  is the Stefan-Boltzmann constant and  $\epsilon_{gl}$  is the emissivity of the glass cover. Finally, the receiver conduction losses through the container insulation are calculated by the following relation:

$$Q_{loss,cond} = \frac{1}{R_{th,ins}} (\bar{T}_{hs} - T_a), \text{ where } R_{th,ins} = \frac{t_{ins}}{k_{ins} A_{hs,ext}} \quad (6.16)$$

and  $t_{ins}$ ,  $k_{ins}$  are the thickness and thermal conductivity of the container insulation;  $A_{hs,ext}$  is the total external area of the heat sink facing the insulation material.

The thermal losses from the system receiver are presented in **Figs. 6.12a-b** for system length of 0.53m and 5.3m, respectively. Regarding the 0.53m-long system, as depicted in **Fig. 6.12a**, the radiative losses are approximately of the same order of magnitude as the convection losses for wind velocity equal to 1.0 m/s and glass temperatures up to 340K and slightly higher for further elevated temperatures. For higher wind velocities, losses due to convection are clearly the dominating heat-loss mechanism. On the contrary, for a 5.3m-long system (**Fig. 6.12b**) the radiative losses are comparable to the convective losses for wind velocity equal to 3.0 m and convective losses dominate only for very high wind velocities. The conduction losses are rendered almost negligible regardless of the system length on account of the small heat-sink outer area and the large insulation thickness. **Fig. 6.12** also elucidates the fact that the thermal losses for a 0.53m-long system operating under conditions similar to that of the experimental evaluation ( $T_{gl} < 330K$ ,  $u_{wind} = 0-2$  m/s) obtain very low values, which are in fact in the same order as the experimental uncertainty, a fact that was also established during the experimental evaluation of the prototype system.

The operating temperature of a typical linear CPVT system primarily oriented for domestic hot water or space heating is expected to lie in the range 340-360K, while the system should be located appropriately or protected by the wind loads so that, in general, it will not face wind streams of velocity larger than 3 m/s. The aforementioned requirement is easily satisfied in locations with climatological conditions similar to Athens [6.16]. For a 5.3m-long system with the geometrical and performance parameters of the experimentally evaluated prototype, the combined nominal electrical

and thermal output is expected to be approximately equal to 4.5kW, considering  $\eta_{tot}=0.5$  and  $G_b=850W/m^2$ . The percentage of thermal-losses would be less than 6% of the useful output for the specified system and it is hence clearly demonstrated that heat losses have a minor influence on the operation of the CPVT system.

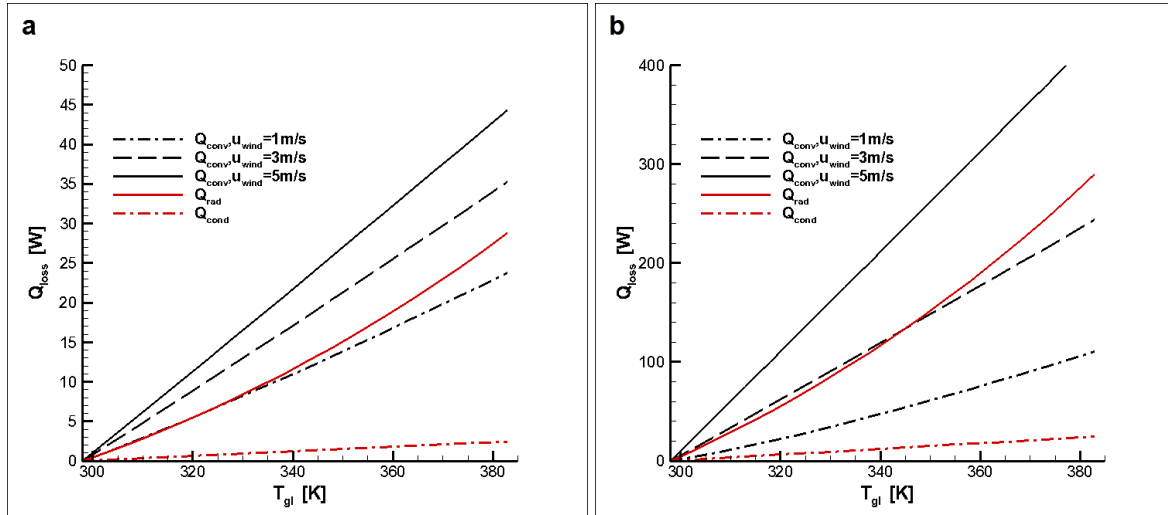


**Fig. 6.12** The various components of the thermal losses of the CPVT system: (a) 0.53m-long system, (b) 5.3m-long system, vs. glass cover temperature.

The results presented in **Fig. 6.12** were calculated with the postulate that the wind direction is aligned with the system main axis. However this is a seldom case, as, firstly, the system receiver is not static and secondly the wind direction is highly fluctuating. The convective thermal losses have been calculated for various angles of the wind direction in reference to the system receiver. The wind-stream angle relative to the receiver is defined as illustrated in **Fig. 6.13**, with  $\theta_{wind}$  equal to  $0^\circ$  and  $90^\circ$  indicating flow parallel and normal to the receiver, respectively. It is important to clarify that the wind direction was considered to lie in the same plane as the receiver bottom surface and thus any effect of possible flow impingement on heat transfer has not been taken into account. Furthermore, possible flow separation from the module leading edge and emergence of secondary flow has also been neglected in the theoretical calculations.

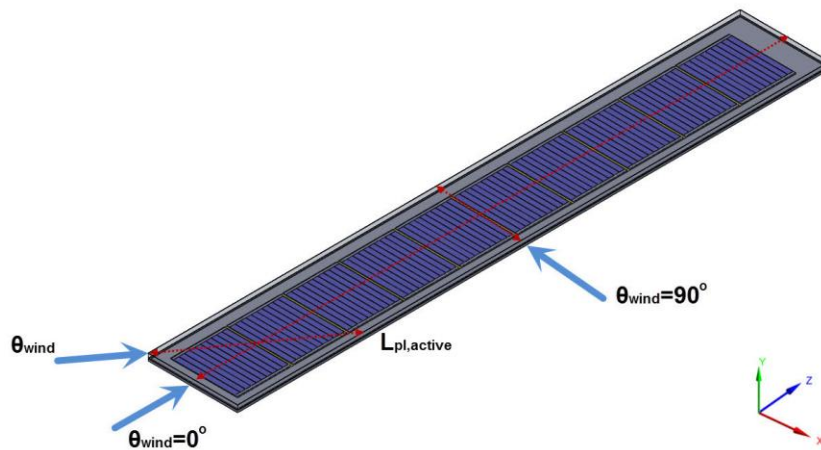


**Fig. 6.13** Definition of the wind direction for the calculation of the receiver heat losses.

The average Nusselt number values under various wind angles for external flow over a 5.3m-long receiver are presented in **Fig. 6.14a**. It must be noted that the values were calculated using once again **Eqs. (6.9-6.13)**; however the active plate length  $L_{plate}$  varied for each case corresponding to a different wind direction. It is evident that the Nusselt number values decrease with the wind angle, owing to the decrease of the plate active length and consequently of the Reynolds number. Besides, the effect of natural convection becomes negligible as the wind angle increases, owing to the strong dependence of the Grashof number on the plate active length. The respective convective thermal losses from the glass cover are presented in **Fig. 6.14b**, as calculated by **Eq. (6.14)**. As can be seen, the higher losses values are obtained for a wind direction  $\theta_{wind}=80^\circ$ , meaning that the worst case in terms of thermal losses occurs when the wind-stream is normal to the system longitudinal axis. This result may seem contradicting to **Fig. 6.14a**, where it is shown that the lowest values of the Nusselt number are obtained for  $\theta_{wind}=80^\circ$ . Yet it must be taken into account that for large angles of the wind direction the plate active length also decreases significantly (see **Fig. 6.13**) and consequently the convective heat transfer coefficient  $h_{conv,ext}$  used for the calculation of the thermal losses (see **Eq. (6.14)**) increases, leading to increased losses as well.

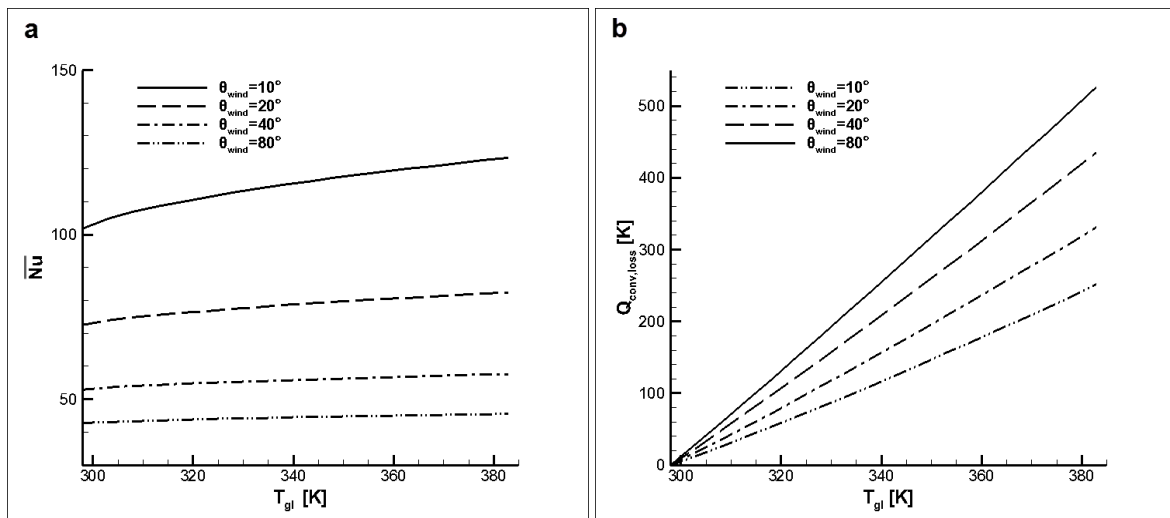


**Fig. 6.14** (a) Overall Nusselt number for external flow and (b) convection losses from the glass cover for various wind directions (5.3m system).

Various empirical correlations have been proposed for the calculation of the external convection coefficient between solar collectors and wind currents [6.17]. Especially regarding PVT systems, the following empirical correlation has been employed for the calculation of the glass cover convection losses [6.18, 6.19].

$$h_{conv,ext} = 2.8 + 3.0 \cdot u_{wind} \tag{6.17}$$

where  $u_{wind}$  is the wind velocity magnitude. **Eq. (6.17)** was derived for external parallel flow over a heated plate and is valid for wind velocities up to 5.0m/s [6.20, 6.21]. **Fig. 6.15** presents the convective heat losses from the glass cover, as calculated using the analytical and empirical expressions for the heat transfer coefficient, respectively. The analytical and empirical predictions for

the convective thermal losses of the 0.53m-long system (Fig. 6.15a) are in agreement for wind velocity equal to 1.0 m/s. However, for higher wind velocities a discrepancy exists between the empirical and analytical predictions, which becomes significant for wind velocity equal to 5.0 m/s. In respect to the 5.3m-long system (Fig. 6.15b), the values of convective losses produced by the empirical correlation are systematically larger than the analytically produced ones for parallel flow. In fact, the empirical predictions are in relative agreement with the analytical values produced considering a wind angle of 20°. It should be beared in mind that the empirical heat transfer coefficient Eq. (6.17) has been derived from fitting of experimental data and thus it includes the effect of possible flow separation. In conclusion, the general assessment can be made that the calculation of the individual convective thermal losses from the receiver bears a considerable degree of uncertainty and consequently the most suitable procedure to provide accurate results in reference to heat losses would be the experimental evaluation of a CPVT system of considerable length under properly monitored (or controlled) environmental conditions.

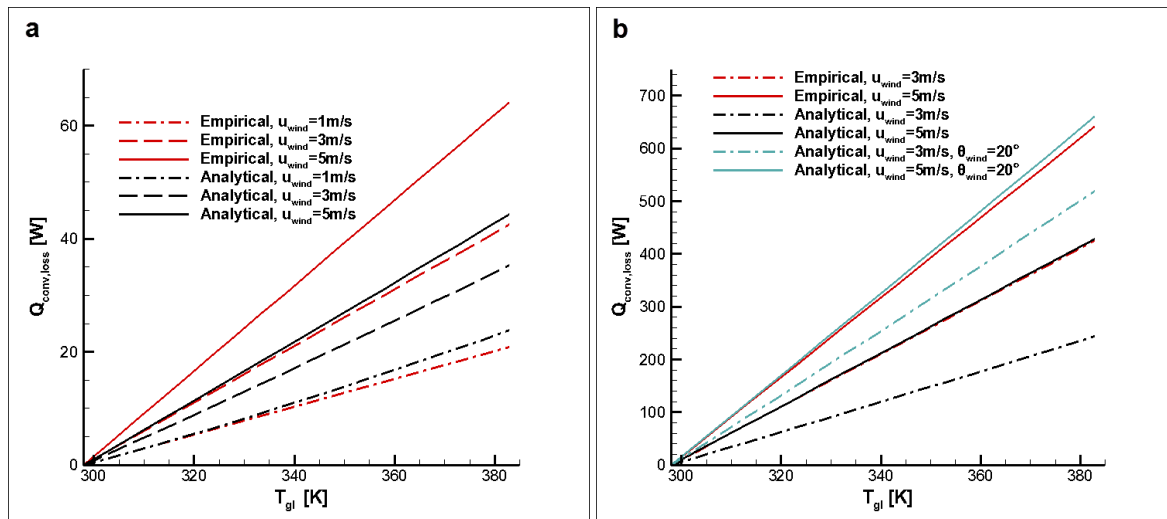


Fig. 6.15 Convective thermal losses from the glass cover as calculated using analytical or empirical correlations: (a) 0.53m-long system, (b) 5.3m-long system.

## 6.6 Heat transfer at the thermal bond

The proper thermal bonding between the PV module and the heat sink constitutes the major technical issue associated with concentrating photovoltaic thermal applications. Poor bonding quality leads to increased solar-cell module temperature, higher thermal losses and consequently decreased electrical and thermal system performance. Besides, elevated module temperature is the main cause for the degradation of its materials, especially of the silicon cells and the thermal tape, and, in general, increases the possibility of a material failure and decreases the life cycle of the application. It has also been reported by Coventry [6.15] that thorough examination of adhesive materials and fastening techniques are required in order to improve the overall performance of a CPVT system.

As was reported in paragraph 5.10, the use of a thermal tape (AIT CB7208-A) was also considered for the bonding of the heat sink onto the module. During the indoor evaluation of the adhesive materials, the thermal tape achieved lower thermal resistance values in comparison to the epoxy resin (see paragraph 5.10.1) and for this reason an initial receiver configuration was assembled

using the thermal tape as bonding material. However, it was established during the testing of the integrated system that the temperature difference between the PV module and the heat sink obtained high values beyond 30K at a very early stage of the testing sequence and certainly before steady-state operating conditions were reached. Therefore the evaluation of the specific receiver configuration had to be called off, in order to prevent the rupture of the solar cells due to the extreme thermal fatigue. It is essential to mention that no clamping configuration was used to fasten the heat sink on the module and this could explain the performance deterioration of the thermal tape. The solid texture of the tape in conjunction with the low pressure at the joint probably allowed the formation of numerous air pockets between the two aluminum substrates leading to poor heat transfer. The epoxy resin was, therefore, used for thermal bonding in all the subsequently assembled receiver configurations.

**Fig. 6.16** presents the temperature difference  $\Delta T = T_{PV} - T_{hs}$  between the PV-module substrate and the heat sink solid wall as a function of the thermal power removed by the fluid ( $Q_{th}$ ) and it is thus indicative of the thermal resistance imposed by the epoxy resin. Each temperature is derived as an average from the readings of three thermocouples mounted on the backside of the module substrate, whereas three more of them were mounted at the backside of the heat sink (**Fig. 6.16a**). It must be noted that the thermocouples had to be mounted on the receiver backside, as they could not be inserted in the holes originally drilled in the heat-sink substrate especially for that purpose (see **Fig. 4.11**). The reason was that those holes had been blocked by the epoxy resin during the adhesion of the heat sink on the PV module. In any case the temperatures occurring at the backside are certainly lower than the respective at the heat-sink substrate and thus the use of the specific temperature difference constitutes a conservative approach. As illustrated in **Fig. 6.16b**, the temperature difference between the module and the heat sink is in the order of 5-7K depending on the system receiver variation. It is essential to point out that each experimental point depicted in **Fig. 6.16b** corresponds to a different value of the water flow rate (20, 30 and 40 mL/s, respectively). Regarding the receiver configurations that employ the VW heat sink, the temperature difference appears insensitive to the cooling fluid flow rate. With respect to the receiver integrated with the FW cooling device, a small discrepancy can be detected in the temperature difference for flow rates equal to 20 and 40 mL/s, which could be attributed to a more significant effect in comparison to the VW configurations of the elevated flow velocity on the convective thermal resistance of the heat sink. However the discrepancy is in the order of experimental uncertainty and it is thus unsafe to draw a solid conclusion. In any case the quality of the bond has a non-negligible effect on heat transfer as revealed by the fact that the two configurations both employing VW exhibit a discrepancy of 1.0 K in the temperature difference values. In fact, the temperature difference is lower for the narrow PV-VW heat sink configuration, although the heat rate is slightly higher.

It can be therefore deduced that the epoxy resin is suitable as a thermal-bonding material; however further investigation is required to further reduce the temperature difference at the bond, which, albeit it is not of great magnitude for the evaluated CPVT system, it is still much higher than the theoretically predicted one considering the resin thermal conductivity. The thermal resistance at the bond could be reduced if uniform resin thickness without voids is assured and, in addition, if the pressure at the joint is increased by mechanically clamping the heat sink on the PV module.

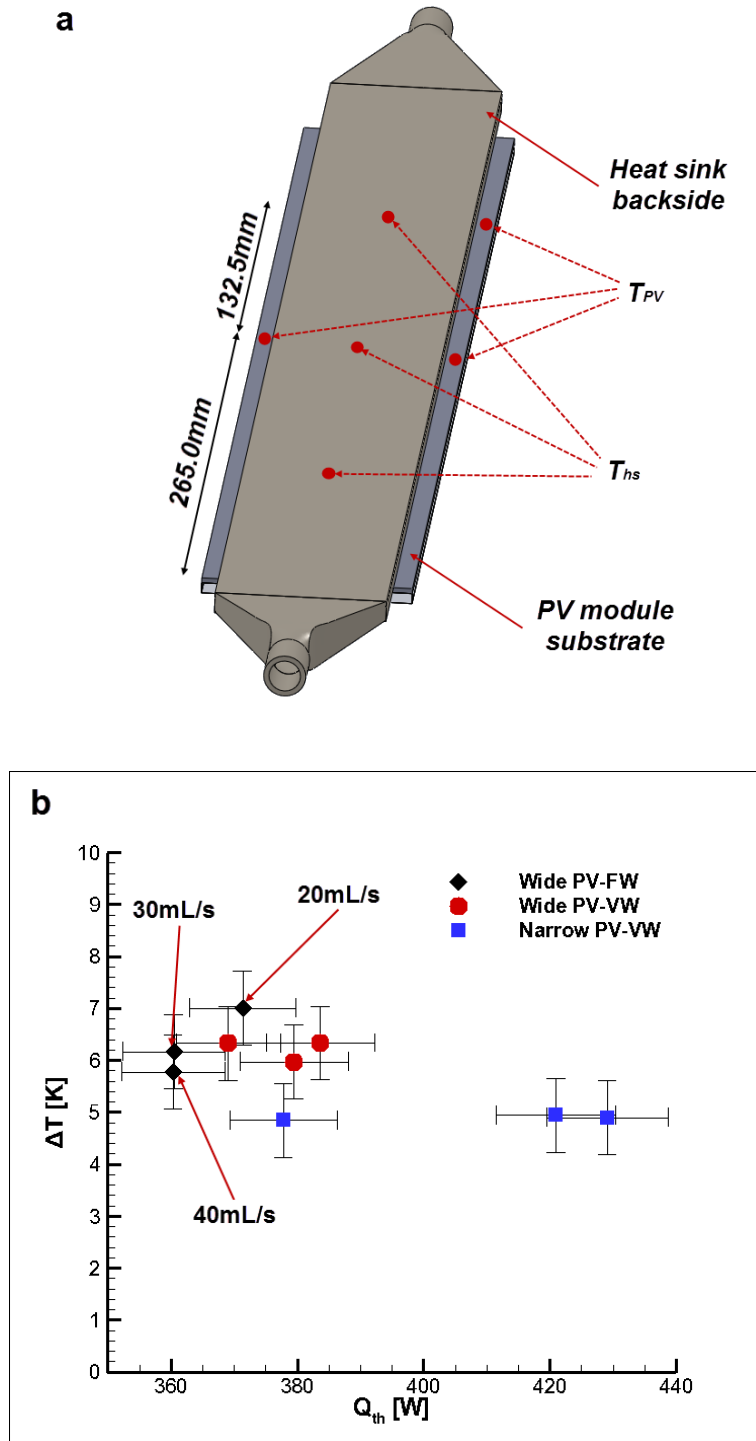


**Fig 6.16** (a) Locations of the thermocouples on the PV module and the heat sink. (b) Temperature difference between the PV-module substrate and the heat sink as a function of the heat removed by the module.

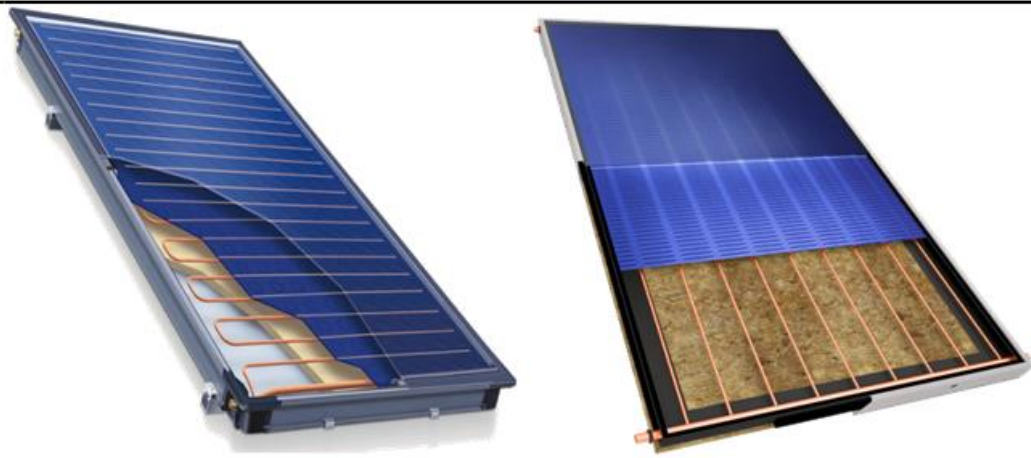
### 6.7 Comparison to flat-plate solar thermal collectors

As the greater part of the system output is in the form of thermal power, it is of importance to examine its thermal performance characteristics in comparison to those of conventional solar thermal collectors. For this reason, the prototype CPVT system has been compared in terms of thermal performance to two state-of-the-art flat-plate solar thermal collectors that are commercially available

in the Greek market. The main design and operating characteristics of the two flat-plate collectors are presented in **Table 6.4**. It must be noted that both collectors employ a selective coating that greatly reduces the absorber emissivity  $\varepsilon_p$  to a value approximately equal to 0.1, but bear different tubing layouts, which are commonly referred to as “harp” and “meander”, respectively.

The performance data of the flat-plate collectors were obtained by the Solar and other Energy Systems Laboratory of NCSR Demokritos through the experimental procedure dictated by the EN12975-2:2006 Standard [6.22], which is similar to the procedure followed for the evaluation of the CPVT system. The cooling fluid flow rate differs between the collectors as the standard dictates that the imposed flow rate should be calculated according to the relation  $\dot{V}_{tot} = 0.02 \cdot A_a$ , where  $A_a$  is the aperture area of the collector.

**Table 6.4** Main characteristics of the commercial flat-plate collectors used for comparison.



Type	Meander	Harp
$A_a$ [m <sup>2</sup> ]	2.31	2.57
$V_{tot}$ [mL/s]	46.14	51.27
$\varepsilon_p$	0.10	0.10

**Fig. 6.17** presents the comparative results for the flat-plate and concentrating configurations. The efficiency curves referring to the CPVT system variations were obtained from the experimental points for water volumetric flow rate equal to 40 mL/s, while the PV module operated at the maximum power point in all cases. However, the electrical output of the CPVT system has been excluded from the comparative evaluation. Additionally, in order to obtain a straightforward comparison between the different types of solar applications, the efficiency points regarding the CPVT system were reduced to the fluid mean temperature  $\overline{T}_f$  and the total irradiation intensity  $G_{tot}$ . As regards the reduction of the radiation values, the assumption was made that for a sunny day the diffuse radiation is 10% of the total solar radiation. The optical efficiency of a flat-plate collector relies solely on the optical properties of the cover and the absorber, i.e. on the product  $\tau\alpha$  of the cover transmissivity and the plate absorptivity; hence, the considered flat-plate collectors achieve high optical efficiencies in the order of 0.8. In contrast, the concentrating system achieves a lower optical efficiency in the order of 0.4, as the integration of a concentrating optical device is accompanied by increased optical losses due to the imperfections in the shape of the concentrator and the reflectivity of the reflector material (see **Eq. 6.7**). However, the major advantage of the concentrating system in terms of thermal performance compared to the flat-plate devices is the very low heat-loss coefficient  $U_0$  achieved, as confirmed by

comparing the slope of the respective sets of curves. In fact, this value lies in the range 0.29-0.93 W/m<sup>2</sup>K for the CPVT system, depending on the heat-sink configuration and the insulation of the receiver, whereas the respective values for the flat plate collectors are in the order of 4.69-4.91 W/m<sup>2</sup>K.

Therefore, the general conclusion that can be drawn is that the present CPVT system, although a prototype application, compares well in terms of performance, especially if the electrical output is also taken into account, to well established, commercial products. The only major drawback of the system is the low optical efficiency, which is exclusively due to the moderate receiver intercept factor. Modern precision manufacturing allows for values of a parabolic trough optical efficiency as high as 0.70-0.75. Such values would render the CPVT system more efficient than flat plate collectors, especially for higher operating temperatures.

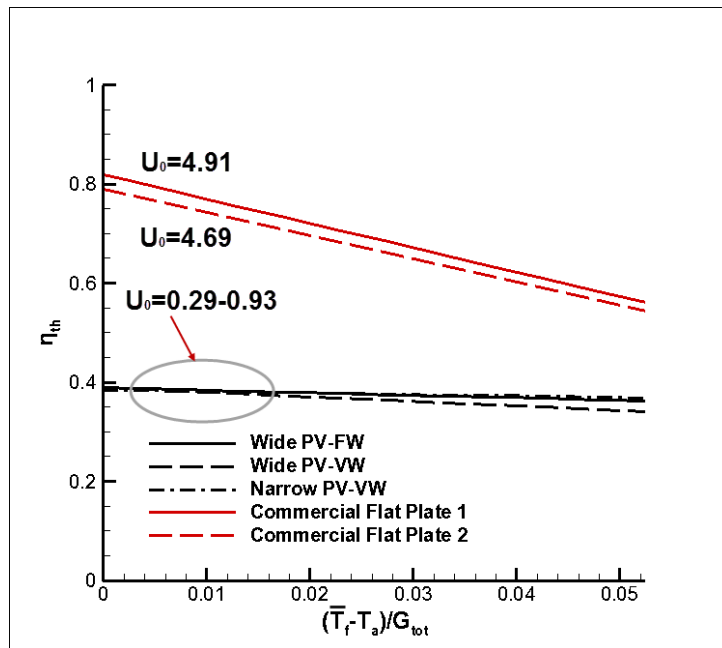


**Fig 6.17** Comparison of the system thermal performance (steady-state efficiency) of the CPVT system against state-of-the-art commercial flat-plate collectors (Flat Plate 1: meander type, Flat Plate 2: harp type).

**Chapter References**

- [6.1] ISO 9060:1990 Standard, Specification and classification of instruments for measuring hemispherical solar and direct solar radiation.
- [6.2] DIN EN 60751:2009 Standard, Usage limitations and accuracies of platinum resistance thermometers in industrial applications.

- [6.3] Agilent Technologies Inc., VEE Pro User's guide, 8<sup>th</sup> ed., Loveland CO, 2004.
- [6.4] R.J. Moffat, Describing the uncertainties in experimental results, *Exp. Therm. Fluid. Sci.* 1 (1988) 3-17.
- [6.5] M.E. Mathioulakis, Measurement, quality of measurement and uncertainty (in Greek), Hellas Lab publications, Athens, 2004.
- [6.6] W. Xiao, W.G. Dunford, A. Capel, A novel method for photovoltaic cells, Proceedings of the 35<sup>th</sup> Annual IEEE Power Electronics Specialists Conference, Aachen, Germany, 2004.
- [6.7] M. Vivar, M. Clarke, J. Pye, V. Everett, A review of standards for hybrid CPV-thermal systems, *Renew. Sustain. Energy Rev.* 16 (2012) 443–448.
- [6.8] ASHRAE 93-2010 Standard, Methods of testing to determine the thermal performance of solar collectors.
- [6.9] ASTM E905-87 Standard, Standard test method for determining thermal performance of tracking concentrating solar collectors, 2007.
- [6.10] L. Xu, Z. Wang, X. Li, G. Yuan, F. Sun, D. Lei, et al., A comparison of three test methods for determining the thermal performance of parabolic trough solar collectors, *Sol. Energy.* 99 (2014) 11–27.
- [6.11] R.H. Pletcher, External Flow Forced Convection, in: S. Kakac, R.K. Shah, W. Aung (Eds.), *Handbook of Single Phase Convective Heat Transfer*, Wiley & sons, New York, 1987.
- [6.12] Y. Jaluria, Basics of Natural Convection, in: S. Kakac, R.K. Shah, W. Aung (Eds.), *Handbook of Single Phase Convective Heat Transfer*, Wiley & sons, New York, 1987.
- [6.13] T.S. Chen, B.F. Armaly, Mixed convection in external flows, in: S. Kakac, R.K. Shah, W. Aung (Eds.), *Handbook of Single Phase Convective Heat Transfer*, Wiley & sons, New York, 1987.
- [6.14] F.P. Incropera, D.P. DeWitt, sixth ed., *Fundamentals of Heat and Mass Transfer*, Wiley, New York, 1996.
- [6.15] J.S. Coventry, A solar concentrating photovoltaic/thermal collector, PhD Thesis, Australian National University, Canberra, AU, 2004.
- [6.16] K. Philippopoulos, D. Deligiorgi, Statistical simulation of wind speed in Athens, Greece based on Weibull and ARMA models, *Int. J. Energy Env.* 4 (2009) 151-158.
- [6.17] J.A. Palyvos, A survey of wind convection coefficient correlations for building envelope energy systems' modeling *Appl. Therm. Eng.* 28 (2008) 801-808.
- [6.18] G. Kosmadakis, D. Manolakos, G. Papadakis, Simulation and economic analysis of a CPV/thermal system coupled with an organic Rankine cycle for increased power generation, *Sol. Energy.* 85 (2011) 308–324.

[6.19] T.T. Chow, Performance analysis of photovoltaic-thermal collector by explicit dynamic model, *Sol. Energy* 75 (2003) 143–152.

[6.20] J.H. Watmuff, W.W.S. Charters, D. Proctor, Solar and wind induced external coefficients for solar collectors, *Comptes. Rend. Acad. Sci. Paris, Ser. II* 2 (1977) 56.

[6.21] W. Nusselt, W. Jürges, Die Kühlung einer ebenen Wand durch einen Luftstrom (The cooling of a plane wall by an air flow), *Gesundheits Ingenieur* 52. Heft, 45. Jahrgang, (30 Dezember 1922) pp. 641–642.

[6.22] EN12975-2:2006 Standard, Thermal solar systems and components - Solar Collectors - Part 2: Test methods.



---

# Chapter 7 Dynamic simulation and optimization of the CPVT system

---

## 7.1 Introduction

Analytical models have been widely used and proven adequate for the prediction of the performance and the daily or annual yield of conventional PVT systems using sheet and tube absorbers, similar to those encountered in flat plate solar thermal collectors. A simple steady-state theoretical model for a flat PVT system that provides low grade heat to an industrial process was proposed by Hazi et al. [7.1]. Amrizal et al. [7.2] predicted the dynamic thermal behavior of a PVT system through linear regression based on constant coefficients that can be specified by measuring the steady-state system efficiency. The simplified approach used in the study assumes the PVT system as a “lumped” component that can be described through averaged quantities. Three steady-state (1-D, 2-D and 3-D) analytical models and a three-dimensional dynamic model were comparatively evaluated by Zondag et al. [7.3] for the prediction of the daily and annual yield of a flat PVT system. The predictions of all models were found in good agreement to measurements regarding the system steady-state efficiency. In addition, it was proved that even the 1-D steady model was adequate for the prediction of the system daily and annual yield. Chow [7.4] developed an explicit analytical model representing a flat plate PVT system. The system receiving plate was divided into segments and the thermal balance was formulated for each segment. The analytical model was used to predict the system response to rapid variations of the operating parameters (irradiation and flow rate).

Theoretical models have also been developed in order to investigate novel flat PVT system layouts and to designate the effect of the system materials on their performance. A flat PVT system using a polycarbonate absorbing plate consisting of parallel channels and thermal storage was modeled by Cristofari et al. [7.5]. The effect of heat capacity was taken into account in the thermal balance equations and the system daily and annual efficiency and yield were calculated. Abu Bakar et al. [7.6] modeled a flat PVT system with fluid (air-water streams) using a two-dimensional steady-state model. Water flows in a serpentine tube enclosed in a rectangular duct, where the air stream flows. The top surface of the duct serves as the system absorber, where the cells are bonded. The focus of the study was on the effect of the two fluid flow rates on the system thermal and electrical efficiency. Da Silva and Fernandes [7.7] performed a sensitivity analysis using a dynamic one-dimensional model and pointed out that the PV module emittance has the most considerable effect on the thermal losses of a flat PVT system, in comparison to other structural and operating parameters. The placement of the absorber in vacuum and the removal of the cell encapsulation material were proposed in order to mitigate thermal losses and it was found that an increase of 8% in the system thermal efficiency could be achieved. The daily trend of the imposed external thermal load was also found to affect the system thermal efficiency. The daily performance of a flat PVT system that also incorporates a layer of PCM material was simulated by Malvi et al. [7.8] using a dynamic one-dimensional model. The focus of the investigation was to determine the influence of the operating conditions and the PCM characteristics on the system performance.

There is a number of studies in the literature that discuss the formulation of analytical models representing concentrating photovoltaic/thermal systems. However, the majority of them do not take transient effects into account. An early study by O'Leary and Clements [7.9] illustrates the formulation of an analytical model of a parabolic trough CPVT system. Transient effects were neglected, as the model was intended for the determination of the optimal coolant flow-rate that maximizes the system net electrical output. A similar study for a compound parabolic concentrator PVT system was conducted by Hedayatizadeh et al. [7.10] who discuss the influence of the environmental conditions and operating parameters on the system overall efficiency. Helmers et al. [7.11] formulated a theoretical model to predict the influence of operating parameters on the efficiency of a point-focus CPVT system. The investigation was focused on the effect of the concentration ratio and cell operating temperature. Their results showed that under high concentration ( $CR > 300$ ), the rate of thermal and electrical losses decreases and a system overall efficiency of 75% can be achieved.

Calise et al. [7.12] developed an analytical steady-state model for a parabolic trough CPVT system with triple-junction cells bonded to a receiver of triangular cross-section and a circular passage where the cooling fluid flows. The receiver was segmented and the mass and energy balances were formulated for each segment. A parametric analysis regarding the variation of system energetic and exergetic efficiency with the system length and the coolant flow rate, respectively, was conducted. It was shown that increase of both parameters leads to increased efficiencies. However, it must be noted that the effect of the parasitic pumping power on the overall efficiency was neglected. In a subsequent study Calise et al. [7.13] included their model of the linear CPVT system into an integrated tri-generation system. The additional system components namely the storage tank and the desiccant air-conditioning unit utilized the thermal output of the CPVT system, while a natural gas boiler served as auxiliary heat input. Researchers from the same group also integrated their developed model to a tri-generation system that uses an absorption chiller to meet cooling loads [7.14]. The investigation illustrated the system capability to cover the annual electricity, heating and cooling demands of a university hospital. In a separate study, Calise et al. [7.15] also evaluated the annual performance of a tri-generation system similar to that presented in [7.14], with the exception of incorporating a point focus dish CPVT system. A parametric analysis taking the overall CPVT system area as a design parameter was also conducted.

Buonomano et al. [7.16] used a one-dimensional algebraic model to predict the performance of a solar dish CPVT system introduced by Kribus [7.17]. Steady state conditions were considered and the system of equations comprising the model was further simplified by neglecting some of the material layers in the receiver. The authors provided predictions for the system thermal and electrical efficiency and, in addition, illustrated the effect of the main geometrical parameters and operating conditions on the system efficiency. A Fresnel lens linear CPVT system that employs high efficiency triple-junction cells with thermal energy storage was modeled by Kerzmann and Schauerer [7.18]. A rectangular duct was considered as the cooling device for the PV module. The thermal balance equations were formulated for each segment of the linear receiver assuming steady-state conditions and the system daily and annual yield were predicted. Renno and Petito [7.19] evaluated the performance of a solar tri-generation system that comprises a point-focus dish CPVT system with a remote duct receiver, a storage tank and a absorption heat pump, in order to meet the electrical, thermal and cooling loads respectively. A one-dimensional model, assuming steady-state operation of all the devices was formulated, and the system yield for two site locations was predicted, by also taking into account the

number of solar cells and the concentration ratio as parameters. In a further study, Renno [7.20] optimized the system reported in [7.19] by coupling the concentration ratio to the system overall area and the working fluid outlet temperature through a fuzzy logic technique. The goal of the optimization procedure was to determine the concentration ratio for which the system occupies a specified overall area and is able to meet the imposed thermal (or cooling) loads.

Few studies have been found, where the effect of heat capacitance has been included in the thermal balance equations and thus the models can predict the transient behavior of the CPVT system as well. Helmers and Kramer [7.21] formulated a quasi-dynamic theoretical model that can predict the thermal and electrical output of a CPVT system by making use of linear regression based on constant coefficients in a procedure similar to that described in [7.2]. A transient model was developed by Coventry [7.22], whereby the formulated set of energy balance differential equations was solved analytically instead of being iteratively approximated. The model was used for the prediction of the annual output of a system coupled to thermal storage. In addition, the effect of basic design parameters, such as the insulation thickness and the conductivity of the thermal interface material, on the annual efficiency was examined. Kosmadakis et al. [7.23] simulated the performance of a linear trough CPVT system which also served as a prime mover for an organic Rankine cycle in order to produce additional electricity.

The scope of the present chapter is to illustrate the influence of the various components geometrical layout, materials and parameters of operation on the CPVT system long-term performance by means of a dynamic theoretical model. The model was employed to conduct a parametric analysis, where the system daily or annual yield was determined for different values of the geometrical and operational parameters. The receiver was divided in segments, so that the temperature distribution at the various material layers along its length can be obtained and consequently the thermal losses and the system electrical performance can be accurately predicted.

### 7.2 Formulation of the dynamic model

The simulation of the CPVT system transient performance was based on energy balances performed on every layer of the system receiver. The model was formulated under the main assumptions of negligible gravitational terms and negligible losses due to end effects. The latter assumption is legitimate, as in reference to configurations with relatively small overall length, the present system could be manufactured as two-axes tracking incorporating a rotational base, whereas longer systems could extend the reflector beyond the receiver active length to prevent the occurrence of end losses. For example, in the extreme case where the system operates at an incidence angle of  $62.4^\circ$ , which occurs at 8am on the summer solstice, an extension of the reflector by 1.3m (for a focal length of 0.69m) beyond the receiver would make the end-loss effects negligible. It is feasible from a manufacturing standpoint for a system having a typical row length e.g. of 10-15m, to incorporate additional reflectors of 2-3m. The effect of non-uniform irradiation distribution on the PV modules surface was taken into account through a constant factor  $F_{uni}$ , whose value is properly set so that the predictions are in agreement with the experimental measurements. Seven material layers were considered and the resulting network of thermal resistances that represents the receiver is depicted in **Fig. 7.1**. For each node  $i$  of the thermal network, i.e. for each material of the receiver, the formulated thermal-balance equation takes the general form:

$$M_i C_i \frac{dT_i}{dt} = \sum_j Q_{in} - \sum_k Q_{out} \quad (7.1)$$

where  $M$  and  $C$  are the material mass and specific heat, respectively. Transient effects are taken into account through the term on the left-hand side of Eq. (7.1), which corresponds to the heat capacitance of the material. Heat flows  $Q$  are correlated to the temperatures of consecutive nodes through the relation:

$$Q = \frac{T_i - T_{i+1}}{R_{th,i-i+1}} \quad (7.2)$$

where  $R_{th,i-i+1}$  is the thermal resistance between consecutive nodes. Each node of the thermal system is placed at the mid-thickness of the material layer and thus the thermal resistance between nodes is treated as half the sum of the thermal resistances of consecutive layers:

$$R_{i-i+1} = \frac{R_i + R_{i+1}}{2} \quad (7.3)$$

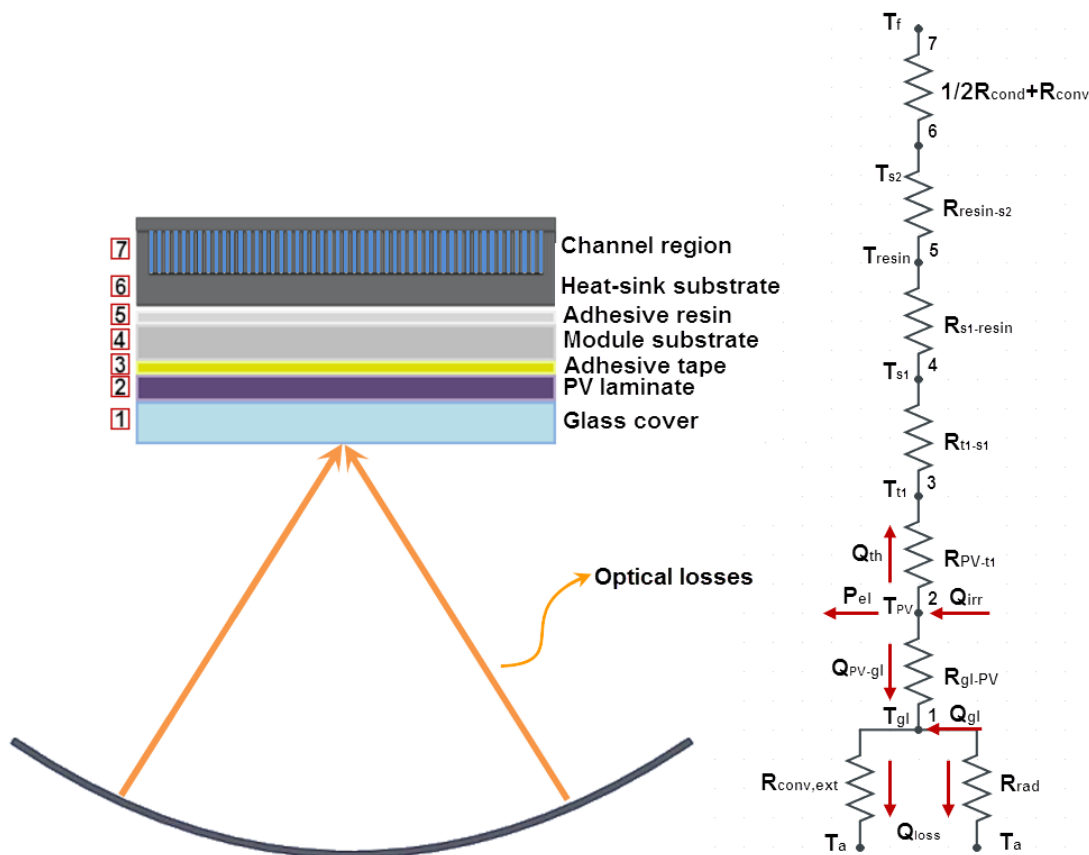


Fig. 7.1 Schematic layout of the CPVT system and thermal network used for the formulation of the energy balances.

By applying **Eqs. (7.1)-(7.2)** on each node of the thermal network, the following set of equations is derived:

- Glass cover of the PV module

$$M_{gl} C_{gl} \frac{dT_{gl}}{dt} = Q_{gl} - Q_{loss} + \frac{T_{pv} - T_{gl}}{R_{gl-PV}} \quad (7.4)$$

where  $Q_{gl}$  is the heat absorbed by the glass cover, which is equal to:

$$Q_{gl} = a_{gl} G_b A_a \eta_{opt} \quad (7.5)$$

with  $a_{gl}$  being the glass absorptivity.  $Q_{loss}$  is the heat dissipated to ambient through external convection and radiation:

$$Q_{loss} = \frac{T_{gl} - T_a}{R_{loss}} \quad (7.6)$$

As depicted in the thermal network of **Fig. 7.1**, the overall external thermal resistance  $R_{loss}$  results by the connection in parallel of the thermal resistances due to convection and radiation:

$$\frac{1}{R_{loss}} = \frac{1}{R_{conv,ext}} + \frac{1}{R_{rad}} \quad (7.7)$$

The heat transfer coefficients required for the calculation of  $R_{conv,ext}$  and  $R_{rad}$ , respectively, are calculated as follows:

$$h_{conv,ext} = \frac{Nu_{MC} \cdot k_{air}}{L} \quad (7.8)$$

$$h_{rad,ext} = \frac{\sigma \epsilon_{gl} (T_{gl}^4 - T_a^4)}{T_{gl} - T_a} \quad (7.9)$$

where the values of the Nusselt number  $Nu_{MC}$  used in **Eq. (7.8)** correspond to external air flow under mixed convection conditions and were calculated using **Eqs. (6.9)-6.13**.

- PV laminate

$$M_{PV} C_{PV} \frac{dT_{PV}}{dt} = Q_{irr} - P_{el} + \frac{T_{gl} - T_{PV}}{R_{gl-PV}} - \frac{T_{PV} - T_{tape}}{R_{PV-tape}} \quad (7.10)$$

where  $Q_{irr}$  is the radiation flux incident on the surface of the solar cells:

$$Q_{irr} = (1 - a_{gl}) (\tau_{gl} a_{cell})_{eff} G_b A_a \eta_{opt} \quad (7.11)$$

and  $P_{el}$  is the electrical power produced by the module:

$$P_{el} = \eta_{el} Q_{irr} \quad (7.12)$$

The degradation in the cell efficiency due to elevated operating temperature was calculated using **Eq. (2.9)** with the values of the temperature coefficient  $\beta$  for each cell design, as were determined by the experimental evaluation (see **paragraph 6.3.2**).

- Adhesive tape (bonding the cells to the module substrate)

$$M_{tape} C_{tape} \frac{dT_{tape}}{dt} = \frac{T_{PV} - T_{tape}}{R_{PV-tape}} - \frac{T_{tape} - T_{s1}}{R_{tape-s1}} \quad (7.13)$$

- PV module substrate  $S_1$

$$M_{s1} C_{s1} \frac{dT_{s1}}{dt} = \frac{T_{tape} - T_{s1}}{R_{tape-s1}} - \frac{T_{s1} - T_{resin}}{R_{s1-resin}} \quad (7.14)$$

- Adhesive resin (bonding the PV module to the heat sink)

$$M_{resin} C_{resin} \frac{dT_{resin}}{dt} = \frac{T_{s1} - T_{resin}}{R_{s1-resin}} - \frac{T_{resin} - T_{s2}}{R_{resin-s2}} \quad (7.15)$$

- Heat sink substrate  $S_2$

$$M_{s2} C_{s2} \frac{dT_{s2}}{dt} = \frac{T_{resin} - T_{s2}}{R_{resin-s2}} - \frac{T_{s2} - T_f}{R_{conv} + R_{cond}/2} \quad (7.16)$$

- Cooling fluid

$$M_f C_f \frac{dT_f}{dt} = \frac{T_{s2} - T_f}{R_{conv} + R_{cond}/2} - \dot{m} C_f (T_{f,max} - T_{f,in}) \quad (7.17)$$

The conductive thermal resistances of the solid materials appearing in the thermal balances were calculated using **Eq. 3.33**, while the convective thermal resistance was calculated using **Eq. 3.35**. The heat capacitance term appearing on the left-hand side of each layer was approximated using finite differences:

$$\frac{dT_i}{dt} = \frac{T_i^n - T_i^{n-1}}{\Delta t} \quad (7.18)$$

where the subscript  $i$  corresponds to each node of the thermal resistance network, i.e to the various material layers that comprise the receiver and to the cooling fluid.

A special note must be made for the calculation of the convective thermal resistance  $R_{conv}$ , as it is dependent on the flow conditions and the geometry of the heat sink. Especially in the case of the VW heat sink configuration, the heat transfer coefficient- required for the determination of the convective thermal resistance- can vary significantly between consecutive sections. Besides, the heat-sink wall temperature distribution has a non-monotonical distribution, as was shown in **paragraph 4.9**. In order to more accurately predict the temperature distribution of the various material layers and consequently the receiver thermal and electrical losses, the receiver of the system was discretized along its longitudinal axis in a number of  $N$  equal-length elements and the system of equations (7.4), (7.10), (7.13)-(7.17) was iteratively solved for each segment  $j$ ,  $j=1,N$  (**Fig 7.2**). Each segment corresponding to a solid material was considered to have a uniform temperature  $T_i$ . On the contrary, a linear temperature distribution was considered for the cooling-fluid layer, with the fluid outlet temperature of each segment imposed as inlet temperature for the next segment, i.e.,  $T_i=T_i(Z)$  for this layer. Global quantities corresponding to the entire receiver length, e.g. the thermal and electrical output, were calculated for each time-step by integrating the elemental output produced by each segment.

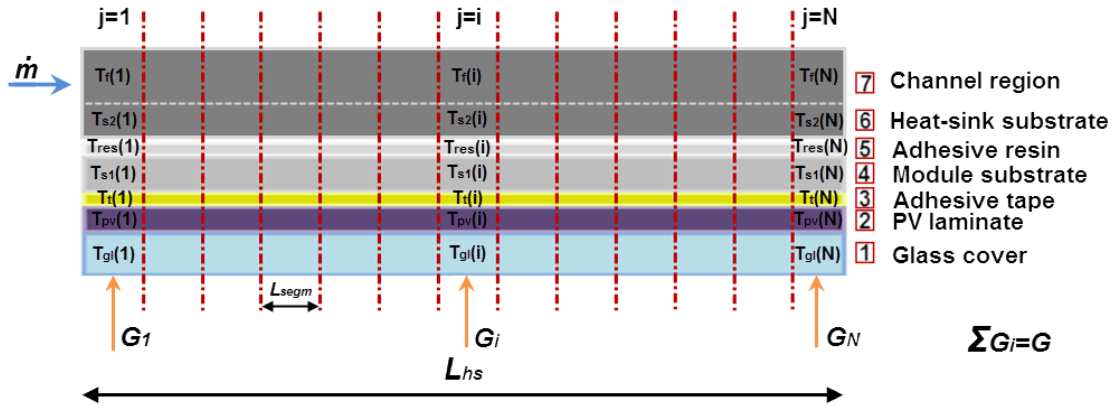


**Fig. 7.2** Segmentation of the material layers comprising the receiver, allowing for variations in the flow direction to be included in the thermal-network model.

The variation of the cooling fluid thermophysical properties with temperature was introduced in the model using the correlations for thermal conductivity  $k_f$ , density  $\rho_f$  and viscosity  $\mu_f$  of water available in [7.24]. Finally, the cooling fluid pressure drop required for the determination of the parasitic pumping power was calculated using **Eqs. (4.5)-(4.11)**. A single calculation was performed for the entire heat sink length using the thermophysical properties based at the coolant average temperature. **Eqs. (7.4), (7.10), (7.13)-(7.17)** constitute a system of seven equations with seven unknowns, namely the temperature  $T_i$  at each layer of the receiver. The system of algebraic equations was iteratively solved using the Gauss-Seidel method. The main model outputs comprise the system energetic (**Eqs. 6.4 and 6.5**) and exergetic efficiency (see **Eq. 7.31** in **paragraph 7.5**) along with the associated losses, as well as the system electrical and thermal yield for a specified time period, i.e. the time

integrals of the system electrical and thermal power produced by the system, respectively (see **Appendices A3, A4**). The temperature distributions at the materials of the receiver are also predicted by the model.

### 7.3 Validation of the theoretical model

As a first step, the theoretical results produced by the transient model were compared against experimental data available from the evaluation of the prototype CPVT system. In order to ensure that the model can accurately predict the transient behavior of the system, the measured system response time, i.e. the time period required for the system to reach steady state once exposed to constant irradiation of high intensity, was compared to that produced by the model for the same environmental conditions. Besides, the predictions produced by the model in regard to the system electrical and thermal efficiency were compared against experimental data. Two receiver configurations were taken into consideration having different heat-sink and PV-module designs. The input parameters required by the model are summarized in **Table 7.1**.

**Table 7.1** Input values required by the theoretical model for the validation case.

Model Input	Symbol	Values
Environmental data	$G_b, V_{air}, T_a, \theta$	TMY file <sup>1</sup>
System aperture area	$A_a$	1.0m <sup>2</sup>
Receiver active length	$L_{rec}$	0.5m
Receive active width (Narrow/Wide cells)	$W_{rec}$	0.04m/0.06m
Number of heat sink sections (FW/VW)	$N_{sec}$	1/3
Channel width (FW/VW)	$W_{ch}$	0.56mm/5.24-2.12-0.56mm
Wall thickness (FW/VW)	$W_w$	0.69mm/1.00mm
Channel height (FW/VW)	$H_{ch}$	3.50mm/10.60mm
Heat-sink substrate thickness (FW/VW)	$t_{sub}$	2.6mm/1.7mm
Resin thickness	$t_{resin}$	152.4 $\mu$ m
Resin thermal conductivity	$k_{resin}$	0.43 W/mK
Absorptance of front glass	$a_{gl}$	0.05
Emmittance of front glass	$\epsilon_{gl}$	0.88
Transmittance of front glass and EVA	$\tau_{eff}$	0.92/0.90
Concentrator optical efficiency	$\eta_{opt}$	0.57
PV module reference efficiency	$\eta_{pv,ref}$	0.138 K
PV module temperature coefficient (wide/narrow cells)	$\beta$	0.00461/0.00603
Irradiation uniformity factor (Narrow cells)	$F_{uni}$	0.85
Cooling fluid volumetric flow rate	$\dot{V}_{tot}$	30/40 mL/s
Cooling fluid inlet temperature	$T_{f,in}$	285K-315K
Simulation time step	$dt$	10s
Simulation total time	time	300-400s
Residual set for convergence	Res	10 <sup>-4</sup>

**Fig. 7.3** depicts the evolution of the fluid, heat sink and PV-module maximum temperatures with time, as predicted by the theoretical model. The respective outlet fluid temperature evolution as measured during the system experimental evaluation is also presented for comparison. The system is

exposed to concentrated sunlight at  $t=0$ . As can be seen the model can accurately predict the system thermal-response time and the fluid temperature rise trend in both receiver variations considered. It is interesting to notice that both configurations obtain steady-state operation in a relatively short time period approximately equal to 150s.

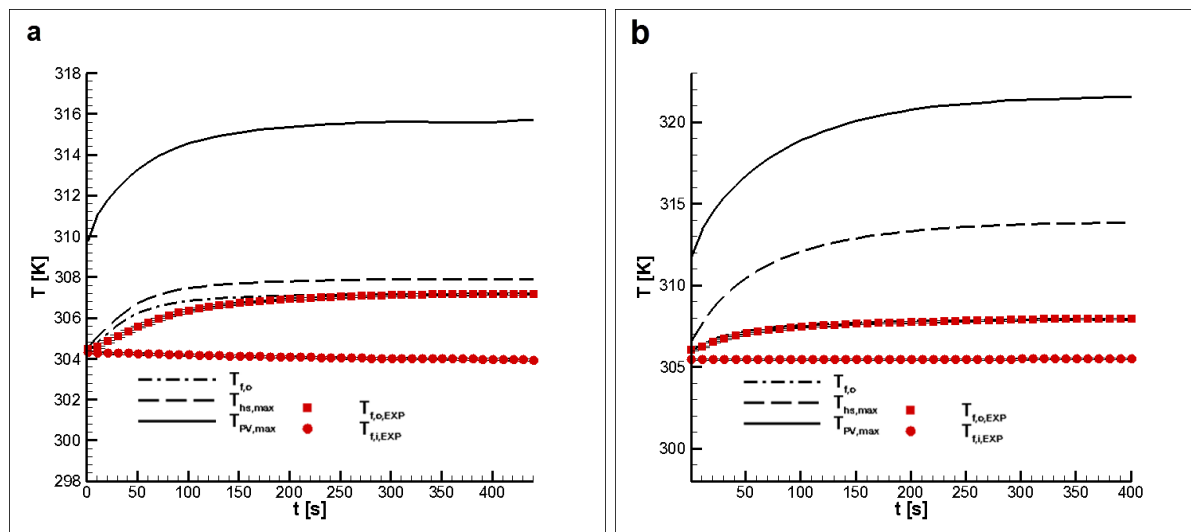


**Fig. 7.3** Thermal response of the CPVT system: (a) FW-Module 1 (wide) configuration, (b) VW-Module 1 (narrow) configuration.

The maximum FW heat-sink temperature (**Fig 7.3a**) is higher than the fluid outlet temperature by approximately 1.0 K. The respective temperature difference in regard to the VW configuration is approximately equal to 6.0 K (**Fig. 7.3b**). It must be reminded that the maximum VW heat-sink temperature occurs at the first section of the device. Nevertheless, the temperature difference between PV module maximum and the fluid outlet temperatures is considerably higher equal to approximately 9.0 K and 14.0 K for the FW and VW devices respectively. It can be therefore deduced that the conductive resistance posed by the solid materials of the receiver has a far more considerable effect on the receiver overall thermal resistance compare to the thermal resistance of the cooling devices.

A further validation study was conducted to verify the accuracy of the model under steady-state conditions as well. The steady-state efficiencies of the two system-receiver configurations considered above, which were measured according to the procedure discussed in **paragraphs 6.3-6.4**, were compared against the theoretically predicted ones for the same environmental and operating conditions. **Fig. 7.4** presents the calculated and measured system thermal and electrical efficiencies for two receiver configurations under a wide range of operating conditions. It is evident that the system steady-state operation can be accurately predicted by the model and the small influence of the operating temperature on the system efficiency is clearly captured. It has therefore been proven that the model can accurately predict both the system transient and steady-state operation and hence it can be used to predict the long-term performance of the system, which will be presented in the following paragraphs.

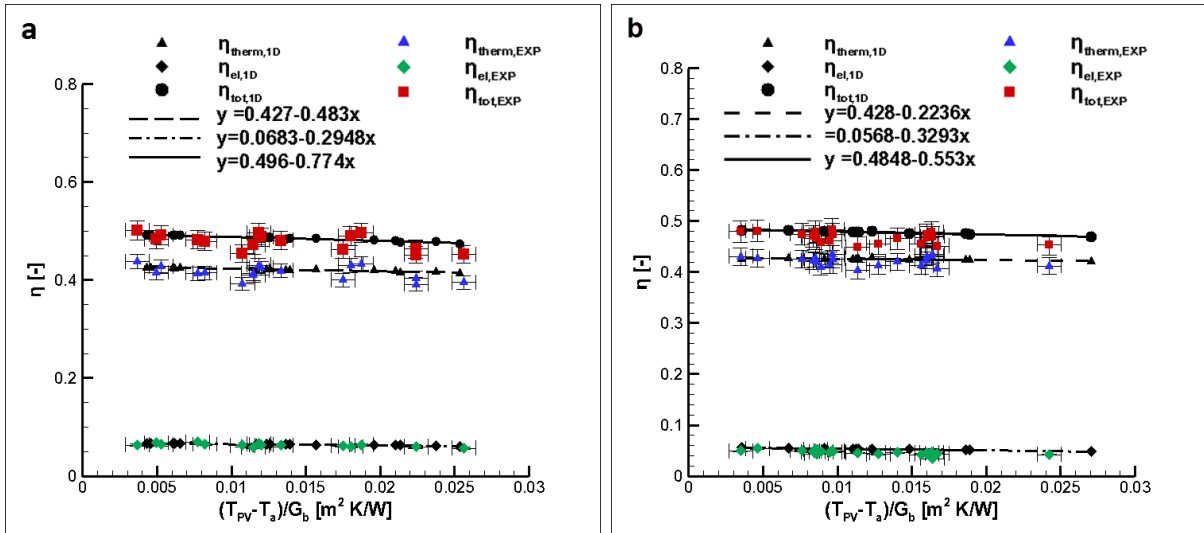


**Fig. 7.4** Steady-state efficiency of the CPVT system: (a) FW-Module 3 configuration ( $\dot{V}_{tot} = 30$  mL/s), (b) VW-Module 2 configuration ( $\dot{V}_{tot} = 40$  mL/s).

Finally, it is interesting to illustrate that the expected form of the temperature distribution at the cooling-devices substrate can be produced by the analytical model. The bottom wall and fluid temperature distributions for the two cooling configurations employed are presented in **Fig. 7.5** for steady-state conditions. In reference to the actual system with aperture area of  $1.0 m^2$  (**Fig. 7.5a**), the stepwise temperature reduction regarding the VW configuration is predicted with the point of maximum wall temperature located at the end of the first section. Regardless of the cooling device employed, the wall temperature at the heat-sink outlet is slightly higher than the fluid outlet temperature.

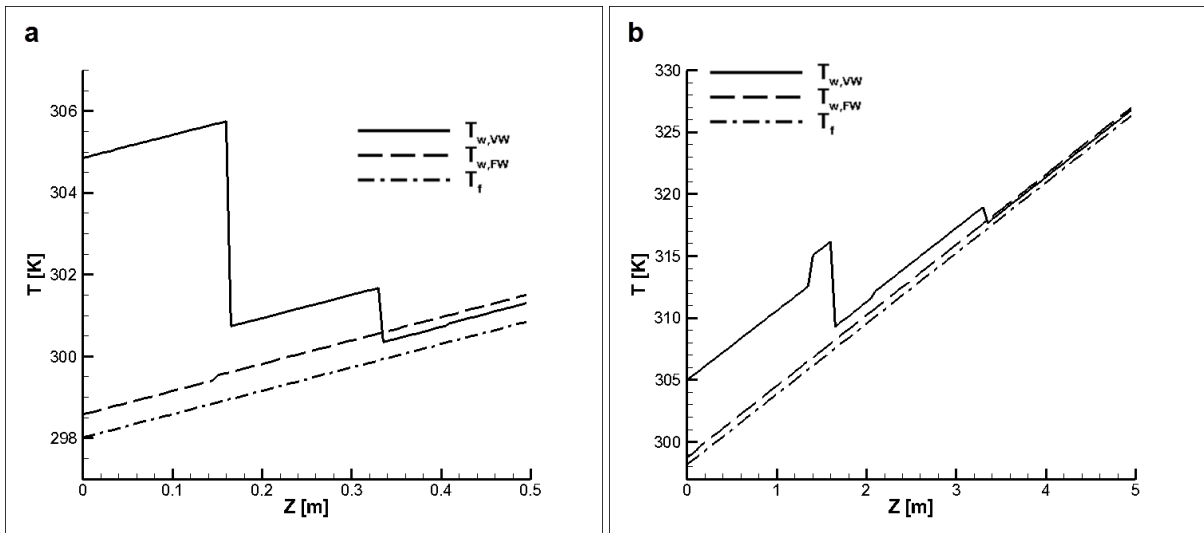


**Fig. 7.5** Longitudinal temperature distribution under steady-state conditions ( $T_{f,i} = 298$  K,  $T_a = 283$  K,  $u_{wind} = 2$  m/s,  $G_b = 850$  W/ $m^2$ ): (a)  $1.0 m^2$  system, (b)  $10.0 m^2$  system.

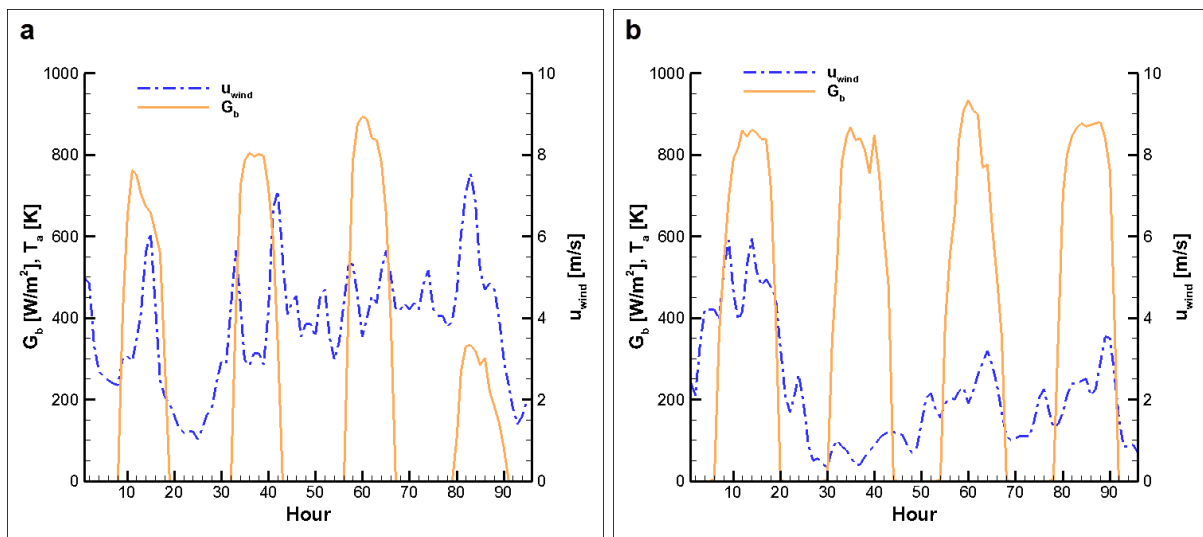
The longitudinal temperature distribution of a similar system with greater length and respective aperture area equal to  $10 m^2$  is depicted in **Fig. 7.5b**. Once again, the temperature distributions over the entire FW heat-sink length and for the most part of the VW heat-sink length closely follow the

respective distribution in the fluid, indicating the small thermal resistance of the devices. In regard to the VW cooling configuration, it is evident that although the wall temperature distribution still exhibits a stepwise trend, its maximum value is located at the heat sink outlet. The steep increase in the distribution gradient discernible in **Fig. 7.5b** at approximately  $Z=1.3$  m occurs because in that location the flow reaches full development and thus the correlations applied for the calculation of the heat transfer coefficient switch from those referring to developing flow to those referring to fully-developed flow, respectively.

### 7.4 Prediction of the system long-term performance

Apart from evaluating the system performance on an annual basis, three time periods in different seasons of the year, namely 1<sup>st</sup>-4<sup>th</sup> of March, 21<sup>st</sup>-24<sup>th</sup> of June and 1<sup>st</sup>-4<sup>th</sup> of December, have been selected in order to illustrate the effect of variable environmental conditions on the system efficiency and output. **Fig. 7.6** presents the prevailing environmental conditions for the time periods in question. The climatological data (wind velocity  $u_{wind}$ , ambient temperature  $T_a$ , insolation  $G_b$ ) were provided by a Meteororm [7.25] TMY (Typical Meteorological Year) file for Athens, Greece. The wind velocity values depicted in **Fig. 7.6**, were reduced at a height of 2.0 m above ground using the respective available values at a height of 10.0 m, according to the relation:

$$u_{wind,2m} = u_{wind,10m} \left( \frac{2}{10} \right)^{1/7} \quad (7.19)$$



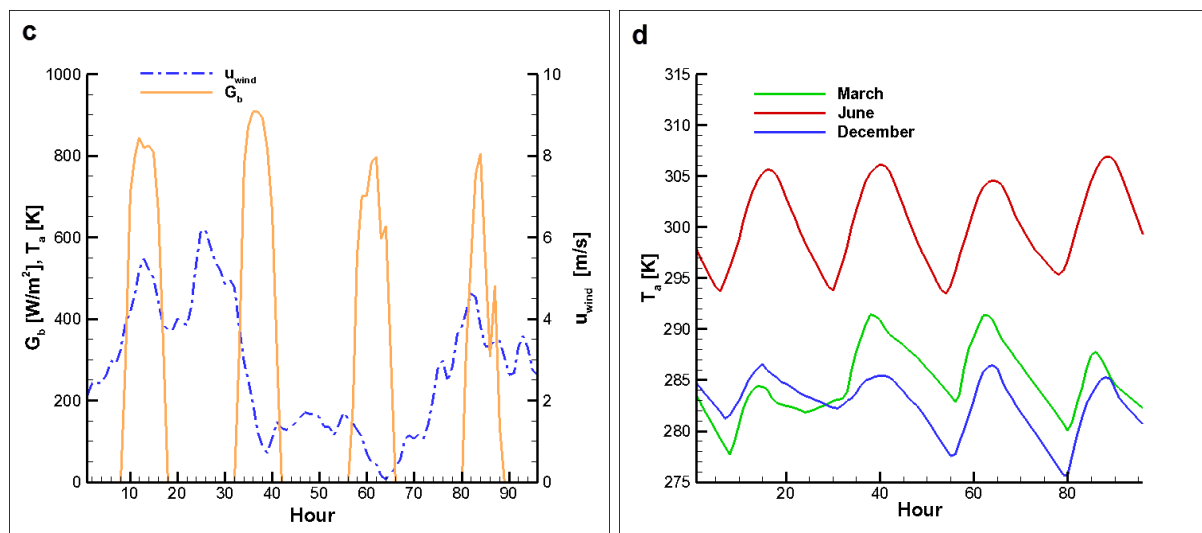


**Fig. 7.6** Climatological data for the evaluation periods considered. Direct solar radiation and wind velocity: (a) 1-4 March, (b) 21-24 June, (c) 1-4 December. (d) Wind velocity for the three time periods.

A CPVT system with the manufacturing and operating characteristics of the manufactured prototype, yet with larger aperture area equal to  $10m^2$ , so that the effect of the thermal losses can be elucidated, has been selected as a “base-case system”. The specific system, the characteristics of which are summarized in **Table 7.2**, will be considered as a reference in the following results, in order to highlight the effect of the various parameters examined on the energetic and exergetic system output and efficiency. It must be noted that the module employing the wide (60.0 mm) cells has been considered for the long term performance, as it was proven to exhibit superior performance during the experimental evaluation.

**Table 7.2** Technical specifications and operating parameters of the base-case system.

Model Input	Values
System aperture area $A_a$ [ $m^2$ ]	10.0 $m^2$
Receiver active length $L_{rec}$ [m]	5.0
Receiver active width $W_{rec}$ [m]	0.06
Heat sink design: FW ( $W_{ch}$ - $W_w$ - $H_{ch}$ ) [mm]	0.56-0.69-3.5
Resin thickness $t_{resin}$ [ $\mu m$ ]	152.4
Resin thermal conductivity $k_{resin}$ [W/mK]	0.43
Absorptance of front glass $a_{gl}$	0.05
Emmitance of front glass $\epsilon_{gl}$	0.88
Transmittance of front glass and EVA $\tau_{eff}$ [-]	0.92
Concentrator optical efficiency $\eta_{opt}$ [-]	0.57
PV module reference efficiency $\eta_{pv,ref}$ [-]	0.138
PV module temperature coefficient $\beta$ [-]	0.00461
Cooling fluid volumetric flow rate $\dot{V}_{tot}$ [mL/s]	30.0
Cooling fluid inlet temperature $T_{f,in}$ [K]	298.0

As an initial step, it must be examined whether the performance of the base-case system varies considerably depending on the incorporated cooling device. For this reason, the influence of the cooling-device design on the system efficiency is presented in **Fig. 7.7a**. It is evident that the effect of

the heat-sink configurations on the efficiency of the base-case system is negligible. The system electrical efficiency for the case where the FW cooling device is employed is higher by up to 1.2% compared to the respective for the VW device, whereas the thermal efficiency remains approximately equal regardless of the incorporated device. According to the formulation of the theoretical model, the elemental electrical power and thermal losses are calculated for each segment of the receiver and thus the respective overall quantities are dependent on the average wall temperature. As was proven in **paragraph 4.9.3**, the thermal resistance based on the average wall temperature is nearly identical for the two configurations and thus the similar overall system performance is justified. Consequently, it is adequate to analyze the performance of the base-case system considering only the FW heat sink as cooling device. It is essential to point out that the effect of temperature non-uniformity on the electrical efficiency could not be predicted by the present model as there are no performance data available from the manufacturer of the actual PV modules with regard to operation at non-uniform temperature.

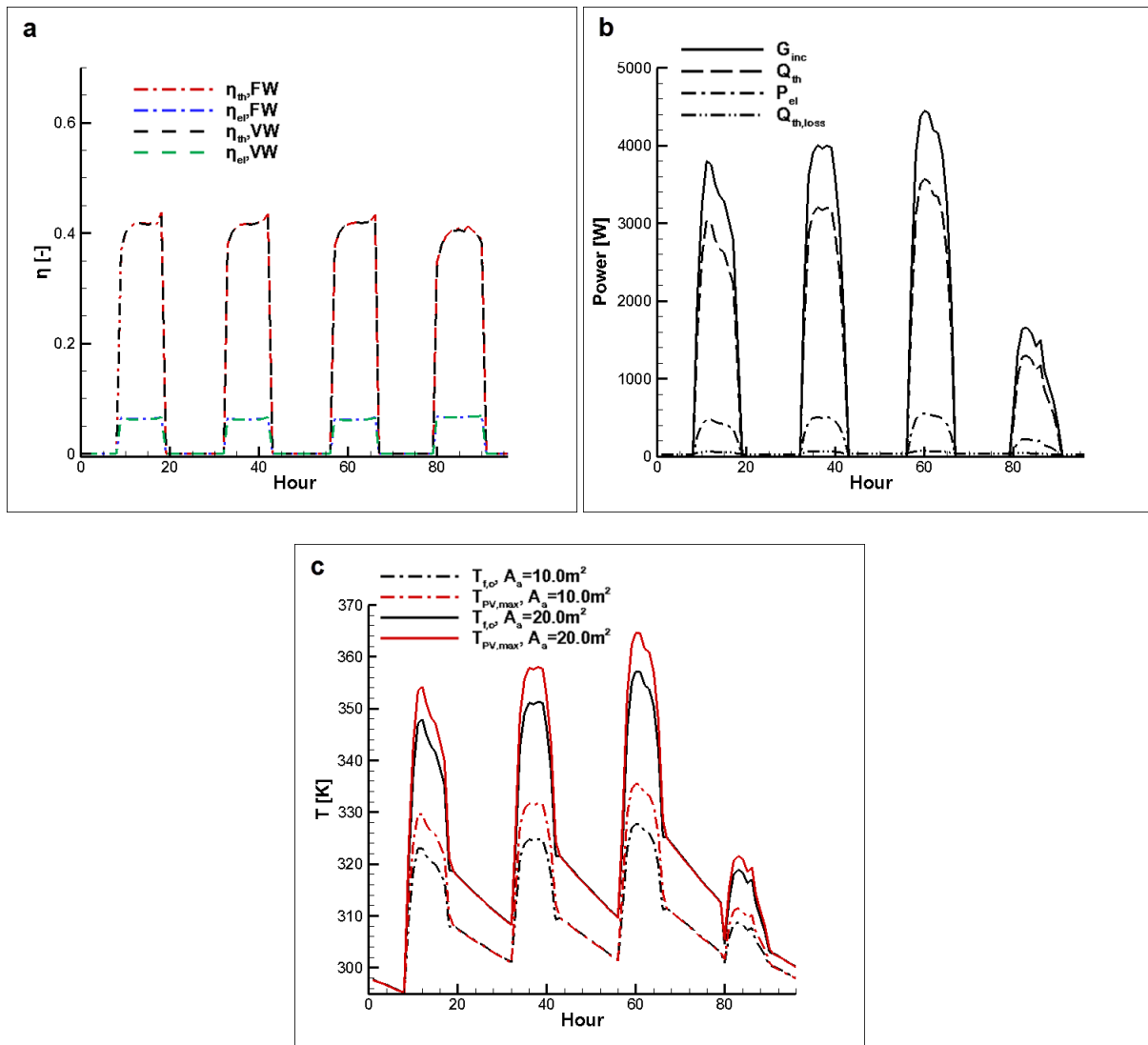


**Fig. 7.7** Performance characteristics of the base-case system in March: (a) efficiency, (b) power production, and (c) maximum fluid and PV-module temperatures.

The power output of the base-case system is depicted in **Fig. 7.7b**. As can be seen, the major percentage of the irradiation incident on the receiver is exploited either as electrical or thermal power, with the thermal losses representing less than 3% of the thermal output. For the environmental conditions corresponding to the time period in March, the base-case system can produce up to 3.5 kW of thermal power and 0.5 kW of net electrical power.

**Fig. 7.7c** illustrates the daily variation of the fluid outlet and the PV-module maximum temperatures, respectively. It can be observed that the system can produce heat at a temperature level of approximately 328.0 K, with the PV-module maximum temperature being higher by as much as 7.5 K. As also revealed by **Fig. 7.7c**, the temperature difference between the PV module and the fluid remains constant even when the system aperture area is increased to 20.0 m<sup>2</sup>, as the system length is actually increased while the heat flux on the receiver remains constant. For completeness purposes, it should be stated that the water within the receiver is considered to be stagnant when there is no solar irradiation and hence it is cooled only due to thermal losses to the environment, as can be seen in **Fig. 7.7c**.

It was demonstrated during the experimental evaluation of the prototype CPVT system (**paragraph 6.3**) that the influence of the water volumetric flow rate on the system efficiency could not be elucidated, as the difference in the system performance was in the order of the experimental uncertainty. The dynamic model has been therefore utilized to illustrate the specific effect on the efficiency of the base-case system, which has a ten-fold larger aperture area than the prototype system. The time period in June was considered for the simulations so that the environmental conditions are similar to the actual ones prevailing during the experimental evaluation.

**Fig. 7.8** reveals that the value of the water volumetric flow rate has only a minor effect on the system energetic efficiency for both the cases of the FW (**Fig. 7.8a**) and VW (**Fig. 7.8b**) configurations. An increase of the flow rate from 20.0 to 40.0 mL/s leads to an increase of the electrical and thermal efficiencies by approximately 6% and less than 2%, respectively. As was stated in **paragraph 6.4**, the thermal losses from the system receiver are of small magnitude and, additionally, the conductive thermal resistance posed by the solid materials has a more significant contribution on the receiver overall thermal resistance compared to the heat-sink convective resistance. It must also be mentioned that even for a system with an overall length of 5.0m, such as the base-case system, the effect of the parasitic pumping power on the system efficiency is negligible; however this cannot be considered a general remark, as linear CPVT systems of larger scale can have overall lengths of several meters.

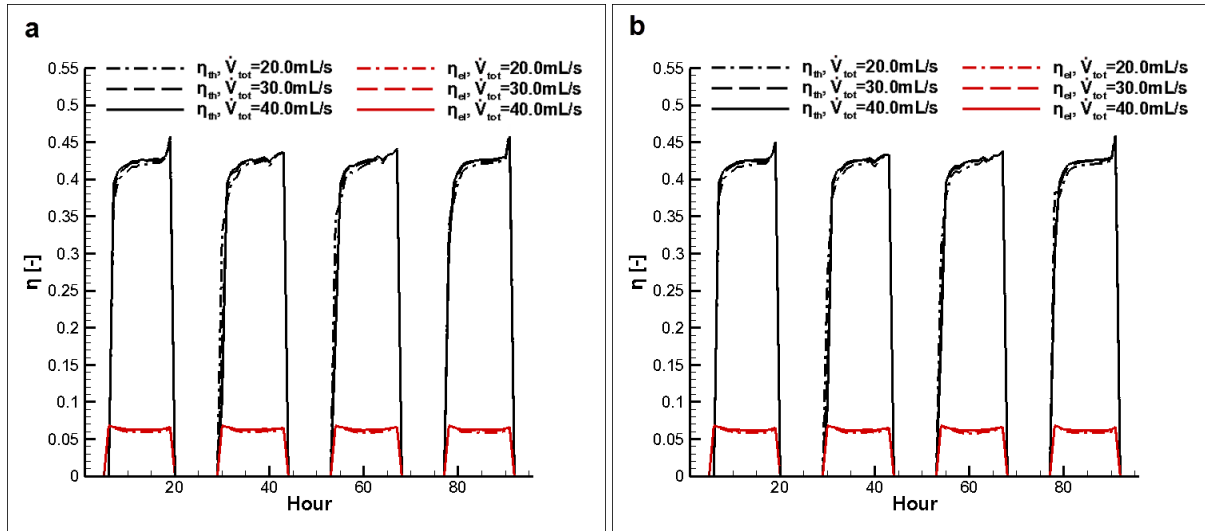


**Fig. 7.8** Effect of the water volumetric flow rate on the system energetic efficiency. The results refer to the base-case system in June employing: (a) the FW and (b) VW devices, respectively.

Moreover, it is of interest to examine the effect of the water inlet temperature on the system efficiency, as the CPVT system is most likely intended to be coupled with heat storage, e.g. in a domestic hot-water system, and thus to be fed with water of elevated temperature from the storage tank during its daily operation. It is evident from **Fig. 7.9**, referring to the base-case system, that water entering the system with an elevated temperature has a considerable detrimental effect on both the system thermal and total efficiency. In fact, the decrease is slightly more substantial in the case of total efficiency (black line) compared to the thermal efficiency (red line), as the increased receiver temperature leads to increased thermal losses and, in addition, to reduced electrical production due to the elevated PV-module temperature. For example, for increase of the water inlet temperature from 298.0 K to 338.0 K and referring to the environmental conditions corresponding to December (**Fig. 7.9b**) the total efficiency decreases by approximately 10% relative to the total, while the thermal efficiency decreases by approximately 8%. The relative deterioration in the system efficiency caused by the increased water inlet temperature is also influenced by the environmental conditions, as the effect is stronger at time periods with low or fluctuating solar irradiation values, e.g. as is evident for the curves corresponding to the 4<sup>th</sup> of March (**Fig. 7.9a**) and the 4<sup>th</sup> of December (**Fig. 7.9b**).

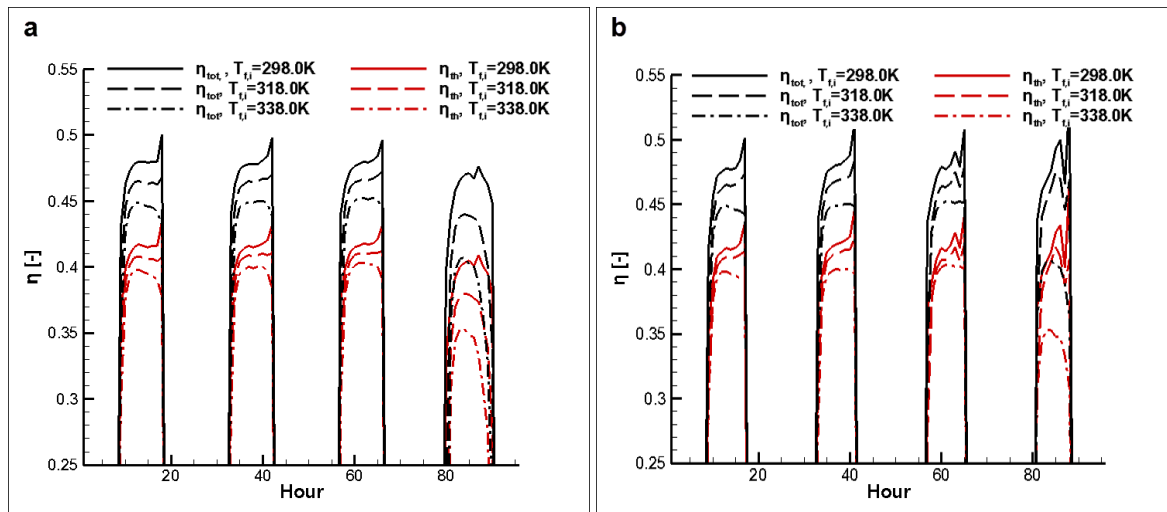


**Fig. 7.9** Effect of the water inlet temperature on the efficiency of the base-case system: (a) March, (b) December.

As has been already mentioned, the effect of the parasitic pumping power on the efficiency of the base-case system is negligible considering the geometrical parameters of the manufactured cooling devices. The channel geometrical parameters were decreased to smaller dimensions to examine whether the thermal performance of the devices can be further enhanced without inducing a severe pressure drop penalty, hence leading to increased overall system efficiency. A water volumetric flow rate of 40.0 mL/s has been considered for all cases, which constitutes a worst-case scenario in terms of pumping power. As shown in **Fig. 7.10a** referring to the FW configuration, reducing the channel width and fin thickness from 500  $\mu\text{m}$  to 100  $\mu\text{m}$  has a negative impact on the system net efficiency, as the net total efficiency decreases by approximately 10%. It must be noted that channel aspect ratio was kept equal to six in all cases. It can also be easily deduced that the deterioration of the device hydrodynamic performance due to increased friction losses exceeds by far the thermal performance enhancement, as heat losses were of small magnitude in the first place.

Regarding the VW configuration (**Fig. 7.10b**) reducing the width of the first-section channel  $W_{ch,1}$  from 5.24 mm to 3.40 mm, leads to a reduction of the third-section channel width identical to that considered for the FW device, i.e. from approximately 500 $\mu\text{m}$  to 100 $\mu\text{m}$ . The fin thickness was maintained equal to 1.00 mm for all cases, while the channel aspect ratio in the first heat-sink section was kept equal to two. The effect of the reduction of channel dimensions is still unfavorable yet far more moderate in comparison to the FW configuration as the net efficiency decreases by approximately 1.5%. It is therefore made evident for both designs that there is no need to add heat transfer surfaces as the potential benefit due to enhanced thermal performance is exceeded by far by the negative impact of increased pumping power.

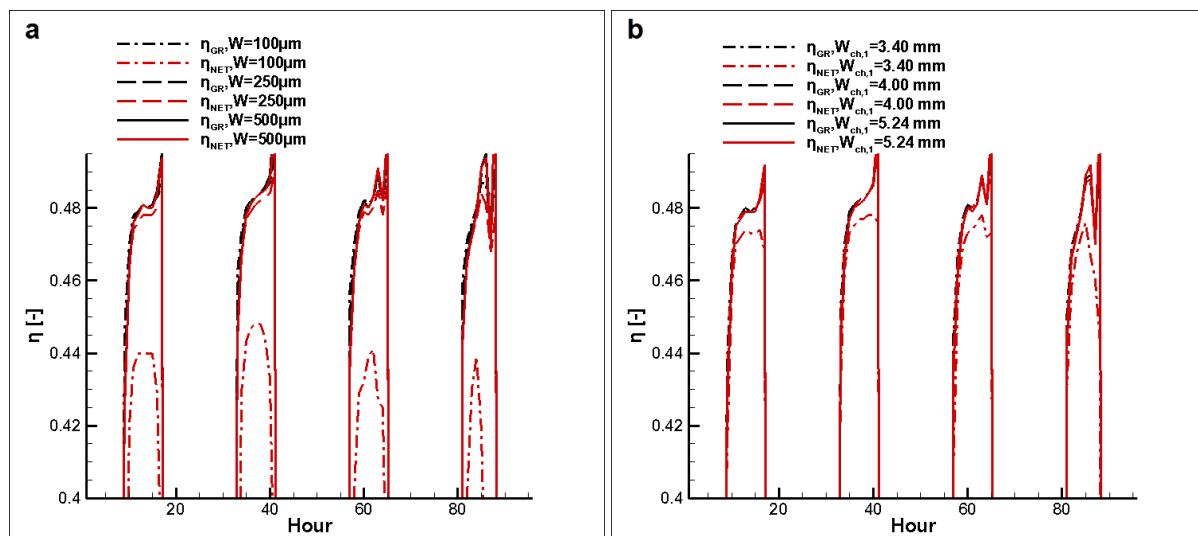
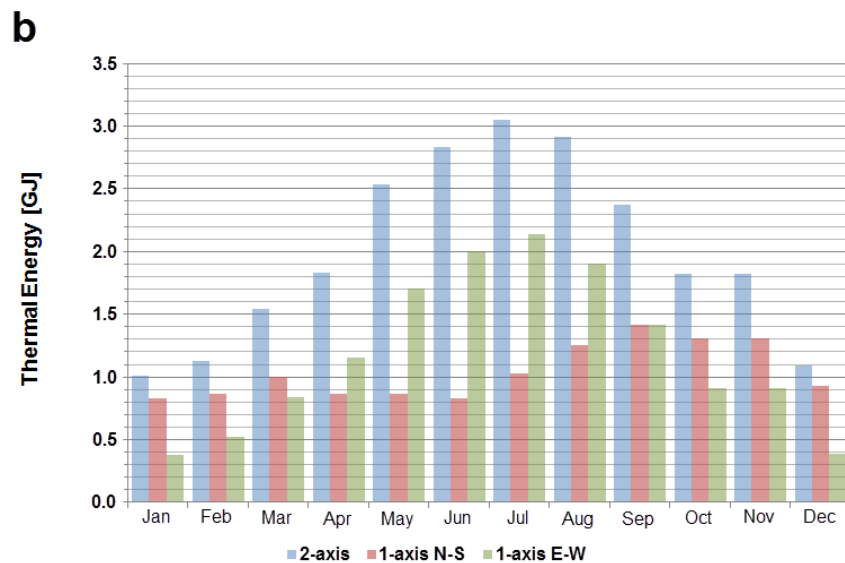
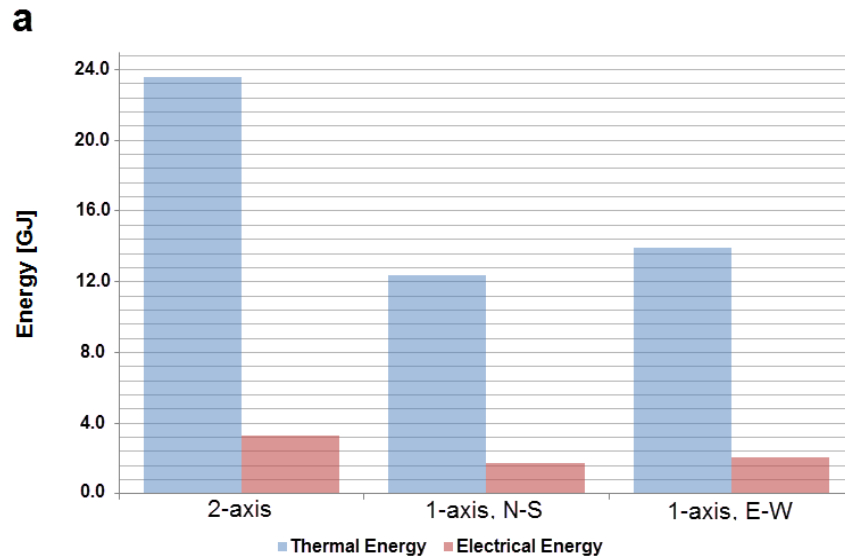


**Fig. 7.10** Effect of the heat-sink geometry on the efficiency of the base-case system (December time period): (a) FW configuration ( $W_{ch}=W_w=W$ ), (b) VW configuration ( $W_w=1.0$  mm).

The type of tracking mechanism can also have a significant influence on the system annual output. As was stated in **paragraph 7.2** end-losses are not taken into consideration in the present simulations and thus cosine losses contribute to the optical losses that are inevitable in the case of single-axis tracking systems. The annual output of the base-case CPVT system for single (both for East-West and North-South orientations) and two-axis tracking is presented in **Fig. 7.11a** , where it can be observed that the total energy output of the two-axis tracking system is 90.5% and 67.5% higher compared to

the single-axis tracking system with North-South and East-West orientations, respectively. For the geographic latitude of Athens, the East-West orientation is preferable for single-axis tracking as cosine losses vanish at solar noon, whereas for the North-South orientation cosine losses obtain their maximum value at solar noon.

The monthly distribution of the thermal and electrical energy produced by the base-case system during a typical meteorological year in Athens is presented in **Figs. 7.11b** and **7.11c**, respectively. As expected the two-axis tracking system produces its maximum output in July, where the monthly insolation is maximum as well. In regard to single-axis tracking, the system with East-West orientation outperforms the respective with North-South orientation in the months with high insolation (May to August) and hence increased system thermal (**Fig. 7.11b**) and electrical (**Fig. 7.11c**) output, which results to a higher annual output as well. The North-South oriented system is more effective in the autumn and winter months (October to February) and thus a general strategy for single-axis tracking system located at the latitude of Athens could be recommended, where the system orientation switches from North-South to East-West in March and vice-versa in September.



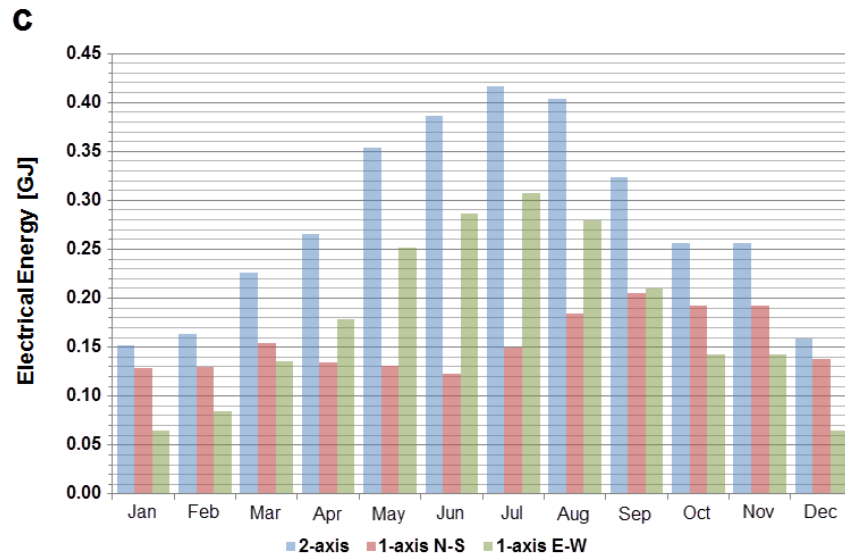


Fig.7.11 Monthly distribution of the base-case system output: (a) total energy, (b) thermal energy and (c) electrical energy.

## 7.5 System optimization

The objective of the following paragraph is to designate the value range of operating parameters, for which the system attains the most effective performance from a second-law of thermodynamics point of view. The latter allows for a straightforward comparison between thermal and electrical output. In addition, the influence of the performance characteristics of key sub-components on the system exergetic performance will also be elucidated. A parametric study is conducted to determine the factors that can lead to increase of the system net exergetic efficiency on a daily and annual basis having as reference the exergetic efficiency of the base-case system (see **Table 7.2**).

### 7.5.1 Exergy analysis

Exergy analysis allows for a straightforward evaluation of a system performance as, in essence, the system is compared to an ideal (reversible) heat engine and the factors that contribute to the deviation of the system from ideal operation are pointed out. The exergetic system efficiency has been widely used for the evaluation of PVT and concentrating solar thermal applications, as well as for the optimization of their design and operation [7.26-7.32]. In a conventional energy analysis, it is assumed that the heat gain of the cooling fluid can be completely converted to useful work. However, this assumption is invalid as there is an upper limit to the conversion of heat to useful work, known as the Carnot efficiency and thus exergy, i.e. the maximum useful work that can be produced until a thermodynamic system reaches thermal equilibrium with a reference environment is defined as:

$$\dot{E}x_{th} = Q_{th} \left( 1 - \frac{T_c}{T_h} \right) \quad (7.20)$$

where  $Q_{th}$  is the available thermal energy,  $T_h$  is the temperature at which the heat is available and  $T_c$  is the dead-state temperature where the useful work that can be produced is equal to zero. The general exergy balance of a thermodynamic system with inbound ( $\dot{E}x_{in}$ ) and outbound exergy flows ( $\dot{E}x_{out}$ ) can be written as:

$$\sum_i \dot{E}x_{in} - \sum_i \dot{E}x_{out} = \sum_i \dot{E}x_{dest} \quad (7.21)$$

where  $\dot{E}x_{dest}$  is the destroyed exergy within the system. Exergy is destroyed when a process involves a temperature change or fluid friction within a duct. The term is also referred to as system irreversibility  $\dot{E}x_{dest} = \dot{I}$ . The exergy destruction is proportional to the entropy increase of the system [7.33]:

$$\dot{S}_{gen} = \frac{1}{T_c} (\dot{E}x_{in} - \dot{E}x_{out}) \quad (7.22)$$

In the case of solar applications, the inbound stream of exergy or exergy fuel is the solar irradiation, which according to Petela [7.34] is:

$$\dot{E}x_{sun} = G_b A_a \left( 1 - \frac{4}{3} \frac{T_a}{T_{sun}} + \frac{1}{3} \left( \frac{T_a}{T_{sun}} \right)^4 \right) \quad (7.23)$$

where  $T_{sun}$  is the sun temperature equal to 4350 K [7.35]. **Eq. (7.23)** provides the maximum work that can be produced from an isotropic blackbody radiation at  $T_{sun}$  [7.36]. The useful exergy streams that comprise the outbound exergy stream are the extracted heat and electrical power:

$$\dot{E}x_{th} = Q_{th} \left( 1 - \frac{T_a}{T_{f,o}} \right) \quad (7.24)$$

$$\dot{E}x_{el} = P_{el} \quad (7.25)$$

As can be directly inferred from **Eq. (7.25)**, the exergy flow associated with photovoltaic electricity is equal to the produced electrical power [7.28, 7.29, 7.35]. The destroyed exergy rate or system irreversibility comprises four terms due to the optical losses, the temperature difference between the receiver and the sun temperature, the thermal losses and the coolant pressure drop respectively:

$$\dot{E}x_{opt,loss} = G_b A_a (1 - \eta_{opt}) (1 - \tau \alpha_{eff}) \left( 1 - \frac{4}{3} \frac{T_a}{T_{sun}} + \frac{1}{3} \left( \frac{T_a}{T_{sun}} \right)^4 \right) \quad (7.26)$$

$$\dot{E}x_{\Delta T, CPVT-sun} = G_b A_a T_a \left( \frac{1}{T_{pv}} - \frac{1}{T_{sun}} \right) \quad (7.27)$$

$$\dot{E}x_{th,loss} = Q_{th,loss} \left( 1 - \frac{T_a}{T_{pv}} \right) \quad (7.28)$$

$$\dot{E}x_{pump} = P_{pump} \quad (7.29)$$

The Petela factor was used for the calculation of the exergy flow associated with optical losses, as **Eq. (7.26)** refers to conversion of solar irradiation to useful work. Furthermore, the term referring to the temperature difference between the receiver and the sun surface, **Eq. (7.27)**, exists, as the heat available at the temperature of the sun surface, which is considered as the “hot reservoir”, could be ideally converted to useful work without having to transition to a lower temperature level  $T_{pv}$ , a process accompanied by exergy loss [7.27]. By combining **Eqs. (7.23)-(7.29)** and **Eq. (7.21)** the exergy flow balance for the CPVT system takes the following form:

$$\begin{aligned} G_b A_a \left( 1 - \frac{4}{3} \frac{T_a}{T_{sun}} + \frac{1}{3} \left( \frac{T_a}{T_{sun}} \right)^4 \right) &= Q_{th} \left( 1 - \frac{T_a}{T_{f,o}} \right) + P_{el} - \\ - G_b A_a (1 - \eta_{opt}) (1 - \tau \alpha_{eff}) &\left( 1 - \frac{4}{3} \frac{T_a}{T_{sun}} + \frac{1}{3} \left( \frac{T_a}{T_{sun}} \right)^4 \right) - G_b A_{refl} T_a \left( \frac{1}{T_{pv}} - \frac{T_a}{T_{sun}} \right) - Q_{th,loss} \left( 1 - \frac{T_a}{T_{gl}} \right) - P_{pump} \end{aligned}$$

$\underbrace{\hspace{15em}}_{\dot{I}}$

(7.30)

where  $\dot{I}$  is the destroyed exergy or system irreversibility. Finally, the exergetic efficiency of the integrated system is defined as the useful, net exergy flows to the sun input exergy:

$$\eta_{II} = \frac{\dot{E}x_{th} + \dot{E}x_{el} - \dot{E}x_{pump}}{\dot{E}x_{sun}} \quad (7.31)$$

An additional quantity which has been used for the optimization of solar applications [7.32, 7.37, 7.38] is the entropy generation number, which quantifies the system irreversibility and is defined as:

$$N_s = \frac{T_a \dot{S}_{gen}}{A_a G_b} \quad (7.32)$$

where the entropy generation rate  $\dot{S}_{gen}$  can be calculated by **Eq. (7.22)**. It is obvious that the system optimal operation is achieved when the entropy generation number is minimized.

### 7.5.2 Effect of the system parameters on overall performance

Since the CPVT system under evaluation is a prototype device employing a number of custom-made components it is necessary to point out the characteristics of the system constituents that have to

be improved, in order to enhance the system overall performance. Besides, it is of importance to determine the system operating conditions, e.g. cooling fluid flow rate and temperature for which optimal performance is achieved and to identify the environmental conditions that are favorable to the system efficient operation. The net exergetic efficiency is reckoned as a suitable quantity to highlight the significance of the operating conditions and the various key-components characteristics on the system overall performance, since it allows the straightforward treatment of the produced thermal and electrical power, which are appropriately reduced to exergy streams of equal “value”.

**Fig. 7.12** depicts the variation in the system exergetic efficiency caused by the increase of the water volumetric flow rate. As was shown in **paragraph 7.3** (see **Fig. 7.8**), the energetic efficiency of the system is relatively independent of the volumetric flow rate value. However the water flow rate appears to have a considerable effect in regard to the system exergetic efficiency, and, in fact, increase of the volumetric flow rate leads to decrease of the overall exergetic efficiency. Although a higher volumetric flow rate tends to decrease the PV module operating temperature and thus increase its efficiency, it also leads to reduced fluid temperature at the outlet of the system  $T_{f,o}$ . According to **Eq. (7.24)**, the exergy stream associated with thermal power, apart from the heat output, is also depended on the temperature at which the heat is delivered and hence a lower fluid outlet temperature decreases exergetic efficiency. It is interesting to notice that the system exergetic efficiency is higher in the winter period due to the lower ambient temperature values, which allow for a greater temperature difference between the fluid at the system outlet and the system dead-state. Decrease of the water volumetric flow rate from 40.0 mL/s to 20.0 mL/s can lead to an increase of the system exergetic efficiency up to approximately 20% for a day with high insolation and low ambient temperature.

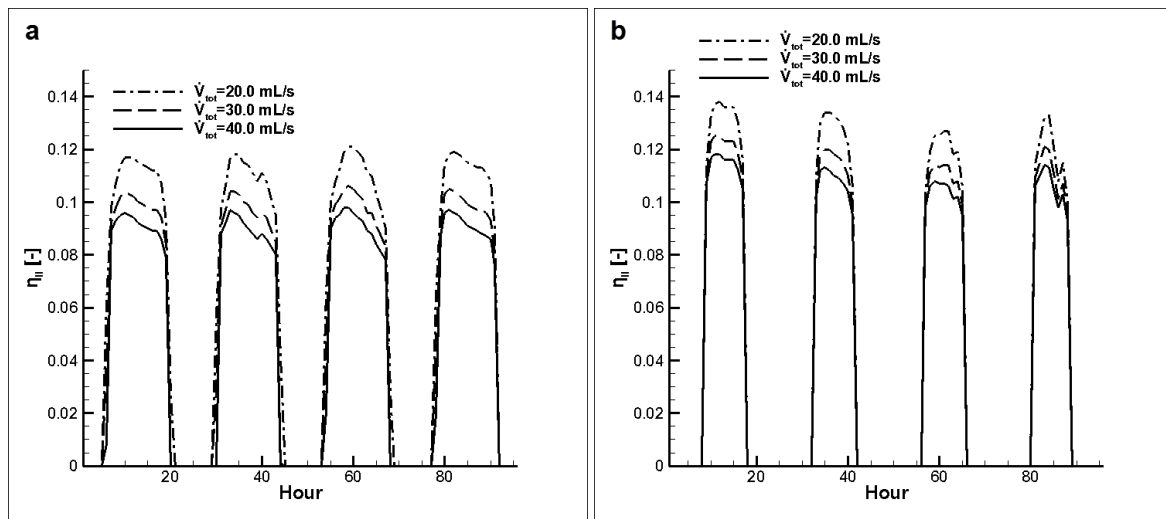


**Fig. 7.12** Effect of water volumetric flow rate on the system exergetic efficiency in regard to the base-case system: (a) June, (b) December

Likewise, as was shown in **Fig. 7.9**, increasing the temperature of the water entering the system has an adverse effect on the system energy efficiency. On the contrary, increased water inlet temperature enhances the system exergetic performance regardless of the environmental conditions, as illustrated in **Fig. 7.13**. The enhanced exergetic performance despite the increased system operating temperature constitutes proof that, from a second-law analysis point of view, it is beneficial to provide heat at elevated temperature despite the fact that the latter is associated with increased thermal losses and

decreases of the system electric efficiency as well. Nevertheless, this conclusion is not of general validity and can only be applied to systems having performance characteristics similar to the developed prototype CPVT system, where the thermal output considerably exceeds the electrical output. As shown in **Fig. 7.13b**, increasing the fluid inlet temperature from 298.0 K to 338.0 K causes an increase of approximately 25% on the system exergetic efficiency that can be achieved in December.

In general the results produced by the dynamic model referring to the base-case system have established that the exergetic efficiency achieved is relatively low and lies in the range 9.0-15.5% depending on the operating and environmental conditions. It was proven during the system experimental evaluation that the system main output is in the form of thermal power. However, as has been already discussed the exergy stream associated with the thermal output is dependent on the temperature level of the delivered heat. Since the intrinsic orientation of the application is the production of relatively low-temperature heat, in the range of 333-363 K, the useful thermal exergy stream is considerably decreased. On the contrary the electrical exergy stream is directly associated with the produced power (see **Eq. 7.25**) and hence it is essential to increase the system electrical output in order to achieve high performance from an exergetic point of view.

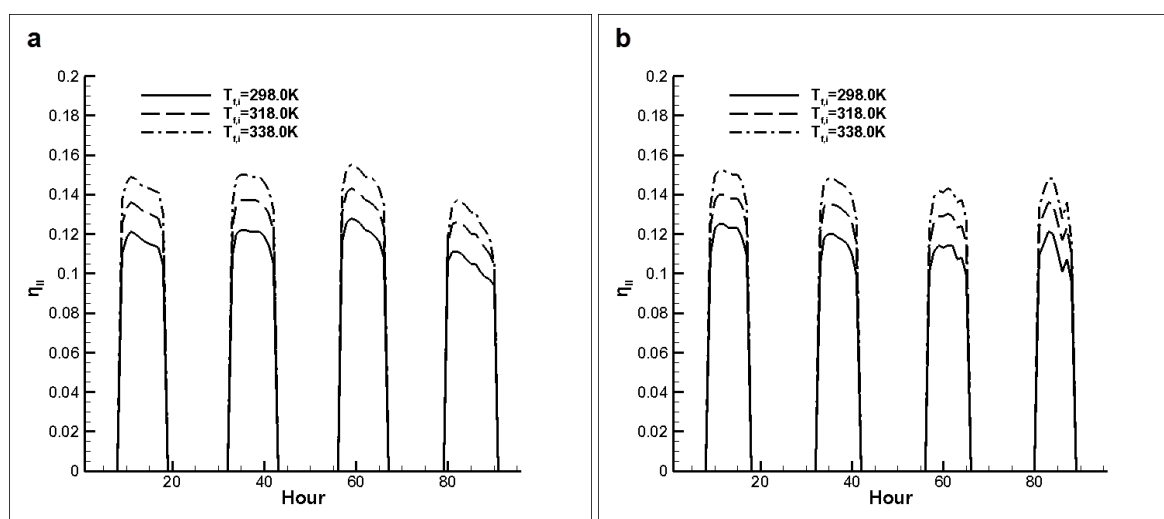


**Fig. 7.13** Effect of fluid inlet temperature on the system exergetic efficiency in regard to the base-case system: (a) March, (b) December.

Depending on application for which the CPVT system is intended, the extent of the aperture area must be properly sized and it is therefore of engineering interest to analyze the performance of different-scale systems. The system aperture area is considered to increase by adding parabolic-trough modules of the same geometrical characteristics, i.e. the system length is increased while the concentration ratio is maintained the same. The exergetic performance of systems having different aperture areas is shown in **Fig. 7.14**. It becomes evident that increasing the system aperture has a beneficial effect on exergetic efficiency, with the effect being relatively independent of the environmental conditions. The temperature level at which heat is delivered appears to be a more significant factor, in terms of exergetic performance, compared to the effect of thermal losses. Even though heat losses also increase as the system aperture and consequently the heat-sink length increase, the influence of the fluid outlet temperature on the second right-hand term of **Eq. 7.24** results to an

increased thermal exergy stream. As depicted in **Fig. 7.14**, the maximum exergetic efficiency obtained for a 20m<sup>2</sup> system is achieved in December and is approximately equal to 15%.

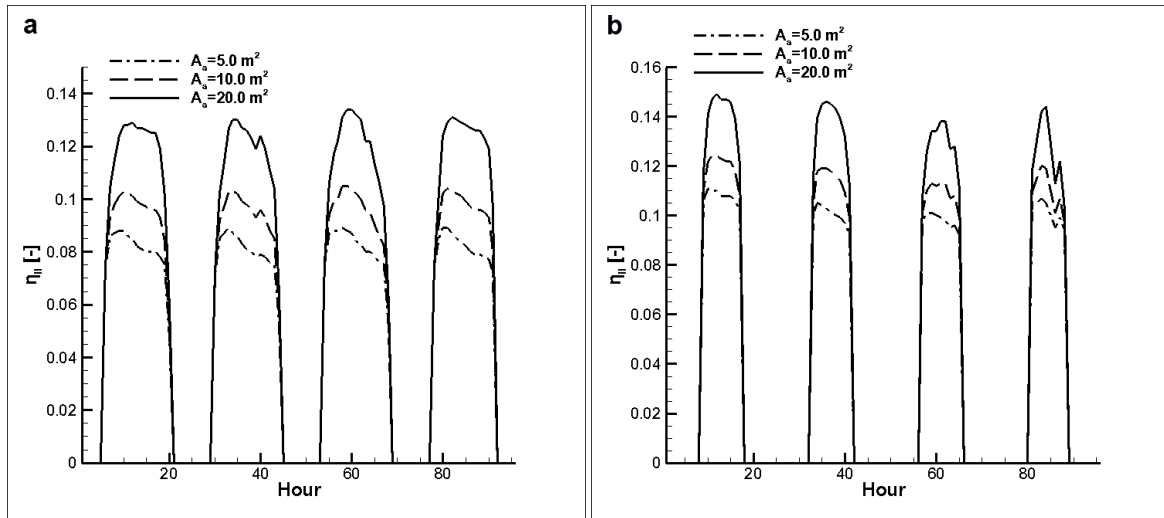


**Fig. 7.14** Effect of the system aperture on the system exergetic efficiency in regard to the base-case system: (a) June, (b) December.

It was established during the system experimental evaluation that the optical losses have the most significant contribution on the reduction of the overall efficiency. **Fig. 7.15** elucidates the influence that a higher optical quality of the parabolic trough would have on the exergetic efficiency. Higher system optical quality leads to augmented irradiation on the system receiver and influences both the useful thermal and electrical exergy streams in a beneficial manner. The system can reach exergetic efficiencies up to 18% and 21% in the summer (**Fig. 7.15a**) and winter (**Fig. 7.15b**) periods, respectively, for an optical efficiency of 85%. These values are significantly larger compared to the 12% achieved by a system with the optical quality of the manufactured prototype (see **Fig. 7.13b**). It is easily perceivable that increased optical quality is of vital importance for the efficient performance of a CPVT system.

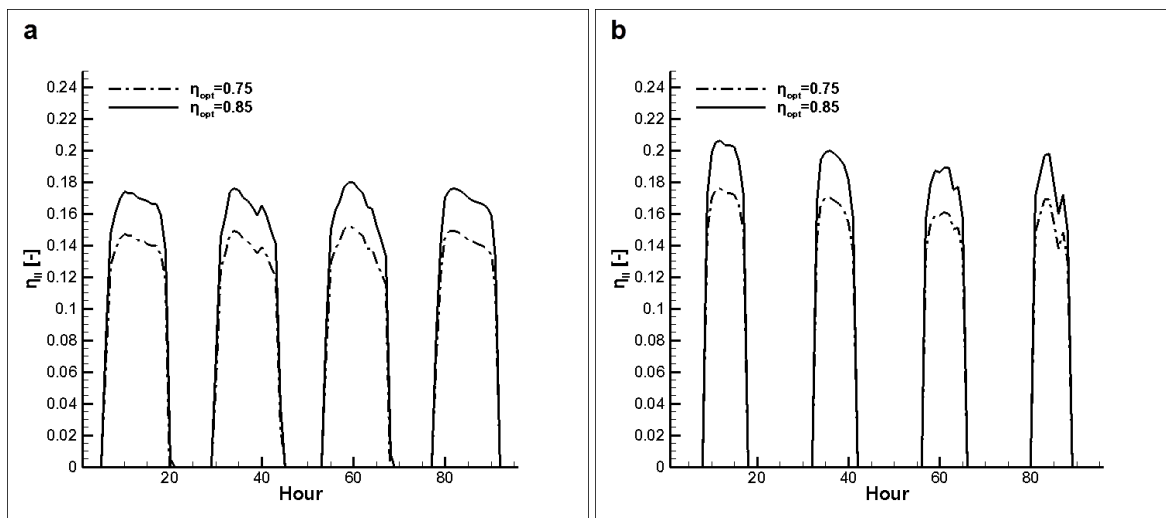


**Fig. 7.15** Effect of optical efficiency on the system exergetic efficiency in regard to the base-case system: (a) June, (b) December.

The relatively low efficiency of the solar-cell modules ( $\eta_{el}=13.8\%$ ) has been identified as a weak point of the prototype system. **Fig. 7.16** presents the influence of the module electrical efficiency on the system exergetic efficiency. Increasing the portion of irradiation converted directly to electricity by the solar cells will certainly reduce the excess heat available for extraction and this effect will also be propagated on the respective exergy stream. It can be observed that a 5% absolute increase of the electrical efficiency leads to an increase of the exergetic efficiency approximately equal to 2%, regardless of the environmental conditions. The graphs of **Fig. 7.16** include an additional curve that corresponds to a system with high, yet certainly achievable, optical and (reference) electrical efficiencies, equal to 75% and 25%, respectively. As can be seen, the system is able to reach exergetic efficiencies up to 24% for low values of the ambient temperature, i.e. in March (**Fig. 7.16a**) and December (**Fig. 7.16c**). By comparing **Figs. 7.15b** and **7.16c**, it can be deduced that, for a day with high insolation in the winter, incorporating high-efficiency cells to a precisely manufactured CPVT system increases the exergy efficiency from 17.5% to 23%. The general conclusion can be drawn that achieving high manufacturing and materials quality in reference to the key components of a CPVT system, such as the PV modules and the optical device, can cause an approximately two-fold increase of its exergetic efficiency (see **Fig. 7.13** for comparison to the base-case system).

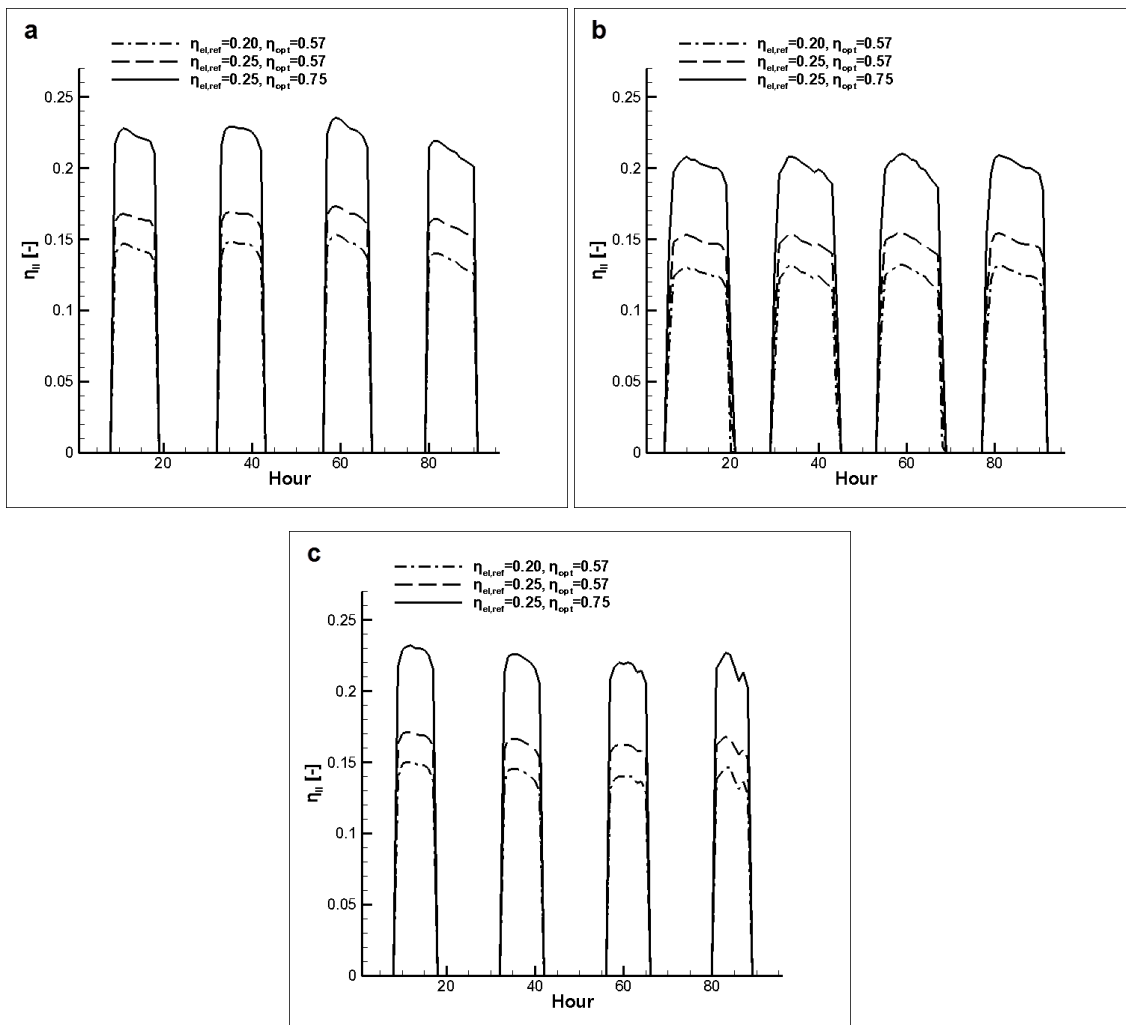


**Fig. 7.16** Effect of the PV module efficiency on the system exergetic efficiency in regard to the base-case system: (a) March, (b) June and (c) December.

As has already been stated in **paragraph 5.10**, the thermal bonding between the PV module and the heat sink is a crucial technical issue concerning CPVT system technology. Apart from the absolute thermal conductivity value of the adhesive material, the thermal bonding could be considerably hindered by the formation of air pockets due to imperfect smearing of the adhesive material on the bonded surfaces. **Fig. 7.17** elucidates the effect of the quality of the thermal bonding on the operation of the base-case system. A value of 0.043 W/mK has also been considered for the effective thermal conductivity of the resin, in order to approximate the case of poor thermal bonding and extensive effect of air pockets on heat transfer. As illustrated in **Fig. 7.17a**, poor thermal bonding ( $k_{resin}=0.043$  W/mK) increases the maximum PV module temperature to values up to 373.0 K for environmental conditions referring to the winter time period, more than 40.0 K higher than the values obtained for a conductivity of 4.3 W/mK, a value achieved by commercial thermally conductive resins. The value of 0.43 W/mK, namely the effective thermal conductivity as achieved by the bonding procedure discussed in **paragraph 5.10.1**, inflicts only a moderately increased thermal resistance compared to the lower limit that can be achieved with commercial resins, as the PV module obtains values as high as 336.0 K, approximately 3.0 K higher than in the case of conductivity equal to 4.3 W/mK. The system exergetic efficiency is decreased by approximately 12.5% for a decrease of the bond active thermal conductivity from 4.3 W/mK to 0.043 W/mK, as revealed by **Fig. 7.17b**. The deterioration in the exergetic efficiency is relatively moderate, as the system output is mainly in the form of thermal power and the magnitude of thermal losses is small due to the general characteristics of the system. Although the system exergetic efficiency is not significantly influenced by the quality of the thermal bond, the cells structural integrity is certainly degraded by the intense thermal cycling leading to increased possibility of failure and reduced life cycle. It is also interesting to notice that increasing the effective thermal conductivity of the bond further, e.g. to a value of 43.0 W/mK, as depicted in **Fig. 7.17b**, has no effect on the exergetic efficiency as the thermal resistance due to the resin is minimized and the overall exergetic losses are dominated by the thermal resistances posed by the other materials comprising the receiver.

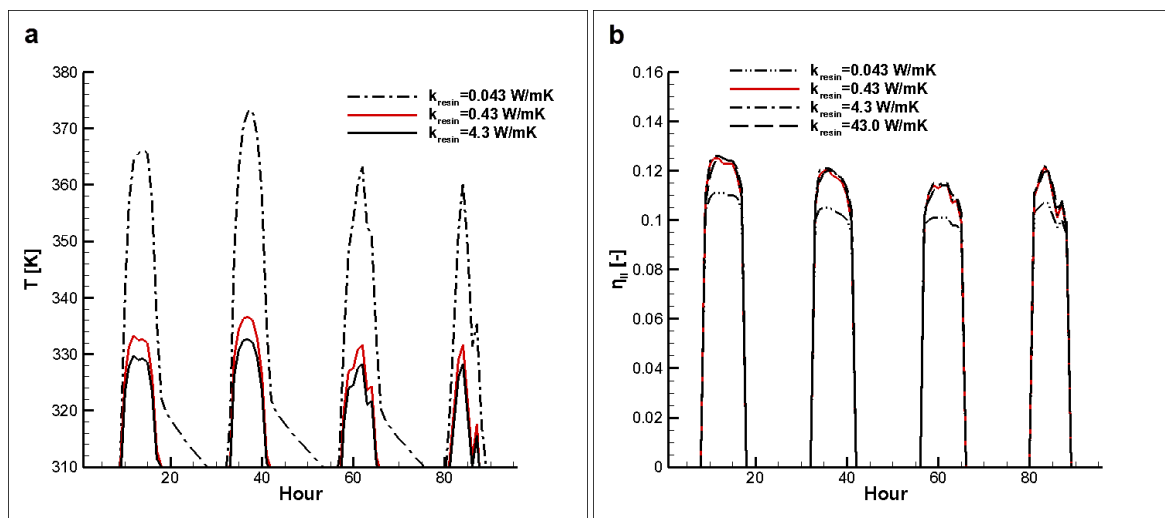


**Fig. 7.17** Effect of the resin thermal conductivity on the base-case system operation: (a) maximum temperature of the PV module and (b) system exergetic efficiency in December.

For completeness purposes and in accordance with the discussion concerning **Fig. 7.10**, the effect of the heat-sink geometrical parameters on the system exergetic efficiency is presented in **Fig. 7.18**. The detrimental effect of decreasing the channel dimensions on the exergetic performance of both configurations is evident, with the effect being more pronounced in the case of the FW device (**Fig. 7.18a**). Besides, for the case of channel width equal to 100  $\mu\text{m}$ , it can be clearly seen that the exergetic efficiency exhibits an intense oscillation due to the fluctuation and subsequent decrease of the solar irradiation during the fourth day of December simulated (see **Fig. 7.6c**). Especially in the case corresponding to channel width of 100  $\mu\text{m}$ . Furthermore, it can be observed in **Fig. 7.18a** that at periods of transient operation the exergetic efficiency is negative, as the pumping power exergy stream is larger than the sum of the useful electrical and thermal exergy streams. It can be therefore concluded that the optimization procedure followed has been proven reliable as the designed and manufactured cooling devices exhibit superior thermal and hydrodynamic performance.

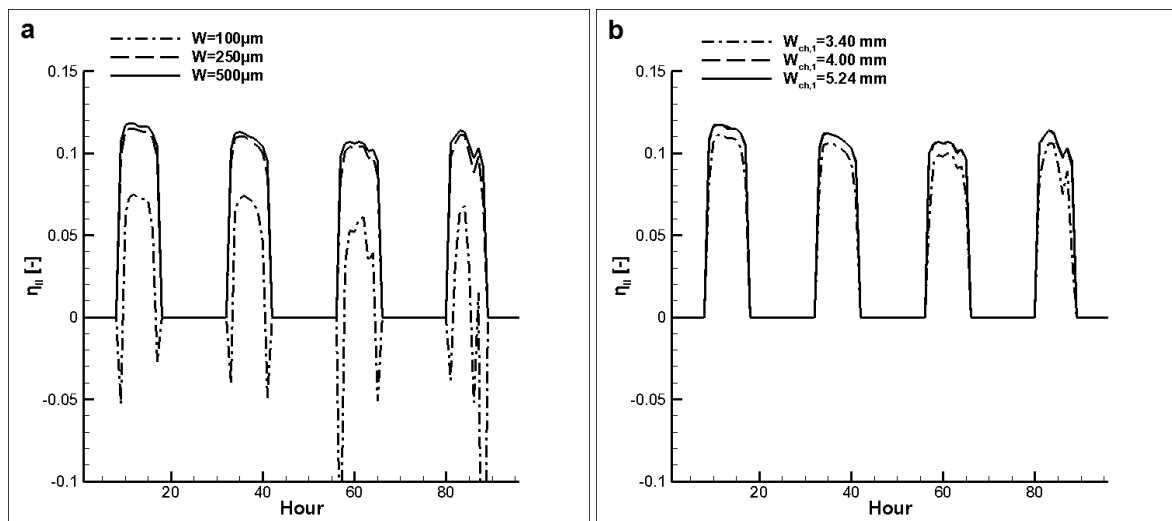


**Fig. 7.18** Effect of the heat-sink geometrical parameters (channel width) on the system exergetic efficiency (base-case system in December): (a) FW configuration, (b) VW configuration.

The monthly distribution of the base-case system exergy output is shown in **Fig. 7.19a** and allows the specification of the time periods where the system achieves its most effective performance. An initial observation is that the electrical exergy exceeds the respective thermal throughout the year and obtains maximum values in the summer months, 2.5 times higher compared to the respective thermal exergy (in July and August). It is interesting to notice that the peak electrical exergy is delivered by the system in July, whereas the maximum thermal exergy is obtained in May. This variation in regard to the two useful exergy streams occurs on grounds that the electrical exergy is primarily depended on the irradiation intensity, whereas thermal exergy is significantly influenced by the ratio of the fluid outlet to the ambient temperature and hence the combination of these two factors in the spring and autumn tend to enhance the thermal exergy produced by the system and render it comparable to that produced during the summer months.

**Fig. 7.19b** illustrates the monthly exergy output of the “high-quality” system for a water volumetric flow rate of 20.0 mL/s. The annual produced thermal and electrical exergy by the “high-quality” system are approximately 1.9 and 2.6 times higher in comparison to the respective of the base-case system. In the case of the “high-quality” system the peak electrical exergy efficiency is still achieved

in July, however, in contrast to the base case system, the respective thermal exergy is achieved in June. In general, it can be deduced that the thermal exergy output of the “high-quality” system is slightly less sensitive to the ratio of the outlet fluid to ambient temperature and for this reason it achieves higher values during the summer months, unlike the base-case system. Moreover, the electricity to thermal exergy ratio is larger in the “high-quality” system due to the increased efficiency of the solar-cell modules.

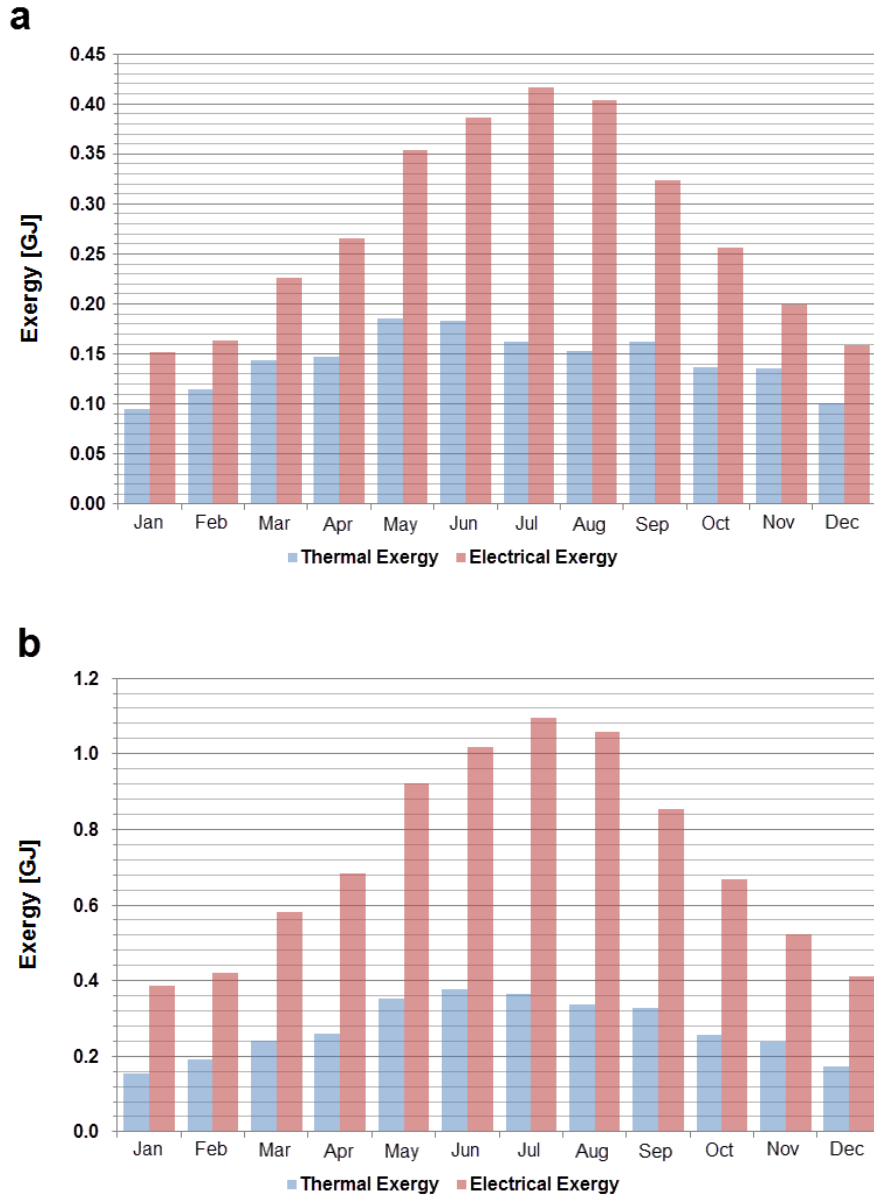


**Fig. 7.19** Monthly exergy output of the CPVT system: (a) base-case system (b) “high-quality” system ( $\eta_{opt}=0.75$ ,  $\eta_{el}=0.25$ ) with water volumetric flow rate  $\dot{V}_{tot}=20.0$  mL/s

The high-quality system is also comparatively evaluated against the base-case system in terms of destroyed exergy rate and entropy generation, so that the main causes of system irreversibility can be identified. **Fig. 7.20** illustrates the main exergy destruction mechanisms for the two system variations in question under variable environmental conditions. It is clearly demonstrated that the main cause of

system irreversibility are the optical losses, as approximately half of the available solar irradiation exergy is destroyed in the optical device. On the contrary, the exergy destroyed due to the system thermal losses is two orders of magnitude lower, indicating thus the high system thermal performance. The destroyed exergy rate closely follows the trend of the solar irradiation intensity and the system output (see Figs. 7.6-7.7b) and consequently it is maximized in time periods with high insolation. As also revealed by Fig. 7.20, increasing the system optical efficiency reduces the respective exergy destruction rate by approximately 53% regardless of the environmental conditions. However, as depicted by the curves in red color of Fig. 7.20 the destroyed exergy stream that corresponds to the thermal losses in fact increased in the high quality system. This variation is justified as the solar irradiation incident on the receiver and therefore the additional heat available for extraction are producing higher temperature gradients in the receiver materials and increased thermal losses. Apparently, the benefit due to the decreased exergy destruction in the optical device exceeds by far the negligible increase in the exergy destruction stream referring to the thermal losses.

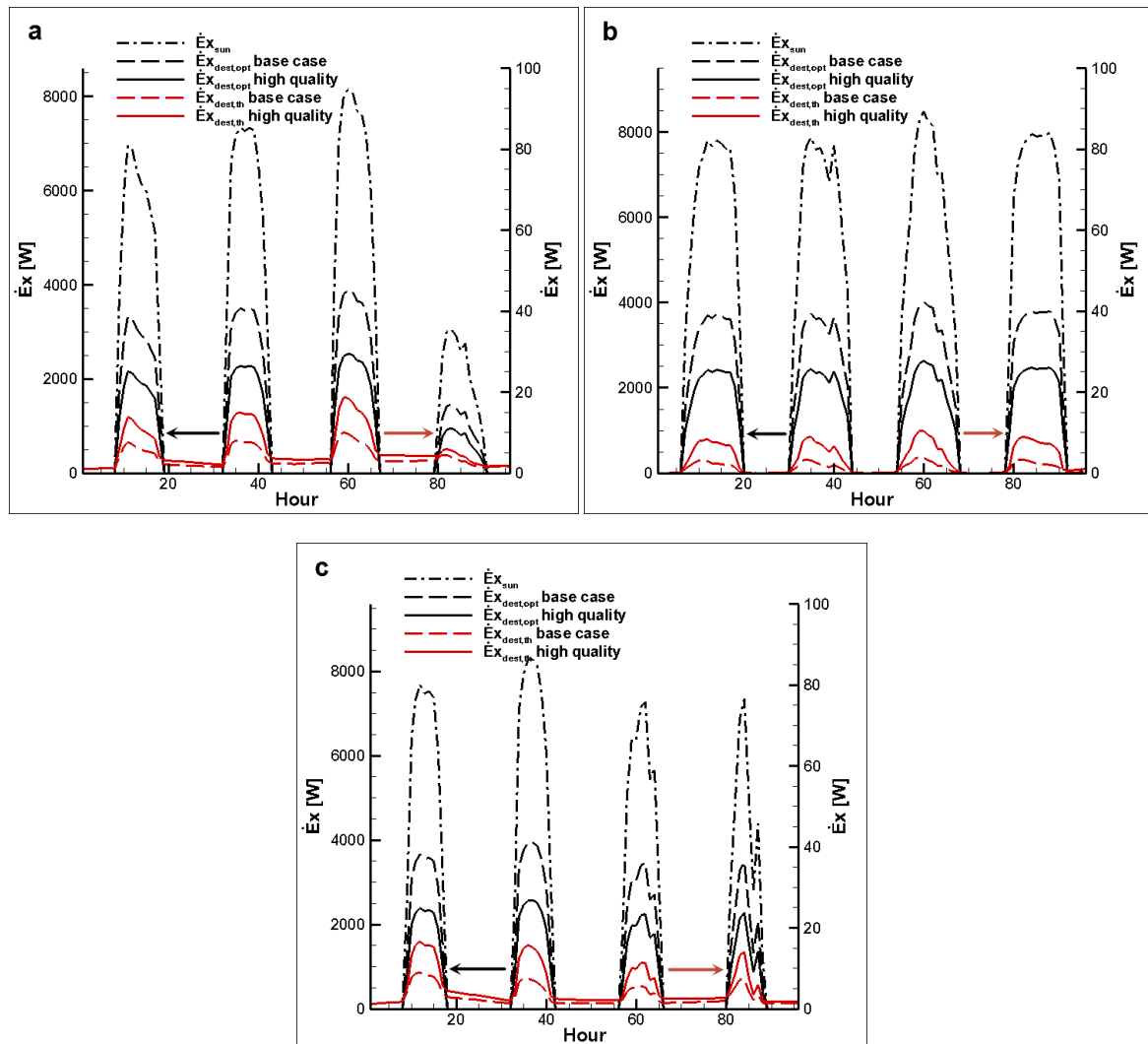
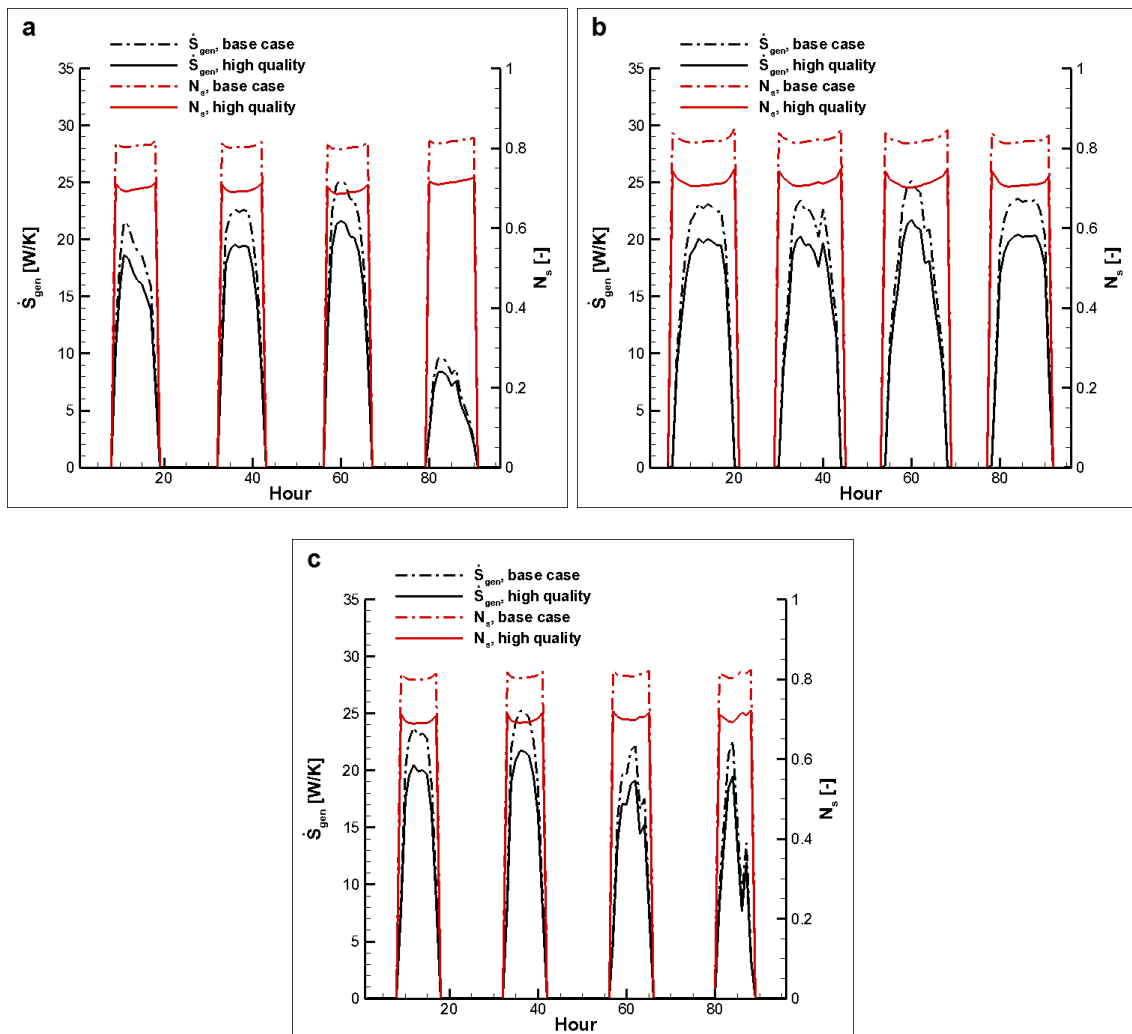


Fig. 7.20 Destroyed exergy rate referring to the base-case and high-quality systems: (a) March, (b) June, (c) December

The system entropy generation rate is presented in **Fig. 7.21** in the form of either absolute values or dimensionless entropy generation number  $N_s$ . In all cases the entropy generation rate is lower for the “high-quality” system, where the exergy destruction due to optical losses and poor electrical performance is considerably reduced. However, it can be seen that the entropy generation rate closely follows the trend of the solar irradiation intensity and consequently of the system output (see **Figs. 7.6-7.7b**). The entropy generation number  $N_s$  (**Eq. 7.32**) appears as a more appropriate quantity for the clarification of the system irreversibilities, as it is independent of the solar irradiation intensity and obtains comparable values regardless of the environmental conditions. As can be observed, the entropy generation number for the base-case system lies in the range 0.80-0.82 for all the time periods considered. In regard to the “high-quality” system, the same quantity is reduced to values in the range 0.69-0.72. It is also interesting to notice that the entropy generation number, which in general exhibits a flatter profile during the day, obtains its minimum daily value when the value of the absolute entropy generation rate is maximized, i.e. when the system output is maximized. The entropy generation number decrease is steeper for the high-quality system. It becomes therefore evident that the minimization of the entropy generation number indicates the time period of the day where the system obtains its most effective operation and coincides with the maximization of the exergetic efficiency  $\eta_{II}$ . Hence, it is recommended as a suitable index for CPVT applications.



**Fig. 7.21** Entropy generation rate for the base-case and high-quality systems: (a) March, (b) June and (c) December.

### 7.6 Concluding remarks

The prediction of the CPVT system long-term energetic and exergetic performance was performed in this chapter using a dynamic theoretical model. The simulations clearly demonstrated the applicability of the manufactured cooling devices to large-scale CPVT systems, as the thermal losses were found to be of small magnitude in reference to systems oriented towards the domestic sector. Additionally, the parasitic pumping power had a negligible effect on the system efficiency for the heat-sink geometrical parameters considered.

The analysis of the system exergetic performance revealed that, for the performance characteristics of the prototype system, namely substantially higher thermal than electrical output, it is beneficial to operate the system using low flow rate and elevated fluid inlet temperature, in order to ensure that heat is delivered at a high temperature level and thus the exergetic efficiency is increased. The basic constituents characteristics identified to have a significant effect on the system exergetic performance are the solar-cell module efficiency and the optical quality of the parabolic trough, with the optical losses being clearly established as the primary source of exergy destruction. Increasing the aforementioned system quality characteristics to higher yet achievable values, e.g.  $\eta_{opt}=0.75$  and  $\eta_{e}=0.25$ , can lead to a two-fold increase of the exergetic efficiency. Finally, an interesting general remark that can be made is that the cooling fluid flow rate and inlet temperature can be utilized as free parameters to adjust the system thermal and electrical output, as the latter two quantities are of interdependent nature, based on the respective thermal and electrical loads required by a specific application.

### Chapter references

- [7.1] A. Hazi, G. Hazi, R. Grigore, V. Sorin, Opportunity to use PVT systems for water heating in industry, *Appl. Therm. Eng.* (2013).
- [7.2] N. Amrizal, D. Chemisana, J.I. Rosell, Hybrid photovoltaic-thermal solar collectors dynamic modeling, *Appl. Energy*. 101 (2013) 797–807.
- [7.3] H.A. Zondag, D.W. De Vries, W.G.J. Van Helden, R.J.C. Van Zolingen, a. a. Van Steenhoven, The thermal and electrical yield of a PV-thermal collector, *Sol. Energy*. 72 (2002) 113–128.
- [7.4] T.T. Chow, Performance analysis of photovoltaic-thermal collector by explicit dynamic model, *Sol. Energy*. 75 (2003) 143–152.
- [7.5] C. Cristofari, G. Notton, J.L. Canaletti, Thermal behavior of a copolymer PV/Th solar system in low flow rate conditions, *Sol. Energy*. 83 (2009) 1123–1138.

- [7.6] M.N. Abu Bakar, M. Othman, M. Hj Din, N.A. Manaf, H. Jarimi, Design concept and mathematical model of a bi-fluid photovoltaic/thermal (PV/T) solar collector, *Renew. Energy*. (2013).
- [7.7] R.M. da Silva, J.L.M. Fernandes, Hybrid photovoltaic/thermal (PV/T) solar systems simulation with Simulink/Matlab, *Sol. Energy*. 84 (2010) 1985–1996.
- [7.8] C.S. Malvi, D.W. Dixon-Hardy, R. Crook, Energy balance model of combined photovoltaic solar-thermal system incorporating phase change material, *Sol. Energy*. 85 (2011) 1440–1446.
- [7.9] M.J. O’Leary, L.D. Clements, Thermal-electric performance analysis for actively cooled, concentrating photovoltaic systems, *Sol. Energy* 25 (1980) 401-406.
- [7.10] M. Hedayatizadeh, Y. Ajabshirchi, F. Sarhaddi, A. Safavinejad, S. Farahat, H. Chaji, Thermal and electrical assessment of an integrated solar photovoltaic thermal (PV / T) water collector equipped with a compound parabolic concentrator (CPC), *Int. J. Green Energy* 10 (2013) 494-522.
- [7.11] H. Helmers, A. Bett, J. Parisi, C. Agert, Modeling of concentrating photovoltaic and thermal systems, *Prog. Photovolt.: Res. Appl.* (2012).
- [7.12] F. Calise, A. Palombo, L. Vanoli, A finite-volume model of a parabolic trough photovoltaic/thermal collector: Energetic and exergetic analyses, *Energy* 46 (2012) 283–294.
- [7.13] F. Calise, M. Dentice d’Accadia, C. Roselli, M. Sasso, F. Tariello, Desiccant-based AHU interacting with a CPVT collector: Simulation of energy and environmental performance, *Sol. Energy* (2013).
- [7.14] A. Buonomano, F. Calise, G. Ferruzzi, L. Vanoli, A novel renewable polygeneration system for hospital buildings: design, simulation and thermo-economic optimization, *Appl. Therm. Eng.* (2014).
- [7.15] F. Calise, M. Dentice d’Accadia, A. Palombo, L. Vanoli, Dynamic simulation of a novel high-temperature solar trigeneration system based on concentrating photovoltaic/thermal collectors, *Energy*. 61 (2013) 72–86.
- [7.16] A. Buonomano, F. Calise, M. Dentice d’ Accadia, L. Vanoli, A novel solar trigeneration system based on concentrating photovoltaic/thermal collectors. Part 1: Design and simulation model, *Energy* 61 (2013) 59-71.
- [7.17] A. Kribus, D. Kaftori, G. Mittelman, A. Hirshfeld, Y. Flitsanov, A. Dayan, A miniature concentrating photovoltaic and thermal system, *Energy Convers. Manag.* 47 (2006).
- [7.18] T. Kerzmann, L. Schaefer, System simulation of a linear concentrating photovoltaic system with an active cooling system, *Renew. Energy*. 41 (2012) 254–261.
- [7.19] C. Renno, F. Petit, Design and modeling of a concentrating photovoltaic thermal (CPV/T) system for a domestic application, *Energy Build.* 62 (2013) 392–402.

- [7.20] C. Renno, Optimization of a concentrating photovoltaic thermal (CPV/T) system used for a domestic application, *Appl. Therm. Eng.* (2014).
- [7.21] H. Helmers, K. Kramer, Multi-linear performance model for hybrid (C)PVT solar collectors, *Sol. Energy* 92 (2013) 313–322.
- [7.22] J.S. Coventry, A solar concentrating photovoltaic/thermal collector, PhD thesis, Australian National University, Canberra, 2004.
- [7.23] G. Kosmadakis, D. Manolakos, G. Papadakis, Simulation and economic analysis of a CPV/thermal system coupled with an organic Rankine cycle for increased power generation, *Sol. Energy*. 85 (2011) 308–324.
- [7.24] B. Gebhart, Y. Jaluria, R.L. Mahajan, B. Sammakia Buoyancy-induced Flows and Transport, 1<sup>st</sup> ed. Hemisphere Publishing Co., New York, 1988.
- [7.25] Meteotest, Meteororm Version 6.1, Bern, Switzerland, 2008
- [7.26] R. Abbas, J. Muñoz, J.M. Martínez-Val, Steady-state thermal analysis of an innovative receiver for linear Fresnel reflectors, *Appl. Energy*. 92 (2012) 503–515.
- [7.27] A. Bejan, Extraction of exergy from solar collectors under time-varying conditions, *Int. J. Heat Fluid Flow*. 3 (1982) 67–72.
- [7.28] S. Agrawal, G.N. Tiwari, Energy and exergy analysis of hybrid micro-channel photovoltaic thermal module, *Sol. Energy*. 85 (2011) 356–370.
- [7.29] A. Tiwari, S. Dubey, G.S. Sandhu, M.S. Sodha, S.I. Anwar, Exergy analysis of integrated photovoltaic thermal solar water heater under constant flow rate and constant collection temperature modes, *Appl. Energy*. 86 (2009) 2592–2597.
- [7.30] D. Kamthania, S. Nayak, G.N. Tiwari, Energy and exergy analysis of a hybrid photovoltaic thermal double pass air collector, *Appl. Sol. Energy*. 47 (2011) 199–206.
- [7.31] C.S. Rajoria, S. Agrawal, G.N. Tiwari, Exergetic and enviroeconomic analysis of novel hybrid PVT array, *Sol. Energy*. 88 (2013) 110–119.
- [7.32] F. Sobhnamayan, A. Hamidi, H.R. Monavari, F. Sarhaddi, S. Farahat, M. a. Alavi, Performance evaluation of a solar photovoltaic thermal air collector using energy and exergy analysis, *J. Renew. Sustain. Energy*. 3 (2011) 043115.
- [7.33] A. Bejan, Entropy Generation Minimization, 1<sup>st</sup> ed., CRC Press, New York, 1996.

- [7.34] R. Petela, Exergy of heat radiation, *J. Heat Transfer* 86 187-192.
- [7.35] F. Calise, A. Palombo, L. Vanoli, A finite-volume model of a parabolic trough photovoltaic/thermal collector: Energetic and exergetic analyses, *Energy* 46 (2012) 283–294.
- [7.36] E. Saloux, A. Teysseidou, M. Sorin, Analysis of photovoltaic (PV) and photovoltaic/thermal (PV/T) systems using the exergy method, *Energy Build.* 67 (2013) 275–285.
- [7.37] E. Torres-Reyes, J.J. Navarrete-Gonzalez, B.A. Ibarra-Salazar, Thermodynamic method for designing dryers operated by flat-plate solar collectors, *Renew. Energy* 26 (2002) 649–660.
- [7.38] E. Torres-reyes, J.G. C. Gortari, B.A. Ibarra-Salazar, M. Picon-Nuñez, A design method of flat-plate solar collectors based on minimum entropy generation, *Exergy Int.* 1 (2001) 46–52.



### 8.1 Conclusions

The concept of concentrating photovoltaics (CPV) accounts for a promising technology in the field of sustainable-energy applications, as it involves the replacement of semiconductor material by inexpensive reflector material, which can lead to significant cost reduction of the specific technology. The vast majority of technologically mature applications, some of which have reached the stage of commercial production, account for high-concentration ( $CR > 1000$ ), large-scale CPV systems that utilize refractive optics and triple-junction solar cells of high efficiency. Nevertheless, none of these applications incorporates an active cooling system to exploit excess heat. In general, concentrating photovoltaic/thermal systems have not yet reached commercialization as vital technical challenges have not been effectively addressed and there are still reliability issues associated with the specific technology. Especially in regard to mid-range ( $10 < CR < 100$ ) concentrating applications that are primarily intended toward the domestic and commercial sectors, only few full-scale integrated installations are known as of today world-wide. During the literature survey performed in the framework of the present dissertation, a lack of innovative designs has been verified regarding devices incorporated for cooling the solar-cell modules, as more elaborate layouts besides simple cylindrical or rectangular ducts have not been considered. The basic objective of the present thesis was to illustrate the design procedure and to highlight all the technical challenges associated with the development of a novel, linear-focus concentrating photovoltaic/thermal system with special attention being given to the design and performance characterization of the active cooling system.

Various types of plate-fin and tube-on-plate heat-sink configurations were considered as devices potentially suitable for the cooling of the solar cells and were numerically investigated. Microchannel heat sinks demonstrated superior thermal performance compared to the other configurations, whereby the implementation of stepwise-varying channels also proved to be an efficient, passive heat transfer enhancement technique, leading to the disruption of the thermal boundary layer development and the inducement of longitudinal vortices. Furthermore, the heat-sink configurations with varying channel width were found to exhibit increased temperature uniformity of the heated substrate than those with straight channels. After a comparative evaluation, the straight and variable width microchannels were deemed as the most prominent geometrical layouts and were selected for fabrication of suitable specimens to be used for the experimental evaluation.

In addition, a multi-objective optimization methodology was formulated to determine the geometrical parameters of the selected plate-fin heat sinks that lead to optimal hydrodynamic and thermal performance. It was also demonstrated that the use of a genetic algorithm in conjunction with surrogate models representative of the device performance can significantly accelerate the optimization procedure. The manufacturing of the optimal designs was realized using conventional machining procedures, which posed a technical challenge in terms of manufacturing feasibility and precision. The manufactured cooling devices were very compact as the overall device thickness was equal to 6.0 mm and 10.6 mm for the FW and VW configurations respectively, for an active (heat-

transfer) area equal to 500.0 mm x 60.0 mm. A manifold system has also been designed and manufactured, allowing for the uniform fluid distribution to the heat-sink channels, while inducing minimal pressure drop. The experimental evaluation of the cooling devices was performed on a test rig specifically developed for this purpose and the quality of the respective designs was verified. It was furthermore established that the thermal resistance and the induced pressure drop by the heat sinks can be predicted by three-dimensional computational fluid dynamics (CFD) and heat transfer numerical models using the “unit-cell” approach to define a computational domain.

The design and manufacturing procedure of the integrated CPVT system has been discussed in detail and the various technical challenges associated with the realization of its sub-components were thoroughly elucidated. In reference to practical aspects of the system development, the experience gained indicates that prior to manufacturing it is essential to confirm whether the parabolic frame has the required rigidity to withstand wind-loads and, in addition, whether the reflective sheets have proper optical properties that remain unaffected by the environmental conditions. Besides, the materials used for the assembly of the PV modules (EVA, cells and thermal tape) must allow for operation up to 350-360 K and the solar cell modules must be rigid in order to allow a good thermal bond to the heat sink. It is of vital importance to give special attention during the system design to the manageable and reliable assembly of the various constituents, in order to ensure that the system can achieve long-term, unimpeded operation. This involves, among others, the proper sealing of the heat sink and connection to the manifold system, as well as the and proper thermal bonding to prevent fluid leakage and system overheating, respectively. A critical issue for the performance of the system is the quality of the thermal bonding between the solar cells and the heat sink.

The optical quality of the parabolic trough is the most significant loss mechanism in the prototype system, which is a common trend for concentrated solar power applications in the temperature range below 373 K. Consequently, manufacturing precision must be achieved in regard to the trough shape so that the highest possible receiver intercept factor could be ensured, as well as illumination uniformity on the receiver active surface. The experimental evaluation of the prototype CPVT system showed that there is considerable margin for improvement in regard to its electrical efficiency, which is considerably affected by the irradiation non-uniformity on the PV-module surface. The PV module employing wide cells (60.0 mm) were found to be insensitive to minor fluctuations of the concentrated irradiation caused by errors in the sun tracking, while the opposite was true for the modules employing narrow cells, as their efficiency showed a considerable deterioration for small misalignment of the receiver in respect to normal incidence.

The thermal efficiency of the prototype was found to be outstanding as the excess heat from the receiver is almost fully exploited and thermal losses were proven to be of minor significance due to the low values of thermal resistance and the compactness of the heat-sink configurations. Overall, the high performance of the novel cooling devices has been confirmed, as both thermal losses and parasitic pumping power were insignificant for the prototype system. It can be furthermore deduced that the cooling devices are capable of managing even higher heat fluxes and hence are suitable for systems of high concentration such as dish systems with “densely-packed” solar cells at the receiver. In regard to the thermal losses, the main mechanism accountable is convection from the receiver glass cover, especially for high wind velocities.

From an exergetic point of view, for a CPVT system where the thermal output considerably surpasses the respective electrical, it is beneficial to operate it in relatively high temperatures or low

flow rates. The system was found suitable to produce heat at the temperature levels required by applications such as domestic water heating, space heating, solar cooling using desiccant dehumidifiers and desalination with the method of membrane distillation. In regard to the prototype system, it was found that exergy is primarily destroyed in the form of optical losses. A parametric analysis conducted revealed that the exergetic efficiency of the CPVT system is primarily influenced by the optical efficiency of the parabolic trough, while also further know-how is required regarding the manufacturing of the PV modules, as increase of their electrical efficiency also has a substantial effect on exergetic performance.

In conclusion, it could be said that the research activities performed in the framework of the dissertation lie in two main axes, i.e. the design and evaluation of cooling devices and the development of the integrated CPVT application. The main findings of the thesis are summarized through the following points referring to the aforementioned groups of activities:

### Cooling devices

- The addition of heat-transfer surfaces in the geometrical layout of a plate-fin heat sink enhances thermal performance yet induces considerable cooling-fluid pressure drop.
- The incitement of secondary flow due to the geometrical layout and/or the prevailing flow conditions has a beneficial effect on the thermal performance of a cooling device.
- The introduction of stepwise-decreasing channel width along the flow direction in a plate-fin heat sink increases the temperature uniformity and significantly decreases the induced pressure drop with a minor increase of the thermal resistance, owing to the beneficial action of longitudinal vortices.
- It is feasible to manufacture heat sinks of considerable length ( $L=0.5$  m) with microchannels of constant and stepwise-varying width using conventional machining techniques. In fact, the machining of microchannels having very high aspect ratio ( $AR\approx 19$ ) was proven to be feasible.
- Suitable design and multi-objective optimization of the cooling-device geometrical layout can result to a device of high thermal performance with minor pressure loss penalty.
- The decoupling of the heat-sink optimization procedure from the physical model through the use of surrogate functions significantly simplified the entire process.
- The manufactured FW device exhibits exceptional thermal performance, as, for negligible heat losses, the maximum solid wall temperature is slightly higher than the fluid outlet temperature.
- The manufactured three-section VW device maintains relatively constant maximum wall temperature regardless of the coolant flow rate in the range 20.0-40.0 mL/s. Even though the maximum wall temperature exceeds the respective value of the FW device, the thermal resistance of the two devices based on the average wall temperature obtains similar values for the range of water

flow rates considered. Nevertheless, the induced fluid pressure drop by the VW device is an order of magnitude smaller compared to that of the FW device.

### Integrated CPVT system

- All the technical challenges associated with the development of a CPVT were properly addressed and a full-scale prototype system was successfully manufactured and experimentally evaluated. The system demonstrated reliable operation for the entire evaluation time period.
- The optical analysis showed that the irradiation flux distribution on the receiver exhibits a profile with two peaks. The experimentally obtained irradiation distribution was verified through ray-tracing simulations performed considering a parabolic trough of slightly distorted shape.
- The irradiation distribution on the receiver active surface has a significant effect on the electrical performance of the system, as the central part of the solar cells is poorly illuminated.
- The prototype CPVT system achieves an overall efficiency of approximately 50% with the thermal and electrical efficiencies of 43-44% and 5-7%, respectively. Hence, the main output of the system is in the form of thermal power. The performance of the system has been found to be independent of the water flow rate in the range of 20.0-40.0 mL/s.
- The design of the cooling system was found to be of high effectiveness as its incorporation in the CPVT system results to negligible thermal losses and parasitic pumping power; however there is margin for improvement in reference to its manufacturing precision.
- The quality of the thermal bond between the PV module and the heat sink was found to be satisfactory as the temperature difference between the PV-module and heat-sink substrates was found not to be significant. The use of thermally conductive epoxy resins instead of adhesive tapes is recommended for large bonding areas.
- The prevailing heat-loss mechanism from the system receiver is heat convection through the front glass cover, while conduction losses through the insulation are negligible.
- A comparative analysis demonstrated that the CPVT achieves a significantly lower heat transfer coefficient compared to state-of-the-art commercial flat-plate solar thermal collectors.
- For the performance characteristics of the prototype CPVT system where the main output is in the form of thermal power, it is suggested in terms of exergetic performance the system to operate at high temperatures. The effect of producing heat at high temperature exceeds by far the negative effect of increased heat losses and lower electrical efficiency on the system exergetic efficiency.
- The exergetic efficiency of the CPVT system is primarily influenced by the optical quality of the parabolic trough and the electrical efficiency of the PV module. Increasing these two factors to

achievable values, e.g.  $\eta_{opt}=0.75$  and  $\eta_{ei}=0.25$ , can yield a two-fold increase of the system exergetic efficiency.

- Technical challenges must still be overcome to enhance the system overall efficiency with the major ones being the precise manufacturing of the parabolic trough and the reliable assembly of concentrating-cell module.

### 8.2 Publications

Several of the subjects investigated in the present dissertation and the main conclusions drawn have resulted in the following list of publications in acclaimed peer-reviewed journals in the fields of energy and heat transfer and in the proceedings of relevant conferences:

#### *Journal Publications*

- [1] I.K. Karathanassis, E. Papanicolaou, V. Belessiotis, G.C. Bergeles, Experimental and numerical evaluation of an elongated plate-fin heat sink with three sections of stepwise varying channel width, *Int. J. Heat Mass Transfer* 84 (2015) 16-34.
- [2] I.K. Karathanassis, E. Papanicolaou, V. Belessiotis, G.C. Bergeles, The flow and temperature fields in cooling devices with embedded serpentine tubes, *Num. Heat Transfer, Part A: Appl.* 66 (2014), 349-378.
- [3] I.K. Karathanassis, E. Papanicolaou, V. Belessiotis, G.C. Bergeles, Effect of secondary flows due to buoyancy and contraction on heat transfer in a two-section plate-fin heat sink, *Int. J. Heat Mass Transfer* 61 (2013), 583-597.
- [4] I.K. Karathanassis, E. Papanicolaou, V. Belessiotis, G.C. Bergeles, Three-dimensional flow effects on forced-convection heat transfer in a channel with stepwise-varying width, *Int. J. Therm. Sci.* 67 (2013) 177-191.
- [5] I.K. Karathanassis, E. Papanicolaou, V. Belessiotis, G.C. Bergeles, Design optimization of a micro heat sink for Concentrating Photovoltaic/Thermal (CPVT) Systems using a genetic algorithm, *Appl. Therm. Eng.* 59 (2013) 733-744.
- [6] I.K. Karathanassis, E. Papanicolaou, V. Belessiotis, G.C. Bergeles, Design and experimental evaluation of a parabolic-trough Concentrating Photovoltaic/ Thermal (CPVT) system, *Ren. Energy*, Under Review.

### Participation in conferences

- [1] I.K. Karathanassis, E. Papanicolaou, V. Belessiotis, G.C. Bergeles, Design and Optimization of a Micro Heat Sink for Concentrating Photovoltaic/Thermal Systems, 3<sup>rd</sup> Micro and Nano Flows Conference, 2011, Thessaloniki, Greece.
- [2] I.K. Karathanassis, E. Papanicolaou, V. Belessiotis, G.C. Bergeles, A novel two-section cooling device employing jets in cross-flow, Proceedings of the 9th Hellenic Conference on Fluid Flow Phenomena, 2014, Athens, Greece.
- [3] I.K. Karathanassis, E. Papanicolaou, V. Belessiotis, G.C. Bergeles, Design and evaluation of linear concentrating photovoltaic/thermal system (in Greek), Proceedings of the 10<sup>th</sup> Hellenic Conference on Renewable Energy Sources, 2014, Thessaloniki, Greece.
- [4] I.K. Karathanassis, E. Papanicolaou, V. Belessiotis, G.C. Bergeles, Flow and conjugate heat transfer in heat exchanging devices employing tubes with 180deg bends (in Greek), Proceedings of the 8th Hellenic Conference on Fluid Flow Phenomena, 2012, Volos, Greece.

### **8.3 Novelty of the work**

As has already been stated, the research activities performed focus on two main subjects: the characterization of novel cooling devices and the development of a prototype CPVT system. Innovative findings have been established in reference to both research topics and valuable technical experience has been gained, which can be valuable to other research fields apart from renewable-energy applications such as electronics cooling. The main points of novelty attributed to the present work can be summarized as follows:

#### Cooling devices

Novel cooling configurations have been proposed and thoroughly evaluated in respect to their pertinence to CPVT systems. By this way a useful data set has been created that enables the appropriate selection of cooling devices for a wide range of concentrating solar applications based on a range of well-established criteria. Insight has been gained on the flow phenomena that lead to heat-transfer enhancement and the mechanisms that lead to their onset have been identified. The secondary-flow effect on heat transfer in particular was thoroughly studied, providing significant contributions to the relevant fluid-mechanics bibliography. Such phenomena were studied both in configurations with rectangular channel geometry and flow contraction as well as in curved tubes. In the former case, the inducement of secondary flows was due to bluff body effects, whereas in the latter due to centrifugal forces. The embedded curved (serpentine-type) tube configuration was in fact examined for the first time in conjunction with conjugate heat transfer effects. The experience gained can be used as guideline for the design of the geometrical layout of novel devices that utilize passive (geometrical) heat-transfer enhancement techniques.

In addition, a fast and robust optimization procedure for the geometrical optimization of plate fin heat sinks has been developed. Optimal heat sink configurations of novel layout suitable for CPVT systems have been manufactured. To the author's knowledge, this is the first time that the manufacturing and experimental evaluation of heat sinks of considerable length employing channels of such high aspect ratio is reported in the literature. It must be pointed out that the configuration designed and manufactured in the course of the present dissertation, employing three sections of channels with stepwise-varying channels exhibits the unique characteristic of maintaining constant maximum wall temperature for a wide range of cooling fluid flow rates, while also it attaining higher temperature uniformity than straight-microchannel heat sinks do.

### *Integrated CPVT system*

An efficient and reliable CPVT system prototype has been developed and all the technical challenges associated with the sizing and manufacturing of all system components have been effectively addressed, along with the proper selection of materials, hence leading to the gain of valuable know-how. To the author's knowledge the specific prototype is the only functional demonstration in Greece and one of the few such worldwide. The operation of the prototype demonstrated that high thermal and electrical output can be produced for a very limited receiver area.

Special attention has been given to the evaluation of the parabolic-trough optical quality and errors associated with the parabolic shape precision have been illustrated. A custom-made, low-cost device has been developed to measure the irradiation distribution on the receiver active surface. The overall analysis demonstrated the proper manufacturing procedure that must be followed in order to ensure high optical quality of the trough. Furthermore, the technical issue of bonding the heat sink and the PV modules has been successfully met and proper adhesive materials have been proposed. The system thermal and electrical performance have been experimentally evaluated and the key characteristics of the constituents that influence the overall prototype efficiency have been identified so that the CPVT system can be further improved and even reach standards of commercial production. Finally, a computational algorithm capable of predicting the system long-term performance has been developed. The predictive tool elucidated the performance characteristics of the system constituents that must be improved, in order to increase the system exergetic efficiency in a decisive manner.

### **8.4 Recommendations for future work**

The present dissertation highlights all the aspects of the design, manufacturing and operation of a concentrating photovoltaic/thermal system. Hence it can stand as a solid groundwork for further investigations associated with the system constituents, aiming at the improvement of their individual performance which could result to a more efficient integrated system as well. Based on the gained experience, the following research topics are regarded as being of importance for obtaining further valuable know-how on CPVT applications and are proposed for future investigation:

### ▪ Further investigation of cooling configurations

Additional heat-sink designs that offer possible heat transfer enhancement such as stacked microchannels, linear vortex generators, and metal foams would constitute interesting subjects for further investigation. In addition, the replacement of pure water with nanoparticle suspensions as cooling fluids could also be examined as an alternative technique to enhance heat transfer. Another novel concept that has been recently introduced is the incorporation of thermoelectric (TE) modules that can utilize waste heat and offer additional electrical production. The use of a TE module in tandem to a heat sink can further increase the electrical output of a CPVT system.

### ▪ Improvement of the integrated CPVT system

It is essential to ensure the effective and reliable CPVT system operation if commercial production is considered as a future step. First of all the design and implementation of a tracking system is necessary so that the system can achieve stand-alone operation. Additionally, the scale-up of the system should be pursued along with the coupling to a properly-sized thermal storage. In respect to the system overall quality, novel PV modules could be tested employing III-V high efficiency cells, e.g. GaAs or CIGS cells, in order to enhance electrical performance. A suitable technique should also be developed that enables the bonding of the solar cells directly onto the heat sink as this would lead to reduction of the overall heat sink thermal resistance. Additional aspects in regard to the manufacturing of the system such as machining precision and cost reduction should be addressed to reach commercialization

### ▪ Design and evaluation of point-focus CPVT systems

The technical experience gained can be applied to the design and development of point-focus CPVT systems. Point-focus systems achieve high concentration ratios ( $CR \approx 1000$ ) that allow the use of triple-junction PV modules of much smaller dimensions in comparison to those applicable to linear-focus systems. Consequently, compact heat-sink designs are also required and the miniaturization of the investigated design concepts constitutes an interesting research topic.

### ▪ Modeling of the CPVT system

The developed code capable of simulating the system performance can be further extended so as to include additional heat-sink configurations. In addition, the code could be implemented within the simulation software for energy systems TRNSYS as a new component. The integration in TRNSYS allows the evaluation the novel CPVT component in conjunction with built-in components corresponding, e.g. to thermal storage, desiccant dehumidifiers or absorption chillers and desalination units. By this way the applicability of coupling CPVT systems to the respective applications can be clearly elucidated. In addition, strategies for the operation of the CPVT system, e.g. regulation of the water flow rate and temperature, can be proposed based on the thermal and electrical loads that must met. It is worth considering making the component available as open-source, as this way it could

## **Chapter 8. Conclusions and recommendations for future work**

---

become useful to a large number of engineers and researchers worldwide dealing with concentrated solar power applications.



## Appendix A1

### Numerical schemes used by the ANSYS CFX package

ANSYS CFX is a general purpose CFD software able to simulate various types of flows such as steady or transient laminar and turbulent flows, single or multi-phase, and compressible or incompressible [A1]. The simulations performed at **Chapter 3** were treated as steady state and incompressible. CFX uses an element-based finite volume method, which requires the discretization of the computational domain using a mesh. All solution variables and fluid properties are stored at the mesh vertices, which are referred as nodes. A control volume is created by lines that join the centers of the mesh elements with the centers of the elements edges and in essence surrounds each node (**Fig. A.1**).

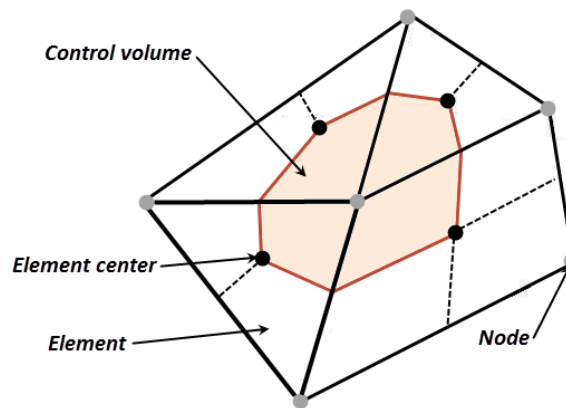


**Fig. A.1** Definition of the control volume.

According to the finite-volume method, the conservation equations for mass, momentum and temperature are integrated over each control volume. The Gauss' divergence theorem is applied to convert the volume integrals to surface integrals. Surface integrals are discretized at the integration points  $ip$  located at the center of each surface segment within an element (see **Fig. A.2**) and are consequently distributed to the adjacent control volumes.

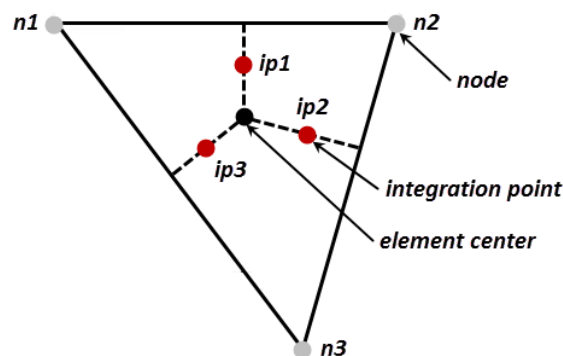


**Fig. A.2** Mesh element

It is therefore essential to approximate the solution field at the integration points. For this reason, finite-element shape functions are used by the software as follows:

$$\phi = \sum_{i=1}^{N_{nodes}} N_i \phi_i \quad (\text{A.1})$$

where  $N_i$  is the shape function for node  $i$  and  $\phi_i$  is the value of a variable  $\phi$  at node  $i$ . The summation is over all nodes of an element. The shape functions used in ANSYS CFX are linear in terms of parametric coordinates.

The advection term of the conservative equations requires values at the integration point of a variable  $\phi$  to be approximated in terms of the nodal values of  $\phi$ . The advection scheme implemented in CFX has the following form [A2]:

$$\phi_{ip} = \phi_{up} + \beta \nabla \phi \cdot \Delta \vec{r} \quad (\text{A.2})$$

where  $\phi_{up}$  is the value at the upwind node and  $\vec{r}$  is the vector from the upwind node to the integration point. The high-resolution scheme, a second-order accurate discretization scheme was employed for the determination of the coefficient  $\beta$ . The spatial derivatives for all the diffusion terms are evaluated using shape functions in accordance to the finite-element approach, e.g. for a derivative at the integration point:

$$\left. \frac{\partial \phi}{\partial x} \right|_{ip} = \sum_n \left. \frac{\partial N_n}{\partial x} \right|_{ip} \phi_n \quad (\text{A.3})$$

The pressure gradient term in the momentum equations is also evaluated using shape functions. CFX uses a co-located grid layout such that the control volumes are identical for all transport equations. The discretization of the mass flow through a surface of the control volume was performed using a discretization scheme proposed by Rhie and Chow [A3] in order to ensure pressure-velocity coupling.

A coupled solver is used by CFX in which all the hydrodynamic equations are solved as a single system, instead of a segregated solver, in order to accelerate the solution procedure. This solution approach uses a fully implicit discretization of the equations. The discrete system of linearized equations is solved using a Multigrid Incomplete Lower Upper factorization technique.

## References

[A1] ANSYS Inc., ANSYS CFX Introduction, Release 13.0, Canonsburg, PA 2010.

[A2] ANSYS Inc., ANSYS CFX-Solver Theory Guide, Release 13.0, Canonsburg, PA 2010.

[A3] C.M. Rhie, W.L. Chow, Numerical study of the turbulent flow past an airfoil with trailing edge separation, AIAA J. 21 (1983) 1525-1532.

## Appendix A2

### Catalogue of the CPVT system components and materials – Cost breakdown

The custom-made system sub-components and the materials procured to realize the prototype CPVT system are listed in **Table B.1**. The cost associated with each constituent is also included in the table. It can be easily deduced by the values of **Table B.1** that the cost of the integrated system is primarily designated by the high manufacturing cost of the main system metallic sub-components, as well as the cost of the custom-made PV module.

The elevated cost associated with the novel metallic items is attributed to the relatively limited know-how of the Greek industry in this area, regarding both the precise manufacturing of metallic structures of complex shape as well as micro-fabrication. Novel technical challenges had to be addressed by the industries, which collaborated in the present project, inevitably accompanied by extensive preparation for the setup of their CNC machines and time-consuming machining procedures consequently leading to elevated cost. The cost of the PV module was primarily determined by the additional charges for the design optimization of the solar cells for operation under concentrated sunlight. Additionally, by the specialized nature of the services provided by NAREC Ltd, given that there is a limited number of companies worldwide that develop silicon-based concentrating PV cells especially in low quantities. Besides, the cost of the consumable materials, e.g. insulation or epoxy resin, is also higher than expected due to the small order placed in each case, since limited quantities were required for the demonstration project.

**Table B.1** Inventory of the prototype CPVT system sub-components, materials and cost breakdown.

Component	Manufacturer	Cost	Comments
Parabolic frame	MEVACO SA	1200 €	Custom-made manufacturing of two frames. The cost refers to a 2.0 m <sup>2</sup> frame, with active area of 1.0 m <sup>2</sup> .
Reflector sheets	ALANOD GmbH	130 €	Commercial product. 65 €/m <sup>2</sup> for an order of 15.0 m <sup>2</sup> .
Heat sink	Petrekas Ltd	300 €	Custom-made manufacturing. The price accounts for an order of four devices.
Nozzles	Petrekas Ltd	500 €	Custom-made manufacturing. 250 €/nozzle for an order of eight nozzles.
PV modules	NAREC Ltd	1438 €	Custom-made assembly. The price accounts for an order of four PV modules.
Insulation	Armacell SA	5 €	Commercial product. 50 €/m <sup>2</sup> for an order of 1.0 m <sup>2</sup> .
Adhesive resin	Cast Coat Inc.	-	Commercial product. 126.60 €/1.33kg pack.
Wiring	Lapp Gruppe GmbH	6 €	Commercial product. 1 €/m for an order of 50.0 m <sup>2</sup> .

Considering an active aperture area of 1.0 m<sup>2</sup> and an overall efficiency of 50% for the CPVT system, the cost per produced power becomes approximately equal to 7.2 €/W. As a reference, the cost per produced power regarding concentrating solar power applications is reported to be in the range 3.0-7.5 €/W. However these values primarily refer to large-scale solar plants, where additional costs, e.g. the cost of the turbine and the generator for production of electric power, also apply. Thus, the

lower value of  $3.0 \text{ €/W}$  should be deemed as representative for relatively small-scale configurations comprising concentrating solar collectors. The respective cost for concentrating photovoltaic systems is estimated approximately equal to  $3.0 \text{ €/W}$ . Both figures are significantly lower compared to that of the prototype CPVT system, however they refer to commercial products manufactured in production lines of high capacity especially developed for that purpose.

In any case, the newly acquired know-how in reference to the design and manufacturing of the CPVT system allows for a great margin in cost reduction, especially if a more extended production is considered. The cost associated with the custom-made metallic parts, as reported by the technical managers of the collaborating industries, can be reduced to  $200 \text{ €/m}^2$  regarding the parabolic frame and to  $380 \text{ €}$  for an integrated heat sink-manifold configuration, considering a higher-volume production, e.g. of 100 items. As shown in **Table B.1**, the most significant cost constituent is that associated to the PV module. However, the cost is primarily designated by the consulting for the module design and optimization. It was stated by *NAREC Ltd* that for significant orders, e.g. in the range of 1000 cells, of a *specified* cell design, the cell cost can be reduced to as much as  $15 \text{ €/cell}$ . A PV module also comprises a low-iron glass front cover, conductive adhesive tape and an aluminum substrate. The values of low-iron glass can reach  $35 \text{ €/m}^2$  for orders in the range of  $50\text{m}^2$ . The cost for the adhesive tape could be estimated equal to  $7 \text{ €/m}$  for large orders (200 m of tape), whereas the cost for the aluminum substrate can be considered negligible.

By taking into account all the cost data mentioned above the overall cost for a PV module per  $\text{m}^2$  of CPVT system active area, provided that out-sourcing for the assembly is not required, is estimated approximately equal to  $155 \text{ €}$ . The cost associated with the receiver insulation (Armaflex) is approximately  $8 \text{ €/m}^2$  for orders of quantities greater than  $10 \text{ m}^2$ . The costs for all the system constituents considering the reduced values for large-scale production are shown in **Table B.2**. The cost of the adhesive resin and the wiring can be considered negligible. Consequently, an estimation for the relative overall cost of a CPVT system having an active area of  $1.0\text{m}^2$  yields a value approximately equal to  $1.75 \text{ €/W}$ . It must be noted that additional cost constituents such as the cost of the converter required in order to allow for the produced electric power to be delivered to the grid or the cost associated with the preparation of the area for mounting the system have not been taken into account in the present analysis. In any case, it is evident that the cost per unit of produced power by the CPVT system, although it merely an initial rough estimation referring to a prototype device, is not prohibitive compared to other concentrated solar power applications and hence a feasibility study on the system commercial viability should be pursued.

**Table B.2** Cost breakdown per  $\text{m}^2$  of active area for “large-scale” production of the CPVT system.

<b>Component</b>	<b>Cost</b>
Parabolic frame	300 €
Reflector sheets	40 €
Heat sink	180 €
Nozzles	200 €
PV modules	155 €
Insulation	0.8 €
Adhesive resin	-
Wiring	-

## Appendix A3

### Dynamic simulation of the CPVT system – Algorithm description

As was discussed in **Chapter 7**, a FORTRAN code was developed for the simulation and exergetic optimization of the prototype CPVT system. The flow chart of the calculations performed by the code is presented in **Fig. C.1**. It is essential to point out that heat conduction within the layers of solid materials of the receiver is considered to occur only in the direction perpendicular to the receiver active surface, whereas heat convection within the heat sink is considered to occur along the longitudinal direction as well. Thus, the code is able to predict the temperature distribution of the receiver materials, instead of a representative average temperature value.

The code takes as inputs the various geometrical parameters of the CPVT system sub-components, as well as the main performance specifications of key components such as the PV module. The environmental conditions are provided in a separate TMY input file. The code allows the selection of a single or dual axis tracking system employing either a FW or VW cooling device. The number of sections for the VW device can also be specified. The thermal resistance of the selected device and the pressure drop induced to the cooling fluid are calculated using separate sub-routines (sub-routines  $R_{conv}$  and  $Dp$  as shown in the flow chart).

The algorithm calculates all the quantities required for the performance characterization of the CPVT system. More specifically, in reference to the energetic characterization, the quantities calculated are the thermal and electrical power production, the optical and heat losses from the system receiver, the parasitic pumping power, the gross and net system energetic efficiency and finally the accumulated thermal and electrical energy yield for the evaluated time period. Besides, in regard to the system exergetic characterization, the outputs of the algorithm comprise the useful exergy streams and the destroyed exergy, as well as the exergetic efficiency. In addition, the entropy generation rate in absolute and relative form is also calculated.

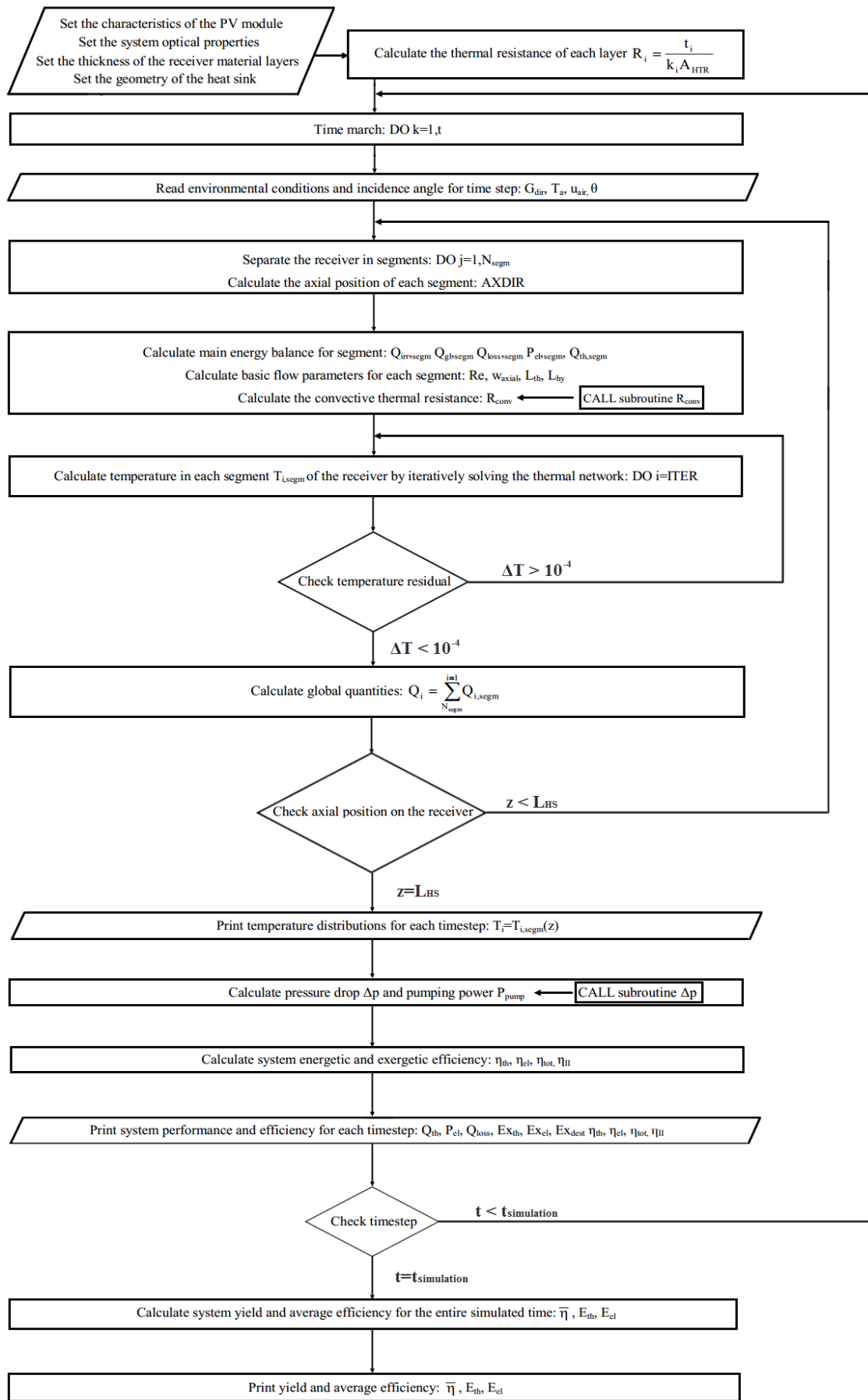


Fig. C.1 Flow chart of the FORTRAN code developed for the dynamic simulation of the CPVT system.



```

double precision eta_opt,eta_trans_eff,eta_abs_gl,eta_el_ref,eta_el_seg,eta_el_sys,beta,eta_th,eta_tot_gr,eta_tot_net,
eta_I_ave,eta_I_ave_net
!
double precision
Tsun,Ex_sun,Ex_th,Ex_el,Ex_pump,Ex_dest_opt,Ex_dest_th,Ex_dest_th_seg,Ex_dest_DT_sun,Ex_dest_DT_sun_seg,S_gen,Ns,eta_ex_
net
!
double precision RE_FW,axial_vel_FW
!
double precision Wch_FW,Ww_FW,a_FW,Hch_FW,Dh_FW
!
double precision L_thdevfl,L_star
!
double precision Wch_VW_1,Ww_VW,a_VW_1,Hch_VW
!
double precision Tf_mean,Tf_in,Tf_out
!
!
DOUBLE PRECISION
Tgl_seg(200),Tpv_seg(200),Tt1_seg(200),Ts1_seg(200),Tt2_seg(200),Tbw_seg(200),Tf_mean_seg(200),&
&Tgl_seg_prev(200),Tpv_seg_prev(200),Tt1_seg_prev(200),Ts1_seg_prev(200),Tt2_seg_prev(200),&
&Tbw_seg_prev(200),Tf_mean_seg_prev(200),Tf_max_seg(200),Tf_in_seg(200)
!
DOUBLE PRECISION Qloss_therm_seg_EX(200)
!
double precision Tf0,Tbw0,Tpv0,RES,Tf_max_prevseg,Tf_mean_seg_rout
!
!
#####
!#I/O#
#####
!
open(1,FILE='meteo_data.txt')
open(2,FILE='CPVT_eff.txt')
open(3,FILE='PV_Temperature.txt')
open(4,FILE='Heat-sink_Temperature.txt')
open(5,FILE='Fluid_Temperature.txt')
open(6,FILE='CPVT_exergy_eff.txt')
open(7,FILE='Overall_Yield.txt')
open(8,FILE='Convergence_check.txt')
open(9,FILE='Mass_check.txt')

write(2,(2X,A15,6X,A4,6X,A4,6X,A4,6X,A3,7x,A5,5X,A10,3X,A6,4X,A10,4X,A10,3X,A12,3X,A12)')&
&'t','Gdir','Qgl','Qirr','Pel','Ppump','Qlos_therm','Qth','eta_th','eta_el_sys','eta_tot_gr','eta_tot_net'
!
write(3,*) 'PV temperature distribution'
write(4,*) 'Heat-sink temperature distribution'
write(5,*) 'Fluid temperature distribution'
!
write(6,(2X,A20,8X,A6,6X,A11,8X,A14,7X,A10,7x,A5,5X,A5,3X,A10,4X,A5,4X,A2)')&
&'t','Ex_sun','Ex_dest_opt','Ex_dest_DT_sun','Ex_dest_th','Ex_th','Ex_el','eta_ex_net','S_gen','Ns'
!
write(7,(A15,4X,A9,4X,A9,4X,A11,4X,A9,4x,A13)') 'Energy_in','Energy_el','Energy_th','Energy_pump','eta_I_ave','eta_I_ave_net'
!
write(9,(A8,8X,A7,8X,A4,8X,A7,8X,A5)') 'M_pv_mod','M_resin','M_hs','M_fluid','M_tot'
!
!ALL UNITS IN SI
!
#####
!System tracking mode 1-axis=1, 2-axis=2
#####
!
ITRACK=2
!
!*****IF N-S orientation provide METEONORM file with solar AZIMUTH angles*****
!*****IF E-W orientation provide METEONORM file with solar ALTITUDE angles*****
!*****IF 2-axis tracking provide METEONORM file with all solar angles equal to zero*****
!
!
#####
!Heat sink design FW=1, VW=2
#####
!
DES=2
!

```

```

!
#####
!Number of SECTIONS for VW design
#####
!
!
IF (DES .EQ. 1) THEN
NSEC=1
ELSE
!
#####
!SPECIFY NUMBER OF SECTIONS
#####
!
NSEC=3
!
ENDIF
!
#####
!SPECIFY METHOD OF CALCULATION FOR THE CALCULATION OF THE EXTERNAL HEAT TRANSFER COEFFICIENT
#####
!
!ih_ext=1 -> analytical, ih_ext=2 empirical
!
ih_ext=1
!
!
#####
!Number of SEGMENTS for the receiver
#####
!
!Obviously the receiver can be treated as a whole if N_seg=1
!
N_seg=100
!
!
write(3,*) 'Number of Segments ',N_seg
write(4,*) 'Number of Segments ',N_seg
write(5,*) 'Number of Segments ',N_seg
!
#####
!Total TIME of the simulation
#####
!
!
time_tot=342001
!
#####
!Number of ITERATIONS for solving the thermal network system
#####
!
!
ITER=100
!
!
#####
!Physical constants
#####
!
!Stefan-Boltzmann constant
!
sigma=5.67e-8
!
!
#####
!Thermal properties
#####
!
!density of SOLID materials [kg/m3]
!
dens_gl=2600.0
dens_pv=2330.0
dens_t1=2200.0
dens_t2=2200.0
dens_al=2700.0

```

```

!
!thermal conductivity of SOLID materials [W/mK]
!
!
k_air=0.02605
k_gl_eva=0.915
k_pv=149.0
k_t1=0.6
k_al_ano=210.0
!
!#####
!SPECIFY EPOXY OR RESIN
!#####
!
k_t2=0.43
!
k_al=237.0
!
k_ins=0.037
!
!
!Specific heat of ALL materials (considered constant for water) [j/kg]
!
Cgl=750.0
Cpv=760.0
Cal=900.0
Cpw=4179.25
!
!Specific heat of the ADHESIVES (Aluminum nitride specific heat 740 J/kgK)
!
Ct1=1500.0
!
!#####
!SPECIFY EPOXY OR RESIN
!#####
!
Ct2=1500.0
!
!
!#####
!PV characteristics
!#####
!
!Reference evaluation temperature of PV efficiency
!
Tref=298.0
!
!PV temperature coefficient (narrow cells:0.00603, wide cells:0.00461)
!
beta=0.00461
!
!PV efficiency at Tref
!
eta_el_ref=0.138
!
!
!#####
!Parameters of operation
!#####
!
!Volumetric flow rate in [m3/s]
!It is defined when the TIME MARCH loop commences
!
!
!fluid inlet temperature
!
Tf_in=298.0
!
!#####
!Optical properties of the system
!#####
!
!optical efficiency of reflector
!
eta_opt=0.57
!

```

```

!Emittance of front glass
!
e_gl=0.88
!
!Absorptance of front glass+EVA
!
eta_abs_gl=0.05
!
!Transmittance-absorptance of front glass+EVA and PV cells (0.90 for narrow cells, 0.92 for wide cells)
!
eta_trans_eff=0.92
!
!
!
!#####
!System Geometrical Parameters
!#####
!
!
!Aperture area of the system in [m2]
!
Aa=10.0
!
!
!contact area between different materials (equal to the heat sink surface)
!
!
!
Wgl_eva=0.08
Wpv=0.06
Whs=0.061
Lhs=5.0
L_SEC=Lhs/NSEC
Acont_segm=Whs*Lhs/N_segm
!
!
!#####
!FW Heat Sink Geometrical parameters
!#####
!
!
!
Wch_FW=0.00056
Ww_FW=0.00069
a_FW=Ww_FW/Wch_FW
N_FW=((Whs-a_FW*Wch_FW)/((a_FW+1)*Wch_FW))
Hch_FW=0.0035
Dh_FW=2*Wch_FW*Hch_FW/(Wch_FW+Hch_FW)
!
!
!#####
!VW Heat Sink Geometrical parameters (only of the first section required)
!#####
!
!
!
Wch_VW_1=0.00524
Ww_VW=0.001
a_VW_1=Ww_VW/Wch_VW_1
Hch_VW=0.0106
!
!
!
DO I1=1,NSEC
IF (I1 .EQ. 1) THEN
Wch_VW(1)=Wch_VW_1
ELSEIF (I1 .GT. 1) THEN
Wch_VW(I1)=0.5*Wch_VW(I1-1)-0.5*Ww_VW
ENDIF
ENDDO
!
!
!
DO I2=1,NSEC
Dh_VW(I2)=2*Wch_VW(I2)*Hch_VW/(Wch_VW(I2)+Hch_VW)
a_VW(I2)=Ww_VW/Wch_VW(I2)
N_VW(I2)=FLOOR(((Whs-a_VW(I2)*Wch_VW(I2))/((a_VW(I2)+1)*Wch_VW(I2))))
ENDDO
!
!

```

```

!
#####
!thickness of each material
#####
!
!
t_gl_eva=0.0045
t_pv=0.0002
t_t1=0.00013
t_al_ano=0.0015
!
t_t2=0.0001524
!
!FW or VW design
!
IF (DES .EQ. 1) THEN
t_al=0.0023
ELSEIF (DES .EQ. 2) THEN
t_al=0.0017
ENDIF
!
!
t_ins=0.05
!
!
#####
!Mass of SOLID materials
#####
!
!
!
Vol_gl_segm=2*Wgl_eva*t_gl_eva*Lhs/N_segm
!
Vol_pv_segm=Wpv*t_pv*Lhs/N_segm
!
!W_t1=Wpv
!
Vol_t1_segm=Wpv*t_t1*Lhs/N_segm
!
!W_t2=Whs
!
Vol_t2_segm=Whs*t_t2*Lhs/N_segm
!
!Wgl_eva=Ws1
!
Vol_s1_segm=Wgl_eva*t_al_ano*Lhs/N_segm
!
!
#####
!Volume of the ENTIRE heat sink (FINS and top cover (t=2mil) included) DEPENDING ON THE DESIGN
#####
!
IF (DES .EQ. 1) THEN
!
Vol_s2_segm=6*(Whs*(t_al+0.002)*Lhs+(N_FW+1)*Ww_FW*Hch_FW*Lhs)/N_segm
!
ELSE
Vol_s2=0.0
DO I4=1,NSEC
!
Vol_s2_SEC=N_VW(I4)*Ww_VW*Hch_VW*L_SEC
!
Vol_s2=Vol_s2+Vol_s2_SEC
ENDDO
!
Vol_s2_segm=3*(Vol_s2+Whs*(t_al+0.002)*Lhs)/N_segm
!
ENDIF
!
!
!
#####
!Volume of water inside each heat sink design
#####
!
!

```

```

Vol_w1_seg=15*N_FW*Wch_FW*Hch_FW*Lhs/N_seg
!
!
Vol_w2=0.0
!
DO I4=1,NSEC
!
Vol_w2_SEC=N_VW(I4)*Wch_VW(I4)*Hch_VW*L_SEC
!
Vol_w2=Vol_w2+Vol_w2_SEC
ENDDO
!
Vol_w2_seg=2*Vol_w2/N_seg
!
!
!Values only for mass check
M_pv_mod=Vol_gl_seg*N_seg*dens_gl+Vol_pv_seg*N_seg*dens_pv+Vol_t1_seg*N_seg*dens_t1+Vol_s1_seg*N_seg*de
ns_al
M_resin=Vol_t2_seg*N_seg*dens_t2
M_hs=Vol_s2_seg*N_seg*dens_al
!
IF (DES.EQ. 1) THEN
!
M_fluid=Vol_w1_seg*N_seg*997
!
ELSE
!
M_fluid=Vol_w2_seg*N_seg*997
!
ENDIF
!
M_tot=M_pv_mod+M_resin+M_hs+M_fluid
!
write(9,('F4.2,8X,F5.3,8X,F4.2,8X,F5.3,8X,F5.2')) M_pv_mod,M_resin,M_hs,M_fluid,M_tot
!
m_gl_seg=dens_gl*Vol_gl_seg
m_pv_seg=dens_pv*Vol_pv_seg
m_t1_seg=dens_t1*Vol_t1_seg
m_t2_seg=dens_t2*Vol_t2_seg
m_s1_seg=dens_al*Vol_s1_seg
!
!
!m_s2 calculated according to Vol_s2, which was calculated above
!
m_s2_seg=dens_al*Vol_s2_seg
!
!
!m_s2 and m_w are modified according to the heat sink design
!
!
!#####
!Internal thermal resistance of the SOLID MATERIALS
!#####
!
!
!Conductive thermal resistance of each material
!
!
R_gl_eva_seg=t_gl_eva/(k_gl_eva*Acont_seg)
!
R_pv_seg=t_pv/(k_pv*Acont_seg)
R_t1_seg=t_t1/(k_t1*Acont_seg)
R_al_ano_seg=t_al_ano/(k_al_ano*Acont_seg)
R_t2_seg=t_t2/(k_t2*Acont_seg)
R_al_seg=t_al/(k_al*Acont_seg)
!
!
!
!Thermal resistances between nodes (each node in the middle of the thickness of each material)
!
Rgl_pv=0.5*R_gl_eva_seg+0.5*R_pv_seg
Rpv_t1=0.5*R_pv_seg+0.5*R_t1_seg
Rt1_s1=0.5*R_t1_seg+0.5*R_al_ano_seg
Rs1_t2=0.5*R_al_ano_seg+0.5*R_t2_seg
Rt2_s2=0.5*R_t2_seg+0.5*R_al_seg

```

```

!
!
!
!#####
!Initialization
!#####
!
!Temperature distribution for t=0.0
!
Tgl_segm_prev=Tf_in
Tpv_segm_prev=Tf_in
Tt1_segm_prev=Tf_in
Tt2_segm_prev=Tf_in
Ts1_segm_prev=Tf_in
Tbw_segm_prev=Tf_in
Tf_mean_segm_prev=Tf_in
!
!
!Energy yield for t=0.0
!
Energy_irr=0.0
Energy_el=0.0
Energy_th=0.0
Energy_pump=0.0
!
!*****
!*Marching in time*
!*****
!
!
!Timestep
!

dt=3600
!
!
DO k=1,time_tot,dt
!
!
!Time
!
t=k
!
!
!#####
!#Environmental conditions#
!#####
!
!
!Meteorological Data: Solar Radiation, wind velocity, Ambient Temperature, Incidence angle
!
!Watch the number of columns of the METEO FILE
!
read(1,*) Gdir_track,u_wind,Ta,theta
!
!
! IF (ITRACK .EQ. 1) THEN
!   Gdir=Gdir_track*cos(theta)
! ELSEIF (ITRACK .EQ. 2) THEN
!   Gdir=Gdir_track
! ENDIF
!
!
!#####
!VOLUMETRIC FLOW RATE#
!#####
!
!***CAUTION***The fluid (within the system) cools faster if it is considered to be stagnant at night, i.e. when Gdir=0 -> Vdot=0
!
! IF (Gdir .EQ. 0.0) THEN
!   V_dot=0.0
! ELSE
!   V_dot=40.0e-6
! ENDIF

```

```

!
!
!
!#####
!GLOBAL quantities (for the entire receiver)
!#####
!
!
!Heat absorbed in glass+EVA
!
Qgl_segm=eta_abs_gl*Gdir*Aa*eta_opt/N_seg
!
!#####
!#Irradiation on PV array#
!#####
!
Qirr_segm=Gdir*Aa*eta_opt*eta_trans_eff*(1-eta_abs_gl)/N_seg
!
!
!INITIALIZATION for DO LOOP "Segmentation of the receiver"
!
!
!
AXDIR=0.0
Qloss_therm_seg=0.0
Pel_seg=0.0
Qth_seg=0.0
!
!
!INITIALIZATION OF GLOBAL QUANTITIES
!
Qgl=0.0
Qirr=0.0
Qloss_therm=0.0
Pel=0.0
Qth=0.0
!
!
!*****
!SEGMENTATION OF THE RECEIVER*
!*****
!
!
!
DO j=1,N_seg
!
write(*,*) '**time**',t,'**SEGMENT**',j
!
!
L_seg=Lhs/N_seg
!
!
!The temperatures are calculated at the MIDDLE of the segment
!
!
AXDIR=L_seg*0.5+(j-1)*L_seg
!
!
!
!Tf_in_segment is explicit and equal to the maximum fluid temperature of the previous segment
!
IF (j .EQ. 1) THEN
Tf_in_seg(j)=Tf_in
ELSEIF (j .GT. 1) THEN
!
!SEE LINE 838: Tf_out(j)=Tf_in(j+1)
!
Tf_in_seg(j)=Tf_max_prevsegm
!
ENDIF
!
!
!

```

```

      !INITIALIZATION (using the segment values of the previous timestep)
      !
      !
IF (J .EQ. 1) THEN
      Tgl_seg(j)=Tf_in+0.6
      Tpv_seg(j)=Tf_in+0.5
      Tt1_seg(j)=Tf_in+0.4
      Tt2_seg(j)=Tf_in+0.3
      Ts1_seg(j)=Tf_in+0.2
      Tbw_seg(j)=Tf_in+0.1
      Tf_mean_seg(j)=Tf_in
!
ELSE
      Tgl_seg(j)=Tgl_seg_prev(j)
      Tpv_seg(j)=Tpv_seg_prev(j)
      Tt1_seg(j)=Tt1_seg_prev(j)
      Tt2_seg(j)=Tt2_seg_prev(j)
      Ts1_seg(j)=Ts1_seg_prev(j)
      Tbw_seg(j)=Tbw_seg_prev(j)
      Tf_mean_seg(j)=Tf_mean_seg_prev(j)
!
ENDIF
!
!*****
!*ITERATIVE SOLUTION FOR EACH SEGMENT AND EACH TIME STEP*
!*****
!
      DO i=1,ITER
!
!Subscript i does not appear anywhere. It counts the iterations for the finite differences
!
!
!Values of the previous iteration stored in order to calculate the residual
!
      Tpv0=Tpv_seg(j)
      Tbw0=Tbw_seg(j)
      Tf0=Tf_mean_seg(j)
!
!
!Electrical efficiency
!
!
!*****CAUTION*****The system is considered to operate using BYPASS DIODES and thus each segment can produce
different current
!
      eta_el_seg=eta_el_ref*(1-beta*(Tpv_seg(j)-Tref))
!
!
!Electrical yield
!
!
      Pel_seg=eta_el_seg*Qirr_seg
!
!
!
!#####
!Loss thermal resistance
!#####
!
!Convection to ambient
!
!
!***Analytical correlation***
!
!Kinematic viscosity
!
      dvisc_air=15.575e-6
!
!Thermal expansion coef.
!
      beta_air=3.26e-3
!
!Prandtl number for air

```

```

!
Pr_air=0.712
!
!Grashof number for air
!
Gr_air=9.81*beta_air
!
!Rayleigh number for air
!
Ra_air=Gr_air*Pr_air
!
!
!Raynolds number for external flow
!
Re_L=u_wind*Whs/dvisc_air
!
!
!Laminar or turbulent flow for forced convection
!
IF (Re_L .LT. 5.0e5) THEN
Nu_FC_air=0.664*Re_L**(1.0/2.0)*Pr_air**(1.0/3.0)
!
ELSE
Nu_FC_air=(0.037*Re_L**(4/5)-871)*Pr_air**(1.0/3.0)
!
ENDIF
!
!Nusselt for natural convection
!
Nu_NC_air=0.56*Ra_air**(1.0/4.0)
!
!
!Nusselt for mixed convection (see respective chapter in Kakac handbook)
!
Nu_MC_air=(Nu_FC_air**3+Nu_NC_air**3)**(1/3)
!
!
IF (ih_ext .EQ. 1) THEN
!
h_ext=Nu_MC_air*k_air/Whs
!
ELSE
!
!***Empirical correlation***
!
      h_ext=2.8+3.0*u_wind
!
ENDIF
!
!Radiation to ambient-The ambient temperature is used instead of the sky temperature as the receiver faces downwards
!
hrad_seg=sigma*e_gl*(Tgl_seg(j)**4-Ta**4)/(Tgl_seg(j)-Ta)
!
!
Rconv_ext_seg=1/(h_ext*Acont_seg)
!
Rrad_seg=1/(hrad_seg*Acont_seg)
!
Rloss_seg=(Rrad_seg*Rconv_ext_seg)/(Rrad_seg+Rconv_ext_seg)
!
!
Rloss_cond_seg=t_ins/(k_ins*Acont_seg)
!
!
Qloss_cond_seg=(Tbw_seg(j)-Ta)/Rloss_cond_seg
!
!
!***TOTAL Thermal losses based on glass temperature (look at the calculation of the term Rloss_seg)***
!
      Qloss_therm_seg=(Tgl_seg(j)-Ta)/Rloss_seg+Qloss_cond_seg
!
!
!Only for the calculation of the Exergy losses after the thermal network is solved
!
Qloss_therm_seg_EX(j)=Qloss_therm_seg
!

```

```

!
!*****Thermal balance: must be verified in each timestep*****
!
!
Qth_seg=Qirr_seg-Qgl_seg-Pel_seg-Qloss_therm_seg-Qloss_cond_seg
!
!*****
!Calculation of BASIC FLOW QUANTITIES for the heat sink designs*
!*****
!
!Prandtl number for water
!
Pr=Cpw*dvisc_w(Tf_mean_seg(j))/k_w(Tf_mean_seg(j))
IF (DES .EQ. 1) THEN
!
!#####
!FW Design#
!#####
!
axial_vel_FW=V_dot/(N_FW*Hch_FW*Wch_FW)
!
Re_FW=axial_vel_FW*Dh_FW/(dvisc_w(Tf_mean_seg(j))/density_w(Tf_mean_seg(j)))
!
!Thermal entrance length for channel flow [Handbook of Single Phase Convective Heat Transfer p. 3.51]
!
L_star=0.0004*(Wch_FW/Hch_FW)**2-0.0101*(Wch_FW/Hch_FW)+0.0756
!
!
L_thdevfl=L_star*Re_FW*Pr*Dh_FW
!
ELSEIF (DES .EQ. 2) THEN
!
!#####
!VW Design#
!#####
!
DO I3=1,NSEC
!
axial_vel_VW(I3)=V_dot/(N_VW(I3)*Hch_VW*Wch_VW(I3))
!
Re_VW(I3)=axial_vel_VW(I3)*Dh_VW(I3)/(dvisc_w(Tf_mean_seg(j))/density_w(Tf_mean_seg(j)))
!
!Thermal entrance length for channel flow [Handbook of Single Phase Convective Heat Transfer p. 3.51]
!
L_star_VW(I3)=0.0004*(Wch_VW(I3)/Hch_VW)**2-0.0101*(Wch_VW(I3)/Hch_VW)+0.0756
!
!
L_thdevfl_VW(I3)=L_star_VW(I3)*Re_VW(I3)*Pr*Dh_VW(I3)
!
ENDDO
!
ENDIF
!
!The same mass flow rate through all the segments
!
m_dot=density_w(Tf_mean_seg(j))*V_dot
!
!

```

```

#####
!CONVECTIVE and CALORIC Thermal resistances#
#####
!
Tf_mean_seg_m_rout=Tf_mean_seg_m(j)
!
IF (DES .EQ. 1) THEN
!
CALL
Thermal_resistance_FW(m_dot,Cpw,k_al,L_seg_m,Tf_mean_seg_m_rout,Wch_FW,Hch_FW,Ww_FW,Dh_FW,N_FW,L_thdevfl,&
&AXDIR,Rconv_int_seg_m,Rcal_seg_m)
!
ELSEIF (DES .EQ. 2) THEN
CALL
Thermal_resistance_VW(m_dot,Cpw,k_al,N_VW,Wch_VW,Ww_VW,Hch_VW,Dh_VW,L_SEC,AXDIR,Tf_mean_seg_m_rout,L_seg_m,&
&L_thdevfl_VW,Rconv_int_seg_m,Rcal_seg_m)
ENDIF
!
!
#####
!
IF (DES .EQ. 1) THEN
m_w_seg_m=density_w(Tf_mean_seg_m(j))*Vol_w1_seg_m
ELSEIF (DES .EQ. 2) THEN
m_w_seg_m=density_w(Tf_mean_seg_m(j))*Vol_w2_seg_m
ENDIF
!
!
#####
!#THERMAL NETWORK CALCULATIONS
#####
!GAUSS-SEIDEL Method
!
!
Tgl_seg_m(j)=(m_gl_seg_m*Cgl*Rgl_pv*Tgl_seg_m_prev(j)+(Qgl_seg_m-
Qloss_therm_seg_m+Tpv_seg_m(j)/Rgl_pv)*dt*Rgl_pv)/(dt+m_gl_seg_m*Cgl*Rgl_pv)
!
!
Tpv_seg_m(j)=(m_pv_seg_m*Cpv*Rgl_pv*Rpv_t1*Tpv_seg_m_prev(j)+(Qth_seg_m+Tgl_seg_m(j)/Rgl_pv+Tt1_seg_m(j)/Rpv_t1)*dt
*Rgl_pv*Rpv_t1)/&
&(m_pv_seg_m*Cpv*Rgl_pv*Rpv_t1+Rpv_t1*dt+Rgl_pv*dt)
!
!
Tt1_seg_m(j)=(m_t1_seg_m*Ct1*Rpv_t1*Rt1_s1*Tt1_seg_m_prev(j)+(Tpv_seg_m(j)/Rpv_t1+Ts1_seg_m(j)/Rt1_s1)*dt*Rpv_t1*Rt1
_s1)/&
&(m_t1_seg_m*Ct1*Rpv_t1*Rt1_s1+Rpv_t1*dt+Rt1_s1*dt)
!
!
Ts1_seg_m(j)=(m_s1_seg_m*Cal*Rt1_s1*Rs1_t2*Ts1_seg_m_prev(j)+(Tt1_seg_m(j)/Rt1_s1+Tt2_seg_m(j)/Rs1_t2)*dt*Rt1_s1*Rs1
_t2)/&
&(m_s1_seg_m*Cal*Rt1_s1*Rs1_t2+Rt1_s1*dt+Rs1_t2*dt)
!
!
Tt2_seg_m(j)=(m_t2_seg_m*Ct2*Rs1_t2*Rt2_s2*Tt2_seg_m_prev(j)+(Ts1_seg_m(j)/Rs1_t2+Tbw_seg_m(j)/Rt2_s2)*dt*Rs1_t2*Rt2
_s2)/&
&(m_t2_seg_m*Ct2*Rs1_t2*Rt2_s2+Rs1_t2*dt+Rt2_s2*dt)
!
!
Tbw_seg_m(j)=(m_s2_seg_m*Cal*Rt2_s2*(Rconv_int_seg_m+0.5*R_al_seg_m)*Tbw_seg_m_prev(j)+(Tt2_seg_m(j)/Rt2_s2+&
&Tf_mean_seg_m(j)/(Rconv_int_seg_m+0.5*R_al_seg_m))*dt*Rt2_s2*(Rconv_int_seg_m+0.5*R_al_seg_m)&
&/(m_s2_seg_m*Cal*Rt2_s2*(Rconv_int_seg_m+0.5*R_al_seg_m)+Rt2_s2*dt+(Rconv_int_seg_m+0.5*R_al_seg_m)*dt)
!
!
!
Tf_mean_seg_m(j)=(m_w_seg_m*Cpw*(Rconv_int_seg_m+0.5*R_al_seg_m)*Tf_mean_seg_m_prev(j)+&
&(Tbw_seg_m(j)/(Rconv_int_seg_m+0.5*R_al_seg_m)+2*m_dot*Cpw*Tf_in_seg_m(j))*dt*(Rconv_int_seg_m+0.5*R_al_seg_m))&
&/(m_w_seg_m*Cpw*(Rconv_int_seg_m+0.5*R_al_seg_m)+dt*dt*(Rconv_int_seg_m+0.5*R_al_seg_m)*2*m_dot*Cpw)
!
!
RES=sqrt((Tf_mean_seg_m(j)-Tf0)**2+(Tbw_seg_m(j)-Tbw0)**2+(Tpv_seg_m(j)-Tpv0)**2)
!
write(8,*) 't,'AXDIR',AXDIR,'RES',RES
!

```

```

!
      IF (RES .LT. 1.0e-4) GOTO 105
      !
      !
      !ENDDO for THERMAL NETWORK CALCULATIONS
      !
      ENDDO
!
!Calculation of maximum segment fluid temperature using Rcal (Rcal is not in the subroutine for thermal resistance)
!
!
!
!Linear interpolation to determine the segment maximum temperature
!
105 Tf_max_seg(j)=2*Tf_mean_seg(j)-Tf_in_seg(j)
      !
      !
      !Maximum fluid temperature of the segment to be used as input temperature for the next segment.
      !
      Tf_max_prevseg=Tf_max_seg(j)
!
!
!#####
!THERMAL Losses
!#####
!
Qgl=Qgl+Qgl_seg
!
Qirr=Qirr+Qirr_seg
!
Qloss_therm=Qloss_therm+Qloss_therm_seg
!
!
!#####
!Useful PRODUCED POWER
!#####
!
!
Pel=Pel+Pel_seg
!
Qth=Qth+Qth_seg
!
!
!ENDDO for RECEIVER SEGMENTATION
!
      ENDDO
!
!*****
!OUTPUT FOR THE TEMPERATURE DISTRIBUTION
!
write(3,'(I6, 3X)',advance='no') t
write(4,'(I6, 3X)',advance='no') t
write(5,'(I6, 3X)',advance='no') t
!
DO j1=1,N_seg
write(3,'(F6.2, 3X)',advance='no') Tpv_seg(j1)
write(4,'(F6.2, 3X)',advance='no') Tbw_seg(j1)
write(5,'(F6.2, 3X)',advance='no') Tf_mean_seg(j1)
ENDDO
!
write(3,'(A1,1X)',advance='yes') ''
write(4,'(A1,1X)',advance='yes') ''
write(5,'(A1,1X)',advance='yes') ''
!*****
!
!
!To be used ONLY in the pressure drop calculations
!
Tf_mean=0.5*(Tf_max_seg(N_seg)+Tf_in)
!
!
!#####
!PARASITICS - Pumping power#
!#####

```

```

!
IF (Gdir .EQ. 0.0) THEN
  Ppump=0.0
ENDIF

IF ((Gdir .GT. 0.0) .AND. (DES .EQ. 1)) THEN
CALL Pressure_drop_FW(Whs,Lhs,Wch_FW,Hch_FW,Dh_FW,N_FW,axial_vel_FW,Re_FW,Tf_mean,DP_tot_FW)
write(*,*) 'FW', DP_tot_FW
Ppump=V_dot*DP_tot_FW
ELSEIF ((Gdir .GT. 0.0) .AND. (DES .EQ. 2)) THEN
CALL Pressure_drop_VW(NSEC,N_VW,Whs,L_SEC,Wch_VW,Hch_VW,Dh_VW,axial_vel_VW,Re_VW,Tf_mean,DP_tot_VW)
Ppump=V_dot*DP_tot_VW
write(*,*) 'VW', DP_tot_VW
ENDIF
!
!
!
!
!#####
!EFFICIENCIES
!#####
!
!FIRST LAW
!
IF (Gdir .EQ. 0.0) THEN
!
eta_th=0.0
eta_el_sys=0.0
!
ELSE
!
eta_th=m_dot*cpw*(Tf_max_segm(N_segm)-Tf_in)/(Gdir*Aa)
!
eta_el_sys=Pel/(Gdir*Aa)
!
ENDIF
!
eta_tot_gr=eta_th+eta_el_sys
!
IF (Gdir .EQ. 0.0) THEN
!
eta_tot_net=0.0
!
ELSE
!
eta_tot_net=eta_th+(Pel-Ppump)/(Gdir*Aa)
!
ENDIF
!
!SECOND LAW
!
!Sun apparent temperature
!
Tsun=4350.0
!
Tf_out=Tf_max_segm(N_segm)
!
!
Ex_sun=Gdir*Aa*(1.0-(4.0/3.0)*(Ta/Tsun)+(1.0/3.0)*(Ta/Tsun)**4)
!
Ex_th=Qth*(1-(Ta/Tf_out))
!
Ex_el=pe1
!
!
!Exergy destruction and entropy generation
!
!
Ex_dest_opt=(Gdir*Aa*(1-eta_opt*eta_trans_eff))*(1.0-(4.0/3.0)*(Ta/Tsun)+(1.0/3.0)*(Ta/Tsun)**4)
!
!
!INITIALIZATION for EXERGY LOSSES
!
Ex_dest_DT_sun=0.0

```

```

Ex_dest_th=0.0
!
!  

!Calculation of Exergy Losses due to TEMPERATURE  

!  

DO j2=1,N_segm  

!  

Ex_dest_DT_sun_segm=Qirr_segm*Ta*((1/Tpv_segm(j2))-(1/Tsun))  

!  

Ex_dest_DT_sun=Ex_dest_DT_sun+Ex_dest_DT_sun_segm  

!  

!  

!  

Ex_dest_th_segm=Qloss_therm_seg_Ex(j2)*(1.0-(Ta/Tpv_segm(j2)))  

!  

Ex_dest_th=Ex_dest_th+Ex_dest_th_segm  

!  

ENDDO  

!  

Ex_pump=Ppump  

!  

S_gen=(1.0/Ta)*(Ex_sun-(Ex_th+Ex_el))  

!  

!Entropy generation number  

!  

IF (Gdir .EQ. 0.0) THEN  

!  

Ns=0.0  

eta_ex_net=0.0  

!  

ELSE  

!  

Ns=Ta*S_gen/(Gdir*Aa)  

!  

eta_ex_net=(Ex_th+Ex_el-Ex_pump)/Ex_sun  

!  

ENDIF  

!  

write(2, '(I20,6X,F6.1,4X,F6.2,5X,F7.2,5X,F6.1,6X,F7.2,8X,F6.2,8X,F7.2,7X,F5.3,6X,F6.4,10X,F5.3,10X,F5.3)')&  

&t,Gdir,Qgl,Qirr,Pel,Ppump,Qloss_therm,Qth,eta_th, eta_el_sys, eta_tot_gr,eta_tot_net  

!  

!  

write(6, '(I20,6X,F6.1,8X,F8.2,10X,F8.2,6X,F6.2,8X,F8.2,6X,F8.2,8X,F5.3,8X,F6.2,8X,F6.3)')&  

&t,Ex_sun,Ex_dest_opt,Ex_dest_DT_sun,Ex_dest_th,Ex_th,Ex_el,eta_ex_net,S_gen,Ns  

!  

!  

!  

!A DO LOOP is not required. The array spots are substituted one by one  

!  

Tgl_seg_prev=Tgl_segm  

Tpv_seg_prev=Tpv_segm  

Tt1_seg_prev=Tt1_segm  

Ts1_seg_prev=Ts1_segm  

Tt2_seg_prev=Tt2_segm  

Tbw_seg_prev=Tbw_segm  

Tf_mean_seg_prev=Tf_mean_segm  

!  

!  

!  

!OVERALL YIELD and losses  

!  

Energy_irr=Energy_irr+Gdir*Aa*dt  

Energy_el=Energy_el+Pel*dt  

Energy_th=Energy_th+Qth*dt  

Energy_pump=Energy_pump+Ppump*dt  

!  

!  

!  

!ENDDO for TIME MARCH  

!  

ENDDO  

!  

!  

!  

!Overall averaged energetic efficiency for the entire simulated time  

!  

eta_I_ave=(Energy_el+Energy_th)/Energy_irr  

eta_I_ave_net=(Energy_el+Energy_th-Energy_pump)/Energy_irr

```

```

!
!
!Write overall yield
write(7, '(F20.2,4X,F20.2,4X,F20.2,4X,F20.3,4X,F5.3,4X,F5.3,4X)') Energy_irr,Energy_el,Energy_th,Energy_pump,eta_I_ave,eta_I_ave_net
!
!
stop
end
!
!
!
SUBROUTINE
Thermal_resistance_FW(m_dot,Cpw,k_al,L_segm,Tf_mean_segm_rout,Wch_FW,Hch_FW,Ww_FW,Dh_FW,N_FW,L_thdevfl,&
&AXDIR,Rconv_int_segm,Rcal_segm)
!
IMPLICIT NONE
!
INTEGER N_FW
DOUBLE PRECISION k_w
DOUBLE PRECISION m_dot,Cpw,k_al,Wch_FW,Ww_FW,Hch_FW,Dh_FW,Tf_mean_segm_rout,Rconv_int_segm,Rcal_segm
DOUBLE PRECISION L_thdevfl,L_segm,AXDIR
DOUBLE PRECISION Nu,HTC_FW,m_fin,FIN_eff
!
!
!Nusselt number according to whether the segment lies in the developing or the fully developed flow region
!
IF (AXDIR.LT.L_thdevfl) THEN
!#####
!THERMALLY DEVELOPING Flow Region
!#####
!
!
!Nu: linear interpolation of the mean values from Shah (thermally developing flow)
!
!
Nu=-9.3716*(Wch_FW/Hch_FW)**3+20.891*(Wch_FW/Hch_FW)**2-15.737*(Wch_FW/Hch_FW)+9.5012
!
!
ELSEIF (AXDIR.GE.L_thdevfl) THEN
!#####
!Fully developed Flow Region#
!#####
!
!
Nu=8.235*(1.0-2.0421*(Wch_FW/Hch_FW)+3.0853*(Wch_FW/Hch_FW)**2-2.4765*(Wch_FW/Hch_FW)**3+&
&1.0578*(Wch_FW/Hch_FW)**4-0.1861*(Wch_FW/Hch_FW)**5)
!
!
ENDIF
!
!
!Heat Transfer Coefficient
!
!
!Takes the temperature of the current segment j
!
HTC_FW=Nu*k_w(Tf_mean_segm_rout)/Dh_FW
!
!fin correction factor
!
m_fin=sqrt(2*HTC_FW/(k_al*Ww_FW))
!
!
FIN_eff=tanh(m_fin*Hch_FW)/(m_fin*Hch_FW)
!
!see Eq. (4) LEE & QU IEEE (2006)
!
!T_w_out_step=T_in_step+(q_dot*W_hex*L_step)/(dens_w*cp*Qt)+q_dot*(a+1)*Wch/(h_c*(Wch+2*FIN_eff*Hch))
!
!
!Convective thermal resistance [LIU & GARIMELLA]

```

```

!
Rconv_int_seg=1.0/(N_FW*HTC_FW*L_seg*(2*FIN_eff*Hch_FW+Wch_FW))
!
!
!Caloric thermal resistance
!
IF (m_dot.EQ. 0.0) THEN
Rcal_seg=1e6
ELSE
Rcal_seg=1.0/(m_dot*Cpw)
ENDIF
!
!
!
return
end
!
!
!
!
!
SUBROUTINE Thermal_resistance_VW(m_dot,Cpw,k_al,N_VW,Wch_VW,Ww_VW,Hch_VW,Dh_VW,&
&L_SEC,AXDIR,Tf_mean_seg_rout,L_seg,L_thdevfl_VW,Rconv_int_seg,Rcal_seg)
!
IMPLICIT NONE
!
INTEGER N_VW(10)
INTEGER POS,SECTION
DOUBLE PRECISION k_w
DOUBLE PRECISION Wch_VW(10),Dh_VW(10),L_thdevfl_VW(10)
DOUBLE PRECISION m_dot,Cpw,k_al,L_seg,L_SEC,AXDIR,Hch_VW,Ww_VW,Tf_mean_seg_rout,Rconv_int_seg,Rcal_seg
DOUBLE PRECISION Nu_VW,HTC_VW,m_fin_VW,FIN_eff_VW,AXDIR_LOCAL
!
!
!Identify SECTION where the SEGMENT j lies
!
POS=FLOOR(AXDIR/L_SEC)
!
!
!If 1<POS<2 the segment lies in the 2nd heat-sink section and so on...
!
SECTION=POS+1
!
!
!Axial direction in Local Coordinates in EACH SECTION
!
AXDIR_LOCAL=AXDIR-POS*L_SEC
!
!
!
IF (AXDIR_LOCAL.LT. L_thdevfl_VW(SECTION)) THEN
!
!#####
!THERMALLY DEVELOPING Flow Region
!#####
!
!
!Nu: linear interpolation of the mean values from Shah (thermally developing flow)
!
!
Nu_VW=-9.3716*(Wch_VW(SECTION)/Hch_VW)**3+20.891*(Wch_VW(SECTION)/Hch_VW)**2-
15.737*(Wch_VW(SECTION)/Hch_VW)+9.5012
!
!
!
ELSEIF (AXDIR_LOCAL.GE. L_thdevfl_VW(SECTION)) THEN
!
!#####
!Fully developed Flow Region
!#####
!
!
!

```

```

Nu_VW=8.235*(1.0-2.0421*(Wch_VW(SECTION)/Hch_VW)+3.0853*(Wch_VW(SECTION)/Hch_VW)**2-
2.4765*(Wch_VW(SECTION)/Hch_VW)**3+&
&1.0578*(Wch_VW(SECTION)/Hch_VW)**4-0.1861*(Wch_VW(SECTION)/Hch_VW)**5)
!
!
ENDIF
!
!
!Heat transfer coefficient
!
!Takes the temperature of the current segment j
!
HTC_VW=Nu_VW*k_w(Tf_mean_segm_rout)/Dh_VW(SECTION)
!
!!
!fin correction factor
!
m_fin_VW=sqrt(2*HTC_VW/(k_al*Ww_VW))
!
!
FIN_eff_VW=tanh(m_fin_VW*Hch_VW)/(m_fin_VW*Hch_VW)
!
!
!Convective thermal resistance [LIU & GARIMELLA]
!
!
Rconv_int_seg=1.0/(N_VW(SECTION)*HTC_VW*L_seg*(2*FIN_eff_VW*Hch_VW+Wch_VW(SECTION)))
!
!
!Caloric thermal resistance
!
IF (m_dot .EQ. 0.0) THEN
Rcal_seg=1e6
ELSE
Rcal_seg=1.0/(m_dot*Cpw)
ENDIF
!
return
end
!
!
!
!
!
*****
!The subroutines for pressure drop make a SINGLE calculation (based on the fluid mean properties)*
*****
!
!
SUBROUTINE Pressure_drop_FW(Whs,Lhs,Wch_FW,Hch_FW,Dh_FW,N_FW,axial_vel_FW,Re_FW,Tf_mean,DP_tot_FW)
!
IMPLICIT NONE
!
!
INTEGER N_FW
DOUBLE PRECISION density_w
DOUBLE PRECISION Whs,Lhs,Hch_FW,Wch_FW,Dh_FW,axial_vel_FW,Re_FW,Tf_mean,DP_tot_FW
DOUBLE PRECISION fRe_FD,K_oo,C_f_app_Re,L_plus,L_devfl,L_FD,DP_contr_FW,DP_exp_FW,DP_FW_devfl,DP_FW_FD
DOUBLE PRECISION K_in_contr,K_out_exp,A2_core,A1_chamb
!
!
*****
!MANIFOLD Inlet-Outlet (Contraction-Expansion)#
*****
!
!
!Correlations and Constants from BLEVINS pp.77-78
!
!
K_in_contr=0.931
A2_core=Wch_FW*Hch_FW*N_FW

```

```

A1_chamb=Whs*Hch_FW
!
K_out_exp=1-(A2_core/A1_chamb)**2
!
!
DP_contr_FW=(1-(A2_core/A1_chamb)**2+K_in_contr)*density_w(Tf_mean)*axial_vel_FW**2
!
!
DP_exp_FW=((A2_core/A1_chamb)**2-1+K_out_exp)*density_w(Tf_mean)*axial_vel_FW**2
!
!
!
#####
!Channel Occupied Region
#####
!
!
!Hydrodynamic entrance length for channel flow
!
L_plus=(0.06+0.07*(Wch_FW/Hch_FW)-0.04*(Wch_FW/Hch_FW)**2)
!
L_devfl=L_plus*Re_FW*Dh_FW
!
!
!Fanning friction factor for fully developed flow
!
!
fRe_FD=24*(1.0-1.355*(Wch_FW/Hch_FW)+1.947*(Wch_FW/Hch_FW)**2-1.701*(Wch_FW/Hch_FW)**3+0.956*&
&(Wch_FW/Hch_FW)**4-0.254*(Wch_FW/Hch_FW)**5)
!
!
!Apparent friction factor for developing flow
!
!
K_oo=0.674+1.2501*(Wch_FW/Hch_FW)-0.3417*(Wch_FW/Hch_FW)**2-0.8358*(Wch_FW/Hch_FW)**3
!
!
C=(0.1811+4.3488*(Wch_FW/Hch_FW)-1.6027*(Wch_FW/Hch_FW)**2)*10**(-4.0)
!
!
f_app_Re=(3.44*L_plus**(-0.5)+(K_oo/(4*L_plus)+fRe_FD-3.44*L_plus**(-0.5))/(1.0+C*L_plus**(-2.0)))
!
!
!
#####
!Developing Flow Region
#####
!
!
DP_FW_devfl=(2*(f_app_Re/Re_FW)*L_devfl*density_w(Tf_mean)*axial_vel_FW**2)/Dh_FW
!
!
#####
!Fully developed Flow Region
#####
!
!
L_FD=Lhs-L_devfl
!
!
DP_FW_fd=(2*(fRe_FD/Re_FW)*L_fd*density_w(Tf_mean)*axial_vel_FW**2)/Dh_FW
!
!
!TOTAL Pressure Drop
!
!
DP_tot_FW=DP_contr_FW+DP_FW_devfl+DP_FW_fd+DP_exp_FW
!
!
return
end
!
!
!

```

```

!
!
!
SUBROUTINE
Pressure_drop_VW(NSEC,N_VW,Whs,L_SEC,Wch_VW,Hch_VW,Dh_VW,axial_vel_VW,Re_VW,Tf_mean,DP_tot_VW)
!
IMPLICIT NONE
!
!
INTEGER kk,m,NSEC
INTEGER N_VW(10)

DOUBLE PRECISION density_w
DOUBLE PRECISION Wch_VW(10),Dh_VW(10),axial_vel_VW(10),Re_VW(10)
DOUBLE PRECISION Whs,L_SEC,Hch_VW,Tf_mean,DP_tot_VW
DOUBLE PRECISION
fRe_FD_VW,K_oo_VW,C_VW,f_app_Re_VW,L_plus_VW,L_devfl_VW,L_FD_VW,DP_contr_VW,DP_inner_contr_VW,DP_step_contr,
&
&DP_exp_VW,DP_VW_devfl,DP_VW_FD,DP_VW_sec,DP_VW_chan
DOUBLE PRECISION
K_in_contr_VW,K_out_exp_VW,K_step_contr,A2_core_in_VW,A2_core_out_VW,A1_chamb_VW,A2_step,A1_step
!
!
!
!
!#####
!MANIFOLD Inlet-Outlet (Contraction-Expansion)
!#####
!
!
!Correlations and Constants from BLEVINS pp.77-78
!
!
K_in_contr_VW=1.281
A2_core_in_VW=Wch_VW(1)*Hch_VW*N_VW(1)
A2_core_out_VW=Wch_VW(NSEC)*Hch_VW*N_VW(NSEC)
A1_chamb_VW=Whs*Hch_VW
!
K_out_exp_VW=(1-A2_core_out_VW/A1_chamb_VW)**2
!
!
DP_contr_VW=(1-(A2_core_in_VW/A1_chamb_VW)**2+K_in_contr_VW)*density_w(Tf_mean)*axial_vel_VW(1)**2
!
!
DP_exp_VW=((A2_core_out_VW/A1_chamb_VW)**2-1+K_out_exp_VW)*density_w(Tf_mean)*axial_vel_VW(NSEC)**2
!
!
!Pressure drop due to contraction in consecutive sections
!
!Blevins pp. 45 & 76
!
!
K_step_contr=1.281
DP_inner_contr_VW=0.0
!
!
DO kk=1,(NSEC-1)
!
!
A2_step=N_VW(kk+1)*Wch_VW(kk+1)*Hch_VW
A1_step=N_VW(kk)*Wch_VW(kk)*Hch_VW
!
!
DP_step_contr=(1-(A2_step/A1_step)**2+K_step_contr)*0.5*density_w(Tf_mean)*axial_vel_VW(kk+1)**2
DP_inner_contr_VW=DP_inner_contr_VW+DP_step_contr
!
ENDDO
!
!#####
!Channel Occupied Region
!#####
!
!

```

```

!Initialization
!
DP_VW_chan=0.0
!
!
DO m=1,NSEC
!
!
!Hydrodynamic entrance length for channel flow
!
L_plus_VW=(0.06+0.07*(Wch_VW(m)/Hch_VW)-0.04*(Wch_VW(m)/Hch_VW)**2)
!
L_devfl_VW=L_plus_VW*Re_VW(m)*Dh_VW(m)
!
!Fanning friction factor for fully developed flow
!
!
fRe_FD_VW=24*(1.0-1.355*(Wch_VW(m)/Hch_VW)+1.947*(Wch_VW(m)/Hch_VW)**2-1.701*(Wch_VW(m)/Hch_VW)**3+0.956*&
&(Wch_VW(m)/Hch_VW)**4-0.254*(Wch_VW(m)/Hch_VW)**5)
!
!Apparent friction factor for developing flow
!
!
K_oo_VW=0.674+1.2501*(Wch_VW(m)/Hch_VW)-0.3417*(Wch_VW(m)/Hch_VW)**2-0.8358*(Wch_VW(m)/Hch_VW)**3
!
!
C_VW=(0.1811+4.3488*(Wch_VW(m)/Hch_VW)-1.6027*(Wch_VW(m)/Hch_VW)**2)*10**(-4.0)
!
!
f_app_Re_VW=(3.44*L_plus_VW**(-0.5)+(K_oo_VW/(4*L_plus_VW)+fRe_FD_VW-3.44*L_plus_VW**(-
0.5))/(1.0+C_VW*L_plus_VW**(-2.0)))
!
!
!#####
!Developing Flow Region
!#####
!
!For EACH SECTION
!
!
DP_VW_devfl=(2*(f_app_Re_VW/Re_VW(m))*L_devfl_VW*density_w(Tf_mean)*axial_vel_VW(m)**2)/Dh_VW(m)
!
!#####
!Fully developed Flow Region
!#####
!
!For EACH SECTION
!
!
L_FD_VW=L_SEC-L_devfl_VW
!
!
DP_VW_fd=(2*(fRe_FD_VW/Re_VW(m))*L_FD_VW*density_w(Tf_mean)*axial_vel_VW(m)**2)/Dh_VW(m)
!
!
!Pressure drop induced in each SECTION
!
!
DP_VW_sec=DP_VW_devfl+DP_VW_fd
!
!
!Pressure drop induced in the ENTIRE channel occupied region
!
!
DP_VW_chan=DP_VW_chan+DP_VW_sec

```

```

!
ENDDO
!
!
DP_tot_VW=DP_contr_VW+DP_inner_contr_VW+DP_VW_chan+DP_exp_VW
!
!
return
end
!
!
!
!
!
!
DOUBLE PRECISION FUNCTION dvisc_w(TK)
!
!#####
!Calculates dynamic viscosity as a function of temperature
!#####
double precision TK,EXPFACT
!
!
EXPFACT=247.8/((TK-273.0)+133.15)
dvisc_w=2.414D-05*10**EXPFACT

return
end
!
!
DOUBLE PRECISION FUNCTION density_w(TK)
!
!#####
!Calculates the fluid density as a function of temperature
!#####
!
double precision TK,DNUMER,DDENOM
double precision CN(0:5),CD(0:1)

!
DATA CN / 999.8396, 18.224944, -0.00792221, -55.44846E-06, &
& 149.7562E-09,393.2952E-12 /
DATA CD / 1, 18.159725E-03 /
!
!
! Water (Gebhart et al., p. 946)

DNUMER=CN(0)+CN(1)*(TK-273.15)+CN(2)*(TK-273.15)**2+CN(3)*(TK-273.15)**3+CN(4)*(TK-273.15)**4+CN(5)*(TK-
273.15)**5
DDENOM=CD(0)+CD(1)*(TK-273.15)
!
density_w=DNUMER/(DDENOM+1.0D-16)
!
!
return
end
!
!
!
DOUBLE PRECISION FUNCTION k_w(TK)
!
!#####
!Calculates the thermal conductivity as a function of temperature#
!#####
!
double precision TK
!
! Water (Gebhart et al., p.946)
!
k_w=-0.92247+2.8395*(TK/273.15)-1.8007*(TK/273.15)**2+0.522577*(TK/273.15)**3-0.07344*(TK/273.15)**4
!
return
end

```